UNIVERSITY OF OKLAHOMA

GRADUATE COLLEGE

The dark universe:

the interplay of cosmological moduli, axions, and the MSSM

A DISSERTATION

SUBMITTED TO THE GRADUATE FACULTY

in partial fulfillment of the requirements for the

Degree of

DOCTOR OF PHILOSOPHY

By

ROBERT WILEY DEAL
Norman, Oklahoma
2023

Downloaded from SHAREOK. Persistent Handle URL: https://hdl.handle.net/11244/337550

THE DARK UNIVERSE:
THE INTERPLAY OF COSMOLOGICAL MODULI, AXIONS, AND THE MSSM

A DISSERTATION APPROVED FOR THE
HOMER L. DODGE DEPARTMENT OF PHYSICS AND
ASTRONOMY

BY THE COMMITTEE CONSISTING OF

Dr. Howard Baer, Chair

Dr. Kuver Sinha

Dr. Brad Abbott

Dr. Kieran Mullen

Dr. Tomasz Przebinda

© Copyright by ROBERT WILEY DEAL 2023
All Rights Reserved.

This work is dedicated to my parents Dr. Don Deal and Cherie Wiley-Deal, my sister Lydia Wiley Deal, my grandma Carol Wiley, my aunt Cari and uncle Jeff, my cat Zeppo, and my partner Angela Bleke. Without the love and support you have given me throughout my entire life, none of this would have been possible.

Thank you.

I also dedicate this work to the memory of my cats, Harpo and Groucho.

I miss you.

Acknowledgements

I would like to thank my advisor, Howard Baer, for directing me through this fascinating line of research, for many insightful discussions on supersymmetry, and for steering me back to the big picture when I delve too deeply into details. I would also like to thank Michele Cicoli for many enlightening discussions about string phenomenology and the Large Volume Scenario, Scott Watson for helping me understand the perturbed Boltzmann equations and structure formation, and Kuver Sinha for many useful discussions about astrophysical constraints, axions, and string cosmology. Additionally, I extend my sincerest gratitude to Vernon Barger for introducing me to Howie; I would not be here today without his support and guidance in my first steps. I hope for many more collaborations with each of you in the future.

I would also like to thank my family, friends, and bandmates for their patience and support during my studies.

Table of Contents

List of Tables **ix**

List of Figures **xvi**

Abstract **xvii**

1 From fields to superfields to strings **1**
1.1 The gauge hierarchy problem . . . 3
1.1.1 The MSSM and the gauge hierarchy problem . . . 5
1.2 The strong-CP problem . . . 7
1.2.1 The Peccei-Quinn solution . . . 9

2 Moduli: a 4D perspective of extra dimensions **14**
2.1 The Kaluza-Klein picture . . . 14
2.1.1 Unification of electromagnetism and gravity . . . 16
2.1.2 Massive scalars in 4d from massless scalars in 5d . . . 21
2.2 The many moduli from string theory . . . 23
2.2.1 Moduli space of string theory . . . 25
2.3 Moduli stabilization . . . 36
2.3.1 Flux compactification . . . 37
2.3.2 The KKLT scheme . . . 43
2.3.3 The Large Volume Scenario . . . 49
2.4 Sequestering in string theory . . . 55
2.5 The cosmological moduli problem . . . 60

3 The PQMSSM - a brief review **63**
3.1 Structure of the PQMSSM . . . 63
3.1.1 Radiative Natural Supersymmetry . . . 64
3.1.2 The Giudice-Masiero mechanism . . . 68
3.1.3 The supersymmetric DFSZ axion and the Kim-Nilles mechanism 71
3.1.4 The axion quality problem . . . 77
3.2 Distribution of μ and f_a from the landscape . . . 79
3.2.1 Distribution of μ and f_a in the GSPQ model . . . 81
3.2.2 Distribution of μ in the Giudice-Masiero model . . . 93

4 The ϕMSSM and the ϕPQMSSM - an EFT approach **96**
4.1 The ϕMSSM and ϕPQMSSM models . . . 97
4.1.1 The superpotential . . . 98
4.1.2 The Kähler potential . . . 101
4.1.3 Connection to GSPQ models . . . 106
4.1.4 The gauge-kinetic function . . . 108
4.2 Modulus decays . . . 109
4.2.1 Decays into gauge bosons and gauginos . . . 110
4.2.2 Decays into Higgses . . . 111
4.2.3 Decays into matter fields . . . 116
4.2.4 Decays into ALPs . . . 118

4.2.5 Decays into DFSZ-type axions . . . 119
4.2.6 Decays into gravitinos . . . 120
4.3 A natural SUSY benchmark point . . . 121
4.3.1 Scenarios from strings . . . 124
4.3.2 Modulus decays in the ϕMSSM - the massive ALP case . . . 130
4.3.3 Modulus decays in the ϕMSSM - the ultralight ALP case . . . 143
4.3.4 Modulus decays in the ϕPQMSSM . . . 146

5 Qualitative cosmological features of the ϕMSSM and ϕPQMSSM 158
5.1 The Boltzmann equations . . . 158
5.2 The temperature scales of interest . . . 163
5.2.1 Decay temperature . . . 163
5.2.2 Oscillation temperature . . . 165
5.2.3 Modulus-radiation equality temperature . . . 170
5.2.4 Entropy injection temperature . . . 172
5.2.5 The temperature scales of the ϕMSSM . . . 173
5.2.6 The temperature scales of the ϕPQMSSM . . . 182
5.3 Estimates of produced abundances . . . 188
5.3.1 Thermal WIMPs and gravitinos - relics of inflation . . . 189
5.3.2 Non-thermal WIMPs - the annihilation scenario . . . 194
5.3.3 Non-thermal WIMPs - the branching scenario . . . 197
5.3.4 Non-thermal WIMP production in the ϕMSSM - case B2 . . . 199
5.3.5 Non-thermal WIMP production in the ϕMSSM - case B1 . . . 205
5.3.6 Dark radiation production in the ϕMSSM with a light ALP . . . 210
5.3.7 Abundance of misalignment produced axions . . . 214

6 Results and discussion 218
6.1 Procedure and initial conditions . . . 218
6.2 Results for the ϕMSSM . . . 222
6.2.1 Cosmological evolution in case B1-GK1 . . . 222
6.2.2 Cosmological evolution in case B2-GK1 . . . 225
6.2.3 Cosmological evolution with kinematically forbidden gravitino . . . 227
6.2.4 Entropy production in the ϕMSSM . . . 228
6.2.5 DM production in case B1 . . . 230
6.2.6 DM production in case B2 . . . 234
6.2.7 Dependence on modulus initial amplitude ϕ_0 . . . 237
6.2.8 Some general comments on the ϕMSSM . . . 240
6.3 Results for the ϕPQMSSM . . . 241
6.3.1 Cosmological evolution in case GK1 . . . 242
6.3.2 Cosmological evolution in case GK2 . . . 246
6.3.3 Entropy production in the ϕPQMSSM . . . 249
6.3.4 DM/DR production in case GK1 - the $\xi = 1$ limit . . . 251
6.3.5 DM/DR production in case GK1 - the $\xi = 0$ limit . . . 258
6.3.6 DM/DR production in case GK2 - the $\xi = 1$ limit . . . 263
6.3.7 DM/DR production in case GK2 - the $\xi = 0$ limit . . . 266
6.3.8 The allowed PQ parameter space . . . 270
6.3.9 Dependence on inflationary reheating temperature T_R . . . 278
6.3.10 Dependence on modulus initial amplitude ϕ_0 . . . 279

6.3.11 Some general comments on the ϕPQMSSM 281

7 Inflation and phenomenology in fibred LVS models 284
7.1 Blow-up/Kähler inflation in LVS 284
7.2 Inflation in fibred LVS 286
7.3 Phenomenology in viable fibred LVS inflationary scenarios 293
7.3.1 Moduli decays 293
7.3.2 Dark radiation production 303
7.3.3 Kähler inflation in fibred LVS with matter fields on $D3$ branes . 307
7.3.4 Fibre inflation with matter fields on $D3$ branes 315

8 Conclusions 320

A Moduli interactions and decay widths 325
A.1 Half superspace integrals of 3 fields 325
A.1.1 Integrals of the form $\hat{A}\overline{\hat{W}^c}_\alpha\hat{W}_\alpha + \text{h.c.}$ 325
A.2 Full superspace integrals of 3 fields 327
A.2.1 Useful Grassmann identities involving scalars 328
A.2.2 Useful Grassmann identities involving spinors 328
A.2.3 Kähler potentials of the form $\hat{A}\hat{B}\hat{C} + \text{h.c.}$ 329
A.2.4 Kähler potentials of the form $\hat{A}\hat{B}\hat{C}^\dagger + \text{h.c.}$ 329
A.3 Toy model Feynman amplitudes and decay widths 332
A.3.1 Modulus decay to real scalars 332
A.3.2 Modulus decay to complex scalars 334
A.3.3 Modulus decay to spin-1/2 fermions 335
A.3.4 Modulus decay to vector bosons 338
A.4 Moduli-gauge sector interactions 341
A.4.1 Electroweak gauge boson interactions 343
A.4.2 Electroweakino interactions 345
A.4.3 Electroweak D-term interactions 347
A.4.4 Electroweak F-term interactions 348
A.4.5 Gluon interactions 349
A.4.6 Gluino interactions 349
A.4.7 QCD D-term interactions 350
A.4.8 Gluino F-term interaction 350
A.5 Moduli-Higgs interactions 350
A.5.1 Charged Higgs interactions 353
A.5.2 Charged higgsino interactions 354
A.5.3 Charged Higgs F-term interactions 356
A.5.4 Neutral Higgs interactions 358
A.5.5 Neutral higgsino interactions 360
A.5.6 Neutral Higgs F-term interactions 362
A.6 Moduli-matter interactions 363
A.6.1 Squark interactions 364
A.6.2 Quark interactions 366
A.6.3 Quark F-term interactions 367
A.6.4 Slepton interactions 368
A.6.5 Lepton interactions 370

A.6.6 Lepton F-term interactions . . . 371
A.7 Moduli-PQ sector interactions . . . 372
A.7.1 Saxion and axion interactions . . . 373
A.7.2 Axino interactions . . . 374
A.7.3 PQ F-term interactions . . . 374
A.8 Moduli decay widths . . . 375
A.8.1 Modulus decay widths to electroweak gauge bosons . . . 375
A.8.2 Modulus decay width to gluons . . . 376
A.8.3 Modulus decay widths to neutral Higgses . . . 377
A.8.4 Modulus decay widths to charged Higgses . . . 378
A.8.5 Modulus decay widths to neutralinos . . . 378
A.8.6 Modulus decay widths to charginos . . . 380
A.8.7 Modulus decay width to gluinos . . . 383
A.8.8 Modulus decay widths to squarks . . . 383
A.8.9 Modulus decay widths to sleptons . . . 385
A.8.10 Modulus decay widths to quarks . . . 386
A.8.11 Modulus decay widths to leptons . . . 387
A.8.12 Modulus decay widths into axions and saxions . . . 387
A.8.13 Modulus decay width into axinos . . . 388

B The Boltzmann equations **389**
B.1 The Boltzmann equations . . . 389

C A list of acronyms **398**

D Conventions **400**

References **401**

List of Tables

4.1 MSSM field content and charge assignments as given in [1]. 98
4.2 Charge assignments for the GSPQ model under a (fundamental) discrete $\mathbb{Z}_{24}^{\mathbf{R}}$ symmetry and the corresponding (approximate) global PQ symmetry as given in [2]. 106
4.3 Input parameters and resulting weak-scale MSSM mass spectra for a natural SUSY benchmark point in the NUHM3 model. Additionally, we take $m_{3/2} = 30$ TeV except where noted otherwise. 122
4.4 Summary of case scenarios on leading decay modes depending on whether or not they receive chirality suppression. 125
4.5 Summary of case scenarios for the expected magnitude of λ_{gauge} depending on whether or not the lightest modulus appears at tree-level or at loop-level. 129
4.6 Parameters for a PQ benchmark point. 146

6.1 Parameter bounds for scanning PQ parameter space. 271

7.1 Benchmark spectrum for Kähler inflation. We take $\omega = 0.01$ and $\tau_3 = 1.5$ which gives the gaugino mass $M_{1/2}$ from Eq. (7.15). 308
7.2 Benchmark spectrum for fibre inflation. We take $\omega = 0.01$ and $\tau_3 = 1.5$ which gives the gaugino mass $M_{1/2}$ from Eq. (7.15). 316

List of Figures

1.1 Quantum corrections to the Higgs two-point correlation function in the MSSM. Each SM loop has a corresponding superpartner loop with opposite sign. Supersymmetry requires the coupling between the Higgs and top quarks to be identical to the coupling between the Higgs and stop squarks, exactly cancelling the quadratic divergences. 7

2.1 Schematic of the Kaluza-Klein geometry. The (infinite) length of the cylinder is the non-compact 4d space, while the "width" is the compact fifth dimension. 17
2.2 A flux F_1 pierces a non-trivial 1-cycle C_1 of the torus T^2. 39
2.3 The KKLT scalar potential in $m_P = 1$ units (see Eq. (2.63)) for $A = 1$, $a = 0.1$, $W_0 = -10^{-4}$. Uplifting choices have $B_1 = 2.7 \times 10^{-11}$ and $B_2 = 3.15 \times 10^{-9}$. Plot reproduced from [3]. 48
2.4 The LVS scalar potential in terms of the blow-up mode in $m_P = 1$ units (see Eq. (2.73)), τ_s. We take here the parameter choices $\langle e^{K'} \rangle = 1$, $A_s = \lambda = 1$, $\xi = 1$, $W_0 = 1$, $a_s = 2\pi$, and $\mathcal{V} = 10^2$. 51
2.5 The LVS scalar potential (in $m_P = 1$ units) in terms of the volume with τ_s stabilized. Here, our parameter choices are $\langle e^{K'} \rangle = 1$, $A_s = \lambda = 1$, $\xi = 1$, $W_0 = 1$, and $a_s = 2\pi$. We also show two uplifting scenarios motivated by [3] and [4], with $B_1 = 0.00315$ and $B_2 = 0.0014$. 53

3.1 Results in A_0 vs μ plane for $n = 1$ scan in GSPQ+MSSM model with $\lambda_\mu = 0.1$ and $f = 1$. The left plot corresponds to all values of $m_{\rm weak}^{PU}$, while the right plot corresponds to $m_{\rm weak}^{PU} < 4m_{\rm weak}^{OU}$. Note the right plot is a blow-up of the red boxed region in the left plot. Figure taken from [5]. 86
3.2 Predicted value of μ in the m_0 vs $m_{1/2}$ plane for $n = 1$ landscape scan with $m_{\rm weak}^{PU}/m_{\rm weak}^{Ou} < 4$ anthropic constraint applied. Here, $f = 1$ and $\lambda_\mu = 0.1$. Figure taken from [5]. 88
3.3 Probability distribution of SUSY μ parameter (left) and PQ scale f_a (right). Here, $f = 1$ and $\lambda_\mu = 0.1$. Figure taken from [5]. 88
3.4 Probability distribution of the light Higgs mass m_h (left) and the gluino mass $m_{\widetilde{g}}$ (right). Here, $f = 1$ and $\lambda_\mu = 0.1$. Figure taken from [5]. . . . 89
3.5 Distribution of μ after imposing $m_{\rm weak}^{PU} < 4m_{\rm weak}^{OU}$ for $\lambda_\mu = 0.2$ (blue), $\lambda_\mu = 0.1$ (red), and $\lambda_\mu = 0.05$ (green). Figure taken from [5]. 91
3.6 Distribution of f_a after imposing $m_{\rm weak}^{PU} < 4m_{\rm weak}^{OU}$ for $\lambda_\mu = 0.2$ (blue), $\lambda_\mu = 0.1$ (red), and $\lambda_\mu = 0.05$ (green). Figure taken from [5]. 92
3.7 Probability distribution for SUSY μ parameter in the Giudice-Masiero model. Here, $\lambda_{\rm GM} = 1$. Figure taken from [5]. 94

4.1 Modulus partial decay widths for the case **B2-GK1** as a function of m_ϕ for the natural SUSY benchmark point in Table (4.3). Here, all λ_i couplings are set to unity. 131
4.2 Modulus branching ratios for the case **B2-GK1** as a function of m_ϕ for the natural SUSY benchmark point in Table (4.3). Here, all λ_i couplings are set to unity. 133

4.3 Upper and lower bounds for total modulus branching ratio to SUSY particles for the case **B2-GK1**. Here, all λ_i couplings are set to unity and we use the natural SUSY benchmark point in Table 4.3. The lower bound LB2 assumes the Higgs cascade decay to SUSY particles with 1% branching ratio, while the upper bound UB assumes 100% Higgs to SUSY branching ratio. The lower bound LB1 assumes no Higgs to SUSY contributions. 134
4.4 Modulus partial decay widths for the case **B2-GK2** as a function of m_ϕ for the natural SUSY benchmark point in Table (4.3). Here, all λ_i couplings are set to unity except for the couplings to the gauge sector, which have $\lambda_{\text{gauge}} = 1/16\pi^2$. 135
4.5 Modulus branching ratios for the case **B2-GK2** as a function of m_ϕ for the natural SUSY benchmark point in Table (4.3). Here, all λ_i couplings are set to unity except for the couplings to the gauge sector, which have $\lambda_{\text{gauge}} = 1/16\pi^2$. 137
4.6 Upper and lower bounds for total modulus branching ratio to SUSY particles for the case **B2-GK2**. Here, we use the natural SUSY benchmark point in Table 4.3 and all λ_i couplings are set to unity except for the couplings to the gauge sector, which have $\lambda_{\text{gauge}} = 1/16\pi^2$. The lower bound LB2 assumes the Higgs cascade decay to SUSY particles with 1% branching ratio, while the upper bound UB assumes 100% Higgs to SUSY branching ratio. The lower bound LB1 assumes no Higgs to SUSY contributions. 138
4.7 Modulus partial decay widths for the case **B1-GK1** as a function of m_ϕ for the natural SUSY benchmark point in Table (4.3). Here, all λ_i couplings are set to unity and decays to gravitinos are unsuppressed. . 139
4.8 Modulus branching ratios for the case **B1-GK1** as a function of m_ϕ for the natural SUSY benchmark point in Table (4.3). Here, all λ_i couplings are set to unity and decays to gravitinos are unsuppressed. 140
4.9 Comparison of the total width for cases **B2-GK1** and **B2-GK2** as a function of m_ϕ for the natural SUSY benchmark point in Table (4.3). Both cases have suppressed decays to gravitinos and gauginos. Case **B2-GK1** sets all couplings, including those to the gauge sector, to unity. Case **B2-GK2** takes the gauge sector couplings to be $\lambda_{\text{gauge}} = 1/16\pi^2$, with all remaining λ_i couplings set to unity. 141
4.10 Modulus partial decay widths for the case **B2-GK1** as a function of m_ϕ for the natural SUSY benchmark point in Table (4.3) with the addition of an ultralight axion-like particle (ALP). Here, all λ_i couplings are set to unity including the coupling to ALPs, λ_{ALP}. 144
4.11 Modulus branching ratios for the case **B2-GK1** as a function of m_ϕ for the natural SUSY benchmark point in Table (4.3) with the addition of an ultralight axion-like particle (ALP). Here, all λ_i couplings are set to unity including the coupling to ALPs, λ_{ALP}. 145
4.12 Modulus decay widths in the case **B2-GK1** for the natural SUSY benchmark point in Table (4.3) and PQ sector parameters in Table (4.6). Here, all λ_i couplings are set to unity. 147

4.13 Modulus branching ratios in the case **B2-GK1** for the natural SUSY benchmark point in Table (4.3) and PQ sector parameters in Table (4.6). Here, all λ_i couplings are set to unity. 148
4.14 Modulus decay widths in the case **B2-GK2** for the natural SUSY benchmark point in Table (4.3) and PQ sector parameters in Table (4.6). Here, all $\lambda_i = 1$ except for $\lambda_{\rm gauge} = 1/16\pi^2$. 149
4.15 Modulus branching ratios in the case **B2-GK2** for the natural SUSY benchmark point in Table (4.3) and PQ sector parameters in Table (4.6). Here, all $\lambda_i = 1$ except for $\lambda_{\rm gauge} = 1/16\pi^2$. 150
4.16 Saxion decay widths for the self-coupling $\xi = 1$ and the natural SUSY benchmark point from Table (4.3) with PQ parameters from Table (4.6). 151
4.17 Saxion branching ratios for the self-coupling $\xi = 1$ and the natural SUSY benchmark point from Table (4.3) with PQ parameters from Table (4.6). 152
4.18 Saxion decay widths for the self-coupling $\xi = 0$ and the natural SUSY benchmark point from Table (4.3) with PQ parameters from Table (4.6). 153
4.19 Saxion branching ratios for the self-coupling $\xi = 0$ and the natural SUSY benchmark point from Table (4.3) with PQ parameters from Table (4.6). 154
4.20 Axino decay widths for the natural SUSY benchmark point from Table (4.3) with PQ parameters from Table (4.6). 155
4.21 Axino branching ratios for the natural SUSY benchmark point from Table (4.3) with PQ parameters from Table (4.6). 155
4.22 Decay widths of the gravitino into the PQMSSM. We again take the natural SUSY benchmark point from Table (4.3) and PQ parameters from Table (4.6). 156
4.23 Gravitino branching ratios to the PQMSSM. We again take the natural SUSY benchmark point from Table (4.3) and PQ parameters from Table (4.6). 157

5.1 Relevant temperature scales for the ϕMSSM using the natural SUSY benchmark point from Table (4.3). We plot both the decay and entropy injection temperatures for all couplings set to $\lambda_i \in \{0.1, 1, 10\}$. We also plot the neutralino freeze-out temperature $T_{\rm f.o.} \sim m_{\widetilde{Z}_1}/20$ and two estimates for the temperature of BBN. 178
5.2 Gravitino decay temperature $T_D^{3/2}$ vs $m_{3/2}$. We also plot the neutralino freeze-out temperature $T_{\rm f.o.} \sim m_{\widetilde{Z}_1}/20$ and two estimates for the temperature of BBN. 181
5.3 Entropy dilution factor $r \simeq T_e^\phi/T_D^\phi$ vs m_ϕ for each $\lambda_i \in \{0.1, 1, 10\}$. . . 191
5.4 Thermally-produced gravitino relic density $\Omega_{3/2}^{\rm TP}h^2$ for $T_R = T_R^{BHLR} = 10^{12}$ GeV. We also show the predicted relic density in the presence of modulus decay for $m_\phi \in \{10, 100, 1000\}$ TeV for case **B2-GK1** with all $\lambda_i = 1$. Figure taken from [6]. 193
5.5 Critical abundance yield $Y_{\widetilde{Z}_1}^C$ (orange) and decay-produced abundance yield $Y_{\widetilde{Z}_1}^D$ (green) for neutralinos. Here we take case **B2-GK1** and assume 1% of Higgses decay to SUSY in addition to all R-parity odd decays. . 200
5.6 Predicted WIMP relic density for each $\lambda_i \in \{0.1, 1, 10\}$. Here we take case **B2-GK1** and assume 1% of Higgses decay to SUSY in addition to all R-parity odd decays. Figure updated from [6]. 202

5.7 Predicted WIMP relic density for each $\lambda_i \in \{0.1, 1, 10\}$. Here we take case **B2-GK1** and assume 100% of Higgses decay to SUSY in addition to all R-parity odd decays. Figure updated from [6]. 203
5.8 Predicted WIMP relic density for each $\lambda_i \in \{0.1, 1, 10\}$. Here we take case **B2-GK1** but assume a flat branching fraction to SUSY $\mathcal{B}(\phi \to \text{SUSY}) = 1\%$ (independent of m_ϕ). Figure updated from [6]. 204
5.9 Critical abundance $Y^C_{\widetilde{Z}_1}$ (orange) and decay-produced abundance $Y^D_{\widetilde{Z}_1}$ (green) for neutralinos. Here we take case **B1-GK1** and assume the gravitino dominates the abundance contribution. Additionally, we fix $m_\phi = 5 \times 10^4$ TeV and take all $\lambda_i = 1$. 207
5.10 Predicted WIMP relic density in case **B1-GK1**. We fix $m_\phi = 5 \times 10^4$ TeV and take all $\lambda_i = 1$. 208
5.11 Predicted dark radiation ΔN_{eff} in case **B2** in the $(m_\phi, \lambda_{\text{ALP}})$ plane. Upper plots and lower left plot assume the **GK1** scenario, while the lower right plot takes the **GK2** scenario. The upper left (right) plot takes all remaining $\lambda_i = 0.1$ (all remaining $\lambda_i = 1$), while the lower left plot takes all remaining $\lambda_i = 10$. The lower right plot takes all remaining $\lambda_i = 1$ except for $\lambda_{\text{gauge}} = 1/16\pi^2$. Horizontal dashed line represents expected minimal LVS value, $\lambda_{\text{ALP}} = 0.816$. Figure reproduced from [7]. 212

6.1 Thermally-averaged cross sections $\langle \sigma v \rangle$ versus temperature for each of neutralinos, saxions, axinos, axions, and gravitinos. 219
6.2 Cosmological evolution of abundance yield $Y_i = n_i/s$ vs scale factor R/R_0 in case **B1-GK1**. Here, we fix $m_\phi = 5 \times 10^3$ TeV and $m_{3/2} = 30$ TeV, and take all allowed $\lambda_i = 1$. 223
6.3 Cosmological evolution of energy densities ρ_i vs scale factor R/R_0 in case **B1-GK1**. Here, we fix $m_\phi = 5 \times 10^3$ TeV and $m_{3/2} = 30$ TeV, and take all allowed $\lambda_i = 1$. 224
6.4 Cosmological evolution of abundance yield $Y_i = n_i/s$ vs scale factor R/R_0 in case **B2-GK1**. Here, we fix $m_\phi = 5 \times 10^3$ TeV and $m_{3/2} = 30$ TeV, and take all allowed $\lambda_i = 1$. 226
6.5 Cosmological evolution of energy densities ρ_i vs scale factor R/R_0 in case **B2-GK1**. Here, we fix $m_\phi = 5 \times 10^3$ TeV and $m_{3/2} = 30$ TeV, and take all allowed $\lambda_i = 1$. 227
6.6 Cosmological evolution of abundance yield $Y_i = n_i/s$ vs scale factor R/R_0 in case **B2-GK1**, but the gravitino is kinematically forbidden. Here, we fix $m_\phi = m_{3/2} = 5 \times 10^3$ TeV and take all allowed $\lambda_i = 1$. 228
6.7 Cosmological evolution of energy densities ρ_i vs scale factor R/R_0 in case **B2-GK1**, but the gravitino is kinematically forbidden. Here, we fix $m_\phi = m_{3/2} = 5 \times 10^3$ TeV and take all allowed $\lambda_i = 1$. 229
6.8 Numerical Boltzmann results for entropy dilution factor r vs modulus mass m_ϕ for in case **B2-GK1** with all $\lambda_i \in \{0.1, 1, 10\}$. Here, we take $T_R = T_R^{BHLR} = 10^{12}$ GeV. 230
6.9 Numerical Boltzmann results for WIMP relic density in case **B1-GK1** as a function of m_ϕ. Here we take all $\lambda_i = 1$ and fix $m_{3/2} = 30$ TeV. . . 231
6.10 Numerical Boltzmann results for WIMP relic density in case **B1-GK1** as a function of $m_{3/2}$. Here we take all $\lambda_i = 1$ and fix $m_\phi = 5 \times 10^4$ TeV. 232

6.11 Numerical Boltzmann results for WIMP relic density in case **B1-GK1** in the ($m_{3/2}$, m_ϕ) plane. Here we take all $\lambda_i = 1$. The diagonal dashed line indicates $m_\phi = 2m_{3/2}$. 233
6.12 Numerical Boltzmann results for WIMP relic density in case **B2-GK1** for each $\lambda_i \in \{0.1, 1, 10\}$. Here we assume 1% of Higgses decay to SUSY in addition to all R-parity odd decays. 235
6.13 Numerical Boltzmann results for WIMP relic density in case **B2-GK1** for each $\lambda_i \in \{0.1, 1, 10\}$. Here we assume a flat branching fraction to SUSY $\mathcal{B}_{\phi\to\text{SUSY}} = 1\%$ (independent of m_ϕ). 236
6.14 Numerical Boltzmann results for WIMP relic density in case **B2-GK1** for kinematically forbidden gravitinos (orange) and gravitino mass fixed at $m_{3/2} = 30$ TeV (green). Here we take $\lambda_i = 1$ and assume 1% of Higgses decay to SUSY in addition to all R-parity odd decays. 237
6.15 Neutralino relic density as a function of ϕ_0/m_P in case **B1-GK1** with $m_\phi = 100$ TeV and $T_R = 10^8$ GeV. Here, all $\lambda_i = 1$ and decays to gravitinos are unsuppressed. 238
6.16 Cosmological evolution of abundance yield $Y_i = n_i/s$ vs scale factor R/R_0 in case **B2-GK1**. Here, we fix $m_\phi = 5 \times 10^3$ TeV and take all allowed $\lambda_i = 1$. Figure reproduced from [8]. 242
6.17 Cosmological evolution of energy densities ρ_i vs scale factor R/R_0 in case **B2-GK1**. Here, we fix $m_\phi = 5 \times 10^3$ TeV and take all allowed $\lambda_i = 1$. Figure reproduced from [8]. 244
6.18 Cosmological evolution of abundance yield $Y_i = n_i/s$ vs scale factor R/R_0 in case **B2-GK2**. Here, we fix $m_\phi = 5 \times 10^3$ TeV and take all allowed $\lambda_i = 1$ except for $\lambda_{\text{gauge}} = 1/16\pi^2$. Figure reproduced from [8]. 247
6.19 Cosmological evolution of energy densities ρ_i vs scale factor R/R_0 in case **B2-GK2**. Here, we fix $m_\phi = 5 \times 10^3$ TeV and take all allowed $\lambda_i = 1$ except for $\lambda_{\text{gauge}} = 1/16\pi^2$. Figure reproduced from [8]. 248
6.20 Entropy dilution factor r vs modulus mass m_ϕ for both case **GK1** and **GK2** in the $\xi = 1$ limit. We adopt our natural SUSY benchmark point from Table (4.3) and our PQ benchmark point from Table (4.6). Here, we fix $T_R = 10^{10}$ GeV. Figure taken from [8]. 250
6.21 Relic densities in case **GK1** with $\xi = 1$ as a function of m_ϕ for neutralinos (blue), TP/DP axions (purple), CO axions (green), and total DM (black) for $\lambda_{\text{PQ}} \in \{0, 0.1, 1\}$ with all other $\lambda_i = 1$. Vertical dashed lines represent where $T_S^\phi \sim T_{\text{osc}}^a$ ($m_\phi \sim 55$ TeV), $T_D^\phi \sim T_{\text{osc}}^a$ ($m_\phi \sim 5 \times 10^3$ TeV), and $T_D^\phi \sim T_{\text{f.o.}}$ ($m_\phi \sim 2 \times 10^4$ TeV). Vertical solid black line at $m_\phi \sim 70$ TeV represents BBN bound. Figure taken from [8]. 251
6.22 Dark radiation production in case **GK1** with $\xi = 1$ as a function of m_ϕ for $\lambda_{\text{PQ}} \in \{0, 0.1, 1\}$ with all other $\lambda_i = 1$. Horizontal red line shows Planck 2018 bounds, while orange dashed line shows forecast CMB-S4 limits. Vertical solid black line at $m_\phi \sim 70$ TeV represents BBN bound. Figure taken from [8]. 254
6.23 Dark matter production as a function of m_s in case B2-GK1 in the $\xi = 1$ limit. Here, we fix $m_\phi = 5 \times 10^5$ TeV and $m_{\widetilde{a}} = 5$ TeV and take all $\lambda_i = 1$. All remaining PQ parameters are as given in Table (4.6). . . . 256

6.24 Relic densities in case **GK1** with $\xi = 0$ as a function of m_ϕ for neutralinos (blue), TP/DP axions (purple), CO axions (green), and total DM (black) for $\lambda_{\rm PQ} \in \{0,\, 0.1,\, 1\}$ with all other $\lambda_i = 1$. Vertical dashed lines represent where $T_S^\phi \sim T_{\rm osc}^a$ ($m_\phi \sim 55$ TeV), $T_D^\phi \sim T_{\rm osc}^a$ ($m_\phi \sim 5 \times 10^3$ TeV), and $T_D^\phi \sim T_{\rm f.o.}$ ($m_\phi \sim 2 \times 10^4$ TeV). Vertical solid black line at $m_\phi \sim 70$ TeV represents BBN bound. Figure taken from [8]. 259
6.25 Dark radiation production in case **GK1** with $\xi = 0$ as a function of m_ϕ for $\lambda_{\rm PQ} \in \{0,\, 0.1,\, 1\}$ with all other $\lambda_i = 1$. Horizontal red line shows Planck 2018 bounds, while orange dashed line shows forecast CMB-S4 limits. Vertical solid black line at $m_\phi \sim 70$ TeV represents BBN bound. Figure taken from [8]. 260
6.26 Dark matter production as a function of m_s in case B2-GK1 in the $\xi = 0$ limit. Here, we fix $m_\phi = 5 \times 10^5$ TeV and $m_{\widetilde{a}} = 5$ TeV and take all $\lambda_i = 1$. All remaining PQ parameters are as given in Table (4.6). . . . 261
6.27 Relic densities in case **GK2** with $\xi = 1$ as a function of m_ϕ for neutralinos (blue), TP/DP axions (purple), CO axions (green), and total DM (black) for $\lambda_{\rm PQ} \in \{0,\, 0.1,\, 1\}$. Vertical dashed lines represent where $T_S^\phi \sim T_{\rm osc}^a$ ($m_\phi \sim 300$ TeV), $T_D^\phi \sim T_{\rm osc}^a$ ($m_\phi \sim 2 \times 10^4$ TeV), and $T_D^\phi \sim T_{\rm f.o.}$ ($m_\phi \sim 2 \times 10^5$ TeV). Vertical solid black line at $m_\phi \sim 200$ TeV represents BBN bound. Figure taken from [8]. 264
6.28 Dark radiation production in case **GK2** with $\xi = 1$ as a function of m_ϕ for $\lambda_{\rm PQ} \in \{0,\, 0.1,\, 1\}$. Horizontal red line shows Planck 2018 bounds, while orange dashed line shows forecast CMB-S4 limits. Vertical solid black line at $m_\phi \sim 200$ TeV represents BBN bound. Figure taken from [8]. 266
6.29 Relic densities in case **GK2** with $\xi = 0$ as a function of m_ϕ for neutralinos (blue), TP/DP axions (purple), CO axions (green), and total DM (black) for $\lambda_{\rm PQ} \in \{0,\, 0.1,\, 1\}$. Vertical dashed lines represent where $T_S^\phi \sim T_{\rm osc}^a$ ($m_\phi \sim 300$ TeV), $T_D^\phi \sim T_{\rm osc}^a$ ($m_\phi \sim 2 \times 10^4$ TeV), and $T_D^\phi \sim T_{\rm f.o.}$ ($m_\phi \sim 2 \times 10^5$ TeV). Vertical solid black line at $m_\phi \sim 200$ TeV represents BBN bound. Figure taken from [8]. 267
6.30 Dark radiation production in case **GK2** with $\xi = 0$ as a function of m_ϕ for $\lambda_{\rm PQ} \in \{0,\, 0.1,\, 1\}$. Horizontal red line shows Planck 2018 bounds, while orange dashed line shows forecast CMB-S4 limits. Vertical solid black line at $m_\phi \sim 200$ TeV represents BBN bound. Figure taken from [8]. 269
6.31 Neutralino relic density from scanning PQ parameter space f_a, θ_i, m_s, $m_{\widetilde{a}}$, and all modulus couplings λ_i as given in Table (6.1). Here, we fix $m_\phi = 5 \times 10^5$ TeV and assume the **B2-GK1** case with $\xi = 1$. Red points are in excess of measured dark matter relic density, $\Omega_{\widetilde{Z}_1} h^2 \gtrsim \Omega_{\rm meas.} h^2 \sim 0.12$. Purple and dark blue points are close to the thermal value and can satisfy DD/ID constraints. Figure taken from [8]. 272
6.32 CO-produced axion relic density from scanning PQ parameter space f_a, θ_i, m_s, $m_{\widetilde{a}}$, and all modulus couplings λ_i as given in Table (6.1). Here, we fix $m_\phi = 5 \times 10^5$ TeV and assume the **B2-GK1** case with $\xi = 1$. Red points are in excess of measured dark matter relic density, $\Omega_{a_{\rm CO}} h^2 \gtrsim \Omega_{\rm meas.} h^2 \sim 0.12$. Note the color schema here is logarithmic. Figure taken from [8]. 274

6.33 Contours of allowed PQ parameter space for given values of m_ϕ in case **B2-GK1** in the $\xi = 1$ limit. Interior regions satisfy $0.09 \leq \Omega_{\rm total}h^2 \leq 0.125$, $\Delta N_{\rm eff} \leq 0.26$, and satisfy DD/ID bounds which are $\Omega_{\widetilde{Z}_1}h^2 \lesssim 0.1\Omega_{meas.}h^2$ for our natural SUSY benchmark point. Here, we take random values of f_a, θ_i, m_s, $m_{\widetilde{a}}$, and all modulus couplings λ_i as given in Table (6.1). Figure taken from [8]. 276
6.34 Dependence of results on inflationary reheating temperature T_R in case **B2-GK1**. Here, we fix $m_\phi = 5 \times 10^3$ TeV and take $\lambda_{\rm PQ} = 0.2$, with all other $\lambda_i = 1$. Figure taken from [8]. 278
6.35 Relic densities in the ϕPQMSSM as a function of the displacement amplitude ϕ_0/m_P. Here, we take case **B2-GK1** with all $\lambda_i = 1$ and $\xi = 1$. Additionally, we set $m_\phi = 100$ TeV, $m_s = m_{\widetilde{a}} = 5$ TeV, $f_a = s_i = 10^{11}$ GeV, and take $T_R = 10^8$ GeV. Figure taken from [8]. 280

7.1 Inflationary potential in fibre inflation for canonically normalized inflaton $\phi/m_P \sim \log\tau_1$. We take $R = g_s^4$ with $g_s = 0.1$, $\beta = 1$, and $\langle\mathcal{V}\rangle = 10^3$. Figure reproduced from [9]. 290
7.2 Dark radiation production $\Delta N_{\rm eff}$ (upper plot) and reheating temperature $T_{\rm rh}$ in GeV (lower plot) in the ultralocal limit for the case $k_1 = 1$ and $k_2 = 0$. Figure taken from [10]. 305
7.3 Dark radiation production $\Delta N_{\rm eff}$ (upper plot) and reheating temperature $T_{\rm rh}$ in GeV (lower plot) in the ultralocal limit for the case $k_1 = 1/2$ and $k_2 = 1/2$. Figure taken from [10]. 306
7.4 Constraints on the branching scenario in the $(m_{\rm DM}, m_u)$ plane. Gray regions are incompatible with the branching scenario, while red regions are excluded by either dark matter overproduction or BBN violation. Figure reproduced from [10]. 311
7.5 Constraints on the annihilation scenario in the $(m_{\rm DM}, T_{\rm rh})$ plane. Red regions are excluded by dark matter overproduction. Blue, green, and yellow contours also indicate dark matter overproduction if $\langle\sigma v\rangle_{\rm f.o.}/\langle\sigma v\rangle^{\rm th}_{\rm f.o.}$ is below 3, 10, and 30 respectively. Figure reproduced from [10]. 313

Abstract

In this work, we introduce two effective field theories which parameterize a light modulus field interacting both with the MSSM (ϕMSSM) and with the MSSM combined with an additional supersymmetric DFSZ axion (ϕPQMSSM). All two-body decays of the modulus are cataloged and connected to explicit string scenarios, with all model-independent decay widths calculated incorporating mixing and phase-space effects for the first time. Dark matter and dark radiation production are studied in both models for a subset of string scenarios, with comments provided on expectations for the remaining scenarios. Quite generally, we find that many string scenarios with a modulus-driven early matter dominated period overproduce dark matter and/or dark radiation. The overproduction of dark matter may be remedied with a sufficiently large modulus mass, however various consistency conditions show that most scenarios are incompatible with weak-scale supersymmetry and with a DFSZ-type axion, at least without additional model-building. We also study statistical properties of the Peccei-Quinn scale f_a and the derived value of the SUSY μ-term in the string landscape. Here, we find the predicted value of f_a is in the cosmological sweet-spot for axion dark matter, while the predicted higgsino masses are slightly above current LHC bounds. Additionally, we study the predicted nature of viable dark matter candidates in explicit inflationary scenarios in string theory, finding a WIMP in Kähler inflation and open string axions in fibre inflation to be natural dark matter candidates.

Chapter 1

From fields to superfields to strings

Our current understanding of the universe can be reduced to a few simple building blocks. These building blocks are described by two extremely well-established frameworks: quantum field theory (QFT) describing extremely small scales and general relativity (GR) describing extremely large scales. Within the framework of quantum field theory, the Standard Model (SM) of particle physics is a specific QFT which describes both the fundamental fermions and the gauge bosons which mediate electromagnetic, weak, and strong interactions. While the framework of general relativity generically describes gravitational interactions as curvature in spacetime, the specific Lambda-Cold Dark Matter (ΛCDM) cosmological model describes the expanding universe on vast scales as homogeneous and isotropic, consisting of baryonic matter, dark matter, and a positive vacuum energy density - the cosmological constant Λ.

However, there are several known experimental and theoretical issues with the SM that indicate it is incomplete, among which include: 1. the SM does not provide a candidate for dark matter, 2. quantum corrections to the mass of the Higgs are expected to pull its physical mass to extremely large values (the gauge hierarchy problem), 3. CP symmetry is expected to be violated in quantum chromodynamics (QCD), however measurements of the neutron electric dipole moment (EDM) indicate that any CP-violation must be extremely weak in stark contrast with theoretical expectations (the strong-CP problem), and 4.

the incorporation of gravity into the theory. One of the primary goals in modern physics is to find some extension or generalization of the SM which will address these issues, while still reproducing the extensive successes of the SM.

The inclusion of a viable dark matter candidate is particularly crucial for a complete understanding of our universe. Planck 2018 data suggests that the current dark matter energy density is over five times greater than that of baryonic matter [11]. However, any non-gravitational dark matter interactions are model-dependent and thus experiments to measure distinct signatures are only sensitive to particular subclasses of dark matter candidates [12]. Furthermore, any existing experimental constraints are typically weakened if dark matter is multi-component [12]. Given the plethora of hypothesized dark matter candidates, perhaps the most motivated approach is to prioritize focus on the models which also solve other theoretical or experimental issues with the SM. This approach both gives promising predictions for the nature of dark matter and for its experimental detection within a particular model, as well as tying these predictions to other problems which - if some alternate solution becomes experimentally confirmed or preferred - may also effectively rule out the model.

One such attempt to address many of the shortcomings of the SM is supersymmetry (SUSY), with the Minimal Supersymmetric Standard Model (MSSM) being arguably the simplest phenomenologically viable model [1, 13, 14, 15]. The MSSM, when embedded in the framework of supergravity or local supersymmetry, provides a remarkably constrained grand unified theory (GUT) and a non-renormalizable theory of gravity, with most models determined completely at the GUT scale by

$\mathcal{O}(5)$ free parameters. A UV-complete theory incorporating gravity, on the other hand, requires another framework. We are naturally led to consider superstring theory as a plausible UV completion for the MSSM, which contains the graviton in its spectrum[1] and can predict the MSSM as the low (sub-Planck) energy effective theory. The main focus of this work is thus to consider the motivated scenario where the MSSM is the low energy limit of string theory, which - as we will see in the next chapter - likely predicts a non-thermal cosmological history before Big Bang Nucleosynthesis (BBN). As we will see throughout this work, this has rather severe implications for the production and composition of dark matter which, despite being an extremely compelling framework, becomes highly constrained.

This introduction is as follows. First, we briefly review the gauge hierarchy problem and how it is addressed in the MSSM. We then review the strong-CP problem and the proposed axionic solution.

1.1 The gauge hierarchy problem

The prediction [20, 21, 22] and experimental discovery [23, 24] of the Higgs boson is perhaps the greatest success of the SM. This discovery gives a considerable degree of evidence that the Higgs mechanism is the correct picture through which the fundamental quarks, leptons, and $W^{\pm}$ and Z^0 bosons of the SM acquire their masses. However, the mass of the Higgs boson itself is a source of

[1]Supergravity - both in 4d and higher-dimensional generalizations - also include a natural inclusion of the graviton [16, 13, 1]. However, supergravity is a non-renormalizable field theory while string theory is finite in the ultraviolet (UV) regime. As realistic string theories can be shown to reduce to supergravity theories in the low energy limit [16, 17, 18, 19], one might be led to consider string theory as the UV-complete theory with a supergravity theory providing an effective description close to the GUT scale but below the string scale.

theoretical mystery, partially because in the SM the Higgs mass is a free parameter. Although several theoretical consistency bounds, including constraints based on renormalization group consistency [25], vacuum stability [26], and perturbative unitarity bounds [27], were proposed, they largely suggested a Higgs mass between $\mathcal{O}(85\text{ GeV}) \lesssim m_h \lesssim \mathcal{O}(1\text{ TeV})$ (see e.g. [14]). Extensions of the SM to the MSSM provided a much more stringent constraint, with $m_h \lesssim \mathcal{O}(135\text{ GeV})$, but in any case there remained a large window of viable Higgs masses to be searched.

There is another (far more disturbing) issue with the Higgs mass in the SM. It is well known that in QFT, particles receive quantum corrections to their tree-level or bare mass. These mass corrections are typically divergent in the UV, which are not expected to be physical divergences but instead imply some high energy cutoff scale Λ_{cutoff}, above which a more fundamental theory makes sense of the divergence. However, in QFT scalar fields are particularly susceptible to quadratic divergences - and the Higgs field, being the sole scalar field in the SM, is no exception. The Higgs mass - to 1-loop order - is then given by the schematic form

$$m_{h,\,\text{phys}}^2 \simeq (125\text{ GeV})^2 = m_{h,\,0}^2 - \frac{c}{16\pi^2}\Lambda_{\text{cutoff}}^2 \tag{1.1}$$

with $m_{h,0}$ the bare Higgs mass, Λ_{cutoff} the UV cutoff of the theory, and c some coefficient set by the relevant couplings and diagrams, predominantly set by the top quark loop, gauge boson loops, and Higgs self-coupling loops.

Based on the running of the gauge couplings in the SM, it is plausible to expect the gauge couplings to unify at an energy scale of around 10^{16} GeV, at

which point some Grand Unified Theory might be expected to describe physics. If we take the cutoff scale for the Higgs mass to be the GUT scale, even by the most conservative estimates, *the bare mass must match the cutoff term to at least 24 decimal places* to get the right Higgs mass. The situation becomes even worse if the scale of new physics is set by the Planck scale, where quantum field theory and general relativity break down and a theory of quantum gravity is needed. It is then highly implausible, although technically possible, that this high degree of fine-tuning happens by pure chance. Certainly, one would expect for some underlying mechanism to explain why the Higgs mass is extremely light when the quantum corrections should pull the Higgs mass to a much higher scale. This is one manifestation of the gauge hierarchy problem.

1.1.1 The MSSM and the gauge hierarchy problem

Supersymmetry, in particular the MSSM which is a supersymmetrization of the Standard Model, provides quite possibly the most elegant solution to the gauge hierarchy problem. In this framework, the notion of a Lie algebra is extended to a graded superalgebra, thus circumventing the Coleman-Mandula theorem [28] which asserts that - assuming all symmetries belong to Lie algebras - the only possible internal and spacetime symmetries of a QFT must be a direct product of the Poincaré group with the internal symmetry group. This simple extension allows for spinorial symmetry generators, which in turn provides a symmetry between bosons and fermions. A supersymmetrization of the SM then predicts a boson superpartner for each fermion, and a fermion superpartner for each boson.

To prevent dangerous operators which induce proton decay, an additional R-parity symmetry is conventionally imposed [1] which forbids the offending terms. This also has the implication that the lightest supersymmetric particle (LSP) is stable - which can provide a compelling weakly interacting massive particle (WIMP) as a dark matter candidate.

Returning to the problem of the stability of the Higgs mass, we can focus on the dominant divergence which is due to the top quark loop[2] [1]. The MSSM then predicts a scalar superpartner, the top squark or stop, which contributes also a quadratically divergent loop contribution to the Higgs mass, which we display in Fig. (1.1.1). However, due to the spin-statistics theorem, the stop and top loops contributions have opposite sign, leading to a cancellation of the quadratic divergences in the amplitude. Additionally, if the supersymmetry is exact, the subleading logarithmic divergences also cancel (see e.g. [31]). Fortunately, this is not required to solve the gauge hierarchy problem, as $\log \Lambda_{\text{cutoff}} \lesssim \mathcal{O}(40)$ with the upper bound set by $\Lambda_{\text{cutoff}} = m_P$, implying that a large tuning is not required to stabilize the Higgs mass unlike when quadratic divergences are untempered.

As we have just alluded, we know that if supersymmetry is to be a fundamental symmetry of nature, it must be a broken symmetry at low energy. If supersymmetry were exact, each SM particle would necessarily have the same mass as its corresponding superpartner - and the superpartners would have been experimentally detected long ago. To maintain the successes of supersymmetry

[2]Crudely speaking, the Higgs couplings to other fields are proportional to their masses. As the top quark is the most massive particle in the SM, with $m_t \simeq 173$ GeV [29, 30], its contribution to this amplitude should dominate.

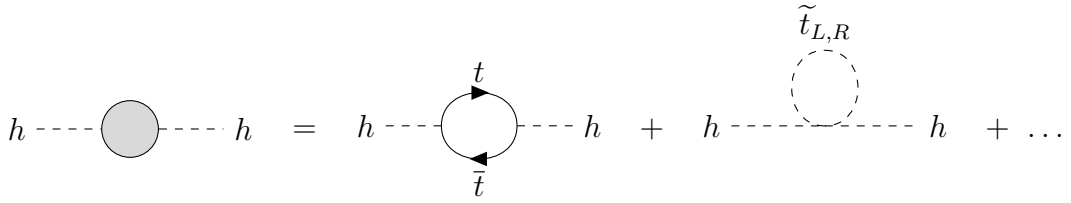


Figure 1.1: Quantum corrections to the Higgs two-point correlation function in the MSSM. Each SM loop has a corresponding superpartner loop with opposite sign. Supersymmetry requires the coupling between the Higgs and top quarks to be identical to the coupling between the Higgs and stop squarks, exactly cancelling the quadratic divergences.

at solving the gauge hierarchy problem, it must be "softly" broken so that the cancellation of quadratic divergences is preserved, although the mild logarithmic divergences reappear [1, 13]. Perhaps the most important open question in supersymmetry is then reconciling the details of how - and at what scale - SUSY is broken with the non-observation of sparticles [32, 33, 34, 35, 36, 37, 38] at the LHC.

1.2 The strong-CP problem

The QCD sector of the SM contains no symmetries to forbid the term

$$\mathcal{L}_{\text{QCD}} \supset \frac{\theta_{\text{QCD}}\, g_s^2}{32\pi^2}\, \text{Tr}\left[G^a_{\mu\nu}\tilde{G}^{\mu\nu,\,a}\right] \tag{1.2}$$

where $G^a_{\mu\nu}$ and $\tilde{G}^{\mu\nu,\,a}$ are respectively the gluon field strength tensor and its Hodge dual, and θ_{QCD} is related to the phase of the quark mass matrix. Initially, this

term seems innocuous as it can be rewritten as a total derivative:

$$G^a_{\mu\nu}\tilde{G}^{\mu\nu,\,a} = \partial_\mu K^\mu, \tag{1.3}$$

where

$$K_\mu = \epsilon_{\mu\nu\rho\sigma}\left[A^a_\nu\, G^a_{\rho\sigma} - \frac{2}{3}\, f^{abc}\, A^a_\nu A^b_\rho A^c_\sigma\right], \tag{1.4}$$

and thus one may expect it to make no contribution to the action. However, K_μ is not a gauge-invariant quantity, and since the gauge field A^a_μ must become pure gauge as we approach infinity [39], the second term in Eq. (1.4) does not vanish from the action integral. Therefore, due to the non-Abelian structure of QCD, non-trivial localized gauge field configurations - known as instantons - provide non-perturbative finite contributions to the action unless $\theta_{\rm QCD} = 0$. Furthermore, since this term violates CP, P, and T symmetries, its presence indicates a source of CP-violation in QCD.

Naively, one might be tempted to force $\theta_{\rm QCD} = 0$ in the Lagrangian by hand. In this case, since QCD has an axial $U(1)_A$ symmetry, the Bell-Adler-Jackiw anomaly [40, 41] regenerates this term if one rotates the quark fields by a chiral transformation [42], e.g. $q \to \exp(i\beta\gamma_5)q$. Additionally, due to the presence of the anomaly, one can eliminate this term by a redefinition of the quark fields at the expense of introducing a phase for the quark mass terms - a result that *also* violates CP. In the quark mass eigenstate basis, the measurable $\theta_{\rm QCD}$ parameter

in Eq. (1.2) is then given by

$$\theta_{\rm QCD} = \tilde{\theta}_{\rm QCD} + \arg\det\left(\mathcal{M}\right) \tag{1.5}$$

where $\mathcal{M}$ is the quark mass matrix, and $\tilde{\theta}_{\rm QCD}$ is the bare θ-parameter.

It thus appears that QCD generically predicts a source of CP-violation. This is problematic, however, since there has yet to be any experimental confirmation that such CP-violation exists. Most stringently, the presence of the term in Eq. (1.2) should induce an electric dipole moment in the neutron, with a magnitude given by [43]

$$d_n \simeq 5.2 \times 10^{-16}\, \theta_{\rm QCD}\, e \cdot {\rm cm}. \tag{1.6}$$

However, experimental measurements of the neutron's electric dipole moment give [44, 45]

$$|d_n| < 1.8 \times 10^{-26}\, e \cdot {\rm cm} \tag{1.7}$$

at the 90% confidence level. This implies that $\theta_{\rm QCD} < 10^{-10}$ for the physical θ-parameter. Such a small value constitutes a large degree of fine-tuning, in particular since the SM provides no motivated reason for $\theta_{\rm QCD} = 0$. This is the strong-CP problem.

1.2.1 The Peccei-Quinn solution

The Peccei-Quinn (PQ) solution to the strong-CP problem [46, 47] effectively promotes the problematic $\theta_{\rm QCD}$ to a field which dynamically relaxes to zero,

naturally solving the strong-CP problem. Originally, this was accomplished by introducing a global $U(1)$ symmetry (conventionally referred to in this context as a $U(1)_{\rm PQ}$ symmetry) along with a second Higgs doublet. Assuming the PQ charges are arranged to allow Yukawa-type couplings with the Higgs doublets, PQ rotations allow for any quark phase to be absorbed into a phase of the Higgs. Once the PQ symmetry is spontaneously broken, quarks (and the rest of the massive SM content) acquire masses through the Higgs mechanism as the two Higgs doublets settle to their vacuum expectation values (VEVs), which are independent of the PQ phase - in essence solving the strong-CP problem.

Of course, as a consequence of the Goldstone theorem, a massless scalar or Nambu-Goldstone boson should be present in the theory after the $U(1)_{\rm PQ}$ symmetry is broken. This was pointed out by Wilczek [48] and Weinberg [49], with the predicted massless particle being named the axion. However, the chiral anomaly explicitly breaks the PQ symmetry - and as such, the axion acquires a small mass from non-perturbative instanton effects and is hence a "pseudo" Nambu-Goldstone boson. In the context of the original PQ framework, the predicted axion is typically coined the Peccei-Quinn-Wilczek-Weinberg (PQWW) axion. The presence of the axion in the theory also makes the PQ solution to the strong-CP problem slightly more apparent. Since the $U(1)_{\rm PQ}$ current should also possess a chiral anomaly, the Lagrangian should contain the terms [50]

$$\mathcal{L} \supset \frac{\theta_{\rm QCD}\, g_s^2}{32\pi^2}\,{\rm Tr}\left[G^a_{\mu\nu}\tilde{G}^{\mu\nu,\,a}\right] + \xi\frac{a}{f_a}\frac{g_s^2}{32\pi^2}\,{\rm Tr}\left[G^a_{\mu\nu}\tilde{G}^{\mu\nu,\,a}\right] \tag{1.8}$$

where ξ is set by PQ charge assignments, a is the axion field, and f_a is the axion decay constant which is determined by the VEV of the additional Higgs field. This effective potential for the axion is then minimized at

$$\langle a \rangle = -\theta_{\mathrm{QCD}} \frac{f_a}{\xi} \tag{1.9}$$

which implies that the physical theory is defined around the CP-conserving vacuum.

The PQWW axion was quickly ruled out for the key reason that the PQ symmetry breaking is inherently tied to electroweak symmetry breaking in this model. The VEV of the additional Higgs field must take a value close to the weak scale, which ties the value of the decay constant to $f_a \sim \mathcal{O}(250\ \mathrm{GeV})$. Since the axion couples to the anomaly terms through couplings of the form $(a/f_a)\, G\tilde{G}$, certain hadronic states should be allowed to decay to an axion and another hadron. Most notably, for the PQWW axion the decay channel $K^+ \to \pi^+ + a$ should occur with a branching ratio [51]

$$\mathcal{B}^{\mathrm{predicted}}_{K^+ \to \pi^+ + a} \gtrsim 1.3 \times 10^{-5} \tag{1.10}$$

which is a factor of $\mathcal{O}(300)$ larger than the measured value [52]

$$\mathcal{B}^{\mathrm{measured}}_{K^+ \to \pi^+ + a} \lesssim 3.8 \times 10^{-8}. \tag{1.11}$$

Furthermore, nuclear reactor experiments, beam dump experiments, and collider

data provide strong evidence against the existence of the PQWW axion (see e.g. [51] for an extensive review from this era, and [53] for a more recent review of collider constraints).

However, these strong constraints are entirely contingent on the magnitude of the PQ scale f_a. Shortly after the PQWW model was introduced, two alternative axion models appeared that incorporated the success of the $U(1)_{\rm PQ}$ symmetry to solve the strong-CP problem, while incorporating an additional field that allows for a significantly larger scale of PQ breaking. In both models, the large increase in f_a predicts an axion that interacts *extremely* weakly which coined the term "invisible axion." As we will see in the following chapters, the invisible axion is also a natural dark matter candidate - potentially explaining another shortcoming of the SM.

The first model introduces a scalar field φ, which is charged under PQ symmetry but otherwise an SM singlet, and a heavy quark doublet $(Q_L\ Q_R)$, which is charged under PQ symmetry and each $Q_{L,R}$ are triplets under $SU(3)_c$. The PQ Lagrangian in this model then includes the Yukawa terms

$$\mathcal{L}_{\rm PQ} \supset -\lambda_Q\, \varphi \overline{Q}_L Q_R + \text{h.c.} \tag{1.12}$$

Since there are no direct tree-level couplings to the SM, φ can acquire a VEV at a high scale, and since the axion couples only to the chiral anomaly, any coupling to SM fields is extremely suppressed. This model is due to Kim [54] and Shifman, Vainshtein, and Zakharov [55], and is thus referred to as the KSVZ axion.

The second model also introduces a scalar field φ, which is similar to the KSVZ case in that it is charged under PQ symmetry but an SM singlet otherwise. Additionally, a second Higgs doublet is added so that both Higgs doublets are charged under PQ symmetry, similar to the original PQWW model. Requiring the usual generation of fermion masses through the Higgs mechanism then implies that the SM fermions should be charged under PQ symmetry as well. This leads to a similar situation as the PQWW model, with the very big exception that the scalar potential

$$V = \lambda_H \, \varphi^2 H_u H_d \tag{1.13}$$

allows for the VEVs of H_u and H_d (v_u and v_d respectively) to remain at the required weak scale values, while the VEV $\langle \varphi \rangle \sim f_a$ is able to be taken extremely large. This is the model proposed by Dine, Srednicki, and Fischler [56] and Zhitnitsky [57], and is referred to as the DFSZ axion. For the remainder of this work, we focus on the DFSZ axion and provide more discussion in Sec. (3.1.3).

Chapter 2

Moduli: a 4D perspective of extra dimensions

In this chapter, we begin by discussing in detail the Kaluza-Klein model and re-derive the key results for both geometric and non-geometric moduli. Although much of this work is focused on moduli from string theory, this introduction serves to show how extra dimensions, when compactified, cause massless scalars in the perspective of the 4d theory to arise rather generically. We then use these concepts to discuss the moduli of string theory. Although we focus predominantly on the Type IIb case, we provide discussion on the moduli present in the heterotic case, as well as for M-theory compactified on a G_2 manifold. Next, we discuss current procedures which stabilize the moduli and the difficulty of this open issue in string theory. Finally, due to its frequent appearance in string literature but scarce appearance in literature on the MSSM, we provide brief discussion on the phenomenon of sequestering. This chapter thus serves as motivation for the generality of moduli in string theory, as background for our case scenario definitions in Ch. (4), and as explicit realizations for our results in Ch. (6).

2.1 The Kaluza-Klein picture

We begin our discussion of moduli within the original context of a five-dimensional theory, which was first proposed by Kaluza [58] and interpreted in a quantum framework by Klein [59, 60]. The resulting Kaluza-Klein (KK) theory showed that both electromagnetism and gravity can occur in a four-dimensional field

theory from the compactification of a five-dimensional field theory containing only gravity, providing the first example of unification of electromagnetism and gravity. The generalization to 10-dimensions (or 11, in the case of M-theory) will be - although substantially more difficult from a technical perspective - much more intuitive.

In our following examples, we will assume a flat background in the extra dimension. This can be generalized to warped backgrounds, which take the general metric decomposition [61]

$$ds^2 = e^{2A(y)}\eta_{\mu\nu}\, dx^\mu\, dx^\nu + dy^2. \tag{2.1}$$

This decomposition is closer to what one might expect from a theory where energy density exists in the higher dimensions - causing a backreaction on the local geometry. Doing so, however, leads to technical complications beyond what we require for this discussion - in particular since the massless spectra of the theory that we are interested in is largely unchanged at the classical level [62].

These warped extra dimension models, such as those originally pioneered by Randall and Sundrum [63], can also lead to interesting phenomenology in any extra-dimensional framework. The original Randall-Sundrum model provided a means of understanding the hierarchy problem from extra dimensions - if two branes are geometrically separated in the additional dimension, the warping caused by the geometric backreaction causes exponential redshifting of the masses in the 4d theory [63]. Distinct collider signatures may be predicted from Kaluza-Klein

graviton exchange [64], additional stable vector bosons if an additional Kaluza-Klein parity symmetry is postulated [65], and radions (or moduli) which could be produced with a mass tentatively of order of the weak scale [66] (see also [67, 68, 69, 70]). However, no experimental collider signatures for these types of models have yet been detected [71, 72, 73, 74, 75, 76, 77, 78, 79, 80, 81, 82, 83]. Additionally, if the extra compact dimension is "large" (as in the Arkani-Hamed - Dimopoulos - Dvali (ADD) model [84], which predicts extra dimensions at or below the millimeter scale), gravity - being intrinsically higher dimensional in this framework - can "leak" out of the effective 4d theory and lead to modifications of general relativity on large scales, which depend on the size of the extra dimension [85, 84, 86]. Experimental analyses using gravitational wave astronomy [87, 88] and black hole astronomy [89, 90] have also put constraints on the size of extra dimensions, which constrain the radius of the extra dimension $R < 170$ AU [89].

2.1.1 Unification of electromagnetism and gravity

For our first example let us consider a five-dimensional field theory containing only gravity, the dimensional reduction of which demonstrates both one particular origin of moduli and shows the unification of electromagnetism and gravity in the original Kaluza-Klein context. Following the Kaluza-Klein picture, we also assume that the topology of the theory is $\mathcal{M}_4 \times S^1$ so that the fifth-dimension is compact. The resulting action is given by

$$S_5 = -\frac{1}{2\kappa_5^2} \int_{\mathcal{M}_4} \int_{\mathcal{M}_{S^1}} d^4x\, dy\, \sqrt{-\det g_5}\, \mathcal{R}_5 \tag{2.2}$$

where $\kappa_5^2 = 8\pi G_N^{(5)}$ is the 5d gravitational constant, $\mathcal{M}_4$ and $\mathcal{M}_{S^1}$ are (respectively) the volumes of the non-compact 4d space and the compact fifth dimension, g_5 is the 5d metric tensor, and $\mathcal{R}_5$ is the 5d Ricci scalar. We display a schematic of this geometry in Fig. (2.1.1).

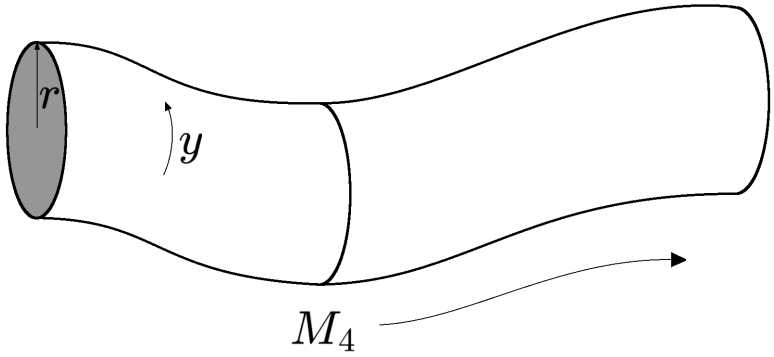


Figure 2.1: Schematic of the Kaluza-Klein geometry. The (infinite) length of the cylinder is the non-compact 4d space, while the "width" is the compact fifth dimension.

In the absence of any matter - i.e. a vacuum compactification - we would expect the 5d metric for this particular topology to decompose as

$$ds^2 = g^{(0)}_{MN}\, dx^M dx^N = g^{(0)}_{\mu\nu}\, dx^\mu dx^\nu + g^{(0)}_{55}\, dy\, dy \tag{2.3}$$

where $g^{(0)}_{MN}$ is the 5d vacuum metric, while $g^{(0)}_{\mu\nu}$ and $g^{(0)}_{55}$ are the 4d and fifth dimension's vacuum metric, respectively. Once matter is incorporated into the 5d theory however, the metric will be deformed as dictated by general relativity and the above decomposition is no longer sufficient.

To build intuition for the Kaluza-Klein metric ansatz, let us first recall that we demand general coordinate invariance within general relativity. If we consider an

infinitesimal coordinate transformation on the fifth dimension so that $y \to y+\epsilon(x)$, the metric will change by

$$g_{\mu 5} \to g_{\mu 5} + \partial_\mu \epsilon(x). \tag{2.4}$$

This coordinate transformation enforces Kaluza's so-called "cylindrical condition," which we will elaborate on shortly. Incidentally, this is precisely the transformation one demands of a $U(1)$ gauge field. Furthermore, under the above coordinate transformation g_{55} has the transformation property of a scalar field, i.e. $g_{55} \to g_{55}$.

We now present the Kaluza-Klein ansatz for the metric, which we choose to parameterize here as:

$$ds^2 = \overline{g}_{MN}\, dx^M dx^N = g_{\mu\nu}\, dx^\mu dx^\nu + \exp(2\phi)\,(A_\mu dx^\mu + dy)^2 \tag{2.5}$$

where we distinguish the 5d metric from the 4d metric with an overline. Here, A_μ is a $U(1)$ gauge field which depends *only* on x^μ, in keeping with Kaluza's "cylindrical condition." We have also introduced the factor $\exp(2\phi)$ where ϕ is a scalar field (which *also* depends only on x^μ). This additional scaling effectively describes the overall strength of any 5d coordinate change relative to the "size" of the coordinate y.

We emphasize that $\overline{g}_{55} = \exp(2\phi)$ is the metric component which defines distances purely within the compact dimension, which we have taken to be S^1. The condition that $\overline{g}_{55}$ and $\overline{g}_{\mu 5}$ depend on x^μ but not on y simply means that

we do not consider any warped regions along the fifth dimension, and hence the geometry is - at least locally - similar to that of a cylinder. For the sake of clarity, let us make a brief analogy to the simple case of cylindrical coordinates in 3d geometry. In 3d cylindrical coordinates, the S^1 metric component is given by $g_{\theta\theta} = r^2$. Comparing to our more complicated case where $\overline{g}_{55} = \exp(2\phi)$, we see that ϕ *parametrizes the size of the compact dimension.* Since ϕ may also vary with x^μ, the size (or volume) of the extra dimension may vary as we move throughout M_4 (although our coordinate choice y remains a fixed length - analogous to the non-dimensional θ coordinate in the 3d cylindrical coordinate system).

To make the metric ansatz a bit more explicit, let us rewrite it in the form:

$$\overline{g}_{\mu\nu} = g_{\mu\nu} + \exp(2\phi) A_\mu A_\nu \tag{2.6}$$

$$\overline{g}_{\mu 5} = \overline{g}_{5\mu} = \exp(2\phi) A_\mu \tag{2.7}$$

$$\overline{g}_{55} = \exp(2\phi) \tag{2.8}$$

which has the inverse metric:

$$\overline{g}^{\mu\nu} = g^{\mu\nu} \tag{2.9}$$

$$\overline{g}^{\mu 5} = \overline{g}^{5\mu} = -A^\mu \tag{2.10}$$

$$\overline{g}^{55} = A^2 + \exp(-2\phi). \tag{2.11}$$

It is now a rather simple matter to now calculate the Christoffel symbols from the above metric and subsequently calculate the Ricci curvature tensor

and scalar. However, as the resulting formulae are extremely lengthy we simply provide the result for the Ricci curvature scalar since the remaining details are largely irrelevant for this discussion. The 5d Ricci scalar in terms of Eqs. (2.6 - 2.11) can be shown to be (see e.g. [13], [18] for similar results):

$$\mathcal{R}_5 = \mathcal{R}_4 + \frac{1}{4}\exp(2\phi)F^{\mu\nu}F_{\mu\nu} - 2\exp(-\phi)\nabla^\mu\nabla_\mu\exp(\phi) \tag{2.12}$$

where $F_{\mu\nu}\,dx^\mu \wedge dx^\nu \equiv dA$ is the $U(1)$ field strength 2-form and ∇_μ is the covariant derivative. We also note that - for our parameterization of the metric ansatz - we have $\det g_5 = \exp(2\phi)\det g_4$.

At long last, we have everything we need to integrate out the fifth dimension in Eq. (2.2). Since our fifth dimension is compact, we take $\mathcal{M}_{S^1} = [0, 2\pi r)$ where r is the radius of the compact dimension. The dy integral is now trivially integrated since (by the Kaluza-Klein metric ansatz) no fields depend on y:

$$\begin{aligned} S_4 = -\frac{2\pi r}{2\kappa_5^2}\int_{\mathcal{M}_4} d^4x\,\sqrt{-\det g_4} \\ \times\left[\exp(\phi)\mathcal{R}_4 + \frac{1}{4}\exp(3\phi)F^{\mu\nu}F_{\mu\nu} - 2\nabla^\mu\nabla_\mu\exp(\phi)\right]. \end{aligned} \tag{2.13}$$

Although the physics is readily apparent, this result is not quite in canonical form. After making the Weyl transformation $g \to \exp(-\phi)g$ and a rescaling $\phi \to \phi/\sqrt{3}$,

we recover the canonical action in the Einstein frame:

$$S_4 = \frac{1}{2\kappa_4^2}\int_{\mathcal{M}_4} d^4x\,\sqrt{-\det g_4}\,\left[-\mathcal{R}_4^{\text{E.H.}} + \frac{1}{2}\nabla^\mu\phi\nabla_\mu\phi - \frac{1}{4}\exp\left(\phi/\sqrt{3}\right)F^{\mu\nu}F_{\mu\nu}\right] \tag{2.14}$$

where we have defined the 4d gravitational constant as $\kappa_4^2 \equiv \kappa_5^2/(2\pi r)$.

Thus, we see that pure gravity in 5d - upon dimensional reduction - looks in 4d like gravity and a $U(1)$ gauge theory such as electromagnetism. Furthermore, we have an additional massless scalar field which, as we have described earlier, parametrizes the size of the extra dimension. In the low energy action, we also see that the VEV of ϕ sets the coupling, g^{-2}, of the gauge kinetic term, $-\frac{1}{4g^2}F^{\mu\nu}F_{\mu\nu}$. The field ϕ is typically labeled as a "radion" or a "dilaton"[1] in Kaluza-Klein theory. For our purposes, we can also refer to this field as a "modulus" in the sense that it is a massless scalar at the classical level.

2.1.2 Massive scalars in 4d from massless scalars in 5d

Before we discuss string compactifications, it is worthwhile to present one more dimensional reduction in Kaluza-Klein theory. Let us now consider a massless scalar field Φ in the above 5d framework - which bears no relation to the ϕ field we encountered in the previous example. Assuming the flat-space limit for simplicity,

[1]The dilaton of Kaluza-Klein theory is similar to the dilaton of string theory in that both describe the size of a compact dimension. In Type IIa string theory, the dilaton appears from compactification of M-theory on a circle.

the action of the free scalar is given by

$$S_\Phi = \int_{\mathcal{M}_4} d^4x \int_{\mathcal{M}_{S^1}} dy \left[\frac{1}{2}\partial_M \Phi\, \partial^M \Phi\right]. \tag{2.15}$$

Since the compact dimension y can be viewed as periodic with a period $2\pi r$ (where r is again the radius of the compact dimension), let us make a Fourier expansion of Φ:

$$\Phi(x,y) = \frac{1}{\sqrt{2\pi r}} \sum_n \phi_n(x) \exp\left(\frac{iny}{r}\right) \tag{2.16}$$

where $1/\sqrt{2\pi r}$ is the normalization factor. Using this expansion, the action can then be written as

$$S_\Phi = \sum_{n,m} \int_{\mathcal{M}_4} d^4x \int_{\mathcal{M}_{S^1}} dy \, \exp\left(\frac{i(n+m)y}{r}\right) \times \frac{1}{2\pi r}\left[\frac{1}{2}\partial_\mu \phi_n(x)\, \partial^\mu \phi_m(x) + \frac{1}{2}\frac{nm}{r^2}\phi_n(x)\phi_m(x)\right]. \tag{2.17}$$

Evaluating the dy integral over $\mathcal{M}_{S^1} = [0, 2\pi r)$ thus reduces the action to

$$S_\Phi = \sum_n \int_{\mathcal{M}_4} d^4x \left[\frac{1}{2}\partial_\mu \phi_n(x)\, \partial^\mu \phi_n(x) - \frac{1}{2}\frac{n^2}{r^2}\phi_n^2(x)\right]. \tag{2.18}$$

It is immediately clear that, although in 5d our theory had a single massless scalar, from the perspective of 4d we have one massless scalar (corresponding to the $n = 0$ case) and an *infinite tower* of massive modes with masses $m^2 = n^2/r^2$. Furthermore, if we take the compact dimension to be of order of the Planck length, then each of the massive scalars would be at least of order m_P! In most cases,

one would expect the resulting 4d effective theory would then be most simply described once these massive modes are integrated out - they are typically far too massive to be relevant.

Comparing results between the previous two explicit compactification examples, we see that massless scalars in the 4d theory can parameterize deformations in the metric, but may also come from massless scalars in the 5d theory where some fundamental symmetry prevents the 5d scalar from acquiring a mass. Following the literature, we refer to these as geometric and non-geometric moduli, respectively. However, in either case, massless scalars present a significant phenomenological problem. Specifically, massless scalars are expected to be cosmologically stable, and are expected to mediate Yukawa-type interactions - leading to a fifth force that is not observed (see e.g. [91, 92] for reviews of theoretical and experimental constraints). These moduli must then acquire a mass (i.e. they must be stabilized) for phenomenological viability.[2] Many other model-dependent issues also arise in this class of models, including modifications to the standard Friedmann-Robertson-Walker (FRW) cosmology [93, 94] or a contracting universe [95].

2.2 The many moduli from string theory

We saw in the previous section how dimensional reduction of a 5d theory to a 4d theory introduced a modulus - which parametrizes the size of the extra dimension

[2] In simple Kaluza-Klein models, quantum corrections in the effective theory tend to provide a mass for the massless scalars. However, in string theory, these corrections which are expected to stabilize the moduli might be incalculable (depending on the regime of interest) as a consequence of the Dine-Seiberg problem, which will be discussed shortly.

- and introduced a low energy gauge theory from pure gravity. By discussing this level of technical detail in the simpler setting of 5d, we are now in a position to productively discuss the far more complicated case of moduli from string theory without requiring explicit computation. It is well known [17, 18, 96, 19, 97, 98] that in string theory, anomaly cancellation requires a spacetime dimension $D = 10$. For a low energy description of string theory that matches physical observation, it is then a phenomenological requirement that the 10d manifold decomposes under compactification as

$$\mathcal{M}_{10} = \mathcal{M}_4 \times \mathcal{M}_6 \tag{2.19}$$

where, similar to the 5d Kaluza-Klein case, $\mathcal{M}_6$ is a 6d compact manifold while $\mathcal{M}_4$ is non-compact.

However, it is not phenomenologically sufficient to simply choose *any* 6d compact space - requiring $\mathcal{M}_4$ to support chiral matter places a considerable constraint on the compactification manifold $\mathcal{M}_6$. Physically, we expect the low energy theory to contain massless fermions (at least, above the EWSB scale) which imposes the requirement that spinors in $\mathcal{M}_6$ are covariantly constant. Since the requirement on spinors to be covariantly constant is linked to the holonomy of the compactification manifold, phenomenology requires $SU(3)$ holonomy for a 6d compactification manifold and thus requires compactification on a Calabi-Yau threefold (see e.g. [97, 98, 96, 19, 18] for additional details and motivation). Similar conditions occur for compactification of M-theory. Since M-theory must have spacetime dimension $D = 11$, the phenomenological requirement of a covariantly

constant spinor on the 7d compact space requires a manifold with G_2 holonomy.

2.2.1 Moduli space of string theory

As one might suspect, the moduli space of string theory is far richer and more complex than a simple extension of the 5d Kaluza-Klein model to 10d. For our purposes, it is useful to deal with the supergravity limit of string theory - so that only the massless string modes are excited. Before we discuss the full moduli space in the supergravity limit, we first present the Type IIb supergravity action in 10d. This will then allow us to proceed with an outline of the generalization of Kaluza-Klein reductions to a 6d Calabi-Yau space - at least in the context of Type IIb supergravity.

In the conventions of [99, 19, 100], the 10d bosonic action for Type IIb supergravity in the string frame is given by

$$\begin{aligned}
S_{\rm NS} &= \frac{1}{2\kappa_{10}^2}\int d^{10}x\,\sqrt{-\det g_{10}}\,e^{-2\phi}\left[\mathcal{R}_{10}+4\,(\partial\phi)^2-\frac{1}{2}|H_3|^2\right]\\
S_{\rm RR} &= -\frac{1}{4\kappa_{10}^2}\int d^{10}x\,\sqrt{-\det g_{10}}\left[|F_1|^2+|\tilde{F}_3|^2+\frac{1}{2}|\tilde{F}_5|^2\right]\\
S_{\rm CS} &= -\frac{1}{4\kappa_{10}^2}\int C_4\wedge H_3\wedge F_3\\
S_{\rm IIb} &= S_{\rm NS}+S_{\rm RR}+S_{\rm CS}+S_{\rm loc}.
\end{aligned} \tag{2.20}$$

Here, we see that the Neveu-Schwarz (NS) sector action $S_{\rm NS}$ contains gravity, the dilaton ϕ, and the 3-form $H_3 \equiv dB_2$ - as expected from the decomposition of the massless string spectrum [19]. In the Ramond-Ramond (RR) sector, the Type

IIb massless modes contain the p-form fields C_p for $p = 0, 2, 4$. Correspondingly, the RR sector action $S_{\rm RR}$ can be built from the corresponding field strengths $F_{p+1} = dC_p$, which is in essence a generalization of a gauge theory in 10d. Following [19, 100], we have defined $\tilde{F}_3 \equiv F_3 - C_0 \wedge H_3$ and $\tilde{F}_5 \equiv F_5 - \frac{1}{2} C_2 \wedge H_3 + \frac{1}{2} B_2 \wedge F_3$. The equations of motion for the four-form are consistent with the self-duality constraint, $\tilde{F}_5 = \star \tilde{F}_5$, which must be imposed on the solutions [19, 101, 102]. The third contribution to the action is the Chern-Simons term $S_{\rm CS}$. Finally, we have included a term $S_{\rm loc}$ to account for local effects in the theory - namely the localized effects of the presence of branes in the theory. We do not display these (model-dependent) terms here, but simply note that these introduce a super-Yang-Mills sector in the 10d low energy limit.

After a Weyl rescaling of the metric to the Einstein frame, the Type IIb action becomes

$$S_{\rm IIb} = \frac{1}{2\kappa_{10}^2} \int d^{10}x \sqrt{-\det \tilde{g}_{10}} \left[\mathcal{R}_{10}^{\rm E.H.} - \frac{|\partial S|^2}{2\,(\mathrm{Re}(S))^2} - \frac{|G_3|^2}{2\ \mathrm{Re}(S)} - \frac{|\tilde{F}_5|^2}{4} \right] - \frac{i}{\kappa_{10}^2} \int \frac{C_4 \wedge G_3 \wedge \overline{G}_3}{\mathrm{Re}(S)} + S_{\rm loc} \quad (2.21)$$

where, following [19], we define[3] the axio-dilaton:

$$S \equiv e^{-\phi} - i C_0 \quad (2.22)$$

[3]Our definition of the axio-dilaton here is rotated by $-i$ compared to [19] to match later conventions.

and the 3-form

$$G_3 \equiv F_3 + iSH_3. \tag{2.23}$$

These quantities will be important when discussing flux compactifications in Sec. (2.3.1).

It is worth reiterating that the supergravity actions listed above are only valid below the string scale M_s, so that the massive string states can be integrated out. There are two perturbative expansions that lead to g_s (string loop) and α' (curvature) corrections which must be considered in order to ensure that the theory has perturbative control and thus that the low energy supergravity limit is a valid approximation. First, the string coupling g_s (which is set by the VEV of the dilaton) must be weak, i.e. $g_s \ll 1$, so that the g_s expansion is sensible.[4] Second, the spacetime curvature must be small compared to the string scale for the α' expansion to be computed.[5] To make matters more difficult, Dine and Seiberg argue in [104] that in order to obtain the expected value of unified gauge couplings in the (MS)SM at the GUT scale, considering a weakly-interacting string theory ($g_s \ll 1$ so that the g_s expansion is under control) then implies the size - and hence radius of curvature - of the compact manifold is relatively small compared to the string length scale, thus causing the α' expansion to break down and invalidating the effective theory approach. In addition, if one considers a large compactification

[4]There are, of course, dualities that relate the five string theories amongst themselves. In the case of strong coupling, one might suspect that the Type IIb string - which is S-dual to itself - could simply be rewritten exploiting this duality. Doing so, however, would invalidate the previous supergravity approximation and require a new supergravity action in this regime.

[5]This is due to the fact that, in flat space, one can compute the spectrum of the theory by simply using the free theory. In curved space, this is (in general) no longer the case - however, if the curvature is small in string units, one can sensibly define a perturbation series and use known methods for calculations. [103]

manifold, non-perturbative effects are expected to induce a runaway to either the decompactification limit or the zero-coupling limit. Dine and Seiberg further argue in [105] that, based on general assumptions relating the expected string coupling to the vacuum energy, one cannot expect to construct a stable deSitter vacuum (although *metastable* deSitter vacua are allowed). Collectively, this is referred to as the Dine-Seiberg problem - and can be elegantly summed up in the phrase [106], "when corrections can be computed, they are not important, and when they are important, they cannot be computed." This is a significant obstacle that any string description (and in particular, any moduli stabilization procedure) must overcome if it claims to reproduce the physics of our universe.

At long last, we are finally ready to describe the moduli in string theory. As with the Kaluza-Klein example, the moduli here are related to the metric of the internal space - albeit in a much more complex manner. Since we are assuming compactification on a Calabi-Yau threefold, we use complexified coordinates, dz^i and $d\bar{z}^{\bar{\jmath}}$, on the manifold. The moduli then correspond to deformations of the (Hermitian) metric that preserves both the Ricci-flatness of the manifold and Hermiticity of the metric. A general metric deformation can be written as [99]

$$\delta g = \delta g_{i\bar{\jmath}}\, dz^i\, d\bar{z}^{\bar{\jmath}} + \delta g_{ij}\, dz^i\, dz^j + \text{c.c.} \tag{2.24}$$

Imposing the Ricci-flatness condition $R_{i\bar{\jmath}} = 0$ on the deformation shows that the $\delta g_{i\bar{\jmath}}$ and $\delta g_{ij} + \text{c.c.}$ deformations decouple.

The first set of deformations $\delta g_{i\bar{\jmath}}$ can then be understood equivalently as

deformations in the Kähler form, J, of the metric, g:

$$\delta J = i\,\delta g_{i\bar{\jmath}}\, dz^i \wedge d\bar{z}^{\bar{\jmath}} \tag{2.25}$$

and are referred to as the Kähler moduli. For the deformations of Kähler form that we are interested in, δJ is a harmonic $(1,1)$-form and thus we can write

$$J \in H^{1,1}_{\bar{\partial}}(\mathcal{M}). \tag{2.26}$$

Here, $H^{1,1}_{\bar{\partial}}(\mathcal{M})$ is the Dolbeault cohomology group of (complex) dimension $(1,1)$ and is required to adequately describe our coordinate choices on the Calabi-Yau manifold $\mathcal{M}$. Unlike our simple 5d Kaluza-Klein example where the topology was trivial, Calabi-Yau manifolds have a non-trivial topology and thus coordinates are not globally well-defined; the Dolbeault cohomology group provides us with the required topological information to properly perform the dimensional reductions. Since the dimension of $H^{(1,1)}_{\bar{\partial}}(\mathcal{M})$ is given by the Hodge number $h^{1,1}$ of the Calabi-Yau, there should thus be $h^{1,1}$ Kähler moduli. It is then convenient to parametrize the moduli by introducing the $h^{1,1}$ harmonic $(1,1)$-forms ω^i that form a basis for $H^{1,1}_{\bar{\partial}}$. We can then write

$$J = t^i(x)\,\omega_i \tag{2.27}$$

where $t^i(x)$ are the 2-cycle moduli [99, 18]. Through Poincaré duality, elements of $H^{1,1}_{\bar{\partial}}(\mathcal{M})$ are related to elements of $H^{2,2}_{\bar{\partial}}(\mathcal{M})$ on a Calabi-Yau manifold [99, 107, 18, 17], providing a relation between the 2-cycle moduli t^i and the 4-cycle moduli

(conventionally denoted by τ_i).

It is useful to briefly discuss the relations between the 2-cycle and 4-cycle moduli since, for our purposes, the 4-cycle moduli are more convenient for our phenomenological work while the 2-cycle moduli are more convenient for our discussion of the origin of the Kähler moduli. Since the Kähler form is a nowhere-vanishing $(1,1)$-form, it is a natural volume measure [108, 109]. The volume of the compactification manifold in terms of the 2-cycle moduli t^i is then given by

$$\mathcal{V} = \frac{1}{3!}\int_{\mathcal{M}_6} J \wedge J \wedge J = \frac{1}{6}\kappa_{ijk} t^i t^j t^k \tag{2.28}$$

where κ_{ijk} are the (fully symmetric) triple-intersection numbers of the manifold [110, 109]. Each of the 4-cycle moduli are then the volumes of the respective 4-cycles they parametrize, and are given by

$$\tau_i = \frac{1}{2}\int_{c_i} J \wedge J \tag{2.29}$$

where c_i is the relevant 4-cycle. The 2-cycle moduli can then be related to the 4-cycle moduli by the relation

$$\tau_i = \frac{\partial \mathcal{V}}{\partial t^i} = \frac{1}{2}\kappa_{ijk}\, t^j t^k. \tag{2.30}$$

The other set of metric deformations, $\delta g_{ij} + \text{c.c.}$, must induce a change in the complex structure $\mathcal{J} \to \mathcal{J} + \delta\mathcal{J}$ in order to preserve Hermiticity of the metric. This shift in the complex structure can be used to build a harmonic $(2,1)$-form χ

as

$$\chi = \Omega_{ijk}\, \delta \mathcal{J}_{\bar{l}}^{k}\, dz^i \wedge dz^j \wedge d\bar{z}^{\bar{l}} = \Omega_{ijk}\, \delta g_{\overline{hl}}\, g^{k\bar{h}}\, dz^i \wedge dz^j \wedge d\bar{z}^{\bar{l}} \tag{2.31}$$

where Ω is the unique non-vanishing $(3,0)$-form on the Calabi-Yau [99, 107, 18, 17]. Since the form χ is harmonic, then

$$\chi \in H_{\bar{\partial}}^{2,1}(\mathcal{M}) \tag{2.32}$$

where $H_{\bar{\partial}}^{2,1}(\mathcal{M})$ is the Dolbeault cohomology group of (complex) dimension $(2,1)$. The dimension of $H_{\bar{\partial}}^{2,1}(\mathcal{M})$ is given by the Hodge number $h^{2,1}$, and we therefore expect $h^{2,1}$ complex structure moduli. We can then parametrize the complex structure moduli as [99]

$$\delta g_{\bar{i}\bar{j}}^{A} = c\zeta^{A}(x)\, (\chi_A)_{\bar{i}}^{kl}\, \overline{\Omega}_{\bar{j}}^{kl} \tag{2.33}$$

where c is a normalization constant and $\zeta^A(x)$ are the complex structure moduli.

Now that we have finally encountered (some of) the moduli of string theory, let us briefly make contact with our main discussion of the 4d theory. Taking analogy to our example in Sec. (2.1.1), we would expect from Eq. (2.21) that the $h^{1,1}$ Kähler moduli and $h^{2,1}$ complex structure moduli to appear as massless scalars in the 4d theory due to the dimensional reduction of gravity $\mathcal{R}_{10}^{\text{E.H.}}$ to $\mathcal{R}_{4}^{\text{E.H.}}$. In addition to the geometric moduli we have just described above, there are also non-geometric moduli. As can be seen from Eq. (2.21), the axio-dilaton is one such field; drawing analogy to our example in Sec. (2.1.2) we would expect the axio-dilaton to show up in the low energy theory as a massless scalar with a

corresponding tower of massive modes.

However, we have not yet discussed the reduction of the gauge fields in Eq. (2.21), such as e.g. $|\tilde{F}_5|^2 \equiv \tilde{F}_5 \wedge \star\tilde{F}_5 \supset dC_4 \wedge \star dC_4$. Utilizing the metric decomposition ansatz, we decompose these forms into 4d and 6d components as e.g.

$$C_4^{(10)} = C_4^{(4)} + c^i(x)\,\tilde{\omega}_i \tag{2.34}$$

where we denote the 10d and 4d 4-forms as $C_4^{(10)}$ and $C_4^{(4)}$ respectively, and have expanded the 6d form in a basis of harmonic $(2,2)$-forms $\tilde{\omega}_i \in H^{2,2}_{\bar{\partial}}$. Focusing on the 6d form, the action becomes

$$S_{\tilde{F}_5} \supset -\frac{1}{8\kappa_{10}^2}\int_{\mathcal{M}_4} d^4x\,\sqrt{-\det g_4}\int_{\mathcal{M}_6}\tilde{\omega}^\alpha \wedge \star_6\,\tilde{\omega}^\beta\left[\frac{1}{4!}\partial_\mu c_\alpha(x)\,\partial^\mu c_\beta(x)\right]. \tag{2.35}$$

As the fields $c_{\alpha,\beta}(x)$ depend on the 4d coordinates only, the 4d action can be trivially isolated - even if the dimensional reduction of $\tilde{\omega}^\alpha \wedge \star_6\,\tilde{\omega}^\beta$ is highly non-trivial. In the 4d theory, we see that the reduction of each of the 10d gauge fields leads to $h^{2,2} = h^{1,1}$ massless scalars since the remaining 6d integral simply provides a field-space metric describing a σ-model. These moduli possess a distinctive continuous shift symmetry, $c_i \to c_i + a$ with a some constant, which is a remnant of the original 10d gauge symmetry. First pointed out by Witten [111] in the context of the heterotic string, the shift symmetry motivates the identification of these particular moduli with axions, which also possess a continuous shift symmetry (at least, for energies above $\Lambda_{\rm QCD} \sim 200$ MeV at which point QCD instantons explicitly break the continuous shift symmetry to a discrete shift symmetry [112]).

Depending on the topological structure of the compactification manifold, this provides potentially hundreds [113, 114] of axion-like particles (ALPs) that may remain in the low energy spectrum - leading to the picture of the string axiverse [115, 116].

As a brief technical aside, we must give mention to orientifolding in the Type II string context. Since Type II strings produce a low energy supergravity theory with $\mathcal{N} = 2$ supersymmetry [19], phenomenology demands this to be broken to $\mathcal{N} = 1$ supersymmetry as $\mathcal{N} = 2$ supersymmetry does not support chiral matter [13]. This is accomplished through use of $O3/O7$ orientifold planes. A complete discussion of orientifold planes is beyond the scope of this work (see e.g. [96, 19, 18] for a more complete treatment), but for the scope of this work it suffices to note that orientifold planes are extended, non-dynamical objects with negative tension that produce unoriented strings and break $\mathcal{N} = 2$ supersymmetry to $\mathcal{N} = 1$ supersymmetry. This also affects the moduli space in a model-dependent way. Under the orientifold action, the cohomology group $H^{1,1}_{\bar{\partial}}$ is broken into

$$H^{1,1}_{\bar{\partial}} = H^{1,1}_{+} \oplus H^{1,1}_{-} \tag{2.36}$$

where the $h^{1,1}_{+}$ elements of $H^{1,1}_{+}$ are even under orientifolding, while the $h^{1,1}_{-}$ elements of $H^{1,1}_{-}$ are odd under orientifolding. This projects out of the spectrum a subset of each of the moduli we have described above, although the decomposition in Eq. (2.36) - and therefore $h^{1,1}_{+}$ and $h^{1,1}_{-}$ - are model-dependent [18]. Once the $\mathcal{N} = 2$ supersymmetry is broken to $\mathcal{N} = 1$ supersymmetry, it is conventional to

complexify the Kähler moduli with the C_4 axions so that our Kähler coordinates are given by $T_i = \tau_i + ic_i$.

As shown by Candelas and Ossa [117], the moduli arising from compactifications on Calabi-Yau manifolds can also be described in a 4d supergravity theory with the Kähler potential

$$K_0 = -2\log(\mathcal{V}) - \log\left(S + \overline{S}\right) - \log\left(-i\int_{\mathcal{M}_6} \Omega \wedge \overline{\Omega}\right) \tag{2.37}$$

where g_s and α' corrections have been neglected. Here, the Calabi-Yau volume $\mathcal{V}$ is in terms of the complexified Kähler moduli T_i, while the second and third terms correspond to the contributions of the dilaton and the complex structure moduli, respectively. This form survives through both orientifolding and the addition of fluxes (i.e. the inclusion of the $|G_3|^2/2\mathrm{Re}(S)$ term in Eq. (2.21)) as shown by Giddings, Kachru, and Polchinski [100] - although the inclusion of fluxes will induce warping of the geometry and thus induce a potential for the complex structure moduli in the 4d theory. The addition of fluxes can be described by the flux superpotential (also known as the Gukov-Vafa-Witten superpotential) [118, 119, 100]

$$W_0 = \int_{\mathcal{M}_6} G_3 \wedge \Omega. \tag{2.38}$$

We will discuss the flux superpotential in more detail when discussing moduli stabilization of the complex structure moduli. Although a far more technical result than in our 5d example, the 4d effective supergravity action specified by the above Kähler potential and superpotential accounts for the Kähler moduli,

complex structure moduli, and the dilaton, in addition to the axionic contributions from the RR field C_4 and the flux contributions from G_3 (which is - by definition - related to the $H_3 = dB_2$ and F_3 forms, as well as the axio-dilaton). Ignoring for the moment any local contributions to the action $S_{\rm loc}$, this 4d supergravity action then accounts for all the moduli we would naively expect to appear from Eq. (2.21).

Finally, we briefly discuss local contributions to the action - specifically the inclusion of branes and open string sectors. The action for a Dp-brane is given by the Dirac-Born-Infeld (DBI) action [99]:

$$S_{\rm DBI} = -g_s T_p \int d^{p+1}\sigma\, e^{-\phi} \sqrt{-\det\left(G_{ab} + \mathcal{F}_{ab}\right)} \tag{2.39}$$

where the action is integrated over the worldvolume of the Dp-brane. Additionally, $\mathcal{F}_{ab} \equiv B_{ab} + 2\pi\alpha' F_{ab}$ is a gauge-invariant field strength, and G_{ab} and B_{ab} are the pullbacks of the 10d metric and 2-form $B_2^{(10)}$ onto the brane worldvolume, respectively. Quantization of open strings living on the Dp-brane gives rise to a gauge sector F_{ab} residing on the brane and a set of massless scalars which parameterize the open string position on the brane. In the case of a stack of branes, the gauge sector is that of an $SU(N)$ super Yang-Mills theory [120]. Since Dp-branes are charged under the RR sector gauge symmetry, $C_{p+1} \to C_{p+1} + d\alpha_p$, we have also the Chern-Simons coupling [99]:

$$S_{\rm CS} = i\mu_p \int_{\Sigma_{p+1}} \sum_n C_n \wedge \exp(\mathcal{F}). \tag{2.40}$$

The reduction of these actions can be expressed by the DeWolfe-Giddings Kähler potential [121] (see also [122, 123]), which for compact volumes well-described by a single Kähler modulus takes the form:

$$K = -3\log\left(T + \overline{T} - k(z_\alpha, \overline{z}_\alpha)\right) \tag{2.41}$$

where $k(z_\alpha, \overline{z}_\alpha)$ is the contribution from the massless complex scalars z_α which are typically taken to be visible sector fields [121, 124], and parameterize the brane position. In addition to possessing no-scale structure [125], this Kähler potential allows for sequestering of soft terms which will be discussed in more detail in Sec. (2.4). This class of open string moduli residing on Dp branes is a conventional way of model-building the MSSM field content in Type IIb string models [126, 127, 128] due to the appearance of a super Yang-Mills gauge theory with scalars (and fermionic partners by supersymmetry) charged under the gauge symmetry.

2.3 Moduli stabilization

Now that we have discussed the naive moduli content appearing in the low energy theory, we now turn to the topic of moduli stabilization. Although quantum corrections are expected to lift any flat directions, due to the aforementioned Dine-Seiberg problem [105, 104] the calculation of these corrections is exceedingly difficult - if not (in various regimes) impossible. We focus here on the leading proposals in Type IIb string theory, and provide some mention to moduli sta-

bilization in heterotic constructions - which is far less understood than in the Type IIb context. We begin with discussion of the stabilization of the complex structure moduli and axio-dilaton from flux compactification, then proceed to the two leading proposals to stabilize Kähler moduli.

2.3.1 Flux compactification

Before discussing the topic of flux compactification and its relevance to the complex structure moduli and axio-dilaton in detail, it is useful to first briefly recap the Dirac quantization condition. We therefore begin by the inclusion of a magnetic monopole into Maxwell's equations - i.e. by making the modification

$$\nabla \cdot \mathbf{B} = \rho_m \tag{2.42}$$

while maintaining the definition for the vector potential

$$\mathbf{B} = \nabla \times \mathbf{A}. \tag{2.43}$$

Since $\nabla \cdot (\nabla \times \mathbf{A}) = 0$ in coordinate patches where $\mathbf{A}$ is well-defined, the result $\nabla \cdot \mathbf{B} = \rho_m$ can only be obtained if $\mathbf{A}$ is *not* globally well-defined. This requires us to define multiple regions each with their own vector potentials (all related by gauge transformations), which then glue together so that $\mathbf{B}$ is globally well-defined. Making the notational shift to differential forms, i.e. $A \equiv A_i\, dx^i$ and $B = dA$ where d is the usual exterior derivative, we can construct two coordinate patches each with their own vector potential 1-form. In order to have a well-defined

magnetic field, the two 1-forms must only vary by an exact form in the region where both coordinate patches overlap:

$$A_1 - A_2 = d\omega \tag{2.44}$$

where we take $A_{1,2}$ to be the vector potential in regions 1 and 2 (respectively). If some particle with charge e - such as an electron - begins at a point a in region 1 and traverses into region 2 to a point b, it should acquire a phase:

$$\psi \to \exp\left(ie\int_{a\to b} d\omega\right)\psi. \tag{2.45}$$

If the charged particle then traverses back to region 1 and returns to point a, the total phase acquired can be written as

$$\psi \to \exp\left(ie\oint d\omega\right)\psi. \tag{2.46}$$

However, since the wavefunction is required to be single-valued we must demand that the total acquired phase vanish. Since $\oint d\omega \in \mathbb{R}\backslash 0$ from our initial assumption that $d\omega$ was non-trivial, we are forced to assume that

$$e\omega = 2\pi n \tag{2.47}$$

for $n \in \mathbb{Z}$, where we have defined $\omega \equiv \oint d\omega$. An equivalent condition follows which will be useful in our discussion of flux quantization. Setting $e = 1$ for simplicity

(or equivalently, absorbing it into ω), we can write the integral in terms of 2-chain boundaries which parameterize the traversal path, then apply Stokes' theorem to arrive at

$$\oint d\omega = \oint (A_1 - A_2) = \int_{\partial c_2} A_1 + \int_{\partial d_2} A_2 = \int_{c_2} dA_1 + \int_{d_2} dA_2 = \int_\Sigma F \tag{2.48}$$

where the 2-cycle Σ is effectively the surface enclosing the traversal path. Thus, we see that an *equivalent* quantization condition is

$$\int_\Sigma F = 2\pi n. \tag{2.49}$$

We therefore see that the presence of magnetic monopoles implies that the electric charge is quantized. More generally, we also see that this quantization condition is forced upon us for any flux F that pierces a non-trivial cycle, which is illustrated in Fig. (2.2).

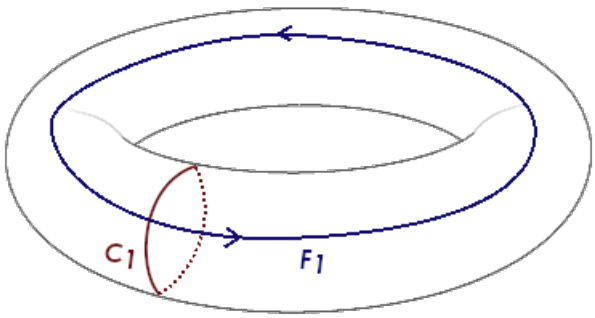


Figure 2.2: A flux F_1 pierces a non-trivial 1-cycle C_1 of the torus T^2.

Returning now to the case of flux compactifications, we saw from Eq. (2.21)

that the 10d action contains the term

$$S_{\text{IIb}} \supset \frac{1}{2\kappa_{10}^2} \int d^{10}x \, \sqrt{-\det \tilde{g}_{10}} \left[-\frac{|G_3|^2}{2\,\text{Re}(S)} \right] \tag{2.50}$$

where $G_3 \equiv F_3 + iSH_3 = dC_2 + iS\,dB_2$. Since these 3-forms are compactified over the non-trivial 3-cycles of the Calabi-Yau, we expect a similar set of quantization conditions to that which we derived from considering magnetic monopoles. This is significant since - once the fluxes are quantized - the integration can be performed over all $h^{2,1}$ of the $(2,1)$-cycles, which provides a potential for the complex structure moduli. Additionally, due to the $\text{Re}(S)^{-1}$ dependence on the axio-dilaton, flux compactifications are expected to also stabilize the axio-dilaton. As shown by Giddings, Kachru, and Polchinski (GKP) [100], the induced superpotential in the 4d effective supergravity theory is of the form postulated by Gukov, Vafa, and Witten [118]:

$$W_0 = \int_{\mathcal{M}_6} G_3 \wedge \Omega_3. \tag{2.51}$$

Following the GKP procedure, we can impose the quantization condition

$$\frac{1}{2\pi\alpha'} \int_A F_3 \in 2\pi\mathbb{Z}, \qquad \frac{1}{2\pi\alpha'} \int_B H_3 \in 2\pi\mathbb{Z} \tag{2.52}$$

where the integrals are understood to be over the relevant 3-cycles of the manifold. Taking the original GKP example where $h^{2,1} = 1$ for simplicity, we can take the integral over the A cycle to have $M \in \mathbb{Z}$ units of F_3 flux while the integral over

the dual B cycle is taken to have $-K \in \mathbb{Z}$ units of H_3 flux.[6] This reduces the flux superpotential to

$$W_0 = (2\pi)^2 \alpha' \left(M \int_B \Omega_3 + iKS \int_A \Omega_3 \right). \tag{2.53}$$

Defining the coordinates

$$z \equiv \int_A \Omega_3, \qquad \mathcal{G}(z) \equiv \int_B \Omega_3 \tag{2.54}$$

so that z now describes the complex structure modulus, this gives us the revealing form of the flux superpotential

$$W_0 = (2\pi)^2 \alpha' \left(M\mathcal{G}(z) + iKSz \right). \tag{2.55}$$

From inspection of the supergravity F-term potential

$$V_F = e^K \left[K^{i\bar{\jmath}} \left(D_i W \right) \left(\overline{D}_{\bar{\jmath}} \overline{W} \right) - 3|W|^2 \right] \tag{2.56}$$

we now expect that the complex structure modulus z and the axio-dilaton S are stabilized. There is a subtle problematic detail in this example: as shown in [100], the complex structure modulus is stabilized at z exponentially small which removes S from the superpotential at $z = 0$, leaving S unstabilized in this vacuum.

[6] We note here that not all charge combinations for multiple fluxes are allowed due to charge conservation of the $D3$ branes. Additionally, the warped geometry does not necessarily allow for all fluxes to be supported on all cycles. We do not focus on these details here as they distract from the main focus of this section, however the original work by GKP [100] and the later review [129] both provide excellent discussions on these points.

This can however be remedied with additional fluxes, which are readily available in more realistic models.

Of course, the quantization requirement combined with charge conservation does not lead to unique combinations of fluxes. As we see from Eq. (2.55), different choices of M and $-K$ will lead to different vacua which are (at least from this vantage point) all equally valid assuming the flux choices satisfy all consistency conditions. This leads to the so-called "flux landscape" or "string theory landscape" of vacua [130, 131, 132, 133], with each vacua giving different low energy physics. Indeed, the number of vacua in realistic compactifications is argued to be finite [134, 135] but exceedingly large - with estimates of the number of flux vacua ranging from $\mathcal{O}(10^{500})$ [136] to $\mathcal{O}(10^{272,000})$ [137]. Given that the scale of (4d, $\mathcal{N} = 1$) supersymmetry breaking is dependent on W_0 in this framework, this motivates the use of statistical studies [133, 131, 5, 138, 139] to uncover generic predictions or salient phenomenological features that flux compactifications may provide. It is, however, possible that some (or perhaps most) of these 4d effective supergravity theories may be inconsistent with string theory [140, 141, 142, 143]. The natural question then arises of whether the MSSM - or at least some form of the SM - are indeed contained in the UV-consistent string landscape or if they instead reside in the so-called "swampland" of 4d supergravity theories which are inconsistent with a UV completion to string theory. In this work, we do not concern ourselves with this issue and simply adopt the optimistic assumption that our models are indeed compatible with the string landscape.

Although we have focused primarily on Type IIb strings here, this methodology

may also have application in heterotic compactifications [129]. Heterotic string constructions may be able to stabilize some complex structure moduli from fluxes [129], although since only the NS flux H_3 is available additional details are required to stabilize all complex structure moduli. In [144], it was shown that constructions with internal gauge fields may be able to stabilize the remaining complex structure moduli in heterotic compactifications. Additionally, it has been proposed by Anderson *et al.* [145] that the gauge bundle required in heterotic compactifications may be sufficient to stabilize all geometric moduli. More work on heterotic moduli stabilization can be found in e.g. [146, 147, 148, 149, 150, 151, 152, 153] while moduli stabilization in M-theory can be found in [154, 155, 156, 157].

2.3.2 The KKLT scheme

In Type IIb models, the Kähler moduli still remain massless at the classical level after turning on fluxes. This is due to the fact that in Type IIb models, the available fluxes are due to the RR forms C_0, C_2, C_4 and the NS form B_2 - which only pierce the "odd-dimensional" cycles of the compactification manifold. The Kähler moduli must therefore be stabilized in a different manner.

One of the most popular Kähler moduli stabilization schemes was developed by Kachru, Kallosh, Linde, and Trivedi [3] (KKLT). This was the first realistic construction to feature both Kähler moduli stabilization and a metastable deSitter (dS) vacuum. After fluxes have stabilized the complex structure moduli and the axio-dilaton, the KKLT approach assumes a tuning of the flux superpotential $W_0 \ll 1$ so that non-perturbative corrections from gaugino condensation

[158, 159] or instanton effects [160] are comparable to the tree-level perturbative superpotential. If W_0 is sufficiently small, the scalar potential then admits an anti-deSitter (AdS), SUSY-preserving minima. In the original work, this AdS minima was uplifted to dS by including a stack of $\overline{D3}$-branes at the tip of a warped throat region [3] which introduces an additional potential contribution and breaks supersymmetry.

To see this more clearly, let us elaborate some details. Once the complex structure moduli and axio-dilaton have been stabilized, we can integrate out these terms which leaves a constant superpotential $W \supset W_0$. At the perturbative level, the shift symmetry of the Kähler moduli $T_i \to T_i + i\alpha$ (which arises as a remnant of the 10d gauge symmetry) prevents them from appearing in the superpotential which is protected by holomorphy. However, the Kähler moduli *can* appear in non-perturbative contributions to the effective superpotential. As discussed in the original work [3], the contributions from gaugino condensation and instanton effects both take effectively the same form:

$$W = W_0 + \sum_i A_i \exp\left(-a_i T_i\right) \tag{2.57}$$

where $a_i = 2\pi$ for instantons and $a_i = 2\pi/N$ for gaugino condensation with N the dimension of the fundamental representation of the condensing gauge group. However, for our discussion it suffices to take both as simply $\mathcal{O}(1)$ parameters.

The Kähler potential then takes the standard no-scale form [125],

$$K = -2\log\mathcal{V} \tag{2.58}$$

where $\mathcal{V}$ is the classical volume of the manifold.

For the purpose of this example, we restrict ourselves to the simplest case, $h^{1,1} = 1$, much as in the original work [3]. The manifold volume in terms of a single 4-cycle modulus is given by Eq. (2.30) which now reads

$$\mathcal{V} = \lambda\tau^{3/2} \tag{2.59}$$

where we have defined $\lambda \equiv 1/(3\sqrt{2\kappa_{111}})$ where κ_{111} is now the only intersection number of the manifold. Complexification of the 4-cycle modulus τ with the reduction of the 4-form gauge field C_4 along the corresponding divisor leads to the Kähler modulus

$$T \equiv \tau + ic \tag{2.60}$$

where, for simplicity, we have absorbed the geometric factor $\lambda^{2/3}$. Thus, the superpotential and Kähler potential take the form

$$W = W_0 + A\exp\left(-aT\right) \tag{2.61}$$

$$K = -3\log\left(T + \overline{T}\right). \tag{2.62}$$

Here, we also make the simplification that a and A are real - the additional phase

will not affect the main point of this discussion. The F-term scalar potential can be computed using the standard supergravity formula, which results in

$$V_F = \frac{\exp(-2a\tau)}{2\tau^2}\left[\frac{1}{3}a^2A^2\tau + aA^2 + aAW_0\exp(a\tau)\right] \tag{2.63}$$

where we have integrated out the axionic component of T in the process. The minimization conditions then read

$$\frac{\partial V_F}{\partial \tau} = 0 = \frac{-2a^2A}{3\tau} - \frac{7aA}{3\tau^2} - \frac{aW_0}{\tau^2}\exp(a\tau) - 2\frac{A}{\tau^3} - 2\frac{W_0}{\tau^3}\exp(a\tau) \tag{2.64}$$

which reduces to the form

$$\left(\frac{2}{3}a\tau + 1\right) = -\frac{W_0}{A}\exp(a\tau). \tag{2.65}$$

This equation in fact *does* have an analytic solution,

$$\langle\tau\rangle = -\frac{1}{a}\mathcal{W}\left(\frac{3W_0}{2A\exp(3/2)}\right) - \frac{3}{2a} \tag{2.66}$$

where $\mathcal{W}(z)$ is the Lambert $\mathcal{W}$-function. For our example, we note that this quantity must be negative to stabilize τ at a positive value given that we have neglected any complex phase associated with A. However, since the Lambert $\mathcal{W}$-function is not defined for arguments below $-1/e$, we immediately have a bound on W_0/A:

$$\frac{|W_0|}{A} < \frac{2}{3}\sqrt{e} \sim 1.1. \tag{2.67}$$

Now that we have a stabilized modulus, let us check to see if SUSY is preserved in this minima. The condition for unbroken/broken SUSY is given by $D_I W \stackrel{?}{=} 0$ evaluated at the minima, where $D_I W$ is the Kähler covariant derivative of the superpotential. Here, the condition reads

$$\langle D_T W \rangle = -A\left(a + \frac{3}{2\tau}\right)\exp(-a\tau) + \frac{3}{2\tau}A\exp(-a\tau)\left(\frac{2}{3}a\tau + 1\right) = 0 \quad (2.68)$$

and thus we see that SUSY is preserved. In the original work [3], the authors instead searched for a stabilized modulus that preserved supersymmetry - making Eq. (2.68) a demand for the minima instead of a consequence as we have done here. Although this is a more pragmatic approach, we will see in the next Kähler moduli stabilization model that not all minima will preserve SUSY.

It is now a simple matter of substituting Eq. (2.66) (or, perhaps more simply, the condition given by Eq. (2.65)) into Eq. (2.63) to reveal that the minima we have found is AdS. Originally, a stack of $\overline{D3}$-branes was placed at the tip of a Klebanov-Strassler [161] throat which was shown to induce a term in the scalar potential $\delta V \sim B_2/\tau^3$ with B_2 a parameter depending on the warp factor. Later work studying this uplifting effect [162, 122] lead to a more precise understanding of the $\overline{D3}$ uplift, producing an uplifting term of the form $\delta V \sim B_1/\tau^2$ where again B_1 is a parameter depending on the warp factor. Fortunately, both B_1 and B_2 are expected to be extremely small due to a large warp factor, otherwise this uplifting effect could destabilize the modulus - leading to a runaway to infinite volume and thus the decompactification limit! In Fig. (2.3), we show the scalar potential

before uplifting (black solid curve) and with both uplifting effects included (blue and green dashed curves).

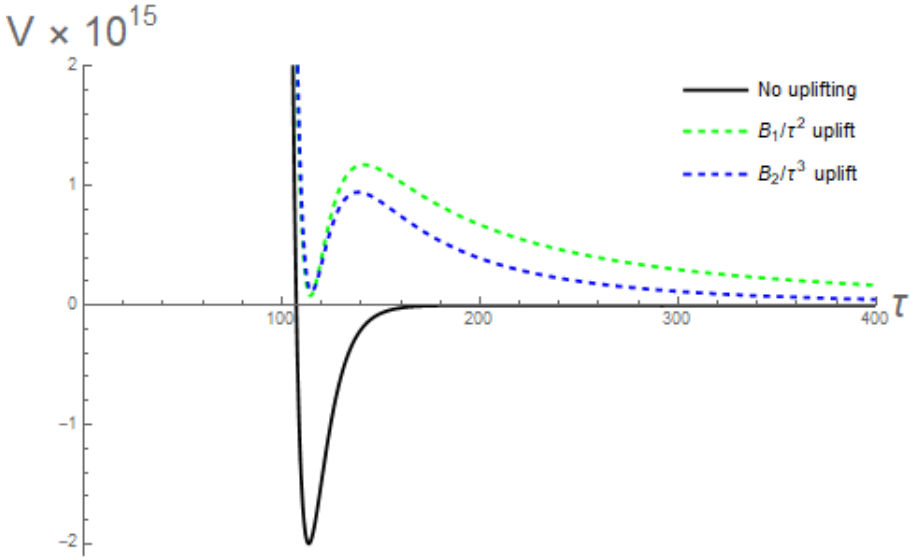


Figure 2.3: The KKLT scalar potential in $m_P = 1$ units (see Eq. (2.63)) for $A = 1$, $a = 0.1$, $W_0 = -10^{-4}$. Uplifting choices have $B_1 = 2.7 \times 10^{-11}$ and $B_2 = 3.15 \times 10^{-9}$. Plot reproduced from [3].

It is also worth mentioning that many variants and generalizations of the KKLT scenario exist in the literature. Although the original work focused on uplifting by $\overline{D3}$-branes, many other uplifting mechanisms exist such as D-term uplifting [163, 164, 165, 166, 167, 168], F-term uplifting [169, 170], and Kähler uplifting [171, 172, 173]. It has also been shown in [174, 175, 176] that the $\overline{D3}$ uplift (which breaks SUSY) can be realized in the nilpotent goldstino formalism, which allows for a supersymmetric formulation of the uplifting effect. Additionally, there are generalizations stabilizing multiple Kähler moduli [177, 178, 179], although as emphasized in [99] it is yet unclear if these situations may be regarded as generic. The KKLT procedure has also been argued [163] to provide viable dS vacua in

heterotic string models, albeit utilizing a D-term uplift as no analogs of $\overline{D3}$ branes exist in this context.

2.3.3 The Large Volume Scenario

The second Kähler moduli stabilization scheme we consider here is the Large Volume Scenario (LVS), which was developed by Conlon *et al.* [180, 181]. The initial setup is similar to KKLT: fluxes stabilize the complex structure moduli and the axio-dilaton, leaving a constant flux superpotential $W \supset W_0$. In LVS however, non-perturbative corrections in the superpotential are balanced against perturbative α' corrections to the Kähler potential. The perturbative corrections within the Kähler potential are computed by expansions in powers of $\mathcal{V}^{-1}$, and by taking $\mathcal{V}$ exponentially large one guarantees the validity of the expansion.

To see this more closely, let us assume the simplest LVS case which has 2 moduli, $T_b = \tau_b + ic_b$ and $T_s = \tau_s + ic_s$, with the geometric hierarchy $\tau_b \gg \tau_s$ so that τ_s is interpreted as a "blow-up mode" - i.e. it resolves a singularity in the Calabi-Yau structure [182, 183]. The volume is assumed to take the form

$$\mathcal{V} \simeq \tau_b^{3/2} - \lambda\tau_s^{3/2} \tag{2.69}$$

and, including leading-order α' corrections to the Kähler potential, we have

$$W = W_0 + A_s \exp(-a_s T_s) + A_b \exp(-a_b T_b) \tag{2.70}$$

$$K = -2\log\left[\mathcal{V} + \frac{\xi}{2}\right] \tag{2.71}$$

where

$$\xi = -\frac{\chi\,\zeta(3)}{2g_s^{3/2}(2\pi)^3} \sim \mathcal{O}(1). \tag{2.72}$$

Here, ξ depends on the Euler number χ of the Calabi-Yau manifold, and g_s follows from the stabilization of the dilaton (i.e. $\xi \equiv \hat{\xi}(S+\overline{S})^{3/2}$ [184, 185, 4]). We assume in this example that there are no additional contributions to the Kähler potential, although in general one expects the additional terms $K \supset K_{\rm matter} + K_{\rm uplift}$, which do not affect the details of stabilization in any significant way. As with the previous example, we again take W_0 and A_s to be purely real - the additional phase does not affect our discussion. Finally, before we calculate the scalar potential, we note that the instanton correction to the big-cycle modulus can be neglected (i.e. we set $A_b \exp(-a_b T_b) \sim 0$) since τ_b is assumed much larger than τ_s, and is thus a highly subleading correction here.

Under these simplifications, it is straightforward to compute the F-term scalar potential from the standard supergravity formula:

$$V_F \simeq e^{K'}\left[\frac{8}{3}\frac{a_s^2 A_s^2}{\lambda}\sqrt{\tau_s}\frac{e^{-2a_s\tau_s}}{\mathcal{V}} - 4a_s A_s W_0 \tau_s \frac{e^{-a_s\tau_s}}{\mathcal{V}^2} + \frac{3\xi W_0^2}{4\mathcal{V}^3}\right] \tag{2.73}$$

where we retain only terms up to $\mathcal{O}(\mathcal{V}^{-3})$ and K' is the remaining Kähler potential which is assumed independent of the Kähler moduli, and we have stabilized the axion c_s in the process. It is clear that both moduli τ_s and τ_b now have a non-vanishing potential - this should not be surprising given the form of the α' corrections in the Kähler potential and our addition of non-perturbative corrections to the small cycle.

We display the scalar potential as a function of τ_s in Fig. (2.4) for $\mathcal{V} = 10^6$. In the limit where $\tau_s \gg 1$, we see that the final term in Eq. (2.73) dominates, yielding an extremely flat potential. Naively, the flatness of the potential in this limit makes the blow-up mode a good candidate for the inflaton. We will discuss this more in Ch. (7).

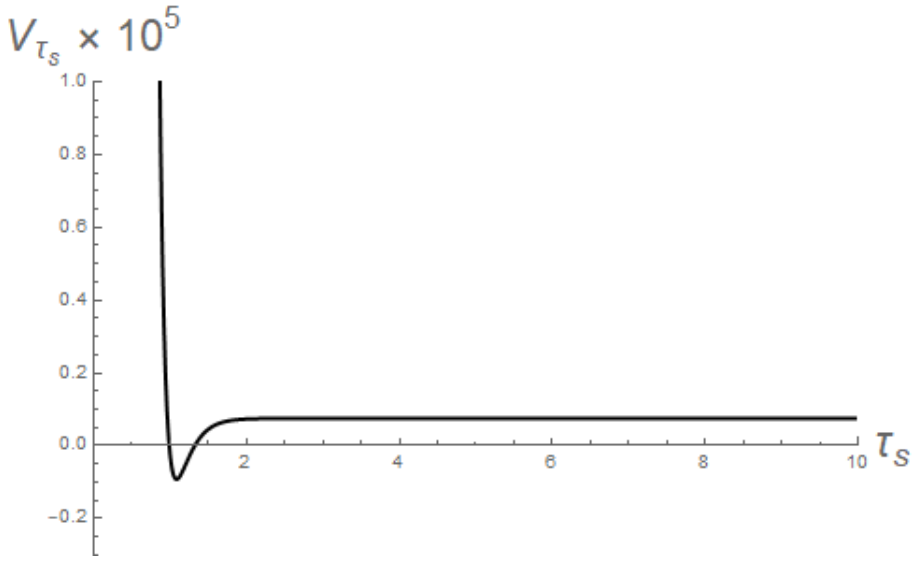


Figure 2.4: The LVS scalar potential in terms of the blow-up mode in $m_P = 1$ units (see Eq. (2.73)), τ_s. We take here the parameter choices $\langle e^{K'} \rangle = 1$, $A_s = \lambda = 1$, $\xi = 1$, $W_0 = 1$, $a_s = 2\pi$, and $\mathcal{V} = 10^2$.

Let us first minimize this potential with respect to τ_s. The minimization condition then becomes

$$\frac{\partial V_F}{\partial \tau_s} = 0 \simeq \left[-\frac{4}{3} \frac{a_s A_s}{\lambda} \sqrt{\tau_s} e^{-a_s \tau_s} + \frac{W_0 \tau_s}{\mathcal{V}} \right] \tag{2.74}$$

which tells us that the small-cycle modulus is stabilized at

$$\langle \tau_s \rangle \simeq \frac{1}{a_s} \log \left[\frac{4 a_s A_s \mathcal{V}}{3 W_0 \lambda} \right] \tag{2.75}$$

where we neglect the second term on the right-hand side, $-\frac{1}{2a_s}\log(\tau_s)$, which is highly subdominant from the assumed hierarchy $\tau_b \gg \tau_s$.

Since we have now stabilized the small cycle modulus, let us briefly check if SUSY is preserved. Taking the condition for unbroken/broken SUSY, i.e. evaluating $D_I W \stackrel{?}{=} 0$ at the minima, we see that

$$\langle D_{T_s} W \rangle \simeq -\frac{3W_0\lambda}{4\langle\mathcal{V}\rangle} + \frac{3}{2\sqrt{a_s}} \frac{\lambda \log^{1/2}\left[\frac{4a_s A_s \langle\mathcal{V}\rangle}{3W_0\lambda}\right]}{\langle\mathcal{V}\rangle + \xi/2} \neq 0. \tag{2.76}$$

Thus, we see that SUSY is broken in this minimum. Let us now proceed to the stabilization of the big-cycle modulus.

Once τ_s is integrated out, we can rewrite the potential as

$$V_F \simeq e^{K'}\left[-\frac{3\lambda}{2a_s^{3/2}}\log^{3/2}\left[\frac{4a_s A_s \mathcal{V}}{3W_0\lambda}\right] + \frac{3\xi}{4}\right]\frac{W_0^2}{\mathcal{V}^3}. \tag{2.77}$$

We display this potential in Fig. (2.5). The minimization for the big-cycle modulus τ_b is effectively the same as the minimization of the volume $\mathcal{V}$ in the large volume limit, and so we consider the minimization condition

$$\frac{\partial V_F}{\partial \mathcal{V}} = 0 \simeq \left[\frac{9\lambda}{2a_s^{3/2}}\log^{3/2}\left[\frac{4a_s A_s \mathcal{V}}{3W_0\lambda}\right] - \frac{9\xi}{4}\right]\frac{W_0^2}{\mathcal{V}^4} \tag{2.78}$$

which tells us that τ_b is stabilized at

$$\langle\mathcal{V}\rangle \simeq \frac{3W_0\lambda}{4a_s A_s}\exp\left(a_s\left(\frac{\xi}{2\lambda}\right)^{2/3}\right) \tag{2.79}$$

and thus, returning to Eq. (2.75), we see that τ_s is stabilized at

$$\langle \tau_s \rangle \simeq \left(\frac{\xi}{2\lambda} \right)^{2/3} \sim \mathcal{O}(g_s^{-1}) \tag{2.80}$$

where we have assumed $\lambda \sim \mathcal{O}(1)$. Finally, let us check if SUSY is broken in the τ_b minima. The SUSY breaking condition reads

$$\langle D_{T_b} W \rangle \simeq -\frac{3}{2} \frac{\langle \tau_b \rangle^{1/2}}{[\langle \mathcal{V} \rangle + \xi/2]} \left[W_0 + \frac{3 W_0 \lambda}{4 a_s \langle \mathcal{V} \rangle} \right] \neq 0. \tag{2.81}$$

As with the τ_s minima, SUSY is broken in the τ_b minima and thus both moduli acquire non-zero F-terms. Furthermore, the value of the potential at the minimum is anti-deSitter.

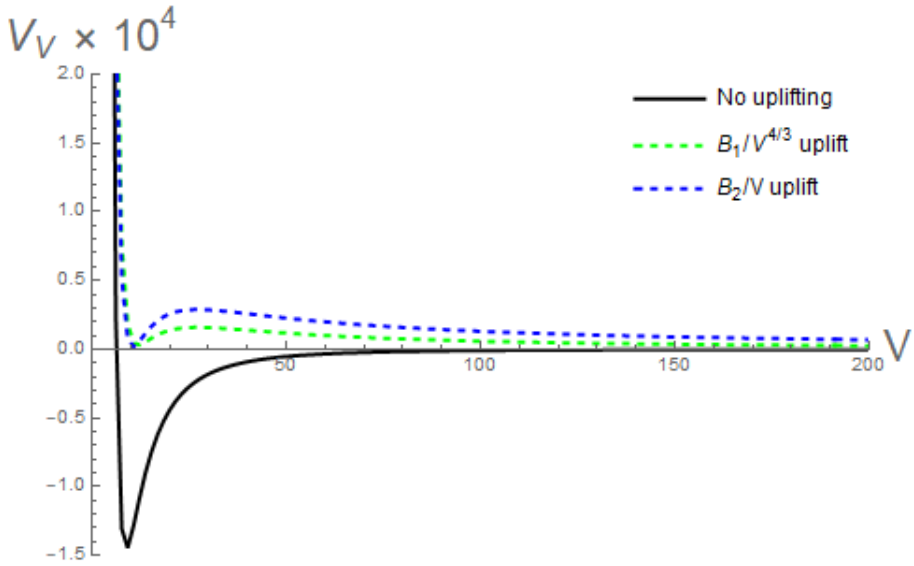


Figure 2.5: The LVS scalar potential (in $m_P = 1$ units) in terms of the volume with τ_s stabilized. Here, our parameter choices are $\langle e^{K'} \rangle = 1$, $A_s = \lambda = 1$, $\xi = 1$, $W_0 = 1$, and $a_s = 2\pi$. We also show two uplifting scenarios motivated by [3] and [4], with $B_1 = 0.00315$ and $B_2 = 0.0014$.

As we have an AdS minima, model-dependent uplifting terms can then be added (as in KKLT) to lift the AdS minima to a dS minima. Much as with the KKLT scenario, it is imperative to construct uplifting scenarios that do not destabilize the moduli. Additionally, uplifting effects can shift the minima of the moduli, and can result in shifts of the soft terms compared to the AdS case [4]. Many uplifting mechanisms in LVS exist, including T-branes [186], non-zero F-terms from complex structure moduli [187], dilaton-dependent non-perturbative effects [188], and (depending on additional model considerations) most if not all uplifting mechanisms that can be applied to KKLT.

We display two examples for uplifting in Fig. (2.5). The first, which we take to be $V_{\rm dS} \sim B_1 \mathcal{V}^{-4/3}$, is of the form of uplifting from $\overline{D}3$-branes at the tip of a warped throat region, similar to the original KKLT uplifting [3]. For our second uplifting scenario, we take the form $V_{\rm dS} \sim B_2 \mathcal{V}^{-1}$ which is motivated from [188] where non-perturbative effects at geometric singularities induce superpotential and Kähler potential terms

$$W_{\rm dS} \sim A_{\rm dS} \exp\left(-a_{\rm dS}(S + \kappa_{\rm dS} T_{\rm dS})\right) \tag{2.82}$$

$$K_{\rm dS} \sim \lambda_{\rm dS} \frac{\tau_{\rm dS}^2}{\mathcal{V}}. \tag{2.83}$$

Once the induced blow-up modulus is stabilized by the hidden sector D-term potential, this leads to the effective scalar potential term $V_{\rm dS} \sim B_2/\mathcal{V}$. For more details and discussion, see e.g. [188, 4].

2.4 Sequestering in string theory

For the purposes of this work, our discussion of string theory would not be complete without a brief mention of the phenomena known as sequestering. In theories with extra dimensions, it is possible [124] to construct models that localize both the Standard Model and the source of SUSY breaking. The effects of SUSY breaking, which can originate from anywhere *other* than the brane that hosts the visible sector, must then be communicated across the bulk geometry. The SM sector then receives a highly suppressed contribution due to the geometric traversal of these effects.

This idea was originally proposed by Randall and Sundrum [124] as a means to solve the SUSY flavor problem. By sequestering the visible sector from the hidden sector, the direct coupling of the two sectors - which leads to dangerous flavor-violating terms - are fundamentally absent. This causes the classical contributions to the squark and slepton masses to vanish, with flavor-symmetric contributions appearing only radiatively through anomaly-mediated contributions. Similarly, other terms such as the $B\mu$ term or problematic CP-violating terms are naturally suppressed, solving other potential issues commonly related to SUSY breaking.

Sequestered Kähler potentials that also possess the desired no-scale structure take the schematic form[7]

$$K = -3\log\left[f_{\text{vis}}(X_i, \overline{X}_i) + g_{\text{hid}}(T_j, \overline{T}_j)\right] \tag{2.84}$$

[7]This is not the most general possible form for Kähler potentials that both exhibit no-scale structure and allow for sequestering, although it suffices for our discussion of the simplest string models. More general forms have been studied in e.g. [189].

where $f_{\rm vis}$ and $g_{\rm hid}$ are unspecified (but suitably analytic) functions of their respective field content. As the two sectors are sequestered from each other, the superpotential is expected to take the form

$$W = W_{\rm vis}(X_i) + W_{\rm hid}(T_j). \tag{2.85}$$

To illustrate how sequestering appears in the low energy effective theory, it is beneficial to show a brief example. Here, we assume for simplicity that each sector contains only a single field, i.e. $W_{\rm vis} \equiv W_{\rm vis}(X)$ and $W_{\rm hid} \equiv W_{\rm hid}(T)$, but our arguments easily generalize to larger visible and/or hidden sectors. Furthermore, we assume here that any visible sector VEVs are negligible compared to those of the hidden sector, and that the visible sector function takes the canonical form

$$f_{\rm vis} \equiv \alpha \overline{X} X \tag{2.86}$$

while we keep $g_{\rm hid}(T, \overline{T})$ arbitrary. Since we demand the visible sector VEVs to be small (or absent) in comparison to the hidden sector VEVs, this motivates the perturbative expansion of Eq. (2.84):

$$K \simeq -3 \log \left[g_{\rm hid}(T, \overline{T}) \right] - \frac{3 f_{\rm vis}(X, \overline{X})}{g_{\rm hid}(T, \overline{T})}. \tag{2.87}$$

The components of the Kähler metric for this example are given by

$$K_{X\overline{X}} = 3\,\frac{\alpha}{g_{\rm hid}} \tag{2.88}$$

$$K_{X\overline{T}} = -3\,\frac{\alpha\,\partial_{\overline{T}} g_{\rm hid}}{g_{\rm hid}^2}\overline{X} \tag{2.89}$$

$$K_{T\overline{T}} = 3\,\frac{g_{\rm hid} + 2\alpha\overline{X}X}{g_{\rm hid}^3}\,\partial_{\overline{T}} g_{\rm hid}\,\partial_T g_{\rm hid} - 3\,\frac{g_{\rm hid} + \alpha\overline{X}X}{g_{\rm hid}^2}\,\partial_{\overline{T}}\partial_T g_{\rm hid} \tag{2.90}$$

where under our assumptions, the metric becomes diagonal once the fields take on their VEVs. Making the Kähler transformation

$$G \equiv K + \log W + \log W^\dagger, \tag{2.91}$$

the visible scalar mass matrix has the diagonal elements [190]

$$m^2_{X\overline{X}} = \langle e^G \left[\nabla_X G_\mu \nabla_{\overline{X}} G^\mu - R_{X\overline{X}\mu\overline{\nu}} G^\mu G^{\overline{\nu}} + K_{X\overline{X}}\right]\rangle. \tag{2.92}$$

We note in our current example, any contributions to this mass matrix from non-Hermitian terms vanish in the VEV so that $m^2_{XX} = m^2_{\overline{X}\overline{X}} = 0$. Thus, in this example Eq. (2.92) gives the classical value of the squared soft mass. Upon evaluating these quantities in their respective VEVs, we obtain the result

$$m^2_{X\overline{X}} = \frac{3\alpha\, e^G}{g_{\rm hid}}\left[1 - \frac{|\partial_T g_{\rm hid}|^2\left(|\partial_T g_{\rm hid}|^2 + g_{\rm hid}^2\,\frac{|\partial_T W|^2}{9|W|^2} - g_{\rm hid}\left(\partial_{\overline{T}} g_{\rm hid}\,\frac{\partial_T W}{3|W|} + \text{h.c.}\right)\right)}{\left(|\partial_T g_{\rm hid}|^2 - g_{\rm hid}\,\partial_T\partial_{\overline{T}} g_{\rm hid}\right)^2}\right] \tag{2.93}$$

where the VEVs of $W_{\rm hid}$ and $g_{\rm hid}$ are implied. Without specification for $g_{\rm hid}$, we

expect that for generic values of the VEVs, the quantity inside brackets should be roughly $\mathcal{O}(0-1)$. As a crude estimation of the gravitationally-mediated contributions to the scalar mass (which we have assumed to be dominant), we expect that

$$m^2_{X\overline{X}} \lesssim \mathcal{O}\left(\frac{m^2_{3/2}}{\langle g_{\rm hid}\rangle}\right). \tag{2.94}$$

The magnitude of the squared soft mass then depends crucially on the details of the hidden sector, which may result in a large suppression depending on its precise form. If the hidden sector has the form $g_{\rm hid} = T + \overline{T}$ and is absent from the superpotential (as in the case of a Calabi-Yau volume which can be well-described by a single Kähler modulus, which takes on the role of the hidden sector and appears only non-perturbatively in the superpotential) then the term in brackets *vanishes*. In this case, the scalar masses vanish at tree-level - reproducing the result of [124]. In a similar way, the gaugino masses in gravity mediation can be computed, which are effectively suppressed by the VEV of $g_{\rm hid}$. Of course, one might then generically expect anomaly-mediated contributions [191, 192] to the soft masses to take precedent.

The structure of soft terms in sequestered string models has been studied extensively [193, 194, 195, 189, 196, 197, 184, 198, 199, 185, 200, 201, 202, 203, 204, 182, 205, 4], and given the plethora of models it is difficult to state any general conclusions as to the pattern of the soft terms. In the context of LVS models, it was shown in [185] that, neglecting uplifting effects, both the leading gravitational and anomaly mediated terms cancel resulting in soft terms arising

from subdominant (suppressed by a factor of $m^2_{\text{string}}/m^2_P$) gravitationally mediated contributions. Depending on the level of sequestering, this can yield either a natural or split SUSY spectrum, referred to as the "ultralocal" and "local" scenarios, respectively. Sensitivity to various uplifting mechanisms in this setting was then studied in [4], which found that, depending on the uplifting mechanism considered, the contributions to the soft terms may be dominant or very mild (and potentially even vanish). Additionally, different uplifting mechanisms were found to predict either universal or non-universal scalar masses in the ultralocal scenario. Furthermore, one might argue that large radiative corrections - which are no longer protected against by supersymmetry - can pull the soft terms to order of the gravitino mass, leading to desequestering. It is, however, possible that this is not necessarily the case in string models. In the context of LVS, [4] argued that due to couplings which are Planck-suppressed, loop corrections may be hierarchically smaller than the classical value. It was also argued in [206, 207] that many physically-separated setups can become desequestered once the backreaction on the geometry is taken into account, however it was argued in [121] that - at least for fields confined to $D3$-branes - such a deformation retains its sequestered form as the solutions remain in the same pseudo-BPS class. Whether or not sequestering is truly viable and generic in string theory remains an open question, although its model-dependent realizations provide rather compelling phenomenology.

2.5 The cosmological moduli problem

We are finally ready to discuss the underlying motivation for the bulk of this work. Given the large number of moduli expected to arise in the 4d theory from string compactifications, it is important to study also their cosmological effects. Major issues related to gravitationally-coupled scalars were first discussed by Coughlan *et al.* [208] in the context of the supergravity Polonyi superpotential. In this seminal work, it was found that strong thermal corrections to the scalar potential displaced the scalar field far from its true minima - but once the temperature falls below the characteristic scale, the scalar "rolls down the potential" towards its true ($T = 0$) minimum. This intriguing behavior leads to cosmological disasters - not only was the scalar field likely to interfere with Big Bang Nucleosynthesis (BBN), but the energy density stored in the scalar field is converted to entropy upon its decay, diluting the baryon-to-photon ratio by an astounding 15 orders of magnitude. This issue, certainly in the context of supergravity models, has been historically coined the "Polonyi problem."

This is very similar to the case of string moduli - during inflation, light moduli are expected to be given large Hubble-induced masses and so are generically displaced far from their true minima [209, 210, 211]. As originally found by Banks *et al.* [212] in the supergravity context and de Carlos *et al.* [213] in the string context, if the moduli are lighter than around $10 - 30$ TeV they decay during BBN while moduli heavier than this (rough) bound may favor low-temperature baryogenesis - with modulus decay possibly even sourcing the baryon

asymmetry. The massive entropy production from modulus decay is, however, likely incompatible with baryogenesis scenarios which occur at high temperatures - with the possible exception of Affleck-Dine baryogenesis [214, 209, 215, 216, 217] which, due to a high efficiency of producing baryon asymmetry, may actually *benefit* from such large entropy production [218]. However, this has prompted new models of baryogenesis which are induced by modulus decay [219, 220, 221, 222, 223, 224]. To make matters worse, it was realized [225, 226, 227, 228, 229, 230] that if the gravitino was an accessible decay of the modulus, BBN considerations from the cascade decay would push the modulus mass to yet larger values. Further yet, the production of dark matter from moduli decay was studied in [231, 232, 233, 234, 235, 236, 237] and found that the produced relic abundance can be satisfied but may also be highly oversaturated depending crucially on the properties of the modulus and the dark matter. As yet one more potentially problematic effect, if moduli are stabilized in a non-supersymmetric fashion (such as in LVS) the shift symmetry of light ALPs may be preserved, leading to substantial dark radiation production from modulus decay [238, 239, 240, 216, 241, 242, 243, 244, 245, 10]. The "cosmological moduli problem" (CMP) - as a moduli-specific version of the original Polonyi problem - then effectively consists of the following parts:

- massive entropy dilution may interfere with BBN if light moduli decay too late,
- if all light moduli decay earlier than BBN, they may still overproduce gravitinos which also may interfere with BBN,

- high-temperature baryogenesis scenarios may be incompatible due to massive entropy production,
- moduli decay may overproduce dark matter, and
- moduli decay may overproduce dark radiation.

Thus, the major aim in this work is to consider the cosmological effects of a light modulus with a natural SUSY spectrum to study the requirements of the modulus to lead to a viable cosmology. Additionally, we will see that matters become even more interesting if one incorporates a supersymmetric DFSZ axion into the model (which allows for a lower Peccei-Quinn scale than the closed string axions from string theory), providing a viable solution to the strong-CP problem.

Chapter 3

The PQMSSM - a brief review

In the next few chapters, we shift focus to the vantage point of supersymmetric models to provide a detailed description of the late-time cosmology before returning to an explicit string realization in Ch. (7). We begin by providing a brief review of the structure of the PQMSSM and previous work done on studying its cosmology in a standard thermal history. We will also briefly review some key results from the perspective of the string landscape, followed by an investigation of statistical predictions from two solutions of the SUSY μ-problem in the context of the string landscape. This chapter thus serves to describe the underlying model which will incorporate a light modulus in the next chapter, and also provide some background description in the standard thermal history of the universe which changes drastically once a modulus is incorporated.[1] The cosmological and phenomenological consequences due to the addition of a post-inflationary light modulus will then be described in the upcoming chapters.

3.1 Structure of the PQMSSM

In this section, we first provide a brief review of radiative natural supersymmetry (RNS) which will serve as our benchmark SUSY model for the following work. We then provide a review of the Giudice-Masiero solution [246] to the SUSY

[1] Of course, a standard thermal history such as in ΛCDM occurs if the lightest modulus decays at or above the inflationary scale. This is the case if the lightest modulus is the inflaton, such as in the model of Sec. (7.3.4).

μ-problem, which will figure prominently into our later work. Following this, we discuss the supersymmetric DFSZ axion and the Kim-Nilles solution [247] to the SUSY μ-problem, which is a highly motivated alternative to the Giudice-Masiero solution. We will also provide a few comments on the axion quality problem.

3.1.1 Radiative Natural Supersymmetry

Although the MSSM is specified by the simple superpotential [1]

$$W_{\rm MSSM} = \mu \hat{H}_u \hat{H}_d + \sum_{i,j=1,3} \left[\lambda_u^{ij} \hat{Q}_i \hat{H}_u \hat{U}_j^c + \lambda_d^{ij} \hat{Q}_i \hat{H}_d \hat{D}_j^c + \lambda_e^{ij} \hat{L}_i \hat{H}_d \hat{E}_j^c \right] \tag{3.1}$$

and supplemented by the set of soft SUSY breaking terms listed in [1], the parameter space is *far* too large to be explored without imposing motivated constraints. Indeed, before any constraints are imposed the MSSM contains around 200 free parameters [1]. Grand Unified Theories (GUTs) based on the incorporation of the MSSM into supergravity frameworks substantially reduces this set (the mSUGRA model [248] is specified by only 5 free parameters [1] - truly a substantial reduction!). Each of these GUTs then predicts the MSSM as its low energy realization, however the phenomenology of the low energy theory varies widely.

In this work, we focus on the framework dubbed "radiative natural supersymmetry" (RNS) which can be incorporated into GUT models with non-universal Higgs masses [249, 250]. RNS is characterized by a mass spectra featuring light ($\sim 100 - 300$ TeV) higgsino-like neutralinos and charginos, gluinos and third-

generation scalars around the TeV scale, and first and second generation scalars at the multi-TeV scale [250]. Another key feature is that a 125 GeV Higgs boson can be generated with very little fine-tuning (specifically, an electroweak fine-tuning measure $\Delta_{\rm EW} \sim 1 - 30$ [250]), which is hardly a universal feature of GUT models featuring weak scale supersymmetry [249]. The motivation for RNS arises from the electroweak symmetry breaking (EWSB) condition which reads [249, 251]

$$\frac{m_Z^2}{2} = \frac{m_{H_d}^2 + \Sigma_d^d - \left(m_{H_u}^2 + \Sigma_u^u\right)\tan^2\beta}{\tan^2\beta - 1} - \mu^2 \simeq -m_{H_u}^2 - \Sigma_u^u - \mu^2 \tag{3.2}$$

where $\tan\beta \equiv v_u/v_d$, μ is the SUSY μ parameter, m_{H_d} and m_{H_u} are the (non-universal) Higgs soft masses, and Σ_u^u and Σ_d^d contain an assortment of radiative corrections. As explained in [250], the electroweak fine-tuning measure $\Delta_{\rm EW}$ is defined as

$$\Delta_{\rm EW} \equiv \frac{|\text{max RHS contribution}|}{m_Z^2/2} \tag{3.3}$$

since - in the absence of fine-tuning - one expects that all terms involved in EWSB are roughly the same order as $m_Z^2/2$. The measure is particularly sensitive to the radiative corrections appearing in Σ_u^u, which are dominated by contributions from the top squarks [249] and takes the form [250]:

$$\Sigma_u^u(\widetilde{t}_{1,2}) = \frac{3}{16\pi^2}F(m_{\widetilde{t}_{1,2}}^2)\left[f_t^2 - g_Z^2 \mp \frac{f_t^2 A_t^2 - 8g_Z^2(\frac{1}{4} - \frac{2}{3}x_W)\Delta_t}{m_{\widetilde{t}_2}^2 - m_{\widetilde{t}_1}^2}\right] \tag{3.4}$$

where f_t is the top quark Yukawa coupling, $x_W \equiv \sin^2\theta_W$, and $\Delta_t \equiv (m_{\widetilde{t}_L}^2 - m_{\widetilde{t}_R}^2)/2 + m_Z^2\cos 2\beta(\frac{1}{4} - \frac{2}{3}x_W)$. For a large value of the trilinear coupling $|A_t|$, the

top squark mass splitting becomes larger [1] - however the term in brackets in Eq. (3.4) exhibits a cancellation for the $\widetilde{t}_1$ contribution. Additionally, the large splitting also leads to a suppression of the $F(m^2_{\widetilde{t}_2})$ term in the $\widetilde{t}_2$ contribution [250] - so that the dominant contributions to Σ^u_u are now highly suppressed. A large *negative* value of the trilinear A_t then also raises the value of m_h [252] towards the observed 125 GeV [24, 23] value while the fine-tuning measure $\Delta_{\rm EW}$ can remain small. Another defining feature of RNS is that the running of the soft mass $m^2_{H_u}$ is driven radiatively to small negative values of order $\sim -m^2_Z$ which triggers EWSB [249]. Although the GUT scale value of $m^2_{H_u}$ may be at the TeV scale, the *weak scale* value is thus driven to the right order of magnitude to achieve the observed Higgs mass without a large degree of fine-tuning, as quantified by $\Delta_{\rm EW}$. RNS can be easily incorporated into models with non-universal Higgses at the GUT scale [249] - in this work we focus mostly on the 2- and 3- extra parameter (NUHM2 and NUHM3, respectively) models as our GUT scale models.

Although the LHC Run 2 constraints seem to require a gluino mass $m_{\widetilde{g}} \gtrsim 2.2$ TeV [34, 35] and a top squark mass $m_{\widetilde{t}_1} \gtrsim 1.2$ TeV [37, 36, 38], such seemingly large masses can be accommodated in RNS without requiring fine-tuning, and may be in reach of the HL-LHC [253, 254]. Due to the expected multi-TeV first and second generation scalars (which are highly subdominant contributions to Σ^u_u [249]), RNS also provides a natural solution to the SUSY flavor and SUSY CP problems [255, 256, 257, 258]. As we will discuss shortly, RNS can also naturally be combined with the DFSZ axion as the Kim-Nilles solution to the SUSY μ-problem can generate a μ term with a value roughly the order of the

weak scale ($\mu \sim 100 - 350$ GeV) [5, 2, 259]. In these classes of models one expects multi-component dark matter consisting of LSPs and axions, and while higgsino-like neutralinos tend to be underproduced (i.e. produce only a fraction of the observed relic density $\Omega h^2 = 0.120 \pm 0.001$ [11]), axions can easily constitute the remaining relic density [260, 261, 262]. For the purposes of this work we thus refer to RNS combined with a (supersymmetric) DFSZ axion as the PQMSSM, which provides a natural solution to the gauge hierarchy problem *and* the strong-CP problem.

Many previous works [263, 251, 264, 265, 138, 266, 267, 254, 268] have also studied RNS in the context of the string landscape. Based on arguments from Douglas and others [133, 131, 269], one naively expects a distribution of the soft SUSY breaking scale $m_{\rm soft}$ to follow a vacua distribution like

$$dN_{\rm vac} \sim f_{\rm SUSY}(m_{\rm soft}) \cdot f_{\rm EWSB}(m_{\rm soft}) \cdot dm_{\rm soft} \tag{3.5}$$

where $f_{\rm SUSY} \sim m_{\rm soft}^{2n_F+n_D-1}$ with n_F (n_D) the number of F-term (D-term) SUSY breaking fields. For non-perturbative sources of SUSY breaking however, it was argued by Dine *et al.* [270, 271] that one would not expect any favored SUSY breaking scale - leading to instead an expectation that $f_{\rm SUSY} \sim m_{\rm soft}^{-1}$. Both of these characteristics were found explicitly in [272] in realistic string models, which found that KKLT models with $\overline{D3}$-brane uplifting suggest $f_{\rm SUSY} \sim m_{\rm soft}^{1}$ while LVS (which, as we have discussed in Sec. (2.3.3) breaks SUSY in the AdS vacua, with uplifting effects contributing only at subleading orders [4]) found $f_{\rm SUSY} \sim m_{\rm soft}^{-1}$.

However, later work utilizing the nilpotent goldstino formalism [273] to model the $\overline{D3}$-brane uplift found instead both KKLT and LVS are tilted towards lower values and stress the sensitivity of results on the details of the uplifting sector. In any case, with RNS assuming a mild statistical draw towards larger soft terms $f_{\rm SUSY} \sim m_{\rm soft}^1$ while also imposing the anthropic constraint based on arguments by Agrawal, Barr, Donoghue, and Seckel [274, 275] puts strong statistical preference on the observed value of the Higgs mass in addition to pulling most sparticle masses above LHC limits [138, 251, 276, 277]. However, a statistical pull towards lower soft terms $f_{\rm SUSY} \sim m_{\rm soft}^{-1}$ results in a low Higgs mass $m_h \sim 118$ GeV with sparticle distributions peaking well within current LHC bounds [277, 267].

3.1.2 The Giudice-Masiero mechanism

As a precursor to the following work, let us briefly review the Giudice-Masiero [246] mechanism for generating a μ-term in gravity-mediated models. In gravity-mediated scenarios, one can write down effective interactions with some hidden sector which are Planck-suppressed, as even if the visible and hidden sectors have no direct couplings between them, they both must couple to gravity. If one prevents the occurrence of the superpotential μ-term with e.g. some postulated symmetry, an effective μ-term can be generated once the hidden sector field acquires a VEV.

To see this more clearly, we write the simple model:

$$K = h^\dagger h + H_u^\dagger H_u + H_d^\dagger H_d + \frac{\lambda_{\rm GM}}{m_P} h^\dagger H_u H_d + \text{h.c.} \tag{3.6}$$

and we assume that h, H_u, and H_d are absent in the superpotential[2] - however we make no further assumptions about the superpotential. Setting $m_P = 1$ for the moment to simplify the calculations, the F-terms can easily be shown to be

$$\overline{\mathcal{F}}_h = e^{K/2} D_h W \simeq e^{K/2} W \left(h^\dagger + \lambda_{\rm GM} H_u^\dagger H_d^\dagger \right) \tag{3.7}$$

$$\overline{\mathcal{F}}_{H_u} = e^{K/2} D_{H_u} W \simeq e^{K/2} W \left(H_u^\dagger + \lambda_{\rm GM} h^\dagger H_d \right) \tag{3.8}$$

$$\overline{\mathcal{F}}_{H_d} = e^{K/2} D_{H_d} W \simeq e^{K/2} W \left(H_d^\dagger + \lambda_{\rm GM} h^\dagger H_u \right) \tag{3.9}$$

where $D_i W$ is the Kähler covariant derivative of the superpotential in the i-th field direction. The scalar potential then can be written as

$$V_F \simeq \left[\overline{\mathcal{F}}_h \mathcal{F}^h + \overline{\mathcal{F}}_{H_u} \mathcal{F}^{H_u} + \overline{\mathcal{F}}_{H_d} \mathcal{F}^{H_d} - 3 e^K |W|^2 \right] \tag{3.10}$$

where indices are raised on the F-terms by use of the inverse Kähler metric. By expanding the F-terms, the scalar potential can also be written as

$$V_F \simeq e^{K/m_P^2} \frac{|W|^2}{m_P^4} \Bigg[h^\dagger h - \frac{\lambda_{\rm GM}}{m_P} h^\dagger H_u H_d + \text{h.c.} \\ - 2 \frac{\lambda_{\rm GM}^2}{m_P^2} h^\dagger h \left(H_u^\dagger H_u + H_d^\dagger H_d \right) - 3 m_P^2 \Bigg] \tag{3.11}$$

where we have explicitly restored the units of m_P. Cancellation of the cosmological

[2]Generically, one *should* expect h to be present in the superpotential at some level. However, any couplings in the superpotential which are relevant to the visible sector should be suppressed by a factor of at least m_P^{-1} due to the assumption that the couplings are purely gravitational. Any contributions to the scalar potential from the superpotential involving hidden sector couplings should then be suppressed by a factor of at least m_P^{-2}, and so we neglect these contributions here as they do not affect our discussion.

constant then implies that the VEV of h should be of order $\langle h \rangle \sim \mathcal{O}(m_P)$ since the VEVs of H_u and H_d should be of order of the weak scale (or vanish, in the case of the charged component of the doublets). Replacing h with its VEV $\langle h \rangle$, we see that the effective μ-terms, $\mu^2 H_u^\dagger H_u$ and $\mu^2 H_d^\dagger H_d$, and the effective $B\mu$ terms, $B\mu\, H_u H_d + \text{h.c.}$, have been generated in the scalar potential. We then expect that

$$\mu^2 \sim 2\lambda_{\text{GM}}^2 e^{K/m_P^2} \frac{|W|^2}{m_P^4} \frac{\langle h \rangle^2}{m_P^2} \sim \lambda_{\text{GM}}^2 \frac{m_{\text{hid.}}^4}{m_P^2} \sim \mathcal{O}\left(m_{3/2}^2\right) \tag{3.12}$$

$$B\mu \sim \lambda_{\text{GM}} e^{K/m_P^2} \frac{|W|^2}{m_P^4} \frac{\langle h \rangle}{m_P} \sim \lambda_{\text{GM}} m_{3/2} \frac{m_{\text{hid.}}^2}{m_P} \sim \mathcal{O}\left(m_{3/2}^2\right) \tag{3.13}$$

where we take $\langle \mathcal{F}_h \rangle \equiv m_{\text{hid.}}^2$ to be the scale of SUSY breaking.

The Giudice-Masiero mechanism is thus a generic way to lower the μ-parameter from its tentatively expected GUT-scale or Planck-scale value, in a way that makes minimal assumptions on the hidden sector besides its existence. However, in weak-scale supersymmetry, one expects μ to be on order of the weak scale - and thus seems to require a very light gravitino mass. Of course, more complete details on the hidden sector than those in our toy model above can significantly ease the requirement of $\langle h \rangle \sim \mathcal{O}(m_P)$. Specifically, as we have seen in Ch. (2), no-scale models naturally cancel the cosmological constant term, which can reduce the expected magnitude of $\langle \mathcal{F}_h \rangle \sim m_{3/2} \langle h \rangle / m_P$ by several orders of magnitude. This can in principle result in natural values of μ, i.e. $\mu \sim \mathcal{O}(100 - 400)$ GeV, depending on the precise details of the model.

There is, though, one caveat if one considers the scaling of μ throughout the string landscape. As we saw in the above example, the μ term should

be proportional to the gravitino mass, even if more realistic models provide a significant suppression of the $\langle h \rangle / m_P$ factor. The gravitino mass - at least in string models with flux compactifications [129, 100] - is set predominantly by the Gukov-Vafa-Witten superpotential W_0. Thus, as we have mentioned in Sec. (2.3.1), the μ parameter should scan in the landscape similar to the soft SUSY breaking terms. If one assumes that the soft terms (and similarly, μ) take a power law distribution in the landscape [133, 131, 269], then μ is *still* expected to be pulled to large values. However, since the μ parameter has direct impact on the value of the weak scale in the MSSM, this issue can be tempered if one considers an anthropic selection which we will explore in Sec. (3.2).

3.1.3 The supersymmetric DFSZ axion and the Kim-Nilles mechanism

The Dine-Fischler-Srednicki-Zhitnitsky (DFSZ) axion model [56, 57] is a particularly compelling solution to the strong-CP problem - especially given the simplicity of constructing a supersymmetrized version within the context of the MSSM. In its original form, a complex scalar, ϕ, is introduced as a Standard Model singlet. Two scalar doublets, ϕ_u and ϕ_d, are also assumed present (which are typically taken to be the Higgs doublets H_u and H_d), and a global $U(1)_{\rm PQ}$ symmetry is imposed such that the assigned charges obey $Q_u + Q_d = -2Q_\phi$. PQ charges for the remaining SM field content then have some freedom in their assignment, so long as the Yukawa coupling structure [56]

$$\mathcal{L} \supset G_u \begin{pmatrix} \overline{u} & \overline{d} \end{pmatrix}_L \phi_u \, u_R + G_d \begin{pmatrix} \overline{u} & \overline{d} \end{pmatrix}_L \phi_d \, d_R + \text{h.c.} \tag{3.14}$$

is allowed (see e.g. [278] for more discussion on phenomenological consequences that arise from differing charge assignments). Here, we have written the structure explicitly for first generation quarks, but the remaining quarks and leptons follow the same pattern.

In the DFSZ model, the addition of an extra SM singlet allows for the spontaneous breaking of PQ symmetry to be independent of the breaking of $SU(2)_L \times U(1)_Y$, allowing PQ breaking to occur at a scale much larger than the electroweak scale which was required in the original PQWW axion model. By demanding that the imposed $U(1)_{\rm PQ}$ symmetry is broken at a high scale f_a and thus ϕ acquires a large VEV

$$\langle \phi \rangle = f_a/\sqrt{2} \gg \sqrt{v_u^2 + v_d^2}, \tag{3.15}$$

the axion is generated as the pseudo Nambu-Goldstone boson with the key feature that the axion's couplings to matter are highly suppressed by a factor $f_a^{-1} \ll (v_u^2 + v_d^2)^{-1/2}$ compared to the original PQWW model [46, 47, 48, 49]. At temperatures below the QCD confinement scale $T \lesssim \Lambda_{\rm QCD} \sim 200$ MeV, the axion acquires a small mass from QCD instanton effects [279, 49, 48, 280]:

$$m_a \simeq \frac{m_\pi f_\pi}{f_a} \sim 360 \ \mu\text{eV} \ \times \left(\frac{10^{11} \ \text{GeV}}{f_a} \right), \tag{3.16}$$

which, since it is also suppressed by a factor of f_a^{-1}, is tiny in comparison to the original PQWW axion which had a predicted mass of $m_a^{\rm PQWW} \sim 100$ keV [49].

Due to the large suppression of its matter couplings and its mass, the DFSZ axion thus evades e.g. beam-dump and collider experiments that quickly excluded the original PQ axion. Some of the most promising searches for axions are resonant microwave cavity experiments such as the Axion Dark Matter Experiment (ADMX) [281, 282]. These experiments rely on the axion-diphoton coupling $g_{a\gamma\gamma}$ to convert axions into microwave photons using strong magnetic fields. Unfortunately, the supersymmetric DFSZ axion couplings are far below any projected sensitivities of current or near-future experiments [283] due to the supersymmetric cancellations in the effective coupling $g_{a\gamma\gamma}$ similar to those which remedy the gauge hierarchy problem in the Higgs sector.

Since the MSSM already possesses the required Higgs doublet structure for the DFSZ model, the simplest supersymmetric extension has a nearly identical setup. Taking $\hat{S}$ to be an SM singlet superfield and assuming the above requirements for PQ charge assignments, one can write the superpotential term

$$W_{\text{DFSZ}} \sim \lambda \frac{\hat{S}^2}{m_P} \hat{H}_u \hat{H}_d. \tag{3.17}$$

The PQ symmetry also forbids the fundamental SUSY μ-term from appearing in the superpotential, since in the DFSZ model both Higgs fields are charged under $U(1)_{\text{PQ}}$. Once the scalar component of $\hat{S}$ acquires its VEV, the axion superfield appears as the phase of $\hat{S}$ and an effective μ-term is induced:

$$W_\mu \sim \lambda \frac{f_a^2}{m_P} \hat{H}_u \hat{H}_d \tag{3.18}$$

where we identify $\mu \sim \lambda f_a^2/m_P$. This is the elegant Kim-Nilles solution [247] to the SUSY μ-problem. Not only is the same mechanism responsible for solving both the strong-CP problem and the SUSY μ-problem, but now the μ-term is related to the intermediate PQ scale which motivates a natural little hierarchy in the MSSM [284].

The remaining terms in the MSSM superpotential (following the conventions of [1]) are given by Eq. (3.1), which we demand to be unchanged by the addition of PQ symmetry. The PQ charge assignments must then reflect this. Assigning a PQ charge $Q_{\hat{S}} \equiv 1$ to the PQ field $\hat{S}$ so that the PQ charges of the two Higgs fields obey $Q_{\hat{H}_u} + Q_{\hat{H}_d} = -2$, we see that the PQ charge assignments for the remaining quark and lepton superfields are highly restricted. Indeed, the choice $Q_{\hat{H}_u} = Q_{\hat{H}_d} = -1$ then dictates that $Q_{\hat{Q}} + Q_{\hat{U}} = Q_{\hat{Q}} + Q_{\hat{D}} = 1$ so that $Q_{\hat{U}} = Q_{\hat{D}}$, while we also have $Q_{\hat{L}} + Q_{\hat{E}} = 1$. Any additional interactions with $\hat{S}$ in the superpotential - depending on PQ charge assignments - then can only possibly arise through dangerous baryon or lepton number violating operators such as $\lambda''_{ijk} m_P^{-1} \hat{S} \hat{U}_i^c \hat{D}_j^c \hat{D}_k^c$ (if left unforbidden by e.g. imposing R-parity) or else appear as highly suppressed corrections (proportional to m_P^{-n}) in the effective theory. Similarly, any interactions with the PQ field $\hat{S}$ appearing in the Kähler potential are likewise highly suppressed by higher powers of m_P^{-n} - the lowest power operators being of the form e.g. $K \supset \frac{\lambda}{m_P^2} \hat{S}^\dagger \hat{S} \hat{H}_u^\dagger \hat{H}_u$. However, this only affects the PQ scalar potential via supergravity interactions $D_I W \supset m_P^{-2} W$, and thus provide only very small corrections to the global SUSY limit.

Once the PQ symmetry is broken and the superfield $\hat{S}$ is integrated out, the

(supersymmetric) axion appears as the phase field of $\hat{S}$. Interactions in the SUSY DFSZ model are then specified by the Lagrangian [285]

$$\mathcal{L}_{\rm DFSZ} = \int d^2\theta \, \left(1 + B\theta^2\right) \mu \exp\left(c_H \hat{A}/v_{\rm PQ}\right) \hat{H}_u \hat{H}_d \tag{3.19}$$

where $(1 + B\theta^2)$ is a SUSY breaking spurion superfield, $-c_H \equiv Q_{\hat{H}_u} + Q_{\hat{H}_d}$, and $v_{\rm PQ} = f_a/\sqrt{2}$. We have also introduced the axion superfield

$$\hat{A} \equiv \frac{1}{\sqrt{2}} \left(s + ia\right) + \sqrt{2}\theta\widetilde{a} + \theta^2 \mathcal{F}_A \tag{3.20}$$

where a is the axion and s is its supersymmetric scalar partner, the saxion, and the fermionic component $\widetilde{a}$ is the axino. The decay rates for the saxion and axino are then primarily produced by the mixing induced by this interaction [285]. It is worth noting that in the DFSZ model, PQ breaking must happen *before or during* inflation if the $U(1)_{\rm PQ}$ symmetry is exact. Otherwise, stable topological defects known as domain walls are present which are highly constrained [286].

Let us briefly comment on some of the features of the saxion and the axino. The saxion is expected to gain a mass through e.g. gravitationally-mediated contributions [287] so that one would expect its mass to be roughly of order of the soft SUSY breaking terms, while the axion is protected against these contributions from its characteristic shift symmetry $A \to A + i\alpha$ [112]. However, the axino mass is much more model-dependent, potentially being as large as the saxion or substantially lighter depending on the model details [288, 289, 290]. If the axino

is sufficiently light (i.e. lighter than the LSP expected from the MSSM alone), it can take on the role as a viable dark matter candidate. Axino dark matter has been studied in [291, 292, 293, 294, 295, 296, 297, 298, 299]. It is generally found that the axino must have a mass $m_{\tilde{a}} \lesssim \mathcal{O}(10 \text{ GeV})$ to be a viable dark matter candidate - heavier axinos tend to be overproduced. Conversely, if the axino mass is too light it may behave as warm or hot dark matter which are highly constrained by CMB measurements [291, 292, 295]. The saxion and axion (in a similar fashion to the modulus) may also be produced from a cosmological phenomenon unique to scalars - coherent oscillations. The coherently oscillating saxion and axion are produced non-thermally and have the equation-of-state of a cold matter distribution, which makes the (stable) axion a highly motivated dark matter candidate. However, as the (unstable) saxion is expected to be of order of the soft terms $\sim \mathcal{O}(1 \text{ TeV})$, its decay will produce a large amount of entropy [286], which dilutes previously existing relics. This was studied in the context of the supersymmetric DFSZ axion in [285, 300] where it was found that large $f_a \gtrsim 10^{14}$ GeV can significantly dilute any relic gravitinos or neutralinos, while $f_a \lesssim 10^{12}$ GeV has a rather minimal effect on any thermal population. Thus, some scenarios that are thermally-excluded may have significantly eased constraints in this non-thermal cosmology, depending on the details of the PQ sector.

The PQMSSM conventionally predicts an admixture of axion and weakly-interacting massive particle (WIMP) dark matter, where the role of the WIMP is played by a higgsino-like neutralino (assuming the MSSM is of RNS type) [285, 301, 302, 300, 284, 260, 261]. Indeed, the PQMSSM can also saturate

the observed dark matter relic density [285, 301, 261], which is measured to be $\Omega h^2 = 0.120 \pm 0.001$ [11], and produce ultra-relativistic axions (which behave as hot dark matter or dark radiation) at a level consistent with CMB observations without fine-tuning [302, 300] (see also [303] for similar results with a wino-like neutralino playing the role of the WIMP). Within the context of the string landscape, it was found in [139] that by assuming a mild statistical draw towards large soft SUSY breaking terms, the PQ VEV was pulled to large values as well - unless additional requirements were imposed on the soft SUSY breaking terms responsible for the PQ VEVs. A pull towards large VEVs - and thus a high PQ scale f_a - was found to typically result in overproduction of *both* the axion and neutralino dark matter. This eliminates a potential solution [304, 305] of the dark matter overproduction problem for large f_a wherein a "tuning" of the axion misalignment angle θ_i can occur in the landscape due to anthropic arguments - if too much dark matter is present, galaxies would collapse on themselves and thus no observers would exist. However, since the WIMPs are overproduced regardless of θ_i this anthropic argument is unlikely to work here - it was found in [139] that we would likely see far more dark matter given the statistical pull towards large f_a. If the soft terms responsible for the PQ VEV *are* constrained however, the PQ scale naturally settles to the sweet spot of $f_a \sim 10^{11} - 10^{13}$ GeV [139].

3.1.4 The axion quality problem

As we have remarked in the previous section, the $U(1)_{\rm PQ}$ symmetry of the DFSZ axion disallows other operators at the m_P^{-1} level from appearing in the super-

potential or Kähler potential. However, in supergravity one generically expects higher dimensional operators which are compatible with the symmetries of the SM but break the global PQ symmetry. This is not unique to the supersymmetric DFSZ model, but rather a general expectation of *all* axion models regardless of the UV completion. Since global symmetries are not expected to survive any inclusion of quantum gravity (even at the classical level, black hole evaporation can destroy global quantum numbers), global-symmetry-violating operators which are gravitationally induced are expected to appear [306, 307, 308, 309, 310, 311]. Naively, one might expect that this has little relevance to the axion solution to the strong-CP problem - all additional operators are expected to be Planck-suppressed, while the leading operators are renormalizable. The work of Kamionkowski and March-Russell [307], Barr and Seckel [312], and Holman *et al.* [308] however showed that for a viable solution to the strong-CP problem, these operators must be suppressed to a level of *at least* $V \sim \phi^{12}/m_P^8$. Thus, the PQ symmetry must be *extremely high quality* in order to provide a solution to the strong-CP problem.

One particularly compelling solution to this "axion quality problem" or "gravity spoliation problem" is the use of discrete symmetries, which appear in the low-energy theory as an *approximate* global $U(1)_{\rm PQ}$ symmetry. However, in the SUSY DFSZ axion case this symmetry must be sufficiently strong to forbid any PQ-violating terms up to m_P^{-8}, forbid the SUSY μ-term, and (preferably) forbid dangerous dimension-5 proton decay operators $\hat{Q}_i\hat{Q}_j\hat{Q}_k\hat{L}_l$ and $\hat{U}_i^c\hat{U}_j^c\hat{D}_k^c\hat{E}_l^c$ from appearing in the superpotential. As discussed in [2], this is elegantly accomplished if the PQ symmetry breaking is tied to SUSY breaking. These models introduce

multiple PQ fields $\hat{X}$ and $\hat{Y}$ which obey a discrete symmetry (which appears as a $U(1)_{\rm PQ}$ symmetry for all non-Planck-suppressed operators) and the axion is then a composite of these fields once they acquire a VEV [313]. Incorporating soft SUSY breaking terms into this model then generates a potential which gives the scalar X and Y fields VEVs at an intermediate scale $v_{X,Y} \sim \mathcal{O}(10^{10} - 10^{12})$ GeV [261]. Most notably, the gravity-safe PQ (GSPQ) model detailed in [2] is based on a $\mathbb{Z}_{24}^{\mathbf{R}}$ symmetry which was shown by Lee *et al.* [314] to be anomaly-free. The GSPQ model also forbids additional PQ-violating operators to order m_P^{-8} - in accordance with the bounds from [307, 312, 308]. Although the remainder of this work will focus on the GSPQ model, many other models postulating discrete symmetries to solve the axion quality problem have been studied in e.g. [315, 316, 317, 318, 319, 320, 321, 314, 322, 323].

3.2 Distribution of μ and f_a from the landscape

Given the two aforementioned solutions to the SUSY μ-problem, we now investigate how these solutions scan in the landscape. Here, we assume a fertile patch of the multiverse so that the MSSM is the low energy effective theory. Based on arguments given in [133, 131, 269], we assume a power-law distribution of soft terms, i.e.

$$f_{\rm SUSY} \sim m_{\rm soft}^n \tag{3.21}$$

where $n = 2n_F + n_D - 1$. In this section, we focus on the case where $n_F = 1$ and $n_D = 0$, and thus we naively expect a linear draw to large soft terms and thus

a high scale of SUSY breaking. However, from the perspective of the landscape, many of these vacua would lead to pocket universes which are incapable of producing larger structures - and thus observers. Namely, large soft terms tend to cause the Higgs potential to have charge-or-color breaking minima (CCB) or no electroweak symmetry breaking (EWSB). Even if the Higgs potential has a possibly viable minima, the magnitude of the soft terms has direct consequence for the expected value of the weak scale. Given the SUSY EWSB conditions which we write here with the specification that m_Z^{PU} is the Z-boson mass set by these conditions in some pocket universe,

$$\frac{\left(m_Z^{PU}\right)^2}{2} = \frac{m_{H_d}^2 + \Sigma_d^d - \left(m_{H_u}^2 + \Sigma_u^u\right)\tan^2\beta}{\tan^2\beta - 1} - \mu^2 \tag{3.22}$$

$$\simeq -m_{H_u}^2 - \Sigma_u^u(\widetilde{t}_{1,2}) - \mu^2, \tag{3.23}$$

one would generically expect the mass of the Z-boson, and hence the magnitude of the weak scale, to be roughly of order of the largest term on the right-hand side of Eq. (3.22). Taking into consideration the results from calculations which investigate the dependence of nuclei on the weak scale, we adopt the Agrawal, Barr, Donoghue, and Seckel (ABDS) window [274, 275] which suggest that the weak scale should be no more than a factor of $(2-5)$ greater than our observed value - otherwise the mass ratio between protons and neutrons would lie outside the range required for complex nuclei to be stable, and thus any observers would be unlikely to exist.

From these assumptions and arguments, it is clear that understanding any

predictions of μ from the landscape is an important endeavor - it plays a direct role in determining the weak scale. Once the anthropic considerations are applied, the statistical distribution of μ then gives predictions for the Higgs mass and sparticle masses, and in the case of the Kim-Nilles mechanism, gives predictions on the PQ scale, f_a.

3.2.1 Distribution of μ and f_a in the GSPQ model

Of course, the PQ models we are interested in should be gravity-safe - i.e. in order to solve the strong-CP problem, it should not suffer from a quality problem induced by effective operators from the UV. As discussed in Sec. (3.1.4), gravity-safe models may be based on discrete symmetries. Namely, here we consider a discrete R-symmetry $\mathbb{Z}_{24}^{\mathbf{R}}$ which was found to be anomaly-free [314] and forbid any potentially dangerous terms such as those inducing proton decay [2]. The low energy limit then looks like an approximate $U(1)_{\rm PQ}$ symmetry, with the axion multiplet given by the phases of two PQ superfields $\hat{X}$ and $\hat{Y}$ once the scalar components acquire their VEVs. Here, we consider as a model the gravity-safe PQ (GSPQ) model which we alluded to in Sec. (3.1.4) and is detailed in [2]. The GSPQ model includes the superpotential terms

$$W \supset \frac{\lambda_\mu}{m_P}\hat{X}^2\hat{H}_u\hat{H}_d + \frac{f}{m_P}\hat{X}^3\hat{Y} \tag{3.24}$$

from which we recover the SUSY μ term from the VEV of X:

$$\mu \equiv \frac{\lambda_\mu}{m_P} v_X^2. \tag{3.25}$$

We augment the superpotential with the following soft SUSY breaking terms

$$\mathcal{L}_{\text{soft}} \supset m_X^2 |\phi_X|^2 + m_Y^2 |\phi_Y|^2 + \left(\frac{f A_f}{m_P} \phi_X^3 \phi_Y + \text{h.c.} \right) \tag{3.26}$$

where A_f is the trilinear coupling in the PQ sector that breaks the $\mathbb{Z}_{24}^{\mathbf{R}}$ symmetry (thus also breaking the approximate $U(1)_{\text{PQ}}$ symmetry) once SUSY is broken.

The scalar potential is now straightforward to compute. The terms relevant to us are

$$V \supset \left| \frac{3f}{m_P} \phi_X^2 \phi_Y \right|^2 + \left| \frac{f}{m_P} \phi_X^3 \right|^2 + m_X^2 |\phi_X|^2 + m_Y^2 |\phi_Y|^2 + \left(\frac{f A_f}{m_P} \phi_X^3 \phi_Y + \text{h.c.} \right). \tag{3.27}$$

We now consider the minimization conditions to find the ϕ_X and ϕ_Y VEVs. Assuming for simplicity that the couplings, f and A_f, and VEVs, v_X and v_Y, are real, the minimization conditions listed in [284] are given by

$$0 \simeq 9 \frac{f^2}{m_P^2} v_X^4 v_Y + \frac{f A_f}{m_P} v_X^3 + m_Y^2 v_Y \tag{3.28}$$

$$0 \simeq 3 \frac{f^2}{m_P^2} v_X^5 + 18 \frac{f^2}{m_P^2} v_X^3 v_Y^2 + 3 \frac{f A_f}{m_P} v_X^2 v_Y + m_X^2 v_X \tag{3.29}$$

where throughout we have neglected the contributions from the Higgs VEVs - which are highly subleading in comparison. It is a simple matter to show that, assuming $m_X = m_Y \equiv m_0$, these minimization conditions are only non-trivial if $|A_f| \geq \sqrt{12}\, m_0$. We must therefore require this condition to be satisfied in order to achieve successful PQ breaking. Additionally, it is worth mentioning that, although the dependence is highly non-trivial, increasing the magnitude of $|A_f|$ increases the magnitude of the VEVs, v_X and v_Y.

For the parameter choice $m_X = m_Y = 10$ TeV, $f = 1$, and $A_f = -35.5$ TeV, the solution to the minimization conditions gives $v_X \simeq 10^{11}$ GeV and $v_Y \simeq 5.8 \times 10^{10}$ GeV, which give a PQ scale of $f_a = \sqrt{v_X^2 + 9v_Y^2} \simeq 2 \times 10^{11}$ GeV. The μ-term then gets a value of $\mu = \lambda_\mu v_X^2 / m_P \simeq 417$ GeV for $\lambda_\mu = 0.1$. Thus, a value of μ close to the weak scale can clearly be achieved with minimal tuning and without imposing anthropic arguments, whereas the Giudice-Masiero mechanism may require additional model-building, tuning, or anthropic tempering in order to achieve a μ-term far below the SUSY breaking scale.

To study the low energy behavior in the landscape, we take the two-extra-parameter non-universal Higgs SUSY model NUHM2 [324, 325, 326, 327, 328, 329] as our GUT-scale model. In this model, all generations of matter scalars have unified soft masses, $m_0(1,2,3) \equiv m_0$, while the two soft Higgs masses, m_{H_u} and m_{H_d}, are independent and may be exchanged instead for weak scale values of μ and m_A. The parameter space for this model then may be entirely specified by

$$m_0,\ m_{1/2},\ A_0,\ \tan\beta,\ \mu,\ m_A \tag{3.30}$$

where μ and m_A are taken at their weak scale values, and all other parameters are taken at the GUT scale. As we have discussed previously, we focus on an independent $n = 1$ draw for the soft terms within the following limits

$$m_0 \quad : \quad 0.1 - 20 \text{ TeV} \tag{3.31}$$

$$m_{1/2} \quad : \quad 0.5 - 5 \text{ TeV} \tag{3.32}$$

$$-A_0 \quad : \quad 0 - 50 \text{ TeV} \tag{3.33}$$

$$m_A \quad : \quad 0.3 - 10 \text{ TeV} \tag{3.34}$$

$$\tan\beta \quad : \quad 3 - 60 \text{ (uniform distribution)} \tag{3.35}$$

where we adopt a uniform distribution for $\tan\beta \equiv v_u/v_d$ since it is not a soft term and thus should not have a favored magnitude in the landscape [138]. Here, the upper bounds of this range are set by our anthropic considerations - values close to any of the upper bound lead to either non-standard minima, no EWSB, or a weak scale much larger than the ABDS limit [276]. Lower bounds for this range are motivated by the current LHC search limits [276]. The soft masses in the PQ sector are then taken to be $m_X = m_Y = m_0$, while we take the coupling $f = 1$. Finally, as we have previously mentioned, we require the soft term $|A_f| \geq \sqrt{12}\, m_0$ for successful PQ breaking. We therefore consider the soft term A_f to be correlated but not equal to A_0, so that $A_f = 2.5A_0$. This is an effective requirement since, for large $|A_0|$, the vacua is a CCB minima due to tachyonic top squark soft-squared masses, which implies that if we were to take equality of A_f and A_0, having successful EW symmetry breaking likely leads to

unsuccessful PQ breaking and vice-versa.

Our procedure here is as follows. For each draw of soft terms in Eqs. (3.31-3.35), we numerically solve the minimization conditions in Eqs.(3.28-3.29) for the smallest non-trivial VEVs, v_X and v_Y. Using these results, we then calculate a value for μ for a specified value of λ_μ, which gives us the full set of input parameters in Eq. (3.30) required by NUHM2. We then use Isajet 7.88 [330] to calculate the SUSY spectrum at the weak scale. Finally, we must impose our anthropic considerations to either accept or veto each point. By adopting the atomic principle advocated by Agrawal *et al.* [275], we require a weak scale in each pocket universe to be within a factor of 4 from the value measured in our universe - i.e. $m_Z^{PU} < 4m_Z^{OU}$. This corresponds to the condition

$$\Delta_{\rm EW} < 30 \tag{3.36}$$

for the $\Delta_{\rm EW}$ fine-tuning measure [249, 250], which is calculated in the Isajet codes.

We begin by considering the case where $\lambda_\mu = 0.1$. As we have already shown, this value of the coupling can produce a value of the μ parameter which is close to the acceptable range for generic values of soft terms, while increasing this to $\lambda_\mu = 1$ far exceeds the constraint $m_Z^{PU} < 4m_Z^{OU} \sim 365$ GeV.

In Fig. (3.1), we display scan results in the A_0 vs μ plane, with the ratio $m_{\rm weak}^{PU}/m_{\rm weak}^{OU}$ being given by the appropriate color scale. The plot on the left shows all standard minima but no restriction on the value of the weak scale, while the plot on the right has the condition $m_{\rm weak}^{PU}/m_{\rm weak}^{OU} < 4$ applied. For the region

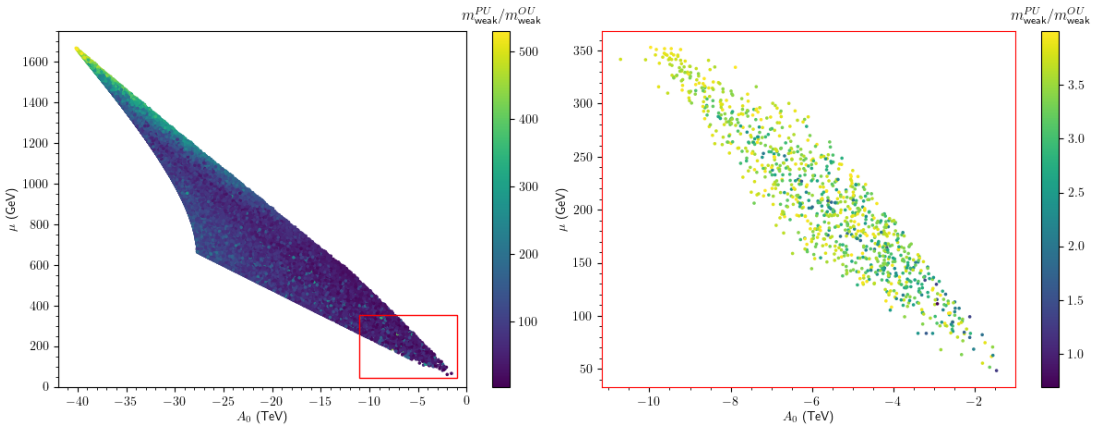


Figure 3.1: Results in A_0 vs μ plane for $n = 1$ scan in GSPQ+MSSM model with $\lambda_\mu = 0.1$ and $f = 1$. The left plot corresponds to all values of m^{PU}_{weak}, while the right plot corresponds to $m^{PU}_{\text{weak}} < 4m^{OU}_{\text{weak}}$. Note the right plot is a blow-up of the red boxed region in the left plot. Figure taken from [5].

below the surviving points in the plot on the left, the lower bound here is imposed by a combination of PQ symmetry breaking requirements (namely the condition $|A_f| \geq \sqrt{12}\, m_0$) and our scan limits. As the magnitude of A_0, and thus A_f, grows towards $|A_0| \sim 27.7$ TeV, there is always a maximal value of m_0 within the scan limits that allows PQ symmetry breaking. Due to this constraint, especially when combined with our $n = 1$ statistical draw towards large soft terms, the region close to $A_0 \sim 0$ becomes sparsely populated as it is extremely disfavored by statistics. When the magnitude of A_0 grows above $|A_0| \gtrsim 27.7$ TeV, the PQ symmetry breaking condition can always be satisfied for any allowed m_0, while any cancellation between A_f and m_0 in determining the VEVs v_X and v_Y quickly becomes small. The shape of the lower boundary reflects these points, although any boundary set from our scan limits is well beyond the ABDS window, as can be seen in the plot on the right. The region above the surviving points in the

plot on the left, however, is bounded by non-standard minima, typically CCB minima in this case. Although there is also a bound above this region from our lower limits of m_0, the bound set by CCB minima is far more stringent here.

The right plot in Fig. (3.1) shows the subset of the scan that obeys our anthropic considerations, and corresponds to an enlargement of the red boxed region in the left plot. In the plot on the right, yellow and green points correspond to points near the upper limit of $m_{\rm weak}^{PU}/m_{\rm weak}^{OU}$. We see that, in the upper left corner of these allowed points, the large values of $|A_0|$ and μ then predict larger values of $m_{\rm weak}^{PU}$. The blue and purple points which predict a weak scale close to $m_{\rm weak}^{OU}$ are then predicted more frequently for smaller values of $|A_0|$ and μ. The dark purple points, which are exceedingly rare in this scan as they require all soft terms to be small, then correspond to a value $\mu \lesssim \mathcal{O}(100\ {\rm GeV})$, which is excluded from LEP2 chargino pair searches [331, 332, 333].

We show the correlation between the soft masses and μ in Fig. (3.2), which displays the predicted value of μ in the m_0 vs $m_{1/2}$ plane after our anthropic considerations have been applied. We see that, as m_0 increases, a larger value of μ is predicted. There is also a correlation between large values of $m_{1/2}$ and large values of μ, which is primarily due to the statistical draw on both $m_{1/2}$ and A_0. Here, it becomes clear that the upper bounds for our parameter space limits in Eqs. (3.31 - 3.35) are well above the maximum values which lead to anthropically viable vacua.

In the left plot of Fig. (3.3), we show the probability distribution of μ from the landscape scan. The blue histogram includes all points that have EW symmetry

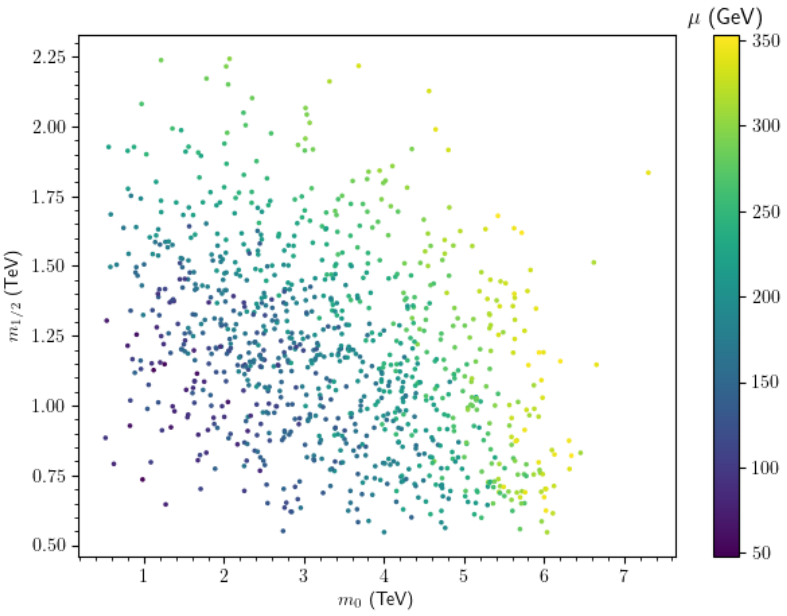


Figure 3.2: Predicted value of μ in the m_0 vs $m_{1/2}$ plane for $n = 1$ landscape scan with $m_{\rm weak}^{PU}/m_{\rm weak}^{Ou} < 4$ anthropic constraint applied. Here, $f = 1$ and $\lambda_\mu = 0.1$. Figure taken from [5].

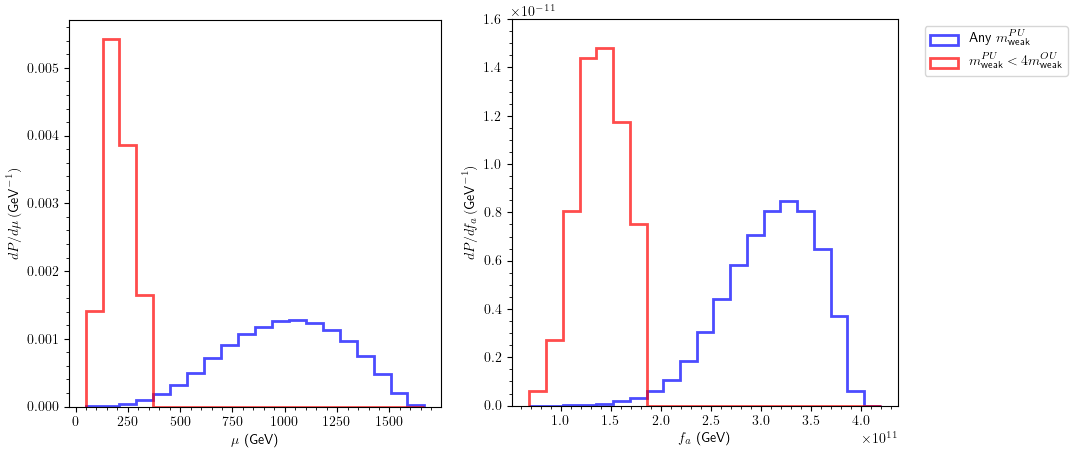


Figure 3.3: Probability distribution of SUSY μ parameter (left) and PQ scale f_a (right). Here, $f = 1$ and $\lambda_\mu = 0.1$. Figure taken from [5].

broken in the appropriate manner, but has no restriction on the predicted value of the weak scale. We see a very broad peak around $\mu \sim 1050$ GeV, while larger values tend to yield CCB minima or are artificially cut off by our scan limits.

The red histogram then gives the probability distribution once our anthropic considerations are applied. Here, we see a sharp peak around $\mu \sim 200$ GeV, while the full distribution is limited to $\mu \lesssim 365$ GeV.

In the right plot of Fig. (3.3), we show the probability distribution of the PQ scale f_a from the landscape scan. Again, the blue histogram includes all points with appropriate EWSB but no restriction on $m_{\rm weak}^{PU}$, while the red histogram includes only points that meet $m_{\rm weak}^{PU}/m_{\rm weak}^{OU} < 4$. Before our anthropic considerations are applied, we find a broad peak around $(3-3.5)\times 10^{11}$ GeV, while a sharper peak around 1.4×10^{11} GeV arises after this constraint is applied. Thus, for anthropically viable vacua, we find a value of the PQ scale predicted at a "cosmological sweet spot" where, for models with both axion and higgsino-like WIMP dark matter, the relic densities of axions and WIMPs are similar and can easily reproduce the observed DM density [139, 300, 285].

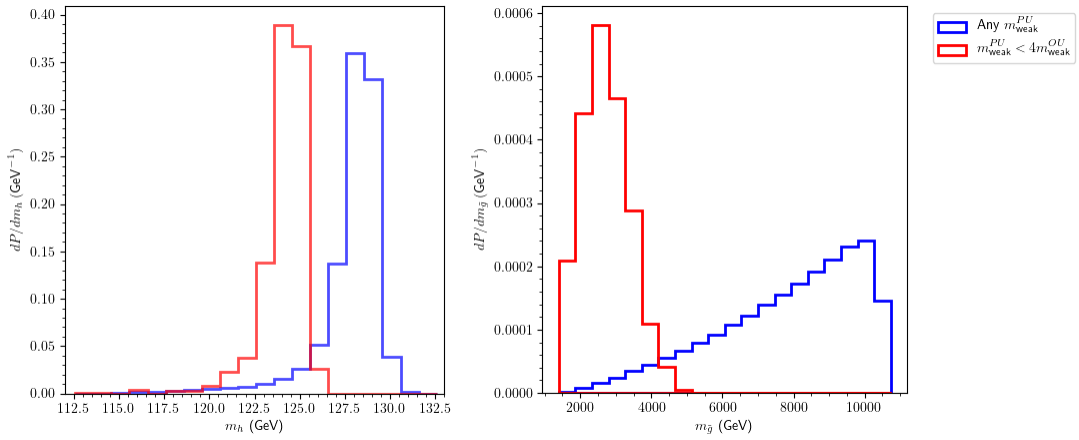


Figure 3.4: Probability distribution of the light Higgs mass m_h (left) and the gluino mass $m_{\tilde{g}}$ (right). Here, $f = 1$ and $\lambda_\mu = 0.1$. Figure taken from [5].

Moving to the left plot Fig. (3.4), we display probability distributions of the

light Higgs mass m_h. Before the application of our anthropic considerations, the blue histogram shows a predicted value of $m_h \sim 128$ GeV. This seemingly low value (at least compared to what one might expect for statistical pulls towards large soft terms) is set primarily by a combination of our scan limits along with the constraint on m_0 from demanding PQ symmetry breaking. Once we apply the $m_{\rm weak}^{PU}/m_{\rm weak}^{OU} < 4$ requirement, we see from the red histogram that the light Higgs mass peak is lowered to $m_h \sim (124 - 125)$ GeV, which is in good agreement with current measurements from CMS [334, 335] and ATLAS [336].

To conclude our study for the value $\lambda_\mu = 0.1$, we display the probability distribution for the gluino mass $m_{\tilde{g}}$ in the right plot of Fig. (3.4). We see in the blue histogram that, before anthropic considerations are applied, the gluino mass is pulled to the largest possible value, cut off only by our artificial scan limits. However, the anthropically allowed values displayed by the red curve are drastically lower, with a peak around $m_{\tilde{g}} \sim 3$ TeV. The tail of the curve is also skewed towards larger values, until the probability vanishes around $m_{\tilde{g}} \sim 5$ TeV. Although the most recent results from CMS exclude gluinos with masses $m_{\tilde{g}} \lesssim 2.2$ TeV [337], this only rules out the leftmost bins - the bulk of the probability narrowly evades this bound, and may be further explored with upcoming results from the LHC Run 3 data. Other light sparticle distributions evade LHC search limits by bigger margins, and thus we do not display these figures in the interest of brevity.

We now briefly investigate how our results change based on the precise value of the PQ coupling, λ_μ. Here, follow the same procedure as before but taking $\lambda_\mu \in$

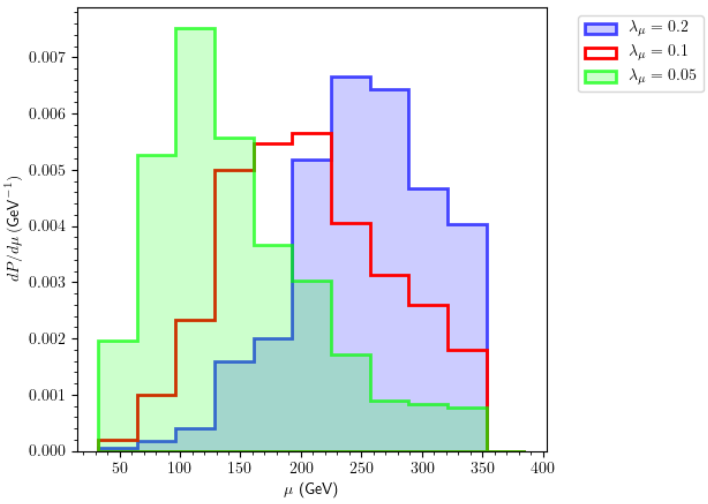


Figure 3.5: Distribution of μ after imposing $m_{\text{weak}}^{PU} < 4m_{\text{weak}}^{OU}$ for $\lambda_\mu = 0.2$ (blue), $\lambda_\mu = 0.1$ (red), and $\lambda_\mu = 0.05$ (green). Figure taken from [5].

$\{0.05, 0.1, 0.2\}$. In Fig. (3.5), we display the resulting probability distributions for the SUSY μ parameter for each of these couplings. As expected, the peak of the probability distribution is raised to larger values of μ as λ_μ increases. We see that for $\lambda_\mu = 0.05$ which is given by the green histogram, the distribution peaks at around $\mu \sim 100$ GeV. This peak value is right at the edge of LEP2 constraints, which require $\mu \gtrsim 100$ GeV. Thus, we expect $\lambda_\mu \lesssim 0.05$ to be ruled out from this constraint - in effect requiring natural values of the coupling λ_μ. When the coupling is increased to $\lambda_\mu = 0.2$, as shown in the blue histogram in Fig. (3.5), we see that the distribution peaks at around $\mu \sim 250$ GeV. Since ATLAS and CMS have yet to observe the soft dilepton plus jets plus $\not{E}_T$ signature from higgsino pair production [333, 338, 339, 340, 341], this model provides a tentative explanation - the μ parameter is pulled towards values larger than the $\mu \sim 200$ GeV limits expected from this process [342, 343].

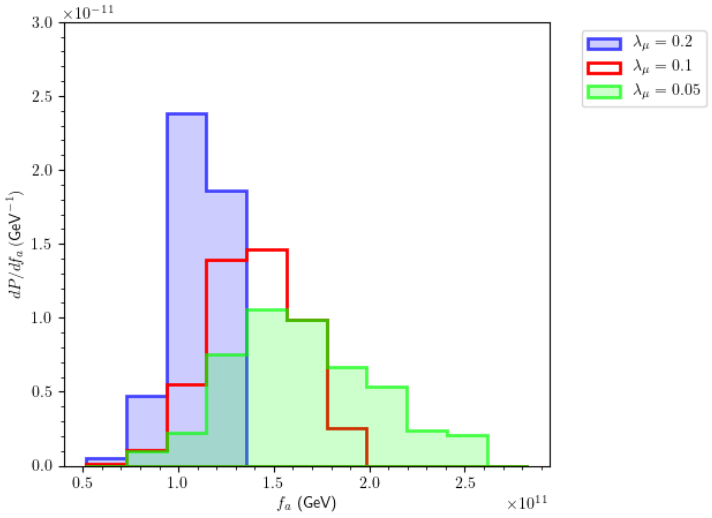


Figure 3.6: Distribution of f_a after imposing $m_{\text{weak}}^{PU} < 4m_{\text{weak}}^{OU}$ for $\lambda_\mu = 0.2$ (blue), $\lambda_\mu = 0.1$ (red), and $\lambda_\mu = 0.05$ (green). Figure taken from [5].

In Fig. (3.6), we display the resulting probability distributions for the PQ scale f_a after our anthropic considerations are applied. It is an intriguing result that, regardless of the value of λ_μ in this plot, the predicted PQ scale is within a fairly narrow window at the $f_a \sim (0.5 - 2.5) \times 10^{11}$ GeV sweet spot. For $\lambda_\mu = 0.05$ shown in the green histogram, we see a comparatively broad distribution which becomes narrower as λ_μ increases. This can be understood from the correlation between the predicted value of μ in this model and the predicted value of f_a - if λ_μ is too large, our anthropic constraint is violated, limiting the distribution for a given set of VEVs, v_X and v_Y. The corresponding axion masses predicted in this scenario are then in the window 144 μeV $\lesssim m_a \lesssim$ 720 μeV. Unfortunately, in the SUSY DFSZ model, the effective axion-diphoton coupling $g_{a\gamma\gamma}$ is highly suppressed due to cancellations in the triangle diagram due to the supersymmetric contributions [283]. In this mass regime, we expect the coupling to have a value

of roughly $g_{a\gamma\gamma} \sim (1-7) \times 10^{-15}$ GeV^{-1} [283] - well below current experimental limits [344].

3.2.2 Distribution of μ in the Giudice-Masiero model

We now move to distributions of μ as predicted from the Giudice-Masiero model [246]. As we have discussed in Sec. (3.1.2), the Giudice-Masiero mechanism assumes that some symmetry forbids the μ-term from appearing in the superpotential. An effective μ term is then generated from integrating out gravitational interactions with some hidden sector in the low energy theory, which has an expected magnitude

$$\mu \sim \lambda_{\rm GM} \frac{m_{\rm hid.}^2}{m_P}. \tag{3.37}$$

The μ term is also expected to scan similarly to the soft terms in the string landscape due to its implicit dependence on the Gukov-Vafa-Witten superpotential W_0.

In this section, we adopt a similar procedure as in the previous section. In the Giudice-Masiero model, a single hidden sector field is responsible for SUSY breaking, thus implying that $n_F = 1$, $n_D = 0$. We therefore take an $n = 2n_F + n_D - 1 = 1$ draw on the soft terms within the parameter space limits given in Eqs. (3.31-3.35) for the same NUHM2 model. We augment this set of soft terms with an $n = 1$ draw on μ with

$$\mu \quad : \quad 0 - 450 \text{ GeV} \tag{3.38}$$

where our upper bound is set by our anthropic considerations, which are saturated at $\mu \sim 365$ GeV. We have also taken $\lambda_{\rm GM} = 1$. Isajet 7.88 [330] is then used to calculate the SUSY spectrum at the weak scale, and the same anthropic requirements are imposed as we have used in the previous section to accept or reject tenable vacua.

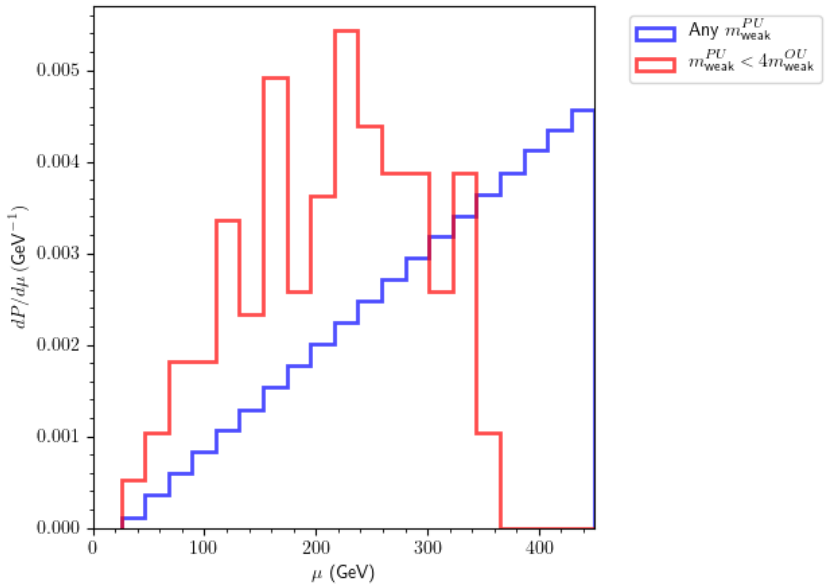


Figure 3.7: Probability distribution for SUSY μ parameter in the Giudice-Masiero model. Here, $\lambda_{\rm GM} = 1$. Figure taken from [5].

In Fig. (3.7), we display our results for the probability distribution of the SUSY μ-parameter in the Giudice-Masiero model. The blue histogram shows vacua with appropriate EWSB conditions, but no restriction on the magnitude of the weak scale. As expected from the $n = 1$ statistical pull, larger values of μ are favored. However, once our anthropic considerations $m_{\rm weak}^{PU}/m_{\rm weak}^{OU} < 4$ are imposed, a fairly broad distribution shown in the red histogram emerges with a slight peak around $\mu \sim 250$ GeV. This is not surprising since, for larger

values of μ, the weak scale also gets contributions from large scalar masses which push the Σ_u^u terms to larger values thus raising the value of the weak scale. The resulting probability distributions for the light Higgs mass and gluino mass are not significantly different from those displayed in the previous section, and hence we omit them here.

Chapter 4

The ϕMSSM and the ϕPQMSSM - an EFT approach

In this chapter, we incorporate a light modulus into the PQMSSM framework. We write down essentially two effective field theories in a single form that parametrize 1. the low energy dynamics of the MSSM, 2. a light modulus that is cosmologically relevant after inflation, and 3. tentative interactions with a PQ sector assumed to be of the DFSZ type. We refer to this EFT as either the ϕPQMSSM or - if the PQ sector is absent - the ϕMSSM. This EFT parametrizes the key features for several models, although additional model-dependent interactions may be present. We provide comments on the connections and applicability to explicit models, and introduce cases to parameterize most of the model-dependent interactions which do not include additional field content. We include detailed computation of the decay modes of the modulus in App. (A), and here provide only simplified results and discussion on the decay widths within different UV models. Finally, we introduce our natural SUSY benchmark point which we adopt for much of the remainder of this work and provide results for various cases using this benchmark. This chapter thus provides the underlying framework to parameterize several explicit string constructions, in addition to providing the relevant decay widths and branching ratios which will play a key role in the resulting cosmology in Ch. (5) and Ch. (6).

4.1 The ϕMSSM and ϕPQMSSM models

Our aim in this section is to write down an appropriate EFT that accommodates all interactions allowed by the symmetries of the MSSM as well as the PQ sector. Certain models then may require various interaction terms to vanish, or posit restrictions on e.g. values of the couplings. Additionally, as we have seen in the previous chapter, for a valid solution to the strong-CP problem, axion quality is extremely important. We show that our model is highly compatible with the class of PQ models based on discrete symmetries discussed in Sec. (3.1.3) without requiring a specific PQ model choice.

In these calculations, we focus on only decay of the scalar component of the modulus supermultiplet $\hat{\Phi}$, denoted here by $\sqrt{2}\Phi = \phi + ic$ with ϕ the modulus and c the corresponding ALP.[1] We also focus only on two-body decay modes which are dominant, but provide comments and expectations on higher-body decays and other model-dependent decays. The full calculation of the partial widths is presented in App. (A) - we discuss only the interaction terms and simplified width results here.

[1]We include the factor $\sqrt{2}$ here as we will assume canonically normalized fields in our global SUSY EFT, which may include e.g. mixing effects with some additional hidden sector fields. As the geometric moduli in Ch. (2) were all in non-canonical form and arose from specific constructions, the normalization constant was spurious and thus omitted as further field redefinitions and rescalings would be required to e.g. compute physical decays.

Field	$SU(3)_C$	$SU(2)_L$	$U(1)_Y$
$\hat{L} = \begin{pmatrix} \hat{\nu}_{eL} \\ \hat{e}_L \end{pmatrix}$	$\mathbf{1}$	$\mathbf{2}$	-1
$\hat{E}^c$	$\mathbf{1}$	$\mathbf{1}$	2
$\hat{Q} = \begin{pmatrix} \hat{u}_L \\ \hat{d}_L \end{pmatrix}$	$\mathbf{3}$	$\mathbf{2}$	$\frac{1}{3}$
$\hat{U}^c$	$\mathbf{3}^*$	$\mathbf{1}$	$-\frac{4}{3}$
$\hat{D}^c$	$\mathbf{3}^*$	$\mathbf{1}$	$\frac{2}{3}$
$\hat{H}_u = \begin{pmatrix} \hat{h}_u^+ \\ \hat{h}_u^0 \end{pmatrix}$	$\mathbf{1}$	$\mathbf{2}$	1
$\hat{H}_d = \begin{pmatrix} \hat{h}_d^- \\ \hat{h}_d^0 \end{pmatrix}$	$\mathbf{1}$	$\mathbf{2}^*$	-1

Table 4.1: MSSM field content and charge assignments as given in [1].

4.1.1 The superpotential

Here, we construct the superpotential for our effective field theory. To begin, we take the MSSM superpotential [1] with the superfields from Table (4.1):

$$W_{\text{MSSM}} = \lambda_u^{ij} \hat{Q}_i \hat{H}_u \hat{U}_j^c + \lambda_d^{ij} \hat{Q}_i \hat{H}_d \hat{D}_j^c + \lambda_e^{ij} \hat{L}_i \hat{H}_d \hat{E}_j^c + \cancel{\mu \hat{H}_u \hat{H}_d} \tag{4.1}$$

where i, j run over generations and we assume that an effective μ-term is been generated by either the Giudice-Masiero mechanism [246] or the Kim-Nilles mechanism [247], but any fundamental μ-term is forbidden by some symmetry. In the case of the Kim-Nilles mechanism, we assume PQ breaking has already occurred and that the massive PQ field(s) have been integrated out of the superpotential.

To write the effective theory for two-body decays of Φ, we now consider any allowed operators in the superpotential. Due to the MSSM charge assignments,

the only potentially allowed 2-body decay terms in the superpotential are

$$W \supset \lambda_{\not L}\, \hat{\Phi}\, \epsilon_{ab} \hat{L}^a \hat{H}_u^b \tag{4.2}$$

and

$$W \supset \lambda_{H_u H_d}\, \hat{\Phi} \hat{H}_u \hat{H}_d. \tag{4.3}$$

The first term does not conserve L symmetry, and conventionally it is forbidden by imposing R-parity - which we adopt here. The second term is effectively a fundamental μ-term if Φ acquires a VEV, with a dimensionless coupling $\lambda_{H_u H_d}$. However, since we are assuming that any fundamental μ-term in $W_{\rm MSSM}$ is forbidden by some additional symmetry, this term should also be forbidden. For the ϕPQMSSM where the effective μ-term is generated by the Kim-Nilles mechanism, we can write down the term

$$W \supset \frac{\lambda_S}{m_P^2} \hat{\Phi} \hat{S}^2 \hat{H}_u \hat{H}_d. \tag{4.4}$$

Once S acquires its VEV, we see that the effective coupling in Eq. (4.3) should have a value $\lambda_{H_u H_d} \sim \lambda_S f_a^2 / m_P^2$. However, in the corresponding Lagrangian this coupling appears as $\mathcal{O}(f_a^4/m_P^4)$ for the $\phi \to H_u H_d$ decay and $\mathcal{O}(f_a^2/m_P^2)$ for the $\phi \to \psi_{H_u} \psi_{H_d}$ decay. This factor can be comparable to the couplings we will encounter in the next section for $f_a \gtrsim \mathcal{O}(10^9$ GeV), although there is one final subtlety to this term. Depending on how well the shift symmetry of Φ, $\Phi \to \Phi + i\alpha$, is preserved in the low energy theory, this term may be expected to be forbidden or

highly suppressed at tree-level in an explicit string construction due to holomorphy restrictions, and thus appears only through loop or non-perturbative effects in the more fundamental supergravity theory. Thus, even if the factor f_a^2/m_P^2 is comparable to the other decays we encounter, the effective coupling λ_S may be extremely suppressed. Additionally, the modulus decay into fermions due to this term receives chiral suppression - and thus is expected only a small difference in the total decay width if this term is included and the effective coupling is sizeable. We thus ignore this decay term as we expect it to be negligible in most string models.

Any generic, sizeable 2-body modulus decay in the superpotential would thus require additional fields beyond the MSSM. At the 3-body level, we can take the MSSM superpotential and simply couple $\hat{\Phi}$ to each term (except, of course, the μ-term). The resulting interaction terms in the superpotential will then be suppressed by a factor m_P^{-1}. As before, the decay to scalars will be suppressed by m_P^{-2}, and the decay to fermions will be suppressed by m_P^{-1}. Additionally, these decay widths will also receive additional phase space suppression - thus we expect only the fermion decays can potentially be appreciable at the 3-body level. However, if the modulus is a geometric modulus with a well-preserved shift symmetry which is left mostly intact, the effective 3-body terms in the superpotential will be highly suppressed since they are forbidden at tree-level and thus might appear only radiatively.

Finally, we note that if the modulus is stabilized in a supersymmetric fashion -

such as in the KKLT model [3] - we can include a supersymmetric mass term

$$W \supset M_\Phi \hat{\Phi}^2 \tag{4.5}$$

which parametrizes the supersymmetric contributions to the modulus mass once the UV physics is integrated out. This will only appear in the F-term interactions upon integrating out the auxiliary fields, as $\mathcal{F}_\phi \sim M_\Phi \Phi$. Furthermore, this term induces model-dependent decays - in LVS [180] M_Φ is approximately 0 as the stabilization of the lightest geometric modulus breaks supersymmetry, leaving its corresponding ALP nearly massless [239] while the massive modulus can be parameterized by the inclusion of a soft mass, $\mathcal{L}_{\text{soft}} \supset \frac{1}{2} M_\phi^2 \phi^2$.

4.1.2 The Kähler potential

Here, we construct the Kähler potential for our effective field theory. Noting the assigned charges in Table (4.1), we can write down the Kähler potential assuming canonically normalized fields:

$$K_{\text{matter}} = \hat{\Phi}^\dagger \hat{\Phi} + \hat{C}_i^\dagger \exp\left(-2g t_A \hat{V}_A\right) \hat{C}_i + \frac{\lambda_{C_i}}{m_P} \hat{\Phi} \hat{C}_i^\dagger \exp\left(-2g t_A \hat{V}_A\right) \hat{C}_i + \text{h.c.} + K_{\text{GM}} + K_{\text{PQ}} \tag{4.6}$$

where $\hat{C}_i$ runs over all superfields listed in Table (4.1), $\hat{\Phi}$ is the modulus superfield, and $\hat{V}_A$ are the appropriate gauge potential superfields with g and t_A the appropriate gauge coupling and generator (respectively) for $\hat{V}_A$. The first two terms in

K_{matter} are simply the kinetic terms for the modulus and the matter fields, e.g. $\partial_\mu \Phi^\dagger \, \partial^\mu \Phi$ and $[D_\mu C_i]^\dagger \, [D^\mu C_i]$ respectively. Since the modulus is an SM singlet, there is no associated gauge potential coupling (and thus takes the $g \to 0$ limit).

The third term - along with its Hermitian conjugate - in K_{matter} are then the couplings of the modulus to all matter fields of the MSSM. Unless one of the matter fields C_i acquires a VEV, any coupling of the modulus to a gauge potential superfield $\hat{V}_A$ through this term is a 3-body or higher decay interaction - and hence the modulus decay width can be well approximated by the simpler form $\hat{\Phi}\hat{C}_i^\dagger \hat{C}_i$. The only possible exceptions to this in the MSSM are when $\hat{C}_i = \hat{H}_u$ or $\hat{C}_i = \hat{H}_d$, which can lead to 2-body decay terms of the modulus once the Higgs fields acquire VEVs.

We also can write the Giudice-Masiero type operator:

$$K_{\text{GM}} = \frac{\lambda_{\text{GM}}}{m_P} \, \hat{\Phi} \hat{H}_u^\dagger \hat{H}_d^\dagger + \text{h.c.} \tag{4.7}$$

This term can appear if it is not forbidden by additional symmetries such as PQ symmetry. As discussed in Sec. (3.1.2) and Sec. (3.1.3), K_{GM} and K_{PQ} are mutually exclusive due to these symmetry considerations, however in the interest of conciseness we treat both simultaneously here as it allows us to write the two similar EFTs in one form. We can then set one of these couplings to be 0 in our later analyses depending on the model under study. If the Giudice-Masiero term is present ($K_{\text{PQ}} \to 0$), we refer to the EFT as the ϕMSSM.

The matter Kähler potential may also be augmented with the PQ sector K_{PQ}.

Taking the simplest supersymmetric DFSZ model as discussed in Sec. (3.1.3), we introduce the new SM singlet field, $\hat{S}$, which carries PQ charge. This of course forbids the Giudice-Masiero type operator so that $\lambda_{\rm GM} = 0$ ($K_{\rm GM} \to 0$) - and so we refer to this EFT as the ϕPQMSSM. Assuming the modulus itself carries no PQ charge, $K_{\rm PQ}$ then takes the form

$$K_{\rm PQ} = \hat{S}^\dagger \hat{S} + \frac{\lambda_{\rm PQ}}{m_P}\, \hat{\Phi} \hat{S}^\dagger \hat{S} + \text{h.c.} \tag{4.8}$$

containing both the kinetic term for $\hat{S}$ and the modulus coupling to $\hat{S}$. Once the PQ symmetry is broken and $\hat{S}$ acquires a VEV, the axion multiplet $\hat{A}$ may then be interpreted as the phase field for fluctuations about $\langle S \rangle$ [290] so that:

$$\hat{S} \sim v_{\rm PQ} \exp\left(q\hat{A}/f_a\right) \tag{4.9}$$

where q is the PQ charge and $v_{\rm PQ} = \langle S \rangle$. The effective Kähler potential after PQ breaking is then given by

$$K_{\rm PQ} = v_{\rm PQ}^2 \exp\left(q\left(\hat{A}^\dagger + \hat{A}\right)/f_a\right)\left(1 + \frac{\lambda_{\rm PQ}}{m_P}\hat{\Phi} + \text{h.c.}\right). \tag{4.10}$$

Expanding the exponential to second order, the terms leading to two-body decay of the modulus are then given by

$$K_{\rm PQ} \supset \frac{1}{2}\left(\hat{A}^\dagger + \hat{A}\right)^2 \left(1 + \frac{\lambda_{\rm PQ}}{m_P}\hat{\Phi} + \text{h.c.}\right) \tag{4.11}$$

where we have performed the field redefinition

$$\hat{A} \to \hat{A}' = \frac{q v_{\rm PQ}}{f_a} \hat{A} \tag{4.12}$$

to obtain canonical kinetic terms for the axion multiplet. Alternatively, in most of the simplest PQ models involving only one PQ superfield $\hat{S}$, we may expect that $f_a^2 = q^2 v_{\rm PQ}^2$ so that this redefinition is trivial. We also note that expanding the exponential to first order[2] induces kinetic mixing between the modulus and the saxion - we ignore here these kinetic mixing effects which are Planck-suppressed. Similarly, expanding the exponential to third order as done in [290] leads to the PQ sector self interactions which we will require to study the cosmology in the presence of the (unstable) saxions and axinos. This also leads to 3-body decay terms for the modulus into PQ sector particles which will be suppressed by a factor of $(m_P f_a)^{-1}$ in addition to receiving phase space suppression.

It is worth noting that global symmetries are expected to be absent in string theory [345], and thus the existence of a global $U(1)_{\rm PQ}$ symmetry is not expected to be consistent with the UV theory. In [346], it was argued that one can successfully construct an approximate global symmetry based on discrete symmetries [347, 348] which *are* compatible with string theory. This approximate global symmetry holds at leading order, while higher order (i.e. terms suppressed by higher powers of m_P) break the approximate global symmetry and restore the exact discrete

[2]Specifically, the expansion at first order leads to kinetic mixing effects between $\hat{A}$ and $\hat{\Phi}$, which are of the form $\lambda_{\rm PQ} q v_{\rm PQ}^2/(m_P f_a)(\hat{\Phi}\hat{A}^\dagger + \text{h.c.})$. While the kinetic mixing may be removed by a field redefinition, we neglect this effect here since it leads to only a small correction in the kinetic terms, $\hat{\Phi}^\dagger\hat{\Phi} \to (1 + f_a^2/m_P^2)\hat{\Phi}^\dagger\hat{\Phi} \sim \hat{\Phi}^\dagger\hat{\Phi}$ as $f_a \gtrsim 10^{12}$ GeV is highly constrained for this model.

symmetry [349]. In Sec. (4.1.3), we will provide an explicit example relating an axion model based on these discrete symmetries to our simple model above - and show that our simple model is sufficient to describe the relevant PQ interactions at our level of approximation.

Finally, in addition to the PQ axions discussed above, moduli stabilization models where the shift symmetry of $\hat{\Phi}$ is left largely intact - such as LVS-type stabilization - may also predict moduli decay to closed string axions or ALPs. These ALPs are the axionic component of a modulus, i.e. the field c for a modulus $T = \tau + ic$ where τ is the geometric modulus and c is, in Type IIb string models, the reduction of the C_4 RR gauge field along the divisor that τ parametrizes. Modulus decay to closed string axions then arises due to the non-linear field redefinitions in the effective theory (see e.g. [239]). Since the ALPs in LVS are typically ultralight and only gravitationally coupled, they behave primarily as dark radiation and can exclude certain models due to stringent limits on the effective number of neutrinos from cosmic microwave background radiation (CMB) measurements [11]. We discuss in Sec. (7.3.1) the explicit form from LVS-type models, but for our purposes here, we simply parameterize the result in the Lagrangian with the terms

$$\mathcal{L}_{\phi cc} \supset -\frac{\lambda_{\rm ALP}}{m_P}\phi\,\partial_\mu c\,\partial^\mu c \tag{4.13}$$

where we take c to be the (massless if relevant) canonical ALP field - i.e. the component from $\Phi = \phi + ic$. Here, $\lambda_{\rm ALP} \simeq 0.816$ corresponds to minimal LVS.

Field	$\hat{L}$	$\hat{E}^c$	$\hat{Q}$	$\hat{U}^c$	$\hat{D}^c$	$\hat{H}_u$	$\hat{H}_d$	$\hat{X}$	$\hat{Y}$
$\mathbb{Z}_{24}^{\mathbf{R}}$	9	5	5	5	9	16	12	-1	5
$U(1)_{\rm PQ}$	1	0	1	0	0	-1	-1	1	-3

Table 4.2: Charge assignments for the GSPQ model under a (fundamental) discrete $\mathbb{Z}_{24}^{\mathbf{R}}$ symmetry and the corresponding (approximate) global PQ symmetry as given in [2].

4.1.3 Connection to GSPQ models

In this section, we provide an explicit example connecting a gravity-safe PQ (GSPQ) model to our simple PQ model we utilize in Sec. (4.1.2). Following along the lines of [2], gravity-safe PQ models based on discrete R symmetries $\mathbb{Z}_N^{\mathbf{R}}$ add a pair of fields $\hat{X}$ and $\hat{Y}$ which are charged under a discrete symmetry which leads to an approximate global symmetry. The fields $\hat{X}$ and $\hat{Y}$ are SM singlets otherwise. As an explicit example, we consider the superpotential of the GSPQ model from [2]:

$$W_{GSPQ} \supset \frac{f}{m_P}\hat{X}^3\hat{Y} + \frac{\lambda_\mu}{m_P}\hat{X}^2\hat{H}_u\hat{H}_d \tag{4.14}$$

which has the charge assignments given in Table (4.2). It was shown in [2] that under these charge assignments, the next leading terms allowed in the superpotential are suppressed by a factor m_P^{-7} - and hence the corrections to the scalar potential are $\mathcal{O}(m_P^{-8})$. This large suppression is sufficient to be "gravity-safe" [307] and thus evades the axion-quality problem [315].

Under this pretext, we may now consider a more complete model coupling the PQ sector to the modulus. The leading terms in the Kähler potential are then

given by

$$K_{\rm PQ} \supset \hat{X}^\dagger \hat{X} + \hat{Y}^\dagger \hat{Y} + \frac{\lambda_X}{m_P} \hat{\Phi} \hat{X}^\dagger \hat{X} + \frac{\lambda_Y}{m_P} \hat{\Phi} \hat{Y}^\dagger \hat{Y} + \text{h.c.} \tag{4.15}$$

Once the approximate $U(1)_{\rm PQ}$ symmetry has been broken, integrating out the $\hat{X}$ and $\hat{Y}$ fields [290] leads to[3]

$$\begin{aligned} K_{\rm PQ} \supset v_X^2 \exp\left(q_X \left(\hat{A}^\dagger + \hat{A}\right)/f_a\right) \left(1 + \frac{\lambda_X}{m_P}\hat{\Phi} + \text{h.c.}\right) \\ + v_Y^2 \exp\left(q_Y \left(\hat{A}^\dagger + \hat{A}\right)/f_a\right) \left(1 + \frac{\lambda_Y}{m_P}\hat{\Phi} + \text{h.c.}\right). \end{aligned} \tag{4.16}$$

Expanding the exponential then leads to interactions of the form

$$K_{\rm PQ} \supset \hat{A}^\dagger \hat{A} + \left[\frac{\lambda_X v_X^2 q_X^2 + \lambda_Y v_Y^2 q_Y^2}{f_a^2}\right] \frac{1}{2m_P} \left(\hat{A}^\dagger + \hat{A}\right)^2 \left(\hat{\Phi} + \hat{\Phi}^\dagger\right) \tag{4.17}$$

where, on the axionic kinetic term, we have taken

$$f_a^2 = \sum_i q_i^2 v_i^2 \tag{4.18}$$

and is hence already normalized. For $\lambda_X = \lambda_Y$, our PQ couplings to the modulus reduce identically to our simple model. However, if we have $\lambda_X \neq \lambda_Y$, we now have an effective coupling of the form

$$\lambda_{\rm PQ} = \left[\frac{\lambda_X v_X^2 q_X^2 + \lambda_Y v_Y^2 q_Y^2}{f_a^2}\right] \tag{4.19}$$

[3]There is also an additional singlet which is orthogonal to the axion multiplet [284], which leads to a similar set of interactions. While this will affect the total decay width of the modulus, we will see in the following chapters that - assuming the additional singlet does not contain the LSP - this will hardly affect our conclusions.

which one should expect to be roughly the same order of magnitude of both λ_X and λ_Y.

4.1.4 The gauge-kinetic function

Here, we discuss the gauge-kinetic function for our effective field theory. We assume the quasi-universal gauge-kinetic function

$$f_{AA} = \frac{\lambda_G}{m_P}\hat{\Phi} \tag{4.20}$$

where, for the sake of notation and future use, we take a separate λ_G for each gauge group to parametrize e.g. mixing effects from a more fundamental, possibly non-universal gauge-kinetic function. However, we assume the gauge couplings to the modulus are indeed unified throughout the rest of this work.

The gauge-kinetic terms then read

$$\mathcal{L}_{\rm GK} \supset -\frac{1}{4}\int d^2\theta\, \frac{\lambda_G}{m_P}\,\hat{\Phi}\overline{\hat{\mathcal{W}}^c}_{\alpha}\hat{\mathcal{W}}_{\alpha} + \text{h.c.} \tag{4.21}$$

where $\hat{\mathcal{W}}_\alpha$ are the gauge superfields belonging to $SU(3)_C$, $SU(2)_L$, and $U(1)_Y$, and $\lambda_G \in \{\lambda_{U(1)}, \lambda_{SU(2)}, \lambda_{SU(3)}\}$ is the appropriate coupling to the gauge superfield.

In many string models where the lightest modulus is a geometric modulus, such as Type IIb models where the MSSM is located on $D3$ branes, the fundamental gauge-kinetic function is typically set by the dilaton. The contribution to the gauge-kinetic function from the lightest (geometric) modulus is then expected to be induced at loop-level, and hence the coupling λ_G should be suppressed.

However, this is not necessarily a universal prediction in string models - we will discuss this point more in Sec. (4.3.1) where we define our several case scenarios based on various string models.

Finally, we include the soft SUSY breaking terms enumerated in [1] to parametrize details of SUSY breaking. We take these to be free parameters for our case at hand (more precisely, these soft terms are set from the reduced set of free parameters in our NUHM3 benchmark model), and provide a motivated benchmark value which yields a natural SUSY spectrum.

We have now enumerated the field content of the model. We do not assume any further details of the hidden sector, although if one postulates that e.g. some non-minimal hidden sector couples gravitationally to the modulus, in addition to implications for SUSY breaking and possible implications for the composition of dark matter, it is possible that the modulus decay would be affected sufficiently to alter our predictions. In this work, we assume that our effective field theory captures most of the relevant effects - at least up to the uncertainty in the couplings of the theory.

4.2 Modulus decays

We are now in a position to discuss the decay formulae for the modulus. Detailed derivation and the full decay widths are included in App. (A) - we provide simplified discussion and formulae here.

4.2.1 Decays into gauge bosons and gauginos

The modulus decays into the gauge field sector is dictated by the gauge kinetic function. This interaction is summarized in Eq. (4.21). After expanding the SM gauge groups, the Lagrangian reads

$$\mathcal{L} \supset -\frac{1}{4}\frac{\lambda_{\text{gauge}}}{m_P}\int d^2\theta \left[\hat{\Phi}\,\overline{\hat{B}^c}\hat{B} + \hat{\Phi}\,\overline{\hat{W}^c_\alpha}\hat{W}_\alpha + \hat{\Phi}\,\overline{\hat{G}^c_\alpha}\hat{G}_\alpha + \text{h.c.}\right] \tag{4.22}$$

Here, $\hat{B}$, $\hat{W}_\alpha$, and $\hat{G}_\alpha$ are the gauge-eigenstate superfields for $U(1)_Y$, $SU(2)_L$, and $SU(3)_C$ gauge groups, respectively. We also assume for our current discussion that the modulus couplings to each gauge group are unified, so that $\lambda_{U(1)} = \lambda_{SU(2)} = \lambda_{SU(3)} \equiv \lambda_{\text{gauge}}$.

Focusing first on the decays to the gauge bosons, once $SU(2)_L \times U(1)_Y$ is broken to $U(1)_{\text{e.m.}}$, the physical gauge bosons become the gluon, photon, and the $W^\pm$ and Z^0 bosons. The modulus decay width to each pair of gauge bosons is then given by

$$\Gamma_{\phi\to\text{gauge boson pairs}} \simeq \frac{N_G\lambda^2_{\text{gauge}}}{32\pi}\frac{m^3_\phi}{m^2_P}. \tag{4.23}$$

Here, $N_G = 8$ for a gluon final pair, $N_G = 2$ for a $W^\pm$ final pair, and $N_G = 1$ for both photon and Z^0 final pairs - giving a total $N_G = 12$. This is an unsuppressed decay mode since the width is proportional to m^3_ϕ/m^2_P. However, depending on whether this effective interaction should be induced at tree level or loop level (which appears in our assumed value of λ_{gauge}), it may be a leading interaction or a subdominant interaction.

Focusing now to the decays to gauginos, we list the leading interaction terms once $SU(2)_L \times U(1)_Y$ is broken. The simplest interaction is that of the modulus and the gluinos since no mixing takes place. This decay width is given by

$$\Gamma_{\phi \to \widetilde{g}\widetilde{g}} \simeq \frac{\lambda^2_{\text{gauge}}}{\pi} \frac{m^3_\phi}{m^2_P} \left(\frac{m^2_{\widetilde{g}}}{m^2_\phi} \right) \tag{4.24}$$

where we have summed over the 8 colored states of the gluinos. This decay width also gains a net factor of 2 enhancement since the final state fermions are Majorana. However, the decay width also receives chirality suppression and is thus typically a very small contribution to the total width if $m_\phi \gg m_{\widetilde{g}}$. The decays to gluinos may, however, also produce a model-dependent decay width which is unsuppressed through the F-term interaction if the modulus has a large supersymmetric mass. This point is discussed more in App. (A) and in Sec. (4.3.1).

Moving now to the decays to electroweakinos, the charged gaugino components combine to give modulus decays to chargino pairs. The neutral gaugino components also combine to give modulus decay to neutralino pairs. However, since both the charged and neutral gauginos also mix with the higgsinos, both the neutralinos and charginos have additional contributions from the higgsino sector. We thus postpone listing these decays until the next section.

4.2.2 Decays into Higgses

The modulus decays into Higgses and higgsinos are primarily dictated by the Kähler potential. Specifically, the modulus couplings to the kinetic terms of the

Higgses is model-independent, while the addition of a Giudice-Masiero term may exist if not forbidden by PQ symmetry.

$$\mathcal{L} \supset \int d^4\theta \left[\frac{\lambda_{\rm GM}}{m_P} \hat{\Phi} \hat{H}_u^\dagger \hat{H}_d^\dagger + \frac{\lambda_H}{m_P} \hat{\Phi} \hat{H}_u^\dagger \hat{H}_u + \frac{\lambda_H}{m_P} \hat{\Phi} \hat{H}_d^\dagger \hat{H}_d + \text{h.c.} \right] \tag{4.25}$$

For simplicity in this discussion, we have assumed the two kinetic couplings are unified, $\lambda_{H_u} = \lambda_{H_d} \equiv \lambda_H$. However, in Ch. (6) we do not always assume this is the case - as one might expect in models with non-universal Higgses. We will discuss this point further in that chapter, however we note that our study there uses the full expressions listed in App. (A).

Let us focus first on the scalar components. After $SU(2)_L \times U(1)_Y$ breaking, the real components of the up-type and down-type neutral Higgs components mix to form the light (h) and heavy (H) scalar Higgses. The imaginary component of the mixed neutral Higgses then becomes the pseudoscalar Higgs (A). A would-be Goldstone boson is also produced, however a gauge transformation to the unitary gauge removes it from the tree-level spectrum as it becomes the longitudinal component of the (now massive) Z^0 boson. The decay to the physical, neutral Higgs bosons is then given by

$$\Gamma_{\phi \to h_i h_i} \simeq \frac{1}{64\pi} \frac{m_\phi^3}{m_P^2} \left(\lambda_{\rm GM} \sin(2x) \pm 2\lambda_H \frac{m_{h_i}^2}{m_\phi^2} \right)^2 \tag{4.26}$$

where we have $x \equiv \alpha$ for $h_i = h, H$ and $x \equiv \beta$ for $h_i = A$. In addition, the $\pm$ becomes $+$ for $h_i = h$, and $-$ for $h_i = H, A$. Finally, there is also the decay to a

light and a heavy scalar Higgs, which is given by

$$\Gamma_{\phi\to hH} \simeq \frac{1}{32\pi}\frac{m_\phi^3}{m_P^2}\lambda_{\rm GM}^2\cos^2(2\alpha). \tag{4.27}$$

In a similar way to the neutral scalars, the up-type and down-type charged Higgs components mix to give a charged Higgs, $H^\pm$. The mixing also produces the charged would-be Goldstone boson, which we have removed from the physical tree-level spectrum by our unitary gauge transformation - and it becomes the longitudinal component for the $W^\pm$ bosons. The decay to the charged Higgs pairs is then given by

$$\Gamma_{\phi\to H^+H^-} \simeq \frac{1}{32\pi}\frac{m_\phi^3}{m_P^2}\left(\lambda_{\rm GM}\sin(2\beta) - 2\lambda_H\frac{m_{H^\pm}^2}{m_\phi^2}\right)^2. \tag{4.28}$$

A few comments are in order. If the Giudice-Masiero coupling is non-zero, i.e. $\lambda_{\rm GM} \neq 0$, then Eq. (4.26), Eq. (4.27), and Eq. (4.28) are rather dominant (unsuppressed) decay terms. The total decay width to Higgs pairs is then well-approximated by

$$\Gamma_{\phi\to\text{Higgs pairs}} \simeq \frac{\lambda_{\rm GM}^2}{32\pi}\frac{m_\phi^3}{m_P^2}\left(1+\frac{3}{2}\sin^2(2\beta)\right). \tag{4.29}$$

However, as in the PQMSSM, if $\lambda_{\rm GM} = 0$ we are left with only the mass-suppressed contributions from Eq. (4.26) - which are *extremely* subdominant. In this case,

the total decay width to Higgs bosons is approximated by

$$\Gamma_{\phi\to\text{Higgs pairs}} \simeq \frac{\lambda_H^2}{16\pi}\frac{m_\phi^3}{m_P^2}\left(\frac{m_h^4+m_H^4+m_A^4+2m_{H^\pm}^4}{m_\phi^4}\right). \tag{4.30}$$

Moving now to the higgsinos, much as with the gauginos, the charged components mix to give contributions to the charginos while the neutral components mix to give contributions to the neutralinos. Combining both the gaugino and higgsino terms, the decays to the physical same-generation chargino pairs is given by

$$\Gamma_{\phi\to\widetilde{W}_i\widetilde{W}_i} \simeq \frac{1}{16\pi}\frac{m_\phi^3}{m_P^2}\left(\frac{m_{\widetilde{W}_i}^2}{m_\phi^2}\right)\left((\lambda_G x_\alpha+\lambda_H x_\beta)^2+(\lambda_G y_\alpha+\lambda_H y_\beta)^2\right) \tag{4.31}$$

where $x_{\alpha,\beta}$ and $y_{\alpha,\beta}$ depend on $\sin^2\gamma_{L/R}$ and $\cos^2\gamma_{L/R}$. Generically, one may expect these are $\mathcal{O}(1)$, however depending on the specific SUSY details, some of these terms may effectively vanish. The decay to the different-generation chargino pairs is given by

$$\Gamma_{\phi\to\widetilde{W}_1\widetilde{W}_2} \simeq \frac{(\lambda_\text{gauge}-\lambda_H)^2}{8\pi}\frac{m_\phi^3}{m_P^2}\left(\frac{m_{\widetilde{W}_1}^2+m_{\widetilde{W}_2}^2}{m_\phi^2}\right) \times\left(\sin^2\gamma_L\cos^2\gamma_L+\sin^2\gamma_R\cos^2\gamma_R\right). \tag{4.32}$$

Intriguingly, if $\lambda_\text{gauge}=\lambda_H$ this interaction vanishes while it is in general highly suppressed due to destructive interference in addition to chirality suppression.

Moving to the decays to neutralino pairs, the decay to same-generation neu-

tralino pairs is given by

$$\Gamma_{\phi\to\widetilde{Z}_i\widetilde{Z}_i} \simeq \frac{\left(\lambda_H\left[(v_1^{(i)})^2+(v_2^{(i)})^2\right]+\lambda_{\text{gauge}}\left[(v_3^{(i)})^2+(v_4^{(i)})^2\right]\right)^2}{8\pi}\frac{m_\phi^3}{m_P^2}\left(\frac{m_{\widetilde{Z}_i}^2}{m_\phi^2}\right). \tag{4.33}$$

Here, $v_j^{(i)}$ are the matrix elements from the matrix that diagonalizes the neutralino mass matrix, which are typically calculated numerically and are at most $\mathcal{O}(1)$. The decay to different generation neutralinos is then given by

$$\Gamma_{\phi\to\widetilde{Z}_i\widetilde{Z}_j} \simeq \frac{\left(\lambda_H\left(v_1^{(i)}v_1^{(j)}+v_2^{(i)}v_2^{(j)}\right)+(-1)^{\theta_i+\theta_j}\lambda_{\text{gauge}}\left(v_3^{(i)}v_3^{(j)}+v_4^{(i)}v_4^{(j)}\right)\right)^2}{16\pi} \times\frac{m_\phi^3}{m_P^2}\left(\frac{m_{\widetilde{Z}_i}^2+m_{\widetilde{Z}_j}^2}{m_\phi^2}\right) \tag{4.34}$$

where θ_i and θ_j are defined to be 0 or 1 so that the corresponding neutralinos $\widetilde{Z}_i$ and $\widetilde{Z}_j$ have a positive mass. It is worth noting that if both neutralino masses $m_{\widetilde{Z}_i}$ and $m_{\widetilde{Z}_j}$ have the same sign (where we refer here to the eigenvalues of the mass matrix - the physical masses have the additional sign from $\theta_{i,j}$ and are thus intrinsically positive), then the gaugino and higgsino components constructively interfere - making this decay width more sizeable. However, if both neutralino masses have *opposite* sign from each other, then they interfere destructively and thus yield a much smaller decay width.

Both the charginos and the neutralinos receive chirality suppression in their widths. Thus, neither one contributes significantly to the total decay width of the modulus. These *are*, however, extremely important modes in determining the modulus branching ratio to R-parity odd final states. Much like the gluinos,

however, the decays to neutralinos and charginos may be unsuppressed if the modulus is stabilized supersymmetrically - this again arises through the F-term interactions of the modulus and is discussed further in App. (A) and Sec. (4.3.1).

4.2.3 Decays into matter fields

The decays to matter fields have the interaction term in the Kähler potential

$$\mathcal{L} \supset \int d^4\theta \left[\frac{\lambda_{L_i}}{m_P} \hat{\Phi}\, \hat{L}_i^\dagger \hat{L}_i + \frac{\lambda_{E_i}}{m_P} \hat{\Phi}\, (\hat{E}_i^c)^\dagger \hat{E}_i^c + \frac{\lambda_{Q_i}}{m_P} \hat{\Phi}\, \hat{Q}_i^\dagger \hat{Q}_i \right. \\ \left. + \frac{\lambda_{U_i}}{m_P} \hat{\Phi}\, (\hat{U}_i^c)^\dagger \hat{U}_i^c + \frac{\lambda_{D_i}}{m_P} \hat{\Phi}\, (\hat{D}_i^c)^\dagger \hat{D}_i^c + \text{h.c.} \right] \quad (4.35)$$

where each of the quark and lepton superfields has a generation index $i \in \{1, 2, 3\}$. Again, for the sake of simplicity in this discussion, we take the quark couplings to be unified, $\lambda_{Q_i} = \lambda_{U_i} = \lambda_{D_i} \equiv \lambda_Q$, and the lepton couplings to be unified, $\lambda_{L_i} = \lambda_{E_i} \equiv \lambda_L$.

Let us focus first on both the squarks and sleptons. For the first two generations of squarks and sleptons, the gauge eigenstates have very minimal mass mixing [1] and thus we approximate the mass eigenstates as simply the gauge eigenstates (e.g. $\widetilde{u}_{L,R} \simeq \widetilde{u}_{1,2}$). The third generation, i.e. the stop, sbottom, and stau, *do* have a non-negligible amount of mixing, and thus we make use of a transformation matrix (detailed in App. (A)) to convert to the mass eigenstates. However, in our unification simplification here, the dependence on the mixing angle drops out. Additionally, although decays to different generation pairs is possible, these are highly subdominant for non-unified couplings - and vanish in the unified limit.

Thus, the modulus decay to sleptons are given by the widths

$$\Gamma_{\phi\to\widetilde{l}_i\widetilde{l}_i} \simeq \frac{\lambda_L^2}{8\pi}\frac{m_\phi^3}{m_P^2}\left(\frac{m_{\widetilde{l}_i}}{m_\phi}\right)^4 \tag{4.36}$$

while the decay to squarks are given by the widths

$$\Gamma_{\phi\to\widetilde{q}_i\widetilde{q}_i} \simeq \frac{3\lambda_L^2}{8\pi}\frac{m_\phi^3}{m_P^2}\left(\frac{m_{\widetilde{q}_i}}{m_\phi}\right)^4 \tag{4.37}$$

where we have summed over colors, resulting in an additional factor of 3.

These decay widths are all *extremely* subleading, due to the mass suppression factor of $(m_{\widetilde{f}}/m_\phi)^4$. Although they do contribute to the branching ratio to R-parity odd particles, we can expect them to be well below the contributions from the neutralinos and charginos, which only have a chirality suppression factor of $(m_f/m_\phi)^2$.

Moving to the decays to the physical quarks and leptons, we combine the doublets and singlets into the physical fields (as described in App. (A)). The decays to leptons are then calculated to be

$$\Gamma_{\phi\to l_i l_i} \simeq \frac{\lambda_L^2}{4\pi}\frac{m_\phi^3}{m_P^2}\left(\frac{m_{l_i}}{m_\phi}\right)^2 \tag{4.38}$$

while the decays to quarks are given by

$$\Gamma_{\phi\to q_i q_i} \simeq \frac{3\lambda_L^2}{4\pi}\frac{m_\phi^3}{m_P^2}\left(\frac{m_{q_i}}{m_\phi}\right)^2 \tag{4.39}$$

where, again, we have summed over colors.

A few immediate comments are in order. From Eq. (4.38), we see that in the massless neutrino limit, this width vanishes. Similarly, the width in Eq. (4.39) vanishes in the limit of massless u, d, and s quarks. Furthermore, we once again see that the fermionic widths are chirality suppressed in comparison to the leading decay modes. We also expect these widths to be subdominant compared to the (suppressed) widths to gluinos, charginos, and neutralinos as the quark and lepton masses are expected to be well below the superparticle masses (except possibly the top quark).

4.2.4 Decays into ALPs

As we have already discussed, the decay of the modulus into ALPs is a model-dependent process. If the ALP is ultralight, as in LVS, the decay mode is always open since the ALP is effectively massless. However, the ALP may also be massive such as in KKLT, and - since supersymmetry is preserved in KKLT before uplifting effects are incorporated providing a large supersymmetric mass M_Φ - may be kinematically forbidden since one expects $m_\phi \simeq m_c$. It is conceivable that one could construct a model in which the ALP is massive but sufficiently light so that the decay channel is kinematically allowed - however we do not consider this case in this work and instead consider only the limits $m_c \sim m_\phi$ and $m_c \sim 0$.

In the case where the ALP is ultralight, the decay width is given by

$$\Gamma_{\phi\to cc} \simeq \frac{\lambda_{\rm ALP}^2}{32\pi}\frac{m_\phi^3}{m_P^2}. \tag{4.40}$$

Since the ALPs are only gravitationally coupled, they do not thermalize once produced. Additionally, since they are effectively massless and are a leading decay mode of the modulus, we will see that these ALPs are potentially very problematic due to tight constraints on the production of dark radiation [11].

4.2.5 Decays into DFSZ-type axions

While the ALPs are assumed to arise from the dimensional reduction of the 10d gauge fields, in this work we consider the QCD axion to be instead of "field theoretic" type - i.e. we assume the QCD axion to be the phase of some massive SM singlet field $\hat{S}$ that acquires a VEV as in the DFSZ model. The modulus couplings are then of the form

$$\mathcal{L} \supset \frac{\lambda_{\rm PQ}}{2m_P} \int d^4\theta \left[\hat{\Phi} \left(\hat{A} + \hat{A}^\dagger \right)^2 + \text{h.c.} \right] \tag{4.41}$$

where the axion superfield $\hat{A} = (s + ia)/\sqrt{2} + \sqrt{2}\theta\tilde{a} + \theta^2 \mathcal{F}_a$. The modulus decay widths to saxions and axions reduce to the same form for $m_\phi \gg m_s, m_a$, and are given by

$$\Gamma_{\phi \to ss(aa)} \simeq \frac{\lambda_{\rm PQ}^2}{64\pi} \frac{m_\phi^3}{m_P^2}. \tag{4.42}$$

Thus, the ϕPQMSSM has two additional unsuppressed modulus decay modes to axions and saxions, while the decays to the Higgs sector become mass-suppressed as the Giudice-Masiero term is forbidden. This can be potentially problematic however, as the axions typically do not thermalize and behave primarily as dark radiation. We will discuss this at great length in Ch. (6).

The modulus decay width to axinos is then given by

$$\Gamma_{\phi\to\widetilde{a}\widetilde{a}} \simeq \frac{\lambda_{\rm PQ}^2}{8\pi}\frac{m_\phi^3}{m_P^2}\left(\frac{m_{\widetilde{a}}^2}{m_\phi^2}\right) \tag{4.43}$$

where the axinos receive a factor of 2 enhancement as they are Majorana. As with the other fermion decay modes, this is chirality suppressed and thus subleading to the total width although it may provide a significant contribution to the total R-parity odd branching fraction. However, similar to the gauginos and higgsinos, the axinos may also have a model-dependent unsuppressed decay through F-term interactions if the modulus has a large supersymmetric mass.

4.2.6 Decays into gravitinos

In addition to the interactions we have already discussed, we also need to include the decays to gravitinos which arise from supergravity interactions of the form

$$\mathcal{L} \supset -\exp(G/2)\psi_\mu\sigma^{\mu\nu}\psi_\nu + \text{h.c.} \tag{4.44}$$

where $G \equiv K + \log W + \log \overline{W}$ is the Kähler function. However, as discussed in [350] the decay widths depend crucially on details of the hidden sector (i.e. other moduli in the UV theory) which can induce different interactions from their mixing in G. In particular, if direct couplings or significant mixing between the modulus and a hidden sector is present, the decay width will be unsuppressed ($\propto m_\phi^3/m_P^2$) while if these direct couplings are absent, the decay width will be chirality suppressed ($\propto m_\phi m_{3/2}^2/m_P^2$). We thus adopt the decay widths computed

in [228, 230, 350] and parameterize them as

$$\Gamma_{\phi\to\psi_{3/2}\psi_{3/2}} \simeq \frac{\lambda_G^2}{288\pi}\frac{m_\phi^3}{m_P^2}\left(\lambda_1+\lambda_2\frac{m_{3/2}^2}{m_\phi^2}\right) \tag{4.45}$$

where we define $\lambda_{1,2} \equiv 0, 1$ depending on which case scenario we are considering. We will discuss this point more in the next section.

4.3 A natural SUSY benchmark point

In order to illustrate the results presented in the previous section, we adopt henceforth a natural SUSY benchmark point based on the three-extra-parameter non-universal Higgs SUSY model NUHM3 [324, 325, 326, 328, 327, 329]. This model has unified soft masses for first and second generation matter scalars $m_0(1) = m_0(2) \equiv m_0(1,2)$, while the third generation soft mass $m_0(3)$ is independent. Additionally, the two soft Higgs masses m_{H_u} and m_{H_d} are independent. The parameter space for this model is entirely specified by

$$m_0(1,2),\ m_0(3),\ m_{1/2},\ A_0,\ \tan\beta,\ \mu,\ m_A \tag{4.46}$$

where μ and m_A are evaluated at the weak scale, while all other parameters are evaluated at the GUT scale.

We display the input data for the benchmark point in Table (4.3), which are listed in the top two sections. The resulting mass spectra is calculated using Isajet 7.88 [330] and is displayed in the third section of Table (4.3). Finally, in

parameter	NUHM3
$m_0(3)$	5 TeV
$m_0(1,2)$	10 TeV
$m_{1/2}$	1.2 TeV
A_0	-8 TeV
$\tan\beta$	10
μ	200 GeV
m_A	2 TeV
$m_{\widetilde{g}}$	2927.4 GeV
$m_{\widetilde{u}_L}$	10209.4 GeV
$m_{\widetilde{u}_R}$	10288.5 GeV
$m_{\widetilde{e}_R}$	9912.9 GeV
$m_{\widetilde{t}_1}$	1251.0 GeV
$m_{\widetilde{t}_2}$	3655.6 GeV
$m_{\widetilde{b}_1}$	3697.1 GeV
$m_{\widetilde{b}_2}$	5104.5 GeV
$m_{\widetilde{\tau}_1}$	4729.8 GeV
$m_{\widetilde{\tau}_2}$	5061.5 GeV
$m_{\widetilde{\nu}_\tau}$	5030.0 GeV
$m_{\widetilde{W}_1^\pm}$	209.1 GeV
$m_{\widetilde{W}_2^\pm}$	1042.8 GeV
$m_{\widetilde{Z}_1}$	197.7 GeV
$m_{\widetilde{Z}_2}$	208.0 GeV
$m_{\widetilde{Z}_3}$	547.1 GeV
$m_{\widetilde{Z}_4}$	1052.6 GeV
m_h	125.3 GeV
$\Omega_{\widetilde{z}_1}^{std}h^2$	0.011
$BF(b\to s\gamma)\times 10^4$	3.0
$BF(B_s\to\mu^+\mu^-)\times 10^9$	3.8
$\sigma^{SI}(\widetilde{Z}_1,p)$ (pb)	1.7×10^{-9}
$\sigma^{SD}(\widetilde{Z}_1,p)$ (pb)	3.6×10^{-5}
$\langle\sigma v\rangle\vert_{v\to 0}$ (cm^3/sec)	2.0×10^{-25}
Δ_{EW}	20

Table 4.3: Input parameters and resulting weak-scale MSSM mass spectra for a natural SUSY benchmark point in the NUHM3 model. Additionally, we take $m_{3/2}=30$ TeV except where noted otherwise.

the fourth section of Table (4.3) we list some estimated quantities which provide insight on current constraints for this benchmark point. These quantities are also computed using the Isajet routines.

It is worth mentioning here that if the lightest supersymmetric particle (LSP) - which in our benchmark point is a higgsino-like neutralino - makes up the entirety of the dark matter density by receiving an enhancement to its thermally-produced relic density, this benchmark point runs into tension with some experimental constraints. Based on the lightest neutralino annihilation cross section and mass, $\langle\sigma v\rangle|_{v\to 0}$ and $m_{\widetilde{Z}_1}$, the neutralino annihilation rate for our benchmark is slightly too large to be consistent with Fermi-LAT searches for dark matter annihilation in dwarf spheroidal galaxies [351], which limits $\langle\sigma v\rangle|_{v\to 0} \lesssim 5 \times 10^{-26}$ cm^{3}s^{-1} in the $b\bar{b}$ channel for a 200 GeV neutralino. Furthermore, recent results from the LUX-ZEPLIN (LZ) [352] experiment constrains the spin-independent cross section $\sigma^{SI}(\widetilde{Z}_1, p) \lesssim 6 \times 10^{-11}$ pb and the spin-dependent cross section $\sigma^{SD}(\widetilde{Z}_1, p) \lesssim 1 \times 10^{-5}$ pb. However, for the purposes of this work we do not expect a different benchmark point that meets these constraints to significantly alter our results for the ϕMSSM. Additionally, when we cover the ϕPQMSSM these constraints become significantly softer as they rely on the assumption that the LSP is the entirety of the dark matter. Specifically, if the produced neutralino relic density takes its thermally-produced value $\Omega_{\widetilde{Z}_1}h^2 \simeq 0.011$ (or at least is a subdominant dark matter component), these constraints are weakened by a factor [353] of $\xi \equiv \Omega_{\widetilde{Z}_1}h^2/0.12$ for the $\sigma^{SI,SD}(\widetilde{Z}_1, p)$ constraints and a factor of ξ^2 for the $\langle\sigma v\rangle|_{v\to 0}$ constraint which eases these bounds sufficiently to allow experimental compatibility. In either case, we will see in the coming chapters that this benchmark point serves as a "best-case scenario" as more efficient cross sections run into experimental tension unless WIMPs are an *extremely* subdominant component of the total dark

matter.

4.3.1 Scenarios from strings

We now enumerate some of the most motivated scenarios that we have alluded to in the previous sections. Although we have already discussed the primary model-independent decay modes of the modulus, there can be significant contributions from model-dependent F-term interactions and assumptions about hidden sector details. In most of the following work, we will only be focused on a subset of these scenarios which provides some semblance of a (string) model-independent reference. Detailing the other scenarios here then allows us to discuss how our results are expected to change for other specific string constructions that may fall into other case scenarios.

As we mentioned in the previous section, the decay of a modulus to gravitinos is sensitive to the details of the hidden sector - which is studied in [350, 230, 228, 354]. Most moduli decays to fermions are expected to receive chirality suppression, which was argued to apply for decays to gravitinos in [355, 225]. However, [350] showed that this amplitude is generically unsuppressed if the modulus has either direct couplings or appreciable non-supersymmetric mixing between longitudinal component of the gravitino (or equivalently the goldstino, by use of the goldstino equivalence theorem) and a SUSY breaking hidden sector field. If the modulus and SUSY breaking hidden fields are not directly coupled and have masses dominated by the supersymmetric contribution, the contributions to the modulus decay width which are unsuppressed cancel, leaving only the suppressed amplitude.

Furthermore, as we have previously mentioned there are cases where modulus decays to gauginos are unsuppressed. As detailed in [350, 356], this may occur through the gaugino mass term which is set by the modulus F-term if the lightest modulus has a large supersymmetric mass (as we show in App. (A)). The same interaction occurs from the Giudice-Masiero term for the higgsinos, so that the modulus decay to the physical charginos and neutralinos is unsuppressed for both gaugino and higgsino components. The simplest way to see this is in the global SUSY limit, where we can parameterize the supersymmetric mass term for the light modulus in the superpotential, $W \supset M_\Phi \Phi^2$, thus leading to an F-term like $\mathcal{F}_\Phi \sim M_\Phi \Phi$. Of course, this only contributes a non-negligible amount if the lightest modulus does not break SUSY, such as in KKLT models. In the ϕPQMSSM, the same effect leads to unsuppressed decays to axinos. However, the ϕPQMSSM forbids the Giudice-Masiero term with a PQ symmetry which also forbids the unsuppressed decays to higgsino components. Since the unsuppressed decay to gaugino components is still allowed as they arise from the gauge-kinetic function, we refer only to unsuppressed gauginos in the following cases - any unsuppressed decays to either higgsino or axino components is then implicit from context.

The above considerations then motivate the four case scenarios for model-dependent decay widths which we enumerate in Table (4.4). Case **A1** has

	Unsuppressed gravitinos	Suppressed gravitinos
Unsuppressed gauginos	Case **A1**	Case **A2**
Suppressed gauginos	Case **B1**	Case **B2**

Table 4.4: Summary of case scenarios on leading decay modes depending on whether or not they receive chirality suppression.

unsuppressed decays to both gravitinos and to gauginos, and thus parametrizes cases where the lightest modulus does not break SUSY, but has direct couplings or appreciable non-supersymmetric mixing to some SUSY breaking hidden sector. This includes some variants and generalizations of KKLT [3] models - and in particular KKLT models with hidden sector fields residing on $D3$ branes which therefore exhibit the sequestered form[4] of Sec. (2.4), such as those described in [271, 228, 354]. Another variant of KKLT in this category is the O'KKLT [169] model, which achieves uplifting by combining the O'Raifeartaigh and KKLT models. This scenario also includes the G_2MSSM model described in [357, 157] where the hidden sector are the other moduli of the M-theory construction, although in this case the lightest modulus is lighter than the gravitino and thus this channel is kinematically forbidden. Case **A2** has suppressed decays to gravitinos but unsuppressed decays to gauginos, and so parametrizes cases where the lightest modulus does not break SUSY and has no direct couplings or non-supersymmetric mixing to some SUSY breaking hidden sector. This includes the KKLT model in its original form [3], the Kallosh-Linde (KL) racetrack-type model [132, 358], and the KKLT model with a D-term uplifting sector [163]. Case **B1** has unsuppressed gravitino decays but suppressed gaugino decays. A tentative example of this would be fibred LVS [9, 10], where the fibre modulus is directly coupled to the transverse mode. The transverse mode is then the lightest modulus which has an effectively vanishing supersymmetric mass. However, it is a generic feature of this framework that the decay of the lightest modulus to

[4]This assumes that, although the Kähler potential may be of sequestered form, the sequestering is sufficiently weak so that the modulus decay to gravitinos is kinematically accessible.

gravitinos is kinematically forbidden [9, 359, 10]. Case **B2** then has suppressed decays to both gauginos and gravitinos. Here, a tentative example would be minimal LVS [181, 180], as any mixing between the bulk modulus and blow-up moduli is extremely suppressed. Although the blow-up moduli break SUSY, they are fixed by non-perturbative effects and have masses dominantly fixed by the supersymmetric contributions, while the bulk modulus is the dominant contribution to SUSY breaking. Much like in fibred LVS, it is a generic feature that moduli decay to gravitinos is kinematically forbidden.

In addition to the specific examples above, there may be as-yet-undiscovered moduli stabilization schemes or extended models based on existing schemes which may generically fall into one or the other of these categories. For much of this work, we concentrate on case **B2** but investigate some implications of case **B1** in the ϕMSSM. As we will see in the next few chapters, we generically expect our results to become slightly more optimistic for models with unsuppressed gaugino decays when compared to both cases **B1** and **B2**.

There are additional model-dependent considerations based on the gauge-kinetic function of the low energy theory. In most Type IIb models that give weak-scale supersymmetry, the MSSM sector is studied by constructions with fractional $D3$ branes at singularities [360, 185, 184, 361]. In this so-called "blow-up" or "singular" regime, the gauge-kinetic function is set primarily by the dilaton,

$$f = S + s_{ik}T_k \tag{4.47}$$

where T_k are the blow-up moduli resolving the singularity [360, 185, 362]. In LVS models, the blow-up moduli are stabilized at a much higher scale than the bulk modulus, while in KKLT models the blow-up moduli may be set to 0 [362, 363]. As the dilaton is expected to be stabilized by fluxes in Type IIb constructions and is thus expected to have a much higher mass (close to the string scale) than the Kähler moduli, any dependence of the gauge-kinetic function on the lighter Kähler moduli is then expected to be induced radiatively [239]. A similar form of the gauge-kinetic function appears in heterotic models [364, 365, 366, 367]. However, in the heterotic case the lightest modulus may in fact be the dilaton depending on the details of stabilization [368, 369]. The MSSM sector can also be located on $D7$ branes in the Type IIb context, which has a gauge-kinetic function of the form

$$f = T_a + \alpha S \tag{4.48}$$

where T_a is the modulus corresponding to the del Pezzo surface that the $D7$ branes wrap [184, 370, 185], so that in the geometric regime our gauge-kinetic function may appear at tree level. In this case, sequestering is not possible and to achieve soft terms close to the TeV scale, either fine-tuning of W_0 or a low string scale, $m_s \sim \mathcal{O}(10^{11} - 10^{12})$ GeV, is required for a sufficiently low gravitino mass [371, 185, 205]. Additionally, in an M-theory construction compactified on a G_2 manifold with N geometric moduli, the gauge-kinetic function is given by

$$f = \sum_{i=1}^{N} \alpha_i T_i \tag{4.49}$$

where α_i are integers determined by topological properties of the manifold [357, 157]. Thus, although one generically expects the couplings to be $\lambda_i \sim \mathcal{O}(1)$ to the quark, lepton, and Higgs sectors, the couplings to the gauge sector may be either $\lambda_{\text{gauge}} \sim \mathcal{O}(1)$ or[5] $\lambda_{\text{gauge}} \sim \mathcal{O}(1/16\pi^2)$ depending on the details of the string model. We enumerate these cases in Table (4.5).

	Tree-level	Loop-level
Gauge-kinetic function	Case **GK1**	Case **GK2**

Table 4.5: Summary of case scenarios for the expected magnitude of λ_{gauge} depending on whether or not the lightest modulus appears at tree-level or at loop-level.

There is one final set of scenarios which we consider in this work. As we saw in Sec. (2.3.2) and Sec. (2.3.3), modulus decay to ALPs may be possible if the ALP is sufficiently light. Specifically, if the shift symmetry of the Kähler modulus is preserved when the lightest modulus is stabilized such as in LVS, the ALP is protected from gaining a mass (except from extremely tiny non-perturbative effects which break this symmetry) and thus is ultralight. If, however, the shift symmetry is broken when the lightest Kähler modulus is stabilized as in KKLT, the ALP becomes massive - and since SUSY is preserved in the KKLT minimum prior to uplifting, it is expected to be roughly the same mass as the modulus. The ALPs which are massive are largely irrelevant for our purposes - not only are they expected to be a kinematically forbidden decay of the lightest modulus, but any thermal population that may exist after inflation will be diluted to negligible

[5]We assume here that the dependence of the gauge-kinetic function on the lightest moduli appears at one-loop order, so that the effective coupling has a magnitude of roughly a loop suppression factor $\sim 1/16\pi^2$.

levels once the modulus injects significant entropy into the thermal bath. The ultralight ALPs, on the other hand, *are* relevant as they are an unsuppressed decay mode and since they are effectively massless and only gravitationally coupled, behave primarily as dark radiation [239, 240]. Thus, we dedicate a section with the ϕMSSM to the study of the dark radiation production estimated by ALPs if they are ultralight.

In the following sections, we display our results for modulus decay widths and branching ratios for a subset of the above scenarios and provide brief discussion on how our results are expected to change for the rest of the cases. Our plots utilize the full set of decay widths which are listed in App. (A), and assume the natural SUSY benchmark point which we have listed in Table (4.3). In the set of **GK1** cases, we take all modulus couplings $\lambda_i = 1$, while in the **GK2** cases we take the modulus couplings to the gauge sector to be $\lambda_{\text{gauge}} = 1/16\pi^2$ and all remaining modulus couplings to be $\lambda_i = 1$. In both cases, we assume that the gauge couplings are unified so that $\lambda_{U(1)} = \lambda_{SU(2)} = \lambda_{SU(3)}$. Finally, for the sake of legibility each curve in the partial width and branching ratio plots are the sum of all relevant contributions (e.g. the sfermion + sfermion curve includes all generations and flavors of squarks and sleptons).

4.3.2 Modulus decays in the ϕMSSM - the massive ALP case

In this section, we display the results of the two-body decays $\phi \to A + B$ in the ϕMSSM where we assume that any ultralight ALPs are absent from the low energy spectrum. In the ϕMSSM, the Giudice-Masiero operator is allowed - and

thus the decay widths to the Higgs sector is unsuppressed. Generically speaking, the possible leading decay modes in this scenario are decays to either gauge boson $(\gamma, g, Z^0, W^\pm)$ pairs or Higgs boson $(h, H, A, H^\pm)$ pairs as these all scale as m_ϕ^3. Specific cases may then add the gravitino $(\psi_{3/2})$ and/or gauginos $(\widetilde{Z}_i, \widetilde{W}_i, \widetilde{g})$ to this list. Of course, the leading decay mode depends on which combination of cases from Tables (4.4) and (4.5) we are considering.

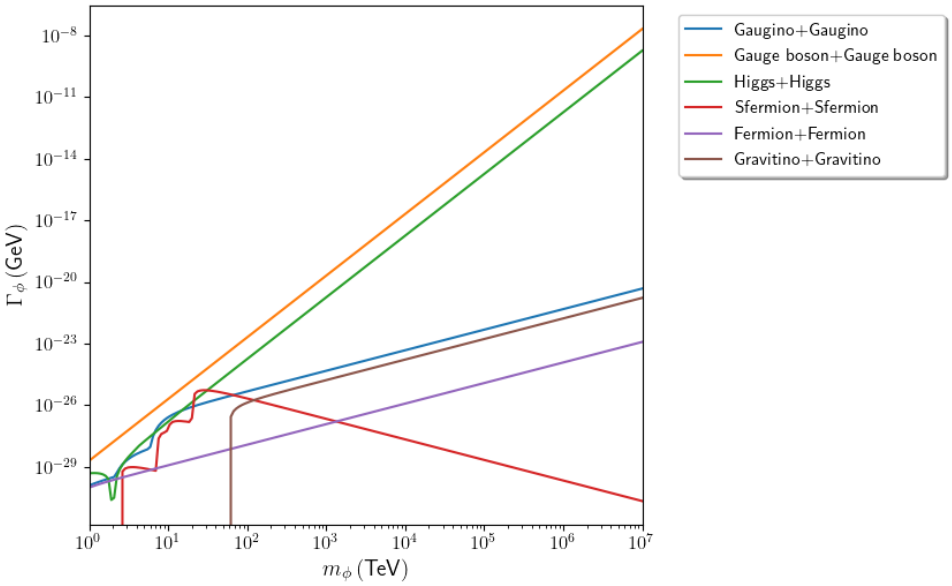


Figure 4.1: Modulus partial decay widths for the case **B2-GK1** as a function of m_ϕ for the natural SUSY benchmark point in Table (4.3). Here, all λ_i couplings are set to unity.

We first focus on the case **B2-GK1**, which assumes suppressed decays to both gauginos and gravitinos and unsuppressed couplings to the gauge sector. We display the modulus partial decay widths in Fig. (4.1) for this scenario. As expected from their m_ϕ^3 scaling behavior, for most of the parameter space the decays to gauge boson pairs (orange curve) are the leading decay channels, with the decays to Higgs pairs (green curve) being the secondary decay channels. All other

modes are highly subleading unless $m_\phi \lesssim 100$ TeV. Note the sharp dip in the width to Higgs pairs around $m_\phi \sim 2$ TeV - this is due to a partial cancellation between the Giudice-Masiero term and the $\Phi H^\dagger_{u,d} H_{u,d}$ + h.c. terms. This cancellation is most pronounced when $m_\phi \sim m_{H,A,H^\pm}$, which all have $m_{H,A,H^\pm} \sim 2$ TeV for our benchmark point. We also see from Fig. (4.1) that the sfermion channel (red curve) is entirely closed until $m_\phi \sim 2.5$ TeV, at which point the decay $\phi \to \widetilde{t}_1 + \widetilde{t}_1$ becomes accessible. The $\widetilde{t}_2$ and $\widetilde{b}_1$ channels then become open around $m_\phi \sim 7.2$ TeV, with the remaining third-generation sfermion decay channels becoming open around $m_\phi \sim 2m_0(3) \sim 10$ TeV. The first and second generation sfermions finally become accessible around $m_\phi \sim 2m_0(1,2) \sim 20$ TeV. Looking at the decay to gauginos (blue curve), the width is comprised of the neutralinos and charginos for $m_\phi \lesssim 6$ TeV, while for $m_\phi \gtrsim 6$ TeV this width is dominated by gluino decay which temporarily makes a sizeable ($\sim 10\%$) contribution to the total width. As expected, decays to gravitino pairs (brown curve) is blocked until $m_\phi \sim 60$ TeV.

In Fig. (4.2), we display the modulus branching ratios for the same scenario, case **B2-GK1**. We see that gauge bosons (orange curve) dominate the branching fraction with roughly $\mathcal{B}(\phi \to \text{G.B.}) \sim 90\%$ for all m_ϕ in the scan limits. The decays to Higgs boson pairs (green curve) then provide the secondary decay channels for $m_\phi \gtrsim 100$ TeV, with $\mathcal{B}(\phi \to \text{Higgs}) \sim 10\%$ in this region. All other decay modes have a branching fraction $\mathcal{B}(\phi \to \text{other}) \ll 1\%$ for $m_\phi \gtrsim 100$ TeV. On the other hand, for $m_\phi \lesssim 100$ TeV we see a bit more competition for the second largest branching fraction, with pairs of Higgs, sfermions, and gauginos each taking the lead when their heavier decay channels open. We see that the sfermions (red

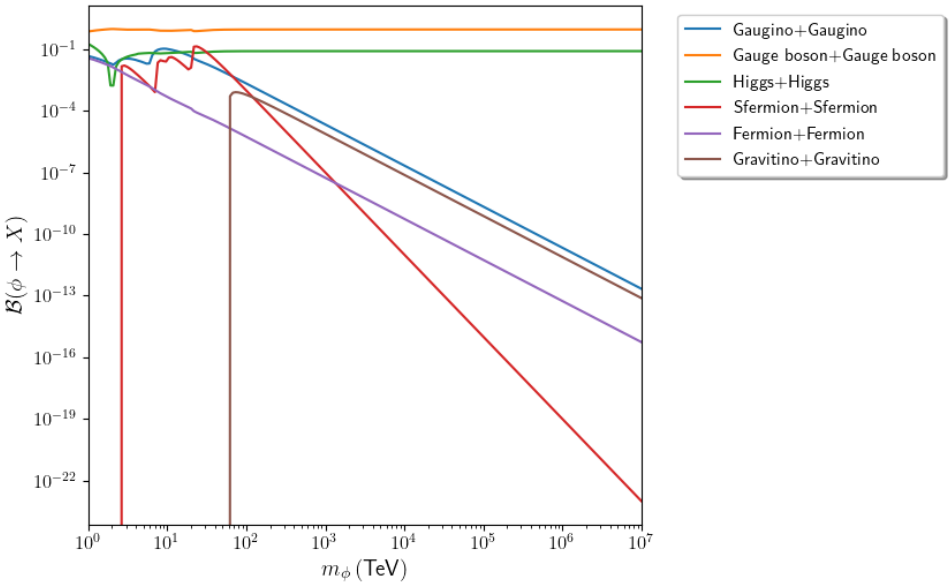


Figure 4.2: Modulus branching ratios for the case **B2-GK1** as a function of m_ϕ for the natural SUSY benchmark point in Table (4.3). Here, all λ_i couplings are set to unity.

curve) are the second leading channel once the first and second generation channels are available at $m_\phi \sim 20$ TeV, but due to the $1/m_\phi$ dependence in their decay widths, this (secondary) dominance is short-lived. Additionally, once the gluino channel (primary contribution to the blue curve) is open around $m_\phi \sim 6$ TeV, it also temporarily has the second largest branching fraction. In cases **A1-GK1** and **A2-GK1**, we would then expect the gluino channel to continue to dominate over the Higgs sector once it becomes accessible.

The total branching fraction into SUSY particles, i.e. decays to R-parity odd pairs, can also be very important when we study the production of WIMP dark matter from modulus decay. In particular, any R-parity odd particle must eventually cascade decay into the LSP. From this, Gelmini and Gondolo [231] emphasized that if LSP annihilations are inefficient, i.e. in the so-called branching

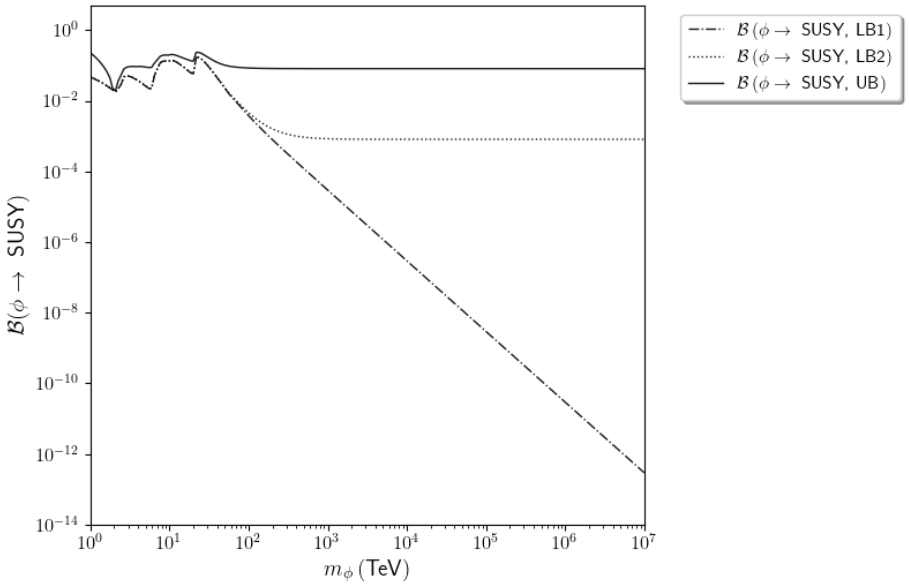


Figure 4.3: Upper and lower bounds for total modulus branching ratio to SUSY particles for the case **B2-GK1**. Here, all λ_i couplings are set to unity and we use the natural SUSY benchmark point in Table 4.3. The lower bound LB2 assumes the Higgs cascade decay to SUSY particles with 1% branching ratio, while the upper bound UB assumes 100% Higgs to SUSY branching ratio. The lower bound LB1 assumes no Higgs to SUSY contributions.

scenario which we discuss in the next chapter, the overall modulus branching ratio to SUSY particles is crucial in determining the relic density of LSPs. Therefore, we show in Fig. (4.3) both upper and lower bounds for the total modulus branching ratio into SUSY particles. Since the Higgs sector can decay into pairs of LSPs, we choose to parameterize this contribution since it is highly model-dependent. For the upper bound, we include all R-parity odd particles and in addition, we assume that the Higgs sector has a 100% branching ratio to SUSY particles. The absolute lower bound, which we notate as $\mathcal{B}(\phi \to \text{SUSY, LB1})$ in Fig. (4.3) is set by taking *only* the R-parity odd branching ratios (no Higgs decay to SUSY particles). Thus, the absolute lower bound LB1 contains no contributions from

possible Higgs sector decay to LSP pairs. Additionally, we display a second lower bound, $\mathcal{B}(\phi \to \text{SUSY, LB2})$, which includes all R-parity odd particles but assumes that the Higgs branching ratio to LSP pairs is $\mathcal{B}(h, H, A, H^{\pm} \to \text{ LSPs}) = 1\%$. We see that, for $m_\phi \lesssim 30$ TeV, the upper and lower bounds are all rather close. For 2.5 TeV $\lesssim m_\phi \lesssim 100$ TeV, gauginos and sfermions both provide comparable contributions to the overall branching fraction into SUSY particles, while for $m_\phi \gtrsim 100$ TeV, the gluino and gravitino are the dominant R-parity odd decays. Additionally, for $m_\phi \lesssim 2.5$ TeV, only the neutralinos and charginos are accessible.

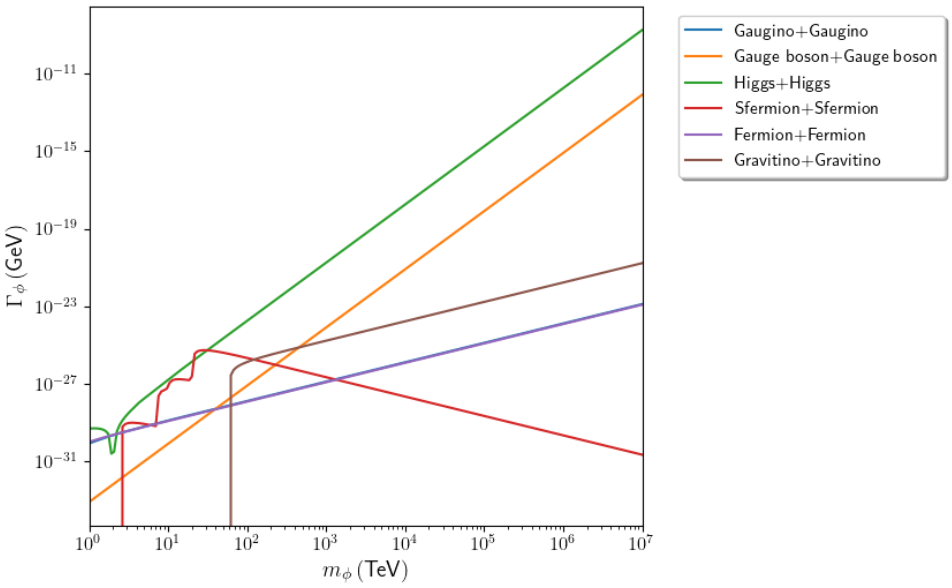


Figure 4.4: Modulus partial decay widths for the case **B2-GK2** as a function of m_ϕ for the natural SUSY benchmark point in Table (4.3). Here, all λ_i couplings are set to unity except for the couplings to the gauge sector, which have $\lambda_{\text{gauge}} = 1/16\pi^2$.

Next, we move on to the case **B2-GK2**, which assumes suppressed decays to both gauginos and gravitinos as well as suppressed couplings to the gauge sector. In Fig. (4.4), we display the partial decay widths of the modulus for this case.

Because the gauge sector in this scenario is taken to be induced radiatively, the Higgs sector (green curve) now provides the dominant decay channels, while the gauge bosons (orange curve) do not become secondary modes until $m_\phi \gtrsim 500$ TeV - even with the m_ϕ^3 scaling! The suppression of this coupling also drastically reduces the decay width into gauginos (blue curve), which is overlapped by the fermion decays (purple curve) in Fig. (4.4). Production of neutralinos and charginos is then dominated by the decay to their higgsino components, while production of gluinos is suppressed below the higgsino channels. It is also interesting to note that, due to the aforementioned cancellation in the Higgs sector around $m_\phi \sim 2$ TeV, there is a small window where the leading decay modes are actually to SM fermions (which are dominated by decays to top quark pairs) and to the higgsino components of the neutralinos and charginos. Similarly, at $m_\phi \sim 2m_0(1,2) \sim 20$ TeV, the sfermions (red curve) are briefly the leading decay mode when the decay to first and second generations become accessible.

The modulus branching ratios for case **B2-GK2** are then shown in Fig. (4.5). For this case, the fermion branching curve (purple) overlaps with the gaugino branching curve (blue) - although a small portion of the gaugino curve can be seen underneath the fermion curve until the heaviest neutralino mode becomes accessible at around 2 TeV. Additionally, we note that the branching ratio to gauge bosons (orange) has been decreased from around 90% in case **B2-GK1** to around 0.1% for case **B2-GK2**. The gravitino (brown) also becomes the dominant R-parity odd decay mode shortly after it becomes accessible, while sfermions (red) are the dominant R-parity odd decay for 7 TeV $\lesssim m_\phi \lesssim$ 100 TeV. For $m_\phi \lesssim 7$

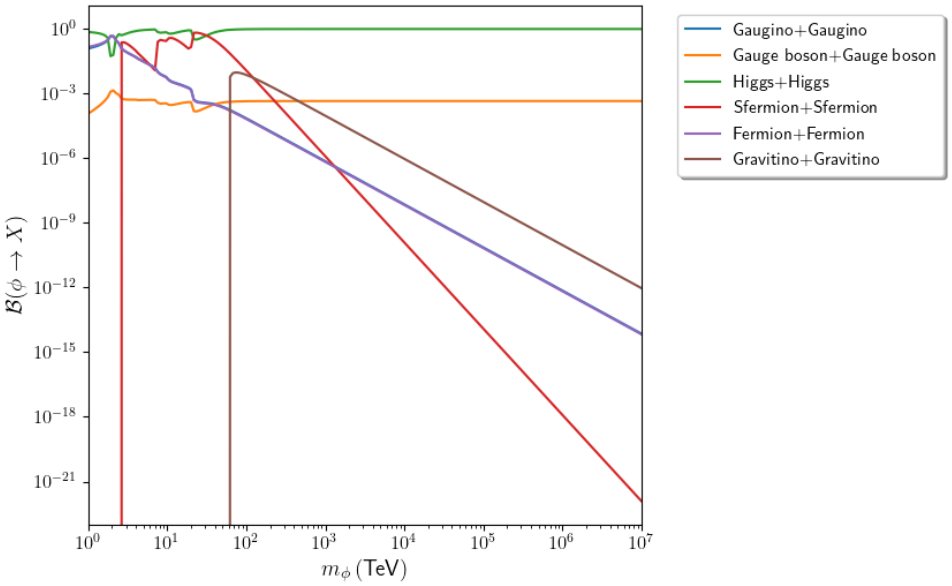


Figure 4.5: Modulus branching ratios for the case **B2-GK2** as a function of m_ϕ for the natural SUSY benchmark point in Table (4.3). Here, all λ_i couplings are set to unity except for the couplings to the gauge sector, which have $\lambda_{\text{gauge}} = 1/16\pi^2$.

TeV, the sfermions, neutralinos, and charginos compete for the leading R-parity odd decays. We display the total branching ratio into SUSY particles in Fig. (4.6), where we again adopt the same upper and lower bounds as for Fig. (4.3). In general, we see that for both lower bounds and the upper bound, there is roughly an order of magnitude increase in the total branching to LSPs compared to case **B2-GK1** in Fig. (4.3).

We now consider case **B1-GK1** which assumes suppressed decays to gauginos but unsuppressed decays to gravitinos. In Fig. (4.7), we display the modulus decay widths for this case. As with the previous cases, the gravitinos (brown curve) are kinematically forbidden until $m_\phi \gtrsim 60$ TeV. However, as the gravitinos are now unsuppressed they now trail the decays to Higgs pairs (green curve) only by

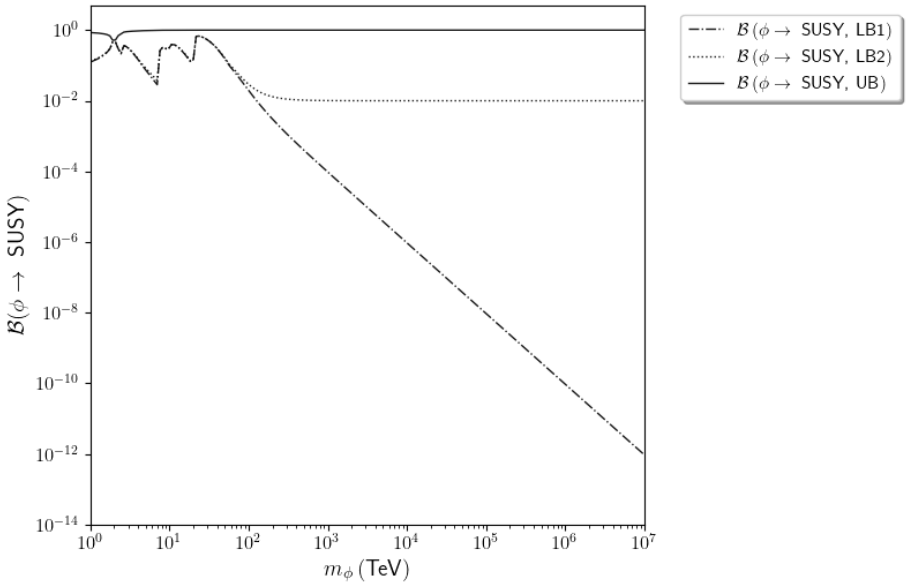


Figure 4.6: Upper and lower bounds for total modulus branching ratio to SUSY particles for the case **B2-GK2**. Here, we use the natural SUSY benchmark point in Table 4.3 and all λ_i couplings are set to unity except for the couplings to the gauge sector, which have $\lambda_{\text{gauge}} = 1/16\pi^2$. The lower bound LB2 assumes the Higgs cascade decay to SUSY particles with 1% branching ratio, while the upper bound UB assumes 100% Higgs to SUSY branching ratio. The lower bound LB1 assumes no Higgs to SUSY contributions.

about an order of magnitude and decays to gauge boson pairs (orange curve) by around two orders of magnitude. We do not expect a significant deviation of the total width of the modulus between cases **B1-GK1** and **B2-GK1**, although the gravitinos may now be produced in significant abundance. In case **B1-GK2**, we do expect a more noticeable change in the total width compared to case **B2-GK2** as the gauge boson decays are suppressed, although in this comparison we only expect roughly a 10% increase in $\Gamma_\phi^{\text{total}}$. In case **A1**, although we expect a change of roughly a factor of 2 in $\Gamma_\phi^{\text{total}}$ compared to the corresponding **B1** case due to the addition of unsuppressed gaugino modes, the addition of unsuppressed gravitino decays will be even less noticeable compared to the corresponding **A2** case.

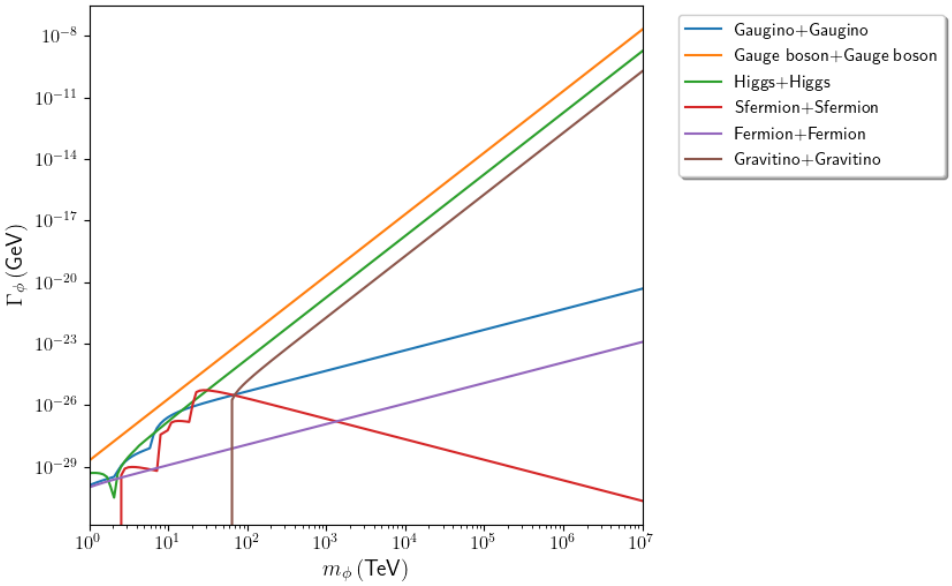


Figure 4.7: Modulus partial decay widths for the case **B1-GK1** as a function of m_ϕ for the natural SUSY benchmark point in Table (4.3). Here, all λ_i couplings are set to unity and decays to gravitinos are unsuppressed.

In Fig. (4.8), we display the corresponding branching ratios in case **B1-GK1**. We see that the modulus decays to gravitinos (if kinematically accessible) now occur at slightly below the 1% level, with all other branching ratios mostly unaffected. This is in good agreement with estimates from [228, 230], which point out a resurgence of the gravitino problem due to a large production of gravitinos from modulus decay. Although moduli lighter than 60 TeV here do not suffer from the moduli-induced gravitino problem (for $m_{3/2} = 30$ TeV) as we will discuss in the next chapter, we will see that a modulus this light will still grossly overproduce dark matter. We will discuss these aspects more in the upcoming chapters.

Now that we have studied modulus decay in a few of the possible cases, we are in a position to compare total decay widths - and discuss the possible quantitative

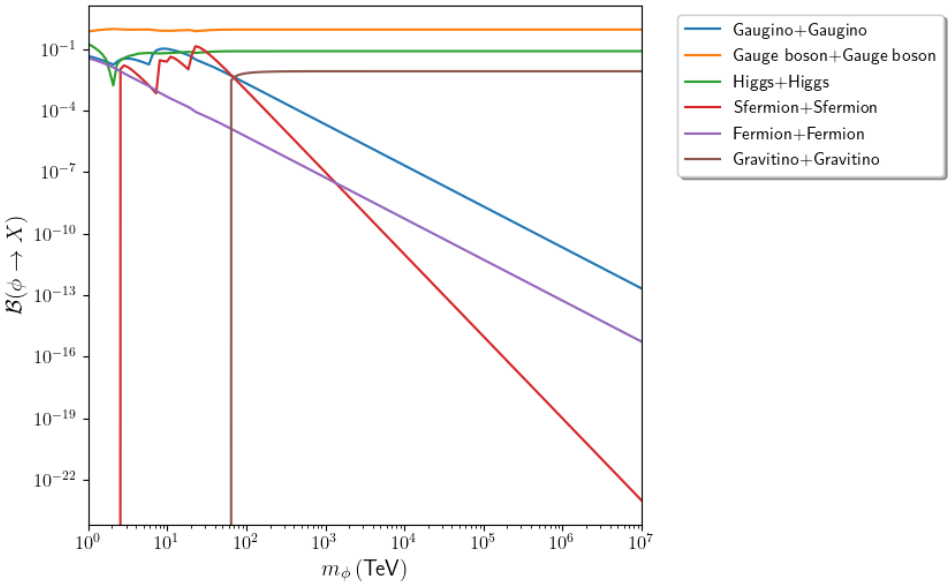


Figure 4.8: Modulus branching ratios for the case **B1-GK1** as a function of m_ϕ for the natural SUSY benchmark point in Table (4.3). Here, all λ_i couplings are set to unity and decays to gravitinos are unsuppressed.

changes for the remaining cases which we did not show above. The total decay width - and by extension, the lifetime - of the modulus is a crucial property to understand from a cosmological standpoint. In particular, if the modulus has too small of a decay width, its lifetime can be long enough that it decays during or after Big Bang Nucleosynthesis (BBN) and can spoil the extremely successful predictions of BBN. It is therefore important to understand the total decay width of the modulus, and to understand if any of our case scenarios can yield significantly different results from the others. This will allow us to draw rather immediate constraints on the modulus when we consider the scale at which it decays, and to understand if these constraints are quantitatively similar across the different moduli scenarios - establishing some potential sense of generality.

We compare the total widths, $\Gamma_\phi^{\text{total}}$, for cases **B2-GK1** and **B2-GK2** in

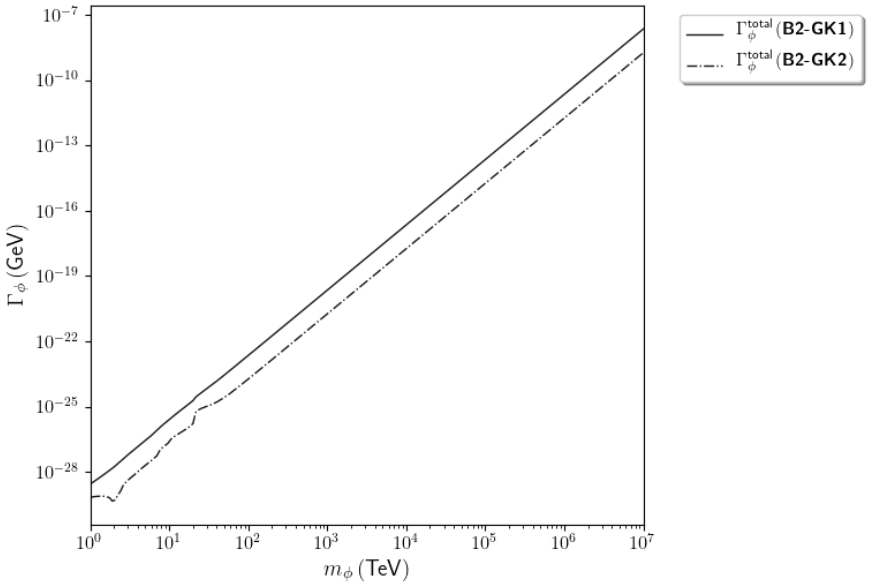


Figure 4.9: Comparison of the total width for cases **B2-GK1** and **B2-GK2** as a function of m_ϕ for the natural SUSY benchmark point in Table (4.3). Both cases have suppressed decays to gravitinos and gauginos. Case **B2-GK1** sets all couplings, including those to the gauge sector, to unity. Case **B2-GK2** takes the gauge sector couplings to be $\lambda_{\text{gauge}} = 1/16\pi^2$, with all remaining λ_i couplings set to unity.

Fig. 4.9. Between these two cases, we see that the value of $\Gamma_\phi^{\text{total}}$ has a difference of approximately one order of magnitude. We also see that the total decay width is largely unaffected as the many decay modes to sparticles become kinematically accessible, although the case **B2-GK2** blatantly sees where the sfermions become dominant ($m_\phi \sim 20$ TeV) and the Higgs cancellation occurs ($m_\phi \sim 2$ TeV). Since case **B2-GK2** has all model-dependent decays suppressed in addition to suppressed couplings to the gauge sector, this case represents the lower limit of $\Gamma_\phi^{\text{total}}$ among the scenarios in Tables (4.4) and (4.5) in the ϕMSSM. Of course, we now must ask how we expect these total widths to change if additional model-dependent decay channels are unsuppressed. In case **B1-GK1**, we saw that the

gravitino was subleading to the Higgs channel by about an order of magnitude. Therefore, we expect the unsuppressed gravitino's contribution to the total decay width to be sub-percent level - and so the case **B1-GK1** will have a value of $\Gamma_\phi^{\text{total}}$ that is nearly identical to the case **B2-GK1**. Case **B1-GK2** will have a more pronounced difference compared to case **B1-GK1** since the gauge boson modes are subdominant, although we expect an increase in total width of only about 10% here - which is still hardly noticeable on this plot.

Considering now the cases where the modulus is stabilized supersymmetrically, the addition of unsuppressed gaugino decay modes can potentially provide a significant difference to $\Gamma_\phi^{\text{total}}$ since they are expected to be comparable to the gauge boson modes. In the **GK1** cases, since the gauge bosons are the dominant decay mode we then expect that the addition of unsuppressed gaugino decays in cases **A1** and **A2** should increase $\Gamma_\phi^{\text{total}}$ by about a factor of 2 over their **B1** and **B2** counterparts. However, in the **GK2** cases, this addition should be mostly washed out from the suppression of λ_{gauge}, and so these modes should only change the total width by about 0.1%. Thus, we expect that all **GK2** cases will be quantitatively very close to the case **B2-GK2** - and thus we largely expect cosmological predictions in the **GK2** scenario to be largely independent of the scenario in Table (4.4). Meanwhile, cases **B1-GK1** and **B2-GK1** should have nearly identical total width, and cases **A1-GK1** and **A2-GK1** both give a $\Gamma_\phi^{\text{total}}$ that is roughly twice as large. As we will see when we study dark matter production, we are typically in the annihilation scenario (where the WIMP DM abundance is set by the annihilation rate and the modulus decay scale) -

and since the LSPs will annihilate somewhat efficiently, the increase in gaugino production is largely irrelevant. However, the small increase in total width will cause the modulus to decay slightly earlier, which actually gives us marginally more optimistic predictions for cases **A1** and **A2** than for case **B1** and **B2** in the **GK1** context.

4.3.3 Modulus decays in the ϕMSSM - the ultralight ALP case

In this section, we display the results of the decays in the ϕMSSM where we assume that the ALP is ultralight - and thus a viable decay mode of the modulus. As we have discussed in Sec. (4.2), the decays to ALPs are an unsuppressed decay mode and thus potentially a leading decay channel. Here, we again adopt the natural SUSY benchmark point from Table (4.3), and take all modulus couplings, including the coupling to the ALP, to unity ($\lambda_i = 1$). For the sake of brevity, we include only the results for case **B2-GK1** - the other case scenarios then follow similar qualitative and quantitative behavior to the results presented in the previous section.

In Fig. (4.10), we display the modulus partial decay widths in the case **B2-GK1** which now includes the ultralight ALP. This case assumes suppressed decays to gravitinos and gauginos, but unsuppressed gauge couplings. Displayed in Fig. (4.11) are the associated branching ratios of the modulus. We see that the decays to ALPs (brown curve) is quantitatively almost identical to the decays to the Higgs sector (green curve), each taking a branching ratio of roughly 10% for $m_\phi \gtrsim 50$ TeV. This is a particularly important consequence for studying the

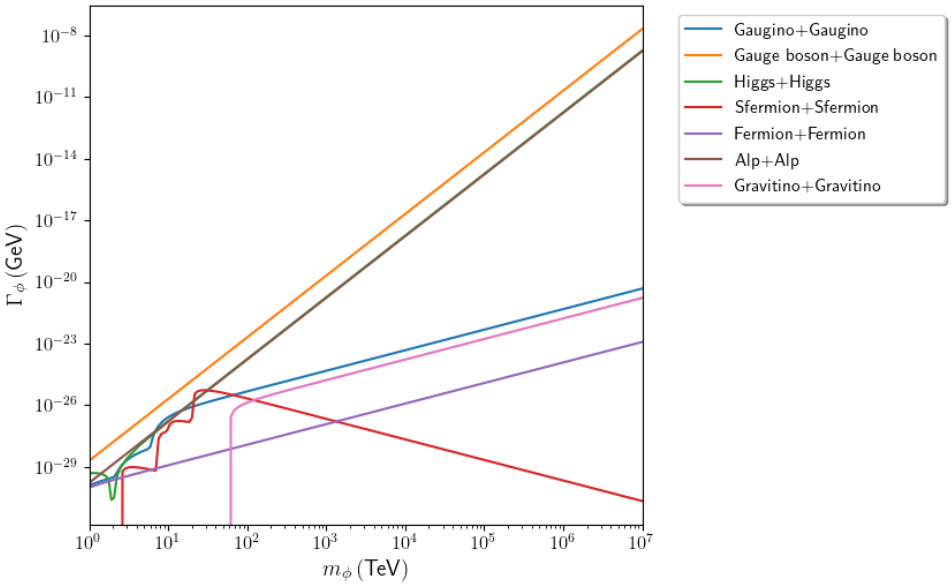


Figure 4.10: Modulus partial decay widths for the case **B2-GK1** as a function of m_ϕ for the natural SUSY benchmark point in Table (4.3) with the addition of an ultralight axion-like particle (ALP). Here, all λ_i couplings are set to unity including the coupling to ALPs, $\lambda_{\rm ALP}$.

production of dark radiation, which is heavily dependent on the modulus branching ratio into ALPs. As we will see later, in case **B2-GK1** dark radiation can be produced at a level consistent with experimental constraints for $\lambda_{\rm ALP} \sim \mathcal{O}(1)$. This is a direct consequence of the assumption that the dominant decays are to gauge bosons, which strongly suppresses the branching fraction to ALPs. We then expect case **B1-GK1** to give a similar branching ratio into ALPs compared to case **B2-GK1** since the decays to gravitinos, if unsuppressed, are still subleading to the Higgs and ALP decays. However, cases **A1-GK1** and **A2-GK1** will include the gauginos as a dominant decay mode, with roughly the same magnitude as the gauge bosons - so we expect the branching ratio to ALPs to be decreased by roughly a factor of 2 in these cases. Thus, cases **A1-GK1** and **A2-GK1** are even more optimistic than case **B2-GK1** from this point of view.

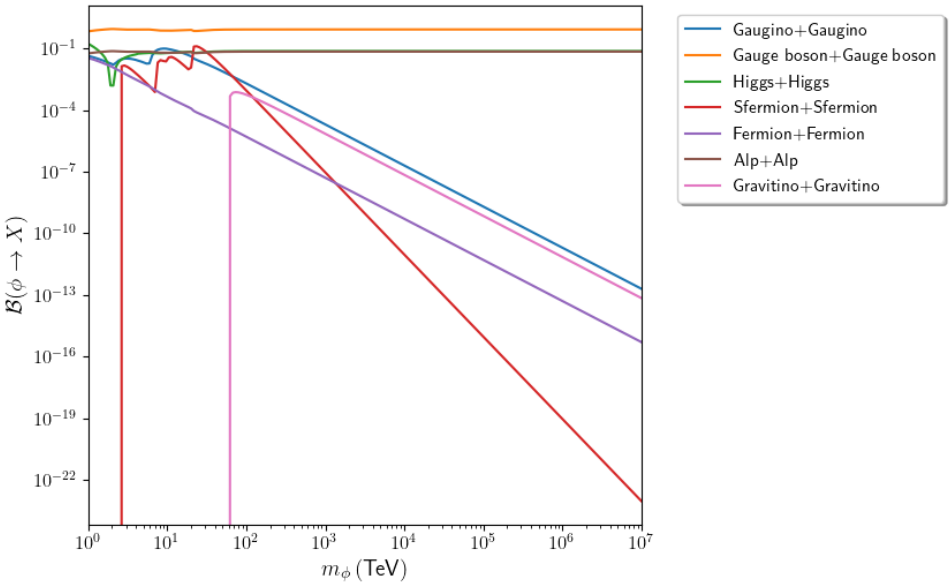


Figure 4.11: Modulus branching ratios for the case **B2-GK1** as a function of m_ϕ for the natural SUSY benchmark point in Table (4.3) with the addition of an ultralight axion-like particle (ALP). Here, all λ_i couplings are set to unity including the coupling to ALPs, $\lambda_{\rm ALP}$.

However, since the gauge sector in case **B2-GK2** is highly suppressed, the leading decays in this scenario are to Higgs and ALPs each with branching ratios of roughly 50% for $m_\phi \gtrsim 100$ TeV. Due to this drastic increase in the branching ratio to ALPs, we expect a significant increase in production of dark radiation in case **B2-GK2** over case **B2-GK1**. In order to keep dark radiation production at a level consistent with current experimental bounds, the coupling $\lambda_{\rm ALP}$ must then be suppressed, i.e. $\lambda_{\rm ALP} \ll 1$. Of course, whether or not a value of $\lambda_{\rm ALP} \ll 1$ can be realized in specific string constructions will be model-dependent. Additionally, using the same arguments we made in the previous section, we expect that all of the scenarios in the **GK2** category will suffer from this problem as the additional unsuppressed modes will still be subdominant to the Higgs and ALP channels.

4.3.4 Modulus decays in the ϕPQMSSM

In this section, we display the results of the two-body decays $\phi \to A + B$ in the ϕPQMSSM. As we have discussed in Sec. (4.1.2), incorporating a DFSZ-type axion sector forbids the Giudice-Masiero [246] term by PQ symmetry, while the SUSY μ term is now generated by the Kim-Nilles mechanism [247]. Thus, in the ϕPQMSSM the decays to the Higgs sector is mass suppressed, i.e. the decay to Higgs pairs scales as m_ϕ^{-1}. Including the PQ sector then introduces both the saxion and the axion as unsuppressed decay modes. The ϕPQMSSM thus generically has unsuppressed decays to gauge bosons, saxions, and axions, with possible additional unsuppressed decays as in Table 4.4. However, any case that assumes unsuppressed gauginos now *also requires* unsuppressed axinos, which arise from the same F-term interaction as the unsuppressed gauginos. This leads to interesting deviations for our results in the **GK2** cases, as the coupling to the PQ sector can yield an additional leading decay mode if the axino decays are unsuppressed.

parameter	PQ
m_s	5 TeV
$m_{\widetilde{a}}$	5 TeV
f_a	10^{11} GeV
θ_i	3.113
$m_a(T=0)$	372 μeV

Table 4.6: Parameters for a PQ benchmark point.

For the sake of brevity, we present results for cases **B2-GK1** and **B2-GK2** which assume suppressed decays into gravitinos, gauginos, and axinos, and again discuss our expectations for the results in the remaining cases. Additionally, we

consider only the case where there are no ultralight ALPs in the spectrum - and leave study for the cases including ultralight ALPs for future work. We again adopt the benchmark values given in Table (4.3), and augment them with the parameters relevant for the PQ sector which are listed in Table (4.6). Additionally, we take $\lambda_{\rm PQ} = 1$ with all remaining couplings also set to unity, except in the **GK2** cases where we again take the couplings to the gauge sector to be unified at $\lambda_{\rm gauge} = 1/16\pi^2$.

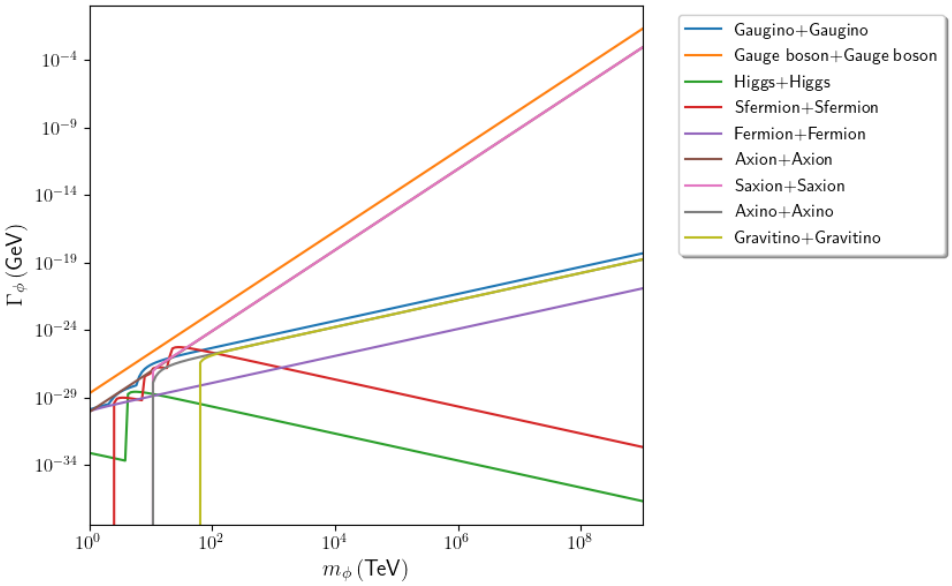


Figure 4.12: Modulus decay widths in the case **B2-GK1** for the natural SUSY benchmark point in Table (4.3) and PQ sector parameters in Table (4.6). Here, all λ_i couplings are set to unity.

We display the results for modulus decay in the ϕPQMSSM for case **B2-GK1** in Fig. (4.12). The decays to Higgs particles (green curve) are now mass-suppressed and are subleading even when compared to the sfermions (red curve) for $m_\phi \gtrsim 7.2$ TeV, when the $\widetilde{t}_2$ and $\widetilde{b}_1$ channels become accessible. Decays to axion pairs (brown curve) have roughly the same partial width that the decay to Higgs pairs had in

the ϕMSSM. Once the saxion channel becomes accessible at $m_\phi \sim 10$ TeV, the decays to saxions (pink curve) give an identical contribution and overlaps the axion curve. Additionally, we see that the decay to axinos (gray curve) overlaps with the decay to gravitinos (yellow curve) once the gravitino channel opens at $m_\phi \sim 60$ TeV.

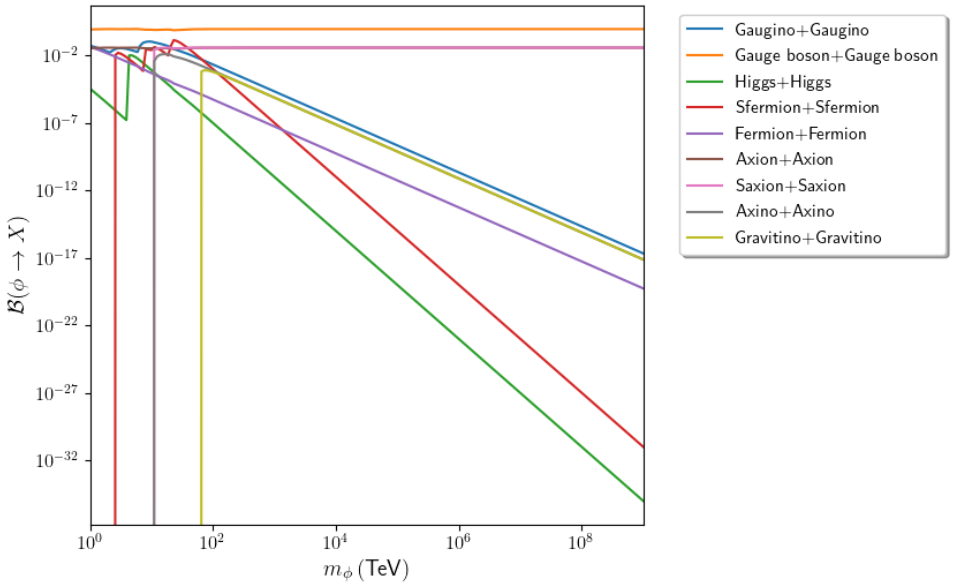


Figure 4.13: Modulus branching ratios in the case **B2-GK1** for the natural SUSY benchmark point in Table (4.3) and PQ sector parameters in Table (4.6). Here, all λ_i couplings are set to unity.

We display the corresponding branching ratios in Fig. (4.13). We see that the axion and saxion each comprise about 4% of the modulus branching ratio, while the gauge bosons have roughly 92%. The branching ratio to SUSY particles thus depends crucially on the details of saxion decay. As discussed by Chun and Lukas [290], self-interactions in the PQ sector are model-dependent and can be parameterized as [300]

$$\mathcal{L} \supset \frac{\xi}{f_a} s \left[\partial_\mu a \, \partial^\mu a + i\bar{\widetilde{a}} \not{\partial} \widetilde{a} \right] \tag{4.50}$$

with the effective self-coupling expected to be $0 \lesssim \xi \lesssim 1$. As the PQ sector self-interactions play a dominant role in the decay of the saxion, we consider both the limiting cases $\xi = 1$ and $\xi = 0$ when we study the cosmology of the ϕPQMSSM. However, the bounds for the total branching ratio to SUSY particles is similar to those for the **B2-GK1** case in the ϕMSSM, which was displayed in Fig. (4.3).

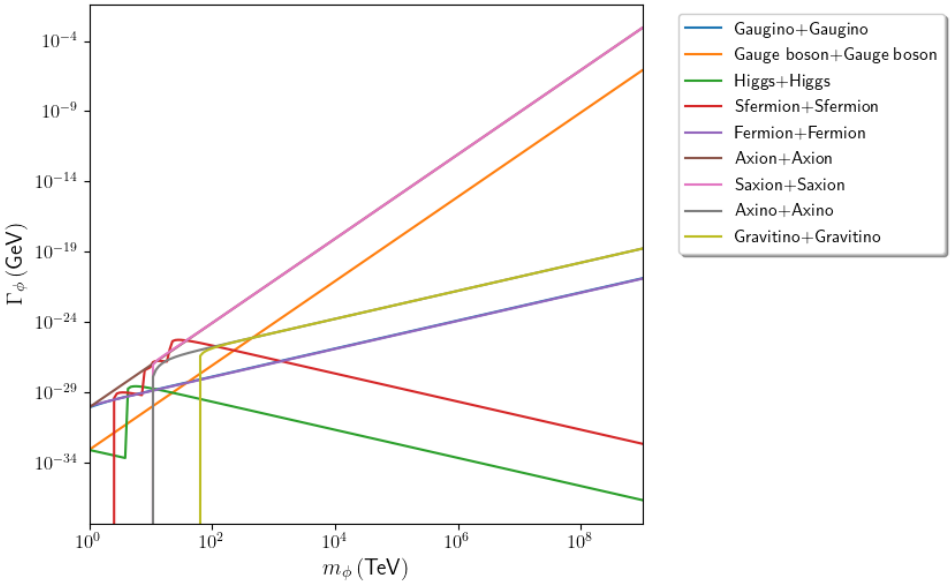


Figure 4.14: Modulus decay widths in the case **B2-GK2** for the natural SUSY benchmark point in Table (4.3) and PQ sector parameters in Table (4.6). Here, all $\lambda_i = 1$ except for $\lambda_{\text{gauge}} = 1/16\pi^2$.

For the case **B2-GK2**, we see from Figs. (4.14) and (4.15) that the dominant decay mode is into axions for $m_\phi \lesssim 10$ TeV, and thus we would expect this regime to be immediately excluded by dark radiation constraints. Once the saxion becomes kinematically available, the saxions and axions are equally dominant decay modes for $m_\phi \gtrsim 30$ TeV, while a brief window between 20 TeV $\lesssim m_\phi \lesssim 30$ TeV has the first and second generations of sfermions dominating the modulus

decay. Because of the large production of axions from modulus decay in this scenario, we might expect overproduction of dark radiation to provide the most stringent constraints on this scenario.

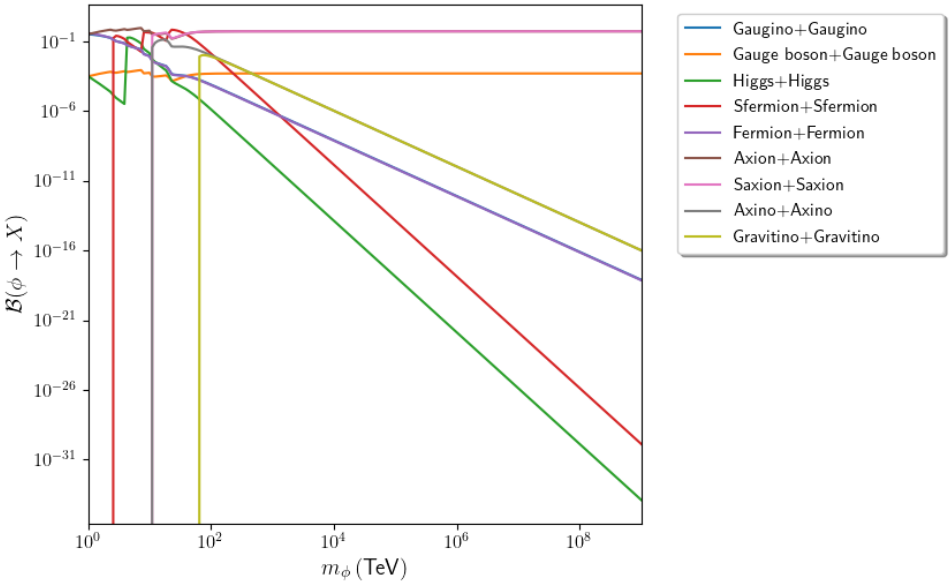


Figure 4.15: Modulus branching ratios in the case **B2-GK2** for the natural SUSY benchmark point in Table (4.3) and PQ sector parameters in Table (4.6). Here, all $\lambda_i = 1$ except for $\lambda_{\text{gauge}} = 1/16\pi^2$.

As we have already mentioned, the decay of the saxion is the dominant contribution in the overall modulus branching fraction to SUSY particles. Here, we investigate the decay of the saxion for both limiting cases for the PQ self-coupling, $\xi = 1$ and $\xi = 0$. For this work, we adopt the saxion and axino decay widths to the MSSM which are provided in the appendix of [285]. As we are considering here only the case with suppressed modulus decays to axinos, we focus our discussion on the decays of the saxion which are dominant once the modulus has decayed. It is worth mentioning that the saxion decays are similar to those of the modulus, with the exception that they are suppressed by the PQ scale f_a

instead of the Planck scale m_P. Since the mass of the saxion is expected to be of

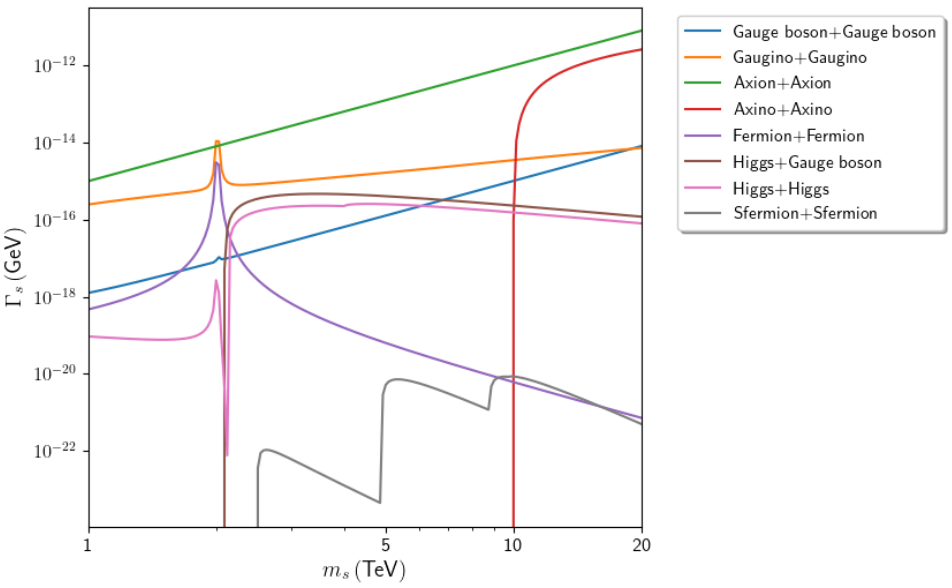


Figure 4.16: Saxion decay widths for the self-coupling $\xi = 1$ and the natural SUSY benchmark point from Table (4.3) with PQ parameters from Table (4.6).

order of the soft SUSY breaking terms [290], many of the interactions which are negligible for the modulus (as we show in App. (A)) must be taken into account for the saxion.

For the PQ sector self-coupling $\xi = 1$, we display the saxion decay widths in Fig. (4.16) and the saxion branching fractions for the same case in Fig. (4.17). We see that the leading decay of the saxion is to pairs of axions (green curve) if the self-interaction of the PQ sector is present. Similarly to the modulus, the decay to axion pairs scales as m_s^3 and thus remains a leading decay channel throughout the range of saxion masses. The other decay channel that has this scaling is to gauge bosons (blue curve), which in this case arises from mixing between the saxion and the Higgs sector [285]. Additionally, we see that the decay to axino pairs, shown

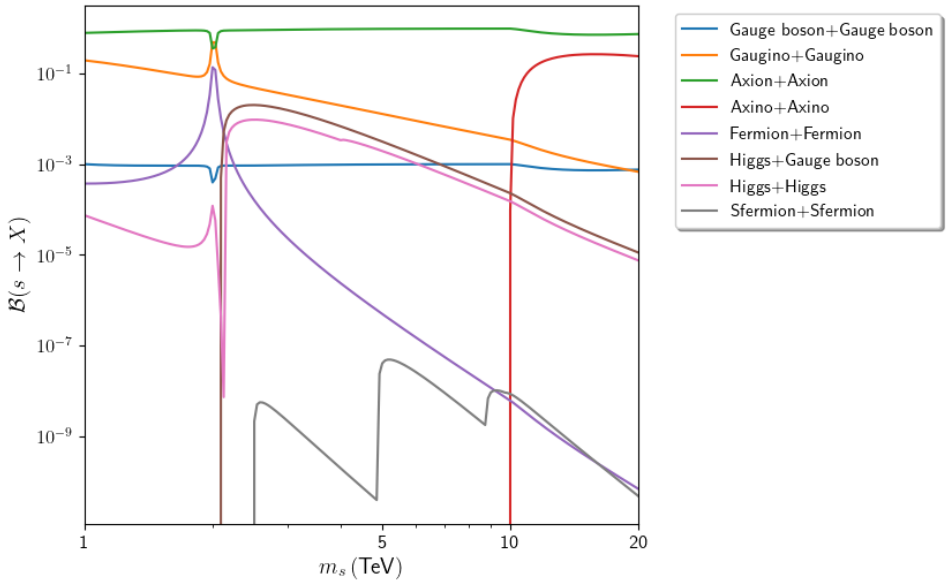


Figure 4.17: Saxion branching ratios for the self-coupling $\xi = 1$ and the natural SUSY benchmark point from Table (4.3) with PQ parameters from Table (4.6).

by the red curve, becomes sizeable once it becomes accessible at $m_s = 2m_{\tilde{a}} \sim 10$ TeV. The saxion decay width to axinos scales as $m_s m_{\tilde{a}}^2$ [285] so if the saxion were to be significantly heavier than the 20 TeV limit we display in Fig. (4.16), we would expect the axino mode to be surpassed by the gauge boson mode. For $m_s \lesssim 2m_{\tilde{a}} \sim 10$ TeV, we see that the second most prominent decay mode is to gauginos. In particular, we note the sharp peak at $m_s \sim 2$ TeV - although this peak coincides with the saxion mass at which the heaviest chargino and neutralino become kinematically accessible decay modes, this peak is primarily due to mixing effects between the saxion and the Higgs sector [285]. When the saxion mass is close to the mass of the heavy scalar Higgs, i.e. $m_s \sim m_H \sim 2$ TeV, the saxion-Higgs mixing leads to a sharp enhancement of the effective couplings for the gauginos, as well as the fermions (purple curve) and the Higgs channels (pink

curve). This mixing would also induce a similar resonance in the sfermion decay channel (gray curve), although this channel is closed until the lightest sfermions become accessible around $m_s \sim 2.5$ TeV. Thus for the $\xi = 1$ limit, we expect the saxion to decay primarily to axions, which behave as dark radiation, and gauginos and/or axinos, which cascade decay to the LSP.

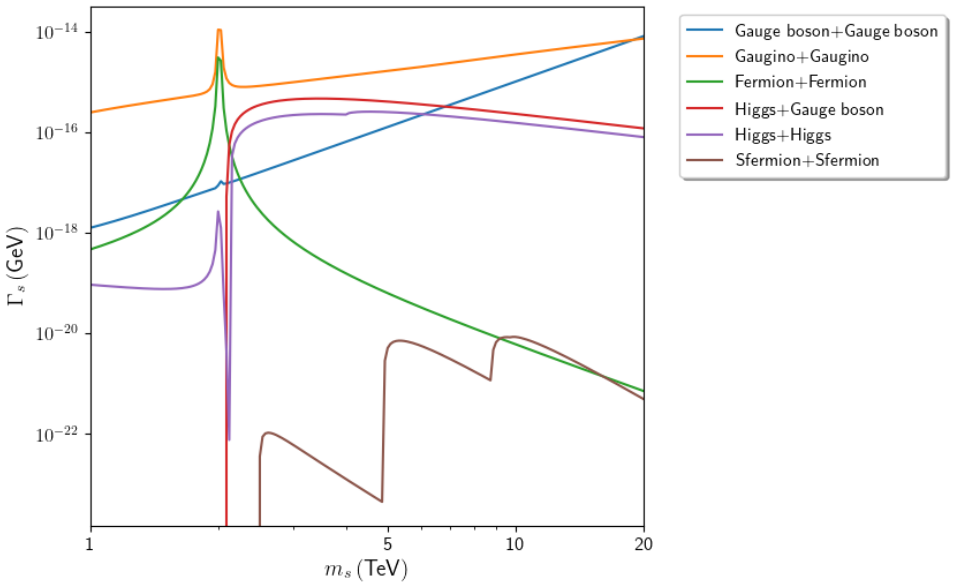


Figure 4.18: Saxion decay widths for the self-coupling $\xi = 0$ and the natural SUSY benchmark point from Table (4.3) with PQ parameters from Table (4.6).

For the PQ sector self-coupling $\xi = 0$, we display the saxion decay widths in Fig. (4.18) and branching fractions in Fig. (4.19). We see that, perhaps as expected, the decay widths are unchanged except that any decay to axions or axinos is forbidden. However, since the axions were the dominant decay mode in the $\xi = 1$ limit, we see from Fig. (4.19) that the dominant branching fraction is now to gauginos, which is only overtaken by the gauge boson channel once $m_s \sim 20$ TeV. Although the $\xi = 0$ limit will not introduce any additional dark

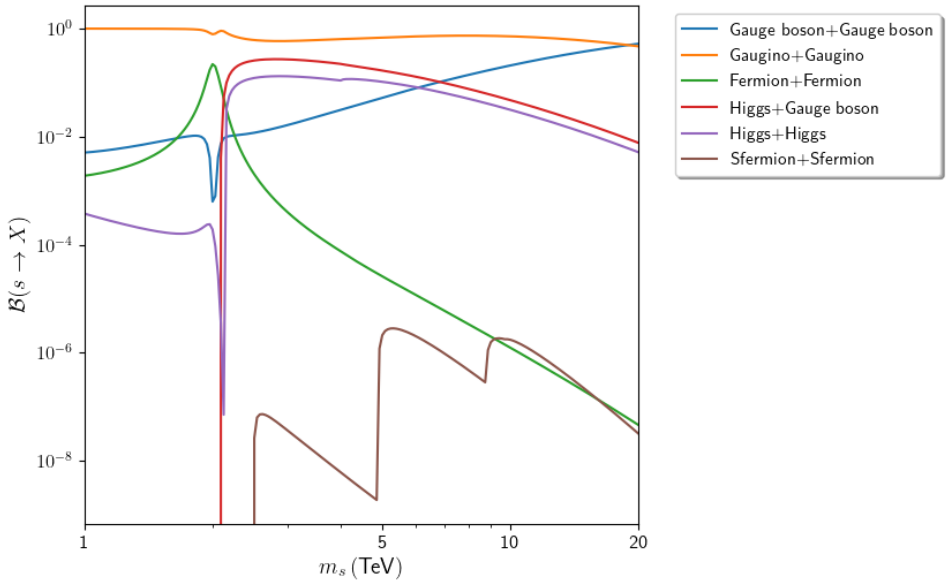


Figure 4.19: Saxion branching ratios for the self-coupling $\xi = 0$ and the natural SUSY benchmark point from Table (4.3) with PQ parameters from Table (4.6).

radiation, the substantial increase in the branching ratio to gauginos compared to the $\xi = 1$ limit suggests the $\xi = 0$ limit may produce significantly more WIMP dark matter if the saxion takes sufficiently long to decay.

For the axino, there is no distinction between the $\xi = 1$ and $\xi = 0$ cases, as can be read from Eq. (4.50). These decay modes arise from axino-higgsino mixing [285], similar to the fashion that the saxion decay modes arise. The axino decay widths are displayed in Fig. (4.20), and the associated branching fractions in Fig. (4.21). We see that the axino decays predominantly to either gauginos and Higgs bosons (green curves) or gauginos and gauge bosons (blue curve). The decays to sfermion + fermion pairs is highly suppressed, and is kinematically forbidden until the top quark + top squark threshold, at roughly 1.4 TeV. Due to R-parity conservation, the axino must cascade decay to the LSP - resulting in a

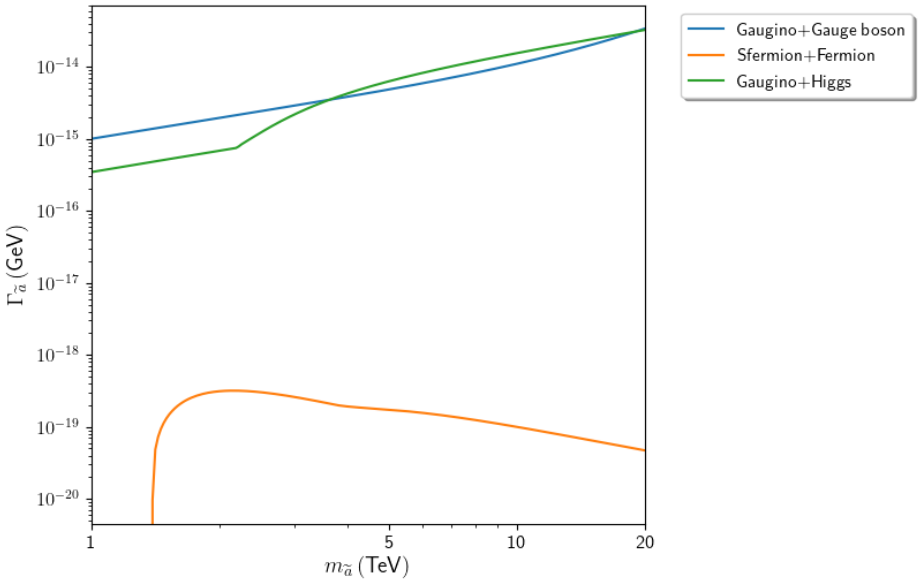


Figure 4.20: Axino decay widths for the natural SUSY benchmark point from Table (4.3) with PQ parameters from Table (4.6).

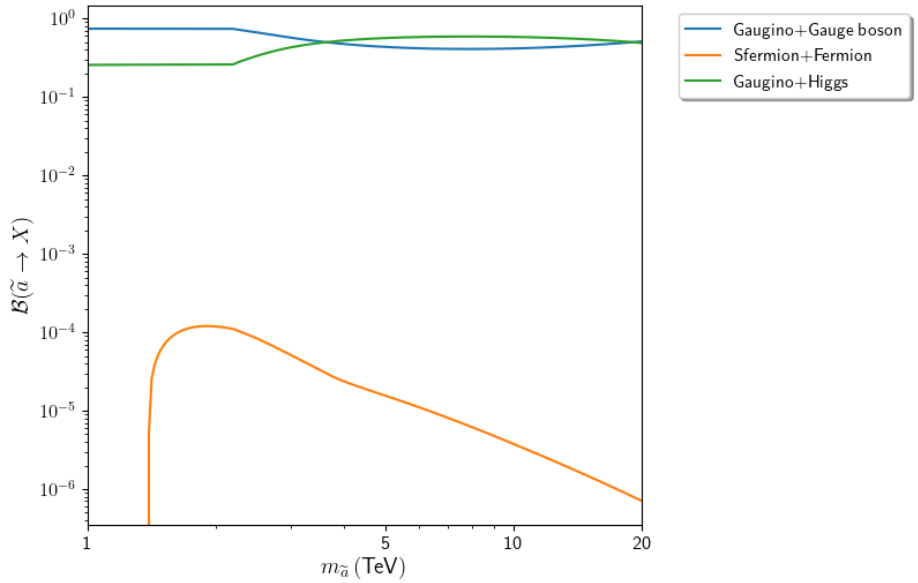


Figure 4.21: Axino branching ratios for the natural SUSY benchmark point from Table (4.3) with PQ parameters from Table (4.6).

100% branching fraction to SUSY. In the cases where modulus decay to axinos is unsuppressed, this may produce a significant excess of WIMP dark matter.

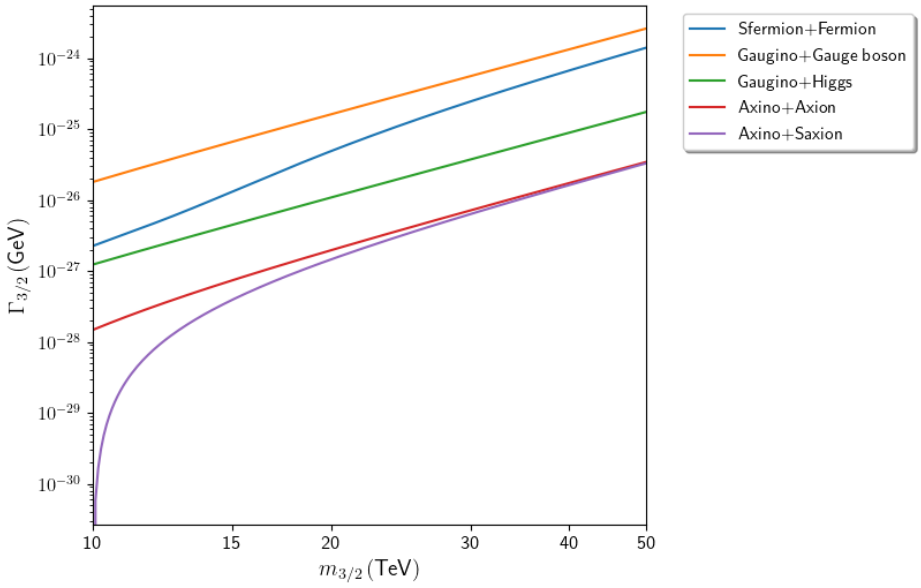


Figure 4.22: Decay widths of the gravitino into the PQMSSM. We again take the natural SUSY benchmark point from Table (4.3) and PQ parameters from Table (4.6).

Finally, we also note that the gravitino may couple to the PQ sector. As we have previously mentioned, a viable cosmology requires the gravitino to decay before BBN. Furthermore, since the gravitinos - at least, in unsequestered scenarios - are expected to decay rather late due to the gravitational nature of their interactions, they can overproduce LSPs when they decay *even if* the decay occurs before BBN. It is therefore crucial to understand the decays of the gravitino into the MSSM and the PQ sector. These decays were computed in a generalized fashion by Kohri *et al.* [227], which we adopt here. In Fig. (4.22), we display the partial widths of the gravitino. We see that the leading decay channels are into the MSSM sparticle-particle pairs, with the decay to axinos and either axions or saxions providing only a small contribution to the total width of the gravitino. From Fig. (4.23), we see that the branching ratio to the PQ sector is $\mathcal{B}(\psi_{3/2} \to \text{PQ}) \lesssim 1\%$, while

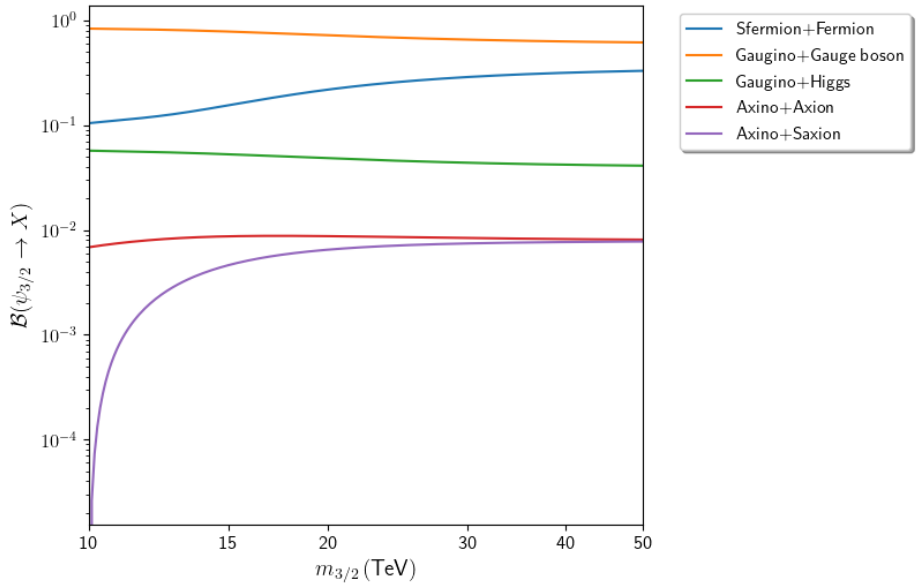


Figure 4.23: Gravitino branching ratios to the PQMSSM. We again take the natural SUSY benchmark point from Table (4.3) and PQ parameters from Table (4.6).

decays to a gaugino/gauge boson pair are the leading decay channel within our scan limits. Due to R-parity conservation, we note that the branching ratio into R-parity odd particles is 1. Thus, if produced in copious quantities (such as in cases **B1** and **A1**), its late decay will produce a large overabundance of LSP dark matter. We also note that, although the branching ratio to an axino/axion pair (shown by the red curve) is around 1%, the decay of the gravitino can make a small contribution to the total amount of dark radiation.

Chapter 5

Qualitative cosmological features of the ϕMSSM and ϕPQMSSM

Now that we have discussed the basic properties of the ϕMSSM and ϕPQMSSM EFTs, we are in a position to study the cosmology of both. We begin this chapter by presenting the relevant Boltzmann equations that describe the cosmological evolution of the model, which are derived in App. (B). We then provide a semi-quantitative treatment of these Boltzmann equations to discuss the key features and predictions for both the ϕMSSM and ϕPQMSSM when applied to our cases enumerated in Tables (4.4) and (4.5). This includes estimates for the production of dark matter and dark radiation, which we will see are rather constraining. We will then include results from numerical solutions of the Boltzmann equations in the next chapter, which in general agree quite well with our semi-quantitative estimates.

5.1 The Boltzmann equations

We begin this section by presenting the general set of Boltzmann equations which are derived in App. (B). We then provide discussion specific to each of the ϕMSSM and of the ϕPQMSSM. In both models, each field that we track utilizes a pair of Boltzmann equations - one which governs the evolution of its comoving number density, and one which governs the evolution of its comoving energy density. This allows us to model the smooth transition between the ultra-relativistic regime and

the non-relativistic regime for any thermally or decay-produced particles as the equations evolve from very high temperatures to very low temperatures. With some simplifications, these equations also describe the evolution of coherently oscillating scalar fields, which we track separately from any thermal counterparts. To close the set of Boltzmann equations, we supplement these with the Boltzmann equation which governs the evolution of entropy.

The Boltzmann equation that governs the i-th species comoving number density n_i is given by:

$$\begin{aligned}\frac{dn_i}{dt} + 3Hn_i = &\sum_j \left(\overline{n}_i\overline{n}_j - n_i n_j\right)\langle\sigma_{i+j\to a+b}|v|\rangle \\ &- \Gamma_i \frac{m_i n_i}{\rho_i}\left(n_i - \overline{n}_i \sum_{i\to a+b}\mathcal{B}_{i\to a+b}\frac{n_a n_b}{\overline{n}_a\overline{n}_b}\right) \\ &+ \sum_a \Gamma_a \frac{m_a n_a}{\rho_a}\left(\mathcal{B}_{a\to i}n_a - \overline{n}_a\sum_{a\to i+b}\mathcal{B}_{a\to i+b}\frac{n_i n_b}{\overline{n}_i\overline{n}_b}\right). \quad (5.1)\end{aligned}$$

The corresponding Boltzmann equation which governs the evolution of the i-th species' energy density is given by:

$$\begin{aligned}\frac{d\rho_i}{dt} + 3H\left(\rho_i + \mathcal{P}_i\right) = &\sum_j \left(\overline{n}_i\overline{n}_j - n_i n_j\right)\langle\sigma_{i+j\to a+b}|v|\rangle\frac{\rho_i}{n_i} \\ &- \Gamma_i m_i\left(n_i - \overline{n}_i \sum_{i\to a+b}\mathcal{B}_{i\to a+b}\frac{n_a n_b}{\overline{n}_a\overline{n}_b}\right) \\ &+ \sum_a \Gamma_a \frac{m_a}{2}\left(\mathcal{B}_{a\to i}n_a - \overline{n}_a\sum_{a\to i+b}\mathcal{B}_{a\to i+b}\frac{n_i n_b}{\overline{n}_i\overline{n}_b}\right). \quad (5.2)\end{aligned}$$

The temperature dependence of the axion also requires a term $\dot{m}/m$ [286] - which

we use in our numerical analysis but omit writing explicitly here for simplicity. In both Eq. (5.1) and Eq. (5.2), the left-hand side is derived from the Liouville operator and governs how the relevant phase space density evolves in an expanding universe. On the right-hand side, the first term in both equations is the annihilation term where $\overline{n}_i$ denotes the equilibrium number density, and $\langle\sigma_{i+j\to a+b}|v|\rangle$ is the thermally averaged annihilation cross section. For most of our analysis, we can make the approximation $i = j$ - e.g. in the case of the lightest neutralino, the total annihilation cross section is dominated by the $\widetilde{Z}_1 + \widetilde{Z}_1 \leftrightarrow a + b$ reaction. It is worth noting that when the interaction rate of the annihilation term, $n_i\langle\sigma_{i+\ldots}|v|\rangle$, is the dominant term in the Boltzmann equation, it acts as an attractor towards equilibrium - i.e. it pushes $n_i \to \overline{n}_i$. However, once the Hubble dilution becomes about the same order (i.e. $3H \sim n_i\langle\sigma_{i+\ldots}|v|\rangle$) the density of i is too dilute to annihilate efficiently, and freeze-out occurs. This effect will factor prominently into our discussion of the abundance of WIMP dark matter in the thermal and non-thermal scenarios. Additionally, for coherently oscillating scalar fields which are effectively zero-momentum condensates [286], this term is set to 0.

The second term on the right-hand side of both Eq. (5.1) and Eq. (5.2) accounts for the decay of a species i. This decay term accounts for the decay $i \to a + b$, as well as inverse decays $a + b \to i$ which arise while chemical equilibrium is maintained. If i is highly relativistic, its lifetime should also be accordingly dilated in the comoving frame (which is implicitly assumed in our Boltzmann equations) when compared to its lifetime in the rest frame. Relativistic dilation of i is thus accounted for in the factor $m_i n_i/\rho_i$, which translates the rest frame of i to the

comoving frame as we show in App. (B). For species which are assumed to be stable, $\Gamma_i = 0$ so that the decay term vanishes.

Finally, the third term on the right-hand side of both Eq. (5.1) and Eq. (5.2) is the injection term, which accounts for the decay of all species a that produce i. This term is, unsurprisingly, very similar to the decay term as they arise due to the same collision operator, as we discuss in App. (B). We note that the addition of the branching ratio $\mathcal{B}_{a\to i}$ is the effective branching ratio of a cascade decaying to i, excluding any other fields which are explicitly tracked by these Boltzmann equations. This term is set to 0 for the Boltzmann equations describing coherently oscillating fields, which are not produced by decays of other particles.

To model the evolution of the thermal background radiation, we utilize the Boltzmann equation for comoving entropy which is given by:

$$\frac{dS}{dt} = \frac{R^3}{T}\sum_i \mathcal{B}_{i\to\mathrm{rad}}\Gamma_i m_i \left(n_i - \overline{n}_i \sum_{i\to a+b} \mathcal{B}_{i\to a+b}\frac{n_a n_b}{\overline{n}_a \overline{n}_b}\right). \tag{5.3}$$

Here, $\mathcal{B}_{i\to\mathrm{rad}}$ is the branching ratio of i to any species that we treat as radiation, and thus excludes decays to the LSP and any species explicitly tracked separately. The relation between the entropy and temperature is then given by [286]:

$$s \equiv \frac{S}{R^3} = \frac{2\pi^2}{45}\, g_{*S}(T)\, T^3 \tag{5.4}$$

where $g_{*S}(T)$ is the number of entropic degrees of freedom. It is then a simple

matter to relate this to the radiation energy density, which is given by

$$\rho_r = \frac{\pi^2}{30}\, g_*(T)\, T^4 \tag{5.5}$$

where $g_*(T)$ is the number of relativistic degrees of freedom. In order to close the above equations, the final constraint we require is the Friedmann equation, which reads:

$$H^2 = \frac{\rho_{\rm total}}{3m_P^2} \tag{5.6}$$

where $\rho_{\rm total}$ is the total energy density of the universe.

Additionally, we need to know the equilibrium number density $\overline{n}_i$. For fields which follow a thermal distribution, a good approximation of the equilibrium number density is given by [286, 372]:

$$\overline{n}_i = \begin{cases} g_i \left(\frac{m_i T}{2\pi}\right)^{3/2} \exp\left(-m_i/T\right) & (T < m_i/10) \\ g_i \left(\frac{m_i^2}{2\pi^2 T}\right) K_2\left(m_i/T\right) & (m_i/10 \leq T \leq 3m_i/2) \\ g_i N_F \left(\frac{\zeta(3)}{\pi^2}\right) T^3 & (T > 3m_i/2) \end{cases} \tag{5.7}$$

where g_i are the number of spin degrees of freedom, $N_F = 1\,(3/4)$ for bosons (fermions), and the modified Bessel function K_2 is required to describe the transition between the non-relativistic and relativistic regimes. For coherently oscillating fields, $\overline{n}_i = 0$.

We are now in a position to discuss some key qualitative features of the Boltz-

mann equations. Although the numerical solutions of the Boltzmann equations will give us more precise predictions, these qualitative features will provide us with significant insight to the relevant physics.

5.2 The temperature scales of interest

We begin our qualitative treatment of the Boltzmann equations by discussing the relevant temperature scales of interest. For our purposes, these scales correspond to when massive particles decay, when scalar fields begin oscillating, when the modulus begins to dominate the energy density of the universe, and when the modulus begins injecting entropy into the thermal bath thus marking the beginning of modulus decay. Once we have the relevant formulae for these temperatures, we estimate these scales for the ϕMSSM and the ϕPQMSSM and investigate their dependence on the details of the modulus.

5.2.1 Decay temperature

The first qualitative result that we discuss is the decay temperature T_D^i of a species i. In the sudden decay approximation, we assume that the decay happens instantaneously when the Hubble scale is sufficiently low, i.e.

$$H(T_D^i) \sim \Gamma_i \tag{5.8}$$

where Γ_i is the decay width of i. This is most easily read from Eq. (5.1), which in this limit reduces to[1]

$$\dot{n}_i + 3Hn_i \simeq -\Gamma_i n_i. \tag{5.9}$$

When the decay interaction dominates over Hubble dilution, the solution of this equation is an exponential decrease of n_i - and once i has begun to decay, the decay process proceeds rapidly.

Assuming that the universe is radiation-dominated after the decay process and that the decay process occurs instantaneously, we have the expression:

$$T_D^i = \sqrt{m_P \Gamma_i} \left(\frac{90}{\pi^2 g_*(T_D^i)} \right)^{1/4} \tag{5.10}$$

which follows directly from the expression for the Hubble parameter in a radiation-dominated universe:

$$H(T) \simeq \frac{T^2}{m_P} \sqrt{\frac{\pi^2}{90} g_*(T)} \tag{5.11}$$

and the aforementioned conditions. Before we continue, it is worth stressing that species with larger decay widths will decay at higher temperatures compared to species with smaller decay widths, regardless of the dominant background.

[1]Here we have assumed i is non-relativistic when it decays. For the case of the modulus or any other coherently oscillating fields, this is a very good approximation. Additionally, the gravitino decays very late and is redshifted towards the non-relativistic limit. These are the two cases that are most of interest for this approximation, as we will see when we discuss the ϕPQMSSM.

5.2.2 Oscillation temperature

Coherent oscillation, sometimes referred to as the misalignment mechanism, is a unique cosmological property of scalar fields, and thus applies to the moduli, saxion, and axion fields. Before we discuss the temperature at which oscillations begin, let us first illustrate the details of this intriguing property for a generic scalar field, φ. A more complete treatment can be found in e.g. [373].

Considering a scalar field φ in an FRW universe and neglecting perturbations, the action for φ is given by

$$S = \int d^4x \sqrt{-\det g} \left[\frac{1}{2} \partial_\mu \varphi \, \partial^\mu \varphi - V(\varphi) \right]. \tag{5.12}$$

The Euler-Lagrange equation of motion can then be written down:

$$\partial_\mu \partial^\mu \varphi + \Gamma^\mu_{\mu\rho} \partial^\rho \varphi = -\frac{\partial V}{\partial \varphi}. \tag{5.13}$$

Assuming that the field is homogeneous (i.e. $\varphi = \varphi(t)$, consistent with our zeroth-order assumptions here), this reduces to

$$\ddot{\varphi} + 3H\dot{\varphi} + V'(\varphi) = 0 \tag{5.14}$$

where V' denotes differentiation of the potential with respect to φ, while $\dot{\varphi}$ denotes differentiation of φ with respect to comoving time. We now assume that the field is initially displaced from its minima - i.e. the inflationary potential shifts the

field $\varphi^{(0)}$ far away from its post-inflationary minima $\langle\varphi\rangle$. We thus approximate the potential as dominated by its quadratic term, $V \sim \frac{1}{2}m^2\varphi^2$ (where, for the sake of this discussion, we have taken $\langle\varphi\rangle \sim 0$ as it is irrelevant for this discussion). The equation of motion now becomes that of a damped harmonic oscillator:

$$\ddot{\varphi} + 3H\dot{\varphi} + m^2\varphi = 0. \tag{5.15}$$

When $3H > m$, the system is overdamped and, assuming that H is varying slowly with respect to the time scale of interest, we have the solution $\varphi \sim \varphi^{(0)} \sim$ const. However, once we have $3H < m$, the system is underdamped and thus begins to oscillate, and for $3H \ll m$, we arrive at the solution $\varphi \sim \mathrm{Re}[A\exp(imt)]$ where A is a constant prefactor. We see that once Hubble friction becomes negligible, the amplitude of φ's oscillations approach a constant value.

It is also worth computing the stress-energy tensor for φ. The time-time component is given by

$$T^0_0 = \rho = \frac{1}{2}\dot{\varphi}^2 + V(\varphi) = m^2A^2\cos^2(mt) \tag{5.16}$$

while the space-space components are given by

$$T^i_i = \mathcal{P} = \frac{1}{2}\dot{\varphi}^2 - V(\varphi) = 0. \tag{5.17}$$

It is now evident that coherently oscillating fields have the equation of state of a cold matter fluid, $w = \mathcal{P}/\rho = 0$. Additionally, we can take the time-average of

the time-time component of the stress-energy tensor, which gives us

$$\rho_0 = \frac{1}{2} m^2 A^2. \tag{5.18}$$

Of course, this expression has assumed that H is slowly varying and is thus applicable to a small window close to when oscillations begin. Since coherently oscillating fields behave as cold dark matter, over cosmological time scales this energy density will decrease like matter so that

$$\rho(t) = \rho_0 \left(\frac{R(t = t_0)}{R(t)} \right)^3. \tag{5.19}$$

To summarize, during the period where Hubble friction is significant, φ is "frozen" in its displacement away from its true minima. When the Hubble friction becomes much smaller, φ is no longer held in place and begins to oscillate about its true minima and acts as cold matter. If φ does not decay, the oscillation phenomenon will continue to the current time (although its energy density will dilute as matter) since the Hubble friction should monotonically decrease. The misalignment mechanism thus can provide a good cold dark matter candidate if the field is cosmologically stable, as is the case with the axion which was first discussed by Abbott *et al.* [374], Dine *et al.* [375], and Preskill *et al.* [376].

Based on the discussion above, we are now in a position to estimate the

temperature at which oscillations begin through the critically damped case:

$$3H(T_{\rm osc}) \sim m(T_{\rm osc}) \tag{5.20}$$

where we have allowed for a temperature dependent mass. The temperature dependence of m is not relevant for the modulus or the saxion, but is required for the axion, which gets a non-zero (albeit tiny) mass through instanton corrections [280, 375]. If we take $T_{\rm osc} \leq T_1$ where T_1 is some reference temperature, the fact that the oscillating fields dilute as matter implies the relation

$$\left(\frac{R(T_{\rm osc})}{R(T_1)}\right)^3 = \begin{cases} \left(\frac{H(T_1)}{H(T_{\rm osc})}\right)^{3/2} & \text{(radiation-dominated)} \\ \left(\frac{H(T_1)}{H(T_{\rm osc})}\right)^{2} & \text{(matter-dominated)} \end{cases} \tag{5.21}$$

for the cases where the universe is either radiation-dominated or matter-dominated between T_1 and $T_{\rm osc}$.

If we assume that no massive particles decay out of equilibrium so that conservation of entropy holds, taking $S_1/S_2 = \text{const.}$ produces the relation

$$\left(\frac{R(T_2)}{R(T_1)}\right)^3 = \frac{g_*(T_1)T_1^3}{g_*(T_2)T_2^3}. \tag{5.22}$$

We should note that Eq. (5.22) holds in both radiation-dominated and matter-dominated backgrounds so long as conservation of entropy holds.

We are also interested in epochs where a field decays out of equilibrium and produces considerable entropy. Specifically, we are interested in the inflationary

reheating period as well as the decay of the modulus and saxions, all of which are assumed to decay in a matter-dominated background. We therefore refer to this period as being "decay-dominated" to distinguish from matter-dominated periods where entropy is conserved. During a decay-dominated epoch, we instead use the result that the radiation is being sourced in the decay and scales instead as $\rho_{\rm rad} \propto R^{-3/2}$ [286]. Thus, during a decay-dominated period, we have the relation

$$\left(\frac{R(T_1)}{R(T_2)}\right)^3 = \left(\frac{g_*(T_2)T_2^4}{g_*(T_1)T_1^4}\right)^2. \tag{5.23}$$

Since we require a reference temperature T_1 to estimate the Hubble parameter $H(T_1)$, we provide here the expression for the oscillation temperature of the modulus taking the inflationary reheat temperature as our reference point, which we denote as T_R. As the hierarchy $m_\phi \gg m_s \gg m_a$ dictates that modulus oscillations begin first, this estimate will be common to both the ϕMSSM and the ϕPQMSSM. We then provide estimates for the saxion and axion oscillation temperatures when we discuss the ϕPQMSSM, as these are more conveniently estimated using model-specific reference points. Assuming that the universe is radiation-dominated at the inflationary reheat temperature[2] T_R, we can combine

[2]We keep this assumption throughout this work. If the universe were matter-dominated at T_R, it is likely that the contributions to the energy density from the modulus would end the inflationary reheating period early. Detailed treatment then requires additional assumptions about the inflationary sector and the details of reheating. This may lead to interesting, non-trivial dynamics similar to those explored in [377]. However, this is beyond the scope of this work.

the above expressions to

$$H(T^{\phi}_{\rm osc}) = \frac{\pi}{3m_P}\sqrt{\frac{g_*(T_R)}{10}} \times \begin{cases} \left(\frac{g_*(T^{\phi}_{\rm osc})}{g_*(T_R)}\right)^{2/3} (T^{\phi}_{\rm osc})^2 & (T^{\phi}_{\rm osc} \leq T_R) \\ \frac{g_*(T^{\phi}_{\rm osc})}{g_*(T_R)} \frac{(T^{\phi}_{\rm osc})^4}{T_R^2} & (T^{\phi}_{\rm osc} \geq T_R) \end{cases} \tag{5.24}$$

where we have used

$$H(T_R) = \sqrt{\frac{\pi^2 g_*(T_R) T_R^4}{90 m_P^2}}. \tag{5.25}$$

Imposing now the oscillation condition $3H(T^{\phi}_{\rm osc}) \sim m_\phi$, we find the oscillation temperature of the modulus is given by

$$T^{\phi}_{\rm osc} \simeq \begin{cases} \sqrt{m_P m_\phi}\left(\frac{10}{\pi^2 g_*(T^{\phi}_{\rm osc})}\right)^{1/4} & (T^{\phi}_{\rm osc} \leq T_R) \\ \left(T_R^2\, m_P\, m_\phi\right)^{1/4}\left(\frac{10\, g_*(T_R)}{\pi^2 g_*^2(T^{\phi}_{\rm osc})}\right)^{1/8} & (T^{\phi}_{\rm osc} \geq T_R). \end{cases} \tag{5.26}$$

As expected, in the limit that $T_{\rm osc} \to T_R$, the two expressions coincide.

5.2.3 Modulus-radiation equality temperature

In this section, we calculate the temperature at which the modulus comes to dominate the energy density of the universe, which we denote as T^{ϕ}_e. [3] Although the saxion and/or axino may also come to dominate over the radiation energy density as studied in [378, 372, 302, 301, 300], we shall see shortly that with the addition of the modulus, the saxion and axino domination is extremely

[3] This temperature of matter-radiation equality is not to be confused with the matter-radiation equality temperature that occurs around the eV scale.

subdominant by comparison. Starting with our expectation for ρ_ϕ from Eq. (5.19), we have the following cases

$$\rho_\phi = \frac{1}{2} m_\phi^2 \phi_0^2 \times \begin{cases} 1 & (T \geq T_{\rm osc}^\phi) \\ \frac{g_*(T)}{g_*(T_{\rm osc}^\phi)} \frac{T^3}{(T_{\rm osc}^\phi)^3} & (T \leq T_R, T_{\rm osc}^\phi \leq T_R) \\ \left(\frac{g_*(T)}{g_*(T_{\rm osc}^\phi)} \frac{T^4}{(T_{\rm osc}^\phi)^4} \right)^2 & (T \geq T_R, T_{\rm osc}^\phi \geq T_R) \\ \frac{g_*(T) g_*(T_R)}{g_*(T_{\rm osc}^\phi)^2} \frac{T^3 T_R^5}{(T_{\rm osc}^\phi)^8} & (T \leq T_R, T_{\rm osc}^\phi \geq T_R) \end{cases} \tag{5.27}$$

where we use $R_{\rm osc}/R(T) = (R_{\rm osc}/R_{T_R})(R_{T_R}/R(T))$ for the case where $T \leq T_R$ but $T_{\rm osc}^\phi \geq T_R$. Setting this equal to $\rho_{\rm rad}$ and plugging in the appropriate expression for $T_{\rm osc}^\phi$, we arrive at our expression for T_e^ϕ:

$$T_e^\phi = \begin{cases} \left(\frac{15}{\pi^2 g_*(T_e^\phi)} \right)^{1/4} \sqrt{m_\phi \phi_0} & (T_{\rm osc}^\phi \leq T_e^\phi) \\ \frac{3}{2} \left(\frac{10}{\pi^2 g_*(T_{\rm osc}^\phi)} \right)^{1/4} \left(\frac{\phi_0}{m_P} \right)^2 \sqrt{m_P m_\phi} & (T_e^\phi \leq T_{\rm osc}^\phi \leq T_R) \\ \left(\frac{2}{3} \right)^{1/4} \left(\frac{g_*(T_R)}{g_*(T_e^\phi)} \right)^{1/4} \sqrt{\frac{m_P}{\phi_0}} T_R & (T_R \leq T_e^\phi \leq T_{\rm osc}^\phi) \\ \frac{3}{2} \left(\frac{\phi_0}{m_P} \right)^2 T_R & (T_e^\phi \leq T_R \leq T_{\rm osc}^\phi) \end{cases} \tag{5.28}$$

We note that we can immediately discard the third case ($T_R \leq T_e^\phi \leq T_{\rm osc}^\phi$) as this case scenario contradicts our assumption that the universe is radiation-dominated at T_R. While we would not expect a significant change in the physics of this case, we leave the study of this case for future work as the details of the reheating period then become interdependent with the details of the lightest modulus.

Before concluding this section, let us first look more closely at the case where

$T_e^\phi \leq T_R \leq T_{\rm osc}^\phi$. We see that if $\phi_0 > \sqrt{2/3}\, m_P$, then $T_e^\phi > T_R$ - contradicting the assumed hierarchy of temperatures for this case. Thus, if the modulus has large enough energy density and oscillations commence during inflationary reheating, the end of inflationary reheating may actually transition directly to a matter-dominated universe instead of a radiation-dominated one.

5.2.4 Entropy injection temperature

The last temperature that we require is the temperature at which entropy begins to be injected due to modulus decay. We denote this temperature as T_S. As we have radiation being sourced by the decay between T_S and T_D, we have a decay-dominated universe and - much as in the reheating scenario - Eq. (5.23) provides a good description of the evolution during this period.

By analogy to the reheating epoch, we can write the relation

$$\frac{H(T_D)^2}{H(T_S)^2} = \left(\frac{g_*(T_D)T_D^4}{g_*(T_S)T_S^4}\right)^2 . \tag{5.29}$$

Assuming that the universe is radiation-dominated after decay, we may use the standard radiation-dominated form for $H(T_D)$. To estimate $H(T_S)$, we can multiply Eq. (5.29) by $H(T_S)^2/H(T_e)^2$ and, by assuming conservation of entropy between T_e and T_S, we can write instead the expression

$$\frac{H(T_D)^2}{H(T_e)^2} = \frac{g_*(T_S)T_S^3}{g_*(T_e)T_e^3}\left(\frac{g_*(T_D)T_D^4}{g_*(T_S)T_S^4}\right)^2 . \tag{5.30}$$

Upon noting that T_D and T_e both mark transitions between matter-domination and radiation-domination (and hence $H(T_D)$ and $H(T_e)$ take on the standard radiation-dominated form), we can retrieve our estimate for the entropy injection temperature:

$$T_S = \left(\frac{g_*(T_D)}{g_*(T_S)} T_e T_D^4\right)^{1/5}. \tag{5.31}$$

5.2.5 The temperature scales of the ϕMSSM

Here, we apply our discussion from the previous sections to the ϕMSSM. We begin by estimating the decay temperature of the modulus. From Fig. (4.9), we estimate the decay width of the case **B2-GK1** to be about $\Gamma_\phi \sim 10^{-20}$ GeV for a modulus with a mass of $m_\phi \sim 10^3$ TeV. Applying this to Eq. (5.10), we would expect a modulus decay temperature of roughly

$$\left(\frac{T_D^\phi}{1\text{ GeV}}\right) \simeq \frac{0.13}{(1\text{ GeV})^{1/2}} \times \left(\frac{\Gamma_\phi}{10^{-20}\text{ GeV}}\right)^{1/2} \left(\frac{20}{g_*(T_D^\phi)}\right)^{1/4}. \tag{5.32}$$

As we have discussed in Sec. (4.3.2), the **GK2** cases all are expected to have a decay width roughly an order of magnitude below the corresponding **GK1** case, and thus we would estimate the modulus decay temperature in the **GK2** cases to be roughly a factor of 3 lower than in the **GK1** case. Additionally, we expect roughly the same result for the **B1** cases as for the corresponding **B2** cases. The cases **A1** and **A2** roughly doubles the decay width, which leads to an increase by

a factor of about 1.4 for the modulus decay temperature.

It is crucial to reiterate that this temperature must be above the scale that BBN occurs. We see from Fig. (4.9) that, optimistically speaking, case **A1-GK1** might produce a decay width around $\Gamma_\phi \sim 10^{-25}$ GeV for $m_\phi \sim 10$ TeV. This pushes the decay temperature down to $T_D^\phi \sim 0.5$ MeV, well below the expected BBN scale, $T \sim (3 - 5 \text{ MeV})$. Clearly, a modulus with $m_\phi \lesssim 10$ TeV (or possibly even much larger, depending on the case scenario) suffers from the cosmological moduli problem (CMP).

Moving to the oscillation temperature of the modulus, we have from Eq. (5.26) the following estimate for $m_\phi \sim 10^3$ TeV:

$$\left(\frac{T_{\rm osc}^\phi}{1 \text{ GeV}}\right) \simeq \begin{cases} 4.04 \times 10^{11} \left(\frac{m_\phi}{10^3 \text{ TeV}}\right)^{1/2} \left(\frac{225}{g_*(T_{\rm osc})}\right)^{1/4} & (T_{\rm osc}^\phi \leq T_R) \\ 6.36 \times 10^{11} \left(\frac{T_R}{10^{12} \text{ GeV}}\right)^{\frac{1}{2}} \left(\frac{m_\phi}{10^3 \text{ TeV}}\right)^{\frac{1}{4}} \left(\frac{225}{g_*(T_{\rm osc})}\right)^{\frac{1}{8}} & (T_{\rm osc}^\phi \geq T_R) \end{cases} \tag{5.33}$$

where in the last line, we take $g_*(T_R) \simeq g_*(T_{\rm osc}) \simeq 225$. We see that for typical values of the modulus mass, the oscillation temperature is very large, and unless $T_R \gtrsim \mathcal{O}(10^{12})$ GeV, oscillations likely commence during inflationary reheating. Indeed, a 10 TeV modulus would still have an oscillation temperature around $T_{\rm osc}^\phi \sim 10^{10}$ GeV.

We have now seen that roughly 12 orders of magnitude separate when the modulus begins to oscillate and when it decays. However, it remains to estimate when the modulus overtakes radiation as the dominant energy density, which gives us a sense of how long the early matter dominated period is. Using again

our benchmark modulus mass, $m_\phi \sim 10^3$ TeV, Eq. (5.28) gives us the estimate

$$\left(\frac{T_e^\phi}{1\text{ GeV}}\right) \simeq \begin{cases} 4.44\times 10^{11}\left(\frac{225}{g_*(T_e^\phi)}\right)^{1/4}\left(\frac{m_\phi}{10^3\text{ TeV}}\right)^{1/2}\left(\frac{\phi_0}{m_P}\right)^{1/2} & (T_{\rm osc}^\phi \leq T_e^\phi) \\ 6.02\times 10^{11}\left(\frac{225}{g_*(T_{\rm osc}^\phi)}\right)^{1/4}\left(\frac{m_\phi}{10^3\text{ TeV}}\right)^{1/2}\left(\frac{\phi_0}{m_P}\right)^{2} & (T_e^\phi \leq T_{\rm osc}^\phi \leq T_R) \\ 1.5\times 10^{12}\left(\frac{\phi_0}{m_P}\right)^{2}\left(\frac{T_R}{10^{12}\text{ GeV}}\right) & (T_e^\phi \leq T_R \leq T_{\rm osc}^\phi) \end{cases} \tag{5.34}$$

where we again assume $g_*(T_{\rm osc}^\phi) \simeq g_*(T_R) \simeq g_*(T_e^\phi) \simeq 225$. We see here that based on some very general assumptions, the modulus will begin to dominate the energy density of the universe at a very high temperature and continue to dominate the energy density until it decays potentially very close to BBN.

Finally, it is worth estimating the scale at which entropy begins to be injected into the thermal bath. This provides us with some intuition on how prolonged the modulus decay is expected to be in the full Boltzmann solution. Additionally, this provides us with our expectations of when the decay-dominated background begins, which will play a crucial role in our semi-quantitative estimates when we study the ϕPQMSSM. Using our benchmarks from this section, Eq. (5.31) provides the estimate

$$\left(\frac{T_S^\phi}{1\text{ GeV}}\right) \simeq 30.2 \times \left(\frac{g_*(T_D)}{20}\right)^{1/5}\left(\frac{90}{g_*(T_S)}\right)^{1/5}\left(\frac{T_e^\phi}{4\times 10^{11}\text{ GeV}}\right)^{1/5}\left(\frac{T_D^\phi}{0.13\text{ GeV}}\right)^{4/5}. \tag{5.35}$$

Thus, we see that the modulus decay-dominated epoch lasts from a radiation

temperature of around 30 GeV to around 0.1 GeV for $m_\phi \sim 10^3$ TeV. Within the ϕMSSM, we do not expect any cosmological effects that we consider to occur in this window. This is not true in the ϕPQMSSM - we will see that axion oscillations are potentially likely to begin during this decay-dominated epoch. We should note that due to the high scale of T_e^ϕ and sensitive m_ϕ-dependence of T_D^ϕ, the duration of the decay-domination can easily change by over a full order of magnitude depending on the precise details of the modulus.

Before we display results of the semi-quantitative estimates as a function of m_ϕ, we emphasize that *the only temperatures that depend on the case scenario* are the decay temperature T_D^ϕ and, by extension, the entropy injection temperature T_S^ϕ. The oscillation temperature and the temperature at which the modulus begins to dominate the background are entirely independent of the assumptions on how the modulus decays. We therefore have our estimates for these temperatures in the ϕPQMSSM. Furthermore, the dependence of the decay temperature on the case scenario is not exceedingly large. For a given value of m_ϕ, we have argued that case **A1-GK1**, which has the largest total width of our 8 case scenarios from Tables (4.4) and (4.5), is expected to be around a factor of 20 larger than case **B2-GK2**, which has the smallest total width. However, since the decay temperature depends on $\sqrt{\Gamma_\phi}$, we expect only a factor of about 5 difference between the best and worst case scenarios, which can be compensated for by tripling the value of m_ϕ. Considering the scales involved with modulus cosmology, we therefore expect only relatively small quantitative differences between our many case scenarios, while the qualitative behavior is largely unchanged.

There is one glaring exception to this statement. If gravitinos are produced in large quantities via modulus decay, they may grossly overproduce dark matter or decay during/after BBN. This is the moduli-induced gravitino problem, which has been studied in [225, 226, 227, 228, 229, 230]. We have seen from Fig. (4.22) that the gravitino total width for $m_{3/2} \sim 30$ TeV is roughly $\Gamma_{3/2} \sim 10^{-24}$ GeV. Thus, we expect the gravitino decay temperature which we denote as (by abuse of notation) $T_D^{3/2}$:

$$\left(\frac{T_D^{3/2}}{1 \text{ GeV}}\right) \simeq \frac{0.0011}{(1 \text{ GeV})^{1/2}} \times \left(\frac{\Gamma_\phi}{10^{-24} \text{ GeV}}\right)^{1/2} \left(\frac{10.75}{g_*(T_D^\phi)}\right)^{1/4} \tag{5.36}$$

where, although clear from context, the superscript 3/2 refers to the gravitino and not exponentiation. Although clearly the decay of the gravitino occurs at roughly the scale of BBN, detailed calculations from Jedamzik [379] and later Kawasaki *et al.* [380, 381] suggest that this bound can be eased slightly, so long as the gravitino abundance is sufficiently low. Our BBN bound on the modulus is thus more conservative than the bound on the gravitino, and although similar calculations can be performed for the modulus which may ease the BBN constraints slightly, we will see that moduli that decay close to BBN still overproduce WIMP dark matter in both the ϕMSSM and the ϕPQMSSM.

In Fig. (5.1), we plot the oscillation temperature $T_{\rm osc}^\phi$, modulus-radiation equality temperature T_e^ϕ, entropy injection temperature T_S^ϕ, and decay temperature T_D^ϕ estimates from the above formulae as a function of m_ϕ using our natural SUSY benchmark point in Table (4.3) and assuming case **B2-GK1**. We also plot the

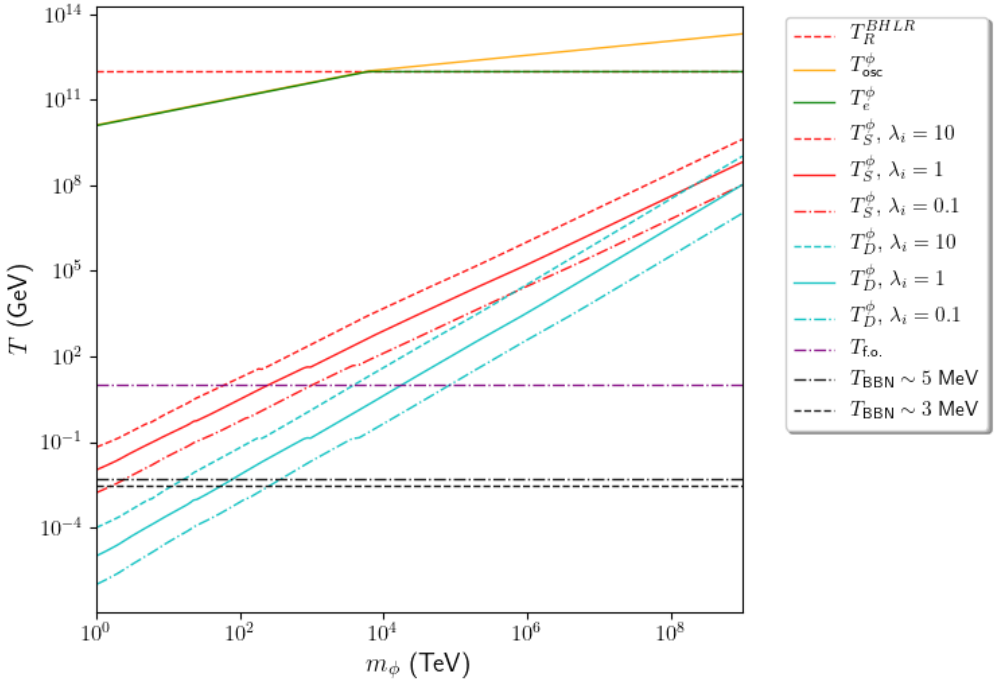


Figure 5.1: Relevant temperature scales for the ϕMSSM using the natural SUSY benchmark point from Table (4.3). We plot both the decay and entropy injection temperatures for all couplings set to $\lambda_i \in \{0.1, 1, 10\}$. We also plot the neutralino freeze-out temperature $T_{\rm f.o.} \sim m_{\widetilde{Z}_1}/20$ and two estimates for the temperature of BBN.

expected upper bound on the inflationary reheating temperature (horizontal red dashed line) based on arguments from Buchmüller, *et al.*, which claim that the dilaton becomes destabilized above $T \gtrsim 10^{12}$ GeV [382, 383][4] - we therefore denote this upper bound on the inflationary reheating temperature as $T_R^{BHLR} \equiv 10^{12}$ GeV, so that $T_R \lesssim T_R^{BHLR}$. Both the oscillation temperature (orange curve) and the modulus-radiation equality temperature (green curve) are, as expected, very

[4]In these works, the finite-temperature effective potential was derived and it was shown to induce a destabilizing term. The authors then found the critical temperature at which destabilization occurs, which is related to the gravitino mass. This work predates the Large Volume Scenario which provides a natural source of sequestering in string theory, which potentially pushes this critical temperature to a much higher bound. We do not consider this here, and adopt this maximum $T_R \sim 10^{12}$ GeV throughout - furthermore, we will show that most of our results are independent of T_R.

close to the reheating temperature which we take here to be $T_R = T_R^{BHLR}$. We see that for $m_\phi \gtrsim 6 \times 10^3$ TeV, the modulus begins to oscillate during the inflationary reheating process for our assumed value of T_R. Any initial radiation-domination at T_R is also almost immediately overcome by the modulus. We also plot the decay (cyan curves) and entropy injection (red curves) temperatures for the modulus for all couplings set to $\lambda_i \in \{0.1, 1, 10\}$ to compensate for the uncertainties in the couplings. The full set of decay widths listed in App. (A) was used to produce Γ_ϕ for each m_ϕ and λ_i in the computation of T_D^ϕ and T_S^ϕ. As we have already discussed, the modulus decay width does not impact the oscillation and modulus-radiation equality temperatures which both depend primarily on the modulus mass. We also plot the neutralino freeze-out temperature $T_{\rm f.o.} \sim m_{\widetilde{Z}_1}/20 \sim 10$ GeV (purple dot-dashed line) for our natural SUSY benchmark point, and two estimates of the BBN temperature $T_{\rm BBN}$ (black dashed lines) which provide a more conservative estimate, $T_{\rm BBN} \sim 5$ MeV, and a more optimistic estimate, $T_{\rm BBN} \sim 3$ MeV (see e.g. [384, 385, 386] for more discussion on determining $T_{\rm BBN}$ in the presence of a late-decaying scalar).

It is immediately apparent that if the modulus mass is below roughly $m_\phi \lesssim 4 \times 10^3$ TeV (if all $\lambda_i = 10$) to $m_\phi \lesssim 7 \times 10^4$ TeV (if all $\lambda_i = 0.1$), the modulus will decay *after* neutralino freeze-out. As we will see in the next section, this results in an enhancement of the neutralino relic density - thus lighter m_ϕ are more susceptible to WIMP dark matter overproduction. Large moduli masses then produce neutralino abundances at the thermally-expected value, unless some late decaying particle (such as gravitinos) produce large quantities of neutralinos

at later times. Additionally, depending on the couplings and how conservative an estimate of $T_{\rm BBN}$, a modulus mass above $m_\phi \gtrsim 10$ TeV to $m_\phi \gtrsim 300$ TeV is required to ensure BBN safety in case **B2-GK1**. Finally, we note that the entropy injection temperature is generally within 1-2 orders of magnitude of the decay temperature. Although this scale is not strictly necessary to understand the relevant scales in the ϕMSSM, it is imperative to understanding the production of coherently-oscillating axions when we study the ϕPQMSSM. As we have previously discussed, we expect the **GK2** cases to have roughly an order of magnitude decrease in Γ_ϕ as compared to the **GK1** cases. Thus, we can expect that the $\lambda_i = 0.1$ curves on this plot will give a decent representation of the **GK2** case with all $\lambda_i = 1$ (except of course for $\lambda_{\rm gauge} = 1/16\pi^2$). In the **GK2** case, we then would expect for $\lambda_i \sim 0.1$ to push the BBN bound to even larger m_ϕ - likely requiring $m_\phi \gtrsim 500$ TeV to ensure BBN safety. Additionally, the **A1** and **A2** cases will only push the curves slightly towards the left - if the inclusion of unsuppressed gaugino decays increases the width by a factor of 2, the corresponding T_D^ϕ increases only by roughly a factor of 1.5. For all $\lambda_i = 1$, this translates to cases **A1** and **A2** falling roughly halfway between the $\lambda_i = 1$ and $\lambda_i = 10$ curves for the shown **B2** case. As the unsuppressed gravitino modes are only expected to be roughly a percent-level increase in Γ_ϕ, we expect this figure to also show accurate temperature scales for case **B1-GK1**.

If gravitinos are produced in large quantities from modulus decay (such as in cases **A1** and **B1**), they may drastically enhance the neutralino relic density or interfere with BBN. We plot the gravitino decay temperature along with the

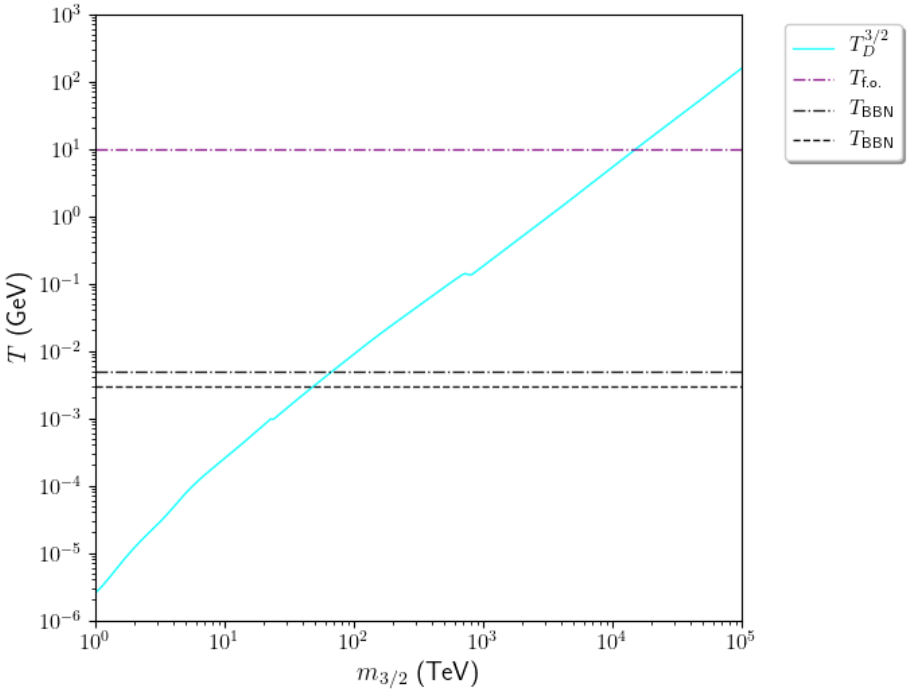


Figure 5.2: Gravitino decay temperature $T_D^{3/2}$ vs $m_{3/2}$. We also plot the neutralino freeze-out temperature $T_{\rm f.o.} \sim m_{\widetilde{Z}_1}/20$ and two estimates for the temperature of BBN.

neutralino freeze-out and BBN temperatures in Fig. (5.2) as a function of the gravitino mass $m_{3/2}$. We see that a large gravitino mass $m_{3/2} \gtrsim 60$ TeV may be required to satisfy BBN constraints if produced in large abundance. Additionally, we see that $m_{3/2} \gtrsim 10^4$ TeV is required to decay before neutralino freeze-out. In unsequestered scenarios, this can run into possibly severe tension with naturalness expectations - TeV-scale soft terms might be viable with a 60 TeV gravitino, but if the overproduction of neutralino dark matter requires $m_{3/2} \sim 10^4$ TeV it is difficult to believe a scenario with TeV-scale soft terms would arise without fairly significant tuning [387, 363, 185]. Incidentally, while this is not an issue with sequestered scenarios which *do* allow for TeV-scale soft terms with $m_{3/2} \gtrsim 10^4$

TeV, in sequestered LVS models the gravitino gains a mass larger than the bulk (lightest) modulus and is thus kinematically forbidden. This may not be the case in sequestered KKLT scenarios, which may give $m_\phi > m_{3/2} \gg \mathcal{O}(1 \text{ TeV})$ [388, 200].

5.2.6 The temperature scales of the ϕPQMSSM

Here, we discuss the relevant temperature scales of the ϕPQMSSM. As we have seen in Sec. (4.3), the modulus decay widths associated with the PQ sector are quantitatively similar to those of the Higgs sector in the ϕMSSM - and thus we expect the decay temperature of the modulus to be roughly unchanged, even when considering the many scenarios from Tables (4.4) and (4.5). We have also remarked in the previous section that the oscillation temperature T^ϕ_{osc} and the temperature of modulus-radiation equality T^ϕ_e are independent of the details of the modulus itself, save for its mass and initial amplitude of oscillation. The ϕPQMSSM thus inherits all of the same temperature estimates we presented for the ϕMSSM - the modulus begins to oscillate at a very high temperature and overtakes the energy density of the universe almost immediately, leading to an early matter dominated period (EMD) until it is expected to decay at a scale not very far from BBN. Within the ϕPQMSSM, however, the addition of the axion and saxion in particular introduce additional scales of interest as both of these scalar fields may have coherently oscillating modes, in addition to the usual thermal or decay production.

We are first tasked with understanding the decay scale of the axino and saxion.

As we saw in Sec. (4.3.4), our benchmark 5 TeV saxion and axino have decay widths of roughly $\Gamma_s \sim 10^{-13}$ GeV and $\Gamma_{\widetilde{a}} \sim 10^{-14}$ GeV. Rough estimates for these decays are then given by

$$\left(\frac{T_D^s}{1\text{ GeV}}\right) \simeq \frac{190}{(1\text{ GeV})^{1/2}} \times \left(\frac{\Gamma_s}{10^{-13}\text{ GeV}}\right)^{1/2} \left(\frac{120}{g_*(T_D^s)}\right)^{1/4} \tag{5.37}$$

and

$$\left(\frac{T_D^{\widetilde{a}}}{1\text{ GeV}}\right) \simeq \frac{62}{(1\text{ GeV})^{1/2}} \times \left(\frac{\Gamma_{\widetilde{a}}}{10^{-14}\text{ GeV}}\right)^{1/2} \left(\frac{10.75}{g_*(T_D^{\widetilde{a}})}\right)^{1/4}. \tag{5.38}$$

There are two issues with the above approximations. First, as we detailed in Sec. (5.2.1), this approximation requires radiation-domination to estimate the temperature at $H(T_D^i) \sim \Gamma_i$. Unless the saxion or axino decays before T_e^ϕ or after T_D^ϕ, this is in general not the case - the universe is expected to be matter-dominated due to the presence of the modulus, resulting in a more complicated dependence between the radiation temperature and the Hubble scale. The second reason is more subtle - it was noted in [300] that in the SUSY DFSZ model, inverse decays such as $h + h \to s$ and $\widetilde{Z}_1 + h \to \widetilde{a}$ can be significant if the decay temperature is large enough to be of order of the saxion or axino mass. This changes the condition for the sudden decay approximation to

$$H(T_D^i) \sim \Gamma_i \left(1 - \frac{\overline{n}_i}{n_i} \sum_{i \to a+b} \mathcal{B}_{i\to a+b} \frac{n_a n_b}{\overline{n}_a \overline{n}_b}\right) \tag{5.39}$$

which has the net effect of reducing the effective Γ_i, and thus prolonging the

decay. However, for our purposes, these estimated decay temperatures serve as a qualitative estimate that predicts the saxion to decay first, followed shortly by the axino, then the modulus. The gravitino, at least in unsequestered scenarios, is then expected to be the final particle to decay. One final comment is that the axino and saxion are produced via the decay of the modulus, which takes place well after these estimated temperatures. At least in the sudden decay approximation, this paints the picture that the coherently oscillating saxions and initial thermal population of saxions and axinos decay entirely during modulus domination, and are then briefly repopulated by modulus decay at a much lower scale.

Our next endeavor will be to estimate the oscillation temperatures of the saxion and the axion. In this case, we can now compare to temperature scales that are set by the modulus, which dominates the cosmological background during this time period. This allows for more convenient formulae, but also allows us insight as to the interplay between these sectors.

Beginning with the saxion, we apply similar logic as we did with the modulus but instead compare to $T_{\rm osc}^{\phi}$ (instead of the inflationary reheating temperature T_R). For the saxion, we have only the case where oscillations begin in a matter-dominated background as dictated by the condition $3H \sim m_s \ll m_\phi$ with the

assumed mass hierarchy.[5] We then have the relation

$$H(T^s_{\rm osc}) = H(T^\phi_{\rm osc}) \left(\frac{g_*(T^s_{\rm osc})}{g_*(T^\phi_{\rm osc})}\right)^{1/2} \left(\frac{T^s_{\rm osc}}{T^\phi_{\rm osc}}\right)^{3/2}. \tag{5.40}$$

Imposing $3H(T^s_{\rm osc}) \sim m_s$, we find the oscillation temperature of the saxion:

$$T^s_{\rm osc} = T^\phi_{\rm osc} \left(\frac{m_s}{m_\phi}\right)^{2/3} \left(\frac{g_*(T^\phi_{\rm osc})}{g_*(T^s_{\rm osc})}\right)^{1/3}. \tag{5.41}$$

Estimating these values, we see

$$\left(\frac{T^s_{\rm osc}}{1\text{ GeV}}\right) \simeq 1.17 \times 10^{10} \left(\frac{T^\phi_{\rm osc}}{4\times 10^{11}\text{ GeV}}\right) \left(\frac{m_s}{5000\text{ GeV}}\right)^{2/3} \left(\frac{10^6\text{ GeV}}{m_\phi}\right)^{2/3} \tag{5.42}$$

where we again have taken $g_*(T^\phi_{\rm osc}) \sim g_*(T^s_{\rm osc}) \sim 225$. Evidently, the saxion oscillations begin soon after the modulus has begun to oscillate, which provides a posteriori justification of our neglection of other background cases. Although $T^\phi_{\rm osc}$ has mild m_ϕ dependence, for both $T^\phi_{\rm osc} \leq T_R$ and $T^\phi_{\rm osc} \geq T_R$ the saxion oscillation temperature is still inversely proportional to m_ϕ (if only mildly). It is straightforward to check that in the limit $m_s \to m_\phi$, we have $T^s_{\rm osc} \to T^\phi_{\rm osc}$.

We now apply our oscillation considerations to the axion, where we *do* expect to have several possible scenarios due to the axion's extremely small mass. If

[5] We ignore the cases where the modulus begins decaying/injecting entropy or completely decays prior to saxion oscillations and assume the modulus dominates the energy density before saxion oscillations begin. This assumption is justified due to the extremely large energy density and relatively low decay temperature of the modulus in comparison to the lighter, more strongly interacting saxion.

the modulus decays very late, we may have $T^a_{\rm osc} > T^\phi_S > T^\phi_D$ so that the modulus still dominates while axion oscillations commence. In this case, it makes sense to compare $T^a_{\rm osc}$ to the oscillation scale of the modulus $T^\phi_{\rm osc}$ as we expect both matter-domination and entropy conservation during this period. We may also have axion oscillations commence during the (non-sudden) modulus decay process, i.e. $T^\phi_S \gtrsim T^a_{\rm osc} \gtrsim T^\phi_D$, which occurs during a decay-dominated background. Here, we compare to the scale of modulus decay T^ϕ_D which marks a transition between decay-domination and radiation-domination. Finally, axion oscillations may also occur once the modulus has decayed. As we have just discussed, we expect the modulus to typically decay after the saxion and hence we focus only on the case where the universe is radiation-dominated after modulus decay, i.e. for the case $T^a_{\rm osc} < T^\phi_D$.

Putting these cases together, we have

$$H(T^a_{\rm osc}) = \begin{cases} H(T^\phi_{\rm osc}) \left(\frac{g_*(T^a_{\rm osc})}{g_*(T^\phi_{\rm osc})}\right)^{1/2} \left(\frac{T^a_{\rm osc}}{T^\phi_{\rm osc}}\right)^{3/2} & (T^a_{\rm osc} > T^\phi_S) \\ H(T^\phi_D) \left(\frac{g_*(T^a_{\rm osc})}{g_*(T^\phi_D)}\right) \left(\frac{T^a_{\rm osc}}{T^\phi_D}\right)^4 & (T^\phi_S \gtrsim T^a_{\rm osc} \gtrsim T^\phi_D) \\ \sqrt{\frac{\pi^2}{90 m_P^2} g_*(T^a_{\rm osc})(T^a_{\rm osc})^4} & (T^a_{\rm osc} < T^\phi_D) \end{cases} \tag{5.43}$$

where we neglect entropy injection due to saxion and axino decays. We are now in a position to impose $3H(T^a_{\rm osc}) \sim m_a(T^a_{\rm osc})$, where we adopt the axion's temperature

dependence as described in [280, 389, 390, 391] which reads

$$m_a(T) = \left(6.2 \times 10^{-3}\ \text{GeV}\right)\left(\frac{N_{\text{DW}}}{f_a/(1\ \text{GeV})}\right) \times \begin{cases} 1 & (T \lesssim \Lambda_{\text{QCD}}) \\ 0.018\left(\frac{\Lambda_{\text{QCD}}}{T}\right)^4 & (T \gtrsim \Lambda_{\text{QCD}}) \end{cases} \tag{5.44}$$

where $\Lambda_{\text{QCD}} \simeq 200$ MeV is the QCD scale and N_{DW} is the domain wall number, which for our DFSZ case is $N_{\text{DW}} = 6$. Taking the ansatz that $T^a_{\text{osc}} \gtrsim \Lambda_{\text{QCD}}$, the oscillation temperature of the axion is then estimated by

$$T^a_{\text{osc}} = \begin{cases} \left(A^{-2}\frac{10m_P^2}{\pi^2 g_*(T^a_{\text{osc}})T^\phi_{\text{osc}}}\right)^{1/11} & (T^a_{\text{osc}} > T^\phi_S) \\ \left(A^{-1}\frac{m_P\left(T^\phi_D\right)^2}{\pi g_*(T^a_{\text{osc}})}\right)^{1/8}\left(10 g_*(T^\phi_D)\right)^{1/16} & (T^\phi_S \gtrsim T^a_{\text{osc}} \gtrsim T^\phi_D) \\ \left(A^{-1}\frac{m_P}{\pi}\right)^{1/6}\left(10/g_*(T^a_{\text{osc}})\right)^{1/12} & (T^a_{\text{osc}} < T^\phi_D) \end{cases} \tag{5.45}$$

where we have made the definition

$$A^{-1} \equiv \left(6.2 \times 10^{-3}\ \text{GeV}\right)\left(\frac{N_{\text{DW}}}{f_a/(1\ \text{GeV})}\right)\left(0.018\Lambda^4_{\text{QCD}}\right) \tag{5.46}$$

for notational convenience. We now are in a position to estimate these results. Here, we take $f_a = 10^{11}$ GeV which has been suggested to be the cosmological sweet-spot for the SUSY DFSZ axion [5, 139] (see also Sec. (3.2.1)). This yields an axion mass at present time $m(T = 0) \sim 378\,\mu$eV. The axion oscillation

temperature is then estimated to be

$$\left(\frac{T^a_{\rm osc}}{1\ {\rm GeV}}\right) = \begin{cases} 0.108 \times \left(\frac{1.09\times10^{-17}\ {\rm GeV}^{-5}}{A}\right)^{2/11} & \\ \qquad \times \left(\frac{75}{g_*(T^a_{\rm osc})}\right)^{1/11} \left(\frac{4\times10^{11}\ {\rm GeV}}{T^\phi_{\rm osc}}\right)^{1/11} & (T^a_{\rm osc} > T^\phi_S) \\ 0.636 \times \left(\frac{1.09\times10^{-17}\ {\rm GeV}^{-5}}{A}\right)^{1/8} \left(\frac{75}{g_*(T^a_{\rm osc})}\right)^{1/8} & \\ \qquad \times \left(\frac{T^\phi_D}{0.13\ {\rm GeV}}\right)^{1/4} \left(\frac{g_*(T^\phi_D)}{20}\right)^{1/16} & (T^\phi_S \gtrsim T^a_{\rm osc} \gtrsim T^\phi_D) \\ 1.20 \times \left(\frac{1.09\times10^{-17}\ {\rm GeV}^{-5}}{A}\right)^{1/6} \left(\frac{75}{g_*(T^a_{\rm osc})}\right)^{1/12} & (T^a_{\rm osc} < T^\phi_D). \end{cases} \tag{5.47}$$

In the first case, we find that in order to be consistent with the assumed temperature hierarchy $T^a_{\rm osc} > T^\phi_S$, one must push the modulus mass far below the rough bound $m_\phi \sim \mathcal{O}(50\ {\rm TeV})$ set by the CMP - even with some tuning of couplings. Hence, we find that in phenomenologically viable scenarios the onset of axion oscillations is expected to start in either the modulus decay-dominated epoch, or when the universe becomes radiation-dominated after the modulus has completely decayed - and in both cases, begins at roughly $T \sim \mathcal{O}(1\ {\rm GeV})$.

5.3 Estimates of produced abundances

In this section, we qualitatively study the production of dark matter in the ϕMSSM and ϕPQMSSM. We then apply similar arguments to study dark radiation production in a qualitative manner within the ϕPQMSSM and (if it contains an ultra-light ALP) the ϕMSSM. This utilizes several approximations to the Boltzmann equations we presented in Sec. (5.1) in addition to our temperature

estimates from the previous section, Sec. (5.2).

5.3.1 Thermal WIMPs and gravitinos - relics of inflation

In standard thermal histories (e.g. ΛCDM), most models incorporating WIMPs assume some form of thermal production. After inflationary reheating, the WIMPs are produced in large quantities through interactions with the radiation, e.g. $i+j \leftrightarrow \widetilde{Z}_1+\widetilde{Z}_1$, with a large enough cross section $\langle\sigma_{\widetilde{Z}_1} v\rangle$ to reach equilibrium. Once the temperature drops sufficiently so that the Hubble rate is comparable to the interaction rate, the WIMPs are dilute enough that annihilations cease and freeze-out occurs. As the Hubble dilution of WIMPs matches the Hubble dilution of entropy, the WIMPs then have a constant abundance yield $Y_{\widetilde{Z}_1}$ assuming no significant source of entropy after freeze-out. However, if a light modulus is present its decay will produce a large amount of entropy which reduces the thermally-produced WIMP abundance. It is generally assumed in cosmological scenarios with light moduli that thermal relics are diluted to negligible amounts, which we show here is typically a good assumption.

We begin by defining the entropy dilution factor to be

$$r \equiv \frac{S_f}{S_0}. \tag{5.48}$$

By taking $S_0 = S(T_S^\phi)$ and $S_f = S(T_D^\phi)$, it is easy to show that

$$r = \frac{g_*(T_D^\phi)}{g_*(T_S^\phi)} \left(\frac{R(T_D^\phi)}{R(T_S^\phi)}\right)^3 \left(\frac{T_D^\phi}{T_S^\phi}\right)^3 \simeq \frac{T_e^\phi}{T_D^\phi} \tag{5.49}$$

where we focus solely on entropy production by the decay of the modulus. Based on our previous numerical estimates of $T_e^\phi \sim \mathcal{O}(10^{11} - 10^{12})$ GeV and $T_D^\phi \sim \mathcal{O}(0.1 - 1)$ GeV for our $m_\phi \sim 10^3$ TeV benchmark, we see immediately that r can easily be $\mathcal{O}(10^{11})$ or larger. We display in Fig. (5.3) the entropy dilution factor r as a function of m_ϕ and see that - except for extremely large modulus masses - the estimated entropy dilution is rather sizeable. As m_ϕ increases, the entropy dilution then decreases due to the early decay. The entropy dilution factor in this approximation also drops at a faster rate once the modulus begins to oscillate during the reheating period, as here T_e^ϕ becomes constant with respect to m_ϕ. If m_ϕ becomes too large, we see that the entropy dilution may become too weak to sufficiently dilute thermal relics. However, we will not consider moduli masses greater than $m_\phi \sim 10^9$ TeV in this work as they decay sufficiently early to effectively decouple from the cosmology, leading to only small deviations from a standard thermal history.

For some thermally-produced species i, we can estimate the relic density $\Omega_i^{\rm TP}$ in the absence of entropy production is given by [286]

$$\Omega_i^{\rm TP} h^2 \simeq \frac{m_i Y_i h^2}{\rho_c / s_0} \tag{5.50}$$

where h is the dimensionless Hubble constant, $s_0 \sim 2970$ cm^{-3} is the present entropy density, and $\rho_c/h^2 \sim 1.05 \times 10^{-5}$ GeV $\cdot$ cm^{-3} is the critical closure density.

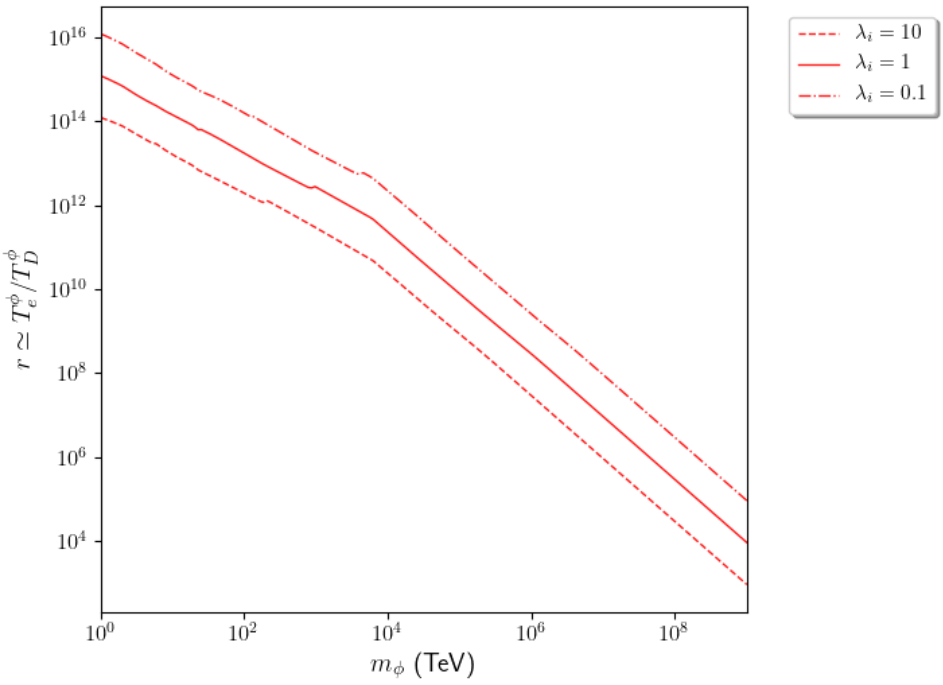


Figure 5.3: Entropy dilution factor $r \simeq T_e^\phi / T_D^\phi$ vs m_ϕ for each $\lambda_i \in \{0.1, 1, 10\}$.

Factoring entropy dilution then changes this to

$$\Omega_i^{\mathrm{TP}'} h^2 \simeq \frac{m_i Y_i^{\mathrm{TP}} h^2}{r \rho_c / s_0} = r^{-1} \Omega_i^{\mathrm{TP}} h^2 \tag{5.51}$$

where Y_i^{TP} is the abundance yield in a standard thermal history (no entropy dilution) and we have denoted the final relic density by $\Omega_i^{\mathrm{TP}'}$. Clearly, any species that has an appreciable relic density in a *standard thermal history* can be expected to be diluted by a significant amount (~ 11 orders of magnitude, depending on m_ϕ) in a *non-thermal history* where modulus decay is present. Unless WIMPs are overproduced by the same magnitude as the dilution factor,[6] the dark matter relic density must then be produced non-thermally. We will discuss non-thermal

[6] See e.g. [392] for a proposal of this sort, which assumes superheavy neutralinos in a high-scale SUSY context are vastly overproduced and diluted to the measured relic density by light modulus decay.

production scenarios in the following sections.

However, this substantial dilution of inflationary relics can in turn be a significant advantage of moduli cosmology. In models of SUSY cosmology, gravitinos are also produced in large quantities in inflationary reheating. Unlike WIMPs, gravitinos are only gravitationally coupled which 1. gives them an extremely suppressed cross section $\langle \sigma_{3/2} v \rangle$ so that gravitinos never annihilate in significant quantities, 2. gives them an extremely long lifetime, which can interfere with the predictions of BBN, and 3. can overproduce WIMPs through the late decay enhancement (which we will discuss in the next section). This is the thermal gravitino problem, and is studied in detail in e.g. [380, 393, 227, 300, 285, 394, 395, 396]. One of the distinct consequences of the thermal gravitino problem is that the gravitino abundance is directly proportional to the inflationary reheating temperature T_R, so large $T_R \gtrsim \mathcal{O}(10^{6-8}$ GeV) is expected to vastly overproduce gravitinos. For lower inflationary reheating temperatures, the production is reduced sufficiently that a viable cosmology is possible. In the modulus-dominated cosmology, the massive entropy dilution can change these predictions significantly - which results in a much larger viable T_R than in a thermal scenario.

To demonstrate this, we adopt thermally-produced gravitino production rates calculated by Pradler and Steffen [394] and plot them vs $m_{3/2}$ in Fig. (5.4). These rates take the form

$$\Omega_{3/2}^{\rm TP} h^2 \simeq \sum_{i=1}^{3} \omega_i g_i^2 \left(1 + \frac{M_i^2}{3m_{3/2}^2}\right) \log\left(\frac{k_i}{g_i}\right) \left(\frac{m_{3/2}}{100 \text{ GeV}}\right) \left(\frac{T_R}{10^{10} \text{ GeV}}\right) \qquad (5.52)$$

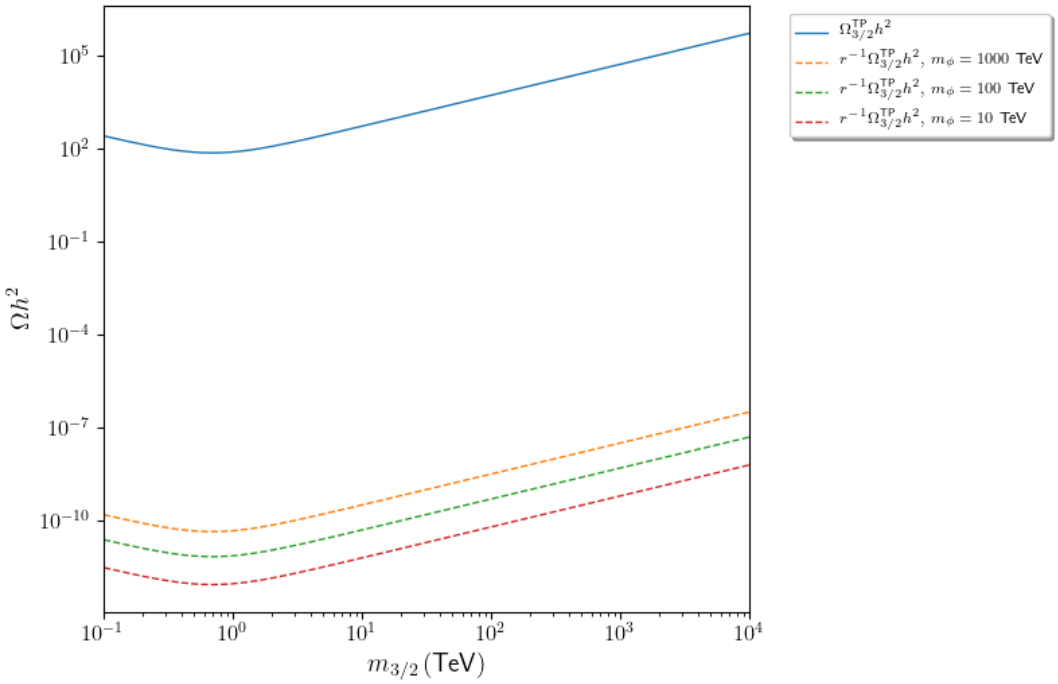


Figure 5.4: Thermally-produced gravitino relic density $\Omega_{3/2}^{\rm TP}h^2$ for $T_R = T_R^{BHLR} = 10^{12}$ GeV. We also show the predicted relic density in the presence of modulus decay for $m_\phi \in \{10, 100, 1000\}$ TeV for case **B2-GK1** with all $\lambda_i = 1$. Figure taken from [6].

where g_i are the $U(1)_Y$, $SU(2)_L$, and $SU(3)_c$ gauge couplings, M_i are the corresponding gaugino masses, and the parameters $c_i \sim \mathcal{O}(10 - 100)$, $k_1 \sim \mathcal{O}(1)$, and $\omega_i \sim \mathcal{O}(0.01 - 0.1)$. Clearly, the expected gravitino production will increase as T_R increases, and as seen from Fig. (5.4) the gravitino abundance (blue curve) is well above acceptable bounds for $T_R = 10^{12}$ GeV. The entropy dilution from the modulus, however, dilutes this tentatively massive abundance to negligible amounts which we see from the entropy dilution curves in the figure for $m_\phi = 10$ TeV (red curve), $m_\phi = 100$ TeV (green curve), and $m_\phi = 1000$ TeV (orange curve). Of course, we see also that as m_ϕ increases, its entropy dilution weakens slightly. We will return to this point later, although we note in passing that this weakening

of the dilution can lead to a resurgence of the thermal gravitino problem if m_ϕ is large enough. Additionally, if $m_{3/2}$ becomes very large ($m_{3/2} \gg 10^4$ TeV) we see that the gravitino abundance may still be problematic even with entropy dilution - though as we saw in Fig. (5.2) a gravitino mass this large might then be expected to decay well before BBN which also alleviates the thermal gravitino problem. This may not be the case if the gravitino is the LSP - though we do not consider this case in this work. Furthermore, a gravitino mass this large is well beyond the expected natural value $m_{3/2} \sim \mathcal{O}(10-50)$ TeV in the absence of sequestering (due to our assumption of TeV-scale soft terms), while in the presence of sequestering one might expect an extremely large gravitino mass which decays sufficiently early to effectively decouple from the late-time cosmology. Thus, for the cases we are interested in here we may safely assume that the thermal gravitino problem is alleviated by the massive entropy production from modulus decay.

5.3.2 Non-thermal WIMPs - the annihilation scenario

Since the thermally-produced relics are expected to be diluted to negligible amounts, dark matter must then be produced non-thermally. First we focus on dark matter that is produced in significant quantities from decay processes (e.g. from moduli or saxion decays) which leads to the so-called *annihilation scenario*. We then discuss in the next section the production of dark matter from decay processes where the produced abundance is relatively low - which is referred to as the *branching scenario* in much of the literature. Finally, we will discuss production of axions from the misalignment mechanism in Sec. (5.3.7).

Let us first focus on neutralinos produced from moduli decay. Close to the neutralino freeze-out, the equilibrium density falls rapidly and - assuming WIMP annihilations are the dominant effect immediately after modulus decay - we can approximate the number density Boltzmann equation for the neutralino as

$$\dot{n}_{\widetilde{Z}_1} + 3Hn_{\widetilde{Z}_1} \simeq -\langle\sigma v\rangle n^2_{\widetilde{Z}_1}. \tag{5.53}$$

Putting this in terms of the abundance yield $Y_{\widetilde{Z}_1} \equiv n_{\widetilde{Z}_1}/s$, we can rewrite this as

$$\dot{Y}_{\widetilde{Z}_1} \simeq -\langle\sigma v\rangle Y^2_{\widetilde{Z}_1} s. \tag{5.54}$$

In the limit of constant $\langle\sigma v\rangle$, we can integrate this equation from T_D^ϕ to the present time to find

$$Y^C_{\widetilde{Z}_1} \simeq \frac{H(T_D^\phi)}{\langle\sigma v\rangle s(T_D^\phi)} \tag{5.55}$$

which may be recast in terms of the number density:

$$n^C_{\widetilde{Z}_1}(T_D^\phi) \simeq \frac{H(T_D^\phi)}{\langle\sigma v\rangle}. \tag{5.56}$$

Here, we have used the superscript C to denote this number density as the "critical density," following the terminology of [357].

This simple result encapsulates some extremely powerful physics. If the produced abundance is large - specifically so that $Y_{\widetilde{Z}_1}(T_D^\phi) \gtrsim Y^C_{\widetilde{Z}_1}(T_D^\phi)$ where

$Y_{\widetilde{Z}_1}(T_D^\phi)$ is the abundance yield produced instantaneously after the decay of the modulus - then the neutralinos will be abundant enough to undergo annihilations. These WIMP annihilations will then continue until the neutralino abundance reaches the critical value $Y^C_{\widetilde{Z}_1}(T_D^\phi)$ - which then remains constant in the absence of any further significant source of production. This is somewhat of a generalization of the freeze-out process, which in the presence of a late-decaying modulus might occur *after* the expected thermal freeze-out temperature is reached. Assuming radiation-domination follows the modulus decay, we can see that $Y^C_{\widetilde{Z}_1} \propto 1/T_D^\phi$, so that a larger modulus decay temperature will have a smaller critical abundance. In particular, if $T_D^\phi > T_{\text{f.o.}}$, then the neutralino abundance is large enough for efficient annihilations to diminish the abundance to the standard thermal freeze-out value. If instead $T_D^\phi < T_{\text{f.o.}}$, then annihilations may still take place, but the dilution of the produced abundance due to Hubble expansion reduces the efficiency of annihilations - giving an enhancement in the final abundance in comparison to the thermal (freeze-out) value. This is the main idea behind the original work of Moroi and Randall [355] which showed that thermally-underproduced dark matter - such as wino-like neutralinos (or in our case, higgsino-like neutralinos) - can be enhanced to levels in accordance with the measured relic density (see also Choi, Kim, and Seto [397]).

Combining these arguments, we can give an extremely concise estimate for the neutralino relic density. Assuming a thermally-produced relic density of $\Omega^{\text{TP}}_{\widetilde{Z}_1}h^2$ (i.e. the expected WIMP relic density in a standard thermal scenario), the WIMP relic density in the annihilation scenario which we denote as $\Omega^C_{\widetilde{Z}_1}h^2$ (the critical

relic density) is given by

$$\Omega^{C}_{\widetilde{Z}_1} h^2 \simeq \Omega^{\rm TP}_{\widetilde{Z}_1} h^2 \times \max\left\{\left(T_{\rm f.o.}/T^{\phi}_{D}\right),\, 1\right\}. \tag{5.57}$$

It is worth reiterating that - at least in the annihilation scenario - if the modulus decay happens *before* thermal freeze-out, the produced dark matter abundance is indistinguishable from that of a standard thermal scenario. We also see that if the modulus decays very late, this enhancement can grossly overproduce dark matter. This is sometimes referred to as the moduli-induced DM overproduction problem [234].

5.3.3 Non-thermal WIMPs - the branching scenario

If the produced abundance is instead too small to annihilate - even inefficiently - the treatment of the previous section does not apply. In this case, the primary contribution to the neutralino's Boltzmann equation close to the time of modulus decay are the injections which can be approximated as

$$\frac{dn_{\widetilde{Z}_1}}{dt} + 3Hn_{\widetilde{Z}_1} \simeq \Gamma_{\phi}\mathcal{B}_{\phi\to\widetilde{Z}_1} n_{\phi} \tag{5.58}$$

where we focus only on neutralinos produced via modulus decay here. Rewriting this in terms of the abundance yield variables $Y_{\widetilde{Z}_1}$ and Y_{ϕ}, this can be rewritten as

$$\dot{Y}_{\widetilde{Z}_1} \simeq \Gamma_{\phi}\mathcal{B}_{\phi\to\widetilde{Z}_1} Y_{\phi}. \tag{5.59}$$

It is now a trivial matter to integrate this expression from T_D^ϕ to the present time. As Y_ϕ is only non-zero for the lifetime of ϕ ($\sim \Gamma_\phi^{-1}$), in the sudden decay approximation we have the result:

$$Y_{\widetilde{Z}_1}^D \simeq \mathcal{B}_{\phi\to\widetilde{Z}_1} Y_\phi(T_D^\phi) \tag{5.60}$$

or, in terms of the neutralino number density:

$$n_{\widetilde{Z}_1}^D(T_D^\phi) \simeq \mathcal{B}_{\phi\to\widetilde{Z}_1} n_\phi(T_D^\phi) \tag{5.61}$$

where we now use the superscript D to denote this abundance as the "decay-produced density." This scenario is sometimes referred to as the "branching scenario" since the WIMP abundance is simply that which is directly produced from the decay of some massive species. The branching scenario also provides a mechanism for thermally-overproduced dark matter - such as bino-like neutralinos - to match the observed relic density.

We are now in a position to estimate the WIMP relic density produced in the branching scenario. In this case, we can use Eq. (5.50) with our expression for $Y_{\widetilde{Z}_1}^D$. However, in evaluating $Y_\phi(T_D^\phi)$ there is one subtlety. Before the modulus decays at T_D^ϕ, it has begun to inject entropy at T_S^ϕ - so in the sudden decay approximation we require $Y_\phi(T_D^\phi)$ to be defined with respect to the produced

entropy from modulus decay. This can be cast in the simple form

$$Y_\phi(T_D^\phi) \simeq \frac{45}{4\pi^2}\frac{r^{-1}m_\phi\phi_0^2}{g_{*S}(T_{\rm osc}^\phi)(T_{\rm osc}^\phi)^3} \tag{5.62}$$

where we have used $n_\phi(T_{\rm osc}^\phi) = \frac{1}{2}m_\phi\phi_0^2$ and used the entropy dilution factor to account for the entropy production between T_S^ϕ and T_D^ϕ. As we expect r to increase as m_ϕ decreases, we see that although $Y_\phi(T_D^\phi)$ is in general quite large due to the expectation that $\phi_0 \sim m_P$, it is possible that the modulus abundance at T_D^ϕ may be very small for small m_ϕ. This then provides us with a fairly concise approximation for the neutralino relic density in the branching scenario:

$$\Omega_{\widetilde{Z}_1}^D h^2 \simeq \frac{45}{4\pi^2}\frac{\mathcal{B}_{\phi\to\widetilde{Z}_1}m_{\widetilde{Z}_1}}{\rho_c/(s_0h^2)}\frac{r^{-1}m_\phi\phi_0^2}{g_{*S}(T_{\rm osc}^\phi)(T_{\rm osc}^\phi)^3}. \tag{5.63}$$

Now that we have expressions for the neutralino relic density in both the annihilation scenario and the branching scenario, we can then in general estimate the WIMP abundance by

$$\Omega_{\widetilde{Z}_1}h^2 \sim \min\left\{\Omega_{\widetilde{Z}_1}^C h^2,\, \Omega_{\widetilde{Z}_1}^D h^2\right\}. \tag{5.64}$$

5.3.4 Non-thermal WIMP production in the ϕMSSM - case B2

We first apply our arguments from the preceding sections to case **B2** utilizing our natural SUSY benchmark point from Table (4.3). Taking a benchmark $m_\phi \sim 10^3$

TeV, in addition to assuming a branching ratio $\mathcal{B}(\phi \to \text{SUSY}) \sim 0.01$, it is clear that we predict the annihilation scenario which gives

$$\Omega_{\widetilde{Z}_1} h^2 \sim \min\{1.7,\, 2600\} \sim 1.7 \quad (m_\phi = 10^3 \text{ TeV}). \tag{5.65}$$

Additionally, it is easy to convince oneself that larger values of m_ϕ should likewise

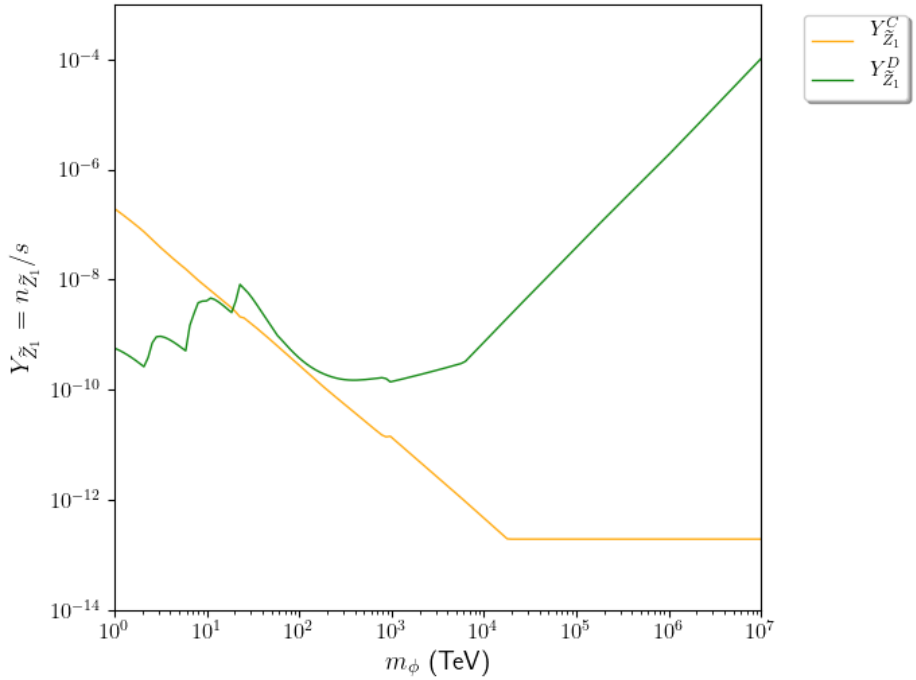


Figure 5.5: Critical abundance yield $Y^C_{\widetilde{Z}_1}$ (orange) and decay-produced abundance yield $Y^D_{\widetilde{Z}_1}$ (green) for neutralinos. Here we take case **B2-GK1** and assume 1% of Higgses decay to SUSY in addition to all R-parity odd decays.

predict the annihilation scenario, based on the scaling of any m_ϕ-dependent parameters. Closer inspection of Eq. (5.63) indicates that smaller values of m_ϕ may predict the branching scenario however, since lowering m_ϕ increases the entropy dilution faster than T^ϕ_{osc}. We display this behavior in Fig. (5.5) for case

B2-GK1, which shows both the critical abundance yield $Y^C_{\widetilde{Z}_1}$ (orange curve) and the decay-produced abundance yield $Y^D_{\widetilde{Z}_1}$ (green curve). We have also assumed that the gravitinos - which are suppressed in this case - are produced in low enough quantities to be ignored. In this figure, we adopt the lower bound LB2 which was shown in Fig. (4.3). This lower bound includes all direct R-parity odd decays (i.e. modulus to sfermions, etc.) and assumes the Higgs sector has a 1% branching ratio to R-parity odd pairs. The critical abundance is computed using the relic density estimate from IsaRED [330] $\Omega_{\widetilde{Z}_1}h^2 \sim 0.011$, as listed in Table (4.3). Evidently the annihilation scenario - given by the critical abundance yield $Y^C_{\widetilde{Z}_1}$ - is predicted for most of the displayed m_ϕ, although the branching scenario given by the decay-produced abundance yield $Y^D_{\widetilde{Z}_1}$ becomes predicted for $m_\phi \lesssim 20$ TeV.

We display the corresponding relic density based on our qualitative arguments in Fig. (5.6) for this same lower bound. In addition, we display the predicted relic density for each $\lambda_i \in \{0.1, 1, 10\}$. Even in this lower bound scenario, we see that the WIMP relic density appears to be a much more stringent constraint on m_ϕ than the BBN bound. For larger values of the modulus couplings, we see $m_\phi \gtrsim 700$ TeV can satisfy the observed relic density, while smaller values push this constraint to $m_\phi \gtrsim 2 \times 10^4$ TeV - both well above our estimated $m_\phi \gtrsim (10 - 300)$ TeV constraint from BBN considerations (again, depending on the assumed values of the couplings). We also see that the branching scenario is predicted for small values of m_ϕ with lower values of the couplings $\lambda_i = 0.1$ predicting the branching scenario at a much larger value of m_ϕ than for $\lambda_i = 1, 10$. However, WIMP dark

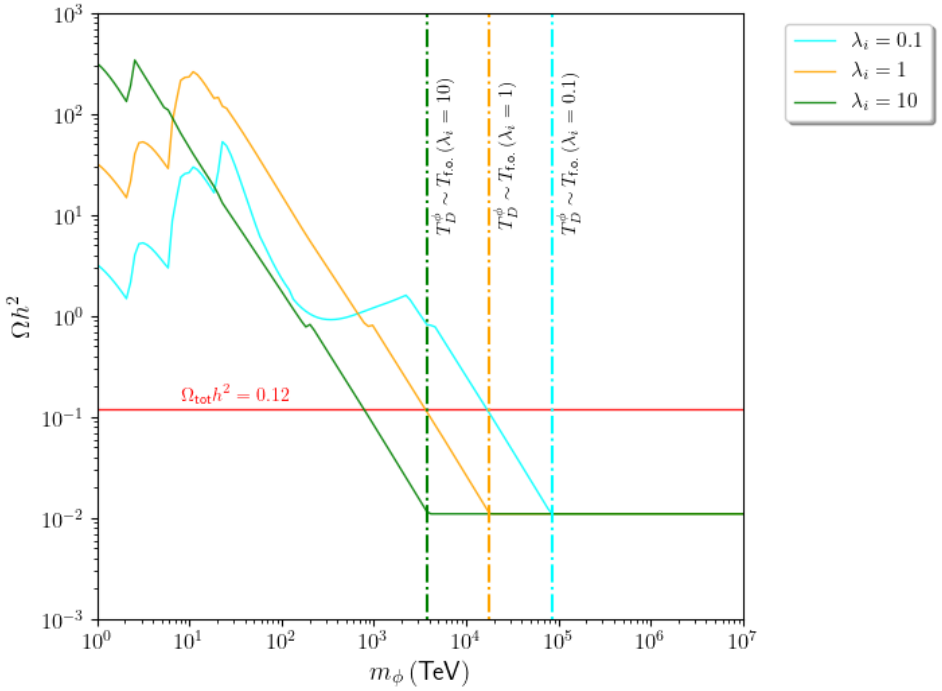


Figure 5.6: Predicted WIMP relic density for each $\lambda_i \in \{0.1, 1, 10\}$. Here we take case **B2-GK1** and assume 1% of Higgses decay to SUSY in addition to all R-parity odd decays. Figure updated from [6].

matter is still grossly overproduced even in this lower bound scenario - one would need to introduce model-dependent considerations to reduce the branching ratio to SUSY particles by more than an order of magnitude without changing the total width significantly in order to reproduce the observed dark matter density in the branching scenario.

We display in Fig. (5.7) the corresponding relic density for the upper bound UB shown in Fig. (4.3), which includes all direct R-parity odd decays and assumes the Higgs sector has a 100% branching ratio to R-parity odd pairs. We see that - especially for $\lambda_i = 0.1$ - small values of m_ϕ now predict even larger WIMP relic densities. Lower values of m_ϕ are also now predicted to be described by the annihilation scenario than in our previous figure. However, since both the

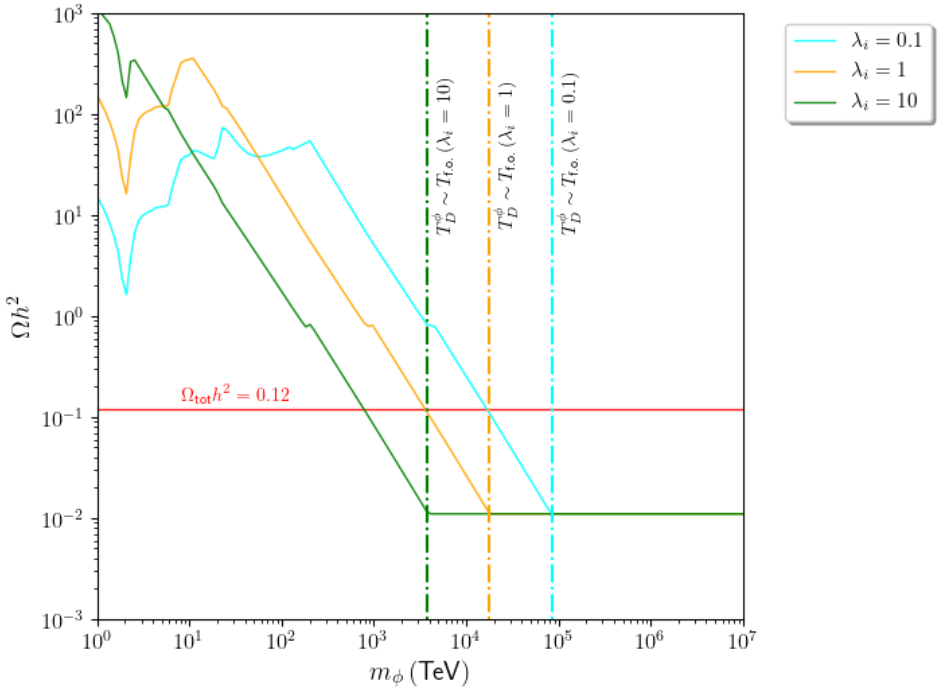


Figure 5.7: Predicted WIMP relic density for each $\lambda_i \in \{0.1, 1, 10\}$. Here we take case **B2-GK1** and assume 100% of Higgses decay to SUSY in addition to all R-parity odd decays. Figure updated from [6].

lower bound in Fig. (5.6) and the upper bound in Fig. (5.7) transition to the annihilation scenario before the WIMP relic density falls below the measured value $\Omega h^2 \sim 0.12$, both branching ratio bounds give identical constraints on m_ϕ.

For the sake of comparison, we display in Fig. (5.8) the predicted WIMP relic density adopting a constant modulus branching ratio to SUSY particles of $\mathcal{B}(\phi \to \text{SUSY}) = 1\%$. Based on our previous discussion in Sec. (4.3.2), this is rather artificial for $m_\phi \lesssim 60$ TeV for the ϕMSSM - although it serves as a useful comparison for what one might expect as a lower bound if one neglects mixing and phase space effects (as is conventional in the literature). Even with this artificial lower bound, we see that - although we still transition between the annihilation scenario and the branching scenario, the total WIMP relic density is still grossly

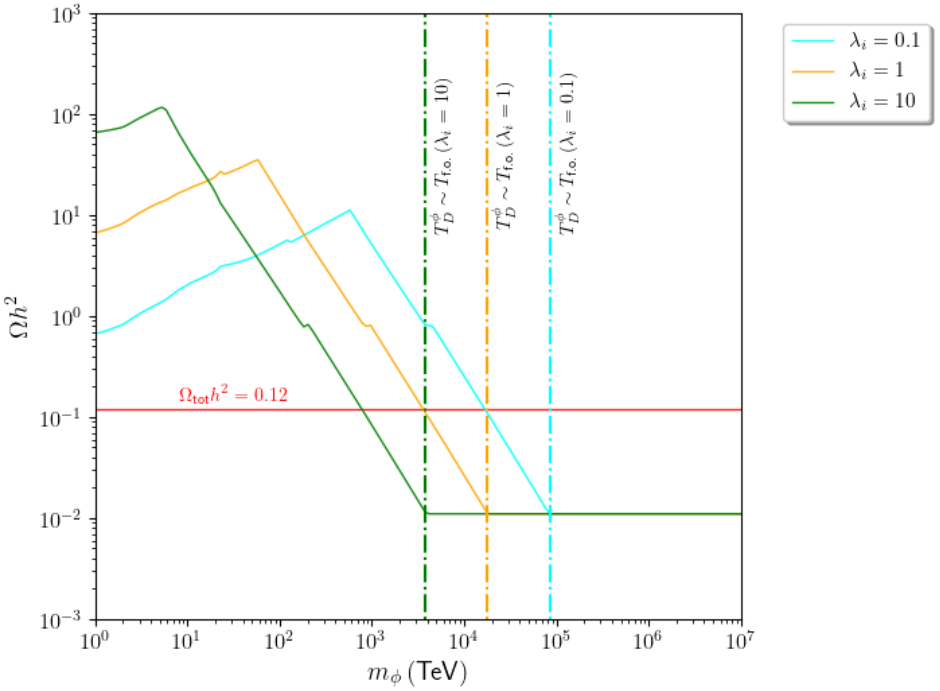


Figure 5.8: Predicted WIMP relic density for each $\lambda_i \in \{0.1, 1, 10\}$. Here we take case **B2-GK1** but assume a flat branching fraction to SUSY $\mathcal{B}(\phi \to \text{SUSY}) = 1\%$ (independent of m_ϕ). Figure updated from [6].

overproduced.

We should note that in the branching scenario, it *may* be possible to reproduce the observed DM relic density for $m_\phi \lesssim 1$ TeV. In particular, for $m_\phi \sim 500$ GeV most decay modes to SUSY particles will be kinematically forbidden, possibly reducing the branching ratio sufficiently to reproduce $\Omega h^2 \sim 0.12$. This scenario however would require the modulus decay to occur after BBN - and is thus excluded. Therefore, we do not expect the branching scenario from modulus decay to be viable in the ϕMSSM - while the annihilation scenario is viable if $m_\phi \gtrsim (700 - 2 \times 10^4)$ TeV - depending on the magnitude of the modulus couplings.

Additionally, we expect similar results for the produced neutralino relic density

in case **A2-GK1**, as well as in **B2-GK2** and **A2-GK2**. This is largely due to the fact that we expect the annihilation scenario for a viable cosmology and the modulus decay temperature will not be significantly affected in any of these cases. Based on our arguments in Sec. (4.3.2) and Fig. (4.9), we would expect a decrease of T_D^ϕ by about a factor of 3 in the **GK2** cases, and an increase of T_D^ϕ by a factor of about 1.5 in the **A2** case - leading to similar results to those we have just discussed. Additionally, in the **A2** cases it is likely that the transition to the branching scenario is pushed to even smaller m_ϕ and results in a larger WIMP abundance - although this enhancement occurs only in the region where neutralinos are already overproduced.

5.3.5 Non-thermal WIMP production in the ϕMSSM - case B1

It is now worth considering case **B1-GK1**, which includes unsuppressed decays to gravitinos. As we saw in Sec. (4.3.2), we do not expect a significant change in the decay width of the modulus so any WIMP abundance from modulus decay in the annihilation scenario will be unchanged. Furthermore, although the modulus branching fraction to SUSY particles is enhanced, we saw in Fig. (5.6) and Fig. (5.7) that even lower (realistic) limits of branching ratios to SUSY particles are likely to overproduce WIMPs in the branching scenario. However, now that gravitinos are produced in tentatively significant abundance they may dominate the cosmology if they are longer-lived than the modulus. In this case, we can use similar arguments to those of the previous sections with a few minor modifications[7]

[7] If $T_D^{3/2} \gtrsim T_D^\phi$, any gravitinos produced by modulus decay will decay rapidly. In this case, we expect no significant deviation from the predictions of case **B2**.

- where we now assume that $T_D^{3/2} < T_D^{\phi}$. The annihilation scenario replacement is straightforward. Since the temperature scale of neutralino production is now the gravitino decay temperature $T_D^{3/2}$ instead of the modulus decay temperature T_D^{ϕ}, we can make the replacements

$$Y_{\widetilde{Z}_1}^{C}(T_D^{3/2}) \simeq \frac{H(T_D^{3/2})}{\langle\sigma v\rangle s(T_D^{3/2})} \tag{5.66}$$

for the critical abundance yield, which gives us

$$\Omega_{\widetilde{Z}_1}^{C} h^2 \simeq \Omega_{\widetilde{Z}_1}^{\mathrm{TP}} h^2 \times \max\left\{\left(T_{\mathrm{f.o.}}/T_D^{3/2}, 1\right)\right\} \tag{5.67}$$

for the critical relic density. The modifications in the branching scenario are not much more involved - taking the modulus abundance yield $Y_{\phi}(T_D^{\phi})$, the gravitino abundance yield is then given by

$$Y_{3/2}(T_D^{\phi}) = \mathcal{B}_{\phi\to\psi_{3/2}} Y_{\phi}(T_D^{\phi}) \simeq \frac{45}{4\pi^2} \frac{r^{-1}\mathcal{B}_{\phi\to\psi_{3/2}} m_{\phi}\phi_0^2}{g_{*S}(T_{\mathrm{osc}}^{\phi})(T_{\mathrm{osc}}^{\phi})^3} \tag{5.68}$$

and, assuming that due to R-parity conservation the gravitino branching ratio to SUSY particles is 100% and that entropy is conserved after T_D^{ϕ}, the decay-produced relic density is given by

$$\Omega_{\widetilde{Z}_1}^{D} h^2 \simeq \frac{45}{4\pi^2} \frac{\mathcal{B}_{\phi\to\psi_{3/2}} m_{\widetilde{Z}_1}}{\rho_c/(s_0 h^2)} \frac{r^{-1} m_{\phi}\phi_0^2}{g_{*S}(T_{\mathrm{osc}}^{\phi})(T_{\mathrm{osc}}^{\phi})^3}. \tag{5.69}$$

Once again, the minimum of $\Omega^D_{\widetilde{Z}_1} h^2$ and $\Omega^C_{\widetilde{Z}_1} h^2$ determines the expected neutralino relic density from gravitino decay.

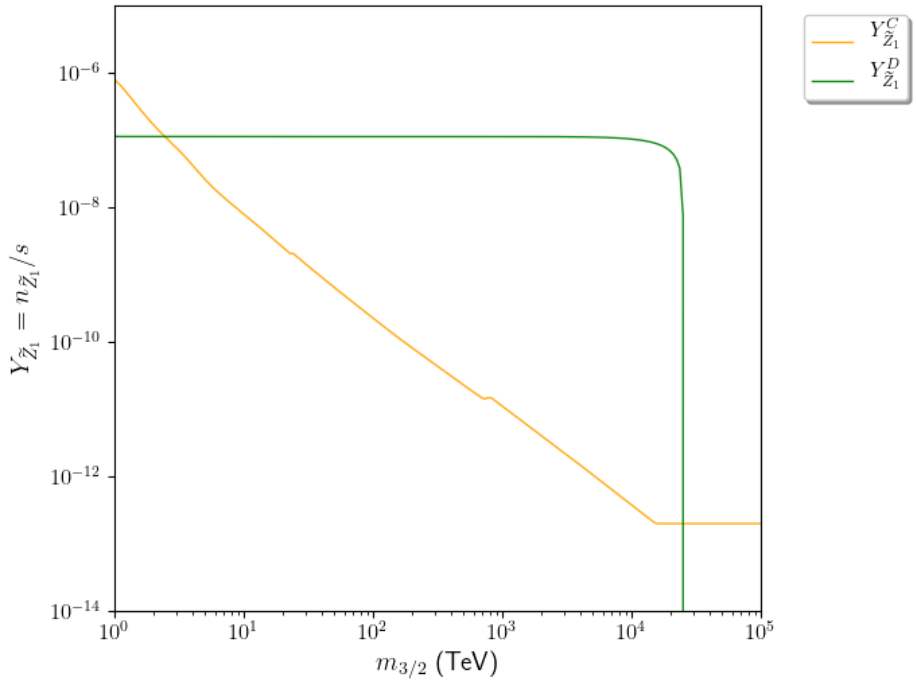


Figure 5.9: Critical abundance $Y^C_{\widetilde{Z}_1}$ (orange) and decay-produced abundance $Y^D_{\widetilde{Z}_1}$ (green) for neutralinos. Here we take case **B1-GK1** and assume the gravitino dominates the abundance contribution. Additionally, we fix $m_\phi = 5 \times 10^4$ TeV and take all $\lambda_i = 1$.

We show in Fig. (5.9) the critical abundance yield (orange curve) and the decay-produced abundance yield (green curve) for neutralinos in case **B1**, where now all neutralinos are assumed to come from the gravitino. We also fix $m_\phi = 5 \times 10^4$ TeV and take all $\lambda_i = 1$, which predicts the thermal WIMP abundance (i.e. no enhancement due to moduli decay) if the gravitino is absent. Evidently, only $m_{3/2} \lesssim 3$ TeV allows for the branching scenario - which is expected to be excluded from BBN constraints as the gravitinos are now produced in large quantities. Since we then expect to be in the annihilation scenario for any viable value of

$m_{3/2}$, we do not expect that neutralinos produced from modulus decay have any significant effect on the WIMP abundance - the gravitinos produced from modulus decay now dominate this aspect of the cosmology. Of course, if the gravitino is kinematically forbidden the modulus is again the dominant factor in neutralino production - we display this in Fig. (5.9) for $m_{3/2} \geq 2.5 \times 10^4$ TeV where the gravitino becomes kinematically forbidden for this benchmark m_ϕ. The WIMP abundance remains at its thermally-expected value in this case, as the modulus decays before neutralino freeze-out for $m_\phi = 5 \times 10^4$ TeV. This also marks the best case scenario within case **B1** since lighter moduli will produce an enhanced neutralino abundance.

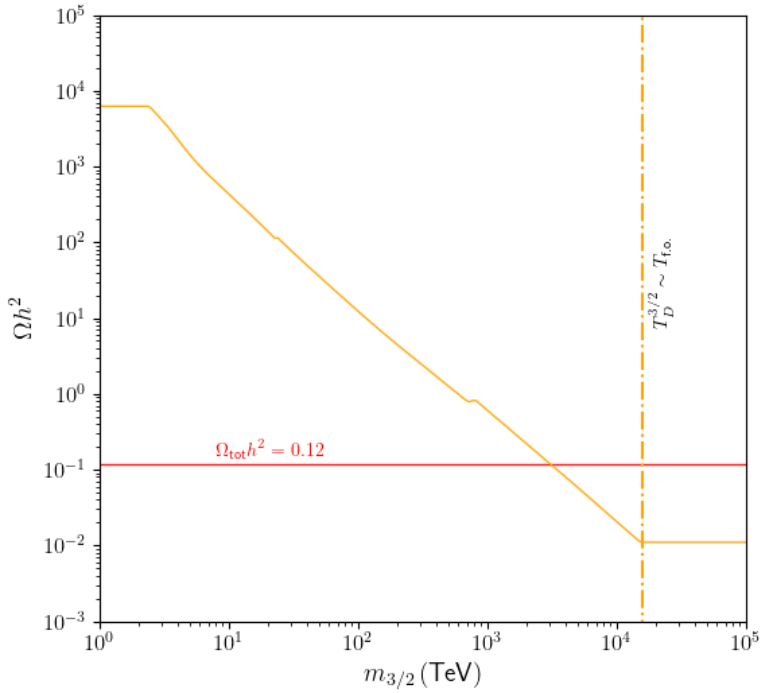


Figure 5.10: Predicted WIMP relic density in case **B1-GK1**. We fix $m_\phi = 5 \times 10^4$ TeV and take all $\lambda_i = 1$.

We also display the predicted neutralino relic density in case **B1** in Fig. (5.10).

We see that dark matter is grossly overproduced here unless $m_{3/2} \gtrsim 3 \times 10^3$ TeV. This marks a big departure from case **B2** - even if the modulus is sufficiently heavy that neutralinos are not overproduced, the same DM overproduction and BBN problems arise from the decay-produced gravitinos. This resurgence of the gravitino problem, or rather the moduli-induced gravitino problem, was previously studied in [229, 354, 228, 230, 350]. The moduli-induced gravitino problem can be resolved quite simply if the gravitino is a kinematically forbidden decay of the modulus or if sequestering is present which allows for $m_{3/2} \gtrsim 10^4$ TeV. However, models which do not predict either of these scenarios will be at severe tension with a natural SUSY spectrum (likely falling into a high-scale SUSY [398, 399] or split-SUSY spectrum [400, 401, 402], see also [403]), unless additional model-building details are considered to evade this rather severe issue.

We should also note that we do not expect any change in results in case **A1** from **B1**. Although the modulus may decay earlier, the gravitinos are produced with roughly the same abundance and will still decay at the same scale - and since we generically expect the annihilation scenario, the additional neutralino abundance from unsuppressed gaugino decays will still annihilate to the critical value. For identical reasons, we also do not expect any significant difference between cases **GK1** and **GK2**. Thus, we expect any case with unsuppressed decays to gravitinos to produce very similar results to those we have presented in this section.

5.3.6 Dark radiation production in the ϕMSSM with a light ALP

If the ϕMSSM contains an light axion-like particle (ALP) in its spectrum, the main contribution of the ALP will be the addition of dark radiation [239, 240, 236]. For a light ALP to exist in the spectrum, the shift symmetry which protects the ALP from gaining a mass must survive moduli stabilization which we assume to be the case in this section. This shift symmetry can then only be broken by small non-perturbative effects, which leave the ALP effectively massless. Since these particles are only gravitationally coupled (in general), they do not thermalize and remain relativistic - only redshifting from Hubble dilution. In this section, we estimate the amount of dark radiation produced in the ϕMSSM if it contains a light ALP in its spectrum.

It is conventional to parametrize the amount of dark radiation produced by an increase in the effective number of neutrinos, $\Delta N_{\rm eff} = N_{\rm eff} - N_{\rm eff}^{\rm SM}$. The Standard Model predicts $N_{\rm eff}^{\rm SM} \simeq 3.046$ [404, 344], while Planck 2018 results require $\Delta N_{\rm eff} < 0.29$ at the 95% C.L. [11]. To estimate $\Delta N_{\rm eff}$, we compare the energy density of additional relativistic degrees of freedom (in the ϕMSSM, we have only the ALP $\rho_{\rm ALP}$) to the energy density of a single neutrino species $\rho_\nu = \frac{7}{8}\frac{\pi^2}{15}T_\nu^4$:

$$\Delta N_{\rm eff} = \frac{\rho_{\rm ALP}}{\rho_\nu} = \frac{120}{7\pi^2}\left(\frac{11}{4}\right)^{4/3}\frac{\rho_{\rm ALP}(T)}{T^4} \tag{5.70}$$

where we relate the radiation temperature T to the neutrino temperature $T_\nu = (4/11)^{1/3}T$ [344, 286]. Our aim now is to estimate $\rho_{\rm ALP}(T)$.

As we have just noted, ALPs are typically expected to be coupled only

gravitationally which implies that production is characterized by the branching scenario (i.e. the ALPs do not annihilate in any significant sense once produced). Using arguments identical to those we made in the previous sections, we can relate the energy density of the ALPs to that of the modulus at T_D^ϕ in the branching scenario by

$$\rho_{\rm ALP}(T_D^\phi) \simeq \frac{1}{2}\mathcal{B}_{\phi\to{\rm ALP}} r^{-1} m_\phi^2 \phi_0^2 \left(\frac{g_{*S}(T_D^\phi)}{g_{*S}(T_{\rm osc}^\phi)}\frac{(T_D^\phi)^3}{(T_{\rm osc}^\phi)^3}\right) \tag{5.71}$$

where we once again require the entropy dilution factor r^{-1} due to entropy having already been injected before T_D^ϕ occurs. At some later temperature $T \lesssim T_D^\phi$, assuming entropy is conserved after T_D^ϕ we can then write down the ALP energy density at some lower temperature T:

$$\rho_{\rm ALP}(T) \simeq \left(\frac{g_{*S}(T)}{g_{*S}(T_D^\phi)}\frac{T^3}{(T_D^\phi)^3}\right)^{4/3} \rho_{\rm ALP}(T_D^\phi) \tag{5.72}$$

where we have used that ALPs dilute as radiation, $\rho_{\rm ALP} \propto R^{-4}$. This then gives us an estimate for $\Delta N_{\rm eff}$:

$$\Delta N_{\rm eff} \simeq \frac{60}{7\pi^2}\left(\frac{11}{4}\right)^{4/3}\left(\frac{g_{*S}(T)}{g_{*S}(T_D^\phi)}\right)^{4/3}\left(\frac{g_{*S}(T_D^\phi)}{g_{*S}(T_{\rm osc}^\phi)}\frac{\mathcal{B}_{\phi\to{\rm ALP}} r^{-1} m_\phi^2 \phi_0^2}{T_D^\phi (T_{\rm osc}^\phi)^3}\right). \tag{5.73}$$

We display the predicted $\Delta N_{\rm eff}$ in Fig. (5.11) in the (m_ϕ, $\lambda_{\rm ALP}$) plane for both the **B2-GK1** and **B2-GK2** scenarios. Here, red dots are in excess of Planck 2018 bounds $\Delta N_{\rm eff} \geq 0.29$, while purple dots contribute a negligible amount of dark radiation due to ALPs. The upper left plot takes all other $\lambda_i = 0.1$ in case

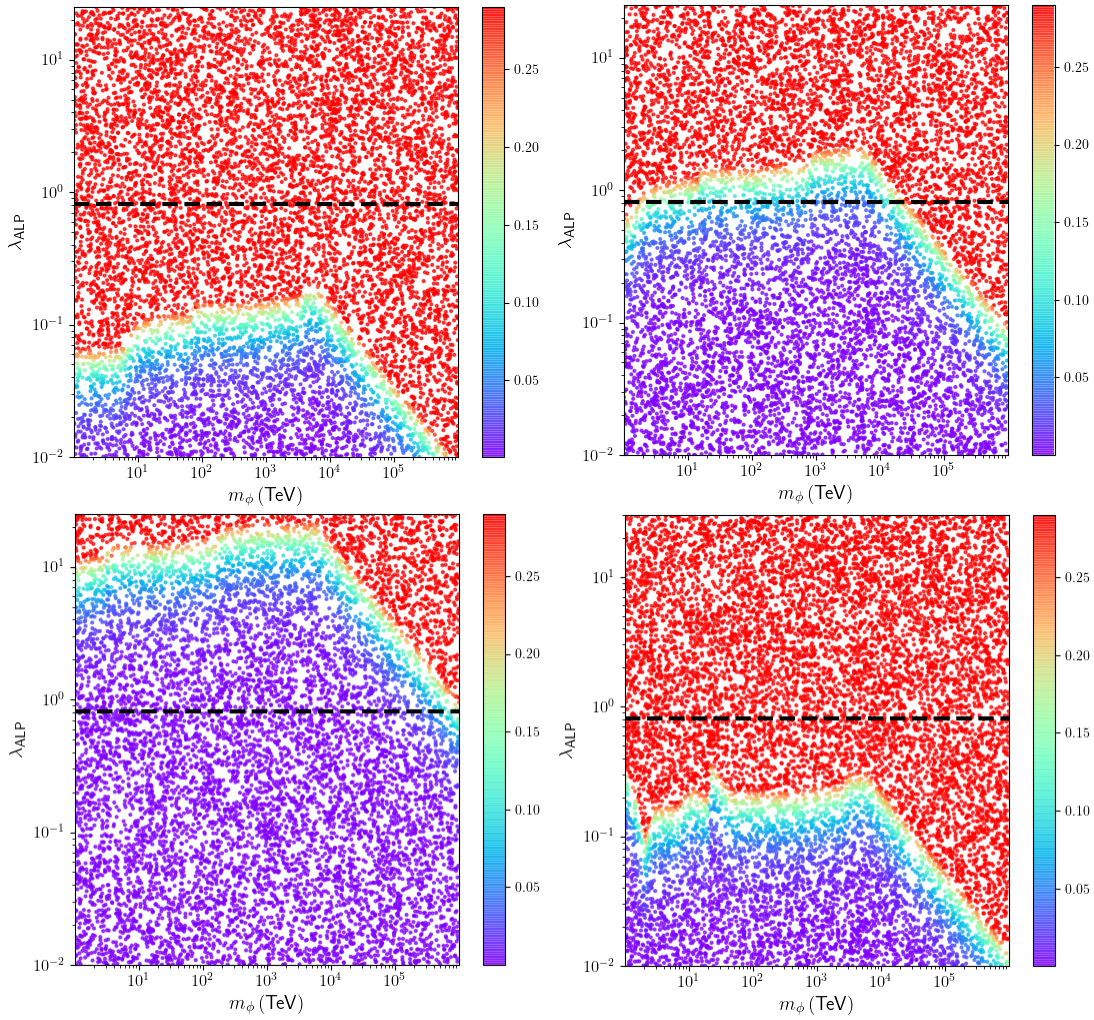


Figure 5.11: Predicted dark radiation $\Delta N_{\rm eff}$ in case **B2** in the (m_ϕ, $\lambda_{\rm ALP}$) plane. Upper plots and lower left plot assume the **GK1** scenario, while the lower right plot takes the **GK2** scenario. The upper left (right) plot takes all remaining $\lambda_i = 0.1$ (all remaining $\lambda_i = 1$), while the lower left plot takes all remaining $\lambda_i = 10$. The lower right plot takes all remaining $\lambda_i = 1$ except for $\lambda_{\rm gauge} = 1/16\pi^2$. Horizontal dashed line represents expected minimal LVS value, $\lambda_{\rm ALP} = 0.816$. Figure reproduced from [7].

B2-GK1. From this plot, we see that a value $\lambda_{\rm ALP} \gtrsim 0.2$ will produce an excess of dark radiation, while far smaller values of $\lambda_{\rm ALP}$ may be required depending on the value of m_ϕ. We also see for $m_\phi \gtrsim 10^4$ TeV, dark radiation seems to be produced in a greater amount than for smaller m_ϕ. This is due to the scaling

behavior of the entropy dilution factor r, which as we saw in Fig. (5.3) decreases more quickly once $T^{\phi}_{\rm osc} \gtrsim T_R$ thus predicting a larger modulus abundance when it decays. The upper right and lower left plots display the same scenario but for all remaining $\lambda_i = 1$ and $\lambda_i = 10$, respectively. In all three of the **B2-GK1** plots, we see very similar behavior and quantitative trends - to avoid overproduction of dark radiation, a $\lambda_{\rm ALP}$ close to the value of the remaining λ_i is required. Referring back to Fig. (4.11), we see that this implies a branching ratio to ALPs of less than roughly 10% is required in the **GK1** scenario. While we would not expect these predictions to change in the **B1-GK1** scenario, they may become marginally more optimistic in the **A1-GK1** and **A2-GK1** scenarios as the introduction of unsuppressed gaugino decays may suppress the branching ratio to ALPs by roughly a factor of 2, which we would expect allows $\lambda_{\rm ALP}$ to be larger by roughly a factor of 1.5.

We also display the predicted $\Delta N_{\rm eff}$ for case **B2-GK2** with all $\lambda_i = 1$ (except $\lambda_{\rm gauge} = 1/16\pi^2$) in Fig. (5.11). Comparing this case to the **B2-GK1** case with all $\lambda_i = 1$, we see that the suppression of the gauge boson decays puts a much larger constraint on $\lambda_{\rm ALP}$ due to the increase in branching fraction to ALPs. Evidently, here a maximum of $\lambda_{\rm ALP} \lesssim 0.3$ is allowed. In LVS, the bulk modulus coupling to the ALP is determined from the geometry and (in minimal LVS) takes the value $\lambda_{\rm ALP} = 0.816$ in our conventions [239, 240]. We display this expected bound as the black dashed line in Fig. (5.11). Clearly, the **GK2** case requires either a much smaller $\lambda_{\rm ALP}$ or larger λ_i couplings (namely, a larger Giudice-Masiero coupling as it is the leading unsuppressed mode). However, as we saw in Sec. (3.1.2) this

may translate to a large value of μ - leading to deviation from our natural SUSY benchmark point. We will also cover this point in Ch. (7) when we consider dark radiation in the fibred LVS model. We do not expect any large deviation in these predictions for any of the **GK2** cases since the branching ratio to ALPs is not expected to be affected significantly.

5.3.7 Abundance of misalignment produced axions

In a standard thermal history, the relic density of axions produced via the misalignment mechanism follows a simple form [374, 376, 375]:

$$\Omega_a^{\rm std} h^2 \simeq 0.23 f(\theta_i)\theta_i^2 \left(\frac{f_a/N_{\rm DW}}{10^{12}\ {\rm GeV}}\right)^{7/6} \tag{5.74}$$

where $f(\theta_i) = [\log(e/(1-\theta_i^2/\pi^2))]^{7/6}$ is the anharmonicity factor [405, 391]. However, in the non-thermal case, the onset of axion oscillations - as shown in Sec. (5.2.2) - is sensitive to the dominant background. In particular, once oscillations begin the number density of the axions decreases as [286]

$$n_a(T) = n_a(T_{\rm osc}^a)\frac{R^3(T_{\rm osc}^a)}{R^3(T)} \tag{5.75}$$

for $T < T_{\rm osc}^a$.

Focusing first on the case where $T_{\rm osc}^a < T_D^\phi$ and assuming a radiation-dominated background after modulus decay, we can immediately write down the abundance yield $Y_a = n_a/s$. The case where $T_S^\phi \gtrsim T_{\rm osc}^a \gtrsim T_D^\phi$ follows similarly, however we now must factor in the decay-dominated epoch from $T_{\rm osc}^a$ to T_D^ϕ, at which

point we again assume a radiation-dominated background. As we have discussed in Sec. (5.2.6), we do not expect a phenomenologically viable scenario where $T^a_{\rm osc} \gtrsim T^\phi_S$ and hence we ignore this case here. The axion abundance is then well approximated by the expressions

$$Y_a = \frac{45}{2\pi^2} \times \begin{cases} \frac{1}{g_*(T^a_{\rm osc})} \frac{n_a(T^a_{\rm osc})}{(T^a_{\rm osc})^3} & (T^a_{\rm osc} < T^\phi_D) \\ \frac{g_*(T^\phi_D)}{g_*(T^a_{\rm osc})^2} \frac{n_a(T^a_{\rm osc})(T^\phi_D)^5}{(T^a_{\rm osc})^8} & (T^\phi_S \gtrsim T^a_{\rm osc} \gtrsim T^\phi_D). \end{cases} \tag{5.76}$$

Let us now parameterize $n_a(T^a_{\rm osc})$ as

$$n_a(T^a_{\rm osc}) = \frac{1}{2} m_a(T^a_{\rm osc}) a_0^2 \tag{5.77}$$

where the axion field's initial amplitude, a_0, is independent of the temperature and background details and is given by [112]

$$a_0^2 = \frac{1.44 f_a^2 \theta_i^2}{N_{\rm DW}^2} f(\theta_i), \qquad f(\theta_i) \equiv \left[\log \left(\frac{e}{1 - \theta_i^2/\pi^2} \right) \right]^{7/6}. \tag{5.78}$$

It is immediately clear that both the misalignment angle, θ_i, and the axion decay constant, f_a, play a large role in determining the final axion abundance. We are now in a position to write down the axion relic density. Making use of Eq. (5.50),

we thus have the expressions

$$\Omega_a h^2 \simeq \frac{45}{4\pi^2}\frac{m_a(T=0)h^2a_0^2}{\rho_c/s_0}\frac{m_a(T^a_{\rm osc})}{g_*(T^a_{\rm osc})}\times\begin{cases}(T^a_{\rm osc})^{-3} & (T^a_{\rm osc}<T^\phi_D)\\ \frac{g_*(T^\phi_D)}{g_*(T^a_{\rm osc})}(T^\phi_D)^5/(T^a_{\rm osc})^8 & (T^\phi_S\gtrsim T^a_{\rm osc}\gtrsim T^\phi_D).\end{cases} \tag{5.79}$$

We now can estimate these relic densities for our standard benchmark data in Table (4.6) and utilize our estimates for the various temperatures from the previous section (again using $m_\phi = 10^3$ TeV as our modulus benchmark). Making the estimate first for the case $T^a_{\rm osc} < T^\phi_D$, we have

$$\Omega_a h^2 \simeq 0.119\times\left(\frac{m_a(T=0)}{378\ \mu{\rm eV}}\right)\left(\frac{a_0^2}{2.54\times 10^{22}\ {\rm GeV}^2}\right)\left(\frac{m_a(T^a_{\rm osc})}{0.00511\ \mu{\rm eV}}\right)\times\left(\frac{75}{g_*(T^a_{\rm osc})}\right)\left(\frac{1.20\ {\rm GeV}}{T^a_{\rm osc}}\right)^3 \tag{5.80}$$

As expected, since this case is specific to axion oscillations which commence *after* the modulus has decayed, it is not surprising that the relic density is entirely independent of the modulus details. Thus, in this case we also restore the thermally-expected result. Our benchmark data also is then expected to saturate the observed DM relic density, $\Omega h^2 \sim 0.12$. Estimating now the second case, $T^\phi_S \gtrsim T^a_{\rm osc} \gtrsim T^\phi_D$, we have the estimate

$$\Omega_a h^2 \simeq 0.0010\times\left(\frac{m_a(T=0)}{378\ \mu{\rm eV}}\right)\left(\frac{a_0^2}{2.54\times 10^{22}\ {\rm GeV}^2}\right)\left(\frac{m_a(T^a_{\rm osc})}{0.00511\ \mu{\rm eV}}\right)\times\left(\frac{75}{g_*(T^a_{\rm osc})}\right)^2\left(\frac{g_*(T^\phi_D)}{20}\right)\left(\frac{T^\phi_D}{0.13\ {\rm GeV}}\right)^5\left(\frac{0.636\ {\rm GeV}}{T^a_{\rm osc}}\right)^8 \tag{5.81}$$

which is a *full two orders of magnitude below the thermally-expected value.* This is perhaps not surprising - if the axion begins oscillations before the modulus has entirely decayed, it will effectively feel a partial amount of the entropy dilution. However, since oscillations do not begin before T_S^ϕ the axions do not feel the full entropy dilution. This is evident if we consider the scaling of this quantity with respect to m_ϕ. Increasing m_ϕ will increase both T_D^ϕ and $T_{\rm osc}^a$, which also has the effect of decreasing the axion mass. Closer inspection of the dependence on m_ϕ for each of these terms then reveals that T_D^ϕ has the dominant effect in this expression - the overall expression scales as roughly m_ϕ^3. Thus, increasing m_ϕ will *increase* the axion relic density - at least until $T_D^\phi \sim T_{\rm osc}^a$, signaling the change in cosmology between the non-thermal and thermal scenarios.

Chapter 6

Results and discussion

In this chapter, we begin by discussing our procedure and initial conditions for numerically solving the Boltzmann equations. We then present results from these numerical solutions for both the ϕMSSM and the ϕPQMSSM. We will also provide discussion throughout on the cosmological and phenomenological impacts that these results suggest.

6.1 Procedure and initial conditions

For all results in the ϕMSSM and ϕPQMSSM, we follow the approach from [372, 300] and set our initial conditions at inflationary reheating T_R. We also assume the universe is radiation-dominated at T_R and therefore take $\phi_0/m_P = \sqrt{2/3}$ since, as we have shown in Sec. (5.2.3), taking $\phi_0/m_P > \sqrt{2/3}$ implies a modulus-dominated universe at T_R (i.e. no initial radiation-dominated epoch). Taking T_R as a free parameter, the initial Hubble rate, entropy, and radiation density are specified from the standard relations we presented in the previous chapter.

To set the initial conditions for the coherently oscillating (CO) components, we compare the field's mass to the Hubble rate. If the field has begun to oscillate during inflationary reheating (i.e. $m > 3H$) we set the initial condition defined by Eq. (5.27), while if $m < 3H$ we set the initial condition to the constant energy density $\rho_0 = \frac{1}{2}m^2\phi_0^2$ (with ϕ_0 the relevant initial oscillation amplitude). As the

coherently oscillating fields are non-relativistic, we always have $\rho = nm$ so that the initial number densities are likewise defined. Additionally, we update the initial conditions of the axion at every integration step until its oscillations begin to account for the temperature-dependence of its mass.

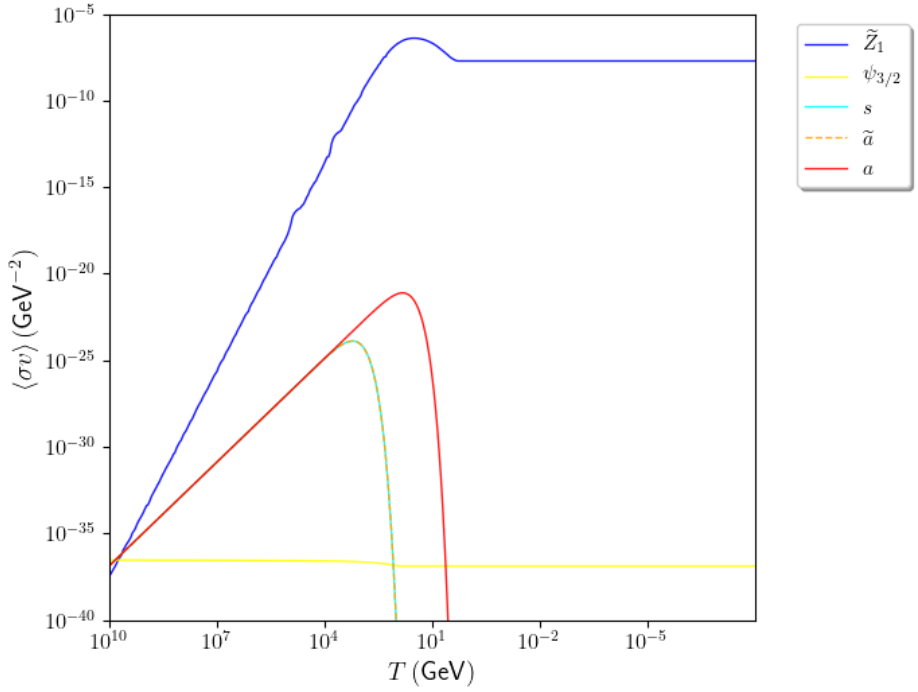


Figure 6.1: Thermally-averaged cross sections $\langle\sigma v\rangle$ versus temperature for each of neutralinos, saxions, axinos, axions, and gravitinos.

Thermally-produced (TP) components follow a simple set of initial conditions. If the annihilation rate is greater than the Hubble rate $\overline{n}\langle\sigma v\rangle > 3H$, we assume that interactions are sufficiently strong to begin the number density at its equilibrium value. We display the thermally-averaged cross sections versus temperature for all fields of interest using our natural SUSY benchmark point from Table (4.3) and PQ benchmark point from Table (4.6). However, if the annihilation rate is smaller than the Hubble rate, we begin the field at the rate expected from the

annihilation rate: $3Hn \sim \langle\sigma v\rangle\overline{n}^2$. The initial energy density then is set to the value expected for a relativistic distribution [286]. For the DFSZ-type axions, saxions, and axinos we adopt the formula for the thermally-averaged cross section given in [300] which follows the expression

$$\langle\sigma_{i+j\to a,s,\widetilde{a}+...}v\rangle n_i n_j \simeq \frac{T^6}{16\pi^4}\int_{M/T}^{\infty} dx\, K_1(x)\, x^4\, \sigma(x^2T^2) \tag{6.1}$$

where M is the threshold mass for the process - i.e. the axino and saxion masses for $\widetilde{a}$ and s (respectively) and the higgsino mass μ for the axion a. The thermally-averaged cross section for the gravitino is adopted from the results of Pradler and Steffen [394]. The neutralino thermally-averaged cross section is computed using a modified version of the IsaRED [330] subroutine, which replaces Bessel functions programmed using Taylor expansions with the Boost library algorithms, which are much better behaved in the low M/T regime. We also utilize the same numerical fit used in [300] to determine the equation of state for thermal components, which tend to begin with an equation of state of radiation and redshifts to a matter distribution at a lower scale based on the relativistic dilation factor ρ/mn.

After the initial conditions are set, we then numerically integrate the Boltzmann equations Eqs. (5.1), (5.2), (5.3) until all decaying fields have entirely decayed *and* $T < 10$ eV. To perform the numerical integration, we use a codebase written in C++ which utilizes Boost's Odeint library. We use the Rosenbrock fourth-order stepper, which is designed to solve numerically stiff equations. At every integration step, decay widths are recalculated for any particles that can decay to axions

to account for the changing mass. Once the Boltzmann equations are evolved to the final step, we can compute the relic density $\Omega_i h^2$ and effective number of neutrinos $\Delta N_{\rm eff}$ for each component tracked using Eq. (5.50) and Eq. (5.70) respectively, assuming that entropy is conserved after the final integration step.

We also note that our Boltzmann results calculate a lower value of the thermally-expected neutralino relic density $\Omega_{\widetilde{Z}_1}^{\rm Boltzmann} h^2 \simeq 0.0044$ than the estimate provided by the IsaRED subroutine $\Omega_{\widetilde{Z}_1}^{\rm IsaRED} h^2 \simeq 0.011$, which is the estimate listed in Table (4.3). This is because of the procedure that IsaRED uses only a semi-analytic formula similar to those we used in Ch. (5) in addition to using only the temperature-independent value of the annihilation cross section at $T_{\rm f.o.}$. Our Boltzmann code uses the full temperature-dependent cross section, which as we see from Fig. (6.1) has a fairly strong temperature dependence affecting the value of $\langle \sigma v \rangle$ by about two orders of magnitude close to $T_{\rm f.o.}$. This results in the neutralino distribution tracking the equilibrium density more closely for a slightly longer time, which produces a lower abundance yield after freeze-out - and hence a lower relic density. We therefore expect our Boltzmann treatment to provide a more accurate estimate of the neutralino relic density than the IsaRED estimate.

In both the ϕMSSM and the ϕPQMSSM, one of our primary goals is to understand the parameter space of both models using our natural SUSY benchmark in Table (4.3) as a reference. As we also mentioned before, if WIMPs compose the entirety of our dark matter then our natural SUSY benchmark point runs into minor tension with recent direct detection (DD) and indirect detection (ID) experiments [352, 406], as well as Fermi-LAT observations of gamma-ray fluxes

from dwarf spheroidal galaxies [351]. Based on the results of [353], we find that if WIMPs compose less than roughly 10% of the observed DM relic density, i.e. $\Omega_{\widetilde{Z}_1} h^2 \lesssim 0.012$, each of these experimental constraints can be met. We will thus adopt this as our DD/ID bound for the neutralino relic density throughout, and we will explicitly state when we impose it onto any selection criteria in our results.

6.2 Results for the ϕMSSM

We begin with discussion of the evolution of the ϕMSSM for a few of the scenarios we have previously defined. Next, we will discuss entropy production in the ϕMSSM and compare to our previous estimates. We then study neutralino (or WIMP) dark matter production in a few scenarios. Throughout this section, we track the modulus, gravitino, and the lightest neutralino - in addition to radiation - in our Boltzmann equations.

6.2.1 Cosmological evolution in case B1-GK1

We begin our discussion of the ϕMSSM by focusing on case **B1-GK1**. In Fig. (6.2), we display the abundance yield $Y_i \equiv n_i/s$ for the four constituents - the modulus, neutralino, gravitino, and radiation. Here, we take all $\lambda_i = 1$ and fix $m_\phi = 5 \times 10^3$ TeV and $m_{3/2} = 30$ TeV. We also take the inflationary reheating temperature to be $T_R = 10^{10}$ GeV. The modulus (black curve) has a constant abundance yield Y_ϕ until it begins injecting entropy at $R/R_0 \sim 10^8$, which continues to dilute the modulus abundance until it decays at $R/R_0 \sim 10^{14}$. The neutralinos (blue curve), on the other hand, begin well below their equilibrium value due to a small cross

section at high temperatures (see Fig. (6.1)). As R/R_0 increases, the radiation

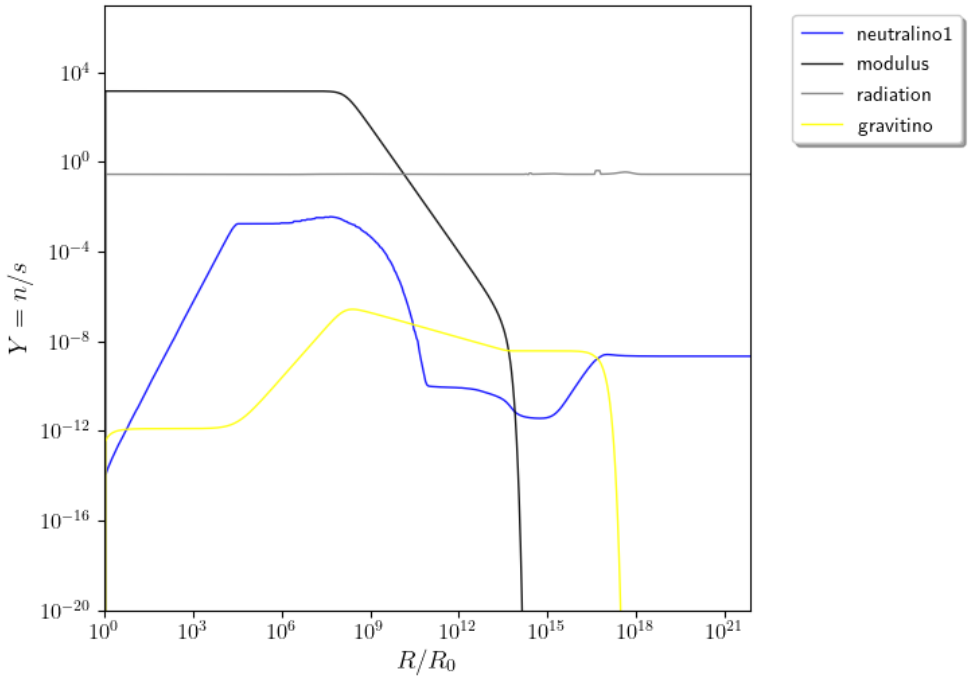


Figure 6.2: Cosmological evolution of abundance yield $Y_i = n_i/s$ vs scale factor R/R_0 in case **B1-GK1**. Here, we fix $m_\phi = 5 \times 10^3$ TeV and $m_{3/2} = 30$ TeV, and take all allowed $\lambda_i = 1$.

temperature cools and the neutralino cross section increases enough to achieve equilibrium around $R/R_0 \sim 10^4$, at which point its abundance yield is conserved until it 1. begins to become sourced from modulus decay, 2. is diluted from the entropy injection of the modulus, and 3. undergoes the freeze-out process (i.e. the equilibrium density drops, pushing the true density lower until Hubble dilution prevents further annihilations) - although clearly this plays no role in the final abundance due to the presence of the modulus and gravitino. We also see that the gravitino (yellow curve) is likewise sourced from the modulus beginning around the time entropy injection begins. Finally, we see that once the modulus has decayed, the gravitinos have an abundance yield of $Y_{3/2} \sim 10^{-9}$ until it decays

around $R/R_0 \sim 10^{17}$, at which point the neutralino abundance yield increases by a large amount ($\Delta Y_{\widetilde{Z}_1} \sim 10^3$). This of course translates to a large increase in the neutralino relic density, as we expect for case **B1**.

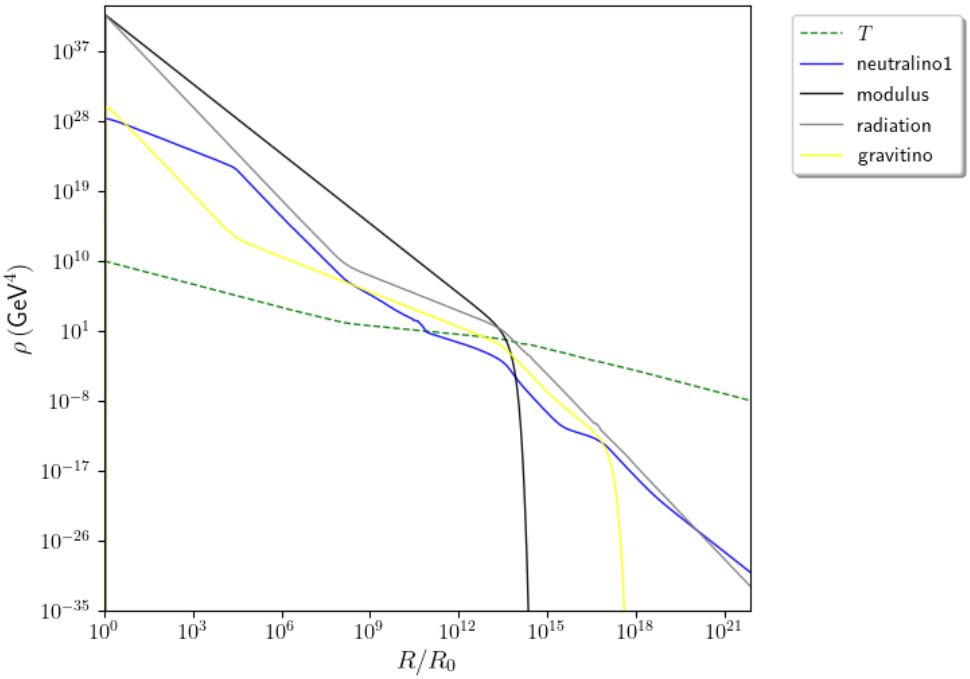


Figure 6.3: Cosmological evolution of energy densities ρ_i vs scale factor R/R_0 in case **B1-GK1**. Here, we fix $m_\phi = 5 \times 10^3$ TeV and $m_{3/2} = 30$ TeV, and take all allowed $\lambda_i = 1$.

We display the corresponding energy density evolution in Fig. (6.3). Here, the features we described for the abundance yield plot are also rather evident. The neutralinos dilute as radiation once they achieve equilibrium, and close to entropy injection (seen by the slowing of the temperature in the dashed green curve) they become sourced by the modulus and hence dilute more slowly. Similarly, close to gravitino decay the neutralinos dilute at a noticeably slower rate. Not long after gravitino decay, the neutralinos become redshifted sufficiently to behave as matter and overtake radiation, leading to a matter-dominated universe at

roughly $T \sim 100$ eV - well above the $T \sim \mathcal{O}(1)$ eV scale in a standard cosmology (e.g. ΛCDM) [407, 286]. We also see that before the gravitinos decay, they have nearly comparable energy density to radiation - trailing by only about an order of magnitude. Finally, we note that this case produces a neutralino relic density of $\Omega_{\widetilde{Z}_1} h^2 = 114.806$ which is in good agreement with our qualitative estimates we presented in Fig. (5.10). (We also reiterate that the order of magnitude change in m_ϕ is inconsequential, as the gravitino abundance is large enough that the neutralinos are in the annihilation scenario).

6.2.2 Cosmological evolution in case B2-GK1

Proceeding now to case **B2-GK1**, we display in Fig. (6.4) the abundance yield $Y_i \equiv n_i/s$ for the modulus, neutralinos, gravitinos, and radiation. We again take all $\lambda_i = 1$ and fix $m_\phi = 5 \times 10^3$ TeV and $m_{3/2} = 30$ TeV, as well as $T_R = 10^{10}$ GeV for the sake of comparison. Many of the details from case **B1-GK1** again appear here - the modulus begins with a constant abundance yield, starts to inject entropy around $R/R_0 \sim 10^8$, and decays around $R/R_0 \sim 10^{14}$. Similarly, the neutralinos again begin well below equilibrium while interactions between the neutralinos and radiation have pushed them to equilibrium around $R/R_0 \sim 10^4$. Shortly after, the neutralinos are both enhanced and diluted from the modulus in addition to the freeze-out process. However due to the now-suppressed decays to gravitinos, the gravitino abundance yield after modulus decay is now around $Y_{3/2} \sim 10^{-13}$ - four orders of magnitude less than case **B1-GK1**. The neutralinos thus do not receive any significant enhancement once gravitinos decay in this case

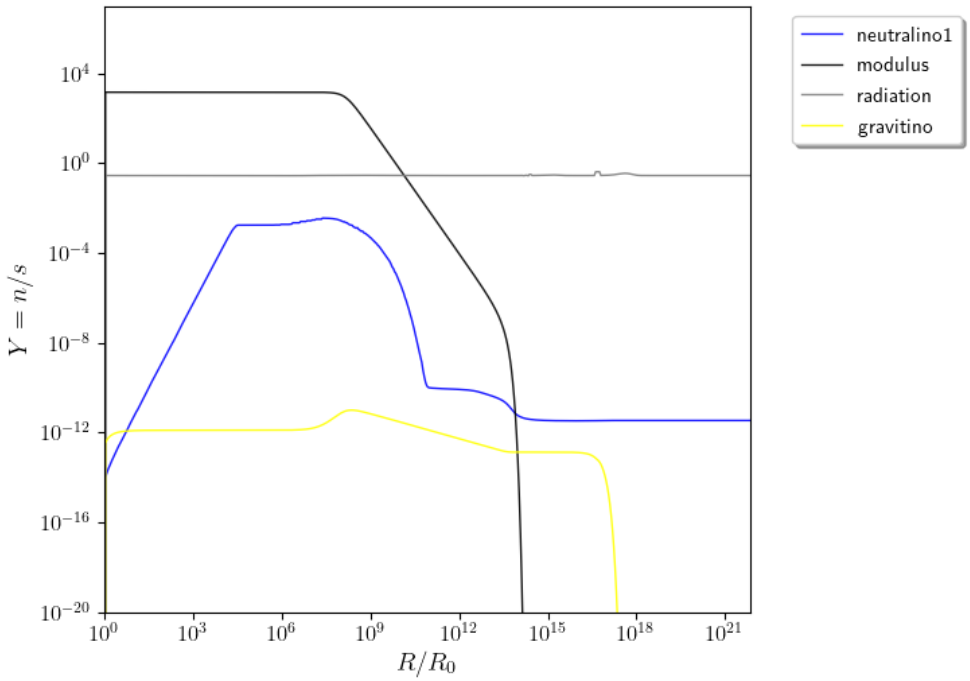


Figure 6.4: Cosmological evolution of abundance yield $Y_i = n_i/s$ vs scale factor R/R_0 in case **B2-GK1**. Here, we fix $m_\phi = 5 \times 10^3$ TeV and $m_{3/2} = 30$ TeV, and take all allowed $\lambda_i = 1$.

- their abundance is now set primarily by the modulus.

We also show the corresponding energy density evolution in Fig. (6.5). Unlike the previous case, the gravitino now remains the lowest energy density for almost the entirety of its existence. As the neutralinos are no longer extensively sourced from gravitino decay, we also see that after they have redshifted sufficiently to behave as a matter distribution (around $R/R_0 \sim 10^{18}$) they will not overcome the radiation energy density until $T < \mathcal{O}(10)$ eV, which is in good accordance with the standard cosmology. Finally, we note that this case produces a neutralino relic density of $\Omega_{\widetilde{Z}_1} h^2 = 0.184067$, about 3 orders of magnitude less than the previous case. This is also in good agreement with our qualitative arguments which can be seen from Fig. (5.6).

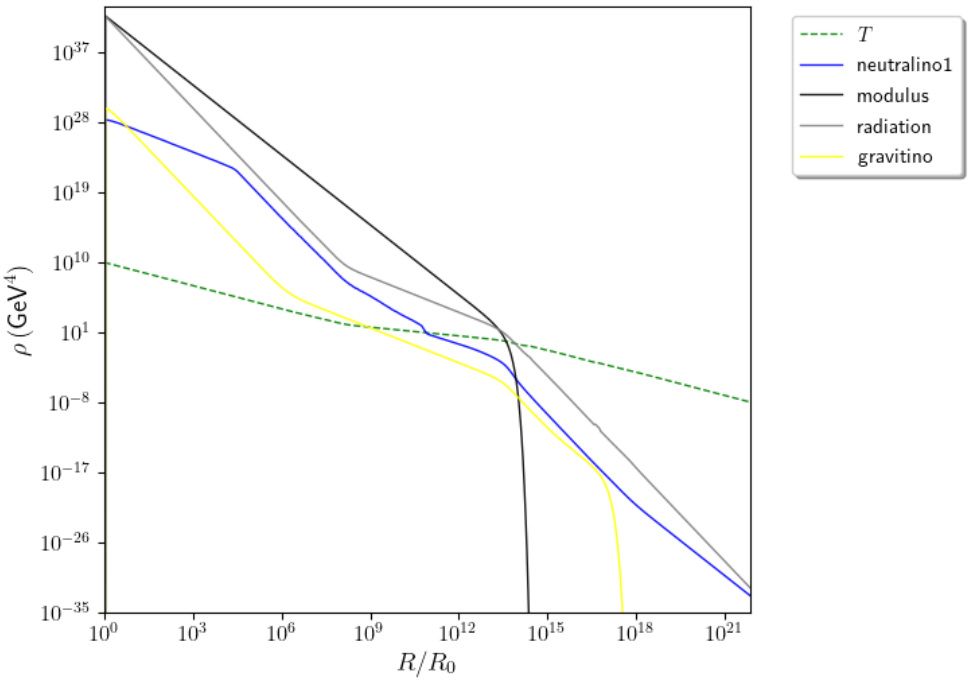


Figure 6.5: Cosmological evolution of energy densities ρ_i vs scale factor R/R_0 in case **B2-GK1**. Here, we fix $m_\phi = 5 \times 10^3$ TeV and $m_{3/2} = 30$ TeV, and take all allowed $\lambda_i = 1$.

6.2.3 Cosmological evolution with kinematically forbidden gravitino

Finally, for the sake of comparison we now consider again case **B2-GK1** but now with a kinematically forbidden gravitino. We once more take all $\lambda_i = 1$ and $T_R = 10^{10}$ GeV, but now fix $m_\phi = m_{3/2} = 5 \times 10^3$ TeV. In Fig. (6.6), we plot the four abundance yields in this scenario. As expected, many features are virtually identical to Fig. (6.4) except that the gravitino abundance yield now disappears around the same time that the modulus decays. The modulus then is the sole determination of the late-time neutralino abundance. Fig. (6.7) then displays the corresponding evolution of energy densities. We see that here, the gravitino plays effectively no role - its energy density is too low to significantly affect the Hubble

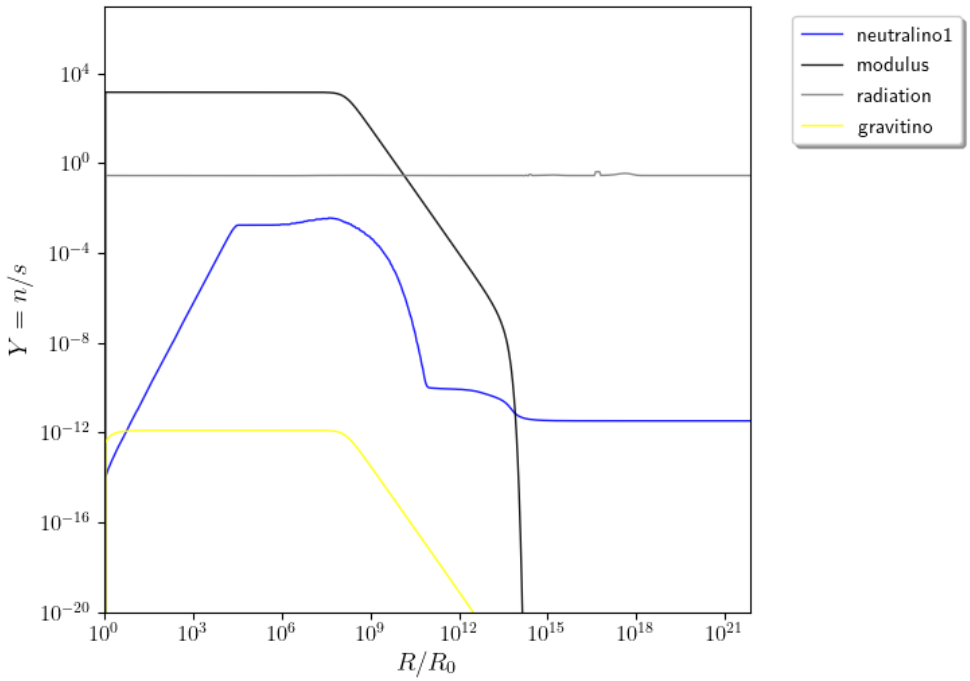


Figure 6.6: Cosmological evolution of abundance yield $Y_i = n_i/s$ vs scale factor R/R_0 in case **B2-GK1**, but the gravitino is kinematically forbidden. Here, we fix $m_\phi = m_{3/2} = 5 \times 10^3$ TeV and take all allowed $\lambda_i = 1$.

constant during modulus domination, and decays slightly before modulus decay providing effectively a decoupling solution. Of course, to realize this scenario in tandem with natural SUSY, one would require sequestering in the UV theory. This case produces a neutralino relic density of $\Omega_{\widetilde{Z}_1} h^2 = 0.176941$, slightly below the previous **B2** case.

6.2.4 Entropy production in the ϕMSSM

In Fig. (6.8), we display the entropy dilution factor $r \equiv S_f/S_0$ in the ϕMSSM for case **B2-GK1**. We also display three values of (unified) couplings, $\lambda_i \in \{0.1, 1, 10\}$. We see remarkable agreement in both qualitative and quantitative

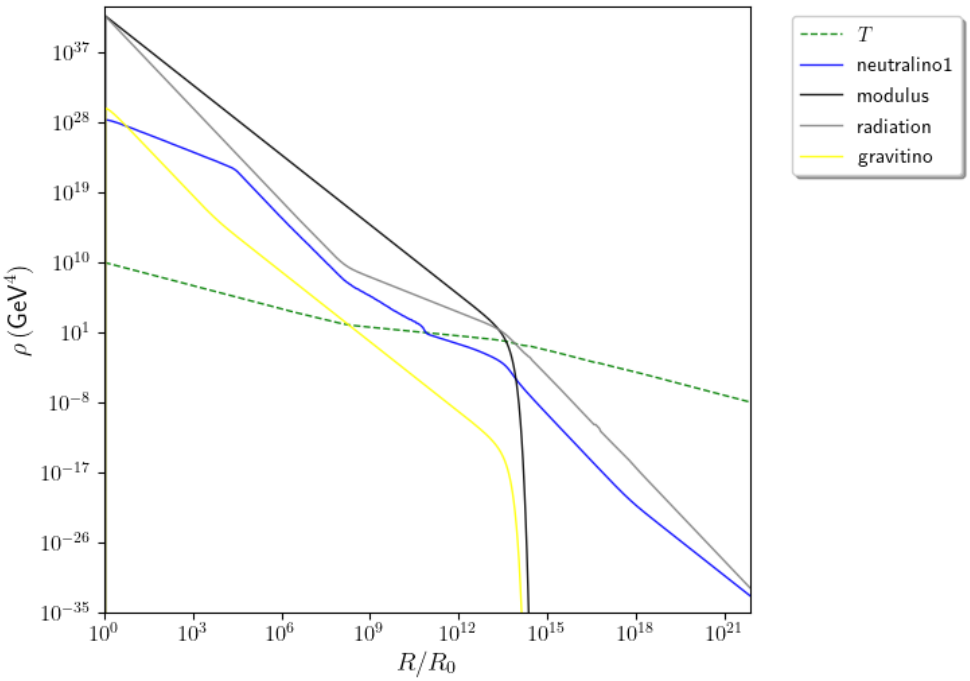


Figure 6.7: Cosmological evolution of energy densities ρ_i vs scale factor R/R_0 in case **B2-GK1**, but the gravitino is kinematically forbidden. Here, we fix $m_\phi = m_{3/2} = 5 \times 10^3$ TeV and take all allowed $\lambda_i = 1$.

behavior between the entropy dilution calculated from numerical solutions of the Boltzmann equations in Fig. (6.8) when compared to Fig. (5.3) which was created using primarily qualitative methods. Here, we emphasize that the entropy density of the modulus, $s \equiv (\rho_\phi + \mathcal{P}_\phi)/T \sim \rho_\phi/T$ [407], decreases as R^{-3} so that the total entropy $S = sR^3$ is effectively independent of the scale factor. However, the amount of entropy stored in the modulus when it is released into the thermal bath is dependent on the decay temperature of the modulus, $S_f \propto (T_D^\phi)^{-1}$. Additionally, the initial entropy stored in the modulus will be more dilute if a prolonged period of radiation-domination has occurred before it begins to oscillate, leading to a softer dependence on T_D^ϕ. Since we have $T_D^\phi \propto m_\phi^{3/2}$ in addition to $T_e^\phi \propto m_\phi^{1/2}$ if $T_{\rm osc}^\phi \leq T_R$ while T_e^ϕ is independent of m_ϕ for $T_{\rm osc}^\phi > T_R$, it is then not

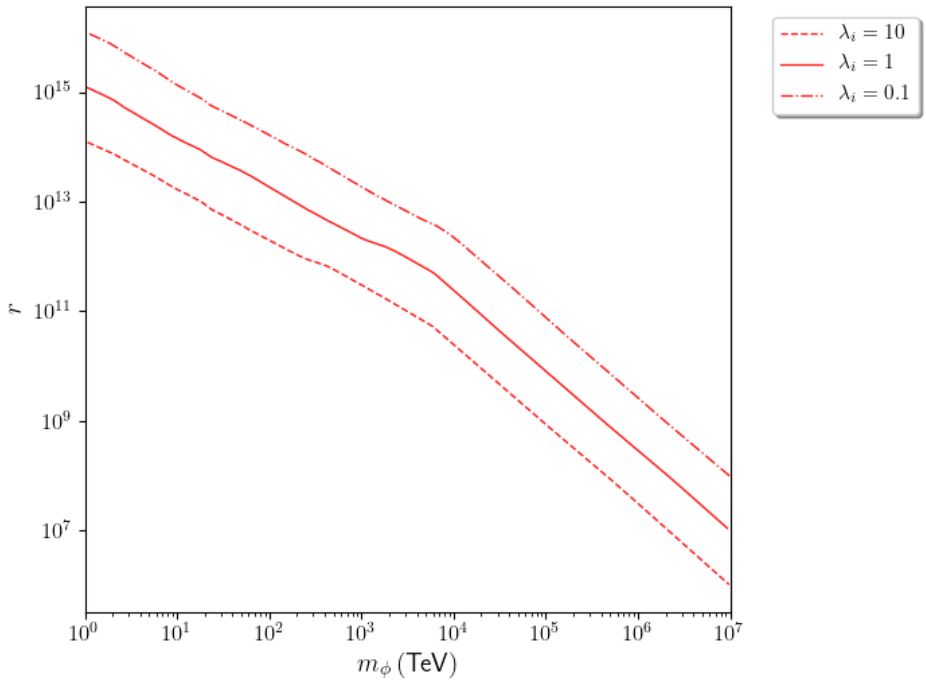


Figure 6.8: Numerical Boltzmann results for entropy dilution factor r vs modulus mass m_ϕ for in case **B2-GK1** with all $\lambda_i \in \{0.1, 1, 10\}$. Here, we take $T_R = T_R^{BHLR} = 10^{12}$ GeV.

surprising that our entropy dilution factor decreases as m_ϕ^{-1} for $m_\phi \lesssim 10^4$ TeV and $m_\phi^{-3/2}$ for $m_\phi \gtrsim 10^4$ TeV in Fig. (6.8). If we had chosen a lower inflationary reheating temperature T_R, the entropy dilution would be expected to scale as $m_\phi^{-3/2}$ beginning at a lower value of m_ϕ. It is also evident that if $m_\phi \gg 10^7$ TeV, the entropy dilution may be sufficiently weak so that thermal relics - thermal gravitinos in particular - are still relevant.

6.2.5 DM production in case B1

In this section, we study WIMP dark matter production in case **B1**. In Fig. (6.9), we display the produced WIMP relic density (orange curve) as a function of m_ϕ and fix $m_{3/2} = 30$ TeV. We see that for $m_\phi \lesssim 60$ TeV, the gravitino is kinematically

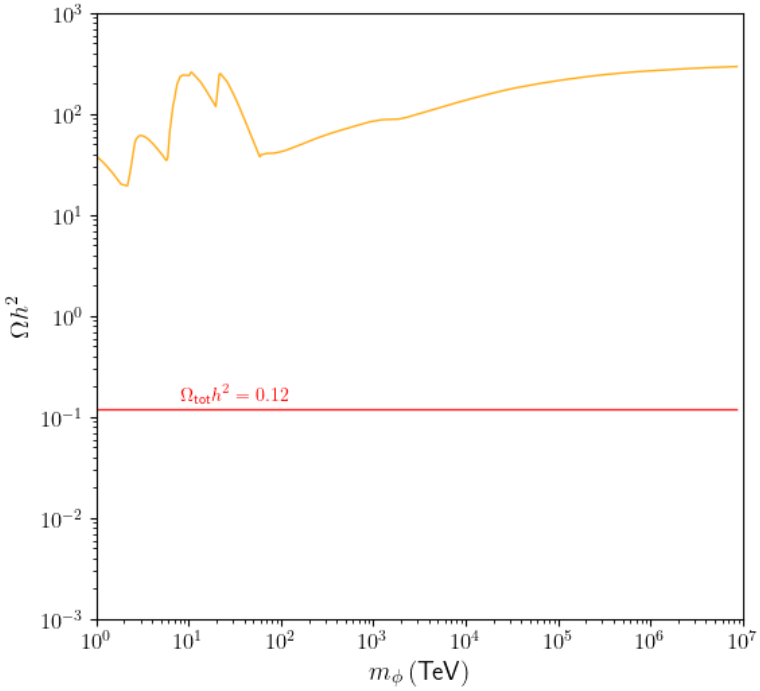


Figure 6.9: Numerical Boltzmann results for WIMP relic density in case **B1-GK1** as a function of m_ϕ. Here we take all $\lambda_i = 1$ and fix $m_{3/2} = 30$ TeV.

forbidden - although the modulus still grossly overproduces dark matter in the branching scenario. Once the gravitino becomes kinematically accessible, the produced dark matter abundance is not only drastically overproduced but also begins to increase slightly as m_ϕ increases. This is due to our inclusion of a relativistic dilation term in the Boltzmann equations: once the modulus is significantly larger than the gravitino, we would expect the modulus decay products to be highly boosted - leading to an enhancement of their lifetime. This then translates to an increase in the produced WIMP abundance as the gravitino decay occurs at a lower temperature. Clearly, it is not feasible to reproduce the observed dark matter density in case **B1** using our natural SUSY benchmark point without raising the gravitino mass.

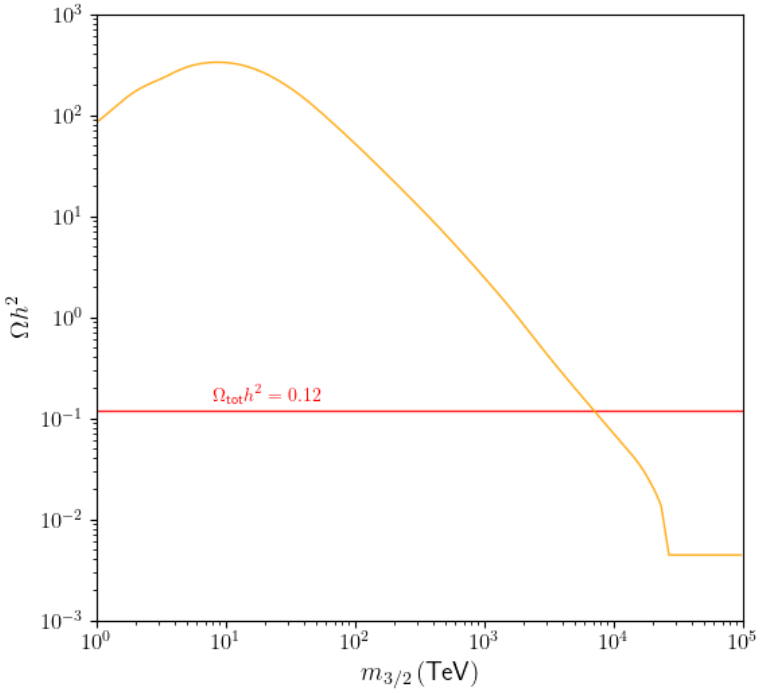


Figure 6.10: Numerical Boltzmann results for WIMP relic density in case **B1-GK1** as a function of $m_{3/2}$. Here we take all $\lambda_i = 1$ and fix $m_\phi = 5 \times 10^4$ TeV.

In Fig. (6.10), we show the produced WIMP relic density (orange curve) as a function of $m_{3/2}$, where we now fix $m_\phi = 5 \times 10^4$ TeV so that there is no enhancement of the thermally-expected relic density due to the modulus. Here we find that $m_{3/2} \gtrsim 7 \times 10^3$ TeV in order to match dark matter production with observation while a value of $m_{3/2} \gtrsim 2 \times 10^4$ TeV is required to meet our DD/ID constraints - both in rather good agreement with the values we expected from our qualitative estimates in Fig. (5.10). In unsequestered scenarios, such a large gravitino mass is in serious tension with our natural SUSY benchmark spectrum!

We display in Fig. (6.11) expected neutralino dark matter production in the ($m_{3/2}$, m_ϕ) plane where $m_{3/2}$ and m_ϕ are now assigned randomly. Red color coding

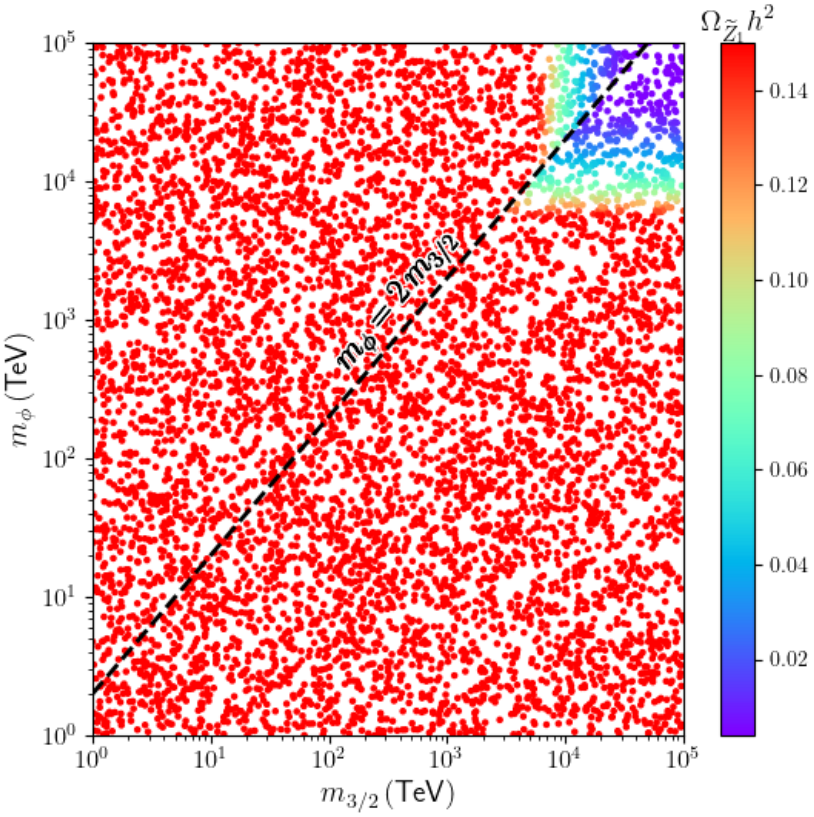


Figure 6.11: Numerical Boltzmann results for WIMP relic density in case **B1-GK1** in the ($m_{3/2}$, m_ϕ) plane. Here we take all $\lambda_i = 1$. The diagonal dashed line indicates $m_\phi = 2m_{3/2}$.

indicates a neutralino relic density in excess of the observed value, $\Omega_{\widetilde{Z}_1} h^2 \gtrsim 0.12$, while purple and dark blue points are expected to satisfy our DD/ID bounds. It is immediately clear that neutralino dark matter production heavily constrains case **B1**, requiring *both* the modulus and gravitino to have very large masses. Below the diagonal dashed line - which indicates where $m_\phi = 2m_{3/2}$ - the gravitino is kinematically blocked. However, here the modulus is still required to have a mass $m_\phi \gtrsim 6 \times 10^3$ TeV to avoid overproduction of the WIMP abundance. Above the diagonal dashed line, we see that the gravitino is now pushed to a slightly larger value - $m_{3/2} \gtrsim 7 \times 10^3$ TeV - to avoid dark matter overproduction. We

also see comparing this plot to the previous figure that this bound is relatively independent of m_ϕ. Thus, in case **B1-GK1** our main result is that unless both the gravitino and modulus are extremely massive (m_ϕ, $m_{3/2} \gtrsim 10^{3-4}$ TeV), either the modulus overproduces dark matter or the gravitino does. As we have previously discussed, we do not expect significant deviation from these results for case **A1** or for the **GK2** cases. Since we are always expected to be in the annihilation scenario, each of these cases results in only a relatively small quantitative shift of the modulus and gravitino masses which we do not expect to change more than a factor of $2 - 3$.

6.2.6 DM production in case B2

We now move to study dark matter production in case **B2**. In Fig. (6.12), we plot the WIMP relic density as a function of m_ϕ for $\lambda_i \in \{0.1, 1, 10\}$. Here we take the lower bound LB2 from Fig. (4.3), which includes all direct R-parity odd decays and assumes the Higgs sector decays to SUSY particles with a 1% branching fraction. Comparing to Fig. (5.6) which estimates neutralino dark matter production using qualitative arguments for the same scenario, we see good agreement both qualitatively and quantitatively. For $\lambda_i = 0.1$, the transition to the branching scenario occurs at a much larger m_ϕ than for larger values of λ_i, which results in diminution of the produced WIMP abundance - although clearly neutralinos are still overproduced in the branching scenario. The annihilation scenario then pushes $m_\phi \gtrsim (2 \times 10^3 - 3 \times 10^4)$ TeV - depending on the value of the couplings - to avoid dark matter overproduction, roughly a factor of 2 larger

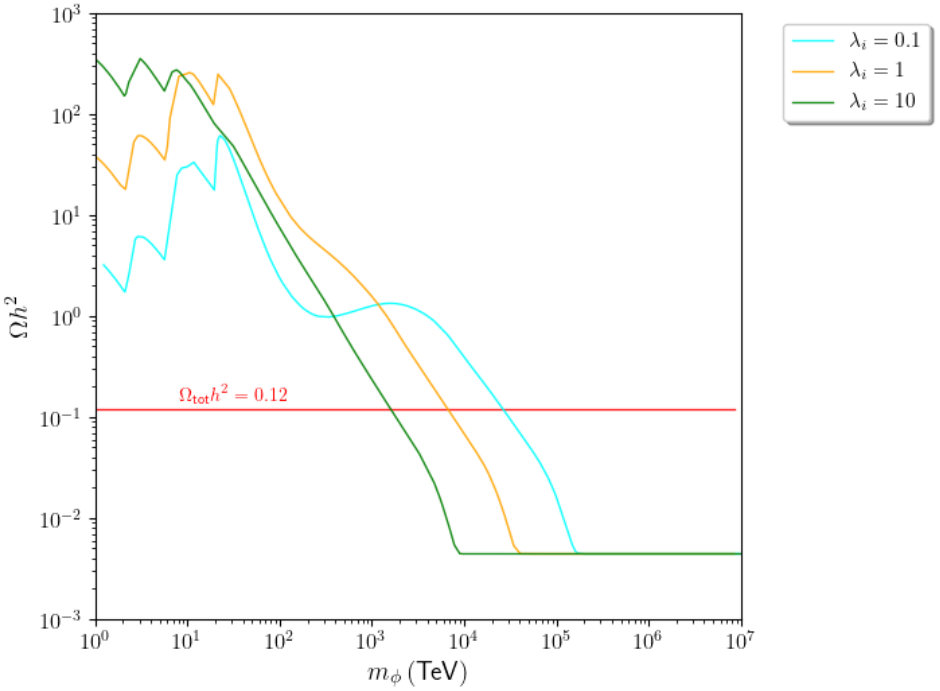


Figure 6.12: Numerical Boltzmann results for WIMP relic density in case **B2-GK1** for each $\lambda_i \in \{0.1, 1, 10\}$. Here we assume 1% of Higgses decay to SUSY in addition to all R-parity odd decays.

than our qualitative arguments in Sec. (5.3.4) have suggested.

We also display results for a flat modulus branching ratio to SUSY particles, $\mathcal{B}(\phi \to \text{SUSY}) = 1\%$, in Fig. (6.13). Once again we see very good qualitative and quantitative agreement with Fig. (5.8), which displays WIMP relic density predictions for the same scenario using only qualitative arguments. Although the transition to the branching scenario looks rather different in comparison to Fig. (6.12), we see that any region that does not overproduce WIMPs is in the annihilation scenario. Similarly, we arrive at the same constraints ($m_\phi \gtrsim 2 \times 10^3 - 3 \times 10^4$ TeV) as in the previous figure - which is in agreement with our assertion that in the annihilation scenario the produced WIMP abundance is largely insensitive to the branching ratio to SUSY particles. As such, we expect

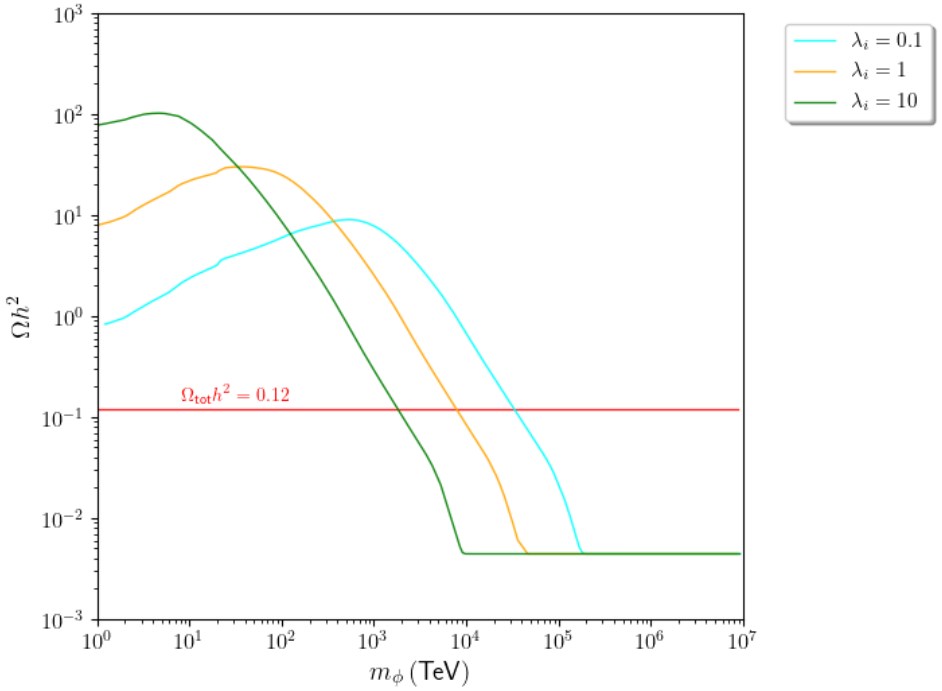


Figure 6.13: Numerical Boltzmann results for WIMP relic density in case **B2-GK1** for each $\lambda_i \in \{0.1, 1, 10\}$. Here we assume a flat branching fraction to SUSY $\mathcal{B}_{\phi\to\text{SUSY}} = 1\%$ (independent of m_ϕ).

very similar results for case **A2** - the additional unsuppressed production of neutralinos should simply annihilate down to the critical value. For the **GK2** cases, due to an order of magnitude decrease (approximately) in $\Gamma_\phi^{\text{total}}$ (see e.g. Fig. 4.9) we expect the WIMP relic density predictions to fall in between the $\lambda_i = 1$ and $\lambda_i = 0.1$ cases, with a slight tilt towards the $\lambda_i = 1$ case.

Finally, one may inquire as to the relevance of a light gravitino $m_{3/2} \sim 30$ TeV to the neutralino relic density in this scenario. We display in Fig. (6.14) the produced WIMP relic density for the lower bound LB2 (all R-parity odd decays with a 1% Higgs to SUSY branching ratio) for a kinematically-forbidden gravitino (orange curve) and for $m_{3/2} = 30$ TeV (green curve). It is immediately evident that the presence of suppressed decays to gravitinos affects results at or below the

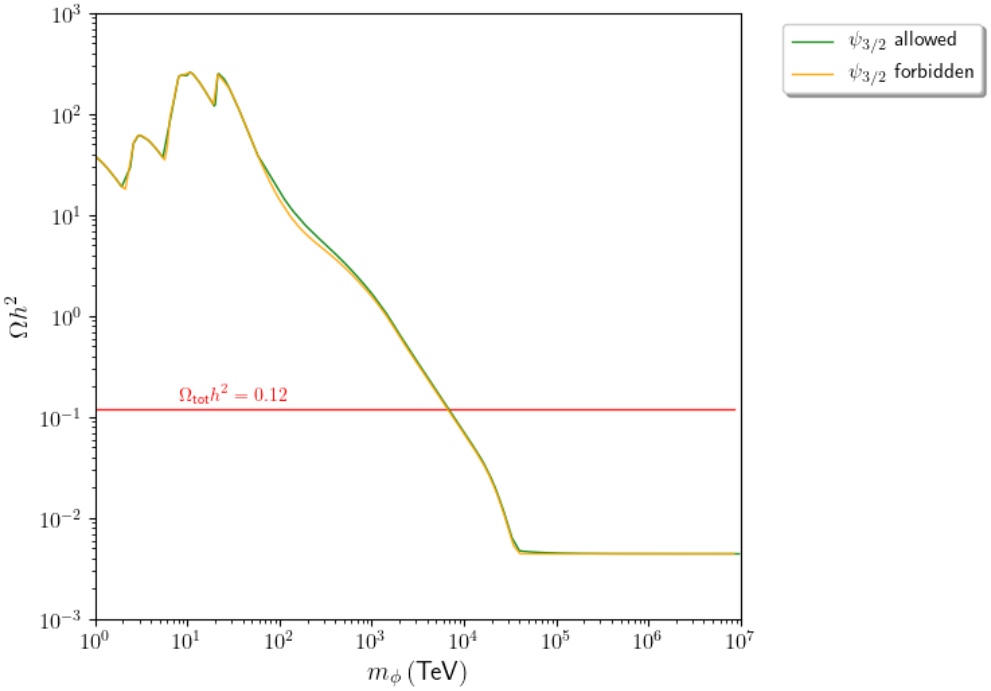


Figure 6.14: Numerical Boltzmann results for WIMP relic density in case **B2-GK1** for kinematically forbidden gravitinos (orange) and gravitino mass fixed at $m_{3/2} = 30$ TeV (green). Here we take $\lambda_i = 1$ and assume 1% of Higgses decay to SUSY in addition to all R-parity odd decays.

percent-level in case **B2** as when compared to the same case with the gravitino effectively decoupled from the cosmology. Thus, case **B2** - and case **A2** by the same arguments as before - seem much more compatible with a natural SUSY spectrum than case **B1** and **A1** if sequestering is absent - requiring only a large modulus mass while a light gravitino can be accommodated.

6.2.7 Dependence on modulus initial amplitude ϕ_0

In this section, we investigate the dependence of our results in the ϕMSSM on the value of the modulus misalignment amplitude ϕ_0. We show in Fig. (6.15) the produced neutralino relic density as a function of ϕ_0/m_P in the bounds

$\phi_0/m_P \in [10^{-8}, \sqrt{2/3}]$ so that the transition at inflationary reheating T_R remains radiation-dominated (if only for an extremely short time). We see that there

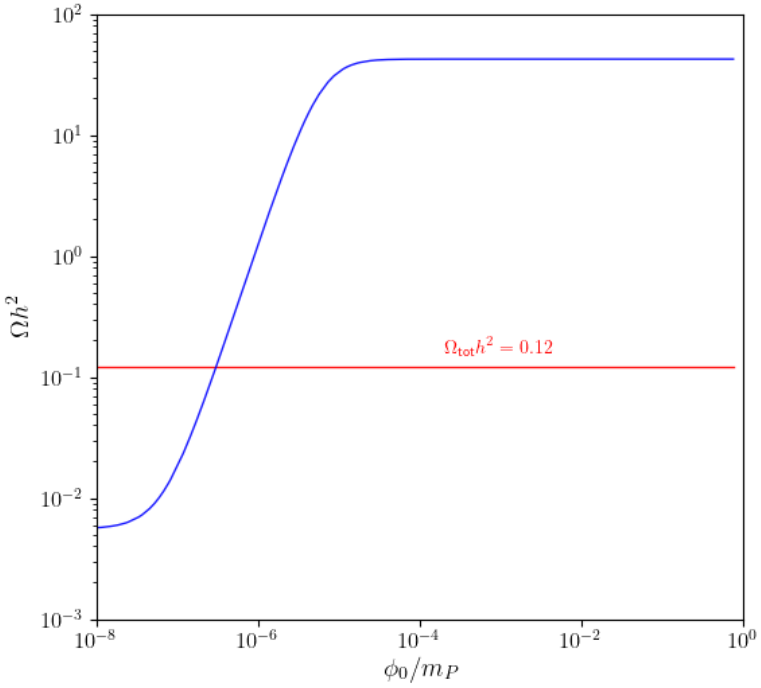


Figure 6.15: Neutralino relic density as a function of ϕ_0/m_P in case **B1-GK1** with $m_\phi = 100$ TeV and $T_R = 10^8$ GeV. Here, all $\lambda_i = 1$ and decays to gravitinos are unsuppressed.

is almost no dependence on the modulus amplitude until $\phi_0/m_P \lesssim 10^{-5}$, and a value of $\phi_0/m_P \lesssim 3 \times 10^{-7}$ (without any other adjustments) would be required so that neutralinos are not overproduced. However, whether or not such a value can actually be realized in string constructions remains an open question. During inflation, the light moduli (i.e. $m_\phi < H$) are displaced from their true minima and held at their misaligned vacuum values by Hubble friction until $H \sim m_\phi$, causing the onset of moduli oscillations. Since the natural scale of the moduli is the Planck scale, one would naively expect a shift from the true minima of $\phi_0 \sim \mathcal{O}(m_P)$

[210, 209]. In [408], an explicit construction in Kähler moduli inflation - which we will discuss in detail in Ch. (7) - studied the vacuum misalignment of the bulk modulus. It was found from rather general arguments in this framework that the modulus displacement is $\phi_0/m_P \sim (0.1 - 1)$, in agreement with EFT expectations. Additionally, in the string landscape one might naively expect variation of this amplitude as was suggested in [409]. Although there is certainly some expected variability, the amplitude of the modulus is directly correlated with the scale of the inflationary potential - and it is rather likely that large changes of W_0 in the landscape would change the curvature of the inflationary potential sufficiently to spoil successful inflation. It is also possible that a sufficiently long period of inflation can dilute the modulus amplitude [410] since the modulus behaves as an overdamped harmonic oscillator as we have discussed in Sec. (5.2.2). Unfortunately, the scenario we consider here would require an extremely fine-tuned inflationary potential to achieve the required value of the amplitude [410]. From this standpoint - in addition to the expectation of the modulus mass to scan in the string landscape - the decoupling solution appears more attractive.

However, it is also feasible that the moduli minimum is entirely independent of the details of inflation. Such an example due to Dine, Randall, and Thomas [210] is if the moduli and inflaton Kähler potentials are independent from each other. In this case, any interaction between the inflationary sector and the moduli sector is due only to supergravity interactions - and it is easy to show that the potential minimum of the moduli is then independent of the inflationary details. Inflation then pushes the moduli to the minimum of their potential - effectively reducing

their amplitude towards 0 and decoupling their cosmological effects. This case would then appear nearly identical to a standard thermal history.

6.2.8 Some general comments on the ϕMSSM

As we have seen, cases **A1** and **B1** seem to require both large modulus and gravitino masses $m_\phi, m_{3/2} \gtrsim 10^{3-4}$ TeV so that neutralino dark matter is not overproduced, with only minor changes between the **GK1** and **GK2** cases. It then appears that unsequestered models will have an extremely difficult time realizing the ϕMSSM in either of these cases, as such large gravitino masses would be expected to raise the soft terms to correspondingly large values. Sequestered models, on the other hand, can accommodate these large values and still provide a natural SUSY spectrum similar to our benchmark mark point from Table (4.3). Additionally, as we have commented in the previous chapters, the neutralino cross section we adopt $\langle \sigma v \rangle (T_{\text{f.o.}}) \sim 2.0 \times 10^{-25}$ cm^3/sec is already at tension with Fermi-LAT results [351] if the neutralinos make up the entirety of the dark matter. We have then effectively studied the lower bound on neutralino dark matter production in the ϕMSSM as larger annihilation cross sections are effectively ruled out by experimental data - and smaller cross sections will result in less efficient annihilations, and therefore raise the produced WIMP relic density.

To contrast this, cases **A2** and **B2** only require large modulus mass $m_\phi \gtrsim 10^{3-4}$ TeV to match the observed DM relic density while a gravitino mass $m_{3/2} \sim 30$ TeV can be easily accommodated - making at most percent-level corrections to our results. This proves a much more optimistic scenario for unsequestered models,

as in e.g. KKLT scenarios various uplifting mechanisms or generalizations may generate different hierarchies between the lightest modulus, the gravitino, and the soft terms [387, 411, 412, 132, 169, 388].

6.3 Results for the ϕPQMSSM

We now discuss results for the ϕPQMSSM from numerical solutions of the coupled Boltzmann equations involving: 1. CO modulus field, 2. CO saxion field, 3. TP/DP saxions, 4. CO axion field, 5. TP/DP axions, 6. TP/DP axinos, 7. TP/DP gravitinos, 8. TP/DP neutralinos, and 9. radiation. Based on our results from the previous section, we focus solely on the case **B2** which provides more optimistic results than case **B1**. However, we now distinguish between the **GK1** and **GK2** cases as we have seen that they give drastically different predictions for dark radiation production, whereas they do not provide significantly different predictions for WIMP dark matter in the ϕMSSM. Throughout this section, we again use the natural SUSY benchmark point from Table (4.3). In several of the following results, we augment these parameters with the PQ benchmark point in Table (4.6), however in some cases we will vary the PQ data to study how our results change with respect to the PQ parameters. In these cases, we will explicitly denote the updated PQ parameter set. We also take the inflationary reheating temperature $T_R = 10^{10}$ GeV throughout, except where explicitly noted otherwise.

6.3.1 Cosmological evolution in case GK1

We begin by displaying Fig. (6.16), which shows the evolution of the abundance yield $Y_i = n_i/s$ for the nine components as the scale factor R/R_0 increases. Here, we again fix $m_\phi = 5 \times 10^3$ TeV and take all $\lambda_i = 1$ to provide comparison with the ϕMSSM abundance yield evolution figures provided in the previous section. As with the ϕMSSM, the modulus begins to inject entropy into the thermal bath

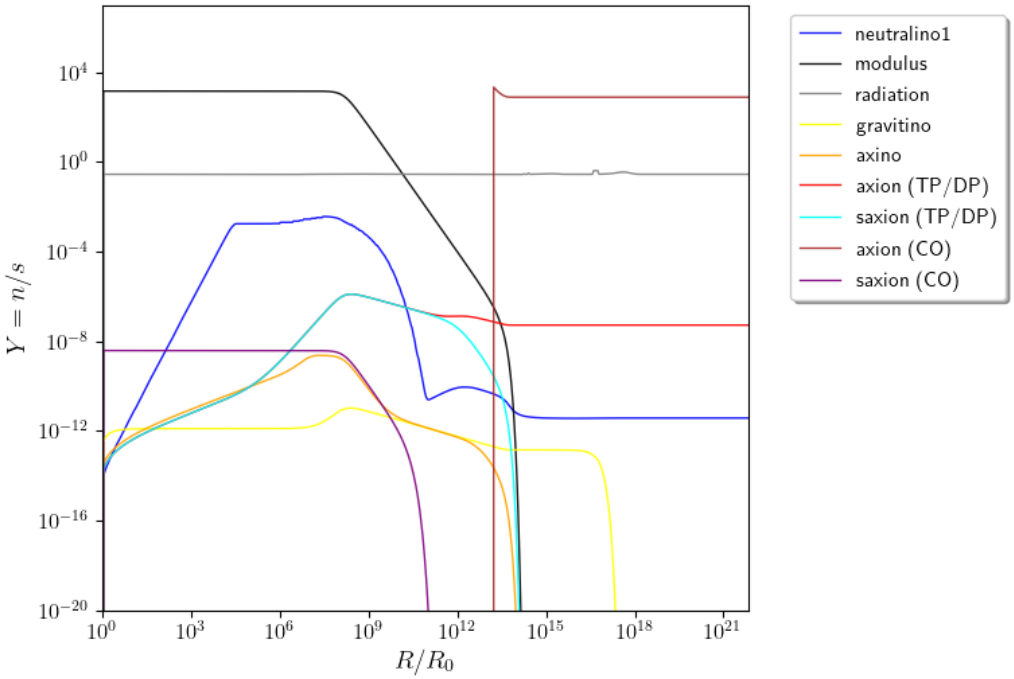


Figure 6.16: Cosmological evolution of abundance yield $Y_i = n_i/s$ vs scale factor R/R_0 in case **B2-GK1**. Here, we fix $m_\phi = 5 \times 10^3$ TeV and take all allowed $\lambda_i = 1$. Figure reproduced from [8].

around $R/R_0 \sim 10^8$, which dilutes all other tracked species (except, of course, radiation) until it decays at $R/R_0 \sim 10^{14}$. The CO saxions then decay around $R/R_0 \sim 10^{11}$. We see that the TP/DP saxions, TP/DP axions, and axinos (as well as neutralinos) all begin with a small abundance due to their small thermally-

averaged cross section at high temperatures. Their abundances then increase towards their respective equilibrium values as T decreases and $\langle \sigma v \rangle$ increases. These populations are sourced by modulus decay, so the late-time abundances of the TP/DP saxions, TP/DP axions, and axinos are predominantly determined by the modulus injections, which overpower the annihilations around $R/R_0 \sim 10^8$. The TP/DP saxions and axinos thus do not fully decay until the modulus decays at $R/R_0 \sim 10^{14}$. We also see that close to the decay of the modulus (and hence decays of the TP/DP saxions and axinos), the neutralino population is noticeably sourced by these decays and - between annihilations and the last of the entropy dilution from the modulus - rapidly approaches a constant value. As expected, the gravitinos are then the final unstable particles to decay at around $R/R_0 \sim 10^{17}$. It is worth noting that once the CO axions begin to oscillate, they are slightly diluted as the onset of oscillations overlaps with modulus decay - although they only are subjected to a small fraction of the entropy dilution from the modulus. Finally, we note that the relative scales from this numerical solution are in very good agreement with our qualitative arguments from Sec. (5.2.6).

We show the evolution of energy densities for the nine components in Fig. (6.17). In addition, we also display the radiation temperature where the ρ-axis gives the magnitude but the units are taken to be GeV. We see that the modulus dominates the energy density almost immediately after inflationary reheating ($R/R_0 = 1$) until it decays close to $R/R_0 \sim 10^{14}$, which is virtually identical to the ϕMSSM case. Briefly focusing on the temperature (green dashed curve), we see the temperature decreases at a noticeably slower rate during the decay-

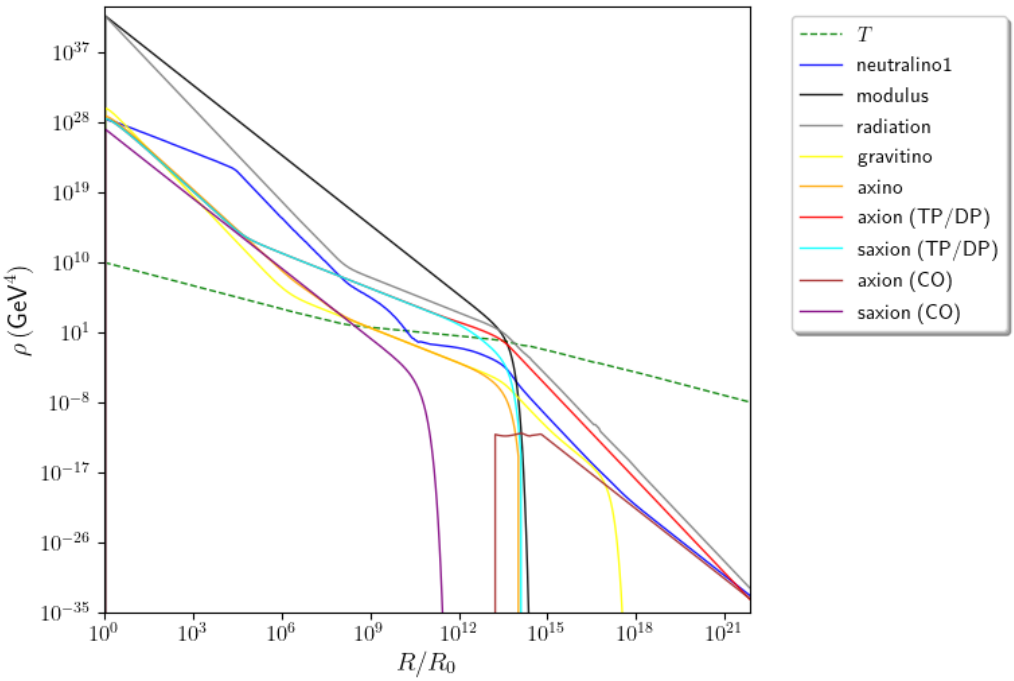


Figure 6.17: Cosmological evolution of energy densities ρ_i vs scale factor R/R_0 in case **B2-GK1**. Here, we fix $m_\phi = 5 \times 10^3$ TeV and take all allowed $\lambda_i = 1$. Figure reproduced from [8].

dominated epoch - from $R/R_0 \sim 10^8$ to $R/R_0 \sim 10^{14}$ - as expected from our previous qualitative arguments. The neutralinos and the thermal components of the PQ sector are produced below their equilibrium value due to a suppressed $\langle \sigma v \rangle$ at high temperatures. As the temperature decreases, the thermally-averaged cross sections for these particles increases which eventually pushes them towards their equilibrium values. Equilibrium is attained for the neutralinos at roughly $R/R_0 \sim 10^4$, although significant injections from the modulus and saxions - along with the freeze-out effect - make sizeable contributions to the neutralino energy density between $R/R_0 \sim 10^8$ and $R/R_0 \sim 10^{14}$. We also see that the TP/DP saxions and TP/DP axions decrease at a slower rate between around $R/R_0 \sim 10^5$ to $R/R_0 \sim 10^{14}$, while the axinos only dilute at a slower rate between around

$R/R_0 \sim 10^8$ to $R/R_0 \sim 10^{14}$. Since the modulus decays to saxions and axions are unsuppressed, the injection term is dominant for these populations from a much earlier time compared to the axinos, which are suppressed modulus decay modes here. In Sec. (5.2.6), we had estimated that the TP/DP saxion would decay shortly before the axinos (albeit, without the rigorous procedure required in this particular case for a true quantitative estimate). Careful inspection of the TP/DP saxion and axino curves reveal that the saxions *do* begin to decay at a slightly earlier time than the axinos - however as the saxions are produced in far larger quantities than axinos by modulus decay, this extends the saxion curve slightly so that they decay slightly later than the axinos. Additionally, the gravitinos do not ever annihilate efficiently - so the injection term dominates the evolution of the gravitinos from an early time ($R/R_0 \sim 10^6$). Finally, we also note that at the end of our scan limit ($T \sim 10^{-8}$ GeV), the CO axions and neutralinos (which are now redshifted sufficiently to behave as a matter distribution) will overcome the radiation-domination around $T \sim 1$ eV, in good agreement with the expected temperature at matter-radiation equality in a standard thermal history (ΛCDM) [407, 286].

We finish this section by listing the late-time values produced from this point.

Here,

$$\Omega_{\widetilde{Z}_1} h^2 = 0.20023$$

$$\Omega_{a_{\rm CO}} h^2 = 0.07789$$

$$\Omega_{a_{\rm TP/DP}} h^2 = 1.48668 \times 10^{-6}$$

$$\Delta N_{\rm eff} = 0.26504$$

and we see that both the total dark matter and dark radiation are overproduced for this point. Additionally, there is a higher WIMP relic density here than in the ϕMSSM case with the same modulus parameters - as we will see shortly, this is due to the same relativistic dilation effect that enhanced the WIMP abundance in the **B1** case with fixed $m_{3/2}$, except that now it is the modulus decay to boosted saxions which enhances the relic density.

6.3.2 Cosmological evolution in case GK2

We now view the cosmological evolution in case **B2-GK2**. In Fig. (6.18), we display the abundance yield $Y_i = n_i/s$ for each of the nine components. Here, we see that the modulus decay occurs later than in case **B2-GK1** - entropy dilution begins around $R/R_0 \sim 10^{10}$ with the modulus decaying at $R/R_0 \sim 10^{15}$. This agrees with our expectations since the gauge boson modes are now suppressed, giving roughly an order of magnitude decrease to the modulus total width. We also see that the CO saxions decay at about the same time as in case **B2-GK1** - while the decay of the TP/DP saxions and axinos still coincides with the modulus

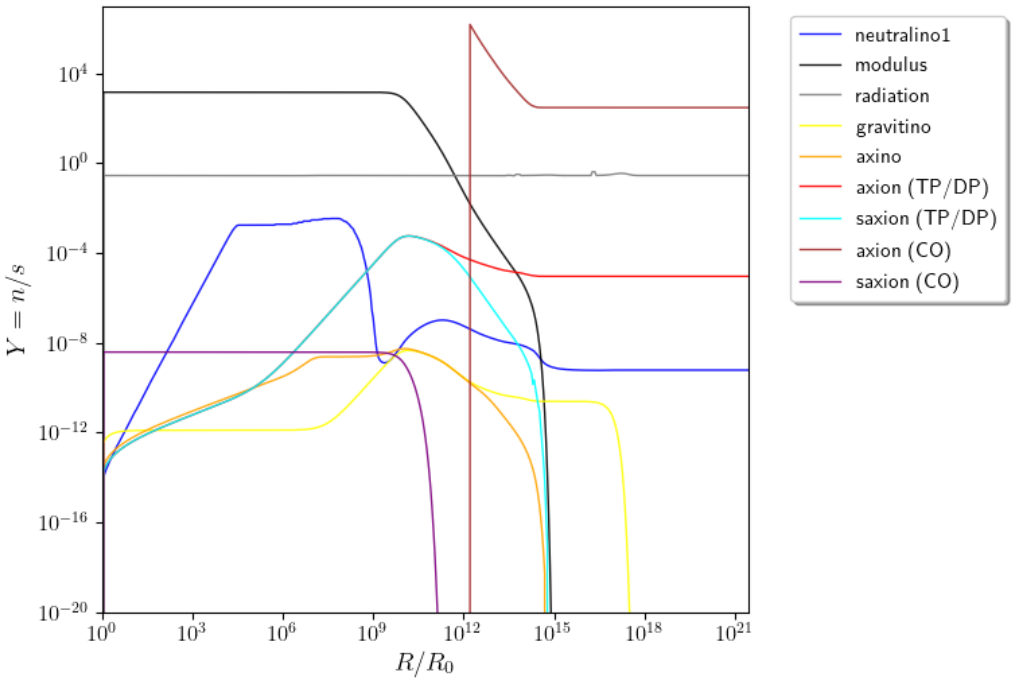


Figure 6.18: Cosmological evolution of abundance yield $Y_i = n_i/s$ vs scale factor R/R_0 in case **B2-GK2**. Here, we fix $m_\phi = 5 \times 10^3$ TeV and take all allowed $\lambda_i = 1$ except for $\lambda_{\rm gauge} = 1/16\pi^2$. Figure reproduced from [8].

decay. Due to the large increase in the effective modulus to WIMP branching ratio (most dominantly through the $\phi \to ss \to$ WIMPs process), we see that between around $R/R_0 \sim 10^9$ to $R/R_0 \sim 10^{12}$ the neutralino abundance yield receives a sizeable enhancement over the previous **GK1** case. Because of the late modulus decay (and therefore late TP/DP saxion and axino decay), we also notice that the final abundance yield $Y_{\widetilde{Z}_1} \sim 10^{-9}$ is enhanced compared to the previous case, which had $Y_{\widetilde{Z}_1} \sim 10^{-11}$. The abundance of TP/DP axions also receives a substantial enhancement over the previous case, due to the large increase in the $\phi \to aa$ branching ratio. Finally, we also notice that the CO axions begin oscillations *earlier* than in case **B2-GK1** (at least in the $\xi = 1$ limit we consider

here). We will comment more on this in Sec. (6.3.6), but for now we note that the CO axions begin with a very large abundance (far more so than in the previous case). The modulus then dilutes this abundance by a significant amount, which gives a final abundance yield similar to the previous case. We will see later that the $\xi = 1$ limit of the **GK2** cases is peculiar in that it can provide an enhancement of the CO axion relic density - a property that is nearly absent in the $\xi = 0$ limit of the same case.

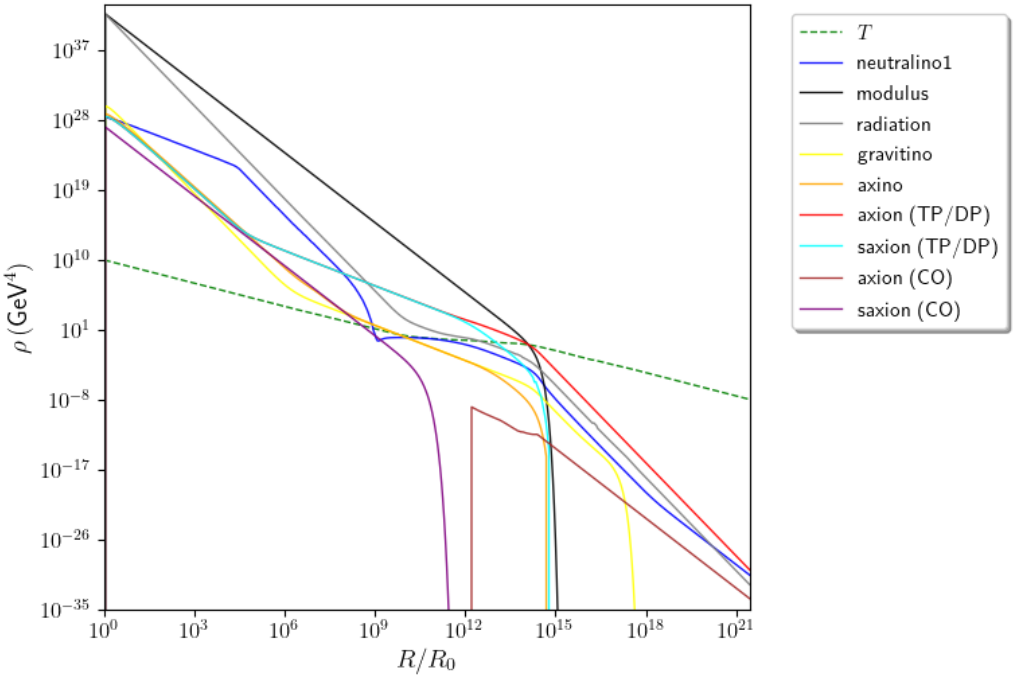


Figure 6.19: Cosmological evolution of energy densities ρ_i vs scale factor R/R_0 in case **B2-GK2**. Here, we fix $m_\phi = 5 \times 10^3$ TeV and take all allowed $\lambda_i = 1$ except for $\lambda_{\rm gauge} = 1/16\pi^2$. Figure reproduced from [8].

In Fig. (6.19), we display the evolution of energy densities for the nine components in case **B2-GK2**. Here, we see a key difference from the previous case is that the energy density of radiation decreases below the TP/DP axions, so that

most of the energy content behaving as radiation is in the form of dark radiation. At this scale, the axions do not thermalize with the rest of the primordial plasma. The corresponding radiation temperature after modulus decay is then expected to be lower than in the previous case.

To conclude this section, we note that this point produces the late-time values

$$\Omega_{\widetilde{Z}_1} h^2 = 32.2581$$

$$\Omega_{a_{\rm CO}} h^2 = 0.03013$$

$$\Omega_{a_{\rm TP/DP}} h^2 = 0.00336$$

$$\Delta N_{\rm eff} = 598.869$$

which overproduces dark matter and *far* overproduces dark radiation. Before we study the production of dark matter and dark radiation in the ϕPQMSSM, we first discuss the entropy production in both the **GK1** and **GK2** cases.

6.3.3 Entropy production in the ϕPQMSSM

In Fig. (6.20), we display the entropy dilution factor $r \equiv S_f/S_0$ as a function of modulus mass m_ϕ for both case **GK1** and **GK2**. As we expect, in both cases **GK1** and **GK2** an increase in m_ϕ translates to a potentially substantial weakening of the entropy dilution factor. From the same arguments we made in Sec. (6.2.4), we note that our entropy dilution factor decreases as $m_\phi^{-3/2}$ in Fig. (6.20) as $T_D^\phi \propto m_\phi^{3/2}$, while we fix $T_R = 10^{10}$ GeV here so that there is no region here where significant radiation-domination occurs before modulus oscillations begin.

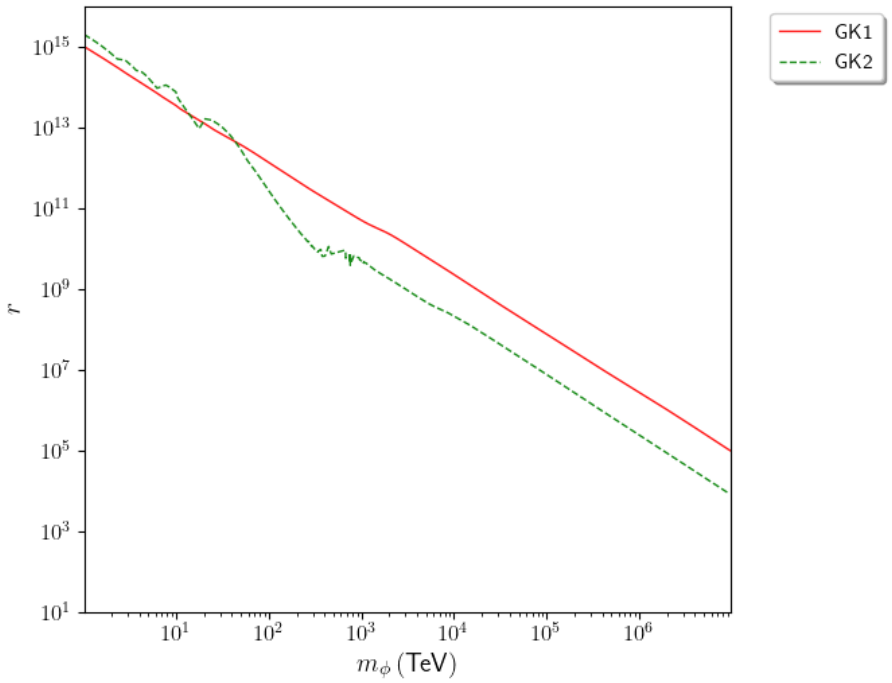


Figure 6.20: Entropy dilution factor r vs modulus mass m_ϕ for both case **GK1** and **GK2** in the $\xi = 1$ limit. We adopt our natural SUSY benchmark point from Table (4.3) and our PQ benchmark point from Table (4.6). Here, we fix $T_R = 10^{10}$ GeV. Figure taken from [8].

In the **GK2** case, we see much more dependence on the various SUSY modes which become kinematically accessible between 1 TeV $\lesssim m_\phi \lesssim$ 60 TeV due to this dependence on T_D^ϕ, while for $m_\phi \gtrsim 100$ TeV the entropy dilution decreases below the value predicted from case **GK1**. This is due to the fact that in case **GK2** in the $\xi = 1$ limit, most of the modulus energy density (and hence entropy) ends up in the production of axions - which behave as dark radiation at this scale - instead of being released into the thermal bath. Case **GK1** has a decay temperature set primarily by λ_{gauge}, and is thus much less affected by these effects than case **GK2**. In the next few sections, we now turn to the study of production of dark matter and dark radiation in the ϕPQMSSM beginning with case **B2-GK1** in the $\xi = 1$

limit.

6.3.4 DM/DR production in case GK1 - the $\xi = 1$ limit

In Fig. (6.21), we show the associated dark matter production for each $\lambda_{\rm PQ} \in \{0, 0.1, 1\}$ with all other $\lambda_i = 1$ as a function of m_ϕ for case **GK1** with $\xi = 1$. We also display the solid black vertical line at $m_\phi \sim 70$ TeV which separates the BBN-safe region ($m_\phi \gtrsim 70$ TeV) from the region excluded by BBN ($m_\phi \lesssim 70$ TeV) - i.e. where the modulus decays during or after the scale of BBN. Additionally,

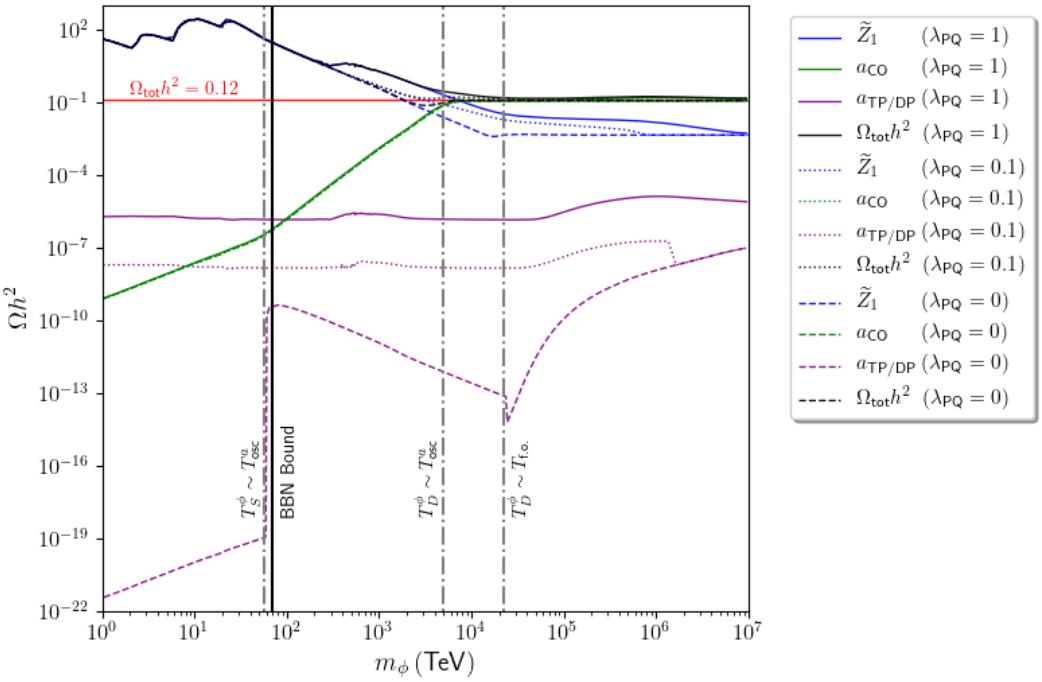


Figure 6.21: Relic densities in case **GK1** with $\xi = 1$ as a function of m_ϕ for neutralinos (blue), TP/DP axions (purple), CO axions (green), and total DM (black) for $\lambda_{\rm PQ} \in \{0, 0.1, 1\}$ with all other $\lambda_i = 1$. Vertical dashed lines represent where $T_S^\phi \sim T_{\rm osc}^a$ ($m_\phi \sim 55$ TeV), $T_D^\phi \sim T_{\rm osc}^a$ ($m_\phi \sim 5 \times 10^3$ TeV), and $T_D^\phi \sim T_{\rm f.o.}$ ($m_\phi \sim 2 \times 10^4$ TeV). Vertical solid black line at $m_\phi \sim 70$ TeV represents BBN bound. Figure taken from [8].

we display three vertical dot-dashed lines at $m_\phi \sim 55$ TeV, $m_\phi \sim 5 \times 10^3$ TeV,

and $m_\phi \sim 2 \times 10^4$ TeV which separate key aspects of the resulting cosmology. The first line ($m_\phi \sim 55$ TeV), indicates where the oscillations of the CO axion begin simultaneously with when the modulus begins releasing entropy into the thermal bath. We notice that, to the right of this line (55 TeV $\lesssim m_\phi \lesssim 5 \times 10^3$ TeV), the produced relic density due to CO axions (shown by the green curve) increases at a faster rate than to the left of this line ($m_\phi \lesssim 55$ TeV). If the axion oscillations do not begin until after the modulus has begun to release entropy, the axion abundance will not be subject to the full dilution - unlike any relics existing before T_S^ϕ. To the left of this line ($m_\phi \lesssim 55$ TeV), the axion relic density increases only because the entropy dilution factor decreases with increasing m_ϕ. The second vertical dot-dashed line ($m_\phi \sim 5 \times 10^3$ TeV) indicates where the decay of the modulus and the beginning of CO axion oscillations coincide. To the right of this line ($m_\phi \gtrsim 5 \times 10^3$ TeV), the entropy dilution from the modulus no longer dilutes the CO axion, and its abundance reaches a constant value. The third vertical dot-dashed line ($m_\phi \sim 2 \times 10^4$ TeV) then denotes where the modulus decay occurs at the same time as neutralino freeze-out. In the case where $\lambda_{\rm PQ} = 0$, we see that the neutralino relic density takes a constant value to the right of this line. However, for $\lambda_{\rm PQ} > 0$ this is clearly not the case.

For the case where $\lambda_{\rm PQ} > 0$, the effect of the relativistic dilation factor $m_s n_s/\rho_s$ in the Boltzmann equations Eqs. (5.1) and (5.2) becomes apparent. Once $m_\phi \gg 2m_s$, the saxions become highly boosted in the comoving frame which leads to a large enhancement of their lifetime. Here, even though the modulus has decayed before neutralino freeze-out, the saxions decay much later. Since

the copiously produced saxions then decay to gauginos with a branching ratio of $\sim 2\% - 5\%$ as we saw in Fig. (4.17), this leads to an enhancement in the neutralino relic density. As m_ϕ increases, the modulus decay temperature rises faster than the saxion lifetime dilation so that eventually the neutralino relic density decreases to its thermal value. For $m_\phi \lesssim 2 \times 10^3$ TeV, we see the neutralino relic density is well above the measured value regardless of the value of $\lambda_{\rm PQ}$ - providing a far more stringent bound than BBN. In order to produce neutralino relic density consistent with the total measured dark matter relic density, here we find that $m_\phi \gtrsim 10^4$ TeV without significant tuning of $\lambda_{\rm PQ}$. However, in order to produce a neutralino relic density consistent with current DD/ID bounds, a much larger value of m_ϕ may be required depending on the precise value of $\lambda_{\rm PQ}$.

Additionally, the contribution of TP/DP axions to the total relic density is very low - below 0.1% of the measured value. The effect of the TP/DP axions is then primarily the production of dark radiation. In Fig. (6.22), we display the dark radiation predictions in the form of the effective number of neutrinos $\Delta N_{\rm eff}$ for $\lambda_{\rm PQ} \in \{0,\, 0.1,\, 1\}$ (where all other $\lambda_i = 1$), as well as the Planck 2018 constraints on $\Delta N_{\rm eff}$ (red line) [11] and the forecasted CMB-S4 limit (orange dashed line) [413]. We see that $\lambda_{\rm PQ} \gtrsim 1$ is excluded from Planck 2018 data, while $\lambda_{\rm PQ} = 0.1$ is still below the forecasted CMB-S4 limit which will probe much of the expected parameter space of this case. Between both Fig. (6.21) and Fig. (6.22), we also see for $\lambda_{\rm PQ} = 0$ a drastic increase in both $\Omega_{a_{\rm TP/DP}} h^2$ and $\Delta N_{\rm eff}$ at $m_\phi \sim 60$ TeV. Although this coincides with the value of m_ϕ where $T_S^\phi \sim T_{\rm osc}^a$, this is purely coincidental - the drastic increase is solely due to the modulus

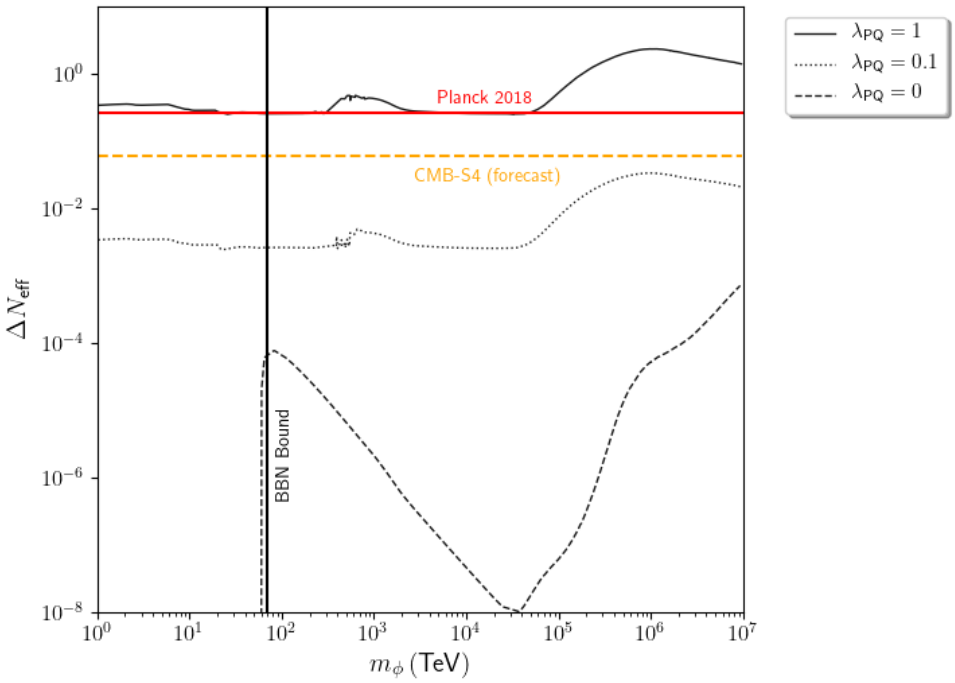


Figure 6.22: Dark radiation production in case **GK1** with $\xi = 1$ as a function of m_ϕ for $\lambda_{\rm PQ} \in \{0, 0.1, 1\}$ with all other $\lambda_i = 1$. Horizontal red line shows Planck 2018 bounds, while orange dashed line shows forecast CMB-S4 limits. Vertical solid black line at $m_\phi \sim 70$ TeV represents BBN bound. Figure taken from [8].

decay to gravitino channel becoming kinematically accessible. The gravitino can then decay to axion+axino pairs (albeit at around a 1% branching fraction, as we saw in Fig. (4.23)), whereas the only other source of TP/DP axions in the $\lambda_{\rm PQ} = 0$ case are the thermal axions produced by inflationary reheating which are heavily diluted from modulus decay. We also notice a sharp increase in $\Delta N_{\rm eff}$ for $m_\phi \gtrsim 3 \times 10^4$ TeV for $\lambda_{\rm PQ} = 0$. Here, the entropy dilution from the modulus has now become sufficiently weak that thermal axions and saxions (which here primarily decay to axions) are no longer diluted to entirely negligible levels - although they are still well below the reach of the CMB-S4 forecasted limits. Since we are considering case **B2** here, which has suppressed modulus decay to

gravitinos, as m_ϕ increases the $\Omega_{a_{\rm TP/DP}}h^2$ and $\Delta N_{\rm eff}$ curves for $\lambda_{\rm PQ} = 0$ decrease until $m_\phi \sim 2 \times 10^4$ TeV. At this point, the entropy dilution from the modulus becomes weak enough that the thermally-produced saxions and axions are no longer diluted to negligible levels, thus increasing the TP/DP axion abundance and corresponding contribution to dark radiation. We also note that there are two bumps in $\Delta N_{\rm eff}$ in Fig. (6.22) for $\lambda_{\rm PQ} > 0$. The first, between $m_\phi \sim 300$ TeV and $m_\phi \sim 2 \times 10^3$ TeV, is due to the relativistic enhancement of the saxions. Here, the saxions begin to be relativistic and have correspondingly higher energy density when they decay, translating to a larger TP/DP axion energy density. However, once the modulus gets much larger than $m_\phi \sim 2 \times 10^3$ TeV, the saxions live sufficiently long to become redshifted, once again behaving as matter once they decay - relaxing the axion energy density back to its expected value. This effect does not happen for the neutralinos produced from saxion decay (at least from the viewpoint of the produced WIMP relic density) since the saxion-produced axions are in the branching scenario while the saxion-produced neutralinos are in the annihilation scenario. The second bump begins at $m_\phi \sim 5 \times 10^4$ and continues for the duration of our plot limits. Once the modulus and saxions decay early enough (i.e. at large enough temperature $T_D^s \gtrsim 3 - 5$ GeV), the axion's cross section $\langle \sigma_a v \rangle$ is large enough to pull the axions up towards their equilibrium value as can be seen from Fig. (6.1). On the other hand, if the modulus and saxions decay *much* earlier the axion population begins to become redshifted - decreasing its energy density and therefore decreasing its contribution to $\Delta N_{\rm eff}$.

We display in Fig. (6.23) the produced dark matter relic densities as a function

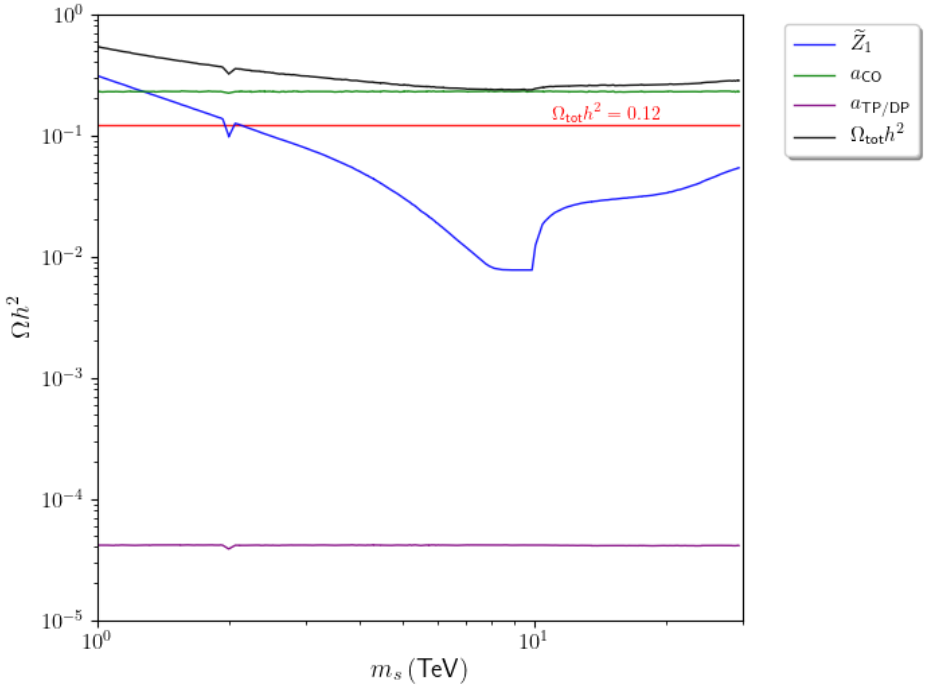


Figure 6.23: Dark matter production as a function of m_s in case B2-GK1 in the $\xi = 1$ limit. Here, we fix $m_\phi = 5 \times 10^5$ TeV and $m_{\widetilde{a}} = 5$ TeV and take all $\lambda_i = 1$. All remaining PQ parameters are as given in Table (4.6).

of the saxion mass m_s, where we have fixed $m_\phi = 5 \times 10^5$ TeV and $m_{\widetilde{a}} = 5$ TeV in addition to taking all $\lambda_i = 1$. We see that as m_s increases, there is a reduction in the produced relic density due to a corresponding decrease in the relativistic dilation factor mn/ρ. Once $m_s \gtrsim 7$ TeV, we see that the decay now happens sufficiently early to return the neutralino relic density to its thermally-expected value (albeit with a slight enhancement due to the modulus decays to axinos, which are both present and constant in this plot). As $m_s \gtrsim 2m_{\widetilde{a}} = 10$ TeV, we can see a sharp increase in the WIMP relic density. This is because the saxion can now decay to axino pairs with a large branching ratio, which further cascade decay to neutralinos. We also notice a slight dip in the neutralino relic density at

$m_s \sim 2$ TeV. As can be seen from Fig. (4.17), this is due to a resonance in the saxion decay width to gauginos. Although the saxion branching ratio to SUSY particles increases sharply here, the saxion lifetime decreases - which produces a net decrease in the neutralino relic density since we are in the annihilation scenario. It is noted in [290] that although the saxion mass is expected to be of order of the soft terms, the axino mass tends to be a truly model-dependent quantity which can be the same magnitude as the saxion or possibly much lighter. Our results here suggest that models predicting a relatively large saxion mass which is close to the axino mass (or at least sufficiently close to block the saxion-to-axino decays) will produce the most optimistic results in the ϕPQMSSM.

Finally, we discuss our anticipations of how these results change for cases **B1**, **A1**, and **A2**. In case **B1**, we do not expect a significant change in the modulus decay temperature since the branching fraction to gravitinos is still only $\sim 1\%$. However, as we saw in the ϕMSSM, the gravitinos decay very late and - as they are now produced in much more abundant quantities than in case **B2** - we expect this to lead to an extremely large enhancement in the neutralino relic density. Since the gravitinos can decay into axion+axino and saxion+axino pairs as well (albeit with only a roughly 1% branching ratio), this may also lead to a slight enhancement in the amount of dark radiation produced. In case **A2**, both gauginos and axinos are unsuppressed - which should increase the modulus total width by roughly a factor of 2. This translates into an increase in the modulus decay temperature by a factor of around 1.4, which lowers the naive expectation of neutralino dark matter production by about the same amount. However,

as the highly boosted saxions significantly enhance the neutralino production for $m_\phi \gtrsim 300$ TeV, the decrease in the neutralino relic abundance may be not be as significant for large m_ϕ - a behavior that is exhibited in Fig. (6.21) for $m_\phi \gtrsim 2 \times 10^4$ TeV. Additionally, axinos are now produced in large quantities and - much like the saxions - are highly boosted. For our PQ benchmark parameters in Table (4.6), we expect that the neutralino relic abundance increases slightly compared to case **B2** for $m_\phi \gtrsim 300$ TeV since, as we saw in Fig. (4.20), the decay width for axinos is slightly lower than the saxion decay width, corresponding to a longer lifetime and less efficient neutralino annihilations. The unsuppressed modulus decays to gauginos and axinos may also ease the production of dark radiation in this scenario since this decreases the effective modulus branching fraction to axions. Case **A1** then provides the most challenging scenario from the perspective of dark matter production - the unsuppressed production of gravitinos should generically overproduce neutralino dark matter unless the gravitino is made extremely massive. Even in sequestered scenarios where this is possible and still compatible with a natural SUSY spectrum, the unsuppressed decays to axinos still may provide severe neutralino overproduction. In all cases, we would not expect a significant change in the CO axion relic density, as the entropy injected from the modulus is expected to only change by a small amount.

6.3.5 DM/DR production in case GK1 - the $\xi = 0$ limit

In Fig. (6.24), we show the associated dark matter production in the PQ self-coupling $\xi = 0$ limit for each $\lambda_{\rm PQ} \in \{0,\, 0.1,\, 1\}$ with all other $\lambda_i = 1$ as a function

of m_ϕ for case **GK1**. We again display the solid black vertical line at $m_\phi \sim 70$ TeV separating the BBN-safe and BBN-violating regions, and the three vertical dot-dashed lines indicating shifts in the resulting cosmology at $m_\phi \sim 55$ TeV, $m_\phi \sim 5 \times 10^3$ TeV, and $m_\phi \sim 2 \times 10^4$ TeV. As can be seen from the figure, this

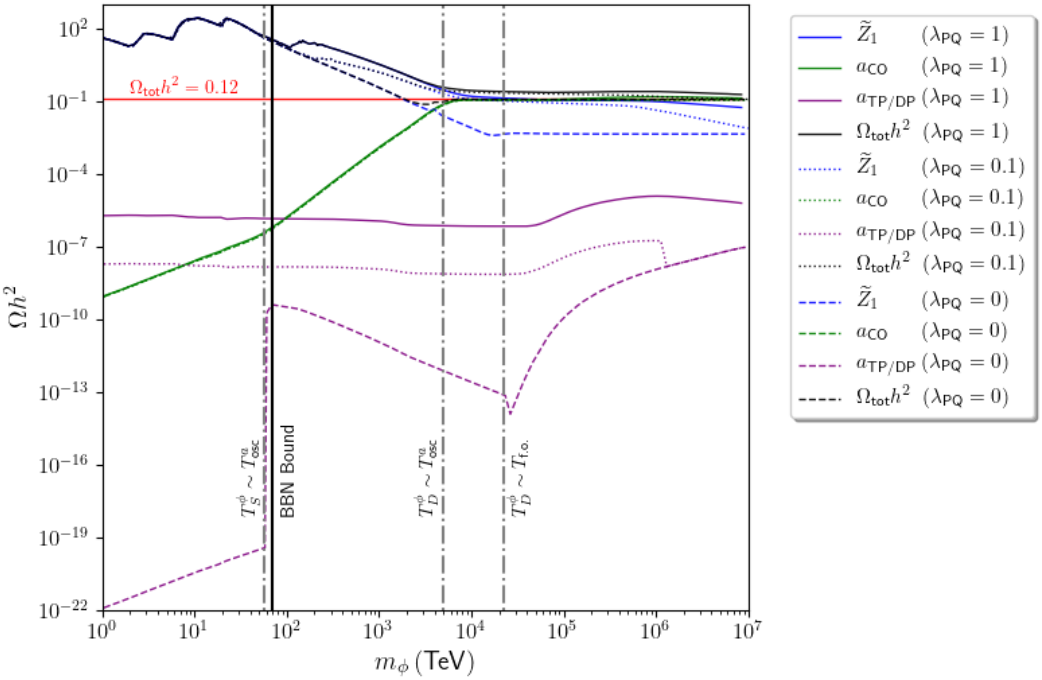


Figure 6.24: Relic densities in case **GK1** with $\xi = 0$ as a function of m_ϕ for neutralinos (blue), TP/DP axions (purple), CO axions (green), and total DM (black) for $\lambda_{\rm PQ} \in \{0, 0.1, 1\}$ with all other $\lambda_i = 1$. Vertical dashed lines represent where $T_S^\phi \sim T_{\rm osc}^a$ ($m_\phi \sim 55$ TeV), $T_D^\phi \sim T_{\rm osc}^a$ ($m_\phi \sim 5 \times 10^3$ TeV), and $T_D^\phi \sim T_{\rm f.o.}$ ($m_\phi \sim 2 \times 10^4$ TeV). Vertical solid black line at $m_\phi \sim 70$ TeV represents BBN bound. Figure taken from [8].

case is very similar to the $\xi = 1$ limit just studied - the key difference being the lack of PQ sector self-interactions. Since the $s \to aa$ mode is now forbidden, the primary saxion decay is into gaugino pairs with a branching fraction of about 90%, as we have seen in Fig. (4.19). The saxion decay width is now also reduced by around two orders of magnitude, thus increasing its lifetime by the same amount.

This increase in the saxion lifetime then predicts much larger enhancements of the neutralino relic density than in the $\xi = 1$ limit. In the $\xi = 0$ limit, we therefore see a much larger value of m_ϕ is required to meet DD/ID bounds - here, $m_\phi \gtrsim 10^7$ TeV for $\lambda_{\rm PQ} = 0.1$, with larger values $\lambda_{\rm PQ}$ requiring even larger values of m_ϕ.

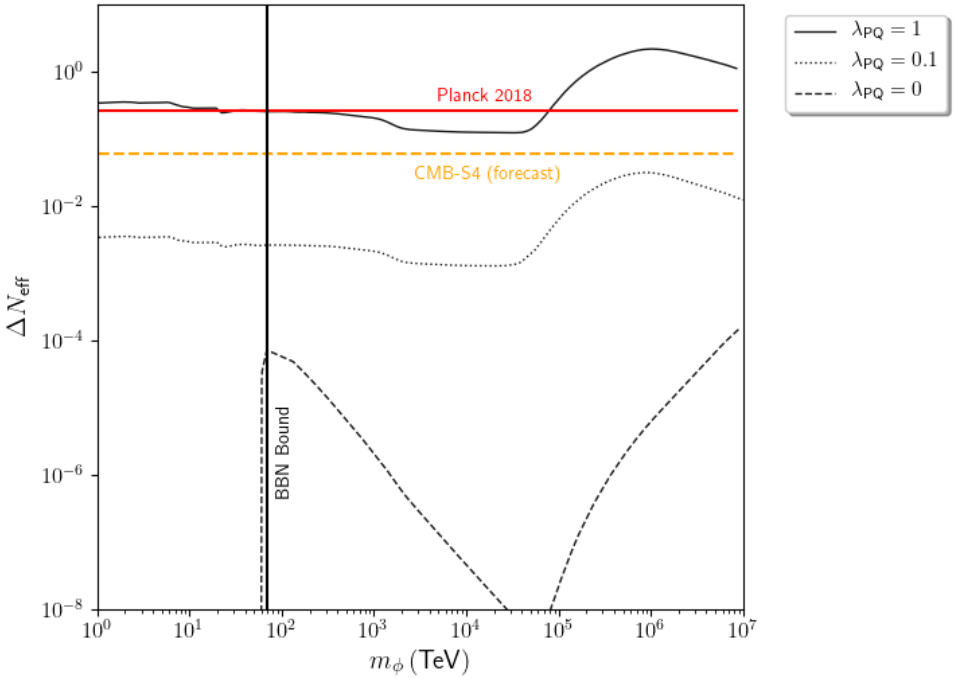


Figure 6.25: Dark radiation production in case **GK1** with $\xi = 0$ as a function of m_ϕ for $\lambda_{\rm PQ} \in \{0, 0.1, 1\}$ with all other $\lambda_i = 1$. Horizontal red line shows Planck 2018 bounds, while orange dashed line shows forecast CMB-S4 limits. Vertical solid black line at $m_\phi \sim 70$ TeV represents BBN bound. Figure taken from [8].

In Fig. (6.25), we plot the produced dark radiation in the $\xi = 0$ limit. A quick comparison with Fig. (6.22) shows that the $\xi = 0$ case generically tends to have a slightly lower $\Delta N_{\rm eff}$ than the $\xi = 1$ limit. This is, of course, due to the lack of saxion decays into axions - so that the only production of dark radiation comes from modulus decay and, to a much lesser extent, gravitino decay. Additionally, we note that the bump that was present in the $\xi = 1$ limit between $m_\phi \sim 300$

TeV and $m_\phi \sim 2 \times 10^3$ TeV is not present in the $\xi = 0$ limit for this reason. We also see that for $\lambda_{\rm PQ} = 0$, the produced dark radiation for $m_\phi \gtrsim 3 \times 10^4$ TeV is correspondingly lower than in the $\xi = 1$ limit. As with the $\xi = 1$ limit, the entropy dilution from modulus decay has become weak at large m_ϕ so that sizeable contributions from the thermally-produced population occur, although the thermal saxions can no longer provide a large contribution to $\Delta N_{\rm eff}$.

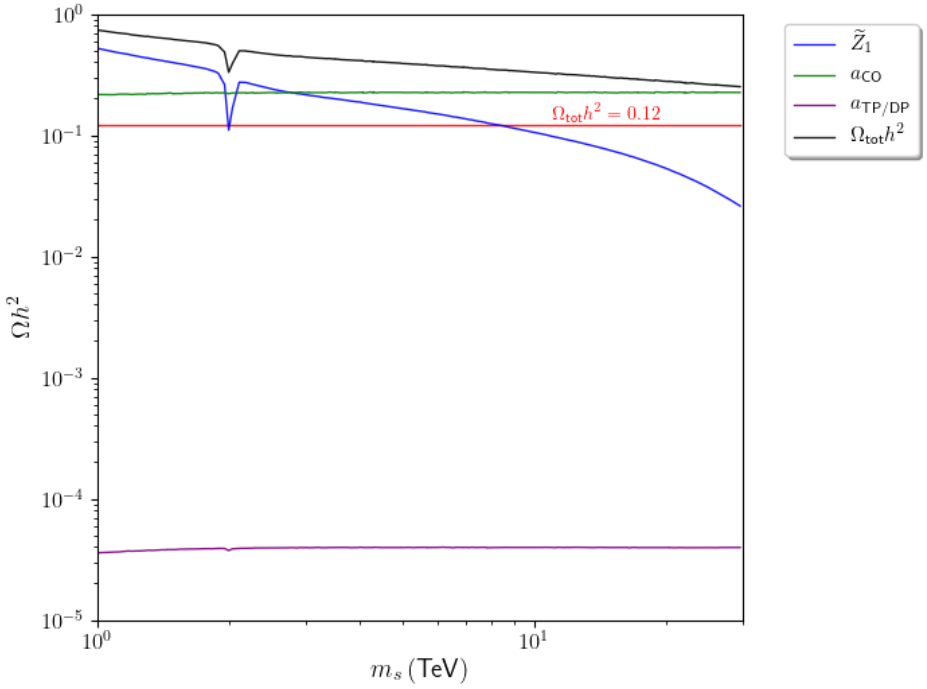


Figure 6.26: Dark matter production as a function of m_s in case B2-GK1 in the $\xi = 0$ limit. Here, we fix $m_\phi = 5 \times 10^5$ TeV and $m_{\widetilde{a}} = 5$ TeV and take all $\lambda_i = 1$. All remaining PQ parameters are as given in Table (4.6).

We display the produced dark matter relic densities as a function of m_s in the $\xi = 0$ limit in Fig. (6.26). Similarly to the $\xi = 1$ limit, here we fix $m_\phi = 5 \times 10^5$ TeV and $m_{\widetilde{a}} = 5$ TeV and take all $\lambda_i = 1$. As the saxion decays to PQ sector pairs are forbidden in the $\xi = 0$ limit, two features are immediately clear: 1. the leading

saxion decays are now to gaugino pairs, which decreases its total width by around $1-2$ orders of magnitude, causing an increase in the neutralino abundance by up to an order of magnitude and 2. now that the decays to axino pairs is forbidden, it appears that larger saxion masses are favored. Much as in the $\xi = 1$ plot, we again see a sharp decrease due to the gaugino resonance in the saxion decay width at $m_s \sim 2$ TeV, however here this drop is far more pronounced as this resonance has a much larger effect on the saxion decay width in the $\xi = 0$ limit.

Evidently, this scenario requires (without any other considerations) a modulus mass at least an order of magnitude larger than in the corresponding $\xi = 1$ limit due to a large increase in the neutralino relic density. In this scenario, we again expect both cases **B1-GK1** and **A1-GK1** to be even more difficult to realize due to the moduli-induced gravitino problem. Case **A2-GK1** may also be difficult to realize due to the unsuppressed decays to axinos. To avoid overproduction of neutralino dark matter, the modulus, saxion, and axino likely all would need to have very large masses - with perhaps saxion and axino masses required to be greater than the expected $\mathcal{O}(1-10)$ TeV based on our soft masses unless the modulus mass is pulled up far higher. However, if the modulus mass is taken large enough that natural values of the saxion and axino masses do not overproduce WIMP dark matter, it is likely that such a large modulus mass will no longer dilute the thermal relics - causing a resurgence of the thermal gravitino problem. Thus it might be that cases **A1** and **A2** are unable to be realized in tandem with natural SUSY - we leave a precise analysis of this statement for future work. There is an additional implication from this scenario due to our expectation of

$m_\phi \gtrsim 10^7$ TeV to meet DD/ID constraints. Consistency of this scenario then puts a requirement on the Hubble scale during inflation $H_I \gtrsim 10^{10}$ GeV so that $H_I > m_\phi$ - *otherwise the modulus begins to oscillate during or before inflation* and would then be irrelevant for the later cosmology. Additionally, our assumption that PQ symmetry is broken before or during inflation requires that $f_a > H_I/2\pi$ [112]. These two consistency arguments put very tight constraints on the viable parameter space of m_ϕ and f_a in the $\xi = 0$ limit - a large enough modulus mass to meet DD/ID constraints requires a higher scale of inflation, which requires an even higher PQ scale. These constraints are eased significantly in the $\xi = 1$ limit, which requires a lower inflationary Hubble scale $H_I \sim 5 \times 10^8$ GeV since we would expect $m_\phi \gtrsim 5 \times 10^5$ TeV to meet DD/ID bounds, allowing for f_a as low as $\sim 10^8$ GeV.

6.3.6 DM/DR production in case GK2 - the $\xi = 1$ limit

We now turn to case **B2-GK2** in the $\xi = 1$ limit. In Fig. (6.27), we display the associated dark matter production in this case as a function of m_ϕ for each $\lambda_{\rm PQ} \in \{0, 0.1, 1\}$, with $\lambda_{\rm gauge} = 1/16\pi^2$ and all remaining $\lambda_i = 1$. A quick comparison to the **GK1** cases shows several notable differences here. To begin, we note that the black vertical line separating BBN-safe from BBN-violating regions has now been pushed up to $m_\phi \sim 200$ TeV. Additionally, the three vertical lines indicating cosmology shifts are (in the case where $\lambda_{\rm PQ} = 1$) pushed to $m_\phi \sim 300$ TeV ($T_S^\phi \sim T_{\rm osc}^a$), $m_\phi \sim 2 \times 10^4$ TeV ($T_D^\phi \sim T_{\rm osc}^a$), and $m_\phi \sim 2 \times 10^5$ TeV ($T_D^\phi \sim T_{\rm f.o.}$). The shift of each of these lines is due to modulus decay occuring

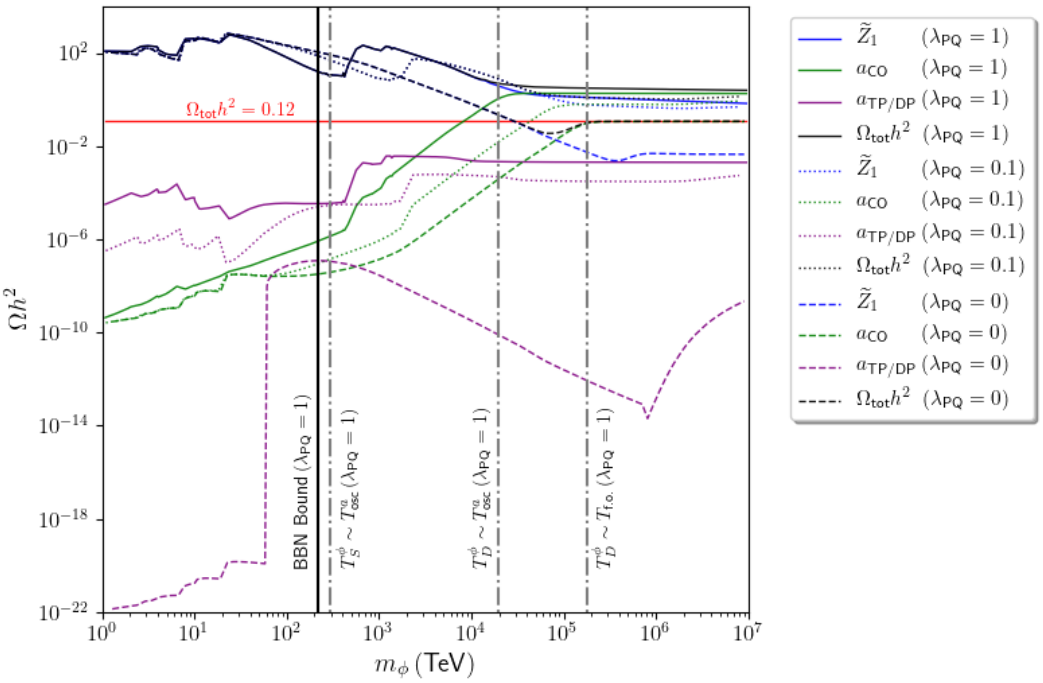


Figure 6.27: Relic densities in case **GK2** with $\xi = 1$ as a function of m_ϕ for neutralinos (blue), TP/DP axions (purple), CO axions (green), and total DM (black) for $\lambda_{\rm PQ} \in \{0, 0.1, 1\}$. Vertical dashed lines represent where $T_S^\phi \sim T_{\rm osc}^a$ ($m_\phi \sim 300$ TeV), $T_D^\phi \sim T_{\rm osc}^a$ ($m_\phi \sim 2 \times 10^4$ TeV), and $T_D^\phi \sim T_{\rm f.o.}$ ($m_\phi \sim 2 \times 10^5$ TeV). Vertical solid black line at $m_\phi \sim 200$ TeV represents BBN bound. Figure taken from [8].

substantially later since the leading decay mode (into gauge bosons) is now highly suppressed. Furthermore, each of these four lines gets pushed to even larger m_ϕ as $\lambda_{\rm PQ}$ decreases.

We also notice a substantial increase in the relic abundance of TP/DP axions for all three values of $\lambda_{\rm PQ}$ considered. As the modulus decays to gauge bosons are now highly suppressed, the modulus branching ratio to both axions and saxions (which primarily decay to axions in this $\xi = 1$ limit) drastically increases - from Figs. (4.15) and (4.17), we see the effective modulus-to-axion branching ratio is above around 95% once the saxions decay. Since the modulus now releases most

of its energy to ultra-relativistic axions which - at the scale they are produced - do not thermalize at all, this energy is not released into the thermal bath at any point. This causes the radiation temperature at a given value of H to be lower after modulus decay in this case than in the others - a key distinction of this case. Since the CO axions have a temperature-dependent mass $m \propto T^{-4}$ for $T \gtrsim \Lambda_{\rm QCD}$, the initial energy density for the axion when it begins to oscillate *increases* in this case due to the lower oscillation temperature. This causes the relic density for the CO axions to receive an enhancement, as we see in Fig. (6.27) for $m_\phi \gtrsim 2 \times 10^4$ TeV. For smaller values of $\lambda_{\rm PQ}$, we also see that the CO axion relic density becomes constant at larger values of m_ϕ due to the sensitive dependence of T_D^ϕ on $\lambda_{\rm PQ}$ here - a feature not present in the **GK1** cases which depend on these couplings only at the percent-level.

Finally, the neutralino relic density receives an extra enhancement over the **GK1** case due to the later decay of the modulus, which causes the boosted saxion population to decay later. For both $\lambda_{\rm PQ} = 0.1$ and $\lambda_{\rm PQ} = 1$, we see that the neutralino relic density is above the measured value throughout the entirety of our scan limits. Even for $\lambda_{\rm PQ} = 0$, a value $m_\phi \gtrsim 10^5$ TeV is required to be consistent with DD/ID constraints - a full order of magnitude above the **GK1** case.

In Fig. (6.28), we display the dark radiation produced in this scenario. We see that for $\lambda_{\rm PQ} = 0.1$ and $\lambda_{\rm PQ} = 1$, the value of $\Delta N_{\rm eff}$ is produced at least two orders of magnitude above the Planck 2018 limit - except for values of m_ϕ well into the BBN-violating region. We also do not expect any significant deviations from this excessive dark radiation and dark matter overproduction in any of the cases **A1**,

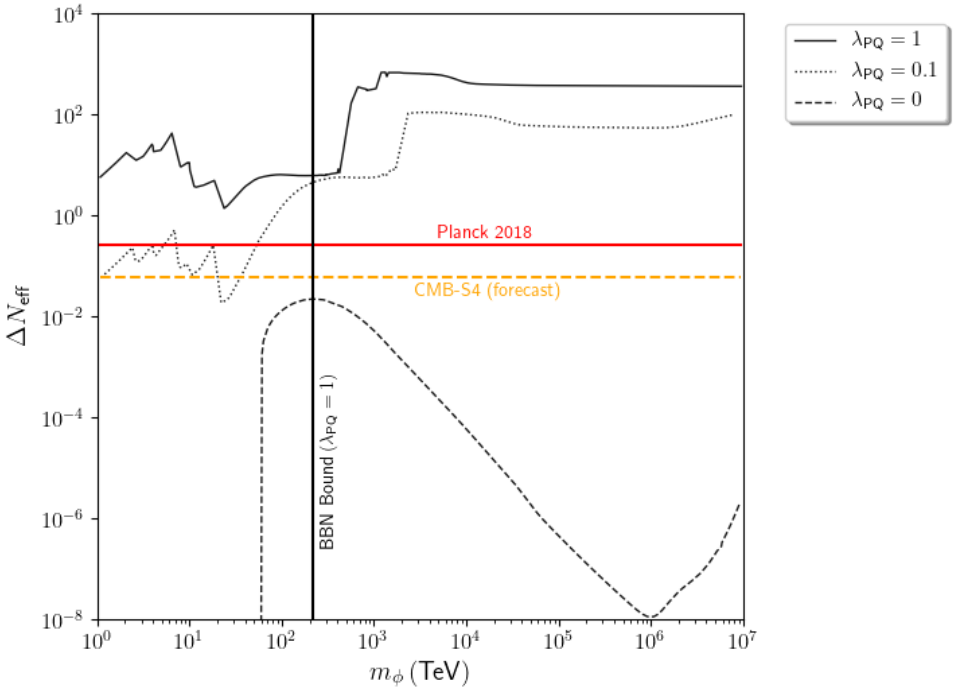


Figure 6.28: Dark radiation production in case **GK2** with $\xi = 1$ as a function of m_ϕ for $\lambda_{\rm PQ} \in \{0, 0.1, 1\}$. Horizontal red line shows Planck 2018 bounds, while orange dashed line shows forecast CMB-S4 limits. Vertical solid black line at $m_\phi \sim 200$ TeV represents BBN bound. Figure taken from [8].

A2, or **B1**. Thus, we conclude this scenario is excluded by overproduction of *both* dark matter and dark radiation, at least without additional symmetries or severe tuning which cause $\lambda_{\rm PQ} \sim 0$.

6.3.7 DM/DR production in case GK2 - the $\xi = 0$ limit

The final case we consider is case **B2-GK2** in the $\xi = 0$ limit. In Fig. (6.29), we plot dark matter production in this case. We see immediately that the $\xi = 0$ limit seems to fare better than the $\xi = 1$ limit. As the saxions can no longer decay to axion pairs, they now decay primarily to gauginos and other particles which *do* thermalize. This returns a significant fraction of the modulus energy back to

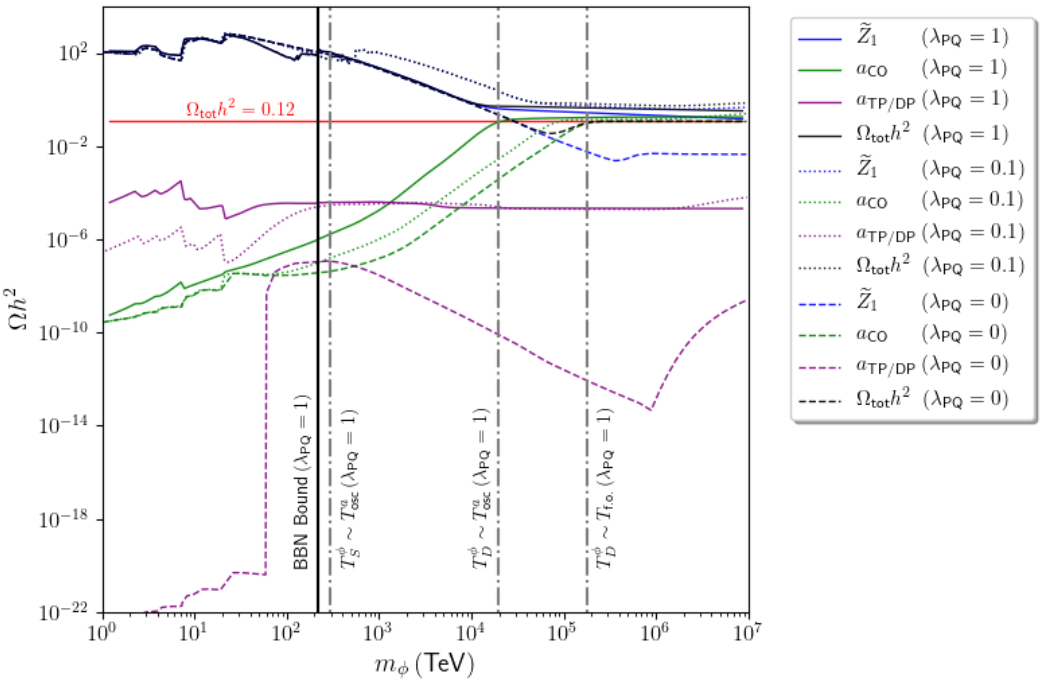


Figure 6.29: Relic densities in case **GK2** with $\xi = 0$ as a function of m_ϕ for neutralinos (blue), TP/DP axions (purple), CO axions (green), and total DM (black) for $\lambda_{\rm PQ} \in \{0, 0.1, 1\}$. Vertical dashed lines represent where $T_S^\phi \sim T_{\rm osc}^a$ ($m_\phi \sim 300$ TeV), $T_D^\phi \sim T_{\rm osc}^a$ ($m_\phi \sim 2 \times 10^4$ TeV), and $T_D^\phi \sim T_{\rm f.o.}$ ($m_\phi \sim 2 \times 10^5$ TeV). Vertical solid black line at $m_\phi \sim 200$ TeV represents BBN bound. Figure taken from [8].

the thermal bath, so that the radiation temperature is now relatively unchanged for differing $\lambda_{\rm PQ}$. We see that the CO axion relic density is still sensitive to the value of $\lambda_{\rm PQ}$ as this coupling predominantly sets the modulus decay temperature - and thus when it ceases to dilute the CO axion abundance. However, since the radiation temperature at $H(T_{\rm osc}^a)$ is now largely unaffected, the CO axions do not receive a large enhancement as in the $\xi = 1$ limit.

On the other hand, the computed relic density for the neutralinos exhibit some seemingly strange behavior at first. We see that for 500 TeV $\lesssim m_\phi \lesssim 2 \times 10^4$ TeV, the neutralino relic density for $\lambda_{\rm PQ} = 0$ and $\lambda_{\rm PQ} = 1$ overlap, while $\lambda_{\rm PQ} = 0.1$

actually yields a *higher* neutralino relic density. This is again due to the sensitive dependence of T_D^ϕ on $\lambda_{\rm PQ}$ in this scenario. For $\lambda_{\rm PQ} = 0$, the modulus decay temperature is set primarily by the (suppressed) couplings to the gauge sector - the decay to saxions and axinos is turned off. Neutralinos are then produced from modulus decay to gauginos with an abundance determined primarily by T_D^ϕ. When $\lambda_{\rm PQ} = 0.1$, the modulus decay temperature is raised but now the boosted saxions set the dominant decay scale, which is lowered due to the relativistic dilation of the saxion lifetime. Here, the net effect is that neutralinos are then produced at a lower scale than for $\lambda_{\rm PQ} = 0$ - leading to the enhancement we see in the plot. However, for $\lambda_{\rm PQ} = 1$ the relativistic dilation factor of the saxion for a given m_ϕ is unchanged, but the modulus decays at a temperature a full order of magnitude larger than for $\lambda_{\rm PQ} = 0.1$. This then roughly reduces the neutralino abundance by an order of magnitude, which is precisely what we see in Fig. (6.29). The overlapping of the $\lambda_{\rm PQ} = 0$ and $\lambda_{\rm PQ} = 1$ cases are then coincidental. This effect was obscured in the $\xi = 1$ limit due to the excessive production of dark radiation, which raises the modulus abundance yield Y_ϕ when it decays due to the lower radiation temperature.

In Fig. (6.30), within the BBN-safe region for $\lambda_{\rm PQ} = 0.1$ and $\lambda_{\rm PQ} = 1$ we see that dark radiation is produced at a level around 2 orders of magnitude above the Planck 2018 limit. Although less extreme, this is similar to the $\xi = 1$ limit of the **GK2** case - dark radiation excludes this case unless fine-tuning or additional symmetries are introduced which we do not consider here.

If we were to instead consider cases **A1** and **A2**, the addition of unsuppressed

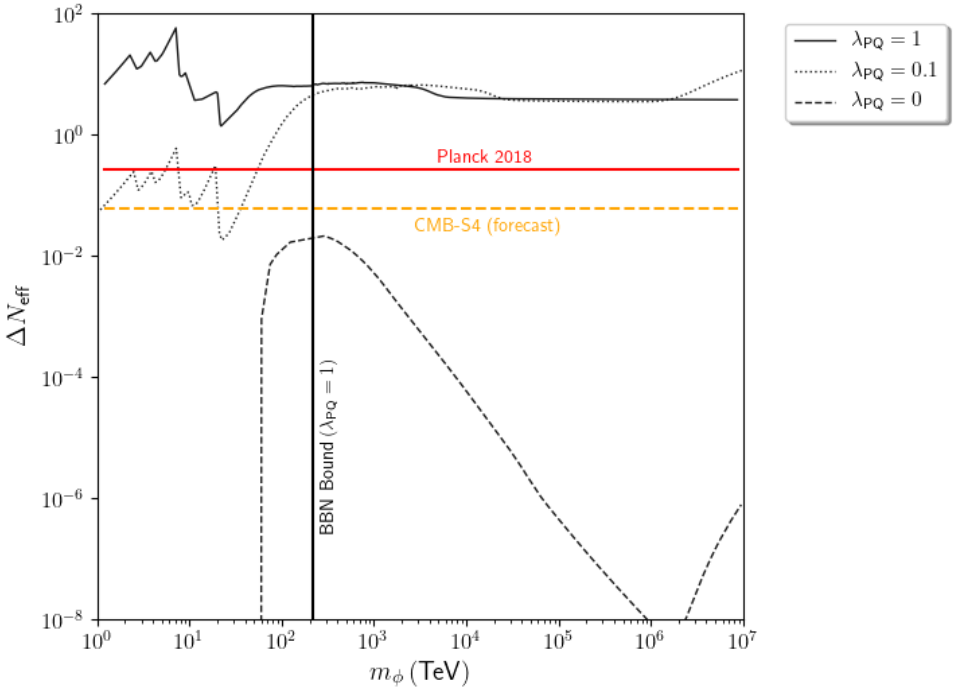


Figure 6.30: Dark radiation production in case **GK2** with $\xi = 0$ as a function of m_ϕ for $\lambda_{\rm PQ} \in \{0, 0.1, 1\}$. Horizontal red line shows Planck 2018 bounds, while orange dashed line shows forecast CMB-S4 limits. Vertical solid black line at $m_\phi \sim 200$ TeV represents BBN bound. Figure taken from [8].

axino decays and gaugino decays (although still suppressed by a loop factor here) will reduce the production of dark radiation since it reduces the effective modulus branching ratio into axions. However, we would then only expect the modulus branching ratio into axions to be reduced from roughly 50% to 33% in this case. Considering that case **B2-GK1** in the $\xi = 0$ limit produced dark radiation at a level close to Planck 2018 bounds with an effective modulus-to-axion branching ratio of roughly $5\% - 10\%$ (as seen from Fig. (4.13)), it is unlikely that the additional decay modes would lower the produced dark radiation to a level consistent with current experimental bounds in this scenario. Furthermore, the boosted axinos would likely contribute an enhancement to the neutralino dark

matter content, leaving the limiting case of $\lambda_{\rm PQ} = 0$ as the only potentially viable case (albeit, at the cost of introducing fine-tuning or additional symmetries). Given the additional constraints on the inflationary Hubble scale H_I and the PQ scale f_a from consistency arguments for large values of m_ϕ, we expect that this case may also be excluded simply by considering consistency in tandem with the DD/ID bounds.

6.3.8 The allowed PQ parameter space

In this section, we abandon the PQ benchmark parameters from Table (4.6) and instead study the production of dark matter and dark radiation as a function of the expected ranges of the PQ parameters. Here, we focus on case **B2-GK1** in the $\xi = 1$ limit for two reasons. The first reason is that although ξ is a model-dependent parameter, generically it is expected to be close to 1 [290]. Since the **GK2** cases are effectively ruled out from dark radiation considerations, this leaves us with case **GK1** in the $\xi = 1$ limit. The second is for consistency reasons: the $\xi = 1$ limit produces a smaller amount of neutralino dark matter than the $\xi = 0$ limit - allowing for easier realization of the required hierarchy $f_a > H_I/2\pi > m_\phi/2\pi$.

Before we delve too deeply, let us first discuss the expected ranges of our parameters which we list in Table (6.1). Of course, we expect the initial misalignment angle of the axion to be in the interval $\theta_i \in [0, \pi)$. We do not make the lack of tuning θ_i a requirement here, but we will discuss this as it pertains to our results later. The axion decay constant is expected to have a lower bound from supernova

cooling [414, 415], which indicate that $f_a \gtrsim 10^9$ GeV. However, too large of f_a tends to overproduce CO axion dark matter unless θ_i is tuned close to 0 - we therefore focus on $f_a \lesssim 3 \times 10^{13}$ GeV. We also take here the axino and saxion masses to be roughly of order of the soft terms, $m_s \sim m_{\tilde{a}} \sim \mathcal{O}(1-30)$ TeV. Additionally, given the uncertainty in the modulus couplings to matter fields we scan over the λ_i as well. Since these couplings are generically expected to be $\lambda_i \sim \mathcal{O}(1)$, we take the range to be within an order of magnitude so that $\lambda_i \in [0.1, 10]$. Furthermore, the modulus couplings are taken to be unified in the sense of what one would expect for the NUHM3 model - e.g. we take unified couplings to first and second generations of lepton superfields $\lambda_{L_1} = \lambda_{L_2} = \lambda_{E_1} = \lambda_{E_2}$, while third generation lepton superfields are unified to a *different* randomly assigned value $\lambda_{L_3} = \lambda_{E_3}$, and similarly for the quarks. The two Higgs couplings, λ_{H_u} and λ_{H_d}, are then taken to be independent as are the gravitino and PQ sector couplings. Finally, the couplings to the gauge sector are also taken to be unified and randomly assigned within the range defined in Table (6.1). Given our ignorance of the underlying parameter set, this allows us to make some rather general statements for this model.

parameter	PQ
m_s	[1 TeV, 30 TeV]
$m_{\tilde{a}}$	[1 TeV, 30 TeV]
f_a	[10^9 GeV, 3×10^{13} GeV]
θ_i	$[0, \pi)$
λ_i	$[0.1, 10]$

Table 6.1: Parameter bounds for scanning PQ parameter space.

For our first scan, we fix $m_\phi = 5 \times 10^5$ TeV. From our results in Sec. (6.3.4),

we expect an m_ϕ this large should be able to produce neutralino relic densities that satisfy the DD/ID constraints on WIMPs, which for our natural SUSY benchmark model requires $\Omega_{\widetilde{Z}_1}h^2 \lesssim 0.012$. In Fig. (6.31), we display the scan

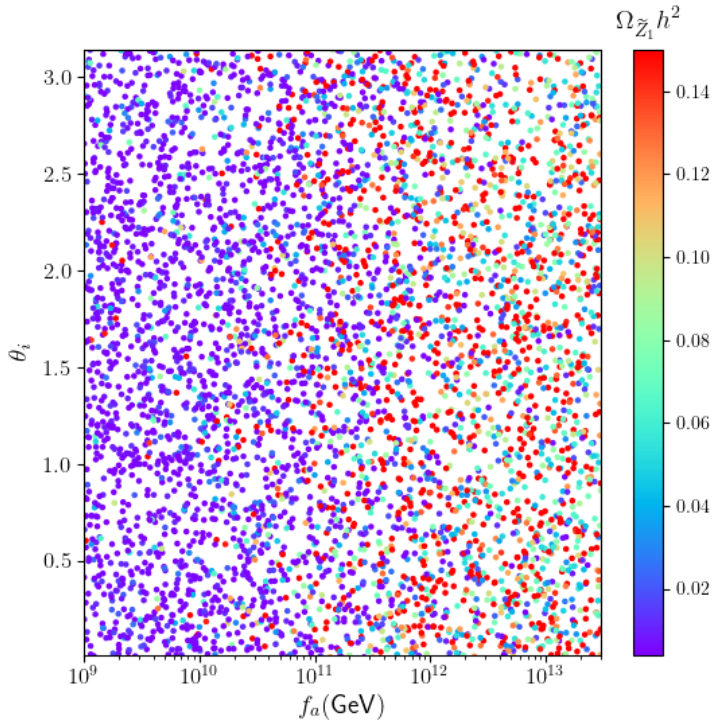


Figure 6.31: Neutralino relic density from scanning PQ parameter space f_a, θ_i, m_s, $m_{\tilde{a}}$, and all modulus couplings λ_i as given in Table (6.1). Here, we fix $m_\phi = 5 \times 10^5$ TeV and assume the **B2-GK1** case with $\xi = 1$. Red points are in excess of measured dark matter relic density, $\Omega_{\widetilde{Z}_1}h^2 \gtrsim \Omega_{\text{meas.}}h^2 \sim 0.12$. Purple and dark blue points are close to the thermal value and can satisfy DD/ID constraints. Figure taken from [8].

results which show the computed relic density for the neutralinos in the (f_a, θ_i) plane. We see that, in general, increasing the PQ scale f_a translates to a larger WIMP abundance as denoted by the color schema. This can be understood by noting that the saxion lifetime in the $\xi = 1$ case is primarily controlled by f_a - the (dominant) decay width to axions is proportional to m_s^3/f_a^2 [285], so that

an increase in f_a produces an increase in the saxion lifetime - thus leading to an enhancement in the neutralino abundance. The red points then oversaturate the observed dark matter abundance, $\Omega_{\text{meas.}}h^2 \sim 0.12$, which occur frequently for $f_a \gtrsim 10^{11}$. Due to the other random parameters in our scan, we see that a large f_a does not necessarily exclude points with very low neutralino relic abundance, although they become more rare. Conversely, we also see some red points in the region $f_a \sim 10^{9-10}$ GeV. Although the mass of the saxions and axinos plays a role in this aspect of the distribution, the primary source for these is the ratio of the leading couplings, $\lambda_{\text{gauge}}/\lambda_{\text{PQ}}$. If the (unified) couplings to the gauge sector are generated towards the top of the scan interval, $\lambda_{\text{gauge}} \sim 10$, while the coupling to the PQ sector is generated towards the bottom, $\lambda_{\text{PQ}} \sim 0.1$, the modulus both decays earlier and produces fewer saxions leading to a substantial reduction in the neutralino relic density. Similarly, if the couplings to the gauge sector are generated quite low, $\lambda_{\text{gauge}} \sim 0.1$, while the coupling to the PQ sector is generated much higher, the modulus will decay later and produce more saxions which cascade decay into neutralinos, producing a higher relic density. Additionally, we note that it is not impossible to find points with $f_a \gtrsim 10^{13}$ GeV which not only satisfy the measured dark matter relic density bound, but also satisfy the DD/ID constraints which are shown by purple or dark blue points. It is perhaps not surprising that θ_i seems to make no effect on the neutralino relic density - although it *does* make a significant difference to the CO axion energy density which we will see shortly, the axion energy density $\rho_{a_{\text{CO}}}$ is never large enough in this case to change the Hubble scale beyond the sub-percent level (and, of course, the CO axions are

effectively decoupled from all other components we consider here outside of any potential impact on the Hubble scale).

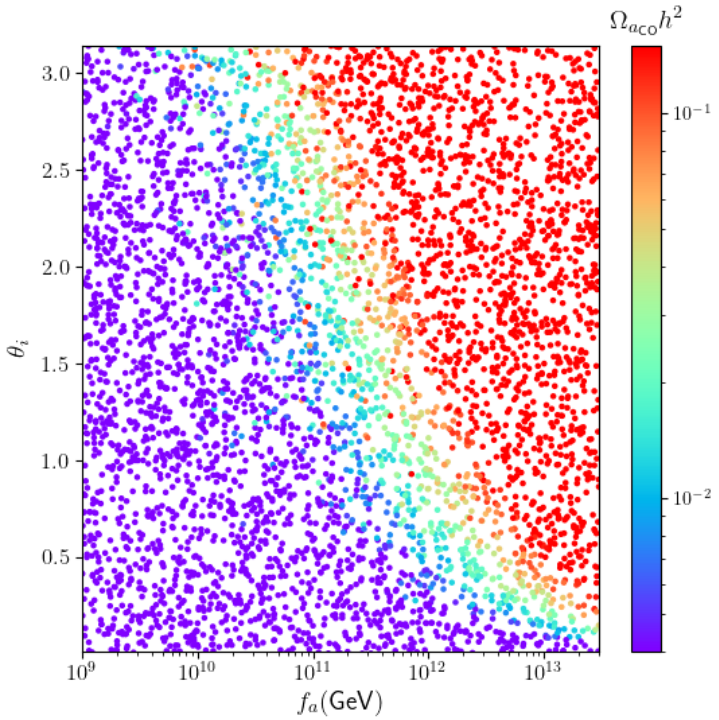


Figure 6.32: CO-produced axion relic density from scanning PQ parameter space f_a, θ_i, m_s, $m_{\widetilde{a}}$, and all modulus couplings λ_i as given in Table (6.1). Here, we fix $m_\phi = 5\times10^5$ TeV and assume the **B2-GK1** case with $\xi = 1$. Red points are in excess of measured dark matter relic density, $\Omega_{a_{\rm CO}}h^2 \gtrsim \Omega_{\rm meas.}h^2 \sim 0.12$. Note the color schema here is logarithmic. Figure taken from [8].

We show the scan results for the axion relic density in the (f_a, θ_i) plane in Fig. (6.32). The axion relic density is extremely sensitive to both parameters, so we adopt here a logarithmic color scale indicating the relic density. Between 5×10^{10} GeV $\lesssim f_a \lesssim 10^{13}$ GeV, we see a distinct predictive band that separates the region where axion dark matter is overproduced (red points) from the region where axion dark matter is extremely underproduced (purple and dark blue points). We also see that the axion relic density is far less sensitive to the other random

parameters (i.e. the saxion and axino masses and the modulus couplings) than the neutralino relic density is. Of course, there are a few overproduced points in the generically underproduced region. These are again determined from the ratio of $\lambda_{\rm gauge}/\lambda_{\rm PQ}$ - if $\lambda_{\rm gauge}$ is small while $\lambda_{\rm PQ}$ is large, most of the modulus energy density goes to the TP/DP axion population (which behaves primarily as dark radiation) thus decreasing the radiation temperature. This leads to an enhancement in the CO axion much like we saw in Sec. (6.3.6). However, these red points then overproduce dark radiation - and are thus excluded from both DM and DR considerations.

Now that we have a small understanding of the parameter space of PQ parameters, we repeat the scan for $m_\phi \in \{5\times 10^4,\, 1\times 10^5,\, 5\times 10^5\}$ TeV. Our aim here is to show the allowed PQ parameter space as m_ϕ increases, while also incorporating the uncertainties in the values of the PQ parameters as indicated by our scan limits in Table (6.1). In Fig. (6.33), we display these contours for each m_ϕ which 1. roughly saturate total dark matter by imposing $0.09 \leq \Omega_{\rm total}h^2 \leq 0.125$, 2. produce neutralinos at a level consistent DD/ID constraints so that $\Omega_{\widetilde{Z}_1}h^2 \leq 0.1\Omega_{\rm meas.}h^2 \sim 0.012$, and 3. do not overproduce dark radiation - i.e. $\Delta N_{\rm eff} \leq 0.26$. In order to have sufficient efficiency to draw sensible contours, we utilize our understanding of the parameter space from Figs. (6.31) and (6.32) to target regions of (f_a, θ_i) where we expect points that meet these criteria to live. The large f_a and small θ_i regime is particularly low efficiency; as we have seen from Fig. (6.31), a large majority of this section of parameter space overproduces neutralinos due to the enhanced saxion lifetime. In all targeted regions, we have

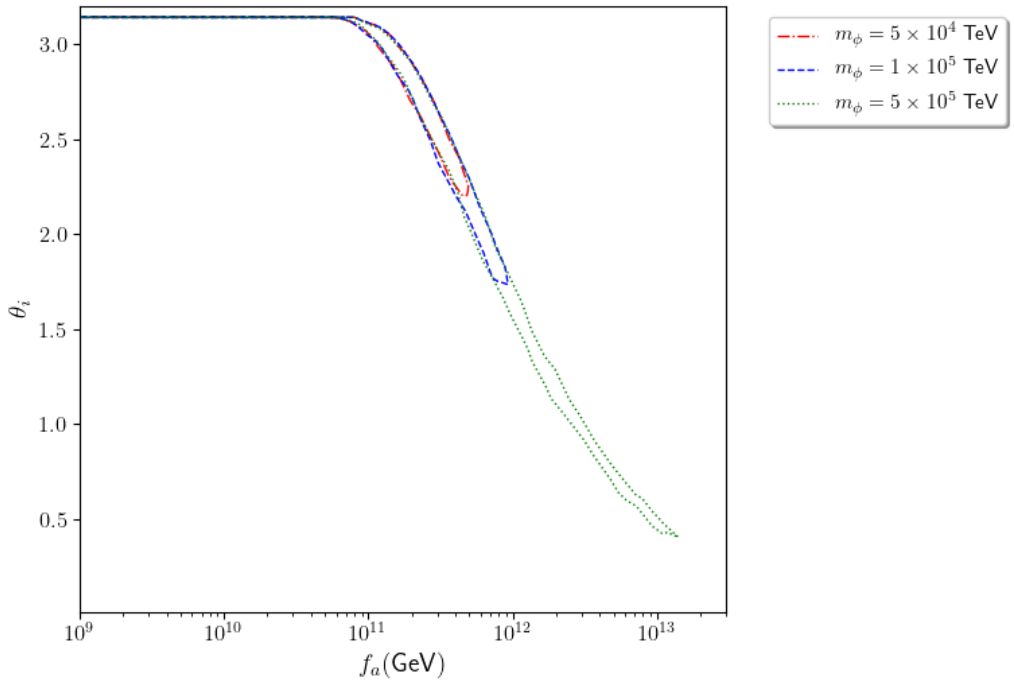


Figure 6.33: Contours of allowed PQ parameter space for given values of m_ϕ in case **B2-GK1** in the $\xi = 1$ limit. Interior regions satisfy $0.09 \leq \Omega_{\rm total}h^2 \leq 0.125$, $\Delta N_{\rm eff} \leq 0.26$, and satisfy DD/ID bounds which are $\Omega_{\widetilde{Z}_1}h^2 \lesssim 0.1\Omega_{meas.}h^2$ for our natural SUSY benchmark point. Here, we take random values of f_a, θ_i, m_s, $m_{\widetilde{a}}$, and all modulus couplings λ_i as given in Table (6.1). Figure taken from [8].

checked that our bounds extend past the contours which gives us confidence in their accuracy. We see that for $m_\phi = 5 \times 10^4$ TeV, only $f_a \lesssim 5 \times 10^{11}$ GeV and $\theta_i \gtrsim 2.2$ is allowed - with the enhancement due to late modulus-to-saxion-to-WIMP cascade decay overproducing neutralinos for larger f_a. As m_ϕ increases to 1×10^5 TeV, its decay temperature has decreased so that now a larger portion of parameter space is allowed: $f_a \lesssim 10^{12}$ GeV and $\theta_i \gtrsim 1.7$. For our largest $m_\phi = 5 \times 10^5$ TeV, we see that a significant portion of the parameter space has opened up, allowing $f_a \lesssim 1 - 2 \times 10^{13}$ GeV and $\theta_i \gtrsim 0.4$. We can also

understand this from referring back to Fig. (6.21) - at $m_\phi \sim 5 \times 10^5$ TeV, the neutralino relic density relaxes close to its thermal value for $\lambda_{\rm PQ} = 0.1$. Thus, we expect points that lie in the large f_a region to have a large $\lambda_{\rm gauge}/\lambda_{\rm PQ}$ ratio within the allowed λ_i scan limits. For smaller values of $f_a \lesssim 8 \times 10^{10}$ GeV, dark matter is typically underproduced - so tuning $\theta_i \sim \pi$ can increase the CO axion's relic density enough through anharmonic effects [391] to saturate the measured value without violating our other constraints. Although we display this value in Fig. (6.33) since it does meet our criteria, the plausibility of such a tuning is rather questionable. We expect larger values of m_ϕ to then exhibit a similar parameter space to $m_\phi = 5 \times 10^5$ TeV, although if $m_\phi \gg 10^{6-7}$ TeV the consistency of this scenario ($f_a > H_I/2\pi > m_\phi$) will exclude lower values of f_a.

It is also worth mentioning that most of the parameter space to the below-left of the contours in Fig. (6.33) are not necessarily excluded. This region, as can also be seen from Figs. (6.31) and (6.32), drastically *underproduces* the total dark matter content although does not generically violate either $\Delta N_{\rm eff}$ or $\Omega_{\widetilde{Z}_1}$ constraints. Thus, this DM-underabundant region can be incorporated into other models which introduce some other primary source of dark matter - such as primordial black holes or possibly other string remnants. We do not consider such cases in this work, but simply note that these cases are not inherently mutually exclusive.

6.3.9 Dependence on inflationary reheating temperature T_R

In a standard thermal history, the inflationary reheating temperature can have a major impact on the abundances of relics present in the late-time cosmology. As we have previously discussed, thermally-produced gravitinos (which do not annihilate efficiently) can be drastically overproduced if $T_R \gtrsim 10^{5-9}$ GeV (depending on model details) [381, 416, 227, 380, 393]. However, the significant entropy released from moduli decay is expected to dilute all thermal relics to negligible quantities. In the early matter dominated framework that is generic with moduli, we then expect that there is no dependence on the inflationary reheating temperature.[1]

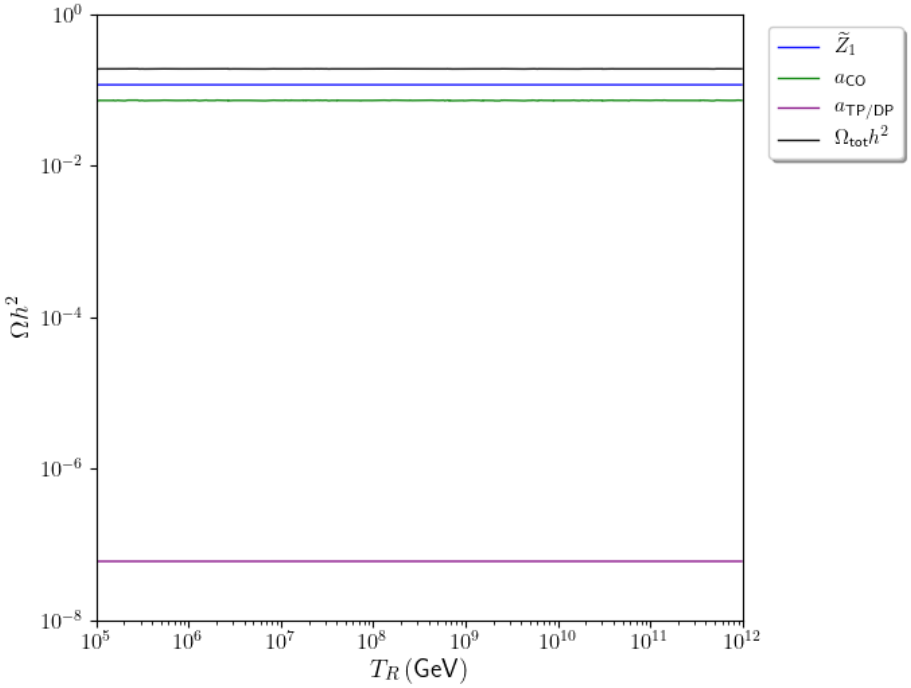


Figure 6.34: Dependence of results on inflationary reheating temperature T_R in case **B2-GK1**. Here, we fix $m_\phi = 5 \times 10^3$ TeV and take $\lambda_{\mathrm{PQ}} = 0.2$, with all other $\lambda_i = 1$. Figure taken from [8].

[1] Of course, as we assume throughout this work, this relies on the assumption that the details of inflationary reheating effectively decouple from the details of the light modulus.

In Fig. (6.34), we plot the produced dark matter abundances as a function of $T_R \in [10^5 \text{ GeV}, 10^{12} \text{ GeV}]$. Here, we fix $m_\phi = 5 \times 10^3$ TeV and take $\lambda_{\rm PQ} = 0.2$ in case **B2-GK1**, with all other allowed modulus couplings set to unity. It is readily apparent that the inflationary reheating temperature plays effectively no role in the late-time cosmology here. Similarly, from the same data set we find that the produced dark radiation $\Delta N_{\rm eff}$ is unchanged, although we do not display this plot in the interest of brevity. Thus, our results from numerical solutions of the Boltzmann equations agrees exceedingly well with our expectations.

6.3.10 Dependence on modulus initial amplitude ϕ_0

In this section, we investigate the dependence of our results in the ϕPQMSSM on the value of the modulus misalignment amplitude ϕ_0. In Fig. (6.35), we display the relic densities for neutralinos and both TP/DP axions and CO axions for $\phi_0/m_P \in [10^{-8}, \sqrt{2/3}]$ so that again we have a radiation-dominated universe at T_R. Here, we again take $m_\phi = 100$ TeV and $T_R = 10^8$ GeV to illustrate the transition between a severely modulus-dominated cosmology to a viable thermal cosmology. Similarly to the **B1-GK1** case we studied in the ϕMSSM, we see that the neutralino relic density is virtually unaffected by the displacement amplitude until $\phi_0/m_P \sim 10^{-5}$, and in order to produce a WIMP relic density below the (total) observed value requires $\phi_0/m_P \lesssim 10^{-6}$. We see that the TP/DP axions also are virtually unaffected by the precise value of the amplitude until the modulus is diluted near $\phi_0/m_P \sim 10^{-5}$. At this point, the relic density of the TP/DP axions decreases extremely rapidly as the modulus is now too dilute

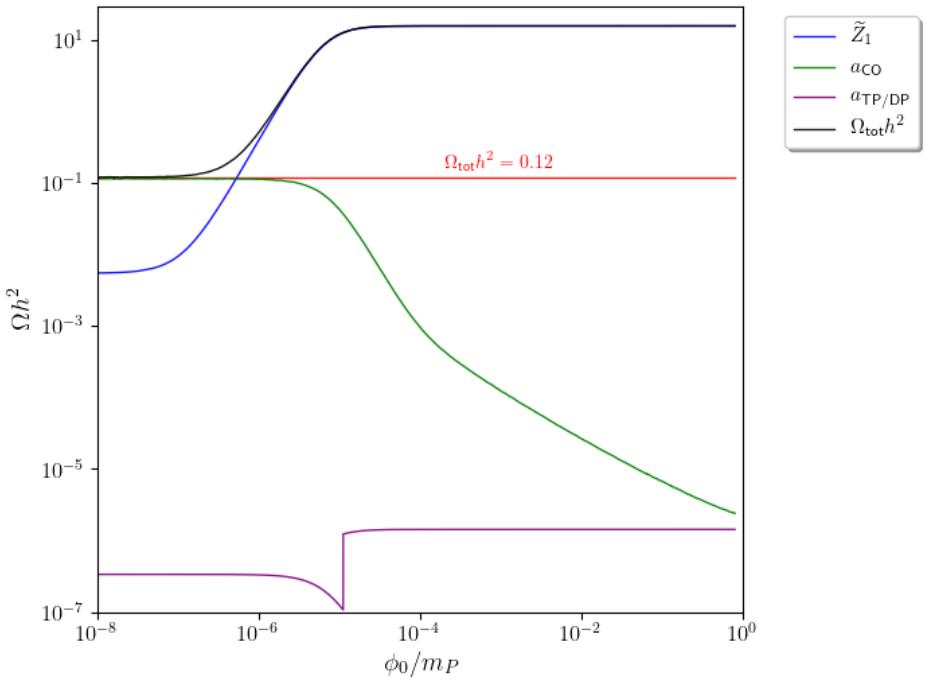


Figure 6.35: Relic densities in the ϕPQMSSM as a function of the displacement amplitude ϕ_0/m_P. Here, we take case **B2-GK1** with all $\lambda_i = 1$ and $\xi = 1$. Additionally, we set $m_\phi = 100$ TeV, $m_s = m_{\widetilde{a}} = 5$ TeV, $f_a = s_i = 10^{11}$ GeV, and take $T_R = 10^8$ GeV. Figure taken from [8].

to contribute significantly to dark radiation - marking the transition between a modulus-dominated cosmology and a radiation-dominated one. For $\phi_0/m_P \lesssim 10^{-5}$, we see that then the modulus entropy dilution effectively vanishes thus leaving the thermal axions produced after inflationary reheating as dark radiation. Finally, we see that the CO axions are the only DM relic that appears sensitive to the amplitude - being critically dependent on the entropy dilution produced from the modulus. We again find that $\phi_0/m_P \lesssim 10^{-7}$ is required to decouple the modulus and provide a viable cosmology in this case.

6.3.11 Some general comments on the ϕPQMSSM

As we have just seen, the **B2-GK2** cases appear to be excluded by dark radiation constraints for the ϕPQMSSM in both the $\xi = 0$ and $\xi = 1$ limits. We also do not expect the addition of unsuppressed axinos and gauginos in case **A2-GK2** nor the addition of unsuppressed gravitinos in cases **A1-GK2** and **B1-GK2** to sufficiently reduce the modulus branching ratio to axions. It may be possible to realize this case if additional symmetries or model-building features are considered that can provide a reasonable explanation for decoupling of the axions - quite likely also decoupling the saxions, which tend to overproduce neutralino dark matter by a large factor in the **GK2** case. However, such additional features should also come with sufficient motivation to warrant their presence other than simply evading current experimental bounds. Without additional model-dependent features, it appears that realizing the ϕPQMSSM in the standard natural SUSY model-building practice of Type IIb models - i.e. confining the matter fields to $D3$ branes at singularities - will be excluded from experimental constraints.

The **B2-GK1** case fairs much better - although Planck 2018 results may be at slight tension with the largest value of the coupling $\lambda_{\rm PQ}$, much of the relevant parameter space will be probed by the upcoming CMB-S4 experiment. Additionally, it appears from neutralino relic density considerations that an extremely massive modulus - more so than the ϕMSSM - is required to successfully realize this case: $m_\phi \gtrsim 10^5$ TeV in the $\xi = 1$ limit, and even larger in the $\xi = 0$ limit. We expect similar results in case **A2-GK1**, although the addition of

unsuppressed axino decays (which are slightly longer lived than the saxions) may further enhance the neutralino relic density, pushing the lowest viable m_ϕ slightly higher. On the other hand, cases **B1-GK1** and **A1-GK1** are expected to suffer from the same moduli-induced gravitino problem as we saw in the ϕMSSM - requiring an extremely massive gravitino which is difficult to realize in unsequestered scenarios. This suggests that our ϕPQMSSM model may be more easily realized in heterotic or M-theoretic constructions - particularly if sequestering is possible - than in Type IIb constructions.

Finally, we also note that our consistency conditions for this scenario ($f_a > H_I/2\pi > m_\phi$) require a higher scale of inflation, especially for the $\xi = 0$ limit. We must then consider isocurvature constraints for the ϕPQMSSM. Based on Planck 2018 results [417], isocurvature constraints require [405]

$$H_I \lesssim 1.4 \times 10^{-5}\, f_a \theta_i. \tag{6.2}$$

Clearly, the $\xi = 0$ limit in the **GK1** cases requires too large of an inflationary scale to be compatible with these bounds. The $\xi = 1$ limit, however, may still be viable - although our benchmark point runs into mild tension with these results, it is possible that similar benchmark points may be compatible with these constraints depending on the precise neutralino annihilation cross section. Although we leave a precise investigation of isocurvature constraints for the $\xi = 1$ limit for future work, it appears that all **GK2** cases and $\xi = 0$ cases are excluded, leaving only the **GK1** cases in the $\xi = 1$ limit. Of course, these results may also suggest

that the standard thermal cosmological history could be preferred such that the inflationary scale is lower than the lightest modulus mass, and all light moduli are inflated away. In this case, the results from e.g. [300, 285] seem far more optimistic in terms of dark matter and dark radiation production.

We can also relate our results for the ϕPQMSSM to one particular aspect of dark matter structure formation. In [418, 419] it was argued that in early matter domination scenarios (such as modulus domination), axion miniclusters with masses of roughly $\mathcal{O}(10^{-13} - 10^{-18})$ times the solar mass can form in the case that PQ symmetry breaking occurs before the end of inflation. This is because perturbations grow linearly in a matter-dominated background, while only logarithmically in a radiation-dominated background [407]. Prior to BBN, small k-modes re-enter the horizon and - if axion oscillations overlap with modulus-domination - these perturbations can become enhanced. However, based on our study of dark matter production in the ϕPQMSSM, we saw that neutralino dark matter is always overproduced - usually by a few orders of magnitude - in the regime where this enhancement is possible. Thus, we do not expect the presence of these axion miniclusters in the ϕPQMSSM.

Chapter 7

Inflation and phenomenology in fibred LVS models

In our final exposition, we shift focus to a specific string construction - that of fibred LVS. One of the many features of string theory is the plethora of light fields which may be good inflaton candidates. Here, we focus on the class of LVS models where the inflaton is one of the Kähler moduli. We first review Kähler moduli inflation - also known as blow-up inflation - in the "minimal" LVS framework that we illustrated in Sec. (2.3.3), where the blow-up moduli appear as natural inflaton candidates due to their extremely flat potential. We then describe the generalization in the fibred LVS framework, where inflation again is driven by a blow-up modulus. Within the fibred LVS framework however, there is one additional flat direction which provides an additional inflaton candidate leading to the scenario known as fibre inflation. In both Kähler moduli inflation and fibre inflation, previous works have fit the available parameters to cosmological observables in the simplest scenarios - here we use these results to study the phenomenology which emerges.

7.1 Blow-up/Kähler inflation in LVS

As we saw in Sec. (2.3.3), the blow-up Kähler moduli - which are stabilized by non-perturbative corrections to the superpotential - have a remarkably flat potential. This particular class of moduli thus make natural inflaton candidates,

and the corresponding inflationary models are referred to as blow-up inflation, Kähler moduli inflation, or simply Kähler inflation [420]. The simplest realization of this model requires $h^{1,1} \geq 3$, with a volume of the form

$$\mathcal{V} = \alpha \left(\tau_b^{3/2} - \lambda_\phi \tau_\phi^{3/2} - \lambda_s \tau_s^{3/2} \right) \tag{7.1}$$

and the assumed hierarchy $\tau_b \gg \tau_\phi \gg \tau_s$. Here, τ_ϕ takes the role of the inflaton and τ_s is required so that the volume mode τ_b (and hence the volume $\mathcal{V}$) is stabilized during inflation, thus maintaining the flatness of the inflaton potential [420]. Once τ_s and τ_b are integrated out, the inflationary potential is given schematically by Eq. (2.73) after the substitution $\tau_s \to \tau_\phi$. In terms of the canonically normalized inflaton ϕ, this potential then takes the schematic form [99]

$$V \simeq V_0 \left(1 - c_1 \mathcal{V}^{5/3} \phi^{4/3} \exp\left[-c_2 \mathcal{V}^{2/3} \phi^{4/3} \right] \right) \tag{7.2}$$

where $V_0 \equiv \mathcal{O}(1) \times W_0^2 \, \xi \, \mathcal{V}^{-3}$ sets the overall scale of the inflationary potential, and $c_1 \equiv \mathcal{O}(1) \times \xi^{-1}$ and $c_2 \equiv \mathcal{O}(1) \times a_\phi$ are set by the details of the perturbative and non-perturbative corrections, although are still expected to be $\mathcal{O}(1)$ parameters.

However, once g_s corrections are taken into account the situation appears to change drastically. The corrections to the potential in terms of the canonically normalized inflaton are conjectured to be [421, 422]

$$\delta V_{g_s} \sim \frac{1}{\phi^{2/3} \, \mathcal{V}^{10/3}}. \tag{7.3}$$

Since this correction is not exponentially suppressed as in Eq. (7.2), this may destroy the flatness of the potential which is required for successful inflation. Indeed, the slow-roll parameter η should receive a correction

$$\delta\eta \sim \frac{\delta V''_{g_s}}{V_0} \sim \frac{1}{\phi^{8/3}\,\mathcal{V}^{1/3}} \sim a_\phi^2 \frac{\mathcal{V}}{(\log \mathcal{V})^2} \gg 1 \tag{7.4}$$

and we are lead to the conclusion that blow-up inflation has a severe η-problem once g_s corrections are considered. However, it is pointed out in [423, 99] this problem can be avoided depending on the brane configuration - e.g. if only $D3$ branes wrap the inflationary cycle instead of $D7$ branes, these g_s corrections may be absent or subdominant while the desired non-perturbative effects in the superpotential are still generated [9].

7.2 Inflation in fibred LVS

In the previous section, we saw that the inclusion of g_s corrections can - depending on the brane configuration - lead to a serious η-problem. The same g_s corrections that may induce the η-problem in Kähler inflation can themselves provide a viable inflationary potential in fibred LVS models. This class of inflationary models are collectively referred to as fibre inflation [9]. Before we discuss inflation and its connections to dark matter and dark radiation phenomenology in fibred LVS models, we first review the fibred LVS framework.

The fibred LVS framework is similar to the (minimal) LVS framework we have detailed in Sec. (2.3.3) - with the key difference that the bulk volume is

determined by two moduli. Specifically, the geometry is that of a $K3$ fibration over a $\mathbb{P}^1$ base, which in terms of the two-cycle moduli takes the form [424, 425]

$$\mathcal{V} = \frac{1}{6}\int_{\mathrm{CY}} J \wedge J \wedge J = \frac{1}{6}\left(3\kappa_{122}t_1 t_2^2 - \sum_{i=3}^{h^{1,1}_+}\kappa_{iii}t_i^3\right) \tag{7.5}$$

where t_1 is the volume of the base, t_2^2 is the volume of the fibre, and t_i are blow-up modes, while the integers κ_{122} and κ_{iii} are the intersection numbers of the Calabi-Yau manifold. This volume can straightforwardly be rewritten in terms of the 4-cycle moduli (see e.g. [359]):

$$\mathcal{V} \simeq \alpha\left(\sqrt{\tau_1}\tau_2 - \sum_{i=3}^{h^{1,1}_+}\gamma_i\tau_i^{3/2}\right) \tag{7.6}$$

where $\alpha = 1/\sqrt{2\kappa_{122}}$ and $\lambda_i = \frac{2}{3}\sqrt{\kappa_{122}/\kappa_{iii}}$. Focusing on the case where $h^{1,1}_+ = 3$ and absorbing any geometrical prefactors into the moduli, this takes the simple form

$$\mathcal{V} = \sqrt{\tau_1}\tau_2 - \tau_3^{3/2}. \tag{7.7}$$

The assumed hierarchy $\tau_2 \gtrsim \tau_1 \gg \tau_3$ ensures the validity of the effective field theory, and allows us to neglect the non-perturbative corrections to τ_1 and τ_2. In this case, similar to Eq. (2.70) the superpotential takes the form

$$W \simeq W_0 + A_3 e^{-a_3 T_3} \tag{7.8}$$

where $T_i = \tau_i + i\,c_i$ are the complexified Kähler moduli, and c_i are the ALPs which

arise from dimensional reduction of the 10d RR 4-form C_4 on the corresponding divisor.

The Kähler potential takes a similar form as to Eq. (2.71) in minimal LVS with one subtlety. In minimal LVS, we saw in Sec. (2.3.3) that the blow-up moduli are stabilized by non-perturbative effects, and the volume (or bulk) modulus is stabilized by the α' corrections in the Kähler potential. In fibred LVS, while the volume can be stabilized similar to minimal LVS, one of the two bulk moduli will remain unstabilized, i.e. a flat direction remains. This flat direction can be lifted by also incorporating g_s corrections in the Kähler potential. Following the procedure of [359, 10], we utilize a perturbative expansion of the Kähler potential incorporating both α' [426] and g_s [421, 422, 427] corrections, which reads

$$\begin{aligned} K_{\text{tree}} &= -2\log\mathcal{V} \\ K_{\alpha'} &= -\frac{\hat{\xi}}{g_s^{3/2}\mathcal{V}} \\ K_{g_s} &= g_s\sum_i \frac{c^i_{g_s}t_i}{\mathcal{V}} \\ K &= K_{\text{tree}} + K_{\alpha'} + K_{g_s} \end{aligned} \tag{7.9}$$

where $c^i_{g_s}$ are $\mathcal{O}(1)$ coefficients for each of the 2-cycle moduli, t_i. These coefficients are dependent on the complex structure moduli, and can be regarded as tunable parameters in the string landscape [359]. Perhaps unsurprisingly, the scalar potential at order $\mathcal{O}(\mathcal{V}^{-3})$ is identical to Eq. (2.73), while the additional K_{g_s} corrections induce corrections to the scalar potential at order $\mathcal{O}(\mathcal{V}^{-10/3})$ which

are given by the schematic form [359]

$$V_{\mathcal{O}(\mathcal{V}^{-10/3})} \simeq \left(g_s^2 \frac{A}{\tau_1^2} - \frac{B}{\mathcal{V}\sqrt{\tau_1}} + g_s^2 \frac{C\tau_1}{\mathcal{V}^2} \right) \frac{W_0^2}{\mathcal{V}^2} \tag{7.10}$$

where A, B, C are parameters that depend on the $c^i_{g_s}$ coefficients. The stabilization of moduli is now entirely analogous to the procedure illustrated in Sec. (2.3.3), with stabilization occurring at

$$\langle \tau_1 \rangle \simeq g_s^{4/3} \lambda \langle \mathcal{V} \rangle^{2/3}, \quad \langle \tau_2 \rangle \simeq g_s^{-2/3} \lambda^{-1/2} \langle \mathcal{V} \rangle^{2/3}, \quad \langle \tau_3 \rangle \simeq \left(\frac{\hat{\xi}}{2} \right)^{2/3} g_s^{-1} \tag{7.11}$$

where $\lambda \equiv (4A/B)^{2/3}$ is effectively an $\mathcal{O}(1)$ tunable parameter. Consequently, the volume $\mathcal{V}$ is stabilized identically to minimal LVS at leading order, and is thus given by Eq. (2.79). The addition of dS uplifting terms may quantitatively affect these VEVs and resulting spectrum by small corrections, but the qualitative behavior will remain unchanged in our regimes of interest.

In fibre inflation, the fibre τ_1 takes the role of the inflaton with the inflationary potential set predominantly by $V_{\mathcal{O}(\mathcal{V}^{-10/3})}$. Integrating out the volume mode and the blow-up mode - whose presence keeps the volume mode stabilized during inflation, much like in Kähler inflation - the inflationary potential in terms of the canonically normalized inflaton $\phi/m_P \simeq \frac{\sqrt{3}}{2} \log \tau_1$ is given by [9, 423]

$$V_{\rm inf} \simeq \frac{\beta}{\langle \mathcal{V} \rangle^{-10/3}} \left(3 - 4 \exp\left(-\frac{\phi}{\sqrt{3} m_P} \right) + \exp\left(-\frac{4\phi}{\sqrt{3} m_P} \right) + R \exp\left(\frac{2\phi}{\sqrt{3} m_P} \right) \right) \tag{7.12}$$

where $R \sim g_s^4 \ll 1$ and $\beta \sim \mathcal{O}(1)$ which can be explicitly determined from the potential Eq. (7.11) with the stabilized values of the moduli, although the precise form is not important for this discussion. We display this potential in Fig. (7.1). From the ϕ/m_P-axis, we see that this model is a large-field inflationary model -

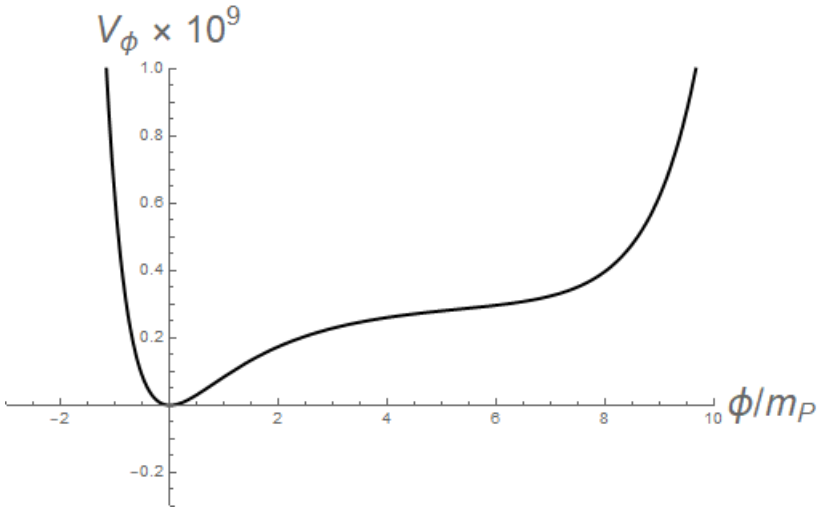


Figure 7.1: Inflationary potential in fibre inflation for canonically normalized inflaton $\phi/m_P \sim \log \tau_1$. We take $R = g_s^4$ with $g_s = 0.1$, $\beta = 1$, and $\langle \mathcal{V} \rangle = 10^3$. Figure reproduced from [9].

i.e. during inflation, ϕ traverses a distance $\Delta\phi \gtrsim m_P$ in field space (see e.g. [99]). One distinguishing feature of the fibre inflation model is - fairly independently of the underlying parameters - the prediction of detectable gravitational waves characterized by a tensor-to-scalar ratio in the range $r \sim \mathcal{O}(0.001 - 0.01)$ [9]. This range of the tensor-to-scalar ratio is expected to be probed in the upcoming CMB-S4 experiment [428], making this scenario quite attractive from a testability standpoint.

In fibred LVS models, Kähler moduli inflation can also be realized where a blow-up modulus again assumes the role of the inflaton. In both minimal

and fibred LVS, an additional blow-up mode is required to keep the inflaton stabilized during inflation. As we have already noted, the potential of the blow-up mode - and thus the details of inflation - are effectively unchanged in fibred LVS compared to minimal LVS. Unlike the fibre inflation scenario, the gravitational waves produced by Kähler inflation are extremely small: $r \lesssim \mathcal{O}(10^{-10})$ [420].

With all moduli stabilized, the characteristic fibred LVS mass spectrum can be computed straightforwardly using the standard formula $(M^2)_{ik} = K^{-1}_{ij} V_{jk}$, where K^{-1}_{ij} is the inverse Kähler metric and V_{jk} is the second derivative of the full scalar potential $V \simeq V_{\mathcal{O}(\mathcal{V}^{-3})} + V_{\mathcal{O}(\mathcal{V}^{-10/3})}$ about the minima. However, in fibred LVS models the mass matrix is not diagonal in the geometric moduli basis - the physical moduli masses are determined by the eigenvalues of the $(M^2)_{ik}$ matrix. The resulting spectrum has been calculated in e.g. [429, 430, 359, 392] and is given by

$$\begin{aligned}
m^2_{\tau_3} &\simeq m^2_{c_3} \simeq (\log\epsilon)^2 \, m^2_{3/2} > m^2_{3/2} \\
m^2_{\mathcal{V}} &\simeq \left(\frac{\epsilon}{g_s^{3/2} W_0 |\, (\log\epsilon)^3 \,|} \right) m^2_{\tau_3} \ll m^2_{\tau_3} \\
m^2_{u} &\simeq \left(\frac{\epsilon^{1/3} g_s^{5/6} |\log\epsilon|}{W_0^{1/3} \sqrt{\lambda}} \right) m^2_{\mathcal{V}} < m^2_{\mathcal{V}} \\
m^2_{c_i} &\simeq \frac{\tau_i^3}{W_0} \, e^{-\mathfrak{a}_i \tau_i} m^2_{3/2} \ll m^2_u \quad \forall i = 1, 2
\end{aligned} \tag{7.13}$$

where we have made the convenient definitions

$$\epsilon \equiv W_0/\mathcal{V} \ll 1 \quad \text{and} \quad \kappa \equiv g_s/(8\pi) \ll 1. \tag{7.14}$$

Additionally, if the visible sector is located on $D3$ branes at singularities - as we consider here - the soft gaugino masses $M_{1/2}$ can be estimated from the results of [4]:

$$M_{1/2} \simeq \frac{3\omega}{2}\frac{m_{3/2}}{\mathcal{V}}\,\tau_3^{3/2} \sim \mathcal{O}\left(\frac{m_{3/2}}{\mathcal{V}}\,(\ln\mathcal{V})^{3/2}\right) \tag{7.15}$$

where ω is dependent on the dilaton and complex structure moduli - and is thus a tunable parameter in the landscape. Incidentally, the SUSY μ term can be cast in terms of $M_{1/2}$ since both are predominantly set by the dilaton [4]. The soft scalar masses m_0 were also computed in [4] for the visible sector on $D3$ branes, which in this context depend on the level of sequestering. The physical (normalized) Yukawa couplings $\hat{Y}_{\alpha\beta\gamma}$ take the following form in terms of the holomorphic Yukawa couplings [431, 371]

$$\hat{Y}_{\alpha\beta\gamma} = e^{K/2}\frac{Y_{\alpha\beta\gamma}(U,S)}{\sqrt{\tilde{K}_\alpha\tilde{K}_\beta\tilde{K}_\gamma}} \tag{7.16}$$

where $\tilde{K}_{\alpha,\beta,\gamma}$ are the matter Kähler metrics. If Eq. (7.16) is independent of the compactification volume $\mathcal{V}$ to *any* expansion order in $\mathcal{V}^{-1}$, we call this the *ultralocal limit*. However, if the sequestering is weaker and Eq. (7.16) is independent of the compactification volume $\mathcal{V}$ at *only leading order* in $\mathcal{V}^{-1}$, we call this the *local limit*. It was found in [4] that the soft scalar masses in each of these limits take the general form

$$m_0 \simeq \begin{cases} M_{1/2}\sqrt{\mathcal{V}} \gg M_{1/2} & \text{(local limit)} \\ \\ M_{1/2} & \text{(ultralocal limit)} \end{cases} \tag{7.17}$$

where the ultralocal limit can lead to a natural SUSY spectrum with all soft terms $\sim \mathcal{O}(1)$ TeV, while the local limit leads to a split-SUSY spectrum with light gauginos but heavy scalars $m_0 \gg \mathcal{O}(10)$ TeV. Although the deSitter uplifting will lead to quantitative deviations (such as non-universality or subleading corrections) [185, 4], this level of approximation will suffice for the following section.

7.3 Phenomenology in viable fibred LVS inflationary scenarios

We now apply the considerations of the previous section to two inflationary models in the fibred LVS framework. We begin by calculating the relevant decays of the lightest modulus. Next, we analyze the produced dark radiation due to decays into closed string axions in a generalized setting of the fibred LVS framework. Finally, we use these results to study the production of dark matter while ensuring a cosmology consistent with dark radiation constraints in both Kähler inflation and fibre inflation scenarios. In both inflationary scenarios, previous work [392, 359] has fitted the fibred LVS parameters to inflationary observables, resulting in a top-down model which is compatible with observation.

7.3.1 Moduli decays

In this section, we compute the relevant decay modes of the lightest modulus - which in fibred LVS, is the direction transverse to the volume mode. We begin by

considering a slight generalization of the volume form:

$$\mathcal{V} = \tau_1^{n_1/2} \tau_2^{n_2/2} \tag{7.18}$$

where $n_1 + n_2 = 3$ and we ignore the blow-up modulus which is irrelevant for studying the decays of the lightest modulus. This allows for quick comparison with the minimal LVS case where $n_1 = 3$ and $n_2 = 0$, while for fibred LVS we have $n_1 = 1$ and $n_2 = 2$. The Kähler potential in terms of the complexified moduli $T_i = \tau_i + ic_i$ is then given by

$$K/m_P^2 = -n_1 \log(T_1 + \overline{T}_1) - n_2 \log(T_2 + \overline{T}_2) \tag{7.19}$$

which produces the Kähler metric

$$K_{i\bar{j}} = \frac{m_P^2}{4} \begin{pmatrix} n_1/\tau_1^2 & 0 \\ 0 & n_2/\tau_2^2 \end{pmatrix}. \tag{7.20}$$

We can then rewrite the moduli kinetic terms

$$\mathcal{L}_{\text{kin.}} = K_{i\bar{j}}\, \partial_\mu T^i\, \partial^\mu \overline{T}^{\bar{j}} \supset \frac{m_P^2}{4} \frac{n_i}{\tau_i^2}\, \partial_\mu \tau_i\, \partial^\mu \tau_i \tag{7.21}$$

in canonical form by the field redefinition

$$\tau_i = \exp\left(\sqrt{\frac{2}{n_i}} \frac{\phi_i}{m_P}\right). \tag{7.22}$$

Here, ϕ_i are the redefined fields which have canonical kinetic terms - however these fields still have, in general, mass mixing. Using the results from [9], the volume mode mass eigenstate is given by

$$\phi_{\mathcal{V}}/m_P \propto \log \mathcal{V}. \tag{7.23}$$

Combining our volume expression from Eq. (7.18) and field redefinitions in Eq. (7.22), the canonical mass eigenstate of the volume mode $\phi_{\mathcal{V}}$ is given by

$$\phi_{\mathcal{V}} = \sqrt{\frac{n_1}{n_1+n_2}}\phi_1 + \sqrt{\frac{n_2}{n_1+n_2}}\phi_2 \tag{7.24}$$

while the transverse mode ϕ_u can be found from imposing orthogonality:

$$\phi_u = -\sqrt{\frac{n_2}{n_1+n_2}}\phi_1 + \sqrt{\frac{n_1}{n_1+n_2}}\phi_2. \tag{7.25}$$

Now that we have the canonical moduli of the theory, we are in a position to study the decays of the lightest (physical) modulus - the transverse mode ϕ_u.

We begin by considering decays to closed string axions, which are the axionic partners c_i of the geometric moduli τ_i. These interactions arise due to the kinetic terms

$$\mathcal{L} = K_{i\bar{\jmath}}\,\partial_\mu T^i\,\partial^\mu \overline{T}^{\bar{\jmath}} \supset \frac{m_P^2}{4}\frac{n_i}{\tau_i^2}\,\partial_\mu c_i\,\partial^\mu c_i \tag{7.26}$$

which, after applying the field redefinitions from Eq. (7.22) and transformations

to the mass eigenstate basis from Eqs. (7.24)-(7.25), take the form

$$\mathcal{L} \supset -\sqrt{\frac{2}{3}}\frac{\phi_{\mathcal{V}}}{m_P}\left(\partial_\mu a_1\,\partial^\mu a_1 + \partial_\mu a_2\,\partial^\mu a_2\right) - \sqrt{\frac{2}{3}}\frac{\phi_u}{m_P}\left(\sqrt{\frac{n_1}{n_2}}\partial_\mu a_2\,\partial^\mu a_2 - \sqrt{\frac{n_2}{n_1}}\partial_\mu a_1\,\partial^\mu a_1\right) \quad (7.27)$$

where we have rescaled the axion fields $a_i = \sqrt{n_i/2}\,m_P\,c_i$ to have canonical kinetic terms. This leads to a decay width of ϕ_u into closed string axions a_1 and a_2

$$\Gamma(\phi_u \to aa) = \frac{1}{48\pi}\left(\frac{n_1^2+n_2^2}{n_1 n_2}\right)\frac{m_u^3}{m_P^2} \equiv c_{\rm hid}\Gamma_0 \quad (7.28)$$

where we have made the following definitions for future convenience:

$$c_{\rm hid} \equiv \left(\frac{n_1^2+n_2^2}{n_1 n_2}\right) \quad (7.29)$$

$$\Gamma_0 \equiv \frac{1}{48\pi}\frac{m_u^3}{m_P^2}. \quad (7.30)$$

In the case of minimal LVS, the transverse mode ϕ_u is set to 0 leaving $\phi_{\mathcal{V}}$ as the lightest modulus - it is then easy to check that with the appropriate rescaling of a_1 the decay into closed string axions in minimal LVS is simply $\Gamma(\phi_{\mathcal{V}} \to aa) = \Gamma_0$ which agrees with the results of [239].

We now consider the decays of ϕ_u to open string axions. Unlike their closed string counterparts, open string axions instead arise as the phase of a matter field, C, which is charged under a $U(1)_{\rm PQ}$ symmetry (possibly an approximate $U(1)$ from a more fundamental discrete symmetry [432, 433]), which is immediately

analogous to e.g. the DFSZ construction that we have already studied.[1] Based on the results of [434] which includes the expected moduli dependence of Kähler potentials for matter fields living on $D3$-branes,[2] the relevant term in the Kähler potential is then taken to be

$$K/m_P^2 = \frac{C\overline{C}}{(T_1+\overline{T}_1)^{x_1}(T_2+\overline{T}_2)^{x_2}} \tag{7.31}$$

where x_1 and x_2 are fixed by the brane configuration.[3] The two cases suggested by [434] are given by $x_1 = 1$, $x_2 = 0$ and $x_1 = 0$, $x_2 = 1$. After rewriting the above Kähler potential in terms of the physical moduli, it is easy to show this leads to the interaction

$$\begin{aligned}\mathcal{L} \supset \frac{m_P}{2\sqrt{6}}\left(C\partial^2\overline{C} + \overline{C}\partial^2 C\right)\,\phi_{\mathcal{V}} \\ + \frac{m_P}{2\sqrt{6}}\left(x_2\sqrt{\frac{n_1}{n_2}} - x_1\sqrt{\frac{n_2}{n_1}}\right)\left(C\partial^2\overline{C} + \overline{C}\partial^2 C\right)\,\phi_u.\end{aligned} \tag{7.32}$$

Once C acquires a VEV, the axion appears as the phase of C - i.e. $C = \rho\,\exp(i\theta)$ where ρ is the radial component and θ is the axion. Rewriting Eq. (7.32) in terms of the canonically normalized radial field $\tilde{\rho}$ and canonically normalized axion

[1] Here, we do not assume a specific open string axion model and so we do not assume the Giudice-Masiero term to be forbidden, which is specific to the DFSZ-type axions.

[2] The cited work presents results for toroidal orientifolds, however these results should be applicable to the fibred LVS case as the volume scaling of toroidal orientifolds ($\mathcal{V} \sim \sqrt{\tau_1\tau_2\tau_3}$) reduces to the fibred LVS volume scaling ($\mathcal{V} \sim \sqrt{\tau_1}\tau_2$) in the $\tau_3 \to \tau_2$ limit. Additionally, we note that this result reduces to the DeWolfe-Giddings Kähler potential [121] in the large volume limit for minimal LVS, which takes the limit $\tau_3 \to \tau_2 \to \tau_1$ limit.

[3] The attentive reader may object that this additional interaction modifies the Kähler metric - requiring corrections to our field redefinitions. This addition does indeed modify the moduli Kähler metric, although the additional terms can be shown to be sufficiently small to neglect.

$\tilde{\theta} = \langle\tilde{\rho}\rangle\theta$, we have the following interaction:

$$\mathcal{L} \supset \frac{1}{2\sqrt{6}m_P}\left(x_2\sqrt{\frac{n_1}{n_2}} - x_1\sqrt{\frac{n_2}{n_1}}\right)\left[2\phi_u\tilde{\theta}\partial^2\tilde{\theta} - \tilde{\theta}^2\partial^2\phi_u\right]. \tag{7.33}$$

Here, the dependence on the canonically normalized radial component $\tilde{\rho}$ of C, which is given by

$$\tilde{\rho} = \frac{m_P\rho}{\sqrt{\langle T_1 + \overline{T}_1\rangle^{x_1}\langle T_2 + \overline{T}_2\rangle^{x_2}}}, \tag{7.34}$$

arises *only* through the canonically normalized axion $\tilde{\theta}$ - i.e. $\tilde{\rho}$ disappears explicitly from the open string axion interactions upon canonical normalization of the axion. It is also worth noting that the axion decay constant is determined by the VEV of $\tilde{\rho}$, i.e. $f_\theta = \langle\tilde{\rho}\rangle$. Clearly, the first interaction ($\sim \phi_u\tilde{\theta}\partial^2\tilde{\theta}$) leads to a mass-suppressed decay width - while the second term ($\sim \tilde{\theta}^2\partial^2\phi_u$) leads to an unsuppressed decay of ϕ_u - both of which we explicitly demonstrate in App. (A) within in a supersymmetric context. Similar results appear in minimal LVS (albeit for $\phi_\mathcal{V}$, which assumes a nearly-identical form from Eq. (7.32)) - this is contrary to the claims in [239] which neglected the unsuppressed term and therefore produced only a suppressed decay to open string axions. As evident from the form of the coupling in Eq. (7.33), depending on the brane configuration which is parametrized by the choices of x_1 and x_2 there are two possible decay widths in the fibred LVS case:

$$\Gamma\left(\phi_u \to \tilde{\theta}\tilde{\theta}\right) = \begin{cases} \Gamma_0/8 & (x_1 = 1 \text{ and } x_2 = 0) \\ \Gamma_0/32 & (x_1 = 0 \text{ and } x_2 = 1) \end{cases} \tag{7.35}$$

where we have restored explicitly that $n_1 = 1$ and $n_2 = 2$ in fibred LVS. Likewise, in minimal LVS the decay width is given by $\Gamma(\phi_{\mathcal{V}} \to \tilde{\theta}\tilde{\theta}) = \Gamma_0/16$ where there is only one choice for the modulus-dependence of the Kähler potential. Thus we see that depending on the assumed brane configuration, one can see either an enhancement or a diminution in the decay to open string axions in fibred LVS when compared to the minimal LVS case. In the remainder of this section, we focus on the more optimistic case where $x_1 = 0$ and $x_2 = 1$, which minimizes its contributions to the dark radiation produced. This case also corresponds to a coupling of $\lambda_{\rm PQ} \simeq 0.41$ if we apply this specific model to the context of our ϕPQMSSM model. However, this application would instead require a construction of the ϕPQMSSM with the KSVZ axion model - since we have seen that forbidding the Giudice-Masiero term in case **GK2** of the ϕPQMSSM with a DFSZ axion drastically overproduced dark radiation.

Our next task is to compute the modulus decays into Higgses. Here, we again take a Kähler potential of the form suggested by the toroidal orientifold case [434]:

$$K/m_P^2 \supset \frac{H_u\overline{H}_u}{(T_1+\overline{T}_1)^{y_1}(T_2+\overline{T}_2)^{y_2}} + \frac{H_d\overline{H}_d}{(T_1+\overline{T}_1)^{w_1}(T_2+\overline{T}_2)^{w_2}} + \frac{ZH_uH_d + \text{h.c.}}{(T_1+\overline{T}_1)^{k_1}(T_2+\overline{T}_2)^{k_2}}. \quad (7.36)$$

We assume the Giudice-Masiero term [246] has a Kähler metric that is of product form, so that $K_{H_uH_d} = \sqrt{K_{H_u}K_{H_d}}$ which implies the relation $k_1 = (y_1 + w_1)/2$ and likewise for k_2. We also assume that Z is constant with respect to T_1 and T_2. Although Z *does* depend on the dilaton and complex structure moduli, these

moduli are integrated out at this scale [4] and so we can adopt the viewpoint that Z is a tunable parameter in the string landscape. Using again the arguments from [434], we have the constraints $y_1 = 1(0)$ and $y_2 = 0(1)$, and $w_1 = 1(0)$ and $w_2 = 0(1)$ (where y_i and w_i are independent from each other as they arise from different fields) for the moduli dependence of the Kähler potential. This implies that the Giudice-Masiero term in Eq. (7.36) may take the following forms:

$$1.)\ k_1 = 1 \text{ and } k_2 = 0$$

$$2.)\ k_1 = 0 \text{ and } k_2 = 1$$

$$3.)\ k_1 = k_2 = 1/2.$$

Putting all this together, the Lagrangian then contains the canonically normalized interactions

$$\begin{aligned}\mathcal{L} \supset\ & \frac{1}{\sqrt{6}m_P}\left(\tilde{H}_u\partial^2\overline{\tilde{H}}_u + \overline{\tilde{H}}_u\partial^2\tilde{H}_u\right)\phi_{\mathcal{V}} + \frac{1}{\sqrt{6}m_P}\left(\tilde{H}_d\partial^2\overline{\tilde{H}}_d + \overline{\tilde{H}}_d\partial^2\tilde{H}_d\right)\phi_{\mathcal{V}} \\ & + \frac{1}{\sqrt{6}m_P}\left(Z\tilde{H}_u\tilde{H}_d + \text{h.c.}\right)\partial^2\phi_{\mathcal{V}} \\ & + \frac{\alpha}{\sqrt{6}m_P}\left(\tilde{H}_u\partial^2\overline{\tilde{H}}_u + \overline{\tilde{H}}_u\partial^2\tilde{H}_u\right)\phi_u + \frac{\beta}{\sqrt{6}m_P}\left(\tilde{H}_d\partial^2\overline{\tilde{H}}_d + \overline{\tilde{H}}_d\partial^2\tilde{H}_d\right)\phi_u \\ & + \frac{\gamma}{\sqrt{6}m_P}\left(Z\tilde{H}_u\tilde{H}_d + \text{h.c.}\right)\partial^2\phi_u \quad (7.37)\end{aligned}$$

where the canonical normalization

$$\tilde{H}_u = \frac{m_P H_u}{\sqrt{\langle T_1 + \overline{T}_1\rangle^{y_1}\langle T_2 + \overline{T}_2\rangle^{y_2}}} \tag{7.38}$$

$$\tilde{H}_d = \frac{m_P H_d}{\sqrt{\langle T_1 + \overline{T}_1\rangle^{w_1}\langle T_2 + \overline{T}_2\rangle^{w_2}}} \tag{7.39}$$

for the Higgs fields has been used and we have made the convenient definitions

$$\alpha \equiv \left(y_2\sqrt{\frac{n_1}{n_2}} - y_1\sqrt{\frac{n_2}{n_1}}\right) \tag{7.40}$$

$$\beta \equiv \left(w_2\sqrt{\frac{n_1}{n_2}} - w_1\sqrt{\frac{n_2}{n_1}}\right) \tag{7.41}$$

$$\gamma \equiv \frac{1}{2}(\alpha+\beta) = \left(k_2\sqrt{\frac{n_1}{n_2}} - k_1\sqrt{\frac{n_2}{n_1}}\right). \tag{7.42}$$

It is easy to see from the form of Eq. (7.37) that only the Giudice-Masiero term leads to an unsuppressed decay width for ϕ_u. Again, we also show this explicitly in App. (A).

Before we compute the decay width to Higgses, we note that in this scenario the level of sequestering plays a dominant role in the masses of the Higgses - and therefore whether or not they are kinematically accessible in the decay of ϕ_u. In the *ultralocal limit* [185, 4], the scalar soft mass has a volume scaling $m_0 \sim M_{1/2} \sim m_P\mathcal{V}^{-2}$ and is thus highly sequestered in the large volume limit - naturally resulting in TeV-scale soft masses for a sufficiently large volume. Since $m_u \sim m_P\mathcal{V}^{-5/3}$, *all* Higgs degrees of freedom are expected to be accessible in the decay of ϕ_u - just as in our previous study of the ϕMSSM EFT. In the *local limit*

[185, 4] however, the sequestering is weaker - the scalar soft mass then scales as $m_0 \sim M_{1/2}\sqrt{\mathcal{V}} \sim m_P \mathcal{V}^{-3/2}$. Evidently, only the *light* Higgs degrees of freedom can be expected to be accessible in the large volume limit - which limits the decays of ϕ_u to the physical h, G^0, and $G^\pm$ modes. In the split-SUSY limit, the physical Lagrangian takes the form [359]

$$\mathcal{L} \simeq -\frac{\gamma Z}{2\sqrt{6}\, m_P} \left(|G^+|^2 - (h^0)^2 + (G^0)^2 \right) \partial^2 \phi_u. \tag{7.43}$$

The decays into Higgs particles can then be written down as

$$\Gamma\left(\phi_u \to H_u H_d\right) = \Gamma_0 \times \begin{cases} 2\gamma^2 Z^2 & \text{(ultralocal limit)} \\ 5\gamma^2 Z^2/8 & \text{(local limit).} \end{cases} \tag{7.44}$$

Since the tree-level gauge-kinetic function is set by the dilaton for $D3$-branes at singularities [185], any decays of ϕ_u to the gauge sector are highly suppressed (i.e. the **GK2** case) and thus we can safely ignore them for our purposes here. Additionally, as we have seen in previous sections all couplings to matter fields lead to either chirality-suppressed decays to fermions or mass-suppressed decays to sfermions, and are also safely neglectable. Finally, since the lightest moduli are stabilized non-supersymmetrically there are no unsuppressed F-term interactions that arise here. To good approximation for $m_u \gtrsim 100$ TeV - which will be the case here - we saw from Fig. (4.10) that the total width in case **B2-GK2** with a light ALP is set to a high precision by the decays to the Higgses and the ALP.

This thus concludes the computation of the leading decay modes we require to study the phenomenology of this scenario.

7.3.2 Dark radiation production

As we have previously discussed, ultra-relativistic particles which interact extremely weakly (such as being only gravitationally coupled) typically do not thermalize and behave as dark radiation which can be parametrized by the effective number of neutrinos $\Delta N_{\rm eff}$. Here we adopt the estimate for $\Delta N_{\rm eff}$ used in [239]:

$$\Delta N_{\rm eff} \simeq \frac{43}{7}\frac{f_{\rm hid}}{1-f_{\rm hid}}\left(\frac{g_*(T_{\rm dec})}{g_*(T_{\rm rh})}\right)^{1/3} \tag{7.45}$$

where $g_*(T_{\rm dec}) \sim 10.75$ is the number of relativistic degrees of freedom at the temperature of neutrino decoupling, $g_*(T_{\rm rh})$ is the number of relativistic degrees of freedom at the modulus decay temperature or reheat temperature,[4] and $f_{\rm hid}$ is the branching fraction into the relativistic hidden sector particles. As we are considering the more optimistic case for open string axions, $f_{\rm hid}$ is given (to good approximation) by

$$f_{\rm hid} \simeq \frac{\Gamma(\phi_u \to aa)}{\Gamma(\phi_u \to aa) + \Gamma(\phi_u \to H_u H_d)}. \tag{7.46}$$

[4]Here, we follow the literature from the string community which conventionally denotes the temperature of modulus decay as $T_{\rm rh}$ and is equivalent to our previous notation T_D^{ϕ}. This reheating temperature is distinct from the inflationary reheating temperature if the lightest modulus is not the inflaton. If the lightest modulus is the inflaton, as is the case in fibre inflation, $T_{\rm rh}$ is also the inflationary reheating temperature.

At our level of approximation, $f_{\rm hid}$ is independent of m_u - a behavior which was observed for moduli masses above $\sim 10-50$ TeV in our detailed treatment in Sec. (4.3.2). Taking our expressions for the decay widths and expanding γ while maintaining generality around the brane configuration hosting the Higgses, we arrive at

$$f_{\rm hid} \simeq \begin{cases} \left[1+2Z^2(k_2 n_1 - k_1 n_2)^2/(n_1^2+n_2^2)\right]^{-1} & \text{(ultralocal limit)} \\ \left[1+\frac{5}{8}Z^2(k_2 n_1 - k_1 n_2)^2/(n_1^2+n_2^2)\right]^{-1} & \text{(local limit).} \end{cases} \tag{7.47}$$

In addition to the expression for $f_{\rm hid}$, we will need the reheating temperature of the modulus to 1. ensure BBN safety of the model and 2. study dark matter production, since we are generally expected to be in the annihilation scenario for viable dark matter production. In the sudden decay approximation, using the results of Sec. (5.2.1) we can write the result[5]

$$\begin{aligned} T_{\rm rh} &= \left|\frac{k_2}{n_2}-\frac{k_1}{n_1}\right|^{1/2}\sqrt{\Gamma_0 m_P} \\ &\times \begin{cases} \left(\frac{80Z^2}{\pi^2 g_*(T_{\rm rh})}\left[2Z^2(k_2 n_1 - k_1 n_2)^2 + n_1^2 + n_2^2\right]\right)^{1/4} & \text{(ultralocal limit)} \\ \left(\frac{25Z^2}{\pi^2 g_*(T_{\rm rh})}\left[\frac{5}{8}Z^2(k_2 n_1 - k_1 n_2)^2 + n_1^2 + n_2^2\right]\right)^{1/4} & \text{(local limit).} \end{cases} \end{aligned} \tag{7.48}$$

Taking $g_*(T_{\rm rh}) \sim 86.25$ and a benchmark modulus mass of $m_u = 2.5\times 10^4$ TeV, we display in Fig. (7.2) and Fig. (7.3) both the dark radiation production (upper plot) and the corresponding reheating temperature (lower plot) in the

[5]Here, we use the condition $3H \sim \Gamma$ instead of $H \sim \Gamma$ for compatibility with previous works. This change is inconsequential to any of our results.

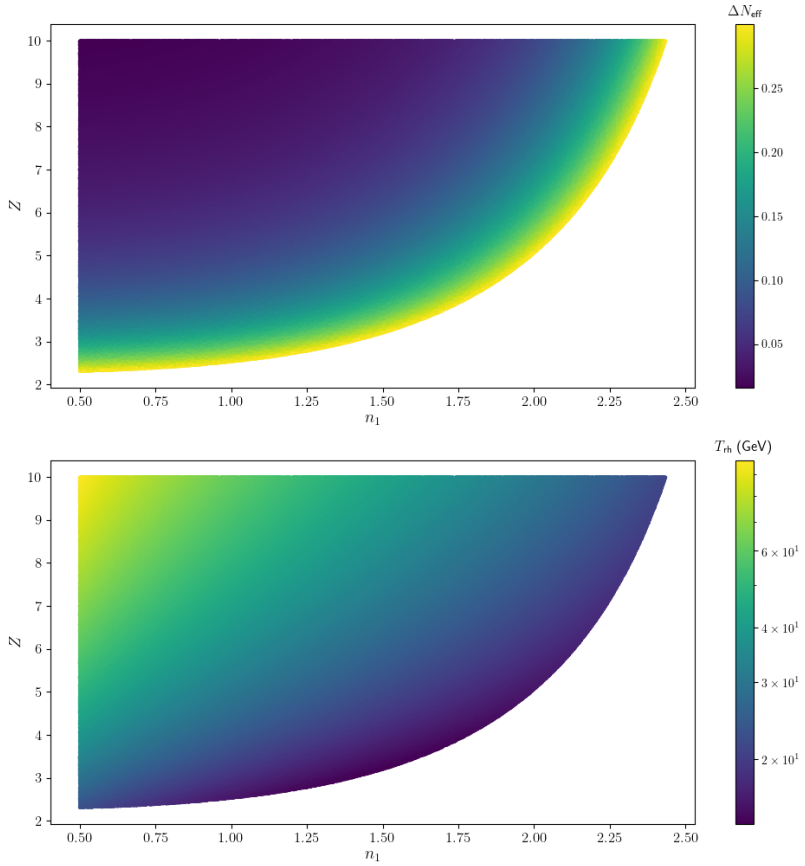


Figure 7.2: Dark radiation production $\Delta N_{\rm eff}$ (upper plot) and reheating temperature $T_{\rm rh}$ in GeV (lower plot) in the ultralocal limit for the case $k_1 = 1$ and $k_2 = 0$. Figure taken from [10].

(n_1, Z) plane for the ultralocal limit. These figures also represent the local limit by scaling Z by a factor of about 1.8. In both upper and lower plots of both figures, the unshaded regions are ruled out by Planck 2018 constraints which require $\Delta N_{\rm eff} \lesssim 0.29$ [11], while color coded regions in each upper plot (lower plot) represents the predicted value of $\Delta N_{\rm eff}$ ($T_{\rm rh}$) if it satisfies the Planck 2018 bound. In Fig. (7.2), we display the more optimistic brane configuration leading to the pair $k_1 = 1$ and $k_2 = 0$. From this figure, we see that a value of $Z \gtrsim 2.5$ is required to satisfy dark radiation constraints for fibred LVS ($n_1 = 1$) in the

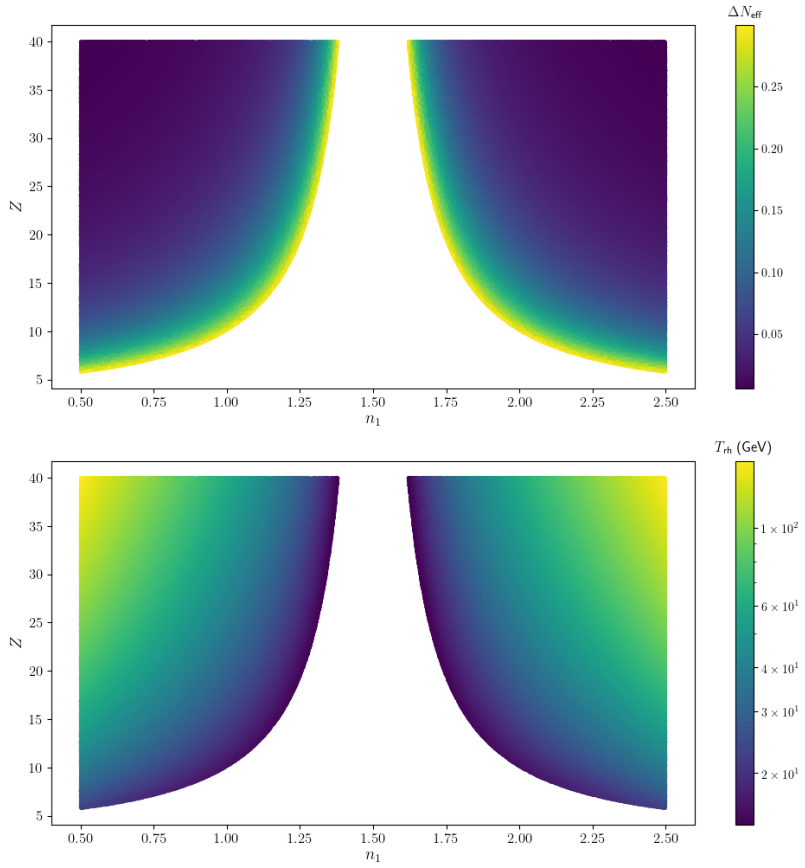


Figure 7.3: Dark radiation production $\Delta N_{\rm eff}$ (upper plot) and reheating temperature $T_{\rm rh}$ in GeV (lower plot) in the ultralocal limit for the case $k_1 = 1/2$ and $k_2 = 1/2$. Figure taken from [10].

ultralocal limit, while the local limit requires $Z \gtrsim 5$. It is worth stressing that this prediction is largely independent of m_u - the only dependence arises through $g_*(T_{\rm rh})$ which only makes very small adjustments to $\Delta N_{\rm eff}$ if m_u is changed. Fibred LVS then predicts a reheating temperature $T_{\rm rh} \gtrsim 15 - 20$ GeV (well above the BBN bound) for our benchmark modulus mass $m_u = 2.5 \times 10^4$ TeV. We note that this figure also describes the case where $k_1 = 0$ and $k_2 = 1$ under the interchange $n_1 \leftrightarrow n_2$. For this case, we see that $Z \gtrsim 5$ in the ultralocal limit would be required for consistency with Planck 2018 results in fibred LVS. From Fig. (7.3) which

displays the case where $k_1 = k_2 = 1/2$, we see that a $Z \gtrsim 10$ in the ultralocal limit is required to satisfy Planck 2018 bounds. Evidently, the $k_1 = 1$ and $k_2 = 0$ case in the ultralocal limit seems preferred from the perspective of tuning Z to avoid dark radiation overproduction. Based on our toy model description of the Giudice-Masiero mechanism in Sec. (3.1.2), we saw that $\mu \sim \lambda_{\rm GM} m_{\rm hid.}^2/m_P$. In the most optimistic brane configuration, we might therefore expect the LSP to be higgsino-like in the ultralocal limit, while $Z \gtrsim 5$ may lead to too large a μ and thus predict either a bino-like or wino-like LSP depending on the remaining model details. We now focus on the best-case scenario - i.e. take $k_1 = 1$ and $k_2 = 0$ - as it does not require unnaturally large Z to satisfy current observational bounds.

7.3.3 Kähler inflation in fibred LVS with matter fields on $D3$ branes

We first apply the results from the previous sections to the case of Kähler moduli inflation (KMI) [420]. In Table (7.1), we list our benchmark spectrum which is based on the results of [392]. As we saw in Sec. (2.3.3), Sec. (7.1), and Sec. (7.2), the scalar potential and mass spectrum in both minimal and fibred LVS are effectively specified by the parameters $\mathcal{V}$, W_0, g_s, and λ since any remaining parameters related to the non-perturbative effects that appear in the superpotential are expected to be $\mathcal{O}(1)$ [435]. It was found in [392] that $\mathcal{V} \lesssim 10^8$ and $W_0 \lesssim 1000$ are able to reproduce the observed density perturbations ($A_s \simeq 2.1 \times 10^{-9}$ [417]), with strong preference for $\mathcal{V} \sim \mathcal{O}(10^7)$ and $W_0 \lesssim 50$. We also take $g_s = 0.1$ to ensure perturbative control, and take $\lambda = 2$ based on the expected ratio of the 1-loop open string correction coefficient to the tree-level winding string coefficient [359].

This produces the mass spectrum in Table (7.1), where we have also taken the parameters $\omega = 0.01$ and $\tau_3 = 1.5$ in Eq. (7.15) so that $M_{1/2}$ is of order the TeV scale.[6] This then fixes the inflationary Hubble scale to be $H_I \sim m_{\mathcal{V}} \sim 5 \times 10^8$ GeV, giving a relatively low inflationary scale. Additionally, we see from Table (7.1) that all moduli in this spectrum are well above the $\mathcal{O}(10 - 300)$ TeV bound set by BBN.

W_0	40
$\mathcal{V}$	10^7
g_s	0.1
λ	2
$m_{3/2}$	6.1×10^8 TeV
$M_{1/2}$	1.7 TeV
m_{τ_3}	7.5×10^9 TeV
$m_{\mathcal{V}}$	3.1×10^5 TeV
m_u	2.5×10^4 TeV

Table 7.1: Benchmark spectrum for Kähler inflation. We take $\omega = 0.01$ and $\tau_3 = 1.5$ which gives the gaugino mass $M_{1/2}$ from Eq. (7.15).

Focusing on the best case scenario ($k_1 = 1$ and $k_2 = 0$) in the ultralocal limit, we can compute the decay width for ϕ_u into the Higgs sector from Eq. (7.44):

$$\Gamma(\phi_u \to H_u H_d) = 4Z^2 \Gamma_0 \tag{7.49}$$

which gives us the branching ratio into hidden sector particles (i.e. closed string axions) from Eq. (7.47):

$$f_{\text{hid}} \simeq \left(1 + \frac{8}{5} Z^2\right)^{-1}. \tag{7.50}$$

[6] As we have noted previously, ω is a tunable parameter in the landscape which allows for this choice without a significant degree of tuning.

Additionally, the reheat temperature is given by Eq. (7.48):

$$T_{\rm rh} = 2\sqrt{5}\left(\frac{Z^2[1+\frac{8}{5}Z^2]}{\pi^2 g_*(T_{\rm rh})}\right)^{1/4}\sqrt{\Gamma_0 m_P}. \tag{7.51}$$

Taking $Z = 3$ so that $\Delta N_{\rm eff} \sim 0.2 < 0.29$ in accord with Planck 2018 constraints [11] and taking $g_*(T_{\rm rh}) \simeq 86.25$, we see that $T_{\rm rh}$ for our benchmark scenario in Table (7.1) is

$$\left(\frac{T_{\rm rh}}{1\ {\rm GeV}}\right) \simeq 18.7 \times \left(\frac{m_u}{2.5\times 10^4\ {\rm TeV}}\right)^{3/2}. \tag{7.52}$$

Clearly, this is well above the BBN scale $T_{\rm BBN} \sim \mathcal{O}(1-5\ {\rm MeV})$, so that this scenario does not suffer from the BBN-violating aspect of the cosmological moduli problem. For the sake of reference, we also have the branching ratio into dark radiation for $Z = 3$

$$f_{\rm hid} \simeq 6.5\% \tag{7.53}$$

which is in accordance with our results which did not violate Planck 2018 bounds in the ϕPQMSSM in Sec. (6.3.4) - albeit within a different context.

Now that we have the relevant cosmological parameters for our KMI benchmark spectrum, we are in a position to analyze the viability of dark matter production. We begin by analyzing dark matter that may be produced in the branching scenario - so that the produced DM abundance after modulus decay is too low to annihilate. We can estimate the produced abundance yield in the branching

scenario by [235] (see also e.g. Sec. (5.3.3) for a derivation):

$$Y_{\rm DM} = Y_{\phi_u}\, \mathcal{B}(\phi_u \to {\rm DM}) \tag{7.54}$$

where the observed abundance yield is given by [235, 236]

$$Y_{\rm DM}^{\rm obs} \simeq 5 \times 10^{-10} \left(\frac{1\ {\rm GeV}}{m_{\rm DM}}\right). \tag{7.55}$$

Adopting a lower bound on the branching ratio to DM as $\mathcal{B}(\phi_u \to {\rm DM}) \gtrsim 5 \times 10^{-3}$ which is motivated from the lower bound set by 3-body modulus decays [220], we see that

$$Y_{\phi_u} \left(\frac{m_{\rm DM}}{1\ {\rm GeV}}\right) \lesssim 10^{-7} \tag{7.56}$$

For $m_{\rm DM} \lesssim \mathcal{O}(10\ {\rm GeV})$, we then expect a modulus abundance yield of $Y_{\phi_u} \lesssim 10^{-8}$ to reproduce the observed DM abundance - with larger DM masses requiring even lower modulus abundances at $T_{\rm rh}$. Additionally, if the dark matter mass is well below the GeV scale we might expect it to behave also as dark radiation without additional model-building details. A simple estimate for the modulus abundance at $T_{\rm rh}$ is given by [235, 236]

$$Y_{\phi_u} = \frac{3T_{\rm rh}}{4m_u}. \tag{7.57}$$

For our benchmark spectrum, we find that this translates to $Y_{\phi_u} \sim 5.6 \times 10^{-7}$ - well above the expected $Y_{\phi_u} \lesssim 10^{-8}$ to successfully realize the branching scenario. Using the required modulus abundance yield, we can also find a rough constraint

on the reheating temperature to realize the branching scenario: $T_{\rm rh} \lesssim 0.3$ GeV - far below the value given by Eq. (7.52). This leads us to the conclusion that the branching scenario is not viable in our benchmark spectrum.

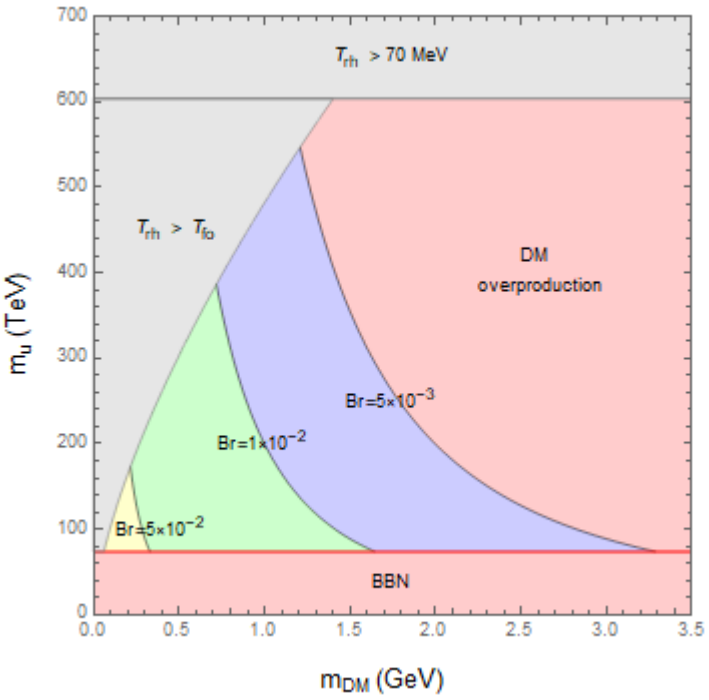


Figure 7.4: Constraints on the branching scenario in the $(m_{\rm DM}, m_u)$ plane. Gray regions are incompatible with the branching scenario, while red regions are excluded by either dark matter overproduction or BBN violation. Figure reproduced from [10].

However, if one instead extends the inflationary sector to include additional fields responsible for generating the observed density perturbations, we can modify the benchmark spectrum to study the requirements on the branching scenario. An increase to the volume $\mathcal{V} \gtrsim 5 \times 10^8$ then corresponds to an abundance yield $Y_{\phi_u} \lesssim 8.7 \times 10^{-8}$ - which is much closer to the required value. This also leads to the rough bound of $T_{\rm rh} \lesssim 70$ MeV required to realize the branching scenario, where larger values of $T_{\rm rh}$ correspond to moduli masses too large to obtain the required

abundance. In Fig. (7.4), we display constraints on the branching scenario in the $(m_{\rm DM}, m_u)$ plane. Here, the gray regions indicate regions that are expected to be inconsistent with the branching scenario - if the reheating temperature is larger than the freeze-out temperature $T_{\rm rh} > T_f \sim m_{\rm DM}/20$ we would expect to be in the thermal scenario, while $T_{\rm rh} > 70$ MeV is likely to overproduce the modulus abundance. The lower red region is set by $T_{\rm rh} = T_{\rm BBN} \sim 3$ MeV - corresponding to the requirement that $m_u \gtrsim 80$ TeV - while the upper-right red region is ruled out by dark matter overproduction. The yellow contour then corresponds to viable branching scenario parameter space with a branching ratio to dark matter $\mathcal{B}(\phi_u \to {\rm DM}) \gtrsim 5 \times 10^{-2}$, while the green and purple contours correspond to $\mathcal{B}(\phi_u \to {\rm DM}) \gtrsim 1 \times 10^{-2}$ and $\mathcal{B}(\phi_u \to {\rm DM}) \gtrsim 5 \times 10^{-3}$, respectively. If the lower bound of the branching ratio to DM can be eased in model-dependent constructions, the viable parameter space can be enlarged - however we see from the plot that one would need an *extremely* suppressed branching ratio to realize the branching scenario with dark matter masses $m_{\rm DM} \gtrsim \mathcal{O}(1-10)$ TeV. We also see that the consistency condition $T_{\rm rh} > T_f$ prevents arbitrarily low dark matter masses from being considered (assuming that the dark matter annihilates strongly enough to reduce to the thermal scenario in this case). Thus, with fairly model-independent considerations we see that the branching scenario can only be realized for a very narrow window of 100 MeV $\lesssim m_{\rm DM} \lesssim$ 3.3 GeV and 80 TeV $\lesssim m_u \lesssim$ 550 TeV, and requires a KMI inflationary model which generates the observed density perturbations through a non-standard mechanism.

This brings us to consider the annihilation scenario. In the annihilation

scenario, we can estimate the produced dark matter abundance yield as [235, 236] (see also e.g. Sec. (5.3.2) for a derivation):

$$Y_{\rm DM} = Y_{\rm DM}^{\rm obs} \frac{\langle \sigma_{\rm ann} v \rangle_{\rm f.o.}^{\rm th}}{\langle \sigma_{\rm ann} v \rangle_{\rm f.o.}} \left(\frac{T_{\rm f.o.}}{T_{\rm rh}} \right) \tag{7.58}$$

where $\langle \sigma_{\rm ann} v \rangle_{\rm f.o.}^{\rm th} \simeq 3 \times 10^{-26}\ {\rm cm}^3\,{\rm s}^{-1}$ is the annihilation cross section required in the thermal scenario to reproduce the observed DM abundance and $Y_{\rm DM}^{\rm obs}$ is given by Eq. (7.55). There is also the consistency condition that $T_{\rm rh} \lesssim T_{\rm f.o.}$,

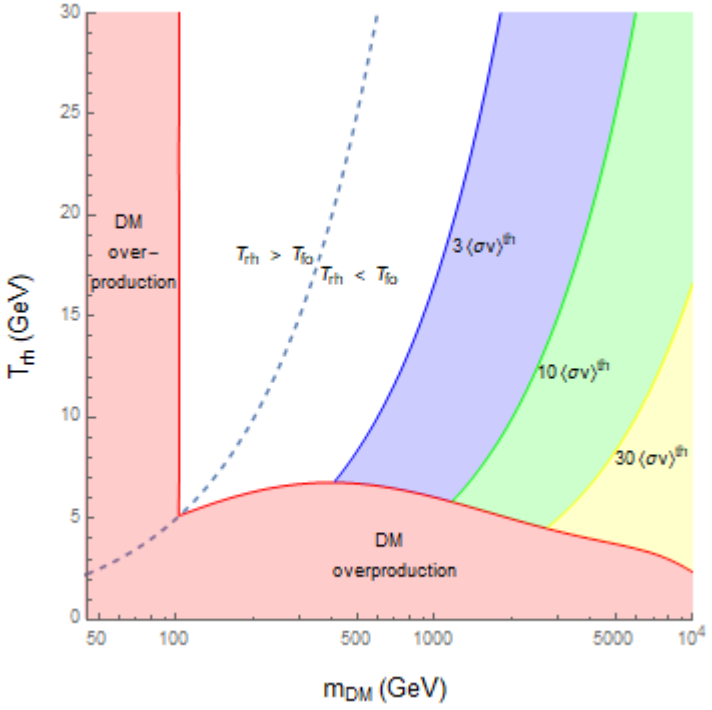


Figure 7.5: Constraints on the annihilation scenario in the $(m_{\rm DM}, T_{\rm rh})$ plane. Red regions are excluded by dark matter overproduction. Blue, green, and yellow contours also indicate dark matter overproduction if $\langle \sigma v \rangle_{\rm f.o.}/\langle \sigma v \rangle_{\rm f.o.}^{\rm th}$ is below 3, 10, and 30 respectively. Figure reproduced from [10].

otherwise we are expected to be in the thermal scenario. This condition then demands that $\langle \sigma_{\rm ann} v \rangle_{\rm f.o.} \gtrsim \langle \sigma_{\rm ann} v \rangle_{\rm f.o.}^{\rm th}$ in order to reproduce the observed DM

abundance. Of course, larger annihilation cross sections imply a larger interaction rate which can be detected from e.g. indirect detection experiments searching for gamma-ray signals from WIMP annihilations such as Fermi-LAT [351] and H.E.S.S [436] (see also [437, 438, 439, 440]). We therefore adopt the upper bound on annihilation cross sections $\langle\sigma_{\rm ann}v\rangle_{\rm f.o.}$ from the limits set by [351] for the $b\bar{b}$ channel as a function of $m_{\rm DM}$. In Fig. (7.5), we display the allowed parameter space for the annihilation scenario in the $(m_{\rm DM}, T_{\rm rh})$ plane. The dashed line separates the thermal ($T_{\rm rh} > T_{\rm f.o.}$) and non-thermal ($T_{\rm rh} < T_{\rm f.o.}$) scenarios. In the red region for $m_{\rm DM} \lesssim 100$ GeV, WIMP-like dark matter in the thermal scenario is expected to be overproduced since any annihilation cross section allowed from Fermi-LAT constraints will result in less efficient annihilations and thus an enhancement above the observed value. The red region below the dashed line then corresponds to DM overproduction based on our fit of $\langle\sigma_{\rm ann}v\rangle_{\rm f.o.}$ from Fermi-LAT constraints which leads to a lower bound of the viable $T_{\rm rh}$ without overproducing DM, while larger $T_{\rm rh}$ with the same $m_{\rm DM}$ and $\langle\sigma_{\rm ann}v\rangle_{\rm f.o.}$ may still be allowed. We also display contours which represent the required annihilation cross section to be consistent with the observed DM abundance, so that $\langle\sigma_{\rm ann}v\rangle_{\rm f.o.}/\langle\sigma_{\rm ann}v\rangle^{\rm th}_{\rm f.o.} \leq n$ will overproduce DM for each contour with $n \in \{3, 10, 30\}$. For our benchmark spectrum from Table (7.1), we have $T_{\rm rh} \simeq 18.7$ GeV with $Z = 3$ and so we find that we would expect to be in the thermal scenario for $m_{\rm DM} \lesssim 400$ GeV while we are in the annihilation scenario for $m_{\rm DM} \gtrsim 400$ GeV.

Incidentally, the local limit leads to exceedingly similar constraints. As we find a value of $Z \gtrsim 5$ is required to be compatible with dark radiation constraints,

we find the reheating temperature for our benchmark spectrum to be

$$\left(\frac{T_{\rm rh}}{1\ {\rm GeV}}\right) \simeq 20.8 \times \left(\frac{m_u}{2.5\times 10^4\ {\rm TeV}}\right)^{3/2} \tag{7.59}$$

where we again have $g_*(T_{\rm rh}) \simeq 86.25$. This puts slightly more stringent restrictions the both the branching scenario. Although an identical analysis to the ultralocal limit can be performed, we can also obtain results by simple scaling arguments. As we have increased $T_{\rm rh}$ and thus the modulus abundance yield Y_ϕ by around 10%, the maximal modulus mass that can realize the branching scenario is correspondingly pushed down to $m_u \lesssim 500$ TeV. Similarly, the maximal dark matter mass that the branching scenario can realize is then pushed down to 3 GeV. The annihilation scenario can also be read off of Fig. (7.5) using the larger value of $T_{\rm rh}$ in the local scenario. We see that in the local limit, we expect a thermal scenario for $m_{\rm DM} \lesssim 430$ GeV while we expect the annihilation scenario for $m_{\rm DM} \gtrsim 430$ GeV. However, in both scenarios it seems that WIMPs produced by the annihilation scenario are the natural dark matter candidate.

7.3.4 Fibre inflation with matter fields on $D3$ branes

We now apply the results from the previous sections to the study of fibre inflation. In this scenario, we update our benchmark spectrum in Table (7.2) which is based on the results of [359]. Similar to the Kähler inflation scenario, these values of W_0, $\mathcal{V}$, g_s, and λ were found to reproduce the observed amplitude of density perturbations in fibre inflation. Due to the inflationary potential now

arising from the g_s corrections, the value of the potential during inflation is now of order $W_0^2/\mathcal{V}^{10/3}$ - so matching the amplitude of density perturbations requires a correspondingly smaller volume, which pushes the resulting mass spectrum to much larger values. We also see that even in the presence of sequestering, the soft gaugino masses are pulled to a much higher scale: $M_{1/2} \sim 10^{10} - 10^{11}$ GeV (and by extension, the soft scalar masses m_0 are pulled up to this scale - or even larger in the local limit). Based on the mass spectrum shown in Table (7.2), the Hubble scale of inflation is also significantly higher than in Kähler inflation: $H_I \sim m_u \sim 5 \times 10^{13}$ GeV. In fibre inflation, there is no period of modulus domination since the lightest modulus is the inflaton. Hence, the reheating temperature $T_{\rm rh}$ is the inflationary reheat temperature, and once the inflaton decays we transition to a standard thermal history.

W_0	15
$\mathcal{V}$	10^3
g_s	0.1
λ	2
$m_{3/2}$	2.3×10^{12} TeV
$M_{1/2}$	6.3×10^{7} TeV
m_{τ_3}	9.5×10^{12} TeV
$m_{\mathcal{V}}$	2.0×10^{11} TeV
m_u	4.4×10^{10} TeV

Table 7.2: Benchmark spectrum for fibre inflation. We take $\omega = 0.01$ and $\tau_3 = 1.5$ which gives the gaugino mass $M_{1/2}$ from Eq. (7.15).

Since the SUSY breaking scale is now much higher than in the Kähler inflation case, here we expect that WIMP dark matter is grossly overproduced. Naively, one expects WIMPs to have an annihilation cross section that scales as $\langle \sigma v \rangle \propto m_{\rm DM}^{-2}$ [12], and since the LSP should have a significantly larger mass this results in a large

suppression of the annihilation cross section - and thus a large enhancement of the relic density in both the thermal and non-thermal scenarios without additional model-building considerations. Since the SUSY breaking scale is fixed roughly 3 orders of magnitude below the lightest modulus (and thus the LSP should be kinematically accessible), the fibre inflation scenario then seems to demand R-parity violating models so that the LSP is unstable.

The fibred LVS scenario *does* however generically predict decays to closed string axions. In [441], it was shown that closed string axions arising from the C_4 reduction along the overall volume can behave as fuzzy dark matter (FDM) [442, 443, 444, 445] - a model where the DM candidate is a cold, ultralight bosonic field which can form dark matter halos as Bose-Einstein condensates while preventing the build-up of potentially problematic substructures. However, this requires a rather specific mass and decay constant range for the closed string axions.[7] Although it was found in [441] that closed string axions arising from a model with $\mathcal{V} \sim 10^2 - 10^4$ can behave as fuzzy dark matter - precisely in the range of our benchmark spectrum, strong isocurvature bounds on axions must also be taken into account. Since our benchmark spectrum (which was determined by fitting the observed amplitude of density perturbations) predicts a high scale of inflation, $H_I \sim 5 \times 10^{13}$ GeV, based on the results of [441] only an inflationary scale $H_I \lesssim 2 \times 10^{11}$ GeV can be accommodated with isocurvature bounds. Thus, we find here that the closed string axions also cannot be the dark matter candidate

[7]Although we have generally neglected the non-perturbative corrections for the τ_1 and τ_2 moduli in our earlier treatment as they are extremely subleading, analyses such as these involving FDM models clearly require their inclusion which give the closed string axions tiny, but non-zero, masses $m_a \sim \mathcal{O}(10^{-22})$ eV.

in fibre inflation.

However, the QCD axion - realized as an open string axion as we studied in Sec. (7.3.1) - can also provide a viable dark matter candidate if produced by the misalignment mechanism (i.e. coherent oscillations). In a similar way to the closed string axions, the QCD axion also is subject to strong isocurvature constraints if the Peccei-Quinn symmetry is broken during inflation ($f_a > H_I$). This then requires us to estimate the decay constant f_θ which, as we have previously discussed, is set by the VEV of the radial component of the PQ field. However, calculation of this VEV is non-trivial as it depends on both F-term and D-term (due to an induced Fayet-Iliopoulos term) stabilization [183]. This calculation has been done in [183], which also shows that the value of the VEV - and thus the decay constant f_θ - depends crucially on the level of sequestering. The result was found to be

$$f_\theta \simeq \begin{cases} m_P/\mathcal{V}^2 \sim M_{1/2} \sim 5 \times 10^{10}\ \text{GeV} & \text{(ultralocal limit)} \\ m_P/\mathcal{V} \sim m_{3/2} \sim 10^{15}\ \text{GeV} & \text{(local limit)} \end{cases} \tag{7.60}$$

where we have assumed the values in our benchmark spectrum in Table (7.2). For scenarios where the PQ symmetry is broken during inflation, the isocurvature bounds are given by [417, 405]

$$H_I \lesssim 1.4 \times 10^{-5}\, f_\theta \theta_i \tag{7.61}$$

where θ_i is again the misalignment angle. Since the local scenario has $f_\theta \sim$

10^{15} GeV $> H_I$ but $1.4 \times 10^{-5} f_\theta \sim 10^{10}$ GeV $< H_I$, we conclude that the local scenario is excluded from isocurvature bounds. However, the ultralocal scenario has $f_\theta \sim 5 \times 10^{10}$ GeV $< H_I$, thus evading the isocurvature bounds as the PQ symmetry remains unbroken until *after* inflation. Thus, in this case we find the QCD axion has a decay constant (and thus mass) in the regime where it can saturate the observed dark matter abundance [446, 112] while also satisfying the isocurvature constraints. Although other dark matter candidates are expected to be viable in this scenario, it appears the ultralocal scenario naturally provides the QCD axion as a viable dark matter candidate without introducing any additional field content or model details.

Finally, we again can estimate the reheating temperature in fibre inflation as with Kähler inflation:

$$\left(\frac{T_{\rm rh}}{1\ {\rm GeV}}\right) \simeq 4.07 \times 10^{10} \left(\frac{m_u}{4.4 \times 10^{13}\ {\rm GeV}}\right)^{3/2} \tag{7.62}$$

where again we take $Z = 3$ to avoid dark radiation overproduction and we take $g_*(T_{\rm rh}) = 106.75$. This inflationary reheating temperature is rather high - however it does not suffer from a thermal gravitino problem as modulus decays to gravitinos are kinematically forbidden due to sequestering and are therefore not produced as inflationary relics.

Chapter 8

Conclusions

In this work, we have studied the interplay of a light modulus with a natural MSSM model based on radiative natural supersymmetry. By parameterizing several cases, we have found motivated benchmark scenarios based on moduli stabilization details and string model-building considerations which allows us to systematically study many different string models with an effective theory approach. We find that a heavy modulus $m_\phi \gg 1000$ TeV is required in order to meet the observed dark matter relic density, regardless of the details of its decays to gravitinos. We also find that if the decays to gravitinos are unsuppressed, $m_{3/2} \gtrsim 7000$ TeV and $m_\phi \gtrsim 6000$ TeV is required to match the observed dark matter relic density - far higher than the bounds set by Big Bang Nucleosynthesis constraints. String models which allow for sequestering then are phenomenologically more attractive in this case, while the restriction to the case of suppressed modulus decays into gravitinos appears to be required in non-sequestered models to avoid running into severe naturalness conflicts. In models where the modulus is stabilized in a non-supersymmetric fashion, the decays to ultralight axion-like particles can contribute significantly to dark radiation depending on the details of the gauge-kinetic function. This potentially excludes a large class of models by stringent constraints set by cosmic microwave background experiments such as the Planck experiment, unless the effective modulus coupling to these axion-like particles is sufficiently small.

We also studied how these results change once a supersymmetric DFSZ axion is incorporated. Generically, the addition of the axino and saxion contribute a large addition to the produced neutralino dark matter, requiring an even larger modulus mass $m_\phi \gtrsim 10000$ TeV. In this case, our scenarios inspired by Type IIb constructions with matter fields hosted on $D3$-branes appears to be excluded due to gross dark radiation overproduction. Additionally, the heterotic and M-theory inspired scenarios are expected to be probed by upcoming CMB experiments. We also find that simple consistency conditions require also a higher scale of inflation due to the requirement of an extremely large modulus mass. These consistency conditions are in severe tension with isocurvature constraints in the scenario where the PQ self-coupling is absent, i.e. $\xi = 0$, thus excluding this scenario. Thus, without additional model-building only the scenario with PQ self-coupling ($\xi = 1$) is potentially viable. We also find that based on our benchmark point and indirect detection limits, we expect these to be "best-case scenario" results unless neutralinos make up a *very* small fraction of dark matter which weakens these constraints and a large neutralino annihilation cross section can be realized in a natural supersymmetry framework. We have therefore excluded a large class of possible string constructions which produce the MSSM and a DFSZ-type PQ sector in the simplest low energy limit, while placing considerable constraints on the remaining viable scenarios. These results may also suggest a preference for a lower inflationary scale, which would inflate away all light moduli and reduce to a standard thermal history instead of one with an early matter dominated period.

It is also interesting that the ϕPQMSSM seems to prefer axions to highly

dominate the dark matter composition. Although our benchmark point required WIMPs to compose (at most) around 10% of the dark matter abundance to be in accordance with direct detection bounds, this put considerable constraints on the minimum modulus mass and, by extension, may run into tension with isocurvature constraints. If the WIMPs were to annihilate more efficiently, this stringent constraint might be eased - however, this comes at the expense of requiring the WIMPs to compose an even smaller percentage of the dark matter composition. Thus, one might not expect to see WIMPs at direct or indirect detection experiments in the near future if they make up e.g. 1% of the total dark matter abundance. However, this implies that (at least in the ϕPQMSSM) the dark matter is almost entirely composed of axions.

These predictions may change slightly if one instead considers a KSVZ-type PQ sector instead of a DFSZ-type model. As the KSVZ model introduces a heavy quark pair which is coupled to the charged PQ field, the Giudice-Masiero term is no longer forbidden. This may drastically ease dark radiation production in the scenarios inspired by Type IIb constructions, in addition to slightly shortening the lifetime of the modulus resulting in a reduced WIMP dark matter abundance in all scenarios. Additionally, if one instead assumes the LSP is the axino, then it is possible that dark matter overproduction might be substantially eased, depending on the ratio $m_{\tilde{a}}/m_{\widetilde{Z}_1}$ [447]. The axino LSP scenario is also largely unaffected by direct and indirect WIMP constraints. Since any axino interactions will be suppressed by the PQ scale f_a, the expected cross sections for axino LSPs are several orders of magnitude below current sensitivities [299, 298]. In our computations of modulus

decay, we have also focused exclusively on perturbative decays. However, in the ϕPQMSSM it is possible that non-perturbative decays to the saxion or axion through a parametric resonance may occur, entirely analogous to preheating effects in inflation. We have also focused exclusively on the case where PQ breaking occurs before or during inflation. Since we expect gravitationally-induced operators to break the $U(1)_{\rm PQ}$ symmetry, it is also possible that PQ breaking may happen after inflation if the domain walls are sufficiently unstable [448, 449, 450], which would trivially evade the isocurvature constraints. Each of these alternate scenarios may drastically change the overall picture, which we leave for future study.

Additionally, we have studied the expected distributions of the SUSY μ-term in the string landscape for each of the Kim-Nilles and Giudice-Masiero solutions to the μ-problem. In both cases, it was found that although requiring an anthropically-allowed window of the weak scale requires $\mu \lesssim 365$ GeV, the Kim-Nilles solution is quite predictive - leading to sharp distributions of μ with its peak value depending on the coupling to the Higgs bilinear $H_u H_d$. The Giudice-Masiero solution, however, produced a rather broad distribution - with tempering at large μ mostly induced from other soft terms leading to anthropically-disallowed vacua. However, both scenarios predicted light higgsinos slightly above current LHC bounds but possibly within reach of upcoming HL-LHC measurements [341]. We also studied the distribution of the Peccei-Quinn scale f_a in the string landscape within the Kim-Nilles solution, and found a sharp peak predicting $f_a \sim (0.5 - 2.5) \times 10^{11}$ GeV with the peak again depending on the coupling to the Higgs bilinear. This agrees well with both previous work and our work here on

the ϕPQMSSM, which seem to favor f_a close to this scale based on dark matter production considerations.

Finally, we have also studied the dark matter and dark radiation production in the context of a fibred Large Volume Scenario string model which produces two viable inflationary scenarios without additional model-building. Based on previous works which fit the parameters of the inflationary potential to the observed density perturbations, we find that in Kähler moduli inflation a massive WIMP is the preferred dark matter candidate while in fibre inflation, the high inflationary scale prefers open string (QCD or QCD-like) axions as the dark matter candidate. In both cases, the "ultralocal limit" appears preferred predicting highly sequestered soft terms. The upcoming CMB-S4 experiment may probe the fibre inflationary scenario, while producing further constraints on general LVS models through measurements of possible dark radiation - which may also further constrain or exclude these scenarios.

Appendix A

Moduli interactions and decay widths

A.1 Half superspace integrals of 3 fields

Following the notation of [1], we expand left-chiral scalar superfields as

$$\hat{A}(x^\mu,\theta,\overline{\theta}) = A + i\sqrt{2}\overline{\theta}\psi_{L,A} + i\overline{\theta}\theta_L\mathcal{F}_A + \frac{i}{2}\left(\overline{\theta}\gamma_5\gamma_\mu\theta\right)\partial^\mu A \\ - \frac{1}{\sqrt{2}}\overline{\theta}\gamma_5\theta\cdot\overline{\theta}\not{\partial}\psi_{L,A} + \frac{1}{8}\left(\overline{\theta}\gamma_5\theta\right)^2\partial^2 A. \tag{A.1}$$

and we expand left-chiral spinor superfields in the Wess-Zumino gauge as

$$\hat{W}_\alpha = \lambda_{L,\alpha} + \frac{1}{2}\gamma^\mu\gamma^\nu F_{\mu\nu,\alpha}\theta_L - i\overline{\theta}\theta_L\left(\not{D}\lambda_R\right)_\alpha - i\mathcal{D}_\alpha\theta_L. \tag{A.2}$$

A.1.1 Integrals of the form $\hat{A}\overline{\hat{W}^c}_\alpha\hat{W}_\alpha$ + h.c.

The form

$$\mathcal{L} = \lambda\int d^2\theta\,\left[\hat{A}\overline{\hat{W}^c}_\alpha\hat{W}_\alpha + \text{h.c.}\right] \tag{A.3}$$

produces the corresponding Lagrangian

$$\lambda^{-1}\mathcal{L} = -4\left[iA\,\left(\overline{\lambda}_\alpha\not{\partial}P_R\lambda_\alpha + gf_{CB\alpha}\overline{\lambda}_\alpha\not{V}_B P_R\lambda_C\right) + \frac{1}{2}A\mathcal{D}_\alpha\mathcal{D}_\alpha\right] \\ + \left[A\,F_{\mu\nu,\alpha}F^{\mu\nu,\alpha} + \frac{i}{2}A\,\epsilon^{\mu\nu\rho\sigma}F_{\mu\nu,\alpha}F_{\rho\sigma,\alpha}\right] + 2\left[i\overline{\lambda}_\alpha\lambda_{L,\alpha}\,\mathcal{F}_A\right] \\ + \sqrt{2}\left[\overline{\psi}_A\sigma^{\mu\nu}\lambda_{L,\alpha}F_{\mu\nu,\alpha}\right] - 2\sqrt{2}\left[\overline{\psi}_A\lambda_{L,\alpha}\mathcal{D}_\alpha\right] + \text{h.c.}$$

This form can be worked out as follows. We expand the left-chiral scalar superfields using Eq. (A.1) and the left-chiral spinor superfields using Eq. (A.2):

$$\begin{aligned}\lambda^{-1}\mathcal{L} \supset & \int d^2\theta \, \left(\overline{\theta}\theta_L\right) A \left[i \left(\left(\overline{\not{D}\lambda_R} \right)^c_\alpha \lambda_{L,\alpha} - \overline{\lambda}_{R,\alpha} \left(\not{D}\lambda_R \right)_\alpha \right) - \mathcal{D}_\alpha \mathcal{D}_\alpha \right] \\ & + \int d^2\theta \, A \left[\frac{1}{4} \overline{\theta}_R \gamma^\nu \gamma^\mu \gamma^\rho \gamma^\sigma \theta_L F_{\mu\nu,\alpha} F_{\rho\sigma,\alpha} - i \frac{1}{2} \overline{\theta}_R \left[\gamma^\nu \gamma^\mu + \gamma^\mu \gamma^\nu \right] \theta_L F_{\mu\nu,\alpha} \mathcal{D}_\alpha \right] \\ & + \int d^2\theta \, \left[\frac{i}{2} \left(\overline{\theta} \gamma_5 \gamma_\mu \theta \right) \partial^\mu A \right] \overline{\lambda}_{R,\alpha} \lambda_{L,\alpha} + \int d^2\theta \, \left[i \overline{\theta} \theta_L \mathcal{F}_A \right] \overline{\lambda}_{R,\alpha} \lambda_{L,\alpha} \\ & + \int d^2\theta \, \left[i\sqrt{2} \overline{\theta} \psi_{L,A} \right] \left[\frac{1}{2} \overline{\lambda}_{R,\alpha} \gamma^\mu \gamma^\nu \theta_L F_{\mu\nu,\alpha} + \frac{1}{2} \overline{\theta}_R \gamma^\nu \gamma^\mu \lambda_{L,\alpha} F_{\mu\nu,\alpha} \right] \\ & + \int d^2\theta \, \left[i\sqrt{2} \overline{\theta} \psi_{L,A} \right] \left[-i \mathcal{D}_\alpha \left(\overline{\lambda}_{R,\alpha} \theta_L + \overline{\theta}_R \lambda_{L,\alpha} \right) \right] \end{aligned} \tag{A.4}$$

Using the identity $\overline{\theta}_R \gamma^\nu \gamma^\mu \gamma^\rho \gamma^\sigma \theta_L = \frac{1}{2} (\overline{\theta}\theta_L) \mathrm{Tr} \left[\gamma^\nu \gamma^\mu \gamma^\rho \gamma^\sigma P_L \right]$ and the defining Clifford algebra for the gamma-matrices, as well as using several Majorana spinor identities, we can rewrite this as

$$\begin{aligned}\lambda^{-1}\mathcal{L} \supset & \int d^2\theta \, \left(\overline{\theta}\theta_L\right) \left[iA \left(\left(\overline{\not{D}\lambda_R} \right)^c_\alpha \lambda_{L,\alpha} - \overline{\lambda}_{R,\alpha} \left(\not{D}\lambda_R \right)_\alpha \right) - A \mathcal{D}_\alpha \mathcal{D}_\alpha \right] \\ & + \int d^2\theta \, \left(\overline{\theta}\theta_L\right) \left[\frac{1}{8} A \, \mathrm{Tr} \left[\gamma^\nu \gamma^\mu \gamma^\rho \gamma^\sigma P_L \right] F_{\mu\nu,\alpha} F_{\rho\sigma,\alpha} \right] \\ & + \int d^2\theta \, \left(\overline{\theta} \gamma_5 \gamma_\mu \theta \right) \left[\frac{i}{2} \overline{\lambda}_\alpha \lambda_{L,\alpha} \, \partial^\mu A \right] + \int d^2\theta \, \left(\overline{\theta}\theta_L\right) \left[i \overline{\lambda}_\alpha \lambda_{L,\alpha} \, \mathcal{F}_A \right] \\ & + \frac{1}{\sqrt{2}} \int d^2\theta \, \left(\overline{\theta}\theta_L\right) \left[\overline{\psi}_A \sigma^{\mu\nu} \lambda_{L,\alpha} F_{\mu\nu,\alpha} \right] - \sqrt{2} \int d^2\theta \, \left(\overline{\theta}\theta_L\right) \left[\overline{\psi}_A \lambda_{L,\alpha} \mathcal{D}_\alpha \right] \end{aligned} \tag{A.5}$$

To evaluate the terms involving the gauge field strengths, we need the identity

$$\begin{aligned}\mathrm{Tr}\left[\gamma^\nu\gamma^\mu\gamma^\rho\gamma^\sigma P_L\right] &= \frac{1}{2}\mathrm{Tr}\left[\gamma^\nu\gamma^\mu\gamma^\rho\gamma^\sigma\right] - \frac{1}{2}\mathrm{Tr}\left[\gamma^\nu\gamma^\mu\gamma^\rho\gamma^\sigma\gamma_5\right] \\ &= 2\left[\eta^{\nu\mu}\eta^{\rho\sigma} - \eta^{\nu\rho}\eta^{\mu\sigma} + \eta^{\nu\sigma}\eta^{\mu\rho}\right] + 2i\epsilon^{\nu\mu\rho\sigma} \qquad \text{(A.6)}\end{aligned}$$

Noting that the integral $\int d^2\theta(\overline{\theta}\theta_L) = 2$ and $\int d^2\theta(\overline{\theta}\gamma_5\gamma_\mu\theta) = 0$, this reduces to

$$\begin{aligned}\lambda^{-1}\mathcal{L} \supset -4\Bigg[iA\,\left(\overline{\lambda}_\alpha\partial\!\!\!/P_R\lambda_\alpha + gf_{CB\alpha}\overline{\lambda}_\alpha\mathcal{V}\!\!\!/_B P_R\lambda_C\right) + \frac{1}{2}A\mathcal{D}_\alpha\mathcal{D}_\alpha\Bigg] \\ + \left[A\,F_{\mu\nu,\alpha}F^{\mu\nu,\alpha} + \frac{i}{2}A\,\epsilon^{\mu\nu\rho\sigma}F_{\mu\nu,\alpha}F_{\rho\sigma,\alpha}\right] + 2\left[i\overline{\lambda}_\alpha\lambda_{L,\alpha}\,\mathcal{F}_A\right] \\ + \sqrt{2}\left[\overline{\psi}_A\sigma^{\mu\nu}\lambda_{L,\alpha}F_{\mu\nu,\alpha}\right] - 2\sqrt{2}\left[\overline{\psi}_A\lambda_{L,\alpha}\mathcal{D}_\alpha\right] + \text{h.c.} \qquad \text{(A.7)}\end{aligned}$$

A.2 Full superspace integrals of 3 fields

Due to the reality condition of the Kähler potential, there are only two entirely unique combinations for products of 3 chiral scalar superfields, namely $\hat{A}\hat{B}\hat{C} + \text{h.c.}$ and $\hat{A}\hat{B}\hat{C}^\dagger + \text{h.c.}$. Our convention for superfields follows [1], which we recap here. Left-chiral scalar superfields are expanded as

$$\begin{aligned}\hat{A}(x^\mu,\theta,\overline{\theta}) = A + i\sqrt{2}\overline{\theta}\psi_{L,A} + i\overline{\theta}\theta_L\mathcal{F}_A + \frac{i}{2}\left(\overline{\theta}\gamma_5\gamma_\mu\theta\right)\partial^\mu A \\ - \frac{1}{\sqrt{2}}\overline{\theta}\gamma_5\theta\cdot\overline{\theta}\partial\!\!\!/\psi_{L,A} + \frac{1}{8}\left(\overline{\theta}\gamma_5\theta\right)^2\partial^2 A. \qquad \text{(A.8)}\end{aligned}$$

A.2.1 Useful Grassmann identities involving scalars

Here we list useful identities involving Grassmann variables which are associated to terms incorporating only Lorentz-scalar terms.

$$\overline{\theta}P_{L/R}\theta\,\left(\overline{\theta}\gamma_5\gamma_\mu\theta\right)=0 \tag{A.9}$$

$$\overline{\theta}P_R\theta\,\overline{\theta}P_L\theta=-\frac{1}{2}\left(\overline{\theta}\gamma_5\theta\right)^2 \tag{A.10}$$

$$\left(\overline{\theta}P_{L/R}\theta\right)^2=0 \tag{A.11}$$

$$\left(\overline{\theta}\gamma_5\gamma_\mu\theta\right)\,\left(\overline{\theta}\gamma_5\gamma_\nu\theta\right)=-g_{\mu\nu}\left(\overline{\theta}\gamma_5\theta\right)^2 \tag{A.12}$$

A.2.2 Useful Grassmann identities involving spinors

Here we list useful identities involving Grassmann variables contracted with spinor fields. Each can be verified by application of Eq. 5.21 in [1].

$$\overline{\theta}P_L\psi_1\left[\overline{\theta}\gamma_5\theta\cdot\overline{\theta}\partial\!\!\!/P_L\psi_2\right]=0 \tag{A.13}$$

$$\overline{\theta}P_L\psi_1\left[\overline{\theta}\gamma_5\theta\cdot\overline{\theta}\partial\!\!\!/P_R\psi_2\right]=\frac{1}{4}(\overline{\theta}\gamma_5\theta)^2\overline{\psi}_1\partial\!\!\!/P_R\psi_2 \tag{A.14}$$

$$\overline{\psi}_1P_R\theta\left[\overline{\theta}\gamma_5\theta\cdot\overline{\theta}\partial\!\!\!/P_L\psi_2\right]=-\frac{1}{4}(\overline{\theta}\gamma_5\theta)^2\overline{\psi}_1\partial\!\!\!/P_L\psi_2 \tag{A.15}$$

$$\overline{\theta}P_L\psi_1\cdot\overline{\theta}P_L\psi_2\left(\overline{\theta}\gamma_5\gamma_\mu\theta\right)=0 \tag{A.16}$$

$$\overline{\theta}P_L\psi_1\cdot\overline{\psi}_2P_R\theta\left(\overline{\theta}\gamma_5\gamma_\mu\theta\right)=\frac{1}{4}\left(\overline{\theta}\gamma_5\theta\right)^2\overline{\psi}_1\gamma_\mu P_R\psi_2 \tag{A.17}$$

$$\overline{\theta}P_L\psi_1\cdot\overline{\psi}_2P_{R/L}\theta\cdot\overline{\theta}P_L\theta=0 \tag{A.18}$$

$$\overline{\theta}P_L\psi_1\cdot\overline{\theta}P_L\psi_2\cdot\overline{\theta}P_R\theta=\frac{1}{4}(\overline{\theta}\gamma_5\theta)^2\overline{\psi}_1P_L\psi_2 \tag{A.19}$$

A.2.3 Kähler potentials of the form $\hat{A}\hat{B}\hat{C} + \text{h.c.}$

The form

$$K \supset \lambda \left[\hat{A}\hat{B}\hat{C} + \text{h.c.} \right] \tag{A.20}$$

gives the corresponding Lagrangian

$$\mathcal{L} = 0 \tag{A.21}$$

Since the Kähler metric vanishes if a term does not contain *both* a holomorphic and anti-holomorphic direction, the corresponding Lagrangian must vanish.

A.2.4 Kähler potentials of the form $\hat{A}\hat{B}\hat{C}^\dagger + \text{h.c.}$

The form

$$K \supset \lambda \left[\hat{A}\hat{B}\hat{C}^\dagger \exp\left(-2g t_a \hat{\Phi}_a \right) + \text{h.c.} \right] \tag{A.22}$$

gives the corresponding Lagrangian

$$\begin{aligned}\lambda^{-1}\mathcal{L} = &-\left[AB\partial^2 C^\dagger\right] + i\left[A\overline{\psi}_B \not{\partial} P_R \psi_C + B\overline{\psi}_A \not{\partial} P_R \psi_C\right] \\ &+ \left[B\mathcal{F}_A \mathcal{F}_C^\dagger + A\mathcal{F}_B \mathcal{F}_C^\dagger - i\overline{\psi}_A P_L \psi_B \mathcal{F}_C^\dagger\right] - g\left[ABC^\dagger\left(t_a D_a\right)\right] \\ &+ g^2\left[ABC^\dagger\left(t_a V_a^\mu\right)\left(t_b V_{b,\mu}\right)\right] + ig\left[AB\partial^\mu C^\dagger - AC^\dagger\partial^\mu B - BC^\dagger\partial^\mu A\right]\left(t_a V_{a,\mu}\right) \\ &- g\sqrt{2}\left[AB\overline{\psi}_C P_R\left(t_a\lambda_a\right) + AC^\dagger\overline{\psi}_B P_L\left(t_a\lambda_a\right) + BC^\dagger\overline{\psi}_A P_L\left(t_a\lambda_a\right)\right] \\ &+ g\left[A\overline{\psi}_B\gamma_\mu P_R\psi_C\left(t_a V_a^\mu\right) + B\overline{\psi}_A\gamma_\mu P_R\psi_C\left(t_a V_a^\mu\right)\right] + \text{h.c.} \quad \text{(A.23)}\end{aligned}$$

This form can be worked out as follows. We expand the left-chiral scalar superfields using A.8 and the gauge potential superfield $\hat{\Phi}_a$ using the identity [1]:

$$\begin{aligned}\exp\left(-2gt_a\hat{\Phi}_a\right) = 1 &- g\left(\overline{\theta}\gamma_5\gamma_\mu\theta\right)\left(t_a V_a^\mu\right) - 2ig\left(\overline{\theta}\gamma_5\theta\right)\overline{\theta}\left(t_a\lambda_a\right) \\ &+ \frac{1}{2}\left(\overline{\theta}\gamma_5\theta\right)^2\left(gt_a D_a - \left(gt_a V_a^\mu\right)\left(gt_b V_{b,\mu}\right)\right). \quad \text{(A.24)}\end{aligned}$$

This gives us

$$\begin{aligned}\mathcal{L} = -\lambda\frac{1}{2}\int d^4\theta\ \left(\overline{\theta}\gamma_5\theta\right)^2 \Bigg[&-\frac{1}{4}\left[AB\partial^2 C^\dagger + AC^\dagger\partial^2 B + BC^\dagger\partial^2 A\right] \\ &+\frac{1}{2}\left[A\partial_\mu B\partial^\mu C^\dagger + B\partial_\mu A\partial^\mu C^\dagger - C^\dagger\partial_\mu A\partial^\mu B\right] \\ &-\frac{i}{2}\left[\overline{\psi}_B\gamma_\mu P_R\psi_C\,\partial^\mu A - A\overline{\psi}_C\partial\!\!\!/ P_L\psi_B - A\overline{\psi}_B\partial\!\!\!/ P_R\psi_C + (A\leftrightarrow B)\right] \\ &+\left[B\mathcal{F}_A\mathcal{F}_C^\dagger + A\mathcal{F}_B\mathcal{F}_C^\dagger - i\overline{\psi}_A P_L\psi_B\mathcal{F}_C^\dagger\right] - \left[ABC^\dagger\left(gt_aD_a - \left(gt_aV_a^\mu\right)\left(gt_bV_{b,\mu}\right)\right)\right] \\ &+i\left[g\left(t_aV_{a,\mu}\right)AB\partial^\mu C^\dagger - g\left(t_aV_{a,\mu}\right)AC^\dagger\partial^\mu B - g\left(t_aV_{a,\mu}\right)BC^\dagger\partial^\mu A\right] \\ &-\sqrt{2}\left[gAB\overline{\psi}_C P_R\left(t_a\lambda_a\right) + gAC^\dagger\overline{\psi}_B P_L\left(t_a\lambda_a\right) + gBC^\dagger\overline{\psi}_A P_L\left(t_a\lambda_a\right)\right] \\ &+\left[gA\overline{\psi}_B\gamma_\mu P_R\psi_C\left(t_aV_a^\mu\right) + gB\overline{\psi}_A\gamma_\mu P_R\psi_C\left(t_aV_a^\mu\right)\right] + \text{h.c.}\Bigg] \quad \text{(A.25)}\end{aligned}$$

where we have made use of the identities Eqs. (A.9-A.19). Evaluating the superspace integral and leveraging several surface term identities, we arrive at the result:

$$\begin{aligned}\lambda^{-1}\mathcal{L} = &-\left[AB\partial^2 C^\dagger\right] + i\left[A\overline{\psi}_B\partial\!\!\!/ P_R\psi_C + B\overline{\psi}_A\partial\!\!\!/ P_R\psi_C\right] \\ &+\left[B\mathcal{F}_A\mathcal{F}_C^\dagger + A\mathcal{F}_B\mathcal{F}_C^\dagger - i\overline{\psi}_A P_L\psi_B\mathcal{F}_C^\dagger\right] - g\left[ABC^\dagger\left(t_aD_a\right)\right] \\ &+g^2\left[ABC^\dagger\left(t_aV_a^\mu\right)\left(t_bV_{b,\mu}\right)\right] \\ &+ig\left[\left(t_aV_{a,\mu}\right)AB\partial^\mu C^\dagger - \left(t_aV_{a,\mu}\right)AC^\dagger\partial^\mu B - \left(t_aV_{a,\mu}\right)BC^\dagger\partial^\mu A\right] \\ &-g\sqrt{2}\left[AB\overline{\psi}_C P_R\left(t_a\lambda_a\right) + AC^\dagger\overline{\psi}_B P_L\left(t_a\lambda_a\right) + BC^\dagger\overline{\psi}_A P_L\left(t_a\lambda_a\right)\right] \\ &+g\left[A\overline{\psi}_B\gamma_\mu P_R\psi_C\left(t_aV_a^\mu\right) + B\overline{\psi}_A\gamma_\mu P_R\psi_C\left(t_aV_a^\mu\right)\right] + \text{h.c.}\end{aligned}$$

A.3 Toy model Feynman amplitudes and decay widths

We make repeated use of the definition

$$\lambda^{1/2}(x,y,z) \equiv \left[x^2+y^2+z^2-2(xy+yz+xz)\right]^{1/2} \tag{A.26}$$

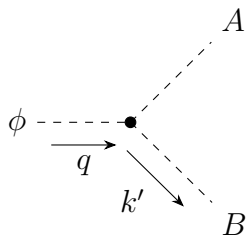
as a shorthand for the phase space factor.

A.3.1 Modulus decay to real scalars

We start with the toy model

$$\mathcal{L} \supset \lambda_1 AB\partial^2\phi + \lambda_2 \phi B\partial^2 A + \lambda_3 \phi A\partial^2 B \tag{A.27}$$

where A and B are assumed to be real scalars, and λ_1, λ_2, λ_3 each have mass dimension -1. Each interaction term corresponds to the diagram



where the vertex factors are $-i\lambda_1 m_\phi^2$, $-i\lambda_2 m_A^2$, and $-i\lambda_3 m_B^2$, respectively. For the case where $A = B$, each of these vertex factors is multiplied by an additional factor of 2.

Assuming no other contributions to the $\phi \to A + B$ decay, the total amplitude

is then

$$i\mathcal{M} = -i\left(\lambda_1 m_\phi^2 + \lambda_2 m_A^2 + \lambda_3 m_B^2\right) \tag{A.28}$$

and hence the squared matrix element is simply given by

$$|\mathcal{M}|^2 = \left(\lambda_1 m_\phi^2 + \lambda_2 m_A^2 + \lambda_3 m_B^2\right)^2 . \tag{A.29}$$

As there is no angular dependence, the decay widths can then be written down immediately. When A and B are distinguishable, we have

$$\Gamma_{\phi AB} = \frac{1}{16\pi m_\phi}\left(\lambda_1 m_\phi^2 + \lambda_2 m_A^2 + \lambda_3 m_B^2\right)^2 \lambda^{1/2}\left(1, \frac{m_A^2}{m_\phi^2}, \frac{m_B^2}{m_\phi^2}\right) \tag{A.30}$$

while for the case where $A = B$, we have

$$\Gamma_{\phi AA} = \frac{1}{8\pi m_\phi}\left(\lambda_1 m_\phi^2 + \lambda_2 m_A^2\right)^2 \lambda^{1/2}\left(1, \frac{m_A^2}{m_\phi^2}, \frac{m_A^2}{m_\phi^2}\right) \tag{A.31}$$

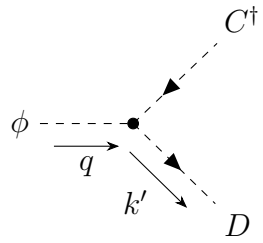
where the amplitude squared introduced an additional factor of 4, while the identical particles in the final state divide the decay width by 2. We have also taken $\lambda_3 = 0$ in this case without loss of generality.

A.3.2 Modulus decay to complex scalars

We start with the toy model

$$\mathcal{L} \supset \lambda_1 C^\dagger D \partial^2 \phi + \lambda_2 \phi D \partial^2 C^\dagger + \lambda_3 \phi C^\dagger \partial^2 D \tag{A.32}$$

where C and D are assumed to be complex scalars, and λ_1, λ_2, λ_3 each have mass dimension -1. Each interaction term corresponds to the diagram



where the vertex factors are $-i\lambda_1 m_\phi^2$, $-i\lambda_2 m_C^2$, and $-i\lambda_3 m_D^2$, respectively. In the case where $C^\dagger = D^\dagger$, the vertex factor remains unchanged as the final state is distinguishable.

Assuming no other contributions to the $\phi \to C^\dagger + D$ decay, the total amplitude is then

$$i\mathcal{M} = -i\left(\lambda_1 m_\phi^2 + \lambda_2 m_C^2 + \lambda_3 m_D^2\right) \tag{A.33}$$

and the squared matrix element is given by

$$|\mathcal{M}|^2 = \left(\lambda_1 m_\phi^2 + \lambda_2 m_C^2 + \lambda_3 m_D^2\right)^2 . \tag{A.34}$$

Like the decay to real scalars, there is no angular dependence and thus the decay width can be written down as

$$\Gamma_{\phi C^\dagger D} = \frac{1}{16\pi} m_\phi^3 \left(\lambda_1 + \lambda_2 \frac{m_C^2}{m_\phi^2} + \lambda_3 \frac{m_D^2}{m_\phi^2} \right)^2 \lambda^{1/2} \left(1, \frac{m_C^2}{m_\phi^2}, \frac{m_D^2}{m_\phi^2} \right). \tag{A.35}$$

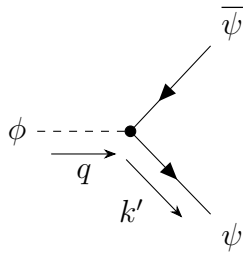
As expected, the contributions from the λ_2 and λ_3 terms are suppressed in comparison to the λ_1 term. This expression is valid also in the case where $C^\dagger = D^\dagger$, where without loss of generality we can take $\lambda_3 = 0$.

A.3.3 Modulus decay to spin-1/2 fermions

We start with the toy model

$$\mathcal{L} \supset i\lambda_1 \, \phi \overline{\psi} \partial\!\!\!/ \, (g_V + g_A \gamma_5) \, \psi \tag{A.36}$$

where ψ is a four-component spinor, and λ_1 has mass dimension -1. This interaction term corresponds to the diagram



where the vertex factor is $-i\lambda_1 k\!\!\!/'(g_V + g_A\gamma_5)$. For the case where ψ is Majorana, this vertex factor is multiplied by an additional factor of 2 due to the indistinguishability of the final state.

Assuming no additional contributions, the matrix element for this process is given by

$$i\mathcal{M} = \overline{u}^{s'}(k')\left(-i\lambda_1 \not{k}'(g_V + g_A\gamma_5)\right)v^s(k). \tag{A.37}$$

Summing over outgoing spins, the squared matrix element becomes:

$$|\mathcal{M}|^2 = 2|\lambda_1|^2\, m_\psi^2 m_\phi^2 \left(g_V^2\left[1 - 4\frac{m_\psi^2}{m_\phi^2}\right] + g_A^2\right) \tag{A.38}$$

where our kinematics gave $k'_\mu k^\mu = \frac{1}{2}m_\phi^2 - m_\psi^2$. Since there is no angular dependence, the decay widths can then be written down immediately. If ψ is simply a Dirac fermion (e.g. quarks and leptons), the decay width is given by

$$\Gamma_{\phi\bar{\psi}\psi} = \frac{1}{8\pi}|\lambda_1|^2\, m_\phi^3 \left(\frac{m_\psi^2}{m_\phi^2}\right)\left(g_V^2\left[1 - 4\frac{m_\psi^2}{m_\phi^2}\right] + g_A^2\right)\lambda^{1/2}\left(1, \frac{m_\psi^2}{m_\phi^2}, \frac{m_\psi^2}{m_\phi^2}\right). \tag{A.39}$$

However, if ψ is Majorana in nature (e.g. gluinos and electroweakinos), the decay width is given by

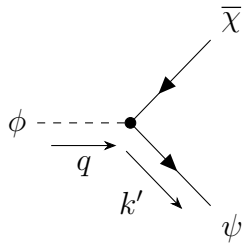
$$\Gamma_{\phi\bar{\psi}_M\psi_M} = \frac{1}{4\pi}|\lambda_1|^2\, m_\phi^3 \left(\frac{m_\psi^2}{m_\phi^2}\right)\left(g_V^2\left[1 - 4\frac{m_\psi^2}{m_\phi^2}\right] + g_A^2\right)\lambda^{1/2}\left(1, \frac{m_\psi^2}{m_\phi^2}, \frac{m_\psi^2}{m_\phi^2}\right) \tag{A.40}$$

where the amplitude squared introduced an additional factor of 4, and we divide the final decay width by 2 as the final state is indistinguishable.

We also consider the toy model

$$\mathcal{L} \supset i\lambda_1 \phi \left[\overline{\chi} \partial\!\!\!/ \left(g_V + g_A\gamma_5\right)\psi + \overline{\psi} \partial\!\!\!/ \left(g_V + g_A\gamma_5\right)\chi\right] \tag{A.41}$$

where ψ and χ are assumed to be four-component Majorana spinors, and λ_1 has mass dimension -1. The first interaction term corresponds to the diagram



where the vertex factor is $-i\lambda_1 k\!\!\!/'(g_V + g_A\gamma_5)$, and the second interaction term can be obtained by the replacements $k \leftrightarrow k'$ and $\psi \leftrightarrow \chi$.

Assuming no other contributions to the $\phi \to \psi + \chi$ decay, the total amplitude is then

$$i\mathcal{M} = -i\lambda_1 \left[\overline{u}^{s'}(k')\left(k\!\!\!/'(g_V + g_A\gamma_5)\right) v^s(k) + \overline{u}^s(k)\left(k\!\!\!/(g_V + g_A\gamma_5)\right) v^{s'}(k')\right]. \tag{A.42}$$

Summing over outgoing spins, the squared matrix element becomes

$$\begin{aligned}|\mathcal{M}|^2 = {} & 2|\lambda_1|^2 m_\phi^2 \left(m_\psi^2 + m_\chi^2\right) \\ & \times \left(g_V^2\left(1 - \frac{(m_\psi + m_\chi)^2}{m_\phi^2}\right) + g_A^2\left(1 - \frac{(m_\psi - m_\chi)^2}{m_\phi^2}\right)\right)\end{aligned} \tag{A.43}$$

where our kinematics gave us $2k'_\mu k^\mu = m_\phi^2 - m_\psi^2 - m_\chi^2$. The decay width can then be written down:

$$\Gamma_{\phi\psi\chi} = \frac{1}{8\pi}|\lambda_1|^2\, m_\phi^3 \left(\frac{m_\psi^2 + m_\chi^2}{m_\phi^2}\right) \times \left(g_V^2\left(1 - \frac{(m_\psi + m_\chi)^2}{m_\phi^2}\right) + g_A^2\left(1 - \frac{(m_\psi - m_\chi)^2}{m_\phi^2}\right)\right)\lambda^{1/2}\left(1, \frac{m_\psi^2}{m_\phi^2}, \frac{m_\chi^2}{m_\phi^2}\right). \tag{A.44}$$

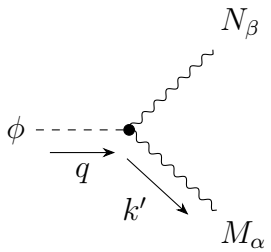
As expected, the decay width to fermions receives chirality suppression.

A.3.4 Modulus decay to vector bosons

We start with the toy model

$$\mathcal{L} \supset -\lambda_1\, \phi\, [\partial_\mu M_\nu \partial^\mu N^\nu - \partial_\mu M_\nu \partial^\nu N^\mu] \tag{A.45}$$

where M and N are (possibly either massive or massless) vector bosons, and λ_1 has mass dimension -1. This interaction term corresponds to the diagram



where the vertex factor is $i\lambda_1[k'_\mu k^\mu g^{\alpha\beta} - k'^\alpha k^\beta]$.

Assuming no other contributions to the $\phi \to M + N$ decay, the total amplitude

is then

$$i\mathcal{M}^{\mu\nu}\epsilon^*_\mu(k)\epsilon^*_\nu(k') = i\lambda_1\left[k'_\gamma k^\gamma g^{\mu\nu} - k'^\mu k^\nu\right]\epsilon^*_\mu(k)\epsilon^*_\nu(k'). \tag{A.46}$$

The squared matrix element then becomes

$$|\mathcal{M}^{\mu\nu}\epsilon^*_\mu(k)\epsilon^*_\nu(k')|^2 = \lambda_1^2\left(k'_\gamma k^\gamma\right)^2\left[g^{\mu\nu} - \frac{k'^\mu k^\nu}{(k'_\gamma k^\gamma)}\right]\left[g^{\alpha\beta} - \frac{k'^\alpha k^\beta}{(k'_\gamma k^\gamma)}\right]$$
$$\times\,\epsilon^*_\mu(k)\epsilon_\alpha(k)\epsilon^*_\nu(k')\epsilon_\beta(k'). \tag{A.47}$$

For a massive boson, we can then sum over polarizations using

$$\sum_\lambda \epsilon(q)^*_\mu\epsilon(q)_\nu = -g_{\mu\nu} + \frac{q_\mu q_\nu}{m^2} \tag{A.48}$$

whereas if a boson is massless, we must use

$$\sum_\lambda \epsilon(q)^*_\mu\epsilon(q)_\nu = -g_{\mu\nu} + \frac{q_\mu n_\nu + q_\nu n_\mu}{q\cdot n} \tag{A.49}$$

where, without loss of generality as two body decays are always colinear in the rest frame of the parent, we assume the decay products move along the z-axis such that $q_\mu = (q, 0, 0, q)$ and $n_\nu = (q, 0, 0, -q)$ so that only the physical polarizations appear in the sum.

We now have the squared matrix element:

$$\sum_{\text{pol.}} |\mathcal{M}^{\mu\nu}\epsilon^*_\mu(k)\epsilon^*_\nu(k')|^2 = \frac{\lambda_1^2}{2}m_\phi^4\left[\left(1-\frac{m_N^2}{m_\phi^2}-\frac{m_M^2}{m_\phi^2}\right)^2+2\frac{m_M^2m_N^2}{m_\phi^4}\right] \tag{A.50}$$

where our kinematics gave us $2k'_\mu k^\mu = m_\phi^2 - m_N^2 - m_M^2$. This formula is valid for both massive and massless bosons. Since there is once again no angular dependence, the decay widths can be written down immediately. If M and N are distinguishable, the decay width is given by

$$\Gamma_{\phi MN} = \frac{\lambda_1^2}{32\pi}m_\phi^3\left[\left(1-\frac{m_N^2}{m_\phi^2}-\frac{m_M^2}{m_\phi^2}\right)^2+2\frac{m_M^2m_N^2}{m_\phi^4}\right]\lambda^{1/2}\left(1,\frac{m_M^2}{m_\phi^2},\frac{m_N^2}{m_\phi^2}\right). \tag{A.51}$$

If $M = N$ is indistinguishable, the decay width is then given by

$$\Gamma_{\phi MM} = \frac{\lambda_1^2}{16\pi}m_\phi^3\left[1-4\frac{m_M^2}{m_\phi^2}+6\frac{m_M^4}{m_\phi^4}\right]\lambda^{1/2}\left(1,\frac{m_M^2}{m_\phi^2},\frac{m_M^2}{m_\phi^2}\right) \tag{A.52}$$

where the amplitude squared introduced an additional factor of 4, and we divide the final decay width by 2 as the final state is indistinguishable.

A.4 Moduli-gauge sector interactions

The leading interaction terms between the modulus and the gauge sector are given by

$$\mathcal{L}_{\text{G.K.}} \supset -\frac{1}{4}\int d^2\theta \left[\frac{\lambda_{U(1)}}{m_P}\,\hat{\phi}\,\overline{\hat{B}^c}\hat{B} + \frac{\lambda_{SU(2)}}{m_P}\,\hat{\phi}\,\overline{\hat{W}^c}_{\alpha}\hat{W}_{\alpha} + \frac{\lambda_{SU(3)}}{m_P}\,\hat{\phi}\,\overline{\hat{G}^c}_{\alpha}\hat{G}_{\alpha} + \text{h.c.}\right] \tag{A.53}$$

where $\hat{B}$ is the gauge-eigenstate superfield for $U(1)_Y$, $\hat{W}_\alpha$ is the gauge-eigenstate superfield for $SU(2)_L$, and $\hat{G}_\alpha$ is the gauge-eigenstate superfield for $SU(3)_C$. Using Eq. (A.4), we can evaluate the superspace integral. Separating into the different gauge groups, we have for the $U(1)_Y$ group

$$\begin{aligned}\mathcal{L}_{\text{G.K., }U(1)} \supset & \frac{\lambda_{U(1)}}{m_P}\left[i\Phi\,\overline{\lambda}_0\partial\!\!\!/ P_R\lambda_0\right] - \frac{\lambda_{U(1)}}{4m_P}\left[\Phi\,B_{\mu\nu}B^{\mu\nu} + \frac{i}{2}\Phi\,\epsilon^{\mu\nu\rho\sigma}B_{\mu\nu}B_{\rho\sigma}\right] \\ & - \sqrt{2}\frac{\lambda_{U(1)}}{4m_P}\left[\overline{\psi}_\phi\sigma^{\mu\nu}B_{\mu\nu}P_L\lambda_0\right] + \sqrt{2}\frac{\lambda_{U(1)}}{2m_P}\left[\mathcal{D}_0^{U(1)}\overline{\psi}_\phi P_L\lambda_0\right] \\ & + \frac{\lambda_{U(1)}}{2m_P}\Phi\mathcal{D}_0^{U(1)}\mathcal{D}_0^{U(1)} - \frac{\lambda_{U(1)}}{2m_P}\left[i\mathcal{F}_\phi\,\overline{\lambda}_0P_L\lambda_0\right] + \text{h.c.}\end{aligned} \tag{A.54}$$

while for $SU(2)_L$ we have

$$\begin{aligned}\mathcal{L}_{\text{G.K., }SU(2)} \supset & \frac{\lambda_{SU(2)}}{m_P}\left[i\Phi\,\overline{\lambda}_\alpha\partial\!\!\!/ P_R\lambda_\alpha + ig\epsilon_{CB\alpha}\,\Phi\,\overline{\lambda}_\alpha W\!\!\!/_B P_R\lambda_C\right] \\ & - \frac{\lambda_{SU(2)}}{4m_P}\left[\Phi\,W_{\mu\nu,\alpha}W^{\mu\nu,\alpha} + \frac{i}{2}\Phi\,\epsilon^{\mu\nu\rho\sigma}W_{\mu\nu,\alpha}W_{\rho\sigma,\alpha}\right] \\ & - \sqrt{2}\frac{\lambda_{SU(2)}}{4m_P}\left[\overline{\psi}_\phi\sigma^{\mu\nu}P_L\lambda_\alpha W_{\mu\nu,\alpha}\right] + \sqrt{2}\frac{\lambda_{SU(2)}}{2m_P}\left[\overline{\psi}_\phi P_L\lambda_\alpha\mathcal{D}_\alpha^{SU(2)}\right] \\ & + \frac{\lambda_{SU(2)}}{2m_P}\Phi\mathcal{D}_\alpha^{SU(2)}\mathcal{D}_\alpha^{SU(2)} - \frac{\lambda_{SU(2)}}{2m_P}\left[i\mathcal{F}_\phi\,\overline{\lambda}_\alpha P_L\lambda_\alpha\right] + \text{h.c.}\end{aligned} \tag{A.55}$$

Finally, for $SU(3)_C$ we have

$$\begin{aligned}\mathcal{L}_{\text{G.K., } SU(3)} \supset & \frac{\lambda_{SU(3)}}{m_P}\left[i\Phi\,\overline{\widetilde{g}}_\alpha \not{\partial} P_R \widetilde{g}_\alpha + ig f_{CB\alpha}\,\Phi\,\overline{\widetilde{g}}_\alpha \not{G}_B P_R \widetilde{g}_C\right] \\ & - \frac{\lambda_{SU(3)}}{4m_P}\left[\Phi\, G_{\mu\nu,\alpha}G^{\mu\nu,\alpha} + \frac{i}{2}\Phi\,\epsilon^{\mu\nu\rho\sigma}G_{\mu\nu,\alpha}G_{\rho\sigma,\alpha}\right] \\ & - \sqrt{2}\frac{\lambda_{SU(3)}}{4m_P}\left[\overline{\psi}_\phi \sigma^{\mu\nu} P_L \widetilde{g}_\alpha G_{\mu\nu,\alpha}\right] + \sqrt{2}\frac{\lambda_{SU(3)}}{2m_P}\left[\overline{\psi}_\phi P_L \widetilde{g}_\alpha \mathcal{D}_\alpha^{SU(3)}\right] \\ & + \frac{\lambda_{SU(3)}}{2m_P}\Phi \mathcal{D}_\alpha^{SU(3)}\mathcal{D}_\alpha^{SU(3)} - \frac{\lambda_{SU(3)}}{2m_P}\left[i\mathcal{F}_\phi\,\overline{\widetilde{g}}_\alpha P_L \widetilde{g}_\alpha\right] + \text{h.c.} \end{aligned} \tag{A.56}$$

We now can separate these results into groupings which are relevant for the decay to the physical gauge bosons and gauginos. The terms involving modulus decay to electroweak gauge boson pairs are given by

$$\begin{aligned}\mathcal{L}_{G,\text{ ewk.}} \supset & -\frac{\lambda_{U(1)}}{4m_P}\left[\left(\Phi+\Phi^\dagger\right)\, B_{\mu\nu}B^{\mu\nu} + \frac{i}{2}\left(\Phi-\Phi^\dagger\right)\,\epsilon^{\mu\nu\rho\sigma}B_{\mu\nu}B_{\rho\sigma}\right] \\ & - \frac{\lambda_{SU(2)}}{4m_P}\left[\left(\Phi+\Phi^\dagger\right)\, W_{\mu\nu,\alpha}W^{\mu\nu,\alpha} + \frac{i}{2}\left(\Phi-\Phi^\dagger\right)\,\epsilon^{\mu\nu\rho\sigma}W_{\mu\nu,\alpha}W_{\rho\sigma,\alpha}\right] \end{aligned} \tag{A.57}$$

while the terms involving modulus decay to gluon pairs is given by

$$\mathcal{L}_{G,\text{ col.}} \supset -\frac{\lambda_{SU(3)}}{4m_P}\left[\left(\Phi+\Phi^\dagger\right)\, G_{\mu\nu,\alpha}G^{\mu\nu,\alpha} + \frac{i}{2}\left(\Phi-\Phi^\dagger\right)\,\epsilon^{\mu\nu\rho\sigma}G_{\mu\nu,\alpha}G_{\rho\sigma,\alpha}\right]. \tag{A.58}$$

The decay to electroweak gaugino pairs is then given by

$$\begin{aligned}\mathcal{L}_{g,\text{ ewk.}} \supset & \, i\frac{\lambda_{U(1)}}{m_P}\left(\Phi\overline{\lambda}_0 \not{\partial} P_R \lambda_0 + \Phi^\dagger\overline{\lambda}_0 \not{\partial} P_L \lambda_0\right) \\ & + i\frac{\lambda_{SU(2)}}{m_P}\left(\Phi\overline{\lambda}_\alpha \not{\partial} P_R \lambda_\alpha + \Phi^\dagger\overline{\lambda}_\alpha \not{\partial} P_L \lambda_\alpha\right) \end{aligned} \tag{A.59}$$

and the decay to gluino pairs is given by

$$\mathcal{L}_{g,\,\text{col.}} \supset i\frac{\lambda_{SU(3)}}{m_P}\left(\Phi\overline{\widetilde{g}}_\alpha \not{\partial} P_R \widetilde{g}_\alpha + \Phi^\dagger \overline{\widetilde{g}}_\alpha \not{\partial} P_L \widetilde{g}_\alpha\right). \tag{A.60}$$

A.4.1 Electroweak gauge boson interactions

Focusing first on the interaction with the electroweak gauge boson pairs, the relevant terms are

$$\begin{aligned}\mathcal{L}_{G,\,\text{ewk.}} \supset & -\frac{\lambda_{U(1)}}{2\sqrt{2}m_P}\left[\phi\, B_{\mu\nu}B^{\mu\nu}\right] - \frac{\lambda_{SU(2)}}{2\sqrt{2}m_P}\left[\phi\, W_{\mu\nu,\alpha}W^{\mu\nu,\alpha}\right] \\ & + \frac{\lambda_{U(1)}}{4\sqrt{2}m_P}\left[c\,\epsilon^{\mu\nu\rho\sigma}B_{\mu\nu}B_{\rho\sigma}\right] + \frac{\lambda_{SU(2)}}{4\sqrt{2}m_P}\left[c\,\epsilon^{\mu\nu\rho\sigma}W_{\mu\nu,\alpha}W_{\rho\sigma,\alpha}\right]\end{aligned} \tag{A.61}$$

where we have used $\Phi = (\phi + ic)/\sqrt{2}$. Expanding the field strengths as

$$B_{\mu\nu} = \partial_\mu B_\nu - \partial_\nu B_\mu \tag{A.62}$$

$$W^\alpha_{\mu\nu} = \partial_\mu W^\alpha_\nu - \partial_\nu W^\alpha_\mu - g\epsilon_{\alpha\beta\gamma}W^\beta_\mu W^\gamma_\nu \tag{A.63}$$

we can express the modulus coupling to the physical electroweak gauge bosons where

$$W^\pm = \frac{1}{\sqrt{2}}\left[W^1 \mp iW^2\right] \tag{A.64}$$

$$Z^0 = -\sin\theta_W B + \cos\theta_W W^3 \tag{A.65}$$

$$A^0 = \cos\theta_W B + \sin\theta_W W^3. \tag{A.66}$$

The interaction between the modulus and $W^{\pm}$ pairs is then given by

$$\mathcal{L}_{\phi W^+W^-} \supset -\frac{2\lambda_{SU(2)}}{\sqrt{2}m_P}\phi\left[\partial_\mu W^-_\nu \partial^\mu W^{+,\nu} - \partial_\nu W^-_\mu \partial^\mu W^{+,\nu}\right] \tag{A.67}$$

where we have neglected the additional terms which arise from the gauge-covariant derivative, as they will introduce only higher-body decays. The interaction between the modulus and Z^0 pairs is given by

$$\mathcal{L}_{\phi Z^0 Z^0} \supset -\frac{\left(\lambda_{U(1)}\sin^2\theta_W + \lambda_{SU(2)}\cos^2\theta_W\right)}{\sqrt{2}m_P}\phi\left[\partial_\mu Z^0_\nu \partial^\mu Z^{0,\nu} - \partial_\nu Z^0_\mu \partial^\mu Z^{0,\nu}\right] \tag{A.68}$$

where once again we have neglected the higher-body interaction terms introduced by the gauge-covariant derivative. The interaction between the modulus and A^0 pairs is given by

$$\mathcal{L}_{\phi A^0 A^0} \supset -\frac{\left(\lambda_{U(1)}\cos^2\theta_W + \lambda_{SU(2)}\sin^2\theta_W\right)}{\sqrt{2}m_P}\phi\left[\partial_\mu A^0_\nu \partial^\mu A^{0,\nu} - \partial_\nu A^0_\mu \partial^\mu A^{0,\nu}\right] \tag{A.69}$$

where, as before, we have neglected higher-body interaction terms. Finally, the interaction between the modulus, a Z^0, and an A^0 is given by

$$\mathcal{L}_{\phi Z^0 A^0} \supset -\frac{2\sin\theta_W\cos\theta_W\left(\lambda_{SU(2)} - \lambda_{U(1)}\right)}{\sqrt{2}m_P}\phi\left[\partial_\mu Z^0_\nu \partial^\mu A^{0,\nu} - \partial_\nu Z^0_\mu \partial^\mu A^{0,\nu}\right]. \tag{A.70}$$

A.4.2 Electroweakino interactions

The relevant terms for the modulus interactions with the electroweakinos are then given by

$$\mathcal{L}_{g,\text{ ewk.}} \supset \frac{\lambda_{U(1)}}{\sqrt{2}m_P}\left(i\phi\overline{\lambda}_0\partial\!\!\!/\lambda_0\right) + \frac{\lambda_{SU(2)}}{\sqrt{2}m_P}\left(i\phi\overline{\lambda}_\alpha\partial\!\!\!/\lambda_\alpha\right) - \frac{\lambda_{U(1)}}{\sqrt{2}m_P}\left(c\overline{\lambda}_0\partial\!\!\!/\gamma_5\lambda_0\right) - \frac{\lambda_{SU(2)}}{\sqrt{2}m_P}\left(c\overline{\lambda}_\alpha\partial\!\!\!/\lambda_\alpha\right). \quad \text{(A.71)}$$

We now move to the mass eigenstates. The neutralino terms may be obtained using [1]

$$\lambda_0 = \sum_i v_4^{(i)}\left(i\gamma_5\right)^{\theta_i}\widetilde{Z}_i \quad \text{(A.72)}$$

$$\lambda_3 = \sum_i v_3^{(i)}\left(i\gamma_5\right)^{\theta_i}\widetilde{Z}_i \quad \text{(A.73)}$$

where $v_j^{(i)}$ are elements of the matrix that diagonalizes the neutralino mass matrix, and θ_i is either 0 or 1 such that the mass of its corresponding neutralino, $\widetilde{Z}_i$, is positive. The modulus interaction with identical neutralino pairs is then given by:

$$\mathcal{L}_{\phi\overline{\widetilde{Z}}_i\widetilde{Z}_i} \supset i\left(\frac{\lambda_{U(1)}(v_4^{(i)})^2 + \lambda_{SU(2)}(v_3^{(i)})^2}{\sqrt{2}m_P}\right)\phi\overline{\widetilde{Z}}_i\partial\!\!\!/\widetilde{Z}_i \quad \text{(A.74)}$$

and the interactions with different pairs of neutralinos is given by:

$$\mathcal{L}_{\phi\overline{\widetilde{Z}}_i\widetilde{Z}_j} \supset i\left(-i\right)^{\theta_i}\left(i\right)^{\theta_j}\left(\frac{\lambda_{U(1)}v_4^{(i)}v_4^{(j)} + \lambda_{SU(2)}v_3^{(i)}v_3^{(j)}}{\sqrt{2}m_P}\right)\phi\overline{\widetilde{Z}}_i\partial\!\!\!/\left(\gamma_5\right)^{\theta_i+\theta_j}\widetilde{Z}_j. \quad \text{(A.75)}$$

The interactions between the modulus and charginos are then obtained by the transformations [1]

$$P_L\lambda = \sin\gamma_L P_L \left(\gamma_5\right)^{\theta_{\widetilde{W}_1}} \widetilde{W}_1 + \theta_x \cos\gamma_L P_L \left(\gamma_5\right)^{\theta_{\widetilde{W}_2}} \widetilde{W}_2 \tag{A.76}$$

$$P_R\lambda = \sin\gamma_R P_R \left(\gamma_5\right)^{\theta_{\widetilde{W}_1}} \widetilde{W}_1 + \theta_y \cos\gamma_R P_R \left(\gamma_5\right)^{\theta_{\widetilde{W}_2}} \widetilde{W}_2 \tag{A.77}$$

where we have defined

$$\lambda = \frac{\lambda_1 + i\lambda_2}{\sqrt{2}} \tag{A.78}$$

and where $\gamma_{L/R}$ are mixing angles between the gauginos and higgsinos, and $\theta_{x,y}$ are signs (which are, loosely speaking, positive if the charginos are higgsino-like and negative if they are gaugino-like). The $\theta_{\widetilde{W}_{1/2}}$ terms are then defined as either 0 or 1 such that the corresponding chargino mass is non-negative.

The interaction of the modulus with the lighter chargino pairs is then given by:

$$\mathcal{L}_{\phi\overline{\widetilde{W}}_1\widetilde{W}_1} \supset \frac{2\lambda_{SU(2)}}{\sqrt{2}m_P}\left(i\phi\overline{\widetilde{W}_1}\partial\!\!\!/\left(x_c - y_c\gamma_5\right)\widetilde{W}_1\right) \tag{A.79}$$

and the interaction between the modulus and heavier chargino pairs is given by:

$$\mathcal{L}_{\phi\overline{\widetilde{W}}_2\widetilde{W}_2} \supset \frac{2\lambda_{SU(2)}}{\sqrt{2}m_P}\left(i\phi\overline{\widetilde{W}_2}\partial\!\!\!/\left(x_s - y_s\gamma_5\right)\widetilde{W}_2\right) \tag{A.80}$$

where we have made the definitions

$$\begin{aligned} x_c &\equiv \frac{1}{2}\left(\sin^2\gamma_L + \sin^2\gamma_R\right) \\ y_c &\equiv \frac{1}{2}\left(\sin^2\gamma_L - \sin^2\gamma_R\right) \\ x_s &\equiv \frac{1}{2}\left(\cos^2\gamma_L + \cos^2\gamma_R\right) \\ y_s &\equiv \frac{1}{2}\left(\cos^2\gamma_L - \cos^2\gamma_R\right). \end{aligned} \tag{A.81}$$

The interaction between the modulus and different generations of charginos is then given by:

$$\mathcal{L}_{\phi\widetilde{W}_1\widetilde{W}_2} \supset i\left(\frac{2\lambda_{SU(2)}}{\sqrt{2}m_P}\right)\left[\phi\overline{\widetilde{W}_1}\partial\!\!\!/\,(x - y\gamma_5)\,\widetilde{W}_2 + \phi\overline{\widetilde{W}_2}\partial\!\!\!/\,(x - y\gamma_5)\,\widetilde{W}_1\right] \tag{A.82}$$

where we have made the definitions:

$$\begin{aligned} x &\equiv \frac{1}{2}\left((-1)^{\theta_{\widetilde{W}_1}+\theta_{\widetilde{W}_2}}\,\theta_x \sin\gamma_L\cos\gamma_L + \theta_y \sin\gamma_R\cos\gamma_R\right) \\ y &\equiv \frac{1}{2}\left((-1)^{\theta_{\widetilde{W}_1}+\theta_{\widetilde{W}_2}}\,\theta_x \sin\gamma_L\cos\gamma_L - \theta_y \sin\gamma_R\cos\gamma_R\right). \end{aligned} \tag{A.83}$$

A.4.3 Electroweak D-term interactions

Most electroweak D-term interactions lead to four-body decays of the modulus to quarks, leptons, and Higgses. However, once the Higgses acquire a vev, there are induced two-body decays of the form

$$m_P\mathcal{L}_{D-\text{term, ewk.}} \supset \Lambda_1\phi v_u^2 H_d^\dagger H_d + \Lambda_2\phi v_d^2 H_u^\dagger H_u + \Lambda_3\phi v_u v_d (H_u^\dagger H_d + \text{h.c.}). \tag{A.84}$$

where the Λ_i are the effective couplings and v_u (v_d) are the up (down) type Higgs vevs. These decay widths are then, up to numerical factors, given by

$$\Gamma \propto \Lambda_1^2 \frac{v_u^4}{m_P^2 m_\phi} + \dots \tag{A.85}$$

Since v_u, $v_d \lesssim \mathcal{O}(100\text{ GeV})$, we neglect these decays as they are extremely subleading.

A.4.4 Electroweak F-term interactions

In models where the modulus is stabilized supersymmetrically, we can parameterize its mass with the superpotential term $W \supset M_\Phi \Phi^2$, where M_Φ is the supersymmetric contribution to the modulus mass. This leads to a modulus F-term $\mathcal{F}_\phi \sim -2iM_\Phi \Phi^\dagger \supset -\sqrt{2}iM_\Phi \phi$. The electroweakinos then have the induced F-term interactions

$$\mathcal{L}_{F-\text{term, ewk.}} \supset -\frac{\lambda_{U(1)}}{\sqrt{2}m_P}\left[M_\Phi \phi\, \overline{\lambda}_0 P_L \lambda_0\right] - \frac{\lambda_{SU(2)}}{\sqrt{2}m_P}\left[M_\Phi \phi\, \overline{\lambda}_\alpha P_L \lambda_\alpha\right] + \text{h.c.} \tag{A.86}$$

These can straightforwardly be rewritten in terms the physical charginos and neutralinos. If $M_\Phi \sim m_\phi$, it is easy to see that these F-term decays will produce proportional to $\sim m_\phi^3/m_P^2$ in our **A** cases.

A.4.5 Gluon interactions

Focusing now on the interaction with gluon pairs, the relevant terms are

$$\mathcal{L}_{G,\text{ col.}} \supset -\frac{\lambda_{SU(3)}}{2\sqrt{2}m_P}\left[\phi\, G_{\mu\nu,\alpha}G^{\mu\nu,\alpha}\right] + \frac{\lambda_{SU(3)}}{4\sqrt{2}m_P}\left[c\,\epsilon^{\mu\nu\rho\sigma}G_{\mu\nu,\alpha}G_{\rho\sigma,\alpha}\right]. \tag{A.87}$$

Expanding the field strength as

$$G^{\alpha}_{\mu\nu} = \partial_\mu G^{\alpha}_{\nu} - \partial_\nu G^{\alpha}_{\mu} - g_s f_{\alpha\beta\gamma}G^{\beta}_{\mu}G^{\gamma}_{\nu} \tag{A.88}$$

we recover the interaction between the modulus and gluon pairs:

$$\mathcal{L}_{G,\text{ col.}} \supset -\frac{\lambda_{SU(3)}}{\sqrt{2}m_P}\phi\left[\partial_\mu G^{\alpha}_{\nu}\partial^\mu G^{\nu,\alpha} - \partial_\mu G^{\alpha}_{\nu}\partial^\nu G^{\mu,\alpha}\right] \tag{A.89}$$

A.4.6 Gluino interactions

The relevant terms containing the modulus interactions with the gluinos are given by:

$$\mathcal{L}_{\widetilde{g},\text{ col.}} \supset i\frac{\lambda_{SU(3)}}{\sqrt{2}m_P}\left(\phi\overline{\widetilde{g}}_\alpha \not{\partial}\widetilde{g}_\alpha + ic\overline{\widetilde{g}}_\alpha \not{\partial}\gamma_5\widetilde{g}_\alpha\right). \tag{A.90}$$

Since $SU(3)_C$ is unbroken, there is no mixing, and we have simply the term

$$\mathcal{L}_{\phi\widetilde{g}\widetilde{g}} \supset i\frac{\lambda_{SU(3)}}{\sqrt{2}m_P}\left(\phi\overline{\widetilde{g}}_\alpha \not{\partial}\widetilde{g}_\alpha\right). \tag{A.91}$$

A.4.7 QCD D-term interactions

All QCD D-term interactions with the modulus lead to four-body decays of the modulus to quarks, and hence the phase space factor is highly suppressed. We neglect these decays.

A.4.8 Gluino F-term interaction

Similarly to the electroweakinos, the gluinos have the induced F-term interaction

$$\mathcal{L}_{F-\text{term, col.}} \supset -\frac{\lambda_{SU(3)}}{\sqrt{2}m_P}\left[M_\Phi \phi \overline{\widetilde{g}}_\alpha P_L \widetilde{g}_\alpha\right] + \text{h.c.} \tag{A.92}$$

where M_Φ is the supersymmetric contribution to the modulus mass. If present (e.g. in the **A** cases), these lead to unsuppressed decays to gluinos.

A.5 Moduli-Higgs interactions

The leading interaction terms between the modulus and Higgs sector is

$$\mathcal{L}_H \supset \int d^4\theta \left[\frac{\lambda_{\text{GM}}}{m_P}\hat{\phi}\hat{H}_u^\dagger \hat{H}_d^\dagger + \frac{\lambda_{H_u}}{m_P}\hat{\phi}\hat{H}_u^\dagger e^{-2gt_a\hat{\Phi}_a}\hat{H}_u + \frac{\lambda_{H_d}}{m_P}\hat{\phi}\hat{H}_d^\dagger e^{-2gt_a\hat{\Phi}_a}\hat{H}_d + \text{h.c.}\right] \tag{A.93}$$

where

$$\hat{H}_u = \begin{pmatrix}\hat{h}_u^+ \\ \hat{h}_u^0\end{pmatrix} \quad \text{and} \quad \hat{H}_d = \begin{pmatrix}\hat{h}_d^- \\ \hat{h}_d^0\end{pmatrix} \tag{A.94}$$

are the two (gauge-eigenstate) Higgs doublets of the MSSM and $\hat{\Phi}_a$ are the $SU(2)_L$ and $U(1)_Y$ gauge potential superfields. Note that gauge invariance requires the gauge potential coupling in the second and third terms, while the Giudice-Masiero interaction is already locally invariant under $SU(2)_L \times U(1)_Y$.

Expanding the doublets, the Giudice-Masiero interaction in terms of the neutral and charged Higgs superfields becomes:

$$\mathcal{L}_H \supset \frac{\lambda_{\rm GM}}{m_P} \int d^4\theta \left[\hat{\phi} \left(\hat{h}_u^+ \right)^\dagger \left(\hat{h}_d^- \right)^\dagger + \hat{\phi} \left(\hat{h}_u^0 \right)^\dagger \left(\hat{h}_d^0 \right)^\dagger + \text{h.c.} \right] \tag{A.95}$$

The interaction with $\hat{H}_u^\dagger \hat{H}_u$ becomes

$$\mathcal{L}_H \supset \frac{\lambda_{H_u}}{m_P} \int d^4\theta \left[\hat{\phi} \left(\hat{h}_u^+ \right)^\dagger \left(\hat{h}_u^+ \right) + \hat{\phi} \left(\hat{h}_u^0 \right)^\dagger \left(\hat{h}_u^0 \right) + \text{h.c.} \right] \tag{A.96}$$

and we have an identical form for the $\hat{H}_d^\dagger \hat{H}_d$ interaction.

Using Eq. (A.23), we can evaluate the superspace integrals for each of the interaction with the charged Higgses. The Giudice-Masiero term becomes

$$\begin{aligned} \mathcal{L}_{H,\text{ charged}} \supset & -\frac{\lambda_{\rm GM}}{m_P} \left[h_u^+ h_d^- \partial^2 \Phi^\dagger \right] + i \frac{\lambda_{\rm GM}}{m_P} \left[h_u^+ \overline{\psi}_{h_d^-} \partial\!\!\!/ P_R \psi_\phi + h_d^- \overline{\psi}_{h_u^+} \partial\!\!\!/ P_R \psi_\phi \right] \\ & + \frac{\lambda_{\rm GM}}{m_P} \left[h_u^+ \mathcal{F}_{h_d^-} \mathcal{F}_\phi^\dagger + h_d^- \mathcal{F}_{h_u^+} \mathcal{F}_\phi^\dagger - i \mathcal{F}_\phi^\dagger \overline{\psi}_{h_u^+} P_L \psi_{h_d^-} \right] + \text{h.c.} \end{aligned} \tag{A.97}$$

while the up-type Higgs interaction becomes

$$\mathcal{L}_{H,\text{ charged}} \supset -\frac{\lambda_{H_u}}{m_P}\left[\Phi h_u^+ \partial^2 \left(h_u^+\right)^\dagger\right] + i\frac{\lambda_{H_u}}{m_P}\left[\Phi \overline{\psi}_{h_u^+} \not{\partial} P_R \psi_{h_u^+} + h_u^+ \overline{\psi}_\phi \not{\partial} P_R \psi_{h_u^+}\right] + \frac{\lambda_{H_u}}{m_P}\left[\Phi \mathcal{F}_{h_u^+} \mathcal{F}^\dagger_{h_u^+} + h_u^+ \mathcal{F}_\phi \mathcal{F}^\dagger_{h_u^+} - i\mathcal{F}^\dagger_{h_u^+} \overline{\psi}_\phi P_L \psi_{h_u^+}\right] + \text{h.c.} \tag{A.98}$$

with an identical interaction for the down-type Higgs after the replacements $h_u^+ \to h_d^-$ and $\lambda_{H_u} \to \lambda_{H_d}$. Here, we have ignored the 3-body decays to gauge modes which may become 2-body decays once one of the Higgs fields takes on its VEV.

After the appropriate interchanges, $h_u^+ \to h_u^0$ and $h_d^- \to h_d^0$, we have identical results for the interaction with the neutral Higgses. Note that in Eq. (A.97), the modulus does not directly couple to higgsinos - however, the moduli F-term leads to a higgsino mass term if it takes on a non-zero VEV (as is expected from the Giudice-Masiero mechanism). Furthermore, based on the form of Eq. (A.97), we would expect the modulus partial widths into Higgses go like $\frac{m_\phi^3}{m_P^2}$. However, Eq. (A.98) *does* couple the modulus directly to the higgsinos, and this term is still allowed even if the Giudice-Masiero term is forbidden by a PQ symmetry. The modulus partial widths into Higgses due to the contribution of Eq. (A.98) is then expected to go like $\frac{m_{H_i}^2}{m_\phi^2}\frac{m_\phi^3}{m_P^2}$ (with $i \in \{u, d\}$) - i.e. these widths should be mass suppressed.

A.5.1 Charged Higgs interactions

Focusing first on the modulus interactions with the charged Higgses, the relevant terms are

$$\begin{aligned} m_P \mathcal{L}_{H,\text{ charged}} \supset & -\frac{\lambda_{\text{GM}}}{\sqrt{2}}\left[h_u^{+*} h_d^{-*} + h_u^{+} h_d^{-}\right]\partial^2\phi - i\frac{\lambda_{\text{GM}}}{\sqrt{2}}\left[h_u^{+*} h_d^{-*} - h_u^{+} h_d^{-}\right]\partial^2 c \\ & -\frac{\lambda_{H_u}}{\sqrt{2}}\left[h_u^{+}\partial^2 h_u^{+*} + h_u^{+*}\partial^2 h_u^{+}\right]\phi - \frac{\lambda_{H_d}}{\sqrt{2}}\left[h_d^{-}\partial^2 h_d^{-*} + h_d^{-*}\partial^2 h_d^{-}\right]\phi \\ & -i\frac{\lambda_{H_u}}{\sqrt{2}}\left[h_u^{+}\partial^2 h_u^{+*} - h_u^{+*}\partial^2 h_u^{+}\right] c - i\frac{\lambda_{H_d}}{\sqrt{2}}\left[h_d^{-}\partial^2 h_d^{-*} - h_d^{-*}\partial^2 h_d^{-}\right] c \end{aligned} \tag{A.99}$$

where we used $\Phi \equiv (\phi + ic)/\sqrt{2}$. Utilizing the following transformation [1],

$$\begin{pmatrix} h_d^{-*} \\ h_u^{+} \end{pmatrix} = \begin{pmatrix} \cos\beta & -\sin\beta \\ \sin\beta & \cos\beta \end{pmatrix} \begin{pmatrix} G^{+} \\ H^{+} \end{pmatrix} \tag{A.100}$$

we may now move to the mass-eigenstate basis. The modulus interaction with the charged Higgs pairs is given by

$$\begin{aligned} \mathcal{L}_{\phi H^+ H^-} \supset & \frac{\lambda_{\text{GM}}\sin(2\beta)}{\sqrt{2}\, m_P} H^+ H^- \partial^2\phi \\ & -\left(\frac{\lambda_{H_u}\cos^2\beta + \lambda_{H_d}\sin^2\beta}{\sqrt{2}\, m_P}\right)\left[H^+\partial^2 H^- + H^-\partial^2 H^+\right]\phi \end{aligned} \tag{A.101}$$

and the modulus interaction with the charged Goldstone boson pairs is given by

$$\mathcal{L}_{\phi G^+G^-} \supset -\frac{\lambda_{\rm GM}\sin(2\beta)}{\sqrt{2}\,m_P}\,G^+G^-\,\partial^2\phi \\ -\left(\frac{\lambda_{H_u}\sin^2\beta+\lambda_{H_d}\cos^2\beta}{\sqrt{2}\,m_P}\right)\left[G^+\partial^2G^-+G^-\partial^2G^+\right]\phi. \qquad \text{(A.102)}$$

Finally, the modulus interaction with a charged Higgs and a charged Goldstone mode is given by

$$\mathcal{L}_{\phi G^\pm H^\mp} \supset -\frac{\lambda_{\rm GM}\cos(2\beta)}{\sqrt{2}\,m_P}\left[H^+G^-+H^-G^+\right]\partial^2\phi \\ -\frac{(\lambda_{H_u}-\lambda_{H_d})\sin(2\beta)}{2\sqrt{2}\,m_P}\left[G^+\partial^2H^-+H^-\partial^2G^+\right]\phi \\ -\frac{(\lambda_{H_u}-\lambda_{H_d})\sin(2\beta)}{2\sqrt{2}\,m_P}\left[H^+\partial^2G^-+G^-\partial^2H^+\right]\phi. \qquad \text{(A.103)}$$

As we work in the unitary gauge, the decay interactions to would-be Goldstone modes can be projected out with the appropriate transformation - here they become the longitudinal components of the $W^\pm$ bosons.

A.5.2 Charged higgsino interactions

The interaction between the modulus and charged higgsinos comes solely from the kinetic couplings. The relevant terms are

$$\mathcal{L}_{H,\text{ charged}} \supset i\frac{\lambda_{H_u}}{\sqrt{2}\,m_P}\left[\phi\overline{\psi}_{h_u^+}\partial\!\!\!/\psi_{h_u^+}+ic\overline{\psi}_{h_u^+}\partial\!\!\!/\gamma_5\psi_{h_u^+}\right] \\ +i\frac{\lambda_{H_d}}{\sqrt{2}\,m_P}\left[\phi\overline{\psi}_{h_d^-}\partial\!\!\!/\psi_{h_d^-}+ic\overline{\psi}_{h_d^-}\partial\!\!\!/\gamma_5\psi_{h_d^-}\right]. \qquad \text{(A.104)}$$

After using the transformation [1]

$$\widetilde{\chi} \equiv P_L \psi_{h_d^-} - P_R \psi_{h_u^+} \tag{A.105}$$

to define our Dirac fields for the negatively charged higgsino, we see that the modulus-charged higgsino interaction becomes

$$\mathcal{L}_{H,\text{ charged}} \supset i \left(\frac{\lambda_{H_u} + \lambda_{H_d}}{\sqrt{2}\, m_P} \right) \phi \overline{\widetilde{\chi}} \not{\partial} \widetilde{\chi}. \tag{A.106}$$

However, we are still using the gauge-eigenstates, and must put these into the appropriate mass-eigenstates, resulting in interactions with the charginos. This can be done with the transformations [1]:

$$P_L \widetilde{\chi} = -\theta_x \sin\gamma_L \left(\gamma_5\right)^{\theta_{\widetilde{W}_2}} P_L \widetilde{W}_2 + \cos\gamma_L \left(\gamma_5\right)^{\theta_{\widetilde{W}_1}} P_L \widetilde{W}_1 \tag{A.107}$$

$$P_R \widetilde{\chi} = -\theta_y \sin\gamma_R \left(\gamma_5\right)^{\theta_{\widetilde{W}_2}} P_R \widetilde{W}_2 + \cos\gamma_R \left(\gamma_5\right)^{\theta_{\widetilde{W}_1}} P_R \widetilde{W}_1 \tag{A.108}$$

where $\gamma_{L/R}$, $\theta_{x,y}$, and $\theta_{\widetilde{W}_{1/2}}$ are defined identically as for the gaugino components of the charginos.

The modulus interaction with pairs of the lighter charginos is governed by the term

$$\mathcal{L}_{\phi \overline{\widetilde{W}}_1 \widetilde{W}_1} \supset i \left(\frac{\lambda_{H_u} + \lambda_{H_d}}{\sqrt{2}\, m_P} \right) \phi \overline{\widetilde{W}_1} \not{\partial} (x_s - y_s \gamma_5) \widetilde{W}_1 \tag{A.109}$$

while the modulus interaction with pairs of the heavier charginos is governed by

$$\mathcal{L}_{\phi\overline{\widetilde{W}}_2\widetilde{W}_2} \supset i\left(\frac{\lambda_{H_u}+\lambda_{H_d}}{\sqrt{2}\,m_P}\right)\phi\overline{\widetilde{W}_2}\not{\partial}(x_c-y_c\gamma_5)\widetilde{W}_2 \tag{A.110}$$

where we have made use of the definitions in Eq. (A.81). Finally, the modulus interaction with a heavy and a light chargino is then given by the terms:

$$\mathcal{L}_{\phi\widetilde{W}_1\widetilde{W}_2} \supset -i\left(\frac{\lambda_{H_u}+\lambda_{H_d}}{\sqrt{2}\,m_P}\right)\left[\phi\overline{\widetilde{W}_2}\not{\partial}(x-y\gamma_5)\widetilde{W}_1+\phi\overline{\widetilde{W}_1}\not{\partial}(x-y\gamma_5)\widetilde{W}_2\right] \tag{A.111}$$

where we have made use of the definitions in Eq. (A.83).

A.5.3 Charged Higgs F-term interactions

The interactions with the relevant F-terms lead to the additional modulus interactions:

$$\mathcal{L}_{\phi\mathcal{F}_{h_u^+}\mathcal{F}_{h_u^+}} \supset \frac{\sqrt{2}\lambda_{H_u}}{m_P}\phi\mathcal{F}_{h_u^+}\mathcal{F}^\dagger_{h_u^+}+\frac{\sqrt{2}\lambda_{H_d}}{m_P}\phi\mathcal{F}_{h_d^-}\mathcal{F}^\dagger_{h_d^-} \tag{A.112}$$

Using the equations of motion for each F-term, we see that there are numerous higher order interactions allowing for 4-body decays (and higher) to the quark and lepton superfields. However, in the presence of a μ-term the following two interactions are induced:

$$\mathcal{L}_{\phi\mathcal{F}_{h_u^+}\mathcal{F}_{h_u^+}} \supset \frac{\sqrt{2}\lambda_{H_u}}{m_P}\mu^2\,\phi h_d^{-*}h_d^-+\frac{\sqrt{2}\lambda_{H_d}}{m_P}\mu^2\,\phi h_u^{+*}h_u^+ \tag{A.113}$$

which are 2-body decay terms. It is straightforward to rewrite these in terms of the physical charged Higgs particles. Clearly, these terms are negligible as they lead to mass-suppressed decay widths of the form $\sim \mu^4/m_P^2 m_\phi$.

We now consider the terms involving the F-term of the modulus. The interactions with the scalar components are

$$\mathcal{L}_{\mathcal{F}_\phi} \supset \frac{\lambda_{\rm GM}}{m_P}\left[h_u^+ \mathcal{F}_{h_d^-} \mathcal{F}_\phi^\dagger + h_d^- \mathcal{F}_{h_u^+} \mathcal{F}_\phi^\dagger\right] + \frac{\lambda_{H_u}}{m_P} h_u^{+*} \mathcal{F}_{h_u^+} \mathcal{F}_\phi^\dagger + \frac{\lambda_{H_d}}{m_P} h_d^{-*} \mathcal{F}_{h_d^-} \mathcal{F}_\phi^\dagger + \text{h.c.} \tag{A.114}$$

Once again replacing the F-terms of the Higgses and the modulus using their equations of motion, the leading interactions are given by

$$\mathcal{L}_{\mathcal{F}_\phi} \supset \frac{\sqrt{2}\lambda_{\rm GM}}{m_P} M_\Phi \mu \left[h_u^+ h_u^{+*} \phi + h_d^- h_d^{-*} \phi\right] + \frac{\sqrt{2}\,(\lambda_{H_u} + \lambda_{H_d})}{m_P} M_\Phi \mu\, h_u^{+*} h_d^{-*} \phi + \text{h.c.} \tag{A.115}$$

where again M_Φ is the supersymmetric contribution to the modulus mass. Evidently, regardless of whether or not the Giudice-Masiero term is allowed, the F-term interactions lead to the helicity-suppressed decay width form $\sim \mu^2 m_\phi/m_P^2$ for decays to charged Higgses if $M_\Phi \sim m_\phi$.

We also have the following F-term interaction from the Giudice-Masiero operator:

$$\mathcal{L} \supset \frac{\sqrt{2}\lambda_{\rm GM}}{m_P}\left[M_\Phi \phi \overline{\psi}_{h_u^+} P_L \psi_{h_d^-}\right] + \text{h.c.} \tag{A.116}$$

This F-term interaction, similar to the previous modulus-higgsino interaction terms, can be rewritten in terms of the physical charginos. As with the F-term interactions through the gaugino mass term, the F-term interactions with the higgsino mass term also lead to unsuppressed decays to charginos if $M_\Phi \sim m_\phi$.

A.5.4 Neutral Higgs interactions

Focusing now on modulus interactions with the neutral Higgses, the relevant terms are

$$\begin{aligned} m_P \mathcal{L}_{H,\text{ neutral}} \supset & -\frac{\lambda_{\text{GM}}}{\sqrt{2}}\left[h_u^{0*} h_d^{0*} + h_u^0 h_d^0\right]\partial^2\phi - i\frac{\lambda_{\text{GM}}}{\sqrt{2}}\left[h_u^{0*} h_d^{0*} - h_u^0 h_d^0\right]\partial^2 c \\ & -\frac{\lambda_{H_u}}{\sqrt{2}}\left[h_u^0 \partial^2 h_u^{0*} + h_u^{0*}\partial^2 h_u^0\right]\phi - \frac{\lambda_{H_d}}{\sqrt{2}}\left[h_d^0 \partial^2 h_d^{0*} + h_d^{0*}\partial^2 h_d^0\right]\phi \\ & -i\frac{\lambda_{H_u}}{\sqrt{2}}\left[h_u^0 \partial^2 h_u^{0*} - h_u^{0*}\partial^2 h_u^0\right] c - i\frac{\lambda_{H_d}}{\sqrt{2}}\left[h_d^0 \partial^2 h_d^{0*} - h_d^{0*}\partial^2 h_d^0\right] c \end{aligned} \tag{A.117}$$

where we again used $\Phi \equiv (\phi + ic)/\sqrt{2}$. Splitting this apart into the real and imaginary components of the Higgses, e.g. $h_u^0 = (h_{uR}^0 + i h_{uI}^0)/\sqrt{2}$ and likewise for h_d^0, this becomes

$$\begin{aligned} m_P \mathcal{L}_{H,\text{ neutral}} \supset & -\frac{\lambda_{\text{GM}}}{\sqrt{2}}\left[h_{uR}^0 h_{dR}^0 - h_{dI}^0 h_{uI}^0\right]\partial^2\phi - \frac{\lambda_{\text{GM}}}{\sqrt{2}}\left[h_{uI}^0 h_{dR}^0 + h_{dI}^0 h_{uR}^0\right]\partial^2 c \\ & -\frac{\lambda_{H_u}}{\sqrt{2}}\left[h_{uR}^0 \partial^2 h_{uR}^0 + h_{uI}^0 \partial^2 h_{uI}^0\right]\phi - \frac{\lambda_{H_d}}{\sqrt{2}}\left[h_{dR}^0 \partial^2 h_{dR}^0 + h_{dI}^0 \partial^2 h_{dI}^0\right]\phi \\ & +\frac{\lambda_{H_u}}{\sqrt{2}}\left[h_{uI}^0 \partial^2 h_{uR}^0 - h_{uR}^0 \partial^2 h_{uI}^0\right] c + \frac{\lambda_{H_d}}{\sqrt{2}}\left[h_{dI}^0 \partial^2 h_{dR}^0 - h_{dR}^0 \partial^2 h_{dI}^0\right] c. \end{aligned} \tag{A.118}$$

Utilizing the transformations [1]

$$\begin{pmatrix} h^0_{uR} \\ h^0_{dR} \end{pmatrix} = \begin{pmatrix} \cos\alpha & -\sin\alpha \\ \sin\alpha & \cos\alpha \end{pmatrix} \begin{pmatrix} h \\ H \end{pmatrix} \tag{A.119}$$

and

$$\begin{pmatrix} h^0_{uI} \\ h^0_{dI} \end{pmatrix} = \begin{pmatrix} \sin\beta & \cos\beta \\ -\cos\beta & \sin\beta \end{pmatrix} \begin{pmatrix} G^0 \\ A \end{pmatrix} \tag{A.120}$$

we may now move to the mass-eigenstate basis. The interaction between the modulus and light Higgs pairs is given by

$$\mathcal{L}_{\phi hh} \supset -\frac{\lambda_{\rm GM}\sin(2\alpha)}{2\sqrt{2}\,m_P}\,hh\,\partial^2\phi - \left(\frac{\lambda_{H_u}\cos^2\alpha + \lambda_{H_d}\sin^2\alpha}{\sqrt{2}\,m_P}\right)\phi h\,\partial^2 h \tag{A.121}$$

while the interaction between the modulus and the heavy Higgs pairs is given by

$$\mathcal{L}_{\phi HH} \supset \frac{\lambda_{\rm GM}\sin(2\alpha)}{2\sqrt{2}\,m_P}\,HH\,\partial^2\phi - \left(\frac{\lambda_{H_u}\sin^2\alpha + \lambda_{H_d}\cos^2\alpha}{\sqrt{2}\,m_P}\right)\phi H\,\partial^2 H. \tag{A.122}$$

The interaction between the modulus and a CP-odd Higgs pair is given by

$$\mathcal{L}_{\phi AA} \supset \frac{\lambda_{\rm GM}\sin(2\beta)}{2\sqrt{2}\,m_P}\,AA\,\partial^2\phi - \left(\frac{\lambda_{H_u}\cos^2\beta + \lambda_{H_d}\sin^2\beta}{\sqrt{2}\,m_P}\right)\phi A\,\partial^2 A. \tag{A.123}$$

The interaction between the modulus and neutral Goldstone boson pairs is given by

$$\mathcal{L}_{\phi G^0 G^0} \supset -\frac{\lambda_{\rm GM}\sin(2\beta)}{2\sqrt{2}\,m_P}\,G^0 G^0\,\partial^2\phi - \left(\frac{\lambda_{H_u}\sin^2\beta + \lambda_{H_d}\cos^2\beta}{\sqrt{2}\,m_P}\right)\phi G^0\,\partial^2 G^0. \tag{A.124}$$

Moving to the interactions of the modulus with mixed pairs of Higgses, we begin with the interaction between the modulus and a light and a heavy Higgs:

$$\mathcal{L}_{\phi h H} \supset -\frac{\lambda_{\rm GM}\cos(2\alpha)}{\sqrt{2}\,m_P}\,hH\,\partial^2\phi - \frac{(\lambda_{H_d}-\lambda_{H_u})\sin(2\alpha)}{2\sqrt{2}\,m_P}\left[\phi H\,\partial^2 h + \phi h\,\partial^2 H\right]. \tag{A.125}$$

Finally, we have the interaction between the modulus and the CP-odd Higgs and the neutral Goldstone boson:

$$\mathcal{L}_{\phi A G^0} \supset -\frac{\lambda_{\rm GM}\cos(2\beta)}{\sqrt{2}\,m_P}\,G^0 A\,\partial^2\phi - \frac{(\lambda_{H_u}-\lambda_{H_d})\sin(2\beta)}{2\sqrt{2}\,m_P}\left[\phi A\,\partial^2 G^0 + \phi G^0\,\partial^2 A\right]. \tag{A.126}$$

A.5.5 Neutral higgsino interactions

The interaction between the modulus and neutral higgsinos once again arises solely from the kinetic couplings. The relevant terms are

$$\begin{aligned}\mathcal{L}_{H,\,\rm neutral} \supset\; & i\frac{\lambda_{H_u}}{\sqrt{2}\,m_P}\left[\phi\overline{\psi}_{h_u^0}\partial\!\!\!/\psi_{h_u^0} + ic\overline{\psi}_{h_u^0}\partial\!\!\!/\gamma_5\psi_{h_u^0}\right] \\ & + i\frac{\lambda_{H_d}}{\sqrt{2}\,m_P}\left[\phi\overline{\psi}_{h_d^0}\partial\!\!\!/\psi_{h_d^0} + ic\overline{\psi}_{h_d^0}\partial\!\!\!/\gamma_5\psi_{h_d^0}\right].\end{aligned} \tag{A.127}$$

In order to move to the mass-eigenstates, we use the following transformations [1]:

$$\psi_{h_u^0} = \sum_{i=1}^{4} v_1^{(i)} \left(-i\gamma_5\right)^{\theta_i} \widetilde{Z}_i \tag{A.128}$$

$$\psi_{h_d^0} = \sum_{j=1}^{4} v_2^{(j)} \left(-i\gamma_5\right)^{\theta_j} \widetilde{Z}_j \tag{A.129}$$

where $v_{1/2}^{(i)}$ are elements of the matrix which diagonalizes the neutral gaugino-higgsino mass matrix, and θ_i is defined to be either 0 or 1 such that the corresponding neutralino mass is non-negative.

The interactions between the modulus and pairs of identical neutralinos is given by

$$\mathcal{L}_{\phi\overline{\widetilde{Z}}_i\widetilde{Z}_i} \supset i \left(\frac{\lambda_{H_u}\left(v_1^{(i)}\right)^2 + \lambda_{H_d}\left(v_2^{(i)}\right)^2}{\sqrt{2}\, m_P} \right) \phi \overline{\widetilde{Z}}_i \partial\!\!\!/ \widetilde{Z}_i. \tag{A.130}$$

The interactions between the modulus and two differing neutralinos ($i \neq j$) is then given by

$$\mathcal{L}_{\phi\overline{\widetilde{Z}}_i\widetilde{Z}_j} \supset i\,(i)^{\theta_i}\,(-i)^{\theta_j} \left(\frac{\lambda_{H_u} v_1^{(i)} v_1^{(j)} + \lambda_{H_d} v_2^{(i)} v_2^{(j)}}{\sqrt{2}\, m_P} \right) \phi \overline{\widetilde{Z}}_i \partial\!\!\!/ \left(\gamma_5\right)^{\theta_i+\theta_j} \widetilde{Z}_j \tag{A.131}$$

A.5.6 Neutral Higgs F-term interactions

The interactions with the neutral Higgs F-terms lead to the additional modulus interactions:

$$\mathcal{L}_{\phi\mathcal{F}_{h_u^0}\mathcal{F}_{h_u^0}} \supset \frac{\sqrt{2}\lambda_{H_u}}{m_P}\phi\mathcal{F}_{h_u^0}\mathcal{F}^\dagger_{h_u^0} + \frac{\sqrt{2}\lambda_{H_d}}{m_P}\phi\mathcal{F}_{h_d^0}\mathcal{F}^\dagger_{h_d^0} \tag{A.132}$$

As with the charged Higgs F-term interactions, the only 2-body decays arise in the presence of a μ-term:

$$\mathcal{L}_{\phi\mathcal{F}_{h_u^0}\mathcal{F}_{h_u^0}} \supset \frac{\sqrt{2}\lambda_{H_u}}{m_P}\mu^2\,\phi h_d^{0*}h_d^0 + \frac{\sqrt{2}\lambda_{H_d}}{m_P}\mu^2\,\phi h_u^{0*}h_u^0 \tag{A.133}$$

which are again negligible as the decay widths are of the form $\sim \mu^4/m_P^2 m_\phi$.

Considering now the modulus F-term interactions, we have

$$\mathcal{L}_{\mathcal{F}_\phi} \supset \frac{\lambda_{\rm GM}}{m_P}\left[h_u^0\mathcal{F}_{h_d^0}\mathcal{F}^\dagger_\phi + h_d^0\mathcal{F}_{h_u^0}\mathcal{F}^\dagger_\phi\right] + \frac{\lambda_{H_u}}{m_P}h_u^{0*}\mathcal{F}_{h_u^0}\mathcal{F}^\dagger_\phi + \frac{\lambda_{H_d}}{m_P}h_d^{0*}\mathcal{F}_{h_d^0}\mathcal{F}^\dagger_\phi + \text{h.c.} \tag{A.134}$$

Once more replacing the F-terms via their equations of motion, the leading interactions are given by

$$\mathcal{L}_{\mathcal{F}_\phi} \supset \frac{\sqrt{2}\lambda_{\rm GM}}{m_P}M_\Phi\mu\left[h_u^0h_u^{0*}\phi + h_d^0h_d^{0*}\phi\right] + \frac{\sqrt{2}\,(\lambda_{H_u}+\lambda_{H_d})}{m_P}M_\Phi\mu\,h_u^{0*}h_d^{0*}\phi + \text{h.c.} \tag{A.135}$$

where again M_Φ is the supersymmetric contribution to the modulus mass. Again

we find that the F-term interactions lead to the helicity-suppressed decay width form $\sim \mu^2 m_\phi / m_P^2$ for decays to neutral Higgses if $M_\Phi \sim m_\phi$, regardless of whether or not the Giudice-Masiero term is allowed.

We also have the F-term interaction from the Giudice-Masiero operator:

$$\mathcal{L} \supset \frac{\sqrt{2}\lambda_{\rm GM}}{m_P}\left[M_\Phi \phi \overline{\psi}_{h_u^0} P_L \psi_{h_d^0}\right] + \text{h.c.} \tag{A.136}$$

which can be rewritten in terms of the physical neutralinos. As with the charginos, the F-term interactions with the higgsino mass term lead to unsuppressed decays to neutralinos if $M_\Phi \sim m_\phi$, much like the F-term interactions through the gaugino mass term.

A.6 Moduli-matter interactions

The leading interaction term between the modulus and matter (i.e. quark and lepton superfields) sector is

$$\mathcal{L}_M \supset \int d^4\theta \left[\frac{\lambda_M}{m_P}\hat{\phi}\hat{M}^\dagger \hat{M} + \text{h.c.}\right] \tag{A.137}$$

where $\hat{M} \in \{\hat{L}, \hat{E}^c, \hat{Q}, \hat{U}^c, \hat{D}^c\}$. Using Eq. (A.23), we can evaluate the superspace integral, which becomes:

$$\begin{aligned}\mathcal{L}_M \supset -\frac{\lambda_M}{m_P}\left[\Phi M \partial^2 M^\dagger\right] + i\frac{\lambda_M}{m_P}\Big[\Phi\overline{\psi}_M \not{\partial} P_R \psi_M + M\overline{\psi}_\phi \not{\partial} P_R \psi_M\Big] \\ + \frac{\lambda_M}{m_P}\Big[\Phi \mathcal{F}_M \mathcal{F}_M^\dagger + M\mathcal{F}_\phi \mathcal{F}_M^\dagger - i\mathcal{F}_M^\dagger \overline{\psi}_\phi P_L \psi_M\Big] + \text{h.c.}\end{aligned} \tag{A.138}$$

A.6.1 Squark interactions

Focusing first on the modulus interactions with squarks, we have the following terms:

$$\begin{aligned}\mathcal{L}_M \supset &-\frac{\lambda_{Q_i}}{\sqrt{2}\,m_P}\Big[\phi\widetilde{u}_{L,i}\partial^2\widetilde{u}^\dagger_{L,i} + \phi\widetilde{u}^\dagger_{L,i}\partial^2\widetilde{u}_{L,i} + \phi\widetilde{d}_{L,i}\partial^2\widetilde{d}^\dagger_{L,i} + \phi\widetilde{d}^\dagger_{L,i}\partial^2\widetilde{d}_{L,i}\Big] \\ &-\frac{\lambda_{U_i}}{\sqrt{2}\,m_P}\Big[\phi\widetilde{U}_i\partial^2\widetilde{U}^\dagger_i + \phi\widetilde{U}^\dagger_i\partial^2\widetilde{U}_i\Big] - \frac{\lambda_{D_i}}{\sqrt{2}\,m_P}\Big[\phi\widetilde{D}_i\partial^2\widetilde{D}^\dagger_i + \phi\widetilde{D}^\dagger_i\partial^2\widetilde{D}_i\Big] \\ &-i\frac{\lambda_{Q_i}}{\sqrt{2}\,m_P}\Big[c\widetilde{u}_{L,i}\partial^2\widetilde{u}^\dagger_{L,i} - c\widetilde{u}^\dagger_{L,i}\partial^2\widetilde{u}_{L,i} + c\widetilde{d}_{L,i}\partial^2\widetilde{d}^\dagger_{L,i} - c\widetilde{d}^\dagger_{L,i}\partial^2\widetilde{d}_{L,i}\Big] \\ &-i\frac{\lambda_{U_i}}{\sqrt{2}\,m_P}\Big[c\widetilde{U}_i\partial^2\widetilde{U}^\dagger_i - c\widetilde{U}^\dagger_i\partial^2\widetilde{U}_i\Big] - i\frac{\lambda_{D_i}}{\sqrt{2}\,m_P}\Big[c\widetilde{D}_i\partial^2\widetilde{D}^\dagger_i - c\widetilde{D}^\dagger_i\partial^2\widetilde{D}_i\Big]\end{aligned} \tag{A.139}$$

where $\widetilde{u}_{L,i}$ and $\widetilde{d}_{L,i}$ are respectively the up and down $SU(2)_L$ doublet squarks, $\widetilde{U}_i$ and $\widetilde{D}_i$ are respectively the up and down $SU(2)_L$ singlet squarks, and $i \in \{1, 2, 3\}$ is the generation index.

Moving to the mass-eigenstates, the first two generations of squarks have minimal mixing and hence the gauge-eigenstates are approximately mass-eigenstates.

Thus, we have the interactions between the modulus and the left-handed squarks

$$\mathcal{L}_{\phi\widetilde{q}_L\widetilde{q}_L} \supset -\frac{\lambda_{Q_i}}{\sqrt{2}\,m_P}\left[\phi\widetilde{q}_L\partial^2\widetilde{q}_L^\dagger + \phi\widetilde{q}_L^\dagger\partial^2\widetilde{q}_L\right] \tag{A.140}$$

where $\widetilde{q}_L \in \{\widetilde{u}_L, \widetilde{d}_L, \widetilde{c}_L, \widetilde{s}_L\}$ and the coupling index $i \in \{1, 2\}$ again labels the generation. Similarly, for the modulus interactions with the right-handed squarks, we have

$$\mathcal{L}_{\phi\widetilde{q}_R\widetilde{q}_R} \supset -\frac{\lambda_{q_i}}{\sqrt{2}\,m_P}\left[\phi\widetilde{q}_R\partial^2\widetilde{q}_R^\dagger + \phi\widetilde{q}_R^\dagger\partial^2\widetilde{q}_R\right] \tag{A.141}$$

where $\widetilde{q}_R \in \{\widetilde{u}_R, \widetilde{d}_R, \widetilde{c}_R, \widetilde{s}_R\}$, the coupling $\lambda_{q_i} \equiv \lambda_{U_i}$ if $\widetilde{q}_R$ is an up-type squark and $\lambda_{q_i} \equiv \lambda_{D_i}$ if it is a down-type squark, and $i \in \{1, 2\}$ is once again the generation index.

For the third-generation squarks, mixing can no longer be neglected. For the top squarks, we use the transformation [1]

$$\begin{pmatrix}\widetilde{t}_L\\ \widetilde{t}_R\end{pmatrix} = \begin{pmatrix}\cos\theta_t & \sin\theta_t\\ -\sin\theta_t & \cos\theta_t\end{pmatrix}\begin{pmatrix}\widetilde{t}_1\\ \widetilde{t}_2\end{pmatrix} \tag{A.142}$$

where θ_t is the top squark mixing angle. The same transformation also holds for the bottom squarks with the interchange $\theta_t \to \theta_b$ and $\widetilde{t} \to \widetilde{b}$. The modulus interactions with pairs of identical top squarks are then

$$\mathcal{L}_{\phi\widetilde{t}_1\widetilde{t}_1} \supset -\frac{\left(\lambda_{Q_3}\cos^2\theta_t + \lambda_{U_3}\sin^2\theta_t\right)}{\sqrt{2}\,m_P}\left[\phi\widetilde{t}_1\partial^2\widetilde{t}_1^\dagger + \phi\widetilde{t}_1^\dagger\partial^2\widetilde{t}_1\right] \tag{A.143}$$

and

$$\mathcal{L}_{\phi\widetilde{t}_2\widetilde{t}_2} \supset -\frac{\left(\lambda_{Q_3}\sin^2\theta_t + \lambda_{U_3}\cos^2\theta_t\right)}{\sqrt{2}\,m_P}\left[\phi\widetilde{t}_2\partial^2\widetilde{t}_2^\dagger + \phi\widetilde{t}_2^\dagger\partial^2\widetilde{t}_2\right] \tag{A.144}$$

while the modulus interaction with mixed pairs of top squarks is then

$$\mathcal{L}_{\phi\widetilde{t}_1\widetilde{t}_2} \supset -\frac{(\lambda_{Q_3} - \lambda_{U_3})\sin(2\theta_t)}{2\sqrt{2}\,m_P}\left[\phi\widetilde{t}_2\partial^2\widetilde{t}_1^\dagger + \phi\widetilde{t}_1\partial^2\widetilde{t}_2^\dagger + \phi\widetilde{t}_2^\dagger\partial^2\widetilde{t}_1 + \phi\widetilde{t}_1^\dagger\partial^2\widetilde{t}_2\right]. \tag{A.145}$$

The modulus interactions with the bottom squarks are then identical to the three interactions above, with the replacements $\widetilde{t}_{1/2} \to \widetilde{b}_{1/2}$, $\theta_t \to \theta_b$, and $\lambda_{U_3} \to \lambda_{D_3}$ (note that λ_{Q_3} couples both top and bottom squarks to the modulus).

A.6.2 Quark interactions

The interaction between the modulus and quarks arises from the following terms:

$$\begin{aligned}\mathcal{L}_M \supset & i\frac{\lambda_{Q_i}}{\sqrt{2}\,m_P}\left[\phi\overline{u}_{L,i}\not{\partial}u_{L,i} + \phi\overline{d}_{L,i}\not{\partial}d_{L,i}\right] + i\frac{\lambda_{U_i}}{\sqrt{2}\,m_P}\phi\overline{U}_i\not{\partial}U_i + i\frac{\lambda_{D_i}}{\sqrt{2}\,m_P}\phi\overline{D}_i\not{\partial}D_i \\ & - \frac{\lambda_{Q_i}}{\sqrt{2}\,m_P}\left[c\overline{u}_{L,i}\not{\partial}\gamma_5 u_{L,i} + c\overline{d}_{L,i}\not{\partial}\gamma_5 d_{L,i}\right] \\ & - \frac{\lambda_{U_i}}{\sqrt{2}\,m_P}c\overline{U}_i\not{\partial}\gamma_5 U_i - \frac{\lambda_{D_i}}{\sqrt{2}\,m_P}c\overline{D}_i\not{\partial}\gamma_5 D_i\end{aligned} \tag{A.146}$$

where $u_{L,i}$ and $d_{L,i}$ are respectively up and down type $SU(2)_L$ doublet quarks, U_i and D_i are respectively up and down type $SU(2)_L$ singlet quarks, and $i \in \{1,2,3\}$

is once again the generation index. We now can define the Dirac quark fields by

$$q \equiv P_L q_L + P_R Q \tag{A.147}$$

where q_L is any left-handed quark, and Q is the corresponding right-handed quark. The interaction with the Dirac quark fields then becomes

$$\mathcal{L}_{\phi \overline{u}_i u_i} \supset i \frac{(\lambda_{Q_i} + \lambda_{U_i})}{\sqrt{2}\, m_P} \phi \overline{u}_i \partial\!\!\!/ u_i \tag{A.148}$$

for up-type quarks and

$$\mathcal{L}_{\phi \overline{d}_i d_i} \supset i \frac{(\lambda_{Q_i} + \lambda_{D_i})}{\sqrt{2}\, m_P} \phi \overline{d}_i \partial\!\!\!/ d_i \tag{A.149}$$

for down-type quarks.

A.6.3 Quark F-term interactions

The interactions with the quark F-terms of the form

$$\mathcal{L} \supset \frac{\lambda_M}{m_P} \Phi \mathcal{F}_M \mathcal{F}_M^\dagger + \text{h.c.} \tag{A.150}$$

typically leads to 4-body (and higher) decays of the modulus. However there is the exception when the Higgs fields take on their VEVs, which lead to interactions of the form

$$\mathcal{L} \supset \frac{\lambda_{D_i}}{\sqrt{2} m_P} f_d^2 v_d^2\, \phi \widetilde{d}_{L,i}^\dagger \widetilde{d}_{L,i} + \text{h.c.} \tag{A.151}$$

and similarly for the $\mathcal{F}_U$ and $\mathcal{F}_Q$ interactions. These interactions are negligible as they lead to decay widths of the form $\sim v_d^4/m_P^2 m_\phi$ and, additionally, only third generation quark components are expected to contribute [1].

The modulus F-term interactions of the form

$$\mathcal{L} \supset \frac{\lambda_M}{m_P} M \mathcal{F}_\phi \mathcal{F}_M^\dagger + \text{h.c.} \tag{A.152}$$

typically lead to 3-body decays, except when the Higgs fields acquire their VEVs. In this case, we have

$$\mathcal{L} \supset \frac{\sqrt{2}\lambda_{D_i}}{m_P} f_d v_d M_\Phi \, \phi \widetilde{d}_{R,i}^\dagger \widetilde{d}_{L,i} + \text{h.c.} \tag{A.153}$$

and similarly for the $\mathcal{F}_U$ and $\mathcal{F}_Q$ terms. If we have $M_\Phi \sim m_\phi$, these lead to decay widths of the helicity-suppressed form $v_d^2 m_\phi / m_P^2$.

A.6.4 Slepton interactions

The slepton interactions with the modulus follow similarly to the squark case. Applying Eq. (A.138) to the lepton superfields, we have

$$\begin{aligned}
\mathcal{L}_M \supset & -\frac{\lambda_{L_i}}{\sqrt{2}\, m_P} \left[\phi \widetilde{e}_{L,i} \partial^2 \widetilde{e}_{L,i}^\dagger + \phi \widetilde{e}_{L,i}^\dagger \partial^2 \widetilde{e}_{L,i} + \phi \widetilde{\nu}_{L,i} \partial^2 \widetilde{\nu}_{L,i}^\dagger + \phi \widetilde{\nu}_{L,i}^\dagger \partial^2 \widetilde{\nu}_{L,i} \right] \\
& - \frac{\lambda_{E_i}}{\sqrt{2}\, m_P} \left[\phi \widetilde{E}_i \partial^2 \widetilde{E}_i^\dagger + \phi \widetilde{E}_i^\dagger \partial^2 \widetilde{E}_i \right] \\
& - i \frac{\lambda_{L_i}}{\sqrt{2}\, m_P} \left[c \widetilde{e}_{L,i} \partial^2 \widetilde{e}_{L,i}^\dagger - c \widetilde{e}_{L,i}^\dagger \partial^2 \widetilde{e}_{L,i} + c \widetilde{\nu}_{L,i} \partial^2 \widetilde{\nu}_{L,i}^\dagger - c \widetilde{\nu}_{L,i}^\dagger \partial^2 \widetilde{\nu}_{L,i} \right] \\
& - i \frac{\lambda_{E_i}}{\sqrt{2}\, m_P} \left[c \widetilde{E}_i \partial^2 \widetilde{E}_i^\dagger - c \widetilde{E}_i^\dagger \partial^2 \widetilde{E}_i \right]
\end{aligned} \tag{A.154}$$

where $\widetilde{e}_{L,i}$ and $\widetilde{\nu}_{L,i}$ are respectively the $SU(2)_L$ doublet selectron and sneutrinos, $\widetilde{E}_i$ is the $SU(2)_L$ singlet selectron, and $i \in \{1,2,3\}$ is the generation index.

Moving to the mass-eigenstates, again the first two generations of selectrons have minimal mixing and thus the gauge-eigenstates are also approximately mass-eigenstates. Additionally, since lepton flavor conservation is assumed and the neutrinos are assumed massless, the sneutrino gauge-eigenstates are also mass-eigenstates. The interactions between the modulus and the left-handed sleptons is thus given by

$$\mathcal{L}_{\phi\widetilde{f}_L\widetilde{f}_L} \supset -\frac{\lambda_{L_i}}{\sqrt{2}\,m_P}\left[\phi\widetilde{f}_L\partial^2\widetilde{f}_L^\dagger + \phi\widetilde{f}_L^\dagger\partial^2\widetilde{f}_L\right] \tag{A.155}$$

where $\widetilde{f}_L \in \{\widetilde{e}_L, \widetilde{\nu}_{e,L}, \widetilde{\mu}_L, \widetilde{\nu}_{\mu,L}, \widetilde{\nu}_{\tau,L}\}$ and the coupling index $i \in \{1,2,3\}$ is again the generation index.

Similarly, the interactions with the right-handed selectrons is given by

$$\mathcal{L}_{\phi\widetilde{f}_R\widetilde{f}_R} \supset -\frac{\lambda_{E_i}}{\sqrt{2}\,m_P}\left[\phi\widetilde{f}_R\partial^2\widetilde{f}_R^\dagger + \phi\widetilde{f}_R^\dagger\partial^2\widetilde{f}_R\right] \tag{A.156}$$

where $\widetilde{f}_R \in \{\widetilde{e}_R, \widetilde{\mu}_R\}$ and once again the coupling index $i \in \{1,2\}$ is the generation index.

The interactions with the staus, however, must take mixing into account - much like the top and bottom squarks. To move to the mass-eigenstates for the

staus, we use the transformation [1]

$$\begin{pmatrix} \widetilde{\tau}_L \\ \widetilde{\tau}_R \end{pmatrix} = \begin{pmatrix} \cos\theta_\tau & \sin\theta_\tau \\ -\sin\theta_\tau & \cos\theta_\tau \end{pmatrix} \begin{pmatrix} \widetilde{\tau}_1 \\ \widetilde{\tau}_2 \end{pmatrix} \tag{A.157}$$

where θ_τ is the mixing angle between staus. The modulus interactions with pairs of identical staus are then

$$\mathcal{L}_{\phi\widetilde{\tau}_1\widetilde{\tau}_1} \supset -\frac{\left(\lambda_{L_3}\cos^2\theta_\tau + \lambda_{E_3}\sin^2\theta_\tau\right)}{\sqrt{2}\,m_P}\left[\phi\widetilde{\tau}_1\partial^2\widetilde{\tau}_1^\dagger + \phi\widetilde{\tau}_1^\dagger\partial^2\widetilde{\tau}_1\right] \tag{A.158}$$

and

$$\mathcal{L}_{\phi\widetilde{\tau}_2\widetilde{\tau}_2} \supset -\frac{\left(\lambda_{L_3}\sin^2\theta_\tau + \lambda_{E_3}\cos^2\theta_\tau\right)}{\sqrt{2}\,m_P}\left[\phi\widetilde{\tau}_2\partial^2\widetilde{\tau}_2^\dagger + \phi\widetilde{\tau}_2^\dagger\partial^2\widetilde{\tau}_2\right] \tag{A.159}$$

while the modulus interaction with mixed pairs of staus is then

$$\mathcal{L}_{\phi\widetilde{\tau}_1\widetilde{\tau}_2} \supset -\frac{(\lambda_{L_3}-\lambda_{E_3})\sin(2\theta_\tau)}{2\sqrt{2}\,m_P}\left[\phi\widetilde{\tau}_2\partial^2\widetilde{\tau}_1^\dagger + \phi\widetilde{\tau}_1\partial^2\widetilde{\tau}_2^\dagger + \phi\widetilde{\tau}_2^\dagger\partial^2\widetilde{\tau}_1 + \phi\widetilde{\tau}_1^\dagger\partial^2\widetilde{\tau}_2\right]. \tag{A.160}$$

A.6.5 Lepton interactions

The lepton interactions with the modulus follow nearly identically to the quark interactions. Applying Eq. (A.138) to the lepton superfields, we have the terms

$$\begin{aligned}\mathcal{L}_M \supset & i\frac{\lambda_{L_i}}{\sqrt{2}\,m_P}\left[\phi\overline{e}_{L,i}\not{\partial}e_{L,i} + \phi\overline{\nu}_{L,i}\not{\partial}\nu_{L,i}\right] + i\frac{\lambda_{E_i}}{\sqrt{2}\,m_P}\phi\overline{E}_i\not{\partial}E_i \\ & - \frac{\lambda_{L_i}}{\sqrt{2}\,m_P}\left[c\overline{e}_{L,i}\not{\partial}\gamma_5 e_{L,i} + c\overline{\nu}_{L,i}\not{\partial}\gamma_5\nu_{L,i}\right] - \frac{\lambda_{E_i}}{\sqrt{2}\,m_P}c\overline{E}_i\not{\partial}\gamma_5 E_i\end{aligned} \tag{A.161}$$

where $e_{L,i}$ and $\nu_{L,i}$ are respectively $SU(2)_L$ doublet electrons and neutrinos, E_i are the $SU(2)_L$ singlet electrons, and once more $i \in \{1,2,3\}$ is the generation index. We define the Dirac lepton fields by

$$l \equiv P_L l_L + P_R L \tag{A.162}$$

where l_L is any left-handed lepton, and L is the corresponding right-handed lepton. The interaction with the Dirac lepton fields then becomes

$$\mathcal{L}_{\phi\overline{e}_i e_i} \supset i\frac{(\lambda_{L_i} + \lambda_{E_i})}{\sqrt{2}\, m_P}\phi\overline{e}_i \not{\partial} e_i \tag{A.163}$$

for the electron generations and

$$\mathcal{L}_{\phi\overline{\nu}_i \nu_i} \supset i\frac{\lambda_{L_i}}{\sqrt{2}\, m_P}\phi\overline{\nu}_i \not{\partial} \nu_i \tag{A.164}$$

for the neutrino generations.

A.6.6 Lepton F-term interactions

The interactions with the lepton F-terms, similar to those of the quark F-terms, only lead to 2-body decays when the Higgs fields take on their VEVs. We then have interactions of the form

$$\mathcal{L} \supset \frac{\lambda_{E_i}}{\sqrt{2} m_P} f_e^2 v_d^2\, \phi \widetilde{e}^{\dagger}_{L,i} \widetilde{e}_{L,i} + \text{h.c.} \tag{A.165}$$

and similarly for the $\mathcal{F}_L$ interaction. Much like in the quark F-term case, these interactions are negligible as they lead to decay widths of the form $\sim v_d^4/m_P^2 m_\phi$ with again only third generation lepton components contributing [1].

The modulus F-term interactions again lead to 3-body decays except when the Higgs fields acquire their VEVs. This leads to interactions of the form

$$\mathcal{L} \supset \frac{\sqrt{2}\lambda_{E_i}}{m_P} f_e v_d M_\Phi \, \phi \widetilde{e}^\dagger_{L,i} \widetilde{e}_{R,i} + \text{h.c.} \tag{A.166}$$

and similarly for the $\mathcal{F}_L$ interaction. For $M_\Phi \sim m_\phi$, these lead to decay widths of the helicity-suppressed form $v_d^2 m_\phi / m_P^2$.

A.7 Moduli-PQ sector interactions

The leading interaction term between the modulus and PQ-axion superfields is given by

$$\mathcal{L}_{\text{PQ}} \supset \int d^4\theta \left[\frac{\lambda_{\text{PQ}}}{2m_P} \hat{\phi} \left(\hat{A} + \hat{A}^\dagger \right)^2 + \text{h.c.} \right] \tag{A.167}$$

Expanding, we see

$$\mathcal{L}_{\text{PQ}} \supset \frac{\lambda_{\text{PQ}}}{2m_P} \int d^4\theta \left[2\hat{\phi}\hat{A}^\dagger\hat{A} + \hat{\phi}\hat{A}^\dagger\hat{A}^\dagger + \text{h.c.} \right] \tag{A.168}$$

where the $\hat{\phi}\hat{A}\hat{A} + \text{h.c.}$ term vanishes due to Eq. (A.21).

Using Eq. (A.23), we can evaluate the above superspace integral. This gives

$$\begin{aligned}\mathcal{L}_{\rm PQ} \supset & \frac{\lambda_{\rm PQ}}{2m_P}\left[-2\Phi A\partial^2 A^\dagger - A^\dagger A^\dagger \partial^2 \Phi\right] \\ & + i\frac{\lambda_{\rm PQ}}{m_P}\left[\Phi\overline{\widetilde{a}}\not{\partial}P_R\widetilde{a} + A\overline{\psi}_\phi\not{\partial}P_R\widetilde{a} - A\overline{\widetilde{a}}\not{\partial}P_R\psi_\phi\right] \\ & + \frac{\lambda_{\rm PQ}}{m_P}\left[\Phi\mathcal{F}_A\mathcal{F}_A^\dagger + (A+A^\dagger)\mathcal{F}_\phi\mathcal{F}_A^\dagger - i\mathcal{F}_A^\dagger\overline{\psi}_\phi P_L\widetilde{a} + \frac{i}{2}\mathcal{F}_\phi\overline{\widetilde{a}}P_R\widetilde{a}\right] + \text{h.c.}\end{aligned} \tag{A.169}$$

A.7.1 Saxion and axion interactions

Focusing first on the modulus interactions with the scalars, the relevant terms are

$$\begin{aligned}m_P\mathcal{L}_{\text{PQ, scalar}} \supset & -\frac{\lambda_{\rm PQ}}{2\sqrt{2}}\left[ss\partial^2\phi + 2\phi s\partial^2 s - aa\partial^2\phi + 2\phi a\partial^2 a\right] \\ & -\frac{\lambda_{\rm PQ}}{\sqrt{2}}\lambda_{\rm PQ}\left[as\partial^2 c - ca\partial^2 s + cs\partial^2 a\right].\end{aligned} \tag{A.170}$$

This breaks into

$$m_P\mathcal{L}_{\phi ss} \supset -\frac{\lambda_{\rm PQ}}{2\sqrt{2}}\left[ss\partial^2\phi + 2\phi s\partial^2 s\right] \tag{A.171}$$

for the modulus-saxion interactions, and after integrating-by-parts the modulus-axion terms, we have

$$m_P\mathcal{L}_{\phi aa} \supset \frac{\lambda_{\rm PQ}}{\sqrt{2}}\left[\phi\,\partial_\mu a\,\partial^\mu a\right] \tag{A.172}$$

for the modulus-axion interaction, where the required shift symmetry of the axion is manifest. We have also dropped the ALP interaction term as it vanishes upon integrating-by-parts.

A.7.2 Axino interactions

Focusing now on the modulus interactions with the axinos, the relevant terms are

$$m_P \mathcal{L}_{\mathrm{PQ},axino} \supset i\frac{\lambda_{\mathrm{PQ}}}{\sqrt{2}}\,\phi\bar{\widetilde{a}}\partial\!\!\!/\widetilde{a} - \frac{\lambda_{\mathrm{PQ}}}{\sqrt{2}}\,c\bar{\widetilde{a}}\partial\!\!\!/\gamma_5\widetilde{a}. \tag{A.173}$$

A.7.3 PQ F-term interactions

The PQ symmetry forbids the axion supermultiplet from appearing in the superpotential at the perturbative level. However, they may appear non-perturbatively as [285]

$$W \supset \mu \exp\left(c_H \hat{A}/v_{\mathrm{PQ}}\right) \hat{H}_u \hat{H}_d \tag{A.174}$$

where we use that $\mu = \lambda_{\mathrm{PQ}} f_a^2/m_P$ and take c_H to be the PQ charge of the Higgs bilinear $H_u H_d$. From this, we see that any axion F-terms $\mathcal{F}_A$ have a suppression factor of μ/v_{PQ}. We therefore focus only on the modulus F-terms, which reduce to the axino mass term. This gives an interaction of the form

$$\mathcal{L} \supset \frac{\lambda_{\mathrm{PQ}}}{\sqrt{2}\,m_P} M_\Phi \phi\bar{\widetilde{a}} P_R \widetilde{a} + \mathrm{h.c.} \tag{A.175}$$

where, once more, M_Φ is the supersymmetric contribution to the modulus mass m_ϕ. If we have $M_\phi \sim m_\phi$, this produces an unsuppressed decay width $\sim m_\phi^3/m_P^2$.

A.8 Moduli decay widths

Here, we list the model-independent decay widths of the modulus - i.e. neglecting the F-term interactions which may be included straightforwardly from our results in the previous section.

A.8.1 Modulus decay widths to electroweak gauge bosons

We list here the model-independent decay widths to electroweak gauge bosons. Application of Eq. (A.51) to Eq. (A.67) gives the decay width to $W^\pm$ boson pairs:

$$\Gamma_{\phi W^+ W^-} = \frac{\lambda_{SU(2)}^2}{16\pi}\frac{m_\phi^3}{m_P^2}\left[1 - 4\frac{m_W^2}{m_\phi^2} + 6\frac{m_W^4}{m_\phi^4}\right]\lambda^{1/2}\left(1, \frac{m_W^2}{m_\phi^2}, \frac{m_W^2}{m_\phi^2}\right) \tag{A.176}$$

Taking now Eq. (A.68) and applying Eq. (A.52), we have the decay width to Z boson pairs:

$$\Gamma_{\phi Z^0 Z^0} = \frac{\left(\lambda_{U(1)}\sin^2\theta_W + \lambda_{SU(2)}\cos^2\theta_W\right)^2}{32\pi}\frac{m_\phi^3}{m_P^2}\left[1 - 4\frac{m_Z^2}{m_\phi^2} + 6\frac{m_Z^4}{m_\phi^4}\right] \times \lambda^{1/2}\left(1, \frac{m_Z^2}{m_\phi^2}, \frac{m_Z^2}{m_\phi^2}\right). \tag{A.177}$$

Similarly, we take Eq. (A.69) and apply Eq. (A.69) to obtain the decay width to photon pairs:

$$\Gamma_{\phi A^0 A^0} = \frac{\left(\lambda_{U(1)} \cos^2\theta_W + \lambda_{SU(2)} \sin^2\theta_W\right)^2}{32\pi} \frac{m_\phi^3}{m_P^2} \tag{A.178}$$

where the phase space factor has dropped out as both final state particles are massless. Finally, applying Eq. (A.51) to Eq. (A.70) gives the decay width to a photon and Z boson:

$$\Gamma_{\phi Z^0 A^0} = \frac{\sin^2\theta_W \cos^2\theta_W \left(\lambda_{SU(2)} - \lambda_{U(1)}\right)^2}{16\pi} \frac{m_\phi^3}{m_P^2} \left[\left(1 - \frac{m_M^2}{m_\phi^2}\right)^2\right] \times \lambda^{1/2}\left(1, 0, \frac{m_M^2}{m_\phi^2}\right). \tag{A.179}$$

A.8.2 Modulus decay width to gluons

We list here the model-independent decay width of the modulus to gluons. Applying Eq. (A.52) to Eq. (A.89) gives us the decay width:

$$\Gamma_{\phi gg} = \frac{\lambda_{SU(3)}^2}{4\pi} \frac{m_\phi^3}{m_P^2} \tag{A.180}$$

where we have summed over the 8 possible final state gluons. Note that the phase space factor drops out as the gluons are massless.

A.8.3 Modulus decay widths to neutral Higgses

We list here the model-independent decay widths of the modulus into the neutral Higgs sector. Starting with Eq. (A.121), application of Eq. (A.31) gives us the decay width to light Higgs pairs:

$$\Gamma_{\phi hh} = \frac{1}{64\pi}\frac{m_\phi^3}{m_P^2}\left(\lambda_{\rm GM}\sin(2\alpha) + 2\left(\lambda_{H_u}\cos^2\alpha + \lambda_{H_d}\sin^2\alpha\right)\frac{m_h^2}{m_\phi^2}\right)^2 \times \lambda^{1/2}\left(1, \frac{m_h^2}{m_\phi^2}, \frac{m_h^2}{m_\phi^2}\right). \quad \text{(A.181)}$$

Similarly, application of Eq. (A.31) to Eq. (A.122) gives the decay width to heavy Higgs pairs:

$$\Gamma_{\phi HH} = \frac{1}{64\pi}\frac{m_\phi^3}{m_P^2}\left(\lambda_{\rm GM}\sin(2\alpha) - 2\left(\lambda_{H_u}\sin^2\alpha + \lambda_{H_d}\cos^2\alpha\right)\frac{m_H^2}{m_\phi^2}\right)^2 \times \lambda^{1/2}\left(1, \frac{m_H^2}{m_\phi^2}, \frac{m_H^2}{m_\phi^2}\right). \quad \text{(A.182)}$$

The decay width to CP-odd Higgs pairs is obtained from application of Eq. (A.31) to Eq. (A.123):

$$\Gamma_{\phi AA} = \frac{1}{64\pi}\frac{m_\phi^3}{m_P^2}\left(\lambda_{\rm GM}\sin(2\beta) - 2\left(\lambda_{H_u}\cos^2\beta + \lambda_{H_d}\sin^2\beta\right)\frac{m_A^2}{m_\phi^2}\right)^2 \times \lambda^{1/2}\left(1, \frac{m_A^2}{m_\phi^2}, \frac{m_A^2}{m_\phi^2}\right). \quad \text{(A.183)}$$

Moving now to the modulus decay to a light Higgs and a heavy Higgs, applying Eq. (A.30) to Eq. (A.125) gives:

$$\Gamma_{\phi hH} = \frac{1}{128\pi}\frac{m_\phi^3}{m_P^2}\left(2\lambda_{\rm GM}\cos(2\alpha) + (\lambda_{H_d}-\lambda_{H_u})\sin(2\alpha)\left(\frac{m_h^2+m_H^2}{m_\phi^2}\right)\right)^2 \times \lambda^{1/2}\left(1, \frac{m_h^2}{m_\phi^2}, \frac{m_H^2}{m_\phi^2}\right). \quad \text{(A.184)}$$

The widths to would-be Goldstone bosons vanish in the unitary gauge.

A.8.4 Modulus decay widths to charged Higgses

We list here the model-independent decay widths of the modulus into the charged Higgs sector. Starting with Eq. (A.101), application of Eq. (A.35) gives us the decay width to charged Higgs pairs:

$$\Gamma_{\phi H^+H^-} = \frac{1}{32\pi}\frac{m_\phi^3}{m_P^2}\left(\lambda_{\rm GM}\sin(2\beta) - 2\left(\lambda_{H_u}\cos^2\beta + \lambda_{H_d}\sin^2\beta\right)\frac{m_{H^\pm}^2}{m_\phi^2}\right)^2 \times \lambda^{1/2}\left(1, \frac{m_{H^\pm}^2}{m_\phi^2}, \frac{m_{H^\pm}^2}{m_\phi^2}\right). \quad \text{(A.185)}$$

The widths to would-be Goldstone bosons vanish in the unitary gauge.

A.8.5 Modulus decay widths to neutralinos

We list here the model-independent decay widths of the modulus into neutralinos. The interactions for decay into identical neutralino pairs are given by Eq. (A.74)

and Eq. (A.130). These combine into

$$\mathcal{L}_{\phi\overline{\widetilde{Z}}_i\widetilde{Z}_i} = i\left(\frac{\lambda_{H_u}\left(v_1^{(i)}\right)^2 + \lambda_{H_d}\left(v_2^{(i)}\right)^2 + \lambda_{SU(2)}\left(v_3^{(i)}\right)^2 + \lambda_{U(1)}\left(v_4^{(i)}\right)^2}{\sqrt{2}\,m_P}\right)\phi\overline{\widetilde{Z}}_i\not{\partial}\widetilde{Z}_i. \tag{A.186}$$

The interactions for decay into a pair of different neutralinos is then given by Eq. (A.75) and Eq. (A.131). These combine into

$$\begin{aligned}\mathcal{L}_{\phi\overline{\widetilde{Z}}_i\widetilde{Z}_j} \supset\; & i\,(i)^{\theta_i}\,(-i)^{\theta_j} \\ & \times\left(\frac{\left(\lambda_{H_u}v_1^{(i)}v_1^{(j)} + \lambda_{H_d}v_2^{(i)}v_2^{(j)}\right) + (-1)^{\theta_i+\theta_j}\left(\lambda_{SU(2)}v_3^{(i)}v_3^{(j)} + \lambda_{U(1)}v_4^{(i)}v_4^{(j)}\right)}{\sqrt{2}m_P}\right) \\ & \times\phi\overline{\widetilde{Z}}_i\not{\partial}\,(\gamma_5)^{\theta_i+\theta_j}\,\widetilde{Z}_j.\end{aligned} \tag{A.187}$$

Applying Eq. (A.40) to Eq. (A.186), we have the decay width into identical neutralino pairs:

$$\begin{aligned}\Gamma_{\phi\widetilde{Z}_i\widetilde{Z}_i} = & \frac{\left(\lambda_{H_u}\left(v_1^{(i)}\right)^2 + \lambda_{H_d}\left(v_2^{(i)}\right)^2 + \lambda_{SU(2)}\left(v_3^{(i)}\right)^2 + \lambda_{U(1)}\left(v_4^{(i)}\right)^2\right)^2}{8\pi} \\ & \times\frac{m_\phi^3}{m_P^2}\left(\frac{m_{\widetilde{Z}_i}^2}{m_\phi^2}\right)\left(1 - 4\frac{m_{\widetilde{Z}_i}^2}{m_\phi^2}\right)\lambda^{1/2}\left(1, \frac{m_{\widetilde{Z}_i}^2}{m_\phi^2}, \frac{m_{\widetilde{Z}_i}^2}{m_\phi^2}\right).\end{aligned} \tag{A.188}$$

Applying now Eq. (A.44) to Eq. (A.187), we have the decay width into pairs of

different neutralinos:

$$\Gamma_{\phi\overline{\widetilde{Z}}_i\widetilde{Z}_j} = \frac{\left(\left(\lambda_{H_u}v_1^{(i)}v_1^{(j)} + \lambda_{H_d}v_2^{(i)}v_2^{(j)}\right) + (-1)^{\theta_i+\theta_j}\left(\lambda_{SU(2)}v_3^{(i)}v_3^{(j)} + \lambda_{U(1)}v_4^{(i)}v_4^{(j)}\right)\right)^2}{16\pi} \times \frac{m_\phi^3}{m_p^2}\left(\frac{m_{\widetilde{Z}_i}^2 + m_{\widetilde{Z}_j}^2}{m_\phi^2}\right)\left(1 - \frac{(|m_{\widetilde{Z}_i}| + |m_{\widetilde{Z}_j}|)^2}{m_\phi^2}\right)\lambda^{1/2}\left(1, \frac{m_{\widetilde{Z}_i}^2}{m_\phi^2}, \frac{m_{\widetilde{Z}_j}^2}{m_\phi^2}\right) \quad \text{(A.189)}$$

where the absolute value on the "masses" allow for the negative mass from diagonalization of the mass matrix (before the field redefinition to make the mass intrinsically positive). Depending on the relative signs of the mass of two neutralinos (before field redefinition), these couplings may interfere either constructively (masses for both $\widetilde{Z}_i$ and $\widetilde{Z}_j$ have same sign) or destructively (differing sign).

A.8.6 Modulus decay widths to charginos

We list here the model-independent decay widths of the modulus into charginos. The interactions for decay to lighter chargino pairs are given by Eq. (A.79) and Eq. (A.109). These combine into

$$\mathcal{L}_{\phi\overline{\widetilde{W}}_1\widetilde{W}_1} = \frac{1}{\sqrt{2}m_P}\, i\phi\, \overline{\widetilde{W}}_1 \partial\!\!\!/ \left(g_V^{\widetilde{W}_1} - g_A^{\widetilde{W}_1}\gamma_5\right)\widetilde{W}_1 \quad \text{(A.190)}$$

where we made the definitions

$$g_V^{\widetilde{W}_1} \equiv \left(2\lambda_{SU(2)}x_c + (\lambda_{H_u} + \lambda_{H_d})x_s\right) \quad \text{(A.191)}$$

$$g_A^{\widetilde{W}_1} \equiv \left(2\lambda_{SU(2)}y_c + (\lambda_{H_u} + \lambda_{H_d})y_s\right). \quad \text{(A.192)}$$

Note that this term couples the modulus to the kinetic term of the lighter chargino - and in the absence of the modulus couplings, we have $x_c + x_s = 1$ and $y_c + y_s = 0$, reducing this term to the canonical kinetic term as expected.

The interactions for decay to heavier chargino pairs are given by Eq. (A.80) and Eq. (A.110). These combine into

$$\mathcal{L}_{\phi\overline{\widetilde{W}}_2\widetilde{W}_2} = \frac{1}{\sqrt{2}m_P}\, i\phi\, \overline{\overline{\widetilde{W}}_2}\partial\!\!\!/ \left(g_V^{\widetilde{W}_2} - g_A^{\widetilde{W}_2}\gamma_5\right)\widetilde{W}_2 \tag{A.193}$$

where we made the definitions

$$g_V^{\widetilde{W}_2} \equiv \left(2\lambda_{SU(2)}x_s + (\lambda_{H_u} + \lambda_{H_d})x_c\right) \tag{A.194}$$

$$g_A^{\widetilde{W}_2} \equiv \left(2\lambda_{SU(2)}y_s + (\lambda_{H_u} + \lambda_{H_d})y_c\right). \tag{A.195}$$

Once more, these terms reduce to the canonical kinetic term in the absence of the modulus coupling.

The interactions for decay to a light chargino and a heavy chargino are given by Eq. (A.82) and Eq. (A.111). These combine into

$$\mathcal{L}_{\phi\widetilde{W}_1\widetilde{W}_2} = \supset i\left(\frac{2\lambda_{SU(2)} - \lambda_{H_u} - \lambda_{H_d}}{\sqrt{2}\, m_P}\right)\left[\phi\overline{\widetilde{W}_2}\partial\!\!\!/(x - y\gamma_5)\widetilde{W}_1 + \phi\overline{\widetilde{W}_1}\partial\!\!\!/(x - y\gamma_5)\widetilde{W}_2\right] \tag{A.196}$$

where, in the absence of the modulus coupling, this term vanishes.

Applying Eq. (A.39) to Eq. (A.190), we have the decay width into light

chargino pairs:

$$\Gamma_{\phi\overline{\widetilde{W}}_1\widetilde{W}_1} = \frac{1}{16\pi}\frac{m_\phi^3}{m_P^2}\left(\frac{m^2_{\widetilde{W}_1}}{m_\phi^2}\right)\left(\left(g_V^{\widetilde{W}_1}\right)^2\left[1-4\frac{m^2_{\widetilde{W}_1}}{m_\phi^2}\right]+\left(g_A^{\widetilde{W}_1}\right)^2\right) \times \lambda^{1/2}\left(1,\frac{m^2_{\widetilde{W}_1}}{m_\phi^2},\frac{m^2_{\widetilde{W}_1}}{m_\phi^2}\right). \quad \text{(A.197)}$$

Similar application of Eq. (A.39) to Eq. (A.193) gives the decay width into heavy chargino pairs:

$$\Gamma_{\phi\overline{\widetilde{W}}_2\widetilde{W}_2} = \frac{1}{16\pi}\frac{m_\phi^3}{m_P^2}\left(\frac{m^2_{\widetilde{W}_2}}{m_\phi^2}\right)\left(\left(g_V^{\widetilde{W}_2}\right)^2\left[1-4\frac{m^2_{\widetilde{W}_2}}{m_\phi^2}\right]+\left(g_A^{\widetilde{W}_2}\right)^2\right) \times \lambda^{1/2}\left(1,\frac{m^2_{\widetilde{W}_2}}{m_\phi^2},\frac{m^2_{\widetilde{W}_2}}{m_\phi^2}\right) \quad \text{(A.198)}$$

Finally, application of Eq. (A.44) to Eq. (A.196) gives the decay width into a light chargino and a heavy chargino:

$$\Gamma_{\phi\widetilde{W}_1\widetilde{W}_2} = \frac{\left(2\lambda_{SU(2)}-\lambda_{H_u}-\lambda_{H_d}\right)^2}{16\pi}\frac{m_\phi^3}{m_P^2}\left(\frac{m^2_{\widetilde{W}_1}+m^2_{\widetilde{W}_2}}{m_\phi^2}\right) \times\left(x^2\left[1-\frac{(m_{\widetilde{W}_1}+m_{\widetilde{W}_2})^2}{m_\phi^2}\right]+y^2\left[1-\frac{(m_{\widetilde{W}_1}-m_{\widetilde{W}_2})^2}{m_\phi^2}\right]\right) \times\lambda^{1/2}\left(1,\frac{m^2_{\widetilde{W}_1}}{m_\phi^2},\frac{m^2_{\widetilde{W}_2}}{m_\phi^2}\right). \quad \text{(A.199)}$$

A.8.7 Modulus decay width to gluinos

We list here the model-independent decay width of the modulus into gluinos. Application of Eq. (A.40) to Eq. (A.91), we have the decay width:

$$\Gamma_{\phi\widetilde{g}\widetilde{g}} = \frac{\lambda_{SU(3)}^2}{\pi}\frac{m_\phi^3}{m_P^2}\left(\frac{m_{\widetilde{g}_\alpha}^2}{m_\phi^2}\right)\left(1-4\frac{m_{\widetilde{g}_\alpha}^2}{m_\phi^2}\right)\lambda^{1/2}\left(1,\frac{m_{\widetilde{g}_\alpha}^2}{m_\phi^2},\frac{m_{\widetilde{g}_\alpha}^2}{m_\phi^2}\right) \tag{A.200}$$

where we have then summed over the 8 different gluinos.

A.8.8 Modulus decay widths to squarks

We list here the model-independent decay widths of the modulus into squarks. Each width is multiplied here by the color factor $N_C = 3$. Starting with Eq. (A.140), application of Eq. (A.35) gives us the decay width to left squark pairs:

$$\Gamma_{\phi\widetilde{q}_L\widetilde{q}_L} = \frac{3}{8\pi}\frac{m_{\widetilde{q}_L}^4}{m_\phi m_P^2}\left(\lambda_{Q_i}\right)^2\lambda^{1/2}\left(1,\frac{m_{\widetilde{q}_L}^2}{m_\phi^2},\frac{m_{\widetilde{q}_L}^2}{m_\phi^2}\right) \tag{A.201}$$

where $\widetilde{q}_L \in \{\widetilde{u}_L, \widetilde{d}_L, \widetilde{c}_L, \widetilde{s}_L\}$ and the coupling index $i \in \{1,2\}$ labels the generation. Similar application of Eq. (A.35) to Eq. (A.141) gives us the decay width to right squark pairs:

$$\Gamma_{\phi\widetilde{q}_R\widetilde{q}_R} = \frac{3}{8\pi}\frac{m_{\widetilde{q}_R}^4}{m_\phi m_P^2}\left(\lambda_{q_i}\right)^2\lambda^{1/2}\left(1,\frac{m_{\widetilde{q}_R}^2}{m_\phi^2},\frac{m_{\widetilde{q}_R}^2}{m_\phi^2}\right) \tag{A.202}$$

where $\widetilde{q}_R \in \{\widetilde{u}_R, \widetilde{d}_R, \widetilde{c}_R, \widetilde{s}_R\}$. The coupling again takes the definitions $\lambda_{q_i} \equiv \lambda_{U_i}$ if $\widetilde{q}_R$ is an up-type squark, and $\lambda_{q_i} \equiv \lambda_{D_i}$ if $\widetilde{q}_R$ is a down-type squark, and the index $i \in \{1,2\}$ again labels the generation.

Moving to the decays to the top squarks, we start with Eq. (A.143) which gives the decay width

$$\Gamma_{\phi\widetilde{t}_1\widetilde{t}_1} = \frac{3}{8\pi}\frac{m_{\widetilde{t}_1}^4}{m_\phi m_P^2}\left(\lambda_{Q_3}\cos^2\theta_t + \lambda_{U_3}\sin^2\theta_t\right)^2 \lambda^{1/2}\left(1, \frac{m_{\widetilde{t}_1}^2}{m_\phi^2}, \frac{m_{\widetilde{t}_1}^2}{m_\phi^2}\right) \tag{A.203}$$

for the lightest top squark, while the decay width to the heavier top squark is obtained from Eq. (A.144):

$$\Gamma_{\phi\widetilde{t}_2\widetilde{t}_2} = \frac{3}{8\pi}\frac{m_{\widetilde{t}_2}^4}{m_\phi m_P^2}\left(\lambda_{Q_3}\sin^2\theta_t + \lambda_{U_3}\cos^2\theta_t\right)^2 \lambda^{1/2}\left(1, \frac{m_{\widetilde{t}_2}^2}{m_\phi^2}, \frac{m_{\widetilde{t}_2}^2}{m_\phi^2}\right). \tag{A.204}$$

Finally, the decay to a light top squark and a heavy top squark is given by Eq. (A.145):

$$\Gamma_{\phi\widetilde{t}_1\widetilde{t}_2} = \frac{3}{32\pi}\frac{\left(m_{\widetilde{t}_1}^2 + m_{\widetilde{t}_2}^2\right)^2}{m_\phi m_P^2}\left(\left(\lambda_{Q_3} - \lambda_{U_3}\right)\sin\left(2\theta_t\right)\right)^2 \times \lambda^{1/2}\left(1, \frac{m_{\widetilde{t}_1}^2}{m_\phi^2}, \frac{m_{\widetilde{t}_2}^2}{m_\phi^2}\right). \tag{A.205}$$

Upon taking the appropriate replacements, $\widetilde{t}_{1/2} \to \widetilde{b}_{1/2}$, $\theta_t \to \theta_b$, and $\lambda_{U_3} \to \lambda_{D_3}$, into the above formulae, we have then the modulus decay into bottom squarks. The decay into the light bottom squarks is given by

$$\Gamma_{\phi\widetilde{b}_1\widetilde{b}_1} = \frac{3}{8\pi}\frac{m_{\widetilde{b}_1}^4}{m_\phi m_P^2}\left(\lambda_{Q_3}\cos^2\theta_b + \lambda_{D_3}\sin^2\theta_b\right)^2 \lambda^{1/2}\left(1, \frac{m_{\widetilde{b}_1}^2}{m_\phi^2}, \frac{m_{\widetilde{b}_1}^2}{m_\phi^2}\right) \tag{A.206}$$

while the decay into the heavy bottom squarks is given by

$$\Gamma_{\phi\widetilde{b}_2\widetilde{b}_2} = \frac{3}{8\pi}\frac{m_{\widetilde{b}_2}^4}{m_\phi m_P^2}\left(\lambda_{Q_3}\sin^2\theta_b + \lambda_{D_3}\cos^2\theta_b\right)^2 \lambda^{1/2}\left(1, \frac{m_{\widetilde{b}_2}^2}{m_\phi^2}, \frac{m_{\widetilde{b}_2}^2}{m_\phi^2}\right) \tag{A.207}$$

and the decay into a light and heavy bottom squark is given by

$$\Gamma_{\phi\widetilde{b}_1\widetilde{b}_2} = \frac{3}{32\pi}\frac{\left(m_{\widetilde{b}_1}^2 + m_{\widetilde{b}_2}^2\right)^2}{m_\phi m_P^2}\left(\left(\lambda_{Q_3} - \lambda_{D_3}\right)\sin\left(2\theta_b\right)\right)^2 \times \lambda^{1/2}\left(1, \frac{m_{\widetilde{b}_1}^2}{m_\phi^2}, \frac{m_{\widetilde{b}_2}^2}{m_\phi^2}\right). \tag{A.208}$$

A.8.9 Modulus decay widths to sleptons

We list here the model-independent decay widths of the modulus into sleptons. Starting with Eq. (A.155), application of Eq. (A.35) gives us the decay width to left slepton pairs:

$$\Gamma_{\phi\widetilde{f}_L\widetilde{f}_L} = \frac{1}{8\pi}\frac{m_{\widetilde{f}_L}^4}{m_\phi m_P^2}\left(\lambda_{L_i}\right)^2 \lambda^{1/2}\left(1, \frac{m_{\widetilde{f}_L}^2}{m_\phi^2}, \frac{m_{\widetilde{f}_L}^2}{m_\phi^2}\right) \tag{A.209}$$

where $\widetilde{f}_L \in \{\widetilde{e}_L, \widetilde{\nu}_{e,L}, \widetilde{\mu}_L, \widetilde{\nu}_{\mu,L}, \widetilde{\nu}_{\tau,L}\}$ and the coupling index $i \in \{1,2,3\}$ labels the generation. Note that the decay width to neutrinos vanishes assuming that the neutrinos are massless. Similar application of Eq. (A.35) to Eq. (A.156) gives us the decay width to right slepton pairs:

$$\Gamma_{\phi\widetilde{f}_R\widetilde{f}_R} = \frac{1}{8\pi}\frac{m_{\widetilde{f}_R}^4}{m_\phi m_P^2}\left(\lambda_{E_i}\right)^2 \lambda^{1/2}\left(1, \frac{m_{\widetilde{f}_R}^2}{m_\phi^2}, \frac{m_{\widetilde{f}_R}^2}{m_\phi^2}\right) \tag{A.210}$$

where $\widetilde{f}_R \in \{\widetilde{e}_R, \widetilde{\mu}_R\}$ and the index $i \in \{1,2\}$ once again labels the generation.

Moving to the decays to the tau sleptons, we start with Eq. (A.158) which gives the decay width

$$\Gamma_{\phi\widetilde{\tau}_1\widetilde{\tau}_1} = \frac{1}{8\pi}\frac{m_{\widetilde{\tau}_1}^4}{m_\phi m_P^2}\left(\lambda_{L_3}\cos^2\theta_\tau + \lambda_{E_3}\sin^2\theta_\tau\right)^2 \lambda^{1/2}\left(1, \frac{m_{\widetilde{\tau}_1}^2}{m_\phi^2}, \frac{m_{\widetilde{\tau}_1}^2}{m_\phi^2}\right) \quad \text{(A.211)}$$

for the light tau slepton, while the decay width to the heavy tau slepton is obtained from Eq. (A.159):

$$\Gamma_{\phi\widetilde{\tau}_2\widetilde{\tau}_2} = \frac{1}{8\pi}\frac{m_{\widetilde{\tau}_2}^4}{m_\phi m_P^2}\left(\lambda_{L_3}\sin^2\theta_\tau + \lambda_{E_3}\cos^2\theta_\tau\right)^2 \lambda^{1/2}\left(1, \frac{m_{\widetilde{\tau}_2}^2}{m_\phi^2}, \frac{m_{\widetilde{\tau}_2}^2}{m_\phi^2}\right). \quad \text{(A.212)}$$

Finally, the decay to a light tau slepton and a heavy tau slepton is given by Eq. (A.160):

$$\Gamma_{\phi\widetilde{\tau}_1\widetilde{\tau}_2} = \frac{1}{32\pi}\frac{\left(m_{\widetilde{\tau}_1}^2 + m_{\widetilde{\tau}_2}^2\right)^2}{m_\phi m_P^2}\left(\left(\lambda_{L_3} - \lambda_{E_3}\right)\sin\left(2\theta_\tau\right)\right)^2 \times \lambda^{1/2}\left(1, \frac{m_{\widetilde{\tau}_1}^2}{m_\phi^2}, \frac{m_{\widetilde{\tau}_2}^2}{m_\phi^2}\right). \quad \text{(A.213)}$$

A.8.10 Modulus decay widths to quarks

We list here the model-independent decay widths into quarks. Each width is multiplied here by the color factor $N_C = 3$. Starting with Eq. (A.148), application of Eq. (A.39) gives the decay width to up-type quark pairs:

$$\Gamma_{\phi\overline{u}_i u_i} = \frac{3\left(\lambda_{Q_i} + \lambda_{U_i}\right)^2}{16\pi}\frac{m_\phi^3}{m_P^2}\left(\frac{m_{u_i}^2}{m_\phi^2}\right)\left(1 - 4\frac{m_{u_i}^2}{m_\phi^2}\right)\lambda^{1/2}\left(1, \frac{m_{u_i}^2}{m_\phi^2}, \frac{m_{u_i}^2}{m_\phi^2}\right) \quad \text{(A.214)}$$

where once again, $i \in \{1,2,3\}$ is the generation index. The decay width to down-type quarks follows identically starting with Eq. (A.149). The result is

$$\Gamma_{\phi\bar{d}_i d_i} = \frac{3\left(\lambda_{Q_i}+\lambda_{D_i}\right)^2}{16\pi}\frac{m_\phi^3}{m_P^2}\left(\frac{m_{d_i}^2}{m_\phi^2}\right)\left(1-4\frac{m_{d_i}^2}{m_\phi^2}\right)\lambda^{1/2}\left(1,\frac{m_{d_i}^2}{m_\phi^2},\frac{m_{d_i}^2}{m_\phi^2}\right). \quad \text{(A.215)}$$

In the massless limit for the u, d, and s quarks, these decay widths vanish.

A.8.11 Modulus decay widths to leptons

We list here the model-independent decay widths into leptons. Starting with Eq. (A.163), application of Eq. (A.39) gives the decay width to the electron-generation lepton pairs:

$$\Gamma_{\phi\bar{e}_i e_i} = \frac{\left(\lambda_{L_i}+\lambda_{E_i}\right)^2}{16\pi}\frac{m_\phi^3}{m_P^2}\left(\frac{m_{e_i}^2}{m_\phi^2}\right)\left(1-4\frac{m_{e_i}^2}{m_\phi^2}\right)\lambda^{1/2}\left(1,\frac{m_{e_i}^2}{m_\phi^2},\frac{m_{e_i}^2}{m_\phi^2}\right) \quad \text{(A.216)}$$

where, once again, $i \in \{1,2,3\}$ is the generation index. The decay width to neutrino pairs is obtained identically, starting from Eq. (A.164):

$$\Gamma_{\phi\bar{\nu}_{e_i}\nu_{e_i}} = \frac{\left(\lambda_{L_i}\right)^2}{16\pi}\frac{m_\phi^3}{m_P^2}\left(\frac{m_{\nu_{e_i}}^2}{m_\phi^2}\right)\left(1-4\frac{m_{\nu_{e_i}}^2}{m_\phi^2}\right)\lambda^{1/2}\left(1,\frac{m_{\nu_{e_i}}^2}{m_\phi^2},\frac{m_{\nu_{e_i}}^2}{m_\phi^2}\right). \quad \text{(A.217)}$$

In the limit of massless neutrinos, these decay widths vanish.

A.8.12 Modulus decay widths into axions and saxions

We list here the model-independent decay widths into PQ-sector axions and saxions. Starting with Eq. (A.171), application of Eq. (A.31) leads to the decay

width to saxion pairs:

$$\Gamma_{\phi ss} = \frac{\lambda_{\rm PQ}^2}{64\pi}\frac{m_\phi^3}{m_P^2}\left(1+2\frac{m_s^2}{m_\phi^2}\right)^2 \lambda^{1/2}\left(1,\frac{m_s^2}{m_\phi^2},\frac{m_s^2}{m_\phi^2}\right). \tag{A.218}$$

Moving to the decay to axions, we can use Eq. (A.172) - or equivalently, the modulus-axion interaction terms in Eq. (A.170), in conjunction with Eq. (A.31) to obtain the decay width to axion pairs:

$$\Gamma_{\phi aa} = \frac{\lambda_{\rm PQ}^2}{64\pi}\frac{m_\phi^3}{m_P^2}\left(1-2\frac{m_a^2}{m_\phi^2}\right)^2 \lambda^{1/2}\left(1,\frac{m_a^2}{m_\phi^2},\frac{m_a^2}{m_\phi^2}\right). \tag{A.219}$$

A.8.13 Modulus decay width into axinos

We list here the modulus decay widths to pairs of PQ-sector axinos. Starting with Eq. (A.173), we apply Eq. (A.40) as the axinos are Majorana. This leads to the decay width:

$$\Gamma_{\phi\bar{\tilde{a}}\tilde{a}} = \frac{\lambda_{\rm PQ}^2}{8\pi}\frac{m_\phi^3}{m_P^2}\left(\frac{m_{\tilde{a}}^2}{m_\phi^2}\right)\left(1-4\frac{m_{\tilde{a}}^2}{m_\phi^2}\right)\lambda^{1/2}\left(1,\frac{m_{\tilde{a}}^2}{m_\phi^2},\frac{m_{\tilde{a}}^2}{m_\phi^2}\right). \tag{A.220}$$

Appendix B

The Boltzmann equations

B.1 The Boltzmann equations

We discuss here the relevant Boltzmann equations for our model. Following [286], the Boltzmann equation may be written simply as

$$\hat{\mathbf{L}}[f] = \mathbf{C}[f] \tag{B.1}$$

where $\hat{\mathbf{L}}$ is the Liouville operator and $\mathbf{C}$ is the collision operator. In an FRW universe, the Liouville operator is given by

$$\hat{\mathbf{L}}[f] = p^{\alpha}\frac{\partial f}{\partial x^{\alpha}} - \Gamma^{\alpha}_{\beta\gamma}p^{\beta}p^{\gamma}\frac{\partial f}{\partial p^{\alpha}} \tag{B.2}$$

which reduces to [286]

$$\hat{\mathbf{L}}[f] = E\frac{\partial f(E,t)}{\partial t} - H|\mathbf{p}|^2\frac{\partial f(E,t)}{\partial E} \tag{B.3}$$

where, at zeroth-order in an FRW universe, the distribution function $f = f(E,t)$ is homogeneous and isotropic. From the definitions of the number density, energy

density, and pressure,

$$n_i \equiv g_i \int \frac{d^3p}{(2\pi)^3}\, f_i(E,t) \tag{B.4}$$

$$\rho_i \equiv g_i \int \frac{d^3p}{(2\pi)^3}\, f_i(E,t)E \tag{B.5}$$

$$\mathcal{P}_i \equiv g_i \int \frac{d^3p}{(2\pi)^3} f_i(E,t)\frac{p^2}{3E} \tag{B.6}$$

we recover the Boltzmann equations governing number density

$$\dot{n}_i + 3Hn_i = g_i \int \frac{d^3p}{(2\pi)^3}\, \frac{\mathbf{C}[f_i]}{E} \tag{B.7}$$

and the energy density

$$\dot{\rho}_i + 3H\left(\rho_i + \mathcal{P}_i\right) = g_i \int \frac{d^3p}{(2\pi)^3}\, \mathbf{C}[f_i]. \tag{B.8}$$

We are now ready to discuss the collision operator, $\mathbf{C}[f_i]$. In our case of interest, we are interested in primarily annihilations, decays, and so-called "injections" (which we will define shortly), so that $\mathbf{C}[f_i] = \mathbf{C}[f_i]_{\rm ann} + \mathbf{C}[f_i]_{\rm dec} + \mathbf{C}[f_i]_{\rm inj}$.

Let us focus first on annihilations. We expect that many N-point annihilations should have taken place in the early universe, with the general reaction schematic $i+j+\cdots \leftrightarrow a+b+\ldots$. Fortunately for our calculations, the higher the dimension of the phase space, the more its contribution should be suppressed. We thus make the approximation of including only interactions that follow the $i+j \leftrightarrow a+b$ schematic. The annihilation collision operator for the number density equation

then takes the general form

$$g_i \int \frac{d^3p_i}{(2\pi)^3} \frac{\mathbf{C}[f_i]_{\rm ann}}{E_i} = -\int d\Pi_i d\Pi_j d\Pi_a d\Pi_b \, (2\pi)^4 \, |\mathcal{M}|^2 \times \delta^{(4)}(p_i + p_j - p_a - p_b) \, [f_i f_j - f_a f_b] \quad \text{(B.9)}$$

where we have assumed CP-invariance so that $|\mathcal{M}|^2_{i+j\to a+b} = |\mathcal{M}|^2_{a+b\to i+j}$. In addition, we have also assumed Maxwell-Boltzmann statistics for simplicity as we are typically modeling temperatures well above where quantum statistical effects take precedence.

Assuming that the decay products, $a + b$, rapidly (i.e. within a Hubble time) approach thermal equilibrium with zero chemical potential, the distribution functions may be related by [286]:

$$f_i f_j = \overline{f}_i \overline{f}_j \quad \text{(B.10)}$$

where $\overline{f}_i$ is the equilibrium distribution function of the species. The annihilation collision operator for the number density equation then reduces to the standard form:

$$g_i \int \frac{d^3p_i}{(2\pi)^3} \frac{\mathbf{C}[f_i]_{\rm ann}}{E_i} = -\sum_j \langle \sigma_{i+j\to a+b} |v| \rangle \, [n_i n_j - \overline{n}_i \overline{n}_j] \quad \text{(B.11)}$$

where, although in many cases we may approximate $i = j$ as the dominant annihilation mode, we account for more general annihilation possibilities.

We now shift focus to the decay terms for the number density equation. First, we consider a generic field i which may decay with a total decay width, which

we denote as Γ_i. As with annihilations, in general when i decays, we expect a multitude of N-body decay processes. To simplify our equations, we make the approximation of considering only two body decays, i.e. $\Gamma_{i\to a+b}$, as three-body and higher decays will be phase space suppressed. Much like the annihilations, due to the high energy scale of the thermal bath, the decay process may also happen in reverse - i.e. we may have the inverse decay process $a+b\to i$. It was shown in [285] that the inverse decay process can be significant in the DFSZ model - specifically for the axino and saxion - and thus we cannot ignore this effect in our decay collision terms. Accounting for these inverse decays and making the approximation that $|\mathcal{M}|^2_{i\to a+b}\simeq|\mathcal{M}|^2_{a+b\to i}\equiv|\mathcal{M}|^2$, the collision operator thus takes the form

$$g_i\int\frac{d^3p}{(2\pi)^3}\frac{\mathbf{C}[f_i]_{\rm dec}}{E}=-\int d\Pi_i d\Pi_a d\Pi_b\,(2\pi)^4\,\delta^{(4)}\left(p_i-p_a-p_b\right)|\mathcal{M}|^2\left[f_i-f_af_b\right]. \tag{B.12}$$

Assuming that the decay products, $a+b$, rapidly approach kinetic equilibrium, we can relate their distribution functions to that of i by

$$f_af_b=\overline{f}_i\exp\left((\mu_a+\mu_b)/T\right)=\overline{f}_i\frac{f_af_b}{\overline{f}_a\overline{f}_b} \tag{B.13}$$

where the factor $f_af_b/(\overline{f}_a\overline{f}_b)$ accounts for the decay products having non-zero chemical potential. When the chemical potential for a and b vanishes, this factor simply reduces to unity.

We are now in a position to write down the form of the decay collision operator

in the number density Boltzmann equation:

$$g_i \int \frac{d^3p}{(2\pi)^3} \frac{\mathbf{C}[f_i]_{\rm dec}}{E} = -\Gamma_i' \left[n_i - \overline{n}_i \sum_{i \to a+b} \mathcal{B}_{i\to a+b} \frac{n_a n_b}{\overline{n}_a \overline{n}_b} \right] \tag{B.14}$$

where we sum over all possible decay channels and $\mathcal{B}_{i\to a+b}$ is the branching ratio for each decay process. There is, however, one final subtlety. In writing down the Boltzmann equations, we have implicitly specified the comoving frame [286]. The decay width, Γ_i', must therefore be evaluated in the comoving frame as it is not Lorentz invariant. We can, however, write instead the transformation

$$\Gamma_i' = \frac{E_{\text{rest frame}}}{E_{\text{comoving frame}}} \Gamma_i = \frac{m_i n_i}{\rho_i} \Gamma_i \tag{B.15}$$

where Γ_i is evaluated in the rest frame of i. The factor, $m_i n_i/\rho_i$, serves as a relativistic dilation factor and suppresses the decay of highly relativistic particles in the comoving frame. In the non-relativistic limit, $\rho_i \to m_i n_i$ and the relativistic dilation factor reduces to unity.

Finally, we turn to the injection terms. Some other field, a, may have also have a non-zero decay width, Γ_a. When a decays, it may produce i based on the branching ratio, $\mathcal{B}_{a\to i}$, where this branching ratio is defined to produce at least one i from the decay of a. As we have alluded to previously, we refer to this process as an injection, as this process "injects" i into the thermal plasma, and hence increases the population of i. Finding the collision operator follows nearly identically to the decay case considered above, except now the decay process is

$a \to i + b$. The collision operator for the number density equation thus takes the form

$$g_i \int \frac{d^3p}{(2\pi)^3} \frac{\mathbf{C}[f_i]_{\rm inj}}{E} = + \sum_a \Gamma'_a \left[\mathcal{B}_{a\to i} n_a - \overline{n}_a \sum_{a\to i+b} \mathcal{B}_{a\to i+b} \frac{n_i n_b}{\overline{n}_i \overline{n}_b} \right] \tag{B.16}$$

where the factor $\mathcal{B}_{a\to i}$ accounts for only the decays of a which produce i, while the factor $\mathcal{B}_{a\to i+b}$ accounts for each possible inverse decay $i + b \to a$. Once again, the decay width here is evaluated in the comoving frame. To relate to the decay width in the rest frame of a, we can again utilize Eq. (B.15) with the replacement $i \to a$.

We now turn to the collision operators in the energy density equation for all three contributions. The procedure is identical, save for the additional factor of E (evaluated in the comoving frame) in each term. Taking the average energy-per-particle, $\langle E_i \rangle = \rho_i / n_i$, the annihilation and decay collision operators can be written down with this simple additional factor. For the injections of the form $a \to i + b$, we must first relate $\langle E_i \rangle \sim \langle E_a \rangle / 2$ where $\langle E_a \rangle$ is now the average energy of the parent, a. The additional factor in the injection terms of the energy density equation is then given by $\rho_a/(2n_a)$.

We now have useful forms of equations governing the evolution of number densities and energy densities in terms of easily calculable equilibrium values, decay widths, branching fractions, and annihilation cross sections. However, we must still model the evolution of radiation in order to close the full set of equations. Here, we choose to model the evolution of radiation as given by the second law of

thermodynamics [286]:

$$\dot{S} = -\frac{1}{T}\sum_i \frac{d}{dt}\left(R^3 \rho_{i\to \mathrm{rad}}\right) \tag{B.17}$$

where $\rho_{i\to\mathrm{rad}}$ is the fraction of each i's energy density that decays to radiation. Assuming that the pressure is negligible at the time of decay (i.e. the decaying particle is redshifted sufficiently to be *cold* - a condition trivially true for coherently oscillating fields), this reduces to the same form as the Liouville operator in the energy density Boltzmann equation. Thus, we can simply write down the decay collision operator multiplied by its branching ratio to radiation. The annihilation and injection collision operators will not change the entropy in any significant way here, and hence can be ignored.

At long last, we have all the required pieces to write down the full set of zeroth-order Boltzmann equations. Rewriting the time derivatives in terms of e-fold derivatives which we denote with a prime, the Boltzmann equation governing the number density of the i-th field is given by

$$\begin{aligned} H\left(n_i' + 3n_i\right) = &\sum_j \left(\overline{n}_i\overline{n}_j - n_i n_j\right)\langle\sigma v\rangle_{ij} \\ &- \Gamma_i \frac{m_i n_i}{\rho_i}\left(n_i - \overline{n}_i \sum_{i\to a+b}\mathcal{B}_{i\to a+b}\frac{n_a n_b}{\overline{n}_a\overline{n}_b}\right) \\ &+ \sum_a \Gamma_a \frac{m_a n_a}{\rho_a}\left(\mathcal{B}_{a\to i} n_a - \overline{n}_a \sum_{a\to i+b}\mathcal{B}_{a\to i+b}\frac{n_i n_b}{\overline{n}_i\overline{n}_b}\right) \end{aligned} \tag{B.18}$$

while the Boltzmann equation governing the energy density of the i-th field is

given by

$$H\left(\rho_i' + 3\left(\rho_i + \mathcal{P}_i\right)\right) = \sum_j \left(\overline{n}_i \overline{n}_j - n_i n_j\right) \langle \sigma v \rangle_{ij} \frac{\rho_i}{n_i} - \Gamma_i m_i \left(n_i - \overline{n}_i \sum_{i \to a+b} \mathcal{B}_{i \to a+b} \frac{n_a n_b}{\overline{n}_a \overline{n}_b} \right) + \sum_a \Gamma_a \frac{m_a}{2} \left(\mathcal{B}_{a \to i} n_a - \overline{n}_a \sum_{a \to i+b} \mathcal{B}_{a \to i+b} \frac{n_i n_b}{\overline{n}_i \overline{n}_b} \right). \quad \text{(B.19)}$$

The entropy equation is then given by

$$HS' = \frac{R^3}{T} \sum_i \mathcal{B}_{i \to \mathrm{rad}} \Gamma_i m_i \left(n_i - \overline{n}_i \sum_{i \to a+b} \mathcal{B}_{i \to a+b} \frac{n_a n_b}{\overline{n}_a \overline{n}_b} \right). \quad \text{(B.20)}$$

Finally, we must supplement these with the Friedmann equation,

$$H^2 = \frac{1}{3 m_P^2} \rho_{\mathrm{total}} \quad \text{(B.21)}$$

where ρ_{total} is the total energy density of the universe. We note that these reproduce exactly the Boltzmann equations used in [300].

Let us briefly discuss a few details of the above equations. Although we derived the above equations in some sense of generality, not all terms apply to all of the fields we want to track. Coherently oscillating fields have the equation-of-state that is identically that of matter in the non-relativistic limit. The annihilation cross sections do not apply to these coherently oscillating fields, and the equilibrium densities and the pressure term also vanish. Furthermore, due to their production mechanism, injection terms do not apply. We are then left with only the Hubble

dilution and decay terms for the coherently oscillating fields, with inverse decays set to 0. In addition, for most particles we wish to track, we assume that the annihilation cross section is dominated for $i = j$. However, for the PQ-sector, it was shown in [299, 298] that the dominant annihilation cross sections is instead given by processes like $\tilde{a} + q$, $\tilde{a} + \tilde{q}$, etc. Thus, we treat j as one of the radiation degrees-of-freedom when tracking thermally-produced or decay-produced PQ-sector particles.

Appendix C

A list of acronyms

Here, we present a list of acronyms for the aid of the reader.

ABDS	Agrawal-Barr-Donoghue-Seckel
ADD	Arkani-Hamed-Dimopoulos-Dvali
ADMX	Axion Dark Matter Experiment
AdS	anti-deSitter
ALP	axion-like particle
BBN	Big Bang Nucleosynthesis
CCB	charge-or-color breaking minima
CMB	Cosmic Microwave Background
CMP	Cosmological Moduli Problem
CO	coherently-oscillating
DD	direct detection
DFSZ	Dine-Fischler-Srednicki-Zhitnitsky
DM	dark matter
DP	decay-produced
DR	dark radiation
dS	deSitter
EDM	electric dipole moment
EFT	effective field theory
EMD	early matter dominated period
EWSB	electroweak symmetry breaking
FI	fibre inflation
FRW	Friedmann-Robertson-Walker
GKP	Giddings-Kachru-Polchinski
GR	general relativity
GSPQ	gravity-safe Peccei-Quinn
GUT	grand unified theory
ID	indirect detection
KK	Kaluza-Klein
KKLT	Kachru-Kallosh-Linde-Trivedi
KMI	Kähler moduli inflation
KSVZ	Kim-Shifman-Vainshtein-Zakharov
LHC	Large Hadron Collider
LSP	lightest supersymmetric particle
LVS	Large Volume Scenario
MSSM	Minimal Supersymmetric Standard Model

NS	Neveu-Schwarz
NUHM2/NUHM3	2/3 extra parameter non-universal Higgs model
PQ	Peccei-Quinn
PQMSSM	Peccei-Quinn + Minimal Supersymmetric Standard Model
PQWW	Peccei-Quinn-Wilczek-Weinberg
QCD	quantum chromodynamics
QED	quantum electrodynamics
QFT	quantum field theory
RNS	radiative natural supersymmetry
RR	Ramond-Ramond
SM	Standard Model
SUSY	supersymmetry
TP	thermally-produced
UV	ultraviolet
VEV	vacuum expectation value
WIMP	weakly interacting massive particle
ΛCDM	Lambda-Cold Dark Matter
ϕMSSM	Modulus + Minimal Supersymmetric Standard Model
ϕPQMSSM	Modulus + Peccei-Quinn + Minimal Supersymmetric Standard Model

Appendix D

Conventions

In this work, we use Einstein summation convention where appropriate. Greek indices usually denote 4d coordinates (e.g. $\mu \in \{0, 1, 2, 3\}$) where 0 is the time coordinate. Latin indices usually denote spatial coordinates, with the relevant dimension clear from context. Upper-case indices usually denote higher-dimensional coordinates prior to a decomposition (e.g. $M \in \{0, 1, 2, 3, 4\}$ which decomposes as $\mu \in \{0, 1, 2, 3\}$ in addition to an explicit 5th dimensional coordinate). Where indices are instead used to denote field-space coordinates (e.g. $g_{i\bar{j}}\, \partial_\mu \phi^i \partial^\mu \overline{\phi}^{\bar{j}}$), Latin indices without overlines denote the holomorphic directions while Latin indices with overlines denote anti-holomorphic directions.

Throughout, we utilize natural units where $\hbar = c = m_P = k_B = 1$ except for where these units are explicitly restored for key results.

All Minkowski and Friedmann-Robertson-Walker (FRW) metrics adopt the mostly-minus signature, (+, −, −, −).

References

[1] H. Baer and X. Tata, *Weak scale supersymmetry: From superfields to scattering events* (Cambridge University Press, Cambridge, UK, 2006).

[2] H. Baer, V. Barger, and D. Sengupta, Phys. Lett. B **790**, 58 (2019).

[3] S. Kachru, R. Kallosh, A. D. Linde, and S. P. Trivedi, Phys. Rev. D **68**, 046005 (2003).

[4] L. Aparicio, M. Cicoli, S. Krippendorf, A. Maharana, F. Muia, and F. Quevedo, JHEP **11**, 071 (2014).

[5] H. Baer, V. Barger, D. Sengupta, and R. W. Deal, Phys. Rev. D **104**, 015037 (2021).

[6] K. J. Bae, H. Baer, V. Barger, and R. W. Deal, JHEP **02**, 138 (2022).

[7] H. Baer, V. Barger, and R. W. Deal, JHEAp **34**, 40 (2022).

[8] H. Baer, V. Barger, and R. Wiley Deal, arXiv: **2301.12546**, (2023).

[9] M. Cicoli, C. P. Burgess, and F. Quevedo, JCAP **03**, 013 (2009).

[10] M. Cicoli, K. Sinha, and R. Wiley Deal, JHEP **12**, 068 (2022).

[11] N. Aghanim *et al.*, Astron. Astrophys. **641**, A6 (2020), [Erratum: Astron.Astrophys. 652, C4 (2021)].

[12] S. Profumo, *An Introduction to Particle Dark Matter* (World Scientific, Singapore, 2017).

[13] M. Dine, *Supersymmetry and String Theory: Beyond the Standard Model* (Cambridge University Press, Cambridge, UK, 2016).

[14] P. Langacker, *The Standard Model and Beyond* (Taylor & Francis, New York, USA, 2017).

[15] S. Dimopoulos and H. Georgi, Nucl. Phys. B **193**, 150 (1981).

[16] D. Z. Freedman and A. Van Proeyen, *Supergravity* (Cambridge Univ. Press, Cambridge, UK, 2012).

[17] K. Becker, M. Becker, and J. H. Schwarz, *String theory and M-theory: A modern introduction* (Cambridge University Press, Cambridge, UK, 2006).

[18] R. Blumenhagen, D. Lüst, and S. Theisen, *Basic concepts of string theory*, *Theoretical and Mathematical Physics* (Springer, Heidelberg, Germany, 2013).

[19] J. Polchinski, *String theory. Vol. 2: Superstring theory and beyond*, *Cambridge Monographs on Mathematical Physics* (Cambridge University Press, Cambridge, UK, 2007).

[20] F. Englert and R. Brout, Phys. Rev. Lett. **13**, 321 (1964).

[21] P. W. Higgs, Phys. Rev. Lett. **13**, 508 (1964).

[22] G. S. Guralnik, C. R. Hagen, and T. W. B. Kibble, Phys. Rev. Lett. **13**, 585 (1964).

[23] CMS Collaboration, Phys. Lett. B **716**, 30 (2012).

[24] ATLAS Collaboration, Phys. Lett. B **716**, 1 (2012).

[25] N. Cabibbo, L. Maiani, G. Parisi, and R. Petronzio, Nucl. Phys. B **158**, 295 (1979).

[26] J. R. Espinosa and M. Quiros, Phys. Lett. B **353**, 257 (1995).

[27] B. W. Lee, C. Quigg, and H. B. Thacker, Phys. Rev. D **16**, 1519 (1977).

[28] S. R. Coleman and J. Mandula, Phys. Rev. **159**, 1251 (1967).

[29] CMS Collaboration, arXiv: **2211.01456**, (2022).

[30] ATLAS Collaboration, arXiv: **2209.00583**, (2022).

[31] J. Terning, *Modern supersymmetry: Dynamics and duality* (Oxford University Press, Oxford, England, 2006).

[32] ATLAS Collaboration, Phys. Rev. Lett. **125**, 051801 (2020).

[33] CMS Collaboration, arXiv: **2208.02717**, (2022).

[34] ATLAS Collaboration, JHEP **02**, 143 (2021).

[35] CMS Collaboration, JHEP **10**, 244 (2019).

[36] ATLAS Collaboration, Eur. Phys. J. C **80**, 737 (2020).

[37] ATLAS Collaboration, JHEP **04**, 174 (2021).

[38] CMS Collaboration, Phys. Rev. D **104**, 052001 (2021).

[39] D. Tong, in *Theoretical Advanced Study Institute in Elementary Particle Physics: Many Dimensions of String Theory* (TASI, Colorado, USA, 2005).

[40] S. L. Adler, Phys. Rev. **177**, 2426 (1969).

[41] J. S. Bell and R. Jackiw, Nuovo Cim. A **60**, 47 (1969).

[42] M. E. Peskin and D. V. Schroeder, *An Introduction to quantum field theory* (Addison-Wesley, Reading, USA, 1995).

[43] R. J. Crewther, P. Di Vecchia, G. Veneziano, and E. Witten, Phys. Lett. B **88**, 123 (1979), [Erratum: Phys.Lett.B 91, 487 (1980)].

[44] C. Abel *et al.*, Phys. Rev. Lett. **124**, 081803 (2020).

[45] C. A. Baker *et al.*, Phys. Rev. Lett. **97**, 131801 (2006).

[46] R. D. Peccei and H. R. Quinn, Phys. Rev. Lett. **38**, 1440 (1977).

[47] R. D. Peccei and H. R. Quinn, Phys. Rev. D **16**, 1791 (1977).

[48] F. Wilczek, Phys. Rev. Lett. **40**, 279 (1978).

[49] S. Weinberg, Phys. Rev. Lett. **40**, 223 (1978).

[50] R. D. Peccei, Lect. Notes Phys. **741**, 3 (2008).

[51] J. E. Kim, Phys. Rept. **150**, 1 (1987).

[52] Y. Asano, E. Kikutani, S. Kurokawa, T. Miyachi, M. Miyajima, Y. Nagashima, T. Shinkawa, S. Sugimoto, and Y. Yoshimura, Phys. Lett. B **107**, 159 (1981).

[53] K. Mimasu and V. Sanz, JHEP **06**, 173 (2015).

[54] J. E. Kim, Phys. Rev. Lett. **43**, 103 (1979).

[55] M. A. Shifman, A. I. Vainshtein, and V. I. Zakharov, Nucl. Phys. B **166**, 493 (1980).

[56] M. Dine, W. Fischler, and M. Srednicki, Phys. Lett. B **104**, 199 (1981).

[57] A. R. Zhitnitsky, Sov. J. Nucl. Phys. **31**, 260 (1980).

[58] T. Kaluza, Sitzungsber. Preuss. Akad. Wiss. Berlin (Math. Phys.) **1921**, 966 (1921).

[59] O. Klein, Nature **118**, 516 (1926).

[60] O. Klein, Z. Phys. **37**, 895 (1926).

[61] Y.-X. Liu, in *Introduction to Extra Dimensions and Thick Braneworlds* (World Scientific, Singapore, 2018).

[62] E. Ponton, in *Theoretical Advanced Study Institute in Elementary Particle Physics: The Dark Secrets of the Terascale* (TASI, Colorado, USA, 2013), pp. 283–374.

[63] L. Randall and R. Sundrum, Phys. Rev. Lett. **83**, 3370 (1999).

[64] H. Davoudiasl, J. L. Hewett, and T. G. Rizzo, Phys. Rev. Lett. **84**, 2080 (2000).

[65] K. Agashe, A. Falkowski, I. Low, and G. Servant, JHEP **04**, 027 (2008).

[66] C. Csaki, M. L. Graesser, and G. D. Kribs, Phys. Rev. D **63**, 065002 (2001).

[67] H. Davoudiasl, J. L. Hewett, and T. G. Rizzo, Phys. Rev. D **63**, 075004 (2001).

[68] H. Davoudiasl, J. L. Hewett, and T. G. Rizzo, Phys. Lett. B **493**, 135 (2000).

[69] G. F. Giudice, R. Rattazzi, and J. D. Wells, Nucl. Phys. B **595**, 250 (2001).

[70] J. E. Kim, B. Kyae, and J. D. Park, J. Korean Phys. Soc. **39**, 736 (2001).

[71] CMS Collaboration, Phys. Lett. B **832**, 137263 (2022).

[72] CMS Collaboration, JHEP **04**, 087 (2022).

[73] CMS Collaboration, JHEP **05**, 005 (2022).

[74] ATLAS Collaboration, Phys. Lett. B **822**, 136651 (2021).

[75] ATLAS Collaboration, Eur. Phys. J. C **81**, 332 (2021).

[76] ATLAS Collaboration, Eur. Phys. J. C **80**, 1165 (2020).

[77] CMS Collaboration, JHEP **10**, 125 (2019).

[78] CMS Collaboration, JHEP **09**, 101 (2018).

[79] CMS Collaboration, JHEP **06**, 120 (2018).

[80] ATLAS Collaboration, Eur. Phys. J. C **78**, 24 (2018).

[81] ATLAS Collaboration, Eur. Phys. J. C **78**, 293 (2018).

[82] ATLAS Collaboration, JHEP **03**, 009 (2018).

[83] ATLAS Collaboration, Phys. Lett. B **775**, 105 (2017).

[84] N. Arkani-Hamed, S. Dimopoulos, and G. R. Dvali, Phys. Lett. B **429**, 263 (1998).

[85] L. Randall and R. Sundrum, Phys. Rev. Lett. **83**, 4690 (1999).

[86] H.-C. Cheng, in *Theoretical Advanced Study Institute in Elementary Particle Physics: Physics of the Large and the Small* (TASI, Colorado, USA, 2011), pp. 125–162.

[87] L. Visinelli, N. Bolis, and S. Vagnozzi, Phys. Rev. D **97**, 064039 (2018).

[88] K. Pardo, M. Fishbach, D. E. Holz, and D. N. Spergel, JCAP **07**, 048 (2018).

[89] S. Vagnozzi and L. Visinelli, Phys. Rev. D **100**, 024020 (2019).

[90] I. Banerjee, S. Chakraborty, and S. SenGupta, Phys. Rev. D **101**, 041301 (2020).

[91] B. Jain and J. Khoury, Annals Phys. **325**, 1479 (2010).

[92] C. M. Will, Living Rev. Rel. **17**, 4 (2014).

[93] D. J. H. Chung and K. Freese, Phys. Rev. D **61**, 023511 (2000).

[94] J. M. Cline, C. Grojean, and G. Servant, Phys. Rev. Lett. **83**, 4245 (1999).

[95] C. Csaki, M. Graesser, C. F. Kolda, and J. Terning, Phys. Lett. B **462**, 34 (1999).

[96] J. Polchinski, *String theory. Vol. 1: An introduction to the bosonic string*, *Cambridge Monographs on Mathematical Physics* (Cambridge University Press, Cambridge, UK, 2007).

[97] M. B. Green, J. H. Schwarz, and E. Witten, *SUPERSTRING THEORY. VOL. 1: INTRODUCTION*, *Cambridge Monographs on Mathematical Physics* (Cambridge University Press, Cambridge, UK, 1988).

[98] M. B. Green, J. H. Schwarz, and E. Witten, *SUPERSTRING THEORY. VOL. 2: LOOP AMPLITUDES, ANOMALIES AND PHENOMENOLOGY*, *Cambridge Monographs on Mathematical Physics* (Cambridge University Press, Cambridge, UK, 1988).

[99] D. Baumann and L. McAllister, *Inflation and String Theory*, *Cambridge Monographs on Mathematical Physics* (Cambridge University Press, Cambridge, UK, 2015).

[100] S. B. Giddings, S. Kachru, and J. Polchinski, Phys. Rev. D **66**, 106006 (2002).

[101] E. Bergshoeff, C. M. Hull, and T. Ortin, Nucl. Phys. B **451**, 547 (1995).

[102] E. Bergshoeff, H. J. Boonstra, and T. Ortin, Phys. Rev. D **53**, 7206 (1996).

[103] D. Tong, (2009).

[104] M. Dine and N. Seiberg, Phys. Rev. Lett. **55**, 366 (1985).

[105] M. Dine and N. Seiberg, Phys. Lett. B **162**, 299 (1985).

[106] F. Denef, Les Houches **87**, 483 (2008).

[107] A. Hebecker, Lectures on Naturalness, String Landscape and Multiverse, 2021.

[108] M. Nakahara, *Geometry, topology and physics* (Taylor & Francis, New York, USA, 2003).

[109] B. R. Greene, in *Theoretical Advanced Study Institute in Elementary Particle Physics (TASI 96): Fields, Strings, and Duality* (TASI, Colorado, USA, 1996), pp. 543–726.

[110] R. Altman, J. Gray, Y.-H. He, V. Jejjala, and B. D. Nelson, JHEP **02**, 158 (2015).

[111] E. Witten, Phys. Lett. B **149**, 351 (1984).

[112] D. J. E. Marsh, Phys. Rept. **643**, 1 (2016).

[113] Y.-H. He, Int. J. Mod. Phys. A **28**, 1330032 (2013).

[114] M. Demirtas, C. Long, L. McAllister, and M. Stillman, JHEP **04**, 138 (2020).

[115] A. Arvanitaki, S. Dimopoulos, S. Dubovsky, N. Kaloper, and J. March-Russell, Phys. Rev. D **81**, 123530 (2010).

[116] B. S. Acharya and C. Pongkitivanichkul, JHEP **04**, 009 (2016).

[117] P. Candelas and X. de la Ossa, Nucl. Phys. B **355**, 455 (1991).

[118] S. Gukov, C. Vafa, and E. Witten, Nucl. Phys. B **584**, 69 (2000), [Erratum: Nucl.Phys.B 608, 477–478 (2001)].

[119] T. R. Taylor and C. Vafa, Phys. Lett. B **474**, 130 (2000).

[120] C. V. Johnson, in *Theoretical Advanced Study Institute in Elementary Particle Physics (TASI 99): Strings, Branes, and Gravity* (TASI, Colorado, USA, 2000), pp. 129–350.

[121] O. DeWolfe and S. B. Giddings, Phys. Rev. D **67**, 066008 (2003).

[122] S. B. Giddings and A. Maharana, Phys. Rev. D **73**, 126003 (2006).

[123] H.-Y. Chen, Y. Nakayama, and G. Shiu, Int. J. Mod. Phys. A **25**, 2493 (2010).

[124] L. Randall and R. Sundrum, Nucl. Phys. B **557**, 79 (1999).

[125] E. Cremmer, S. Ferrara, C. Kounnas, and D. V. Nanopoulos, Phys. Lett. B **133**, 61 (1983).

[126] R. Blumenhagen, M. Cvetic, P. Langacker, and G. Shiu, Ann. Rev. Nucl. Part. Sci. **55**, 71 (2005).

[127] H. Verlinde and M. Wijnholt, JHEP **01**, 106 (2007).

[128] R. Blumenhagen, B. Kors, D. Lust, and S. Stieberger, Phys. Rept. **445**, 1 (2007).

[129] M. R. Douglas and S. Kachru, Rev. Mod. Phys. **79**, 733 (2007).

[130] L. Susskind, arXiv: **hep-th/0302219**, 247 (2003).

[131] L. Susskind, in *From Fields to Strings: Circumnavigating Theoretical Physics: A Conference in Tribute to Ian Kogan* (World Scientific, Singapore, 2004), pp. 1745–1749.

[132] R. Kallosh and A. D. Linde, JHEP **12**, 004 (2004).

[133] M. R. Douglas, arXiv: **hep-th/0405279**, (2004).

[134] B. S. Acharya and M. R. Douglas, arXiv: **hep-th/0606212**, (2006).

[135] G. Torroba, JHEP **02**, 061 (2007).

[136] S. Ashok and M. R. Douglas, JHEP **01**, 060 (2004).

[137] W. Taylor and Y.-N. Wang, JHEP **12**, 164 (2015).

[138] H. Baer, V. Barger, S. Salam, and D. Sengupta, Phys. Rev. D **102**, 075012 (2020).

[139] H. Baer, V. Barger, D. Sengupta, H. Serce, K. Sinha, and R. W. Deal, Eur. Phys. J. C **79**, 897 (2019).

[140] C. Vafa, arXiv: **hep-th/0509212**, (2005).

[141] H. Ooguri and C. Vafa, Nucl. Phys. B **766**, 21 (2007).

[142] J. J. Heckman and C. Vafa, Phys. Lett. B **798**, 135004 (2019).

[143] E. Palti, Fortsch. Phys. **67**, 1900037 (2019).

[144] L. B. Anderson, J. Gray, A. Lukas, and B. Ovrut, JHEP **02**, 088 (2011).

[145] L. B. Anderson, J. Gray, A. Lukas, and B. Ovrut, Phys. Rev. D **83**, 106011 (2011).

[146] G. Curio and A. Krause, Nucl. Phys. B **643**, 131 (2002).

[147] K. Becker, M. Becker, K. Dasgupta, and P. S. Green, JHEP **04**, 007 (2003).

[148] G. Lopes Cardoso, G. Curio, G. Dall'Agata, and D. Lust, JHEP **10**, 004 (2003).

[149] K. Becker, M. Becker, P. S. Green, K. Dasgupta, and E. Sharpe, Nucl. Phys. B **678**, 19 (2004).

[150] E. I. Buchbinder and B. A. Ovrut, Phys. Rev. D **69**, 086010 (2004).

[151] S. Gukov, S. Kachru, X. Liu, and L. McAllister, Phys. Rev. D **69**, 086008 (2004).

[152] G. Curio, A. Krause, and D. Lust, Fortsch. Phys. **54**, 225 (2006).

[153] B. de Carlos, S. Gurrieri, A. Lukas, and A. Micu, JHEP **03**, 005 (2006).

[154] P. S. Aspinwall and R. Kallosh, JHEP **10**, 001 (2005).

[155] B. S. Acharya, arXiv: **hep-th/0212294**, (2002).

[156] B. S. Acharya, K. Bobkov, G. L. Kane, P. Kumar, and J. Shao, Phys. Rev. D **76**, 126010 (2007).

[157] B. S. Acharya and K. Bobkov, JHEP **09**, 001 (2010).

[158] M. Dine, R. Rohm, N. Seiberg, and E. Witten, Phys. Lett. B **156**, 55 (1985).

[159] J. P. Derendinger, L. E. Ibanez, and H. P. Nilles, Phys. Lett. B **155**, 65 (1985).

[160] E. Witten, Nucl. Phys. B **474**, 343 (1996).

[161] I. R. Klebanov and M. J. Strassler, JHEP **08**, 052 (2000).

[162] S. Kachru, R. Kallosh, A. D. Linde, J. M. Maldacena, L. P. McAllister, and S. P. Trivedi, JCAP **10**, 013 (2003).

[163] C. P. Burgess, R. Kallosh, and F. Quevedo, JHEP **10**, 056 (2003).

[164] G. Villadoro and F. Zwirner, Phys. Rev. Lett. **95**, 231602 (2005).

[165] A. Achucarro, B. de Carlos, J. A. Casas, and L. Doplicher, JHEP **06**, 014 (2006).

[166] E. Dudas and Y. Mambrini, JHEP **10**, 044 (2006).

[167] M. Haack, D. Krefl, D. Lust, A. Van Proeyen, and M. Zagermann, JHEP **01**, 078 (2007).

[168] C. P. Burgess, J. M. Cline, K. Dasgupta, and H. Firouzjahi, JHEP **03**, 027 (2007).

[169] R. Kallosh and A. D. Linde, JHEP **02**, 002 (2007).

[170] O. Lebedev, H. P. Nilles, and M. Ratz, Phys. Lett. B **636**, 126 (2006).

[171] A. Westphal, JHEP **03**, 102 (2007).

[172] M. Rummel and A. Westphal, JHEP **01**, 020 (2012).

[173] J. Louis, M. Rummel, R. Valandro, and A. Westphal, JHEP **10**, 163 (2012).

[174] S. Ferrara, R. Kallosh, and A. Linde, JHEP **10**, 143 (2014).

[175] R. Kallosh and T. Wrase, JHEP **12**, 117 (2014).

[176] E. A. Bergshoeff, K. Dasgupta, R. Kallosh, A. Van Proeyen, and T. Wrase, JHEP **05**, 058 (2015).

[177] F. Denef, M. R. Douglas, and B. Florea, JHEP **06**, 034 (2004).

[178] F. Denef, M. R. Douglas, B. Florea, A. Grassi, and S. Kachru, Adv. Theor. Math. Phys. **9**, 861 (2005).

[179] K. Bobkov, V. Braun, P. Kumar, and S. Raby, JHEP **12**, 056 (2010).

[180] V. Balasubramanian, P. Berglund, J. P. Conlon, and F. Quevedo, JHEP **03**, 007 (2005).

[181] J. P. Conlon, F. Quevedo, and K. Suruliz, JHEP **08**, 007 (2005).

[182] M. Cicoli, S. Krippendorf, C. Mayrhofer, F. Quevedo, and R. Valandro, JHEP **09**, 019 (2012).

[183] M. Cicoli, D. Klevers, S. Krippendorf, C. Mayrhofer, F. Quevedo, and R. Valandro, JHEP **05**, 001 (2014).

[184] J. P. Conlon, A. Maharana, and F. Quevedo, JHEP **05**, 109 (2009).

[185] R. Blumenhagen, J. P. Conlon, S. Krippendorf, S. Moster, and F. Quevedo, JHEP **09**, 007 (2009).

[186] M. Cicoli, F. Quevedo, and R. Valandro, JHEP **03**, 141 (2016).

[187] D. Gallego, M. C. D. Marsh, B. Vercnocke, and T. Wrase, JHEP **10**, 193 (2017).

[188] M. Cicoli, A. Maharana, F. Quevedo, and C. P. Burgess, JHEP **06**, 011 (2012).

[189] D. Farquet and C. A. Scrucca, JHEP **09**, 025 (2012).

[190] J. Wess and J. Bagger, *Supersymmetry and supergravity* (Princeton University Press, Princeton, NJ, USA, 1992).

[191] J. A. Bagger, T. Moroi, and E. Poppitz, JHEP **04**, 009 (2000).

[192] S. P. de Alwis, Phys. Rev. D **77**, 105020 (2008).

[193] B. D. Nelson, in *1st String Phenomenology 2002* (World Scientific, Singapore, 2003), pp. 295–298.

[194] C. A. Scrucca, Mod. Phys. Lett. A **20**, 297 (2005).

[195] M. Ibe, K. I. Izawa, Y. Nakayama, Y. Shinbara, and T. Yanagida, Phys. Rev. D **73**, 035012 (2006).

[196] K. S. Jeong, Mod. Phys. Lett. A **23**, 1981 (2008).

[197] S. Kachru, L. McAllister, and R. Sundrum, JHEP **10**, 013 (2007).

[198] K. Choi, AIP Conf. Proc. **1078**, 138 (2009).

[199] G. Perez, T. S. Roy, and M. Schmaltz, Phys. Rev. D **79**, 095016 (2009).

[200] M. Berg, D. Marsh, L. McAllister, and E. Pajer, JHEP **06**, 134 (2011).

[201] C. Andrey and C. A. Scrucca, Nucl. Phys. B **851**, 245 (2011).

[202] J. P. Conlon and L. T. Witkowski, JHEP **12**, 028 (2011).

[203] S. P. de Alwis, Phys. Lett. B **708**, 314 (2012).

[204] S. P. de Alwis, JHEP **05**, 026 (2012).

[205] M. Cicoli, S. Krippendorf, C. Mayrhofer, F. Quevedo, and R. Valandro, JHEP **07**, 150 (2013).

[206] A. Anisimov, M. Dine, M. Graesser, and S. D. Thomas, Phys. Rev. D **65**, 105011 (2002).

[207] A. Anisimov, M. Dine, M. Graesser, and S. D. Thomas, JHEP **03**, 036 (2002).

[208] G. D. Coughlan, W. Fischler, E. W. Kolb, S. Raby, and G. G. Ross, Phys. Lett. B **131**, 59 (1983).

[209] M. Dine, L. Randall, and S. D. Thomas, Nucl. Phys. B **458**, 291 (1996).

[210] M. Dine, L. Randall, and S. D. Thomas, Phys. Rev. Lett. **75**, 398 (1995).

[211] G. Kane, K. Sinha, and S. Watson, Int. J. Mod. Phys. D **24**, 1530022 (2015).

[212] T. Banks, D. B. Kaplan, and A. E. Nelson, Phys. Rev. D **49**, 779 (1994).

[213] B. de Carlos, J. A. Casas, F. Quevedo, and E. Roulet, Phys. Lett. B **318**, 447 (1993).

[214] I. Affleck and M. Dine, Nucl. Phys. B **249**, 361 (1985).

[215] G. Kane, J. Shao, S. Watson, and H.-B. Yu, JCAP **11**, 012 (2011).

[216] T. Higaki, K. Kamada, and F. Takahashi, JHEP **09**, 043 (2012).

[217] R. Allahverdi, M. Cicoli, and F. Muia, JHEP **06**, 153 (2016).

[218] M. Dine and A. Kusenko, Rev. Mod. Phys. **76**, 1 (2003).

[219] R. Allahverdi, B. Dutta, and K. Sinha, Phys. Rev. D **82**, 035004 (2010).

[220] R. Allahverdi, B. Dutta, and K. Sinha, Phys. Rev. D **83**, 083502 (2011).

[221] K. Ishiwata, K. S. Jeong, and F. Takahashi, JHEP **02**, 062 (2014).

[222] K. Ishiwata, JHEP **09**, 122 (2014).

[223] M. Dhuria, C. Hati, and U. Sarkar, Phys. Lett. B **756**, 376 (2016).

[224] G. Kane and M. W. Winkler, JCAP **02**, 019 (2020).

[225] M. Hashimoto, K. I. Izawa, M. Yamaguchi, and T. Yanagida, Prog. Theor. Phys. **100**, 395 (1998).

[226] K. Kohri, M. Yamaguchi, and J. Yokoyama, Phys. Rev. D **70**, 043522 (2004).

[227] K. Kohri, T. Moroi, and A. Yotsuyanagi, Phys. Rev. D **73**, 123511 (2006).

[228] S. Nakamura and M. Yamaguchi, Phys. Lett. B **638**, 389 (2006).

[229] T. Asaka, S. Nakamura, and M. Yamaguchi, Phys. Rev. D **74**, 023520 (2006).

[230] M. Endo, K. Hamaguchi, and F. Takahashi, Phys. Rev. Lett. **96**, 211301 (2006).

[231] G. B. Gelmini and P. Gondolo, Phys. Rev. D **74**, 023510 (2006).

[232] S. Nakamura and M. Yamaguchi, Phys. Lett. B **655**, 167 (2007).

[233] B. S. Acharya, G. Kane, S. Watson, and P. Kumar, Phys. Rev. D **80**, 083529 (2009).

[234] N. Blinov, J. Kozaczuk, A. Menon, and D. E. Morrissey, Phys. Rev. D **91**, 035026 (2015).

[235] R. Allahverdi, M. Cicoli, B. Dutta, and K. Sinha, Phys. Rev. D **88**, 095015 (2013).

[236] R. Allahverdi, M. Cicoli, B. Dutta, and K. Sinha, JCAP **10**, 002 (2014).

[237] M. Reece and T. Roxlo, JHEP **09**, 096 (2016).

[238] S. Angus, JHEP **10**, 184 (2014).

[239] M. Cicoli, J. P. Conlon, and F. Quevedo, Phys. Rev. D **87**, 043520 (2013).

[240] T. Higaki and F. Takahashi, JHEP **11**, 125 (2012).

[241] T. Higaki, K. Nakayama, and F. Takahashi, JHEP **07**, 005 (2013).

[242] J. P. Conlon and M. C. D. Marsh, JHEP **10**, 214 (2013).

[243] A. Hebecker, P. Mangat, F. Rompineve, and L. T. Witkowski, JHEP **09**, 140 (2014).

[244] M. Cicoli and F. Muia, JHEP **12**, 152 (2015).

[245] M. Cicoli, A. Hebecker, J. Jaeckel, and M. Wittner, JHEP **09**, 198 (2022).

[246] G. F. Giudice and A. Masiero, Phys. Lett. B **206**, 480 (1988).

[247] J. E. Kim and H. P. Nilles, Phys. Lett. B **138**, 150 (1984).

[248] A. H. Chamseddine, R. L. Arnowitt, and P. Nath, Phys. Rev. Lett. **49**, 970 (1982).

[249] H. Baer, V. Barger, P. Huang, D. Mickelson, A. Mustafayev, and X. Tata, Phys. Rev. D **87**, 115028 (2013).

[250] H. Baer, V. Barger, P. Huang, A. Mustafayev, and X. Tata, Phys. Rev. Lett. **109**, 161802 (2012).

[251] H. Baer, V. Barger, and S. Salam, Phys. Rev. Research. **1**, 023001 (2019).

[252] M. Carena and H. E. Haber, Prog. Part. Nucl. Phys. **50**, 63 (2003).

[253] H. Baer, V. Barger, X. Tata, and K. Zhang, Symmetry **14**, 2061 (2022).

[254] H. Baer, V. Barger, X. Tata, and K. Zhang, arXiv: **2212.09198**, (2022).

[255] M. Dine, A. Kagan, and S. Samuel, Phys. Lett. B **243**, 250 (1990).

[256] N. Arkani-Hamed and H. Murayama, JHEP **06**, 030 (2000).

[257] K. Agashe and M. Graesser, Phys. Rev. D **59**, 015007 (1999).

[258] A. G. Cohen, D. B. Kaplan, and A. E. Nelson, Phys. Lett. B **388**, 588 (1996).

[259] K. J. Bae, H. Baer, V. Barger, and D. Sengupta, Phys. Rev. D **99**, 115027 (2019).

[260] K. J. Bae, H. Baer, H. Serce, and Y.-F. Zhang, JCAP **01**, 012 (2016).

[261] K. J. Bae, H. Baer, V. Barger, M. R. Savoy, and H. Serce, Symmetry **7**, 788 (2015).

[262] M. Throm, R. Thornberry, J. Killough, B. Sun, G. Abdulla, and R. E. Allen, Mod. Phys. Lett. A **34**, 1930001 (2019).

[263] H. Baer, V. Barger, M. Savoy, and H. Serce, Phys. Lett. B **758**, 113 (2016).

[264] H. Baer, V. Barger, S. Salam, H. Serce, and K. Sinha, JHEP **04**, 043 (2019).

[265] H. Baer, V. Barger, and D. Sengupta, Phys. Rev. Res. **1**, 033179 (2019).

[266] H. Baer, V. Barger, D. Martinez, and S. Salam, JHEP **09**, 125 (2022).

[267] H. Baer, V. Barger, S. Salam, and D. Sengupta, in *2022 Snowmass Summer Study* (arXiv, New York, USA, 2022).

[268] H. Baer, V. Barger, D. Martinez, and S. Salam, JHEP **03**, 186 (2022).

[269] N. Arkani-Hamed, S. Dimopoulos, and S. Kachru, arXiv: **hep-th/0501082**, (2005).

[270] M. Dine, E. Gorbatov, and S. D. Thomas, JHEP **08**, 098 (2008).

[271] M. Dine, JHEP **01**, 162 (2006).

[272] I. Broeckel, M. Cicoli, A. Maharana, K. Singh, and K. Sinha, JHEP **10**, 015 (2020).

[273] M. Cicoli, M. Licheri, A. Maharana, K. Singh, and K. Sinha, JHEP **01**, 013 (2023).

[274] V. Agrawal, S. M. Barr, J. F. Donoghue, and D. Seckel, Phys. Rev. D **57**, 5480 (1998).

[275] V. Agrawal, S. M. Barr, J. F. Donoghue, and D. Seckel, Phys. Rev. Lett. **80**, 1822 (1998).

[276] H. Baer, V. Barger, H. Serce, and K. Sinha, JHEP **03**, 002 (2018).

[277] H. Baer, V. Barger, S. Salam, and H. Serce, Phys. Rev. D **104**, 115025 (2021).

[278] J. Sun and X.-G. He, Phys. Lett. B **811**, 135881 (2020).

[279] C. G. Callan, Jr., R. F. Dashen, and D. J. Gross, Phys. Rev. D **17**, 2717 (1978).

[280] D. J. Gross, R. D. Pisarski, and L. G. Yaffe, Rev. Mod. Phys. **53**, 43 (1981).

[281] N. Du *et al.*, Phys. Rev. Lett. **120**, 151301 (2018).

[282] T. Braine *et al.*, Phys. Rev. Lett. **124**, 101303 (2020).

[283] K. J. Bae, H. Baer, and H. Serce, JCAP **06**, 024 (2017).

[284] K. J. Bae, H. Baer, and H. Serce, Phys. Rev. D **91**, 015003 (2015).

[285] K. J. Bae, H. Baer, and E. J. Chun, JCAP **12**, 028 (2013).

[286] E. W. Kolb and M. S. Turner, *The Early Universe*, *Frontiers in physics* (Westview Press, Boulder, CO, 1990).

[287] H. P. Nilles, Phys. Rept. **110**, 1 (1984).

[288] T. Goto and M. Yamaguchi, Phys. Lett. B **276**, 103 (1992).

[289] E. J. Chun, J. E. Kim, and H. P. Nilles, Phys. Lett. B **287**, 123 (1992).

[290] E. J. Chun and A. Lukas, Phys. Lett. B **357**, 43 (1995).

[291] L. Covi, J. E. Kim, and L. Roszkowski, Phys. Rev. Lett. **82**, 4180 (1999).

[292] L. Covi, H.-B. Kim, J. E. Kim, and L. Roszkowski, JHEP **05**, 033 (2001).

[293] L. Covi, L. Roszkowski, R. Ruiz de Austri, and M. Small, JHEP **06**, 003 (2004).

[294] A. Brandenburg and F. D. Steffen, JCAP **08**, 008 (2004).

[295] K. Jedamzik, M. Lemoine, and G. Moultaka, JCAP **07**, 010 (2006).

[296] E. J. Chun and H. B. Kim, JHEP **10**, 082 (2006).

[297] K.-Y. Choi, L. Covi, J. E. Kim, and L. Roszkowski, JHEP **04**, 106 (2012).

[298] K. J. Bae, K. Choi, and S. H. Im, JHEP **08**, 065 (2011).

[299] K. J. Bae, E. J. Chun, and S. H. Im, JCAP **03**, 013 (2012).

[300] K. J. Bae, H. Baer, A. Lessa, and H. Serce, JCAP **10**, 082 (2014).

[301] K. J. Bae, H. Baer, and A. Lessa, in *Community Summer Study 2013: Snowmass on the Mississippi* (arXiv, New York, USA, 2013).

[302] K. J. Bae, H. Baer, and A. Lessa, JCAP **04**, 041 (2013).

[303] K. J. Bae, H. Baer, A. Lessa, and H. Serce, Front. in Phys. **3**, 49 (2015).

[304] A. D. Linde, Phys. Lett. B **201**, 437 (1988).

[305] M. Tegmark, A. Aguirre, M. Rees, and F. Wilczek, Phys. Rev. D **73**, 023505 (2006).

[306] L. M. Krauss and F. Wilczek, Phys. Rev. Lett. **62**, 1221 (1989).

[307] M. Kamionkowski and J. March-Russell, Phys. Lett. B **282**, 137 (1992).

[308] R. Holman, S. D. H. Hsu, T. W. Kephart, E. W. Kolb, R. Watkins, and L. M. Widrow, Phys. Lett. B **282**, 132 (1992).

[309] M. Dine and N. Seiberg, Nucl. Phys. B **273**, 109 (1986).

[310] M. Dine, in *Conference on Topics in Quantum Gravity* (arXiv, New York, USA, 1992).

[311] R. Kallosh, A. D. Linde, D. A. Linde, and L. Susskind, Phys. Rev. D **52**, 912 (1995).

[312] S. M. Barr and D. Seckel, Phys. Rev. D **46**, 539 (1992).

[313] E. J. Chun, J. E. Kim, and H. P. Nilles, Nucl. Phys. B **370**, 105 (1992).

[314] H. M. Lee, S. Raby, M. Ratz, G. G. Ross, R. Schieren, K. Schmidt-Hoberg, and P. K. S. Vaudrevange, Nucl. Phys. B **850**, 1 (2011).

[315] P. N. Bhattiprolu and S. P. Martin, Phys. Rev. D **104**, 055014 (2021).

[316] G. Choi and T. T. Yanagida, JHEP **12**, 067 (2022).

[317] K. S. Babu, I. Gogoladze, and K. Wang, Phys. Lett. B **560**, 214 (2003).

[318] K. Harigaya, M. Ibe, K. Schmitz, and T. T. Yanagida, Phys. Rev. D **88**, 075022 (2013).

[319] A. G. Dias, V. Pleitez, and M. D. Tonasse, Phys. Rev. D **67**, 095008 (2003).

[320] F. Björkeroth, E. J. Chun, and S. F. King, Phys. Lett. B **777**, 428 (2018).

[321] J. Kawamura and S. Raby, Phys. Rev. D **103**, 015002 (2021).

[322] H. M. Lee, S. Raby, M. Ratz, G. G. Ross, R. Schieren, K. Schmidt-Hoberg, and P. K. S. Vaudrevange, Phys. Lett. B **694**, 491 (2011).

[323] Q. Bonnefoy, (2022).

[324] D. Matalliotakis and H. P. Nilles, Nucl. Phys. B **435**, 115 (1995).

[325] M. Olechowski and S. Pokorski, Phys. Lett. B **344**, 201 (1995).

[326] P. Nath and R. L. Arnowitt, Phys. Rev. D **56**, 2820 (1997).

[327] J. R. Ellis, K. A. Olive, and Y. Santoso, Phys. Lett. B **539**, 107 (2002).

[328] J. R. Ellis, T. Falk, K. A. Olive, and Y. Santoso, Nucl. Phys. B **652**, 259 (2003).

[329] H. Baer, A. Mustafayev, S. Profumo, A. Belyaev, and X. Tata, JHEP **07**, 065 (2005).

[330] F. E. Paige, S. D. Protopopescu, H. Baer, and X. Tata, arXiv: **hep-ph/0312045**, (2003).

[331] A. Heister *et al.*, Phys. Lett. B **533**, 223 (2002).

[332] D. Buskulic *et al.*, Phys. Lett. B **373**, 246 (1996).

[333] H. Baer, V. Barger, and P. Huang, JHEP **11**, 031 (2011).

[334] CMS Collaboration, JHEP **11**, 185 (2018).

[335] CMS Collaboration, JHEP **11**, 047 (2017).

[336] ATLAS Collaboration, Phys. Lett. B **784**, 345 (2018).

[337] CMS Collaboration, Phys. Rev. D **104**, 012015 (2021).

[338] Z. Han, G. D. Kribs, A. Martin, and A. Menon, Phys. Rev. D **89**, 075007 (2014).

[339] H. Baer, A. Mustafayev, and X. Tata, Phys. Rev. D **90**, 115007 (2014).

[340] C. Han, D. Kim, S. Munir, and M. Park, JHEP **04**, 132 (2015).

[341] H. Baer, V. Barger, S. Salam, D. Sengupta, and X. Tata, Phys. Lett. B **810**, 135777 (2020).

[342] CMS Collaboration, JHEP **04**, 091 (2022).

[343] ATLAS Collaboration, Phys. Rev. D **101**, 052005 (2020).

[344] R. L. Workman *et al.*, PTEP **2022**, 083C01 (2022).

[345] T. Banks and L. J. Dixon, Nucl. Phys. B **307**, 93 (1988).

[346] K.-S. Choi, H. P. Nilles, S. Ramos-Sanchez, and P. K. S. Vaudrevange, Phys. Lett. B **675**, 381 (2009).

[347] T. Kobayashi, H. P. Nilles, F. Ploger, S. Raby, and M. Ratz, Nucl. Phys. B **768**, 135 (2007).

[348] T. Araki, T. Kobayashi, J. Kubo, S. Ramos-Sanchez, M. Ratz, and P. K. S. Vaudrevange, Nucl. Phys. B **805**, 124 (2008).

[349] S. Weinberg, Phys. Rev. Lett. **29**, 1698 (1972).

[350] M. Dine, R. Kitano, A. Morisse, and Y. Shirman, Phys. Rev. D **73**, 123518 (2006).

[351] A. Albert *et al.*, Astrophys. J. **834**, 110 (2017).

[352] L. Collaboration, arXiv: **2207.03764**, (2022).

[353] H. Baer, V. Barger, and H. Serce, Phys. Rev. D **94**, 115019 (2016).

[354] M. Kawasaki, F. Takahashi, and T. T. Yanagida, Phys. Lett. B **638**, 8 (2006).

[355] T. Moroi and L. Randall, Nucl. Phys. B **570**, 455 (2000).

[356] M. Reece and W. Xue, JHEP **04**, 045 (2016).

[357] B. S. Acharya, P. Kumar, K. Bobkov, G. Kane, J. Shao, and S. Watson, JHEP **06**, 064 (2008).

[358] J. J. Blanco-Pillado, R. Kallosh, and A. D. Linde, JHEP **05**, 053 (2006).

[359] M. Cicoli and G. A. Piovano, JCAP **02**, 048 (2019).

[360] J. F. G. Cascales, M. P. Garcia del Moral, F. Quevedo, and A. M. Uranga, JHEP **02**, 031 (2004).

[361] G. Aldazabal, L. E. Ibanez, F. Quevedo, and A. M. Uranga, JHEP **08**, 002 (2000).

[362] H. Abe, T. Higaki, and T. Kobayashi, Phys. Rev. D **73**, 046005 (2006).

[363] L. Aparicio, F. Quevedo, and R. Valandro, JHEP **03**, 036 (2016).

[364] S. Stieberger, Nucl. Phys. B **541**, 109 (1999).

[365] S. Gurrieri, A. Lukas, and A. Micu, Phys. Rev. D **70**, 126009 (2004).

[366] M. Cicoli, S. de Alwis, and A. Westphal, JHEP **10**, 199 (2013).

[367] H. Abe, T. Kobayashi, H. Otsuka, Y. Takano, and T. H. Tatsuishi, PTEP **2016**, 053B01 (2016).

[368] V. Lowen and H. P. Nilles, Phys. Rev. D **77**, 106007 (2008).

[369] V. Lowen, H. P. Nilles, and A. Zanzi, Phys. Rev. D **78**, 046002 (2008).

[370] R. Blumenhagen, Phys. Rev. Lett. **102**, 071601 (2009).

[371] J. P. Conlon, S. S. Abdussalam, F. Quevedo, and K. Suruliz, JHEP **01**, 032 (2007).

[372] H. Baer, A. Lessa, and W. Sreethawong, JCAP **01**, 036 (2012).

[373] M. S. Turner, Phys. Rev. D **28**, 1243 (1983).

[374] L. F. Abbott and P. Sikivie, Phys. Lett. B **120**, 133 (1983).

[375] M. Dine and W. Fischler, Phys. Lett. B **120**, 137 (1983).

[376] J. Preskill, M. B. Wise, and F. Wilczek, Phys. Lett. B **120**, 127 (1983).

[377] K. R. Dienes, J. Kost, and B. Thomas, Phys. Rev. D **93**, 043540 (2016).

[378] H. Baer, A. Lessa, S. Rajagopalan, and W. Sreethawong, JCAP **06**, 031 (2011).

[379] K. Jedamzik, Phys. Rev. D **74**, 103509 (2006).

[380] M. Kawasaki, K. Kohri, T. Moroi, and A. Yotsuyanagi, Phys. Rev. D **78**, 065011 (2008).

[381] M. Kawasaki, K. Kohri, T. Moroi, and Y. Takaesu, Phys. Rev. D **97**, 023502 (2018).

[382] W. Buchmuller, K. Hamaguchi, O. Lebedev, and M. Ratz, JCAP **01**, 004 (2005).

[383] W. Buchmuller, K. Hamaguchi, O. Lebedev, and M. Ratz, Nucl. Phys. B **699**, 292 (2004).

[384] M. Kawasaki, K. Kohri, and N. Sugiyama, Phys. Rev. Lett. **82**, 4168 (1999).

[385] M. Kawasaki, K. Kohri, and N. Sugiyama, Phys. Rev. D **62**, 023506 (2000).

[386] T. Hasegawa, N. Hiroshima, K. Kohri, R. S. L. Hansen, T. Tram, and S. Hannestad, JCAP **12**, 012 (2019).

[387] K. Choi, K. S. Jeong, T. Kobayashi, and K.-i. Okumura, Phys. Lett. B **633**, 355 (2006).

[388] K. Choi, A. Falkowski, H. P. Nilles, and M. Olechowski, Nucl. Phys. B **718**, 113 (2005).

[389] P. Fox, A. Pierce, and S. D. Thomas, arXiv: **hep-th/0409059**, (2004).

[390] M. Beltran, J. Garcia-Bellido, and J. Lesgourgues, Phys. Rev. D **75**, 103507 (2007).

[391] L. Visinelli and P. Gondolo, Phys. Rev. D **81**, 063508 (2010).

[392] R. Allahverdi, I. Broeckel, M. Cicoli, and J. K. Osiński, JHEP **02**, 026 (2021).

[393] M. Kawasaki and T. Moroi, Prog. Theor. Phys. **93**, 879 (1995).

[394] J. Pradler and F. D. Steffen, Phys. Rev. D **75**, 023509 (2007).

[395] H. Eberl, I. D. Gialamas, and V. C. Spanos, Phys. Rev. D **103**, 075025 (2021).

[396] V. S. Rychkov and A. Strumia, Phys. Rev. D **75**, 075011 (2007).

[397] K.-Y. Choi, J. E. Kim, H. M. Lee, and O. Seto, Phys. Rev. D **77**, 123501 (2008).

[398] L. J. Hall and Y. Nomura, JHEP **03**, 076 (2010).

[399] S. A. R. Ellis and J. D. Wells, Phys. Rev. D **96**, 055024 (2017).

[400] J. D. Wells, in *11th International Conference on Supersymmetry and the Unification of Fundamental Interactions* (World Scientific, Singapore, 2003).

[401] N. Arkani-Hamed and S. Dimopoulos, JHEP **06**, 073 (2005).

[402] G. F. Giudice and A. Romanino, Nucl. Phys. B **699**, 65 (2004), [Erratum: Nucl.Phys.B 706, 487–487 (2005)].

[403] G. F. Giudice and A. Strumia, Nucl. Phys. B **858**, 63 (2012).

[404] P. F. de Salas and S. Pastor, JCAP **07**, 051 (2016).

[405] L. Visinelli and P. Gondolo, Phys. Rev. D **80**, 035024 (2009).

[406] E. Aprile *et al.*, Phys. Rev. Lett. **121**, 111302 (2018).

[407] S. Dodelson, *Modern Cosmology* (Academic Press, Amsterdam, 2003).

[408] M. Cicoli, K. Dutta, A. Maharana, and F. Quevedo, JCAP **08**, 006 (2016).

[409] H. Baer, V. Barger, and R. W. Deal, JHEAp **34**, 33 (2022).

[410] L. Randall and S. D. Thomas, Nucl. Phys. B **449**, 229 (1995).

[411] R. Blumenhagen, A. Gligovic, and S. Kaddachi, Fortsch. Phys. **71**, 2200167 (2023).

[412] A. Linde, Y. Mambrini, and K. A. Olive, Phys. Rev. D **85**, 066005 (2012).

[413] C.-S. Collaboration, arXiv: **1907.04473**, (2019).

[414] J. W. Brockway, E. D. Carlson, and G. G. Raffelt, Phys. Lett. B **383**, 439 (1996).

[415] J. A. Grifols, E. Masso, and R. Toldra, Phys. Rev. Lett. **77**, 2372 (1996).

[416] M. Kawasaki, K. Kohri, and T. Moroi, Phys. Rev. D **71**, 083502 (2005).

[417] Y. Akrami *et al.*, Astron. Astrophys. **641**, A10 (2020).

[418] A. E. Nelson and H. Xiao, Phys. Rev. D **98**, 063516 (2018).

[419] N. Blinov, M. J. Dolan, and P. Draper, Phys. Rev. D **101**, 035002 (2020).

[420] J. P. Conlon and F. Quevedo, JHEP **01**, 146 (2006).

[421] M. Berg, M. Haack, and B. Kors, JHEP **11**, 030 (2005).

[422] M. Berg, M. Haack, and E. Pajer, JHEP **09**, 031 (2007).

[423] M. Cicoli and F. Quevedo, Class. Quant. Grav. **28**, 204001 (2011).

[424] M. Cicoli, M. Kreuzer, and C. Mayrhofer, JHEP **02**, 002 (2012).

[425] M. Cicoli, C. P. Burgess, and F. Quevedo, JHEP **10**, 119 (2011).

[426] K. Becker, M. Becker, M. Haack, and J. Louis, JHEP **06**, 060 (2002).

[427] M. Cicoli, J. P. Conlon, and F. Quevedo, JHEP **01**, 052 (2008).

[428] K. Abazajian *et al.*, Astrophys. J. **926**, 54 (2022).

[429] M. Cicoli and A. Mazumdar, Phys. Rev. D **83**, 063527 (2011).

[430] M. Cicoli and A. Mazumdar, JCAP **09**, 025 (2010).

[431] J. P. Conlon, D. Cremades, and F. Quevedo, JHEP **01**, 022 (2007).

[432] G. Honecker and W. Staessens, Fortsch. Phys. **62**, 115 (2014).

[433] G. Honecker and W. Staessens, J. Phys. Conf. Ser. **631**, 012080 (2015).

[434] L. Aparicio, D. G. Cerdeno, and L. E. Ibanez, JHEP **07**, 099 (2008).

[435] R. Blumenhagen, M. Cvetic, S. Kachru, and T. Weigand, Ann. Rev. Nucl. Part. Sci. **59**, 269 (2009).

[436] H. Abdallah *et al.*, Phys. Rev. Lett. **117**, 111301 (2016).

[437] H. Abdalla *et al.*, PoS **ICRC2021**, 528 (2021).

[438] H. Abdalla *et al.*, Astron. Astrophys. **619**, A71 (2018).

[439] L. Oakes *et al.*, PoS **ICRC2019**, 012 (2021).

[440] J. Rico, M. Wood, A. Drlica-Wagner, and J. Aleksić, PoS **ICRC2015**, 1206 (2016).

[441] M. Cicoli, V. Guidetti, N. Righi, and A. Westphal, JHEP **05**, 107 (2022).

[442] W. Hu, R. Barkana, and A. Gruzinov, Phys. Rev. Lett. **85**, 1158 (2000).

[443] H.-Y. Schive, T. Chiueh, and T. Broadhurst, Nature Phys. **10**, 496 (2014).

[444] L. Hui, J. P. Ostriker, S. Tremaine, and E. Witten, Phys. Rev. D **95**, 043541 (2017).

[445] L. Hui, Ann. Rev. Astron. Astrophys. **59**, 247 (2021).

[446] M. Gorghetto, E. Hardy, and G. Villadoro, SciPost Phys. **10**, 050 (2021).

[447] H. Baer and A. Lessa, JHEP **06**, 027 (2011).

[448] G. B. Gelmini, M. Gleiser, and E. W. Kolb, Phys. Rev. D **39**, 1558 (1989).

[449] S. E. Larsson, S. Sarkar, and P. L. White, Phys. Rev. D **55**, 5129 (1997).

[450] A. Ringwald and K. Saikawa, Phys. Rev. D **93**, 085031 (2016), [Addendum: Phys.Rev.D 94, 049908 (2016)].

[451] K. Choi, E. J. Chun, and J. E. Kim, Phys. Lett. B **403**, 209 (1997).